Karlsruhe Institute of Technology

Modeling of the response function and measurement of transmission properties of the KATRIN experiment

Zur Erlangung des akademischen Grades eines

Doktors der Naturwissenschaften

von der Fakultät für Physik
des Karlsruher Instituts für Technologie
genehmigte

Dissertation

von

Dipl.-Phys. Stefan Groh

aus Tübingen

Erstgutachter:	Prof. Dr. G. Drexlin Institut für Experimentelle Kernphysik, KIT
Zweitgutachter:	Prof. Dr. W. de Boer Institut für Experimentelle Kernphysik, KIT

Tag der mündlichen Prüfung: 13. 2. 2015

Erklärung

Hiermit versichere ich, die vorliegende Arbeit selbständig angefertigt, alle dem Wortlaut oder Sinn nach entnommenen Inhalte anderer Werke an den entsprechenden Stellen unter Angabe der Quelle kenntlich gemacht und keine weiteren Hilfsmittel verwendet zu haben.

Stefan Groh
Karlsruhe, Januar 2015

Zusammenfassung

Neutrinos und ihre Eigenschaften spielen eine Schlüsselrolle in der Teilchenphysik und Kosmologie, da sie die häufigsten massebehafteten Elementarteilchen im Universum sind. Ursprünglich als exakt masselos betrachtet, wurde durch eine Reihe von Experimenten bewiesen, dass eine nicht verschwindende Umwandlung zwischen verschiedenen Neutrinoarten existiert und damit eine von Null verschiedene Masse etabliert. Der grundlegende Wert der Neutrinomasse ist zurzeit noch nicht bekannt, da Experimente bis heute nur eine Obergrenze von $\approx 2\,\mathrm{eV}/c^2$ bestimmen konnten. Massebehaftete Neutrinos geben einen Einblick in neue Physik jenseits des Standardmodells der Elementarteilchenphysik und sie beeinflussen die Bildung und Entwicklung von großräumigen Strukturen im Universum. Dieser grundlegende Einfluss der Neutrinomasse auf unterschiedlichste Gebiete der Physik ist die Hauptmotivation für die großen Anstrengungen die aktuell unternommen werden, um die Größenordnung der fundamentalen Massenskala von Neutrinos zu bestimmen. Dabei würde eine verbesserte obere Schranke bereits einen deutlichen Fortschritt in Teilchenphysik und Kosmologie bedeuten.

Von mehreren heute verfolgten Methoden zur Messung der Neutrinomasse, verkörpert die hochpräzise Elektronenspektroskopie des Tritium β-Spektrums die sensitivste modellunabhängige Methode, die durch das Karlsruhe Tritium Neutrino Experiment (KATRIN) an das technologische Limit getrieben wird. Dieses Schlüsselexperiment der nächsten Generation hat sich das Ziel gesetzt, die absolute Neutrinomasse mit einer Sensitivität von $200\,\mathrm{meV}/c^2$ (90% C.L.) zu vermessen. Das Experiment befindet sich zurzeit im Aufbau am Tritiumlabor Karlsruhe (TLK) am Campus Nord des Karlsruher Instituts für Technologie (KIT). Es wird eine fensterlose, gasförmige, molekulare Tritiumquelle mit hoher Luminosität mit einem großen hochauflösenden, integrierenden Spektrometer verbinden, das auf dem MAC-E Filter Prinzip beruht.

Die beim Tritium β-Zerfall emittierten Elektronen werden von der Quellregion zum Detektor durch ein System von supraleitenden Solenoiden über eine Länge von 70m geführt. Die Wahrscheinlichkeit, dass ein Signalelektron mit einer bestimmten Energie für eine spezifisches, eingestelltes Retardierungspotential am Spektrometer vom Detektor gezählt wird, wird durch die Antwortfunktion des Experiments beschrieben. Diese beinhaltet alle Energieverluste in der Quelle oder der Transportstrecke, sowie die nicht-trivialen Transmissionseigenschaften des Hauptspektrometers. Aufgrund der integrierenden Eigenschaft der MAC-E Filtertechnik ist die präzise Kenntnis der Antwortfunktion des Experimentes von zentraler Bedeutung, um die ehrgeizig ausgelegte Sensitivität der Neutrinomassenmessung von $200\,\mathrm{meV}/c^2$ (90% C.L.) zu erreichen.

Ein unerlässliches neues Werkzeug zur Untersuchung der Antwortfunktion basiert auf Hochstatistik-Monte-Carlo Simulationen von Elektronen, die durch die Strahlrohrführung des Experimentes propagieren. Ein zentraler Gesichtspunkt hierbei ist die Charakterisierung der Transmissionseigenschaften des Hauptspektrometers. Zu ihrer Bestimmung müssen zunächst geeignete Messstrategien und Analysemodelle entwickelt werden. Von entscheidender Bedeutung hierbei sind dedizierte Messungen mit einer quasi-monoenergetischen, winkelselektiven Elektronenkanone während der Inbetriebnahmephase des Hauptspektrometers. Für beide Zielsetzungen wird ein detailliertes Simulationsprogramm benötigt.

Diese Überlegungen definieren die Hauptziele dieser Dissertation: zum einen die Durchführung von umfangreichen Monte-Carlo Simulationen von Signalelektronen, um die Eigenschaften der Antwortfunktion des Experimentes mit großer Genauigkeit zu untersuchen und zu modellieren. Zum anderen umfasst diese die experimentelle Untersuchung der Transmissionsbedingungen das Hauptspektrometers. Um beide Ziele zu erreichen, musste zunächst das bestehende Programmpaket zur Teilchenbahnberechnung KASSIOPEIA ganz entscheidend erweitert und verbessert werden.

Die vorliegende Dissertation hat diese Aufgaben erfolgreich umgesetzt. Die drei dabei wichtigsten erreichten Ziele werden im Folgenden zusammengefasst:

- Das entwickelte Software-Framework zur Berechnung von Teilchenbahnen, KASSIOPEIA, ist ein modulares, erweiterbares, effizientes und weltweit einzigartiges Simulationspaket. Es ist nun ein unverzichtbares Werkzeug, das von der gesamten KATRIN Kollaboration, sowie externen Nutzern, für die Modellierung experimenteller Effekte und die Analyse von Messdaten genutzt wird.
- Die im Rahmen dieser Arbeit entwickelten Strategien und Analysemethoden zur Bestimmung der radialen Potentialinhomogenität der Analysierebene des Hauptspektrometers haben grundlegende neue Erkenntnisse erbracht. Ein zentraler Gesichtspunkt hierbei waren die durchgeführten Transmissionsmessungen mit einer quasi-monoenergetischen, winkelselektiven Elektronenkanone. Unter Einbeziehung der spezifischen Feldkonfiguration der ersten Messphase mit dem Hauptspektrometer und dem Detektor (SDS-I Phase) konnte eine hervorragende Übereinstimmung von Messdaten mit entsprechenden Simulationen erzielt werden. Diese liegen innerhalb der berechneten Genauigkeitsanforderung für eine erfolgreiche Neutrinomassenbestimmung.
- Eine erste umfangreiche Monte-Carlo Simulation zur Antwortfunktion des Experimentes wurde erfolgreich durchgeführt, bei der Bahnen von Elektronen nahe des Tritiumendpunktes E_0 durch den gesamten experimentellen Aufbau von der Quelle bis zum Detektor berechnet wurden. Auf Basis dieses Datensatzes wurde ein verbessertes analytisches Modell der Antwortfunktion entwickelt, welches eine Gesamtzahl von sieben einzelnen, vorher unberücksichtigten Effekten enthält. Jeder dieser Effekte wurde quantifiziert und bezüglich seines Einflusses auf die Neutrinomassensensitivität untersucht.

Kassiopeia - Ein Framework zur Berechnung von Teilchenbahnen

Das Software-Framework KASSIOPEIA zur Teilchenbahnberechnung ist ein gemeinsames Produkt der KATRIN Kollaboration. Die Weiterentwicklung dieses mächtigen Instruments wurde in den letzten Jahre angeführt und in wesentlichen Teilen implementiert durch D. Furse (MIT) und dem Autor dieser Arbeit. Die aktuelle Version KASSIOPEIA 3 ist ein erweiterbares, objektorientiertes Framework zur detaillierten Berechnung von Teilchenbahnen, das moderne C++ Methoden beinhaltet. Seine modulare und flexible

Struktur, sowie seine vielen Features, ermöglichen eine große Anzahl von Detailanwendungen, speziell im Hinblick auf die Modellierung eines so komplexen und anspruchsvollen Experimentes wie KATRIN. KASSIOPEIA ermöglicht eine effiziente und genaue Bahnverfolgung von Elektronen durch die komplexen Geometrien und elektromagnetischen Felder des gesamten Experimentes. Dies ist unerlässlich für viele Aufgabenstellungen, die zurzeit durchgeführt werden, speziell im Hinblick auf Untersuchungen von Untergrundprozessen und zur Abschätzung entsprechender Raten. Des weiteren ist die Untersuchung von Transmissionseigenschaften unter Einbeziehung von Streuprozessen und Energieverlusten eine ideale Anwendung von KASSIOPEIA. Dabei sind detaillierte Simulationen zum Vergleich mit Daten aus Inbetriebnahmemessungen ein wichtiges, präzises Werkzeug, um die Sensitivität des gesamten Experimentes zu untersuchen. Die benutzerfreundliche XML Konfigurationsdatei erlaubt es auch neuen Nutzern mit einfachen Mitteln eine anspruchsvolle Simulation zur Teilchenbahnberechnung zu starten. Die modulare und erweiterbare Struktur erlaubt auch ein problemloses Hinzufügen von neuen Physikmodulen z.B. zur Beschreibung neuer Untergrundprozesse.

Die Integration von KASSIOPEIA in das KASPER Simulation- und Analyse-Framework ermöglicht den Zugriff auf Geometriemodule und spezifische Algorithmen zur elektromagnetischen Feldberechnung. Dies ermöglicht es, eine einheitliche Geometriedefinition für die gesamte Simulation zu benutzen, sowohl für die Navigation als auch für die Feldberechnung. Dazu werden einzelnen Geometrien spezifische elektromagnetische Attribute zugewiesen. Eine implementierte Schnittstelle zur KATRIN-Datenbank ermöglicht es auf Sensorwerte des Experimentes zuzugreifen und diese als Eingangsparameter für die aktuelle Simulation zu benutzen. Zusammen mit einer Schnittstelle zur Simulation der Detektorelektronik erlaubt es dies zum ersten Mal, durch Simulationen ein realistisches Messspektrum zu erzeugen, wie es im realen Experiment beobachtet wird.

Mit KASSIOPEIA ist es ferner möglich auf automatischer Basis eine Simulationskonfiguration zu erstellen, welche die gleichen Parameter benutzt wie sie in einer spezifischen durchgeführten Messung beobachtet werden. Dies erlaubt die Berechnung von Teilchenbahnen von β-Zerfallselektronen für die "Ist-Feldkonfiguration" des 70 m langen Experimentieraufbaus. Dabei sind Prozesse wie inelastische und elastische Streuung an Tritiummolekülen, radiative Energieverluste durch Synchrotronabstrahlung, sowie Festkörperprozesse im Siliziumwafer des Detektors bis hin zur entsprechenden Signalverarbeitungskette enthalten.

Das KASSIOPEIA Framework wird sowohl innerhalb als auch außerhalb von KATRIN intensiv benutzt. Ohne dieses Programm wäre es nicht möglich gewesen, die Ergebnisse der ersten SDS Messphase korrekt zu analysieren und interpretieren. Auch bei der Bestimmung der experimentellen Sensitivität, vor allem im Hinblick auf die abschließende Neutrinomassenanalyse haben sich mit KASSIOPEIA durchgeführte Simulationen als entscheidend erwiesen.

SDS Inbetriebnahmemessungen und Bestimmung der Transmissionseigenschaften des Hauptspektrometers

Im Sommer 2013 wurde eine umfangreiche viermonatige Messkampagne durchgeführt, bei der das Hauptspektrometer und der Fokalebenendetektor das erste Mal gemeinsam betrieben wurden. Diese Inbetriebnahme der Spektrometer und Detektor Sektion (SDS) bildet einen wichtigen und wesentlichen Teil dieser Dissertation. Der Autor hat durch elektromagnetische Simulationen, die Koordination des Messbetriebs, sowie durch das Durchführen von Spezialmessungen und Analysen zur Bestimmung der Transmissionseigenschaften des Hauptspektrometers erheblich zu den ersten KATRIN-Ergebnissen beigetragen. Diese Messphase hat sich als sehr erfolgreich herausgestellt, da insbesondere das

fehlerlose Zusammenspiel von allen Hardware und Slowcontrol Komponenten gezeigt werden konnte. Außerdem konnte die komplexe Simulationssoftware mit experimentellen Daten überprüft werden. Eine besondere Errungenschaft dieser Messphase bildet die Bestätigung der einwandfreien Funktion sowohl der magnetischen Führung als auch der elektrostatischen Retardierung des hochauflösendes MAC-E Filter System des Hauptspektrometers. Die gemessenen Transmissionseigenschaften stellen zudem eine wertvolle Bereicherung für die aktuell durchgeführten detaillierten Messreihen der SDS Messphase-II dar.

Um die Transmissionseigenschaften des Hauptspektrometers zu bestimmen, wurde eine von der Universität Münster aufgebaute quasi-monoenergetische, winkelselektive Elektronenkanone eingesetzt. Durch das Messen von Transmissionsfunktionen können das elektrostatische Potential sowie das magnetische Feld einer konkreten Position innerhalb des Hauptspektrometers bestimmt werden. Um dies zu erreichen, muss zuerst der kleine aber unvermeidbare Versatz der Elektronenkanone von der Symmetrieachse des Spektrometers bestimmt werden. Nur dann können die Elektronenbahnen durch das Hauptspektrometer präzise berechnet werden, um daraus die benötigten Analysierpunkte bestimmen zu können. Dieser Versatz relativ zum magnetischen Flussschlauch konnte präzise bestimmt werden, indem durch die bewegliche Elektronenkanone eine vertikale und horizontale Linie auf dem Detektor abgebildet wurde. Durch den Vergleich der Raten auf benachbarten Pixeln konnte dabei der exakte Mittelpunkt des Kreuzes bestimmt werden. Nach Abzug des Versatzes des Detektorsystems konnte der Versatz der Elektronenkanone bei dieser Messreihe zu $\Delta x = -14.154\,\mathrm{mm}$ and $\Delta y = -2.590\,\mathrm{mm}$ bestimmt werden. Die entsprechende Messung zeigt eine pixelgenaue Übereinstimmung mit den Monte-Carlo Teilchenbahnsimulationen. Es konnte außerdem gezeigt werden, dass durch hardwarebedingte Effekte, die zuvor optimierten Transmissionsbedingungen modifiziert wurden. Diese Hardwareeffekte umfassen die Spannungsbelegung der inneren Drahtelektrodenmodule mit nur einer Offsetspannung, sowie eine asymmetrische Potentialkonfiguration durch das eingesetzte Hochspannungssystem. Dadurch bildeten die Analysierpunkte für verschiedene Elektronenbahnen keine gemeinsame Ebene in der Mitte des Spektrometers mehr, sondern zeigten Abweichungen von bis zu mehreren Metern für die äußersten Feldlinien. Eine korrekte Analyse der Transmissionsmessungen war nur möglich unter Einbeziehung dieses Effektes.

Eine anspruchsvolle Mess- und Analysestrategie wurde entwickelt, die es ermöglicht, grundlegende Eigenschaften der Elektronenkanone zu bestimmen, insbesondere ihre Energie- und Winkelverteilung. Nur durch die Charakterisierung dieser Quelleigenschaften ist es möglich, die grundlegenden Spektrometereigenschaften wie das elektrostatische Potential und das Magnetfeld zu messen. Dabei wurde ein analytisches Modell der Transmissionsfunktion verwendet, das nur von den Eigenschaften der Elektronenquelle abhängt. Die Gültigkeit dieses Modells wurde durch die Berechnung von Teilchenbahnen mit KASSIOPEIA bestätigt, die eine hervorragende Übereinstimmung zeigen.

Aufgrund von hardwarebedingten Einschränkungen bei der erreichten Winkelselektivität der Elektronenkanone war es nicht möglich, das Magnetfeld in der Analysierebene des Spektrometers durch Transmissionsmessungen alleine zu bestimmen. Dem gegenüber konnte jedoch das elektrostatische Potential und sein radialer Verlauf detailliert untersucht werden. Die sich dabei ergebenden radialen Potentialverläufe für zwei verschiedene elektrostatische Konfigurationen zeigten ein asymmetrisches Verhalten in Ost-West Richtung, die durch asymmetrische Potentialbelegungen auf den inneren Elektroden des Spektrometers verursacht wurden. Der Nachweis dieses minimalen Effektes zeigt die Wichtigkeit der durchgeführten Transmissionsmessungen, die das Vorhandensein kleiner, aber nicht vernachlässigbarer elektrischer Dipolfelder im Spektrometer aufgedeckt haben.

Die Ergebnisse der radialen Potentialmessung wurden im Anschluss mit durchgeführten

Potentialsimulationen eines realistischen 3D-Modells des Hauptspektrometers verglichen. Mit Ausnahme eines konstanten Offsets, als Resultat von Unsicherheiten in der absoluten Energieskala der generierten Elektronen sowie der nur näherungsweise bekannten Arbeitsfunktion des Spektrometertankes, stimmen gemessener und simulierter Potentialverlauf innerhalb von 30 mV überein. Diese exzellente Übereinstimmung ist von großer Bedeutung für das Experiment.

Um den Einfluss von verschiedenen Spektrometereigenschaften wie Potential und Magnetfeld, sowie ihres radialen Verlaufs, auf die Neutrinomassensensitivität von KATRIN zu bestimmen, wurden eine Reihe von Monte-Carlo basierten Ensembletests durchgeführt. Aus den Ergebnissen dieser Untersuchungen lassen sich spezifische Anforderungen an die erforderliche Richtigkeit und Präzision der Parameter festlegen. Dabei muss das Potential für jeden Pixelring mit einer Präzision besser als 50 mV bestimmt werden. Ein globaler Offset des Gesamtpotentials hingegen verschlechtert die Neutrinomassensensitivität nicht, solange die Messzeitverteilung entsprechend angepasst wird. Für das Magnetfeld ist der radiale Verlauf weniger wichtig, solange sein genauer Wert besser als 2 μT bestimmt wird.

Ein wesentliches Resultat dieser Untersuchungen ist, dass der radiale Potentialverlauf im Hauptspektrometer mithilfe der hier entwickelten Messstrategie und Analysemodell mit einer Präzision gemessen werden kann, die innerhalb der berechneten Anforderungen für eine erfolgreiche Neutrinomassenmessung liegt.

Monte-Carlo Simulation und Modellierung der Antwortfunktion

Mit der neusten Version von KASSIOPEIA wurde eine umfangreiche Monte-Carlo Simulation zur Untersuchung der Antwortfunktion des KATRIN Experimentes durchgeführt. Mit Hilfe der Monte-Carlo Simulation wurde der Einfluss von mehreren physikalischen Prozessen untersucht, zum Beispiel der Einfluss von Energieverlusten durch Synchrotronstrahlung, sowie durch Streuungprozesse in der Quelle. Dabei wurde gezeigt, dass die adiabatische Näherung des Elektronentransportes eine gültige Annahme für die gestellte Aufgabe ist. Durch diese, sowie weitere Optimierungen, konnte die erforderliche Rechenzeit um mehrere Größenordnungen verkleinert werden. Dies führt zu einer Rechenzeit von aktuell unter einer Stunde für 1000 β-Elektronen nahe des Endpunktes E_0.

Insgesamt wurden 75 Millionen Elektronen generiert und berechnet und die so erhaltene Antwortfunktion wurde mit dem analytischen Modell des KATRIN Designreportes verglichen. Es konnte gezeigt werden, dass dieses vereinfachte analytische Modell aufgrund von großen Abweichungen zu den Monte-Carlo Daten für eine Neutrinomassenanalyse nicht geeignet ist. Insgesamt wurden sieben einzelne Effekte identifiziert, die im bisherigen Modell nicht berücksichtigt wurden und von denen einige die Form der Antwortfunktion nachhaltig beeinflussen. Für jeden einzelnen Effekt wurde eine Erweiterung des analytischen Modells entwickelt, grafisch präsentiert und anhand von Monte-Carlo Daten überprüft und bestätigt. Außerdem wurde erneut eine Reihe von Ensembletests durchgeführt, um die Auswirkung einzelner Effekte auf die Neutrinomassensensitivität zu bestimmen. Als wichtigste Effekte manifestierten sich radiative Energieverluste durch Synchrotronstrahlung, eine von der Isotropie abweichende Winkelverteilung für ungestreute Elektronen, relativistische Korrekturen sowie Magnetfeldinhomogenitäten in der Tritiumquelle. Ohne die Berücksichtigung dieser Effekte ist die angestrebte Neutrinomassensensitivität von 200 meV/c^2 nicht möglich.

Als Beispiel sei an dieser Stelle die Auswirkung des Ignorierens der Synchrotronabstrahlung zu nennen, was zu einer Sensitivität von 235.9 meV/c^2 führen würde. Es konnte außerdem gezeigt werden, dass eine Genauigkeit von 10% bei der Beschreibung von Synchrotronenergieverlusten ausreichend ist. Dieses Ziel lässt sich mit der hochentwickelten Software

KASSIOPEIA problemlos erreichen. Andererseits konnte gezeigt werden, dass Energieverluste in der Quelle durch elastische Streuung, sowie Winkeländerungen im Allgemeinen bei Streuprozessen eine untergeordnete Rolle spielen, da die resultierenden systematischen Fehler auf die Neutrinomasse vernachlässigbar sind.

Weiterhin wurden die Anforderungen an Präzision für kritische Parameter des Experimentes im Hinblick auf die Neutrinomassensensitivität untersucht. Besonderes Augenmerk ist dabei auf die Modellierung des Magnetfelds der Quelle zu legen. Dies muss mit einer Genauigkeit von 0.6% bekannt sein. Weitere wichtige Beiträge zur korrekten Definition der Antwortfunktion bilden der inelastische Streuquerschnitt, sowie die entsprechende Energieverlustfunktion. Es wurde gezeigt, dass der Wirkungsquerschnitt mit einer Genauigkeit von 0.2% bekannt sein muss, um den maximalen Fehler auf die Neutrinomasse auf $|\Delta m_\nu^2| = 2.4 \cdot 10^{-3}\,\mathrm{eV}^2$ zu beschränken. Die Anforderungen an die Energieverlustfunktion wurden durch das Einbeziehen eines Skalierungsfaktors, sowie einer Energieverschiebung berechnet. Dies resultiert in einem maximal erlaubten Fehler für den Skalierungsfaktor von 0.1% und der Energieverschiebung von 5.8 meV.

Zusammenfassend lässt sich festhalten, dass im Rahmen dieser Arbeit gezeigt werden konnte, dass Monte-Carlo Simulationen auf der Basis von Bahnberechnungen von Signalelektronen durch den gesamten experimentellen Aufbau eine unentbehrliche Methode sind, um die Antwortfunktion des Experiments zu beschreiben. Dabei hat sich gezeigt, dass nur über die Entwicklung des KASSIOPEIA Frameworks ein besseres Verständnis des Experimentes ermöglicht wird. Das im Rahmen dieser Arbeit grundlegend verbesserte Modell der Antwortfunktion wird unverzichtbar sein, um die Messung der Neutrinomasse sogar besser als mit der ehrgeizigen Sensitivität von $200\,\mathrm{meV}/c^2$ bei 90% C.L. zu bestimmen.

Introduction

Neutrinos play a key role in particle physics and cosmology, highlighted by the fact that relic neutrinos are the most abundant massive elementary particles in the universe. Originally believed to be massless, non-zero neutrino masses were established by a suite of experiments which have proven neutrinos to undergo flavor oscillation. The fundamental values of neutrino masses are not known at present, as experiments up to now only provide an upper limit of about $2\,\mathrm{eV}/c^2$ (95% C.L.). Massive neutrinos thus yield insight into new physics beyond the Standard Model and also influence the formation and evolution of large-scale structures of the universe. The significant impact of neutrino masses in these diverse fields of physics is a key motivation for the large efforts to measure their absolute mass scale. It is important to note here that even an improved constraint would trigger major progress in particle physics and cosmology.

Among several existing approaches to measure the neutrino mass scale today, high precision electron spectroscopy of tritium β-decay embodies the most sensitive model-independent method. This promising approach will be pushed to its technological limits by the Karlsruhe Tritium Neutrino experiment (KATRIN), the next-generation large-scale direct neutrino mass experiment, targeted to determine the absolute neutrino mass scale with a unprecedented sensitivity of $200\,\mathrm{meV}/c^2$ (90% C.L.). Presently under construction at Tritium Laboratory Karlsruhe (TLK) at the Campus North site of Karlsruhe Institute of Technology (KIT), KATRIN will combine a high-luminosity windowless gaseous molecular tritium source with a large high resolution integrating spectrometer based on the MAC-E filter principle.

The electrons emitted from tritium β-decay will propagate from the source region to the detector guided by a complex electromagnetic setup over a length of 70 m. The probability of signal electrons of a specific energy to be counted as function of the retarding voltage at the spectrometer is described by the response function of the experiment, which includes all possible source and transport related energy losses, as well as the non-trivial transmission characteristics of the main spectrometer. Due to the integrating properties of the MAC-E filtering technique, the precises knowledge of the response function of the experiment is of central importance to achieve the ambitious design sensitivity for the neutrino mass of $200\,\mathrm{meV}/c^2$ (90% C.L.).

An essential new tool to study the response function is based on Monte Carlo simulations of electrons propagating through the entire experimental beam line. A central aspect here are the transmission properties of the main spectrometer which need to be determined by

developing measurement strategies and analysis models. Of key importance thereby are corresponding measurements with a quasi mono-energetic angular selective electron emitter during the commissioning measurements of the main spectrometer. For both objectives, a sophisticated simulation framework is required.

In line with these considerations, the main goals of the thesis in hand were to perform large-scale Monte Carlo simulations of signal electrons to investigate and model the properties of the response function of the experiment with great precision as well as to optimize and determine the transmission properties of the main spectrometer. To do so, the existing particle tracking framework Kassiopeia had to be significantly extended, improved and refined beforehand.

Outline

In the first chapter, a brief introduction to neutrino physics will be given. Specific highlights in the history of neutrino physics will be presented, and the phenomenology of neutrino flavor oscillations will be introduced. Different approaches to assess the neutrino mass scale will be discussed, from model-dependent cosmological methods to dedicated laboratory experiments.

The focus of the second chapter is set on a description of the working principle of the KATRIN experiment. The corresponding MAC-E filter technique, as well as the concept of transmission and response function will be detailed and the individual main components of the experimental setup will be presented.

In chapter 3, the simulation and analysis tools in use by the collaboration will be introduced. A significant contribution to this sophisticated software package was developed within the course of of this thesis. The main focus here will be set on the particle tracking framework Kassiopeia and its modular and user-friendly design together with the implemented tracking algorithms. Additionally, modules to implement complex geometries and electromagnetic fields will be presented, as well as mathematical tools for sensitivity calculations together with optimization and analysis procedures to investigate the electromagnetic spectrometer properties.

The first commissioning measurements of the spectrometer and detector section (SDS) in 2013 will be highlighted in chapter 4. The detailed experimental setup of this successful four-month measurement campaign will be presented. In doing so the required preconditions for the measurement of the spectrometer properties will be discussed, including the alignment of individual sub-components as well as the key part of calculation and optimization of the transmission conditions. Furthermore, results obtained from background measurements will be highlighted.

The measurement of the electrostatic retarding potential and its radial inhomogeneity in the analyzing plane of the main spectrometer will be described in chapter 5. The main focus here will be set on the implemented measurement strategy and analysis methods. Comparisons of the measured values for different spectrometer configurations with realistic potential simulations will be presented, yielding an excellent agreement. Of particular importance is the fact that the required accuracy as obtained by corresponding sensitivity simulations has been reached.

In chapter 6, the overall response function of the experiment is discussed. In the framework of this thesis the first large-scale Monte Carlo simulations propagating particles through the entire experiment with the use of Kassiopeia were performed. By comparing the small yet significant deviations of the Monte Carlo-based response function to a previous analytical calculation, a total of seven individual effects were identified which need to be incorporated into a final neutrino mass analysis. For each effect an extension of the

analytical model has been derived and a quantitative characterization of the impact of each contribution on the estimated neutrino mass sensitivity was calculated. Finally, it will be shown that the resulting refined analytical model of the response function is in excellent agreement with the Monte Carlo simulation.

The thesis in hand is completed with chapter 7 by giving a detailed summary and conclusion of the performed works and achieved results.

Contents

Zusammenfassung v

Introduction xi

1 Neutrino physics 1
- 1.1 Postulation and discovery of the neutrino . . . 1
- 1.2 Neutrino oscillation . . . 3
  - 1.2.1 The solar neutrino problem . . . 3
  - 1.2.2 Theory of neutrino oscillation . . . 5
  - 1.2.3 Measurements of neutrino oscillation parameters . . . 7
- 1.3 Determination of the neutrino mass . . . 10
  - 1.3.1 Cosmology . . . 11
  - 1.3.2 Neutrinoless double beta-decay . . . 12
  - 1.3.3 Single beta-decay . . . 14

2 The KATRIN-Experiment 19
- 2.1 Measurement principle . . . 19
  - 2.1.1 MAC-E-Filter . . . 21
  - 2.1.2 Transmission function . . . 24
  - 2.1.3 Response function . . . 26
- 2.2 Main components . . . 27
  - 2.2.1 Tritium source . . . 28
  - 2.2.2 Rear section . . . 29
  - 2.2.3 Transport section . . . 29
  - 2.2.4 The Spectrometers . . . 31
  - 2.2.5 Aircoil system . . . 32
  - 2.2.6 Focal plane detector . . . 34
- 2.3 Sensitivity . . . 35

3 Simulation and analysis software 37
- 3.1 Overview of the simulation and analysis software package . . . 38
- 3.2 The particle tracking framework Kassiopeia . . . 38
  - 3.2.1 General design . . . 39
  - 3.2.2 Initialization . . . 43
  - 3.2.3 Generation of particles . . . 45
  - 3.2.4 Propagation of particles . . . 47
  - 3.2.5 Interaction of particles . . . 51
  - 3.2.6 Termination of particles . . . 52
  - 3.2.7 Output . . . 53
  - 3.2.8 Navigation . . . 56
  - 3.2.9 Visualization . . . 57
  - 3.2.10 KATRIN-specific code . . . 58

3.3 Geometry and electromagnetic field calculations . . . 61
3.3.1 Geometry module . . . 61
3.3.2 Field calculation methods . . . 63
3.3.3 KEMField . . . 67
3.4 Tools to estimate the neutrino mass sensitivity . . . 68
3.4.1 Source and Spectrum Calculation . . . 68
3.4.2 KaFit . . . 71
3.5 Simulation and analysis of transmission properties . . . 74
3.5.1 Determination and optimization of the analyzing point positions . . 74
3.5.2 Transmission function simulation and analysis . . . 75

4 Commissioning measurements of the spectrometer and detector section 77
4.1 Hardware configuration and performance . . . 78
4.1.1 Main spectrometer vessel and vacuum system . . . 79
4.1.2 Inner electrodes and high voltage system . . . 80
4.1.3 Magnet system . . . 84
4.1.4 Focal plane detector . . . 89
4.1.5 Electron gun . . . 90
4.2 Alignment of the sub components . . . 94
4.2.1 Alignment of the FPD system . . . 94
4.2.2 Alignment of the EGun system . . . 96
4.3 Optimization of the electromagnetic field . . . 98
4.3.1 Determination of the analyzing point . . . 101
4.3.2 Optimization of the analyzing points . . . 101
4.3.3 Optimization of the LFCS currents . . . 104
4.3.4 Results . . . 106
4.3.5 Transmission conditions during the SDS commissioning measurements 107
4.4 Monitoring of the magnetic field . . . 117
4.4.1 Magnetic field monitor . . . 117
4.5 Measurements . . . 119
4.5.1 Background processes in a MAC-E filter . . . 119
4.5.2 Background measurements . . . 120
4.5.3 Muon induced background . . . 121
4.5.4 Radon induced background . . . 122
4.5.5 Results . . . 124
4.6 Conclusion . . . 125

5 Measurement of the transmission properties of the main spectrometer 127
5.1 Theoretical aspects of the transmission function . . . 128
5.1.1 Basic formulas for transmission function calculation . . . 128
5.1.2 Transmission functions during SDS commissioning measurements . . 129
5.1.3 Influence of the source properties . . . 131
5.1.4 Influence of the spectrometer properties . . . 135
5.1.5 Correlation of the parameters . . . 136
5.2 Extracting the source properties from transmission function measurements . 138
5.2.1 Energy distribution of the source . . . 138
5.2.2 Angular selectivity of the source . . . 142
5.2.3 Angular distribution of the source . . . 145
5.3 Monte Carlo simulation of the transmission function with particle tracking . 148
5.3.1 Settings of the Monte Carlo simulation . . . 149
5.3.2 Results of the Monte Carlo simulation . . . 149
5.3.3 Comparison with measured data . . . 151

5.4 Measurement of the radial potential inhomogeneity in the analyzing plane . 152
5.4.1 Determination of the analyzing plane positions 154
5.4.2 Determination of the analyzing plane potentials 155
5.4.3 Error estimation 158
5.4.4 Results 160
5.4.5 Comparison with potential simulations 161
5.4.6 Measurements without high voltage 162
5.5 Influence on the neutrino mass sensitivity 167
5.5.1 Requirement 167
5.5.2 Settings 167
5.5.3 Influence of the analyzing plane electrostatic potential 169
5.5.4 Influence of the analyzing plane magnetic field 172
5.6 Conclusion 175

6 Precise modeling of the response function via global Monte Carlo simulations 177
6.1 Analytical calculation of the response function 178
6.1.1 Transmission function for an isotropic, mono-energetic source 179
6.1.2 Energy loss due to inelastic scattering 180
6.1.3 Scattering probabilities 181
6.2 Motivation for a full Monte Carlo simulation 183
6.3 Implementation with Kassiopeia and validation of involved physics processes 184
6.3.1 Setup of the Monte Carlo simulation 184
6.3.2 Adiabatic approximation of the electron transport 186
6.3.3 Scattering probabilities 188
6.3.4 Energy loss due to scattering 189
6.3.5 Energy loss due to synchrotron radiation 190
6.3.6 Numerical energy loss and performance 191
6.4 Results and comparison with the analytical model 194
6.5 Refinement of the analytical model and systematic shifts of the neutrino mass 196
6.5.1 Magnetic field inhomogeneities in the WGTS 198
6.5.2 Relativistic corrections 203
6.5.3 Synchrotron radiation 204
6.5.4 Modified angular distribution 206
6.5.5 Angular changes by inelastic scattering 211
6.5.6 Energy losses and angular changes by elastic scattering 214
6.5.7 Requirement on the accuracy of the inelastic cross section and energy losses 220
6.5.8 Summary of the individual effects and resulting refined response function model 221
6.6 Conclusion 227

7 Summary and Outlook 229

Appendix 235
A Potential setting during the transmission function measurements 235
B Settings used for the Monte Carlo Simulation of the response function . . . 238
C Calculation of the scattering probabilities including angular changes 240

Bibliography 249

1. Neutrino physics

Since the last few decades, neutrino physics has emerged as one of the most exciting fields of science, owing to a large number of groundbreaking discoveries, which have changed our understanding in particle physics and cosmology substantially. Neutrinos are by far the most abundant and lightest fundamental massive particles in the universe. Due to their elusive nature, the observation and investigation of neutrino properties is a challenging branch of astroparticle physics. After the recent discovery and mass measurement of the Higgs boson, neutrinos are the sole particles of the Standard Model (SM), where the rest mass is unknown. The discovery of the phenomenon of neutrino oscillation has given clear evidence that neutrinos are massive particles, in contrast to the SM assumption. However, up to the present day all attempts to access their absolute mass scale were unsuccessful.

In this chapter an overview of neutrino physics will be given, starting with a brief historical outline of the postulation and discovery of the neutrinos up to our modern view of their properties in section 1.1. The principle of neutrino oscillations, its important influence on solar neutrino experiments, and its theoretical description up to today's state-of-the-art experiments to measure neutrino oscillation parameters will be introduced in section 1.2. Finally, in section 1.3, different approaches to assess the absolute neutrino mass scale are compared, and the corresponding past, recent and future experiments will be presented. The KATRIN experiment as one of the leading approaches in this field is presented in chapter 2.

More information about neutrino physics can be found in these following text books, which also were used in the writing of this chapter [Zub11, Per03, AW03, Sch97].

1.1 Postulation and discovery of the neutrino

In the early years of the last century, physicists studying the then recent discovery of radioactive decay modes were encountering a curious effect. While for the case of α- and γ-decay processes only discrete energy lines were measured, the energy spectrum of β-decay was found to be continuous, as shown in figure 1.1. This was in apparent contradiction to conservation of energy and angular momentum in a two-body decay process. This decay mode was assumed for the β-decay, as a mother nucleus transformed to a daughter nucleus while emitting an electron [Cha14].

Only much later, in the year 1930, this puzzle could be solved by W. Pauli in his famous letter to his colleagues at a conference in Tübingen [Pau30]. He postulated the existence

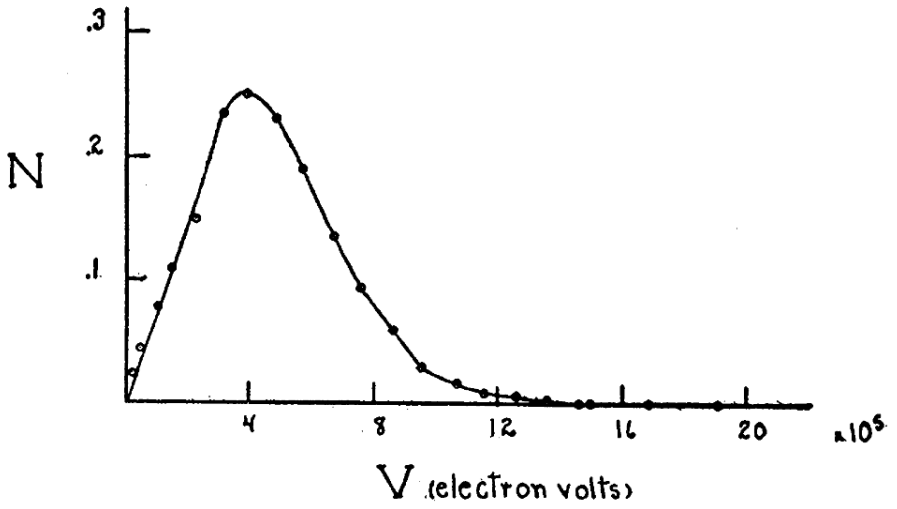

Figure 1.1: Continuous energy spectrum of the β-decay from radium. Figure from [Sco35].

of an electrically neutral spin 1/2 particle, then called neutron, with a very small mass to be produced and emitted alongside the electron during the β-decay. This additional yet undetectable particle transforms the β-decay into a three-body decay process:

$$\mathrm{n} \;\rightarrow\; \mathrm{p} + \mathrm{e}^- + \bar{\nu}_\mathrm{e}. \tag{1.1}$$

When the neutron was discovered by Chadwick in 1932 [Cha32], it was quickly realized that its mass was evidently too high to be Pauli's missing particle from β-decay. When the Italian physicist E. Fermi published his theoretical description of the β-decay shortly afterward [Fer34], he named the particle, which was emitted alongside the electron, the neutrino. He already concluded from the then available experimental data, that the mass of the neutrino must be much smaller than the rest mass of the electron, or even be vanishing. Fermi's theory of β-decay was a milestone in particle physics, which is still valid and in use today as the low-energy limit for weak interactions, for example to describe the tritium β-decay in KATRIN, as detailed in section 1.3.3.

Because of the very low cross section of low-energy neutrinos with matter of about $10^{-44}\,\mathrm{cm}^2$ [BP34] it took more than 20 further years until the neutrino was finally discovered in 1956. This was only possible by making use of a nuclear reactor as neutrino source, being the by far strongest type of source available then and now. The discovery was achieved in a suite of experiments, with the famously labelled "Poltergeist" experiment being one of them. Led by F. Reines and C. Cowan [CRH$^+$56, RCH$^+$60], these experiments made use of the inverse β-decay reaction

$$\bar{\nu}_\mathrm{e} + \mathrm{p} \;\rightarrow\; \mathrm{e}^+ + \mathrm{n} \tag{1.2}$$

to detect electron antineutrinos $\bar{\nu}_\mathrm{e}$, with the free protons of H_2O serving as target. The resulting positron e^+ quickly annihilates with an electron, resulting in the emission of two 511 keV photons as a first part of a spatially correlated delayed coincidence. The neutron was captured a few μs later by cadmium, which was added to the water tank in the form of cadmium-chloride $CdCl_2$. The coincidence signal between the e^-e^+ annihilation photons and neutron capture gammas from the transition of the exited cadmium to its ground stated was a clear proof for the inverse β reaction and therefore for the existence of the neutrino.

Table 1.1: Leptons and their antiparticles in the Standard Model. They are divided into 3 generations, also called flavors.

Generation			Electric	Spin	Interaction
1	2	3	Charge		
e	μ	τ	$-\|e\|$	1/2	weak, electromagnetic
ν_e	ν_μ	ν_τ	0|	1/2	weak
e^+	μ^+	τ^+	$+\|e\|$	1/2	weak, electromagnetic
$\bar{\nu}_e$	$\bar{\nu}_\mu$	$\bar{\nu}_\tau$	0	1/2	weak

Two other types of neutrino flavours coupling to mouns and tau leptons were subsequently discovered in accelerators. The ν_μ, which is related to the muon, was discovered in the year 1962 by Ledermann, Steinberger and Schwartz [D+62]. These neutrinos were produced by pion decay at a proton accelerator and only create muons when interacting with the detector material. The tau neutrino ν_τ, was discovered in a similar way in the year 2000 by the DONUT collaboration [K+01].

The decay width of the Z^0-boson allows to constrain and fix the number of light neutrino flavors. This important SM parameter was measured with very high precision at the LEP e^+e^- collider, resulting in $N_\nu = 2.9840 \pm 0.0082$ for weakly interacting neutrinos with masses below $\approx 45\,\mathrm{GeV}$ [ALE06].

In the Standard Model of particle physics neutrinos are fermions (spin 1/2) and belong to the three generations of leptons: the electron e, the muon μ and the tau τ. For each of these a corresponding neutrino exists, which only interacts via the weak force. However, only the left-handed neutrinos and right-handed antineutrinos take part in the charged current weak interaction, as parity is maximally violated. Together with their antiparticles, there are 6 neutrinos in the Standard Model and a total number of 12 leptons, as listed in table 1.1.

1.2 Neutrino oscillation

After the discovery of the neutrino, many years no compelling experimental evidence for a non-zero mass existed for many decades, so that the neutrino was implemented as mass-less fermion in the Standard Model of particle physics. However, in the year 1998, the discovery of neutrino oscillation finally gave convincing proof that neutrinos must in fact possess a non-zero mass. In the following section the solar neutrino problem will be described, which historically first pointed to the existence of oscillations. This is followed by a section where the theory of neutrino oscillation will be detailed and subsequently recent measurements of oscillation parameters will be presented.

1.2.1 The solar neutrino problem

The Sun is an intense source of astrophysical electron neutrinos emitted in large numbers in the nuclear fusion processes in its inner core. Thereby, protons are fused to form helium with a net reaction of

$$2e^- + 4p \;\rightarrow\; {}^4He + 2\nu_e + 26.73\,\mathrm{MeV}, \tag{1.3}$$

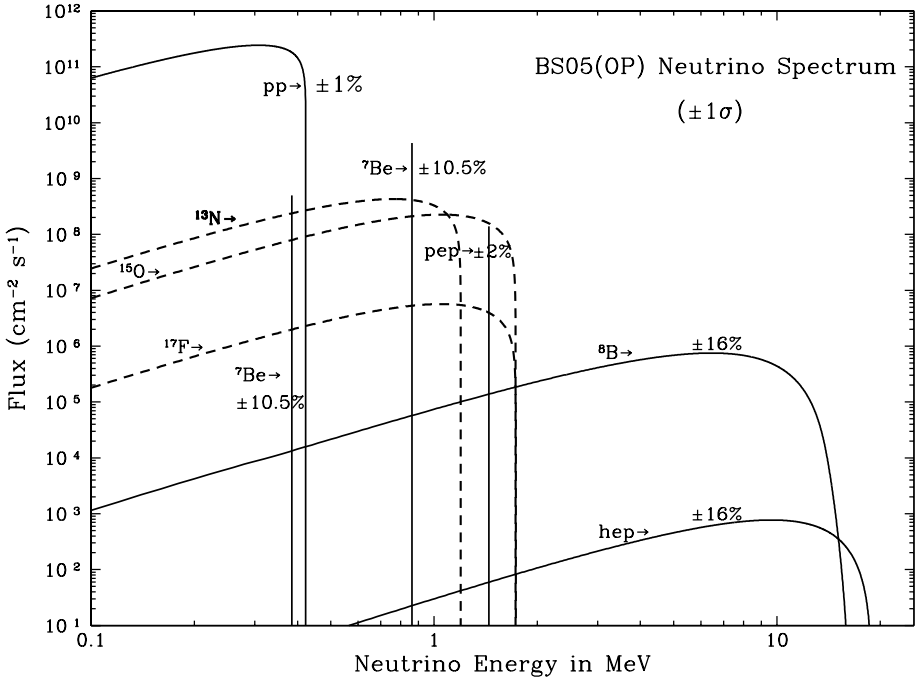

Figure 1.2: Solar neutrino energy spectrum in double-logarithmic presentation. Most of the neutrinos originate from the pp-reaction, with kinetic energies below 0.42 MeV. The neutrinos from ^{8}B-decay are easier to detect, owing to their higher energy, despite the reduced flux. Figure from [BSB05].

where also two electron-type neutrinos are emitted. This reaction proceeds within multiple steps, which can be divided into two main contributions: the pp-cycle and the CNO-cycle. For a core temperature regime equivalent to our Sun, the pp-cycle is dominant by far and accounts for almost all the energy production [Zub11]. The most important reaction in the pp-cycle is the start of the pp-chain

$$\mathrm{p} + \mathrm{p} \;\rightarrow\; {}^2\mathrm{De} + \mathrm{e}^+ + \nu_\mathrm{e}, \tag{1.4}$$

where a deuteron is formed. This reaction gives rise to the dominant part of the neutrino flux of the Sun. However, the energy of these pp-neutrinos is below 0.42 MeV, which makes their detection rather challenging [Zub11]. Neutrinos with higher energies of up to 15 MeV, which can be measured more easily, are emitted by the decay of ^{8}B, which is created within the pp-cycle

$${}^8\mathrm{B} \;\rightarrow\; {}^8\mathrm{Be} + \mathrm{e}^+ + \nu_\mathrm{e}. \tag{1.5}$$

The Standard Solar Model (SSM) [BSB05] describes all relevant reactions in the Sun together with their rates and corresponding energy spectra. The SSM neutrino flux as function of the neutrino energy is shown in figure 1.2.

Neutrinos emitted from the solar core are of special interest, as they not only allow to study neutrino oscillation parameters in a unique regime, however they also yield information on the conditions of the inner core of the sun and the ongoing fusion processes there.

In the year 1970, R. Davis and co-workes started the Homestake [Dav94] experiment with the purpose to perform the first measurement of the solar neutrino flux and to confirm the theoretical calculations of the SSM. The experiment was located in the Homestake gold mine in South Dakota at a depth of 4100 meter water equivalent (mwe). A tank filled with

615 t perchloro-ethylene (C_2Cl_4) was used as a target material to detect solar neutrinos via the transformation of chlorine into argon

$$^{37}\mathrm{Cl} + \nu_e \rightarrow {}^{37}\mathrm{Ar} + e^-. \tag{1.6}$$

The resulting ^{37}Ar isotope decays back into chlorine with a half-life of 35 days via electron capture. Radiochemical methods are used to detect it by extracting it from the tank after a few weeks of solar exposure.

Surprisingly, the measured neutrino flux, as measured over a time interval of more than 20 years, turned out to be only about a third of the predictions of the SSM. This deficit became a significant open issue in astrophysics and particle physics and was called the "solar neutrino problem". It was later on confirmed by other experiments using also radio-chemical detection methods, such as GALLEX [GAL99], GNO [GNO05] and SAGE [SAG02]. Also experiments providing real-time information, such as the Kamiokande experiment, which made use of neutrino-electron scattering in a large water-based Cherenkov detector, confirmed the deficit [Kam96].

Early on, a possible explanation to the solar neutrino problem was given by the theory of neutrino oscillations, where a neutrino can change its flavor state while traveling from the source to the detector. However, as all experiments listed above were only sensitive to electron neutrinos, no definitive proof for the existence of neutrino flavor transformations could be established.

This was possible with the SNO experiment [SNO02], which finally solved the solar neutrino problem. In contrast to previous experiments, SNO was able to measure the flux of all neutrino flavors, in addition to measuring the electron neutrino fraction. This was achieved using a target of 1000 t of pure heavy water (D_2O), which allowed to observe elastic scattering (ES) processes of electrons, as well as charged current (CC) and neutral current (NC) interactions with deuterons:

$$\begin{aligned} \nu_\alpha + e^- &\rightarrow \nu_\alpha + e^- && \text{(ES)}, \\ \nu_e + d &\rightarrow e^- + p + p && \text{(CC)}, \\ \nu_\alpha + d &\rightarrow \nu_\alpha + p + n && \text{(NC)}. \end{aligned} \tag{1.7}$$

The CC interaction is sensitive only to ν_e, while the ES (still dominated by ν_e) and NC interactions are sensitive to all three flavors $\alpha = e, \mu, \tau$ [Zub11]. This allows to measure the total neutrino flux via NC processes, and the flux of ν_e separately via the CC reaction. With an observed electron neutrino flux of about 1/3 of the total neutrino flux, and, most importantly, of the full SSM-flux in NC reactions, the process of neutrino flavor transformation was confirmed by the SNO experiment [SNO02].

1.2.2 Theory of neutrino oscillation

The theoretical formalism of neutrino oscillations was pioneered by B. Pontecorvo [Pon58], and later refined by Maki, Nakagawa and Sakata [MNS62]. It is analogous to the mixing in the quark sector, where the weak and mass eigenstates are not identical but mixed via the CKM matrix. In the leptonic case this leads to the phenomenon of flavor oscillation, which is described in quantum field theory [Zub11].

The description of this phenomenon relies on the fundamental fact that neutrinos can be represented by two sets of states:

- Flavor eigenstates $|\nu_\alpha\rangle$ with $\alpha = e, \mu, \tau$, defined by the weak interaction,
- Mass eigenstates $|\nu_i\rangle$ with $i = 1, 2, 3$, defined by the mass of the states.

In case of mixing the weak interaction eigenstates of neutrinos can be expressed as superposition of mass eigenstates

$$|\nu_\alpha\rangle = \sum_i U_{\alpha i} |\nu_i\rangle, \tag{1.8}$$

with the Pontecorvo-Maki-Nakagawa-Sakata (PMNS) mixing matrix $U_{\alpha i} |\nu_i\rangle$. This unitary matrix thus allows to describe the contribution of mass eigenstates to a specific flavor eigenstate. It is parametrized by three mixing angles θ_{12}, θ_{23} and θ_{13}, a CP-violating phase δ_D, and two complex Majorana-phases δ_{Mi}:

$$U = \begin{pmatrix} 1 & 0 & 0 \\ 0 & c_{23} & s_{23} \\ 0 & -s_{23} & c_{23} \end{pmatrix} \begin{pmatrix} c_{13} & 0 & s_{13}e^{-i\delta_D} \\ 0 & 1 & 0 \\ -s_{13}e^{-i\delta_D} & 0 & c_{13} \end{pmatrix} \begin{pmatrix} c_{12} & s_{12} & 0 \\ -s_{12} & c_{12} & 0 \\ 0 & 0 & 1 \end{pmatrix} \begin{pmatrix} e^{i\delta_{M_1}} & 0 & 0 \\ 0 & e^{i\delta_{M_2}} & 0 \\ 0 & 0 & 1 \end{pmatrix},$$

with $s_{ij} = \sin\theta_{ij}$ and $c_{ij} = \cos\theta_{ij}$.

The mass eigenstates $|\nu_i\rangle$ are stationary and show a time dependence according to

$$|\nu_i(t)\rangle = \exp(\frac{-iE_i t}{\hbar}) |\nu_i\rangle \tag{1.9}$$

being a solution of the Schrödinger equation. As the energy E_i of a neutrino depends on its mass m_i, it is evident that different mass eigenstates will propagate with a different phase. As a specific neutrino flavor eigenstate is a specific superposition of mass eigenstates, transformations of one to another flavor eigenstate are possible. It is thus the propagation of neutrinos which is responsible for flavor changes.

The probability P of a flavor state α to oscillate into a flavor state β can be expressed as

$$P_{\nu_\alpha \to \nu_\beta}(L, E) = \sum_{i,j} U_{\alpha i} U^*_{\beta i} U^*_{\alpha j} U_{\beta j} \exp\left(-i \frac{\Delta m^2_{ij} c^3 L}{2\hbar E}\right), \tag{1.10}$$

with L denoting the distance between source and detector, and the important parameter $\Delta m^2_{ij} = m^2_i - m^2_j$ the difference of the squared masses [Zub11].

In the generic case of two-flavor oscillations between ν_α and ν_β, and masses eigenstates ν_1 and ν_2, the unitary mixing matrix is reduced to a simple 2×2 form, which can be parametrized by a single mixing angle θ. The transformation matrix is then given by

$$\begin{pmatrix} \nu_\alpha \\ \nu_\beta \end{pmatrix} = \begin{pmatrix} \cos(\theta) & \sin(\theta) \\ -\sin(\theta) & \cos(\theta) \end{pmatrix} \cdot \begin{pmatrix} \nu_1 \\ \nu_2 \end{pmatrix}. \tag{1.11}$$

The two-flavor transition probability does not further incorporate a CP violation phase and is given by

$$P_{\nu_\alpha \to \nu_\beta}(L, E) = \sin^2(2\theta) \sin^2\left(\frac{\Delta m^2 c^3 L}{4\hbar E}\right), \tag{1.12}$$

with the characteristic oscillation length

$$L_0 = \frac{4\pi\hbar}{c^3}\frac{E}{\Delta m^2}. \tag{1.13}$$

Here the mixing angle θ determines the amplitude of the oscillation, while the mass difference Δm^2 governs the oscillation length [Zub11].

The oscillation length L_0 is an important experimental parameter, as the distance L between the source and the detector for a given neutrino oscillation experiment should be $L \approx L_0$. In this case, the sensitivity to observe the characteristic oscillation pattern is maximal. The other cases are listed in the following:

- $L \ll L_0$: The transition probability is very small, so no oscillation effect can be observed. The detector is placed too close to the source, or equivalently the neutrino energy is too large.
- $L \gg L_0$: In this case the oscillation frequency is very high, so that only an average transition probability can be measured in view of the finite source size or detector resolution. This occurs if the detector is placed too far away from the source, or if the neutrino energy is too small.

1.2.3 Measurements of neutrino oscillation parameters

In order to determine the three leptonic mixing angles θ_{ij} and the two independent squared mass differences Δm^2_{ij}, neutrinos from a variety of different sources have to be observed, covering a large range of involved energies E and possible base-lengths L. These neutrino oscillation experiments can be classified into two generic types:

- Appearance experiments: This class of experiments searches for a new flavor not present in the source. The appearance probability $P_{\nu_\alpha \to \nu_\beta}$ is thus measured directly.
- Disappearance experiments: Here, the survival probability $P_{\nu_\alpha \to \nu_\alpha}$ of a initial neutrino flavor is measured. To do so, the source activity has to be known precisely, which typically involves the concept of a near and a far detector.

In the following an overview will be given of typical experiments and the latest oscillation results. Four different type of neutrino sources are involved which will be discussed below: the Sun, our atmosphere, particle accelerators and nuclear reactors.

Solar neutrinos

The case of solar neutrinos in the range of up to 15 MeV was already discussed above. Solar neutrinos are created as ν_e and propagate over a distance of $L \approx 150 \cdot 10^6$ km to the earth, while their flavor eigenstate will transform on the path. Solar neutrino experiments are thus sensitive to very small mass differences Δm^2_{21} in principle, and to rather small mixing angles θ_{12}. The results of SNO, in addition to giving proof for neutrino flavor transitions, has confirmed the SSM. The results of all SNO measurement phases are summarized in [SNO13] and yield the following parameters

$$\tan^2(\theta_{12}) = 0.427^{+0.033}_{-0.029}, \tag{1.14}$$

$$\Delta m^2_{21} = 5.6^{+1.9}_{-1.4} \cdot 10^{-5}\ \mathrm{eV}^2/c^2. \tag{1.15}$$

There are other notable experiments studying solar neutrinos at present, for example the Borexino experiment [Bor11]. Borexino was able to directly detect neutrinos in real

time from the pep- and pp-chains the first time [Bor12]. Taken together it has confirmed the transition of the survival probability of high-energy electron neutrinos due to the Mikheyev-Smirnov-Wolfenstein (MSW) effect [Wol78, MS85] to the vacuum oscillation regime at lower energies.

Atmospheric neutrinos

Primary cosmic rays interacting with the upper atmosphere of the earth produce secondary particles. In the decay processes of these particles neutrinos, among others, are produced. The dominant part of the production processes of atmospheric ν's is the decay chain

$$\begin{array}{lll} \pi^+ \rightarrow & \mu^+ + \nu_\mu & \pi^- \rightarrow \quad \mu^- + \bar{\nu}_\mu \\ & \downarrow & \downarrow \\ & \mu^+ \rightarrow e^+ + \nu_e + \bar{\nu}_\mu & \mu^- \rightarrow e^- + \bar{\nu}_e + \nu_\mu \end{array} \tag{1.16}$$

which results in a flavor ratio of $\nu_\mu : \nu_e$ of $2 : 1$ over a large energy range. Above an energy of $E_\nu \approx 1\,\mathrm{GeV}$, an additional contribution from kaon decays becomes dominant [Zub11]. As the earth is transparent for atmospheric neutrinos with energy $E_\nu < 1\,\mathrm{TeV}$, the base length of an experiment between source and detector varies over several orders of magnitude. For neutrinos produced in the atmosphere directly above the neutrino detector the length is $L \approx 10\,\mathrm{km}$, while neutrinos produced in the atmosphere on the other side of the earth have to travel $L \approx 10^4\,\mathrm{km}$.

The Super-Kamiokande experiments [Sup98] has made use of this fact as its Cherenkov technique allows to identify the incoming neutrino direction by measuring the path of the produced lepton. Thereby the oscillation probability can be probed as function of the ratio L/E. To do so, a detector of 50 kt of water is being used, which is surrounded by photomultipliers. Neutrinos scattering off electrons and nucleii produce electrons or muons, resulting in a Cherenkov light cone of the propagating leptons, which can be used to reconstruct the incoming neutrino direction. Present results on the oscillation parameters obtained from the Super-Kamiokande experiment are [Sup10]:

$$0.407 \leq \sin^2(\theta_{23}) \leq 0.583 \text{ (90\% C.L.)}, \tag{1.17}$$

$$1.9 \cdot 10^{-3}\,\mathrm{eV}^2/c^2 < |\Delta m^2_{23}| < 2.6 \cdot 10^{-3}\,\mathrm{eV}^2/c^2 \text{ (90\% C.L.)}, \tag{1.18}$$

The resulting mass splitting is significant larger than the one observed for solar neutrinos. While the size of the mass splitting of Δm^2_{23} is known, its sign is not defined, allowing different mass scenarios.

Accelerator neutrinos

Artificial sources such as particle accelerators allow to study the parameters of oscillation of atmospheric neutrinos in the laboratory. The advantage here is that the neutrino energy can be tuned to achieve the highest sensitivity for the fixed baseline between source and detector. Thereby the measurements of Δm^2_{23} can be performed with higher precision, in particular.

In general, neutrino beams are produced by particle accelerators by irradiating a target (for example aluminium) with a proton beam. The resulting pions propagate through a decay tunnel so that a ν_μ beam with energies of the order of GeV is available. In addition to a near detector to measure the undistorted energy spectrum and radiale profile of the neutrino beam, a main detector is typically placed at a very long base length of up to several hundred km [Zub11].

Table 1.2: Recent parameters for neutrino mixing and oscillation as listed in [Par14] for the normal mass hierarchy.

parameter	best fit value
Δm^2_{21}	$(7.53 \pm 0.18) \cdot 10^{-5}\,\mathrm{eV}^2/c^2$
$\lvert\Delta m^2_{32}\rvert$	$(2.44 \pm 0.06) \cdot 10^{-3}\,\mathrm{eV}^2/c^2$
$\sin^2(2\theta_{12})$	0.846 ± 0.021
$\sin^2(2\theta_{23})$	$0.999^{+0.001}_{-0.017}$
$\sin^2(2\theta_{13})$	0.093 ± 0.008

The pioneering K2K and then the T2K experiment, which uses the J-PARC facility to produce a ν_μ beam directed at the Super-Kamiokande detector, have reported oscillation parameters of [T2K14]:

$$\sin^2(\theta_{23}) = 0.514^{+0.055}_{-0.056}, \tag{1.19}$$

$$|\Delta m^2_{23}| = 2.51 \pm 0.10 \cdot 10^{-3}\ \mathrm{eV}^2/c^2. \tag{1.20}$$

Reactor neutrinos

Nuclear fission reactors are the strongest terrestrial neutrino source available[1]. The electron anti-neutrinos $\bar{\nu}_e$ is released from β-decays of neutron-rich fission products of uranium or plutonium fission. An average fission process yields about 200 MeV and emits 6 $\bar{\nu}_e$. With a thermal power in the order of 1 GW, a total neutrino flux of $\Phi_\nu = 2 \cdot 10^{20}\mathrm{s}^{-1}$ is obtained [Zub11].

With reactor neutrino energies of a few MeV, a typical baseline in the order of $1 - 2$ km is required to probe the region of $\Delta m^2_{23} \approx 10^{-3}\,\mathrm{eV}^2/c^2$. When using detectors at different distances, i.e. at least one near and one far detector, systematic effects can be significantly reduced, which are caused by the limited knowledge of the operational parameters of the reactor and the relative contribution of its fission products [Zub11].

Reactor neutrinos can be detected by the inverse β-decay, as detailed in section 1.1. Multiple experiments using similar detector technologies have published important results in the last years: Double Chooz in France [Dou12], Daya Bay in China [Day12], and RENO in South Korea [REN12]. The results of all three experiments are consistent and can be combined [Par14] to a best fit value of

$$\sin^2(2\theta_{13}) = 0.093 \pm 0.008, \tag{1.21}$$

which is proof of generic 3-flavor neutrino mixing.

Summary

The parameters describing neutrino mixing and oscillation phenomena listed in table 1.2 have been obtained by combining the results of a large variety of experiments. As the sign of Δm^2_{32} and in addition the absolute mass scale, are not known yet, the following generic mass scenarios are possible:

[1] Nuclear bombs are even much stronger neutrino sources on short time scales, but are not practical to study neutrino oscillation due to their devastation influence on a detector placed nearby.

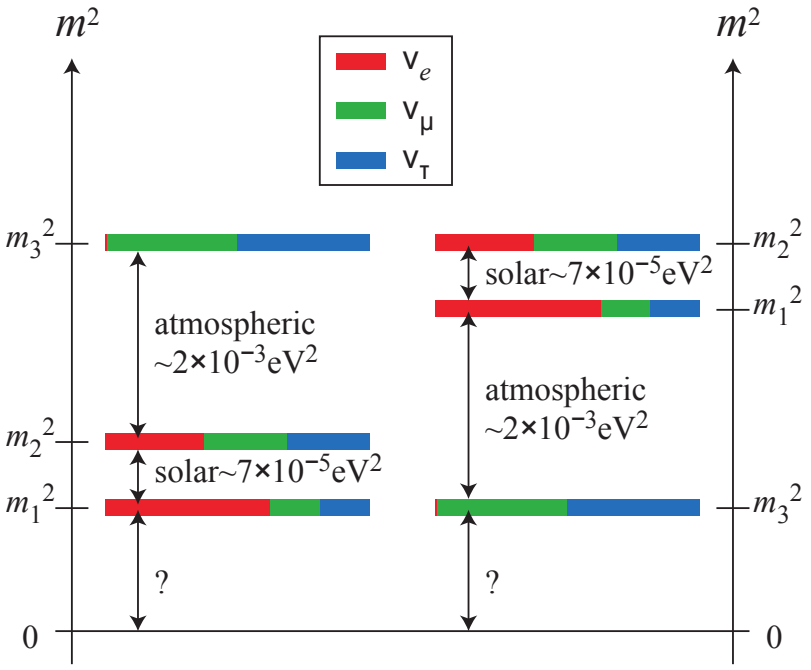

Figure 1.3: Neutrino mass hierarchy and flavor content of mass eigenstates for the two generic scenarios of normal and inverted hierarchy. Figure from [KL13].

- Normal hierarchy case: $m_1 < m_2 \ll m_3$
- Inverted hierarchy case: $m_3 \ll m_1 < m_2$
- Quasi-degenerated case: $m_1 \cong m_2 \cong m_3$

The cases for normal and inverted hierarchy, as well as the flavor content of the mass eigenstates are illustrated in figure 1.3. In case of normal and inverted hierarchy, the value of the lightest mass eigenstate is small compared to the mass splittings, i.e. there are three distinct neutrino masses. In the quasi-degenerated case, the mass of the lightest mass eigenstate is much larger than the mass splittings, i.e. the masses for all mass eigenstates can be approximated by a single neutrino mass. As only mass differences can be obtained with neutrino oscillation experiments, a different approach to measure the absolute mass scale is mandatory. In the next section, several experimental approaches will be introduced.

1.3 Determination of the neutrino mass

This section gives an overview of methods for neutrino mass determination, based on different laboratory approaches as well as cosmological observations. At present, these studies provide an upper limit only for the heaviest neutrino mass in the sub-eV range. As the different experimental approaches all measure specific and non-identic effective neutrino mass parameters, they can be sub-divided into the classes of direct and indirect methods.

- Direct methods rely purely on the kinematics of a β-decay process with the relativistic energy-momentum relation

$$E^2 = p^2c^2 + m_0^2c^4, \tag{1.22}$$

with the energy E, momentum p and rest mass m_0 of the particle. Such methods are usually model-free, as they do not rely on additional assumptions. The β-decay of tritium, which will be investigated by the KATRIN experiment, is a prime example of this direct method and will thus be discussed in detail in section 1.3.3.

- Indirect methods require specific theoretical and modeling assumptions, thereby introducing uncertainties on the neutrino mass. The examples given for indirect methods are the search for neutrinoless double β-decay processes, which is discussed in section 1.3.2, and the deduction of the neutrino mass sum from cosmological observations, introduced in the following.

1.3.1 Cosmology

The current standard model of cosmology is the so called ΛCDM model, which describes the universe starting in a Big Bang. It evolved from a hot dense state to the cold era today, dominated by dark energy (Λ) and cold dark matter (CDM). An important proof of this theory is the cosmic microwave background (CMD), which originates from the decoupling of photons from matter about $3.8 \cdot 10^5$ years after the Big Bang, when neutral atoms were forming and photons started to stream freely. This cosmic microwave background, discovered in the year 1965 [PW65], is an isotropic and homogenously distributed perfect black-body background radiation, permeating the entire universe. Today it has a temperature of $T = 2.725\,\mathrm{K}$ and a photon number density of $n_\gamma = 411\,\mathrm{cm}^{-3}$ [Per03].

Analogue to the CMB, the ΛCDM model predicts a relic neutrino background with a temperature today of $T = 1.95\,\mathrm{K}$, and a density of $n_\nu = 336\,\mathrm{cm}^{-3}$ [Zub11]. Due to their low-energy nature in the sub-meV region, these relic neutrinos have not yet been detected. However, due to their abundant number density they play an important role in structure formation of the early universe, with the impact depending on their mass. The contribution of the energy density of neutrinos Ω_ν to the total energy density of the universe Ω_{tot} can be calculated using the sum of the mass eigenstates of all non-relativistic neutrinos

$$\Omega_\nu = \frac{\sum_i m_i}{93.14 \cdot h^3\ \mathrm{eV}/c^2} \tag{1.23}$$

with the dimensionless Hubble parameter h [LP12]. For a neutrino mass of about 2 eV for each mass eigenstate, the energy density of all relic neutrinos would already exceed a fraction of 10 % of the total energy density of the universe, which would surpass the contribution of the baryonic matter content. This fact emphasizes the importance of neutrinos masses when describing the evolution of the whole universe.

When investigating the role of neutrinos in the evolution of large-scale structures, the sum of all neutrino masses $m_{\mathrm{tot}} = \sum_i m_i$ can be deduced from cosmological observations. This is typically achieved by fitting a large number of parameters to the different cosmological data sets. Recently the Planck collaboration [Pla14] has released an analysis which quotes an upper limit of

$$\sum_i m_i < 0.230\,\mathrm{eV}/c^2 \ (95\%\ \mathrm{C.L.}), \tag{1.24}$$

by combining Planck measurements of the CMB temperature fluctuations with polarization measurements from WMAP [HLK$^+$13] and large scale structure data from surveys of baryon acoustic oscillations [Pla14].

As limits obtained from cosmological observations are highly model-dependent, and as multiple, rather strongly correlated fit parameters have to be adjusted at the same time, these limits can not substitute laboratory measurements of the neutrino mass, which are performed under controlled conditions. Vice versa, a future determination of the neutrino mass in a laboratory experiment will allow to refine cosmological models by breaking parameter degeneracies.

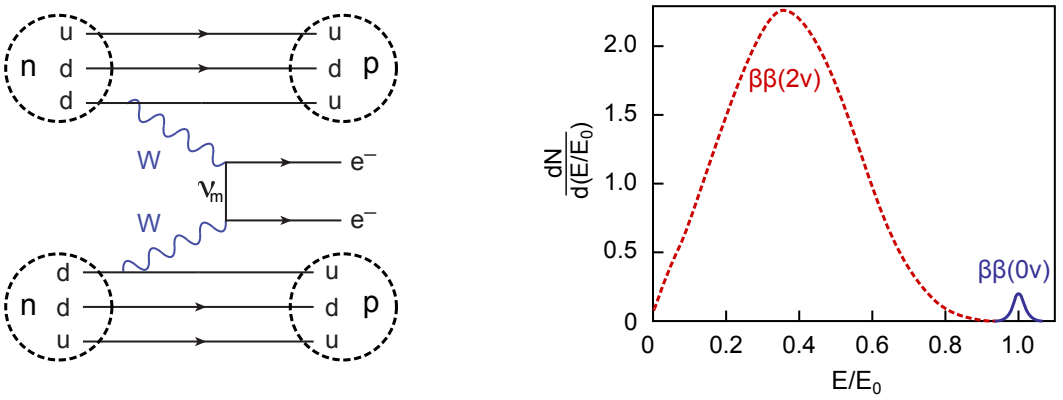

(a) Feynman diagram (b) Energy spectrum

Figure 1.4: Feynman diagram for the neutrinoless double β-decay ($0\nu\beta\beta$) (a). Two neutrons decay simultaneously into two protons and two electrons via the W boson by exchanging a virtual Majorana neutrino ν_m. The energy spectrum of both electrons is shown for $0\nu\beta\beta$ as well as for $2\nu\beta\beta$ (b). The neutrinoless double β-decay results in a peak at the endpoint E_0, which is broadened by the energy resolution of the detector of here 5 % and increased artificially for the shown example. Figures adapted from [Sch13].

1.3.2 Neutrinoless double beta-decay

Double β-decay is a rare nuclear decay process, which can be considered as two simultaneous β-decays within one nucleus [GM35]. This process changes the nuclear charge Z by two units, while emitting two charged leptons and two neutrinos:

$$(Z, A) \rightarrow (Z+2, A) + 2e^- + 2\bar{\nu}_e \ (2\nu\beta\beta). \tag{1.25}$$

The $2\nu\beta\beta$-decay is only relevant for nuclei, which for energetic reasons can not decay via single β-decay. This is only possible for nuclei with an even number of protons and neutrons. Due to the pairing energy term in the Bethe-Weizsäcker mass formula [Wei35] two separate mass parabolas exist for isobars with an even mass number. In this case decay scheme can emerge, where single β-decay is energetically forbidden.

As the $2\nu\beta\beta$-decay is a second order process of weak interactions, the decay rate is extremely low, corresponding to half-life periods in the order of 10^{20} years [Zub11]. The first $2\nu\beta\beta$-decay was thus observed only in the year 1987 for the isotope ^{82}Se [EHM87]. Today, a total of 36 possible double β-decay emitters are known [Zub11].

Far more interesting for neutrino physics would be the observation of the neutrinoless double β-decay

$$(Z, A) \rightarrow (Z+2, A) + 2e^- \ (0\nu\beta\beta). \tag{1.26}$$

Instead of the emission of two neutrinos, a virtual Majorana neutrino [Maj37] is exchanged between the two nucleons involved. The Feynman diagram of the decay is shown in figure 1.4, together with the corresponding energy spectrum of the emitted electrons. While the spectrum is of continuous nature for the $2\nu\beta\beta$-decay, the $0\nu\beta\beta$-decay leads to a monoenergetic electron spectrum so that a peak at the endpoint energy E_0 of the decay is observed.

For this process to occur, two conditions need to be fulfilled [Zub11]:

- As the neutrino is emitted as $\bar{\nu}_e$ in one β-decay and absorbed as ν_e in the other one, neutrinos have to be their own antiparticles, i.e. of Majorana nature.
- Also the helicity of the neutrino has to match. In the first β-decay the neutrino is emitted as a right-handed particle, but absorbed as a left-handed particle at the second vertex. Hence, a non-zero mass for the neutrino is required, otherwise this "spin-flip" is not possible.

The mass of the neutrino is directly related to the probability of the "spin-flip" or change of helicity, and thus to the half-life of the process. By measuring this half-life, the effective Majorana neutrino mass can be obtained

$$\langle m_{\beta\beta} \rangle = \left| \sum_{i=1}^{3} U_{ei}^2 m_i \right| = \left| \sum_{i=1}^{3} |U_{ei}|^2 \, m_i e^{i\delta_{M_i}} \right|, \tag{1.27}$$

which is a coherent superposition of the neutrino mass eigenvalues m_i, weighted by the complex matrix elements U_{ei}. The CP-violating Majorana phases δ_{M_i} may lead to cancellations so that $\langle m_{\beta\beta} \rangle < m_i$. In order to obtain the effective Majorana mass from the half-life of the decay, complicated nuclear matrix elements have to be calculated precisely, which is a dominant source of systematics.

The GERDA experiment [GER06], located in the Laboratori Nationali del Gran Sasso (Italy), searches for the $0\nu\beta\beta$-decay of ^{76}Ge with a Q-value of 2039 keV

$$^{76}\mathrm{Ge} \rightarrow {}^{76}\mathrm{Se} + 2\mathrm{e}^-. \tag{1.28}$$

This experiment employs a detector array of high-purity enriched ^{76}Ge diodes which acts as source as well as detector. In 2013 the GERDA collaboration published results from the first measurement phase based on a total exposure of 21.6 kg yr [GER13]. No $0\nu\beta\beta$ signal was observed, and a limit for the half-life could be derived of

$$T_{1/2}^{0\nu} > 2.1 \cdot 10^{25} \,\mathrm{yr} \ (90\% \ \mathrm{C.L.}), \tag{1.29}$$

corresponding to an upper limit on the effective Majorana neutrino mass in the range of

$$\langle m_{\beta\beta} \rangle < (0.2 - 0.4) \,\mathrm{eV}/c^2. \tag{1.30}$$

The spread for the neutrino mass depends on the model used for the calculation of the nuclear matrix elements. This limit is in severe tension with a previously published claim of a group from the Heidelberg-Moscow experiment, which reported an observation of $0\nu\beta\beta$-decay [KK$^+$01, KKK06], which is controversially discussed in the neutrino physics community, however [A$^+$02].

A large number of experiments is currently investigating the $0\nu\beta\beta$-decay. These projects include among others EXO-200 [EXO14], MAJORANA [MAJ14] and KamLAND-Zen [Kam13].

At this point it has to be emphasized that neutrino mass limits derived from $0\nu\beta\beta$ cannot be directly compared to kinematic neutrino mass results deduced from single β-decay. This important fact is due to the different types of neutrino masses these experiments are sensitive to. Additionally, neutrino masses from $0\nu\beta\beta$ rely on detailed models of the decay process, such as the nuclear matrix elements, and, on the Majorana nature of neutrinos.

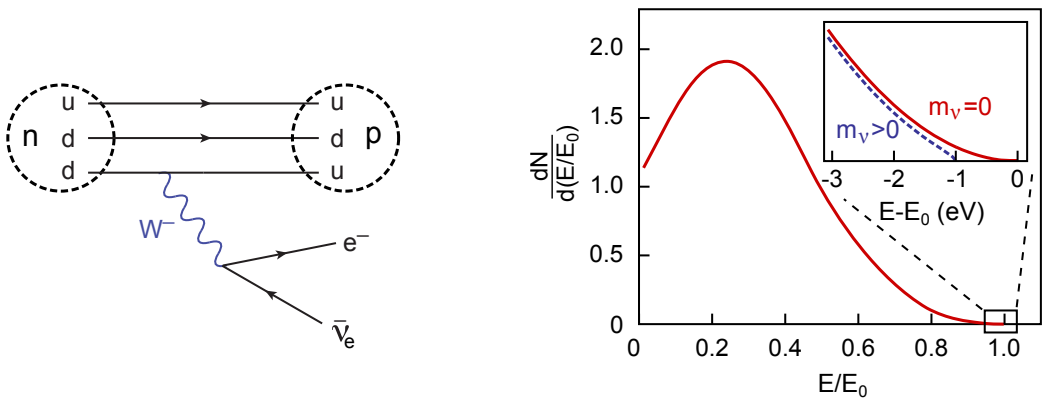

(a) Feynman diagram

(b) Energy spectrum

Figure 1.5: Feynman diagram for the single β-decay (a). A down-quark decays into an up-quark and a lepton pair (e^-, $\bar{\nu}_e$) via the W boson. The energy spectrum of the electron (b) is shown for two different neutrino masses of $m_\nu = 0\,\mathrm{eV}$ and $m_\nu = 1\,\mathrm{eV}$. The spectrum is only sensitive to a non-zero neutrino mass very close to the endpoint, as shown in the inset. Figures adapted from [Sch13].

1.3.3 Single beta-decay

Currently, the best method to measure neutrino masses in based on the investigation of the kinematics of β-decays, as this model-independent approach relies on momentum and energy conversation only. In a nuclear β-decay process a neutrino is transformed into a proton, while an electron and an electron-antineutrino is emitted

$$\mathrm{n} \;\rightarrow\; \mathrm{p} + \mathrm{e}^- + \bar{\nu}_\mathrm{e}. \tag{1.31}$$

The released energy of the decay is shared between the decay products. As the mass of the remaining nucleus is very large in comparison to the mass of the electron and the neutrino, the decay energy is split only between the latter two particles. The neutrino energy is given by

$$E_\nu = \sqrt{m_\nu^2 c^4 + p_\nu^2 c^2}, \tag{1.32}$$

with its rest mass m_ν. Therefore, a neutrino with non-zero mass always takes away some energy of the decay, even though its momentum is close to zero. Consequently, the maximum kinetic energy of the electron is reduced by this finite rest mass of the neutrino.

Figure 1.5 shows the Feynman diagram for the β-decay and a corresponding electron energy spectrum. Only very close to the endpoint E_0 of the spectrum the influence of a non-zero neutrino mass emerges, as it shifts the position of the spectrum endpoint and, much more important, modifies the spectral shape.

Fermi's Golden Rule [Fer34] can be used to describe the transition rate T of the decay [AW03]:

$$T = \frac{\mathrm{d}^2 N}{\mathrm{d}t\,\mathrm{d}E} = \frac{2\pi}{\hbar}|\mathcal{M}|^2 \rho(E), \tag{1.33}$$

describing the transition rate of a particular initial state to a final state with the transition matrix element $\mathcal{M}$ between both states and the final state density $\rho(E)$. When integrating

this particular transition rate over all possible discrete and continuous final states, a decay rate as function of the electron energy can be obtained according to [OW08, DHMW13, AW03]:

$$\frac{\mathrm{d}\dot{N}}{\mathrm{d}E} = C{\cdot}F(Z',E){\cdot}p{\cdot}(E{+}m_e c^2){\cdot}(E_0{-}E){\cdot}\sqrt{(E_0-E)^2 - m^2_{\bar{\nu}_\mathrm{e}}c^4}{\cdot}\Theta(E_0{-}E{-}m_{\bar{\nu}_\mathrm{e}}c^2), \quad (1.34)$$

with the Heaviside step function Θ guaranteeing energy conservation, as a neutrino state can only be produced if the available energy is larger than its rest mass. The constant C

$$C = \frac{G_F^2 \cos^2(\theta_\mathrm{C})}{2\pi^3 c^5 \hbar^7} \cdot |\mathcal{M}|^2, \quad (1.35)$$

incorporates the Fermi coupling constant G_F, the Cabibbo angle θ_C and the nuclear matrix element $\mathcal{M}$. The Fermi function $F(Z',E)$ accounts for the Coulomb interaction between the emitted electron and the daughter nucleus with nuclear charge Z'. The maximum kinetic energy is given by the endpoint energy E_0.

The experimental observable in the differential spectrum in equation 1.34 is the squared neutrino mass $m^2_{\bar{\nu}_\mathrm{e}}$, which is given by the incoherent sum of the three neutrino mass eigenstates m_i.

$$m^2_{\bar{\nu}_\mathrm{e}} = \sum_i \left|U^2_{ei}\right| m^2_{\nu_i}. \quad (1.36)$$

This leads to a fine structure in the electron energy spectrum at the endpoint due to the superposition of three spectra with different neutrino mass. However, individual masses can only be resolved if the energy resolution ΔE of an experiment would be much smaller than the differences of the masses $\sqrt{\Delta m^2_{ij}}$, which is not the case with current technology. Therefore, the actual observable of β-decay experiments is the effective mass of the electron-antineutrino, according to equation 1.36.

Tritium experiments

Since several decades, tritium ($^3_1\mathrm{H}$) is considered to be the most feasible candidate in direct neutrino mass measurements, requiring high precision electron spectroscopy:

$$^3_1\mathrm{H} \rightarrow {}^3_2\mathrm{He}^+ + \mathrm{e}^- + \bar{\nu}_\mathrm{e}. \quad (1.37)$$

Its almost ideal characteristics have resulted in a series of experiments using tritium-based sources [OW08]. The advantages of tritium are based on the following important facts:

- **Low endpoint energy:** Tritium has a comparatively low endpoint energy of $E_0 \approx 18.6\,\mathrm{keV}$ [NFB$^+$05]. As the fraction of β-decay electrons in the endpoint region decreases with E_0, a small endpoint energy is favorable, although the absolute events there will decrease due to $T \propto E_0^5$ [OW08]. Most importantly, a low E_0 has technical benefits, as the required retarding voltage for electron spectroscopy has to be as large as the endpoint of the examining β-decay source in an experiment such as KATRIN. Also, the stringent requirements on the stability of the high voltage (HV) are much better to handle for a correspondingly lower endpoint energy.

- **Short half-life:** The very short half-life of $T_{1/2} = 12.3\,\mathrm{yr}$ [LU00] results in a high decay rate and optimized statistics for a rather small amount of source material.
- **Super-allowed decay:** In super-allowed decays the matrix element does not depend on the energy of the electron and therefore energy-dependent corrections do not have to be taken into account in calculations of the differential β-spectrum [DHMW13].
- **Simple atomic-shell structure:** Due to its low charge of $Z = 1$ and the resulting simple atomic shell configuration, the electromagnetic interaction between the outgoing β-electrons and the nucleus can be computed with high precision [KAT05].
- **Gaseous phase:** Even at cryogenic temperatures of 30 K tritium remains in gaseous form, which has the distinct advantage that no solid-state effects have to be considered.

Tritium sources are typically based on its molecular form T_2, so that the actual tritium decay in an experiment such as KATRIN is given by

$$T_2 \rightarrow {}^3HeT^+ + e^- + \bar{\nu}_e. \tag{1.38}$$

The resulting daughter ion ${}^3HeT^+$ can be excited to rotational and vibrational as well as electronic final states, resulting in specific systematic uncertainties correlated with the precision of the final state calculations.

The currently best limits on the neutrino mass from tritium β-decay experiments were published by the experiments in Mainz [B+01] and Troitsk [L+99]. Both experiments were based on the then new MAC-E filter principle, which allows high-resolution spectrometry by combining magnetic adiabatic collimation with electrostatic filtering as will be detailed in section 2.1.

The Mainz experiment, which used a solid quench-condensed tritium source, published a final limit of [K+05]:

$$m(\bar{\nu}_e) < 2.3\,\mathrm{eV}/c^2 \text{ (95\% C.L.)}. \tag{1.39}$$

The Troitsk experiment, which uses a windowless gaseous tritium source, obtained a marginally better result of [A+11]:

$$m(\bar{\nu}_e) < 2.05\,\mathrm{eV}/c^2 \text{ (95\% C.L.)}. \tag{1.40}$$

A combined analysis by the Particle Data Group [Par14] yields the currently best lower limit from direct measurements:

$$m(\bar{\nu}_e) < 2.0\,\mathrm{eV}/c^2 \text{ (95\% C.L.)}. \tag{1.41}$$

A new concept of measuring the electron spectrum from tritium β-decay is currently being investigated by the Project 8 collaboration [MF09]. There β-decay electrons will be guided through strong magnetic fields so that they emit synchrotron radiation. By detecting this radiative emission with an array of radio-frequency antennas, the energy of the corresponding electron can be determined and consequently a β-spectrum obtained, in principle. The current aim of the collaboration is to demonstrate the feasibility of this new detection technology.

Rhenium and Holmium experiments

When discussing precision kinematic investigations of single β-decays, the use of cryogenic bolometers is a rather new approach, which will be discussed in the following. In a calorimetric setup the source also acts as detector. Accordingly, the entire decay energy should be detected, which eliminates some of the systematic uncertainties. The released energy leads to an increase in detector temperature, which can be measured by a sensitive thermometer. As only a small fraction of the decays contains sufficient information on the neutrino mass, countermeasures against pile-up of low-energetic events have to be implemented, as electrons from all decays are measured. This can be achieved by segmentation of the detector into multiple small micro-calorimeters to reduce the activity and hence the count rate per detector [DHMW13].

An excellent source candidate for this approach is rhenium with a Q-value of $Q = 2.67\,\mathrm{keV}$ [FCB99], making the isotope ^{187}Re the emitter with the lowest endpoint energy of all known β^- decaying isotops.

The Milano experiment published an upper limit on the electron antineutrino mass of [S$^+$04]

$$m(\bar{\nu}_\mathrm{e}) < 15\,\mathrm{eV}/c^2 \text{ (90\% C.L.)}. \tag{1.42}$$

The successor experiment MARE plans to improve the sensitivity down to the technical challenging sub-eV range [MAR06, MAR12].

A new isotope suitable to measure the neutrino mass with cryogenic bolometers has generated a lot of interest recently: the holmium isotope ^{163}Ho, which decays via electron capture. The ECHo experiments plans to reach a future sensitivity in the sub-eV range in the measurement of the electron neutrino mass [GBD$^+$14].

However, the most promising and most advanced model-independent approach to determine neutrino masses is tritium β-decay, where a high resolution spectrometer is used for spectroscopy. Based on the experiences of the successful Mainz and Troitsk experiments, the KATRIN experiment [KAT05], currently being built up at KIT, will push this principle to its technological limits to reach an ambitious design sensitivity of $200\,\mathrm{meV}/c^2$ (90 % C.L.). A detailed overview of the experiment will be given in the following chapter.

2. The KATRIN-Experiment

The **Ka**rlsruhe **Tri**tium **N**eutrino experiment (KATRIN) is the next-generation tritium β-decay experiment targeted to determine the "effective mass of the electron anti-neutrino" $m_{\bar{\nu}_e}$ with a model-independent measurement. With a sensitivity of $200\,\mathrm{meV}/c^2$ at 90% C.L. ($350\,\mathrm{meV}/c^2$ at $5\,\sigma$) after five calender years of operation, KATRIN will improve the current neutrino mass sensitivity obtained by its predecessors by one order of magnitude (see chapter 1.3.3). This chapter will give a short introduction to the measurement principle of the KATRIN experiment with a detailed explanation of the so called MAC-E filter in section 2.1.1 and an introduction of the transmission (section 2.1.2) and response functions (section 2.1.3), both playing a crucial role in KATRIN's measurement principle as well as being a main purpose of this work. After that the main components of the KATRIN experiment, presently under construction at the Karlsruhe Institute of Technology (KIT) in Germany, will be described, starting with the high-luminosity source in section 2.2.1, followed by the transport section for signal electron guidance and gas flow reduction in section 2.2.3, the spectrometers for high-precision energy analysis of the β-decay electrons in section 2.2.4, and finally the detector at the very end in section 2.2.6, counting the transmitted particles. In the last section (2.3) of this chapter, a brief summary about the statistical and systematical uncertainties and the sensitivity of the KATRIN experiment is given.

More details about KATRIN, complementing the outline given in this chapter, can be found in the original KATRIN design report [KAT05].

2.1 Measurement principle

To directly determine the neutrino mass in the previously unexplored sub-eV region, the electron energy spectrum of the tritium beta decay has to be measured close to its endpoint E_0 with very high precision. To obtain this challenging high-precision spectroscopy, KATRIN utilizes an electrostatic high-pass filter. The differential tritium β-decay spectrum (see figure 2.1 a) is measured at different retarding potentials U to obtain an integral spectrum (see figure 2.1 b). The implementation of the electrostatic high-pass filter, the MAC-E filter, is described in the next section, followed by the introduction of the transmission and the response function, whose detailed knowledge and understanding is fundamental for a successful neutrino mass analysis.

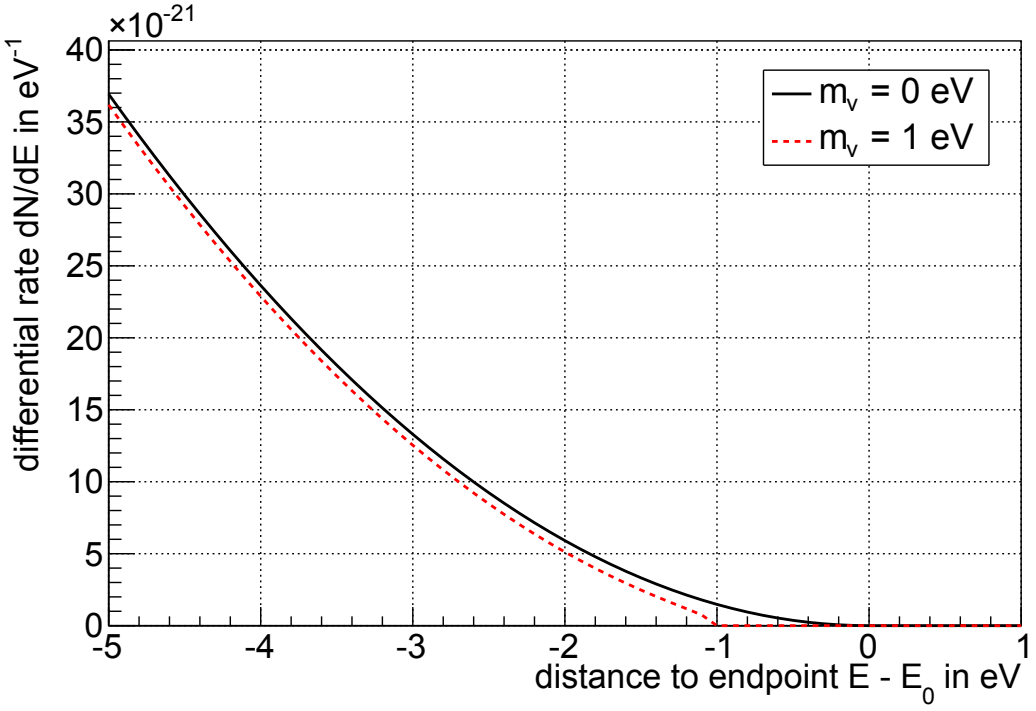

(a) Differential tritium spectrum

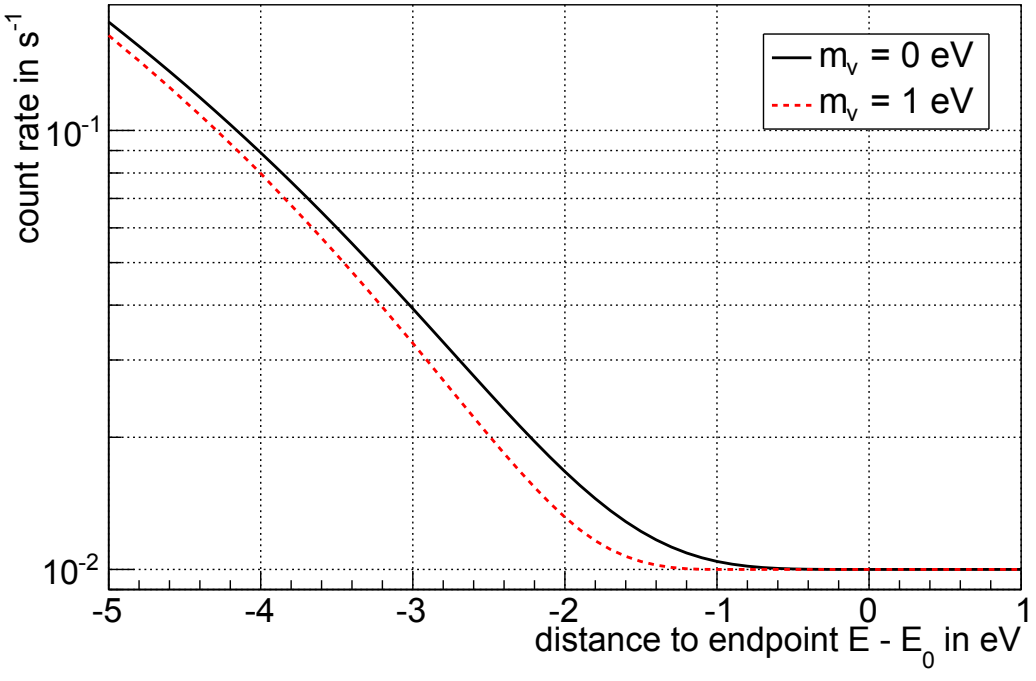

(b) Integrated tritium spectrum

Figure 2.1: Tritium beta decay spectra in its differential form (a) and as measured at the KATRIN experiment in its integrated form in logarithmic scale (b). While the black line represents a spectrum with a vanishing neutrino mass, the red dashed line represents a spectrum with a neutrino mass of $m_\nu = 1\,\mathrm{eV}$.

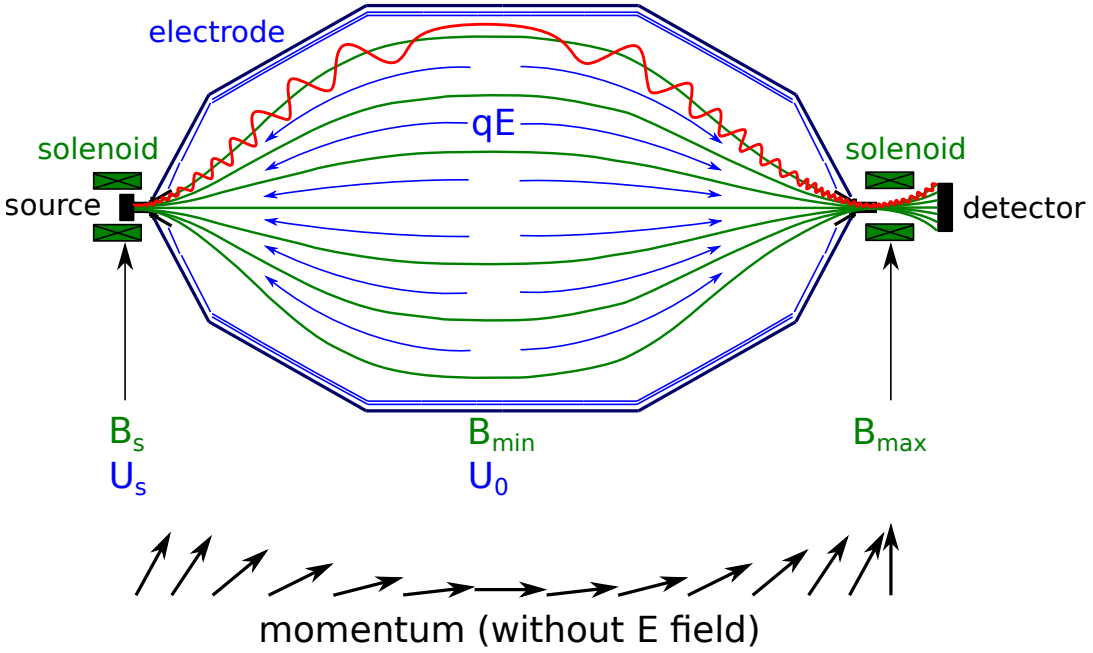

Figure 2.2: MAC-E filter principle. Superconducting magnets (green) produce a guiding field which is minimal in the center of the spectrometer. The magnetic field gradient transforms the electron's (red) transversal momentum into longitudinal momentum (lower part), as the magnetic moment remains constant along the trajectory that is shown in exaggerated size. The electric field (blue) acts on the longitudinal energy $E_{||}$ only, filtering out those electrons with $E_{\|} < qU_0$. Figure adapted from [Wan13].

2.1.1 MAC-E-Filter

As already discussed in section 1.3.3, the count rate near the endpoint of the tritium β-decay spectrum is extremely small, as only about 10^{-13} of all decays take place in the region within 1 eV of the endpoint. Also, the tiny spectral distortion of a non-vanishing neutrino mass can only be detected with a sufficient energy resolution. Therefore the KATRIN spectrometers are based on the MAC-E filter[1] principle, which inherently features large angular acceptance and a high luminosity. This fundamental principle was first proposed in [BPT80] and [KR83] and further refined and adapted for neutrino-mass measurements in Troitsk [LS85] and Mainz [P$^+$92].

In figure 2.2 the principle of the MAC-E filter is schematically illustrated and its details are explained below.

Magnetic guidance

The basis of a MAC-E filter is an axially symmetric magnetic guidance field reaching from the source to the detector, created by multiple sequentially arranged superconducting magnets. All electrons originating from the β-decay in the source region will, independent of their polar angle θ, perform a cyclotron motion around the magnetic field lines due to the Lorentz force, as schematically visualized in figure 2.3. This leads to a large acceptance angle of up to 2π, which means that half of all decay electrons can reach the detector, in principle. Because of the gyration around the magnetic field lines, the momentum and also the kinetic energy is composed of a longitudinal component, parallel to the magnetic field line, and a transversal component, perpendicular to the latter:

$$E_{\text{kin}} = E_{\|} + E_{\perp}. \tag{2.1}$$

[1] **M**agnetic **A**diabatic **C**ollimation combined with an **E**lectrostatic filter

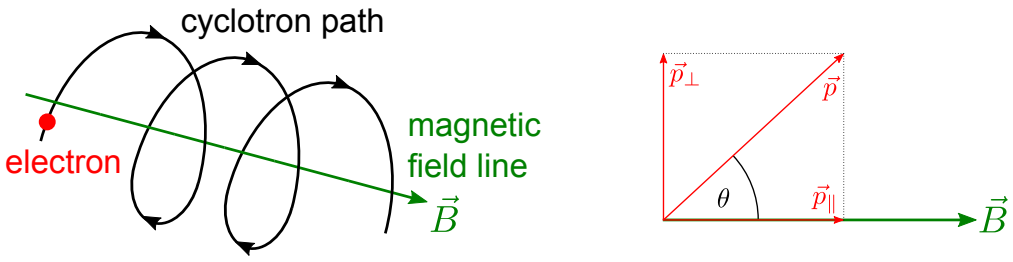

(a) Cyclotron motion (b) Polar angle θ

Figure 2.3: Simple sketch of a the cyclotron motion of an electron in a constant magnetic field (a) and definition and illustration of the polar angle θ (b).

Electrostatic filtering

To filter the electrons according to their energy, an electrostatic retarding potential is used with an electric field parallel to the magnetic field lines. Thus, only electrons with sufficient kinetic energy can pass the potential barrier to reach the detector, while electrons with insufficient kinetic energy are reflected back to the source where they are absorbed at the rear wall. At KATRIN this electrostatic retarding potential is created by putting the spectrometer vessel on negative high voltage of about -18.6 kV, see section 2.2.4. This creates a symmetric potential barrier with its maximum in the center of the spectrometer, the so called analyzing plane. As the electric field is aligned parallel to the magnetic field lines, only the longitudinal Energy $E_\parallel$ of the electrons can be filtered. However, as electrons are isotropically emitted during β-decay in the source, nearly all of them have a significant fraction of their kinetic energy in the transversal component, as they are being guided magnetically from the source to the spectrometer. The solution to overcome this dilemma relies on magnetic adiabatic collimation, as explained in the following.

Magnetic adiabatic collimation

As only the longitudinal energy component $E_\parallel$ can be filtered by the electrostatic potential, the polar angle θ needs to be minimized at the analyzing point, which results in a conversion from transversal into longitudinal energy. This can be done by reducing the magnetic field at the analyzing point and making sure that the first adiabatic invariant

$$\gamma\mu = \frac{\gamma+1}{2} \cdot \frac{E_\perp}{B} \tag{2.2}$$

remains constant along the electron's trajectory, with γ being the relativistic Lorentz factor and μ the orbital magnetic moment of the electron. For tritium β-decay electrons with a maximum kinetic energy of $E_{\mathrm{kin}} = E_0 \approx 18.6\,\mathrm{keV}$, a non-relativistic approximation can still be used here to explain the measurement principle, as $\gamma = 1.04 \approx 1$. The adiabatic invariant of the electron's motion is therefore its magnetic moment

$$\mu = \frac{E_\perp}{B} = \text{const.} \tag{2.3}$$

Following this equation, the reduction of the magnetic field at the analyzing point results in an appropriate reduction of the transversal energy component. Due to the conservation of the total energy according to equation 2.1, the longitudinal energy component increases accordingly. In short terms, the magnetic field gradient enforces a conversion from the transversal to the longitudinal kinetic energy component ($E_\perp \rightarrow E_\parallel$) as the magnetic field from the source to the analyzing point ($B_{\mathrm{S}} \rightarrow B_{\mathrm{min}}$) decreases, and the electrostatic

filtering according to the longitudinal energy component leads to the required high pass filtering.

As the conversion $E_\perp \rightarrow E_\parallel$ happens at the same time as the electrostatic potential reduces the longitudinal kinetic energy component $E_\parallel$, the interplay between magnetic field and electric potential needs to be adjusted and optimized precisely to prevent electrostatic reflection before the conversion from $E_\perp \rightarrow E_\parallel$ has finished, which is called early retardation. The required optimization is discussed in section 4.3.

Also, this derivation is only true if the adiabatic invariant $\gamma\mu$ remains constant along the electron's trajectory, which can be assured by keeping small magnetic and electric field gradients within a cyclotron motion of the electron

$$\frac{\Delta B}{B} \ll 1 \quad \text{and} \quad \frac{\Delta E}{E} \ll 1. \tag{2.4}$$

The KATRIN main spectrometer, see section 2.2.4, was designed to guide electrons fully adiabatically, so it has a considerable length of 23.3 m, resulting in sufficiently low field gradients for the required magnetic adiabatic collimation.

Magnetic mirror

In addition to the process of electrostatic reflection by the potential barrier, electrons can also get reflected magnetically, independent of their kinetic energy. As the magnetic adiabatic collimation also works the other way round, the polar angle θ increases when electrons propagate towards an increasing magnetic field, as their longitudinal kinetic energy component gets converted to the transversal one ($E_\parallel \rightarrow E_\perp$). At the specific point where the polar angle θ reaches a values of 90° and the longitudinal kinetic energy component $E_\parallel$ vanishes, the electron gets reflected. Accordingly, in a MAC-E filter where the maximal magnetic field is not in the source ($B_{\max} > B_S$), all electrons with a starting polar angle θ_S larger than the maximum accepted angle

$$\theta_{\max} = \arcsin\left(\sqrt{\frac{B_S}{B_{\max}}}\right) \tag{2.5}$$

will turn around at the position of the magnetic field maximum and propagate back to the source, independent of their kinetic energy.

At the KATRIN experiment the design values for the magnetic fields are $B_S = 3.6\,\mathrm{T}$ for the source and $B_{\max} = 6\,\mathrm{T}$ for the pinch magnet, which results in a maximum starting polar angle of $\theta_{\max} = 50.77°$. The intentionally rather small maximum starting polar angle causes nearly two-thirds of all electrons created in forward direction to be reflected magnetically. This is advantages, as electrons with a large polar angle θ have an increased path length through the experiment, resulting in increased synchrotron losses and enhanced scattering probabilities in the gaseous source, contributing significantly to the systematic uncertainty budget.

Energy resolution

As the magnetic field in the center of the MAC-E filter can not drop to zero, the conversion from transversal to longitudinal kinetic energy ($E_\perp \rightarrow E_\parallel$) is not perfect, so that a certain fraction of the kinetic energy of the electron remains in the transversal component. This amount can not be analyzed by the electrostatic filter, implying that at a given potential U_0 electrons with a kinetic energy of $E_{\mathrm{kin}} = qU_0$ can only pass the potential if their starting polar angle θ is zero. Otherwise they need a surplus energy of up to ΔE for the maximal starting angle to pass the filter and reach the detector.

This surplus energy ΔE is called energy resolution of the MAC-E filter, or more precisely the filtering width of the spectrometer. It can be calculated directly given the maximal kinetic energy and the ratio of the minimal and maximal magnetic field. The maximal polar angle that an electron can possess at $B_{\max}$ amounts to $\theta = 90°$, where all of the kinetic energy of the electron is stored in its transversal component $E_\perp$. Assuming an adiabatic motion, making use of equation 2.3, the remaining transversal energy component ΔE at the analyzing plane at $B_{\min}$ is given by the relation

$$\frac{E_{\text{kin,max}}}{B_{\max}} = \frac{\Delta E}{B_{\min}}. \tag{2.6}$$

At the KATRIN main spectrometer the design values are $B_{\min} = 3{\cdot}10^{-4}\,\text{T}$ at the analyzing plane at the middle of the spectrometer and $B_{\max} = 6\,\text{T}$ at the pinch magnet. As the maximal kinetic energy for tritium β-decay electrons is $E_{\text{kin}} = E_0 \approx 18.6\,\text{keV}$, the energy resolution of the KATRIN main spectrometer results in a filter width of

$$\Delta E = 18.6\,\text{keV} \cdot \frac{3 \cdot 10^{-4}\,\text{T}}{6\,\text{T}} = 0.93\,\text{eV}. \tag{2.7}$$

It should be mentioned here that KATRIN's designed energy resolution of $\Delta E = 0.93\,\text{eV}$ does not limit the ambitious goal of measuring the neutrino mass with a sensitivity of $200\,\text{meV}/c^2$ (90% C.L.), as long as the width and shape of this filter is known precisely (see section 5.5). The presented formula is a non-relativistic approximation and also neglects additional modifications such as synchrotron radiation. In chapter 6 all relevant effects will be included and realistic magnetic field values will be used resulting in an energy resolution of $\Delta E = 1.17\,\text{eV}$.

Conservation of magnetic flux

While the length of the main spectrometer is a consequence of the required adiabatic motion of the electrons, its radius is an implication of the conserved magnetic flux

$$\Phi = \int_A \vec{B} \cdot \mathrm{d}\vec{A} = \text{const.} \tag{2.8}$$

A reduction of the magnetic field results in an appropriate increase of the flux-tube cross section area A, which means that the maximum area of transported electrons is reached at the minimal magnetic field $B_{\min}$ at the center of the MAC-E filter.

The design value for the magnetic flux at the KATRIN experiment is $\Phi = 191\,\text{Tcm}^2$, resulting in a radius of $r_{\max} = 4.5\,\text{m}$ in the analyzing plane, where the magnetic field is minimal with $B_{\min} = 3 \cdot 10^{-4}\,\text{T}$.

2.1.2 Transmission function

When discussing the selectivity of the MAC-E filter with regards to the kinematic parameters of signal electrons, one usually neglects energy losses in the source (these are described in the response function in section 2.1.3). In this approximation the count rate at the detector can be expressed as a function of the retarding potential U_0 by

$$\dot{N}(qU_0) \propto \int_{qU_0}^{E_0} \frac{\mathrm{d}N}{\mathrm{d}E}(E_0, m_\nu^2) \cdot T(E, qU_0)\mathrm{d}E, \tag{2.9}$$

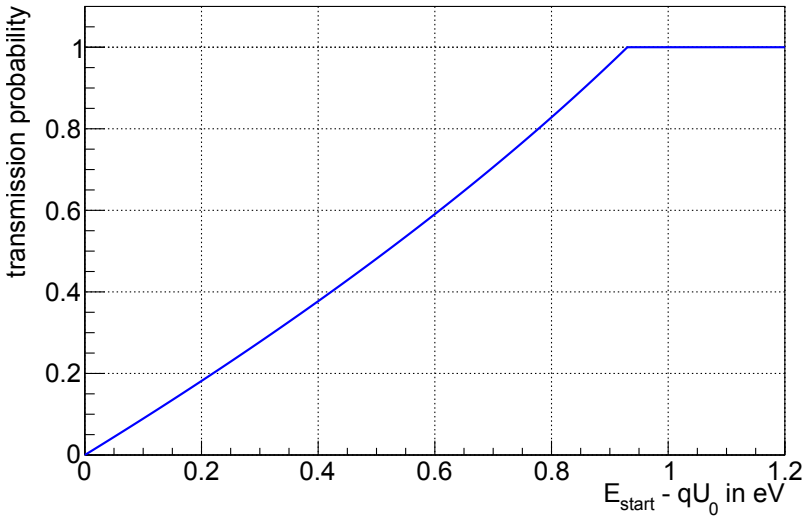

Figure 2.4: Transmission function for an isotropic source and the KATRIN design values of $U_0 = 18.6\,\mathrm{kV}$, $B_\mathrm{S} = 3.6\,\mathrm{T}$, $B_\mathrm{a} = 3 \cdot 10^{-4}\,\mathrm{T}$ and $B_\mathrm{max} = 6\,\mathrm{T}$. The transmission starts at a surplus energy of $E_\mathrm{start} - qU_0 = 0\,\mathrm{eV}$. For larger surplus energies accordingly electrons with larger starting angles are transmitted until the full transmission is reached at a surplus energy of $\Delta E = 0.93\,\mathrm{eV}$.

with the differential tritium decay spectrum $\frac{\mathrm{d}N}{\mathrm{d}E}(E_0, m_\nu^2)$ and the transmission function $T(E, qU_0)$, being discussed in this section. The information about the neutrino mass is hidden in the differential tritium spectrum, however, KATRIN measures an integrated spectrum due to the MAC-E filter principle. As can be seen from equation 2.9, a precise knowledge of the transmission function is thus of uttermost importance for a successful neutrino mass analysis.

To first order the transmission function can be described fully analytically and does only depend on the magnetic field in the source B_S, the maximal magnetic field B_max, the analyzing plane magnetic field B_a and electrostatic potential U_0. The measurement of the latter will be discussed in detail in chapter 5.

As discussed in the section above, the probability for an electron to be transmitted through the spectrometer depends on its starting polar angle and starting kinetic energy. For a fixed retarding potential U_0 and starting polar angles lower than θ_max, electrons with a kinetic energy less than the electrostatic potential qU_0 will not be transmitted, while electrons with a surplus energy of the filter width ΔE will always pass the filter. For all electrons with a kinetic energy in between the transmission depends on the polar angle θ. While electrons with lower values of θ need less surplus energy, electrons with higher θ values will need more. The exact shape of the transmission function depends on the angular distribution of the source. For an isotropic source the transmission function can be described by

$$T(E, qU_0) = \begin{cases} 0 & E - qU_0 < 0 \\ \dfrac{1 - \sqrt{1 - \frac{E - qU_0}{E} \cdot \frac{B_\mathrm{S}}{B_\mathrm{A}}}}{1 - \sqrt{1 - \frac{B_\mathrm{S}}{B_\mathrm{max}}}} & 0 \leq E - qU_0 \leq \Delta E \\ 1 & E - qU_0 > \Delta E \end{cases} , \tag{2.10}$$

shown visually in figure 2.4 for the KATRIN design values. A detailed derivation of this formula can be found in 6.1.1.

As already mentioned, this simple description of the transmission function is only valid to first order, as multiple effects need to be taken into account, naming the most important ones in the following:

- The electric potential and also the magnetic field are not constant over the area of the analyzing plane, but posses a distinct radial dependency. Depending on the exact electromagnetic field settings in the main spectrometer, the width of the transmission function can increase by about 50 %. As the focal plane detector is composed of 148 individual pixels, see section 2.2.6, a transmission function for each pixel has to be calculated. The effect of a pixel-dependent transmission function will be discussed in section 5.5.
- Even for a fixed electron trajectory the position of the analyzing point may not be constant, but also depends on the starting polar angle θ and thus may vary on the order of several cm. This effect can be minimized by a careful optimization of the magnetic field settings in the main spectrometer, see section 4.3.
- The magnetic field in the source is not constant, but experiences small variations along its z-axis of the order of a few percent. Consequently, the maximal polar starting angle $\theta_{\max}$ is also not constant over the source region, which leads to the necessity of summing up multiple transmission functions and weighing them according to the corresponding tritium density, see section 6.5.
- The acceleration of charged particles in electromagnetic fields leads to energy loss due to synchrotron radiation. Although the maximal radiative energy losses are less than 100 meV, the shape of the transmission function gets modified significantly, see section 6.5.

2.1.3 Response function

While the transmission function describes the spectroscopic features of the MAC-E filter, where electrons do not lose any energy on their trajectory from the source to the detector, the overall response function will also include energy losses in the gaseous tritium source. Equation 2.9 needs then to be rewritten as

$$\dot{N}(qU_0) \propto \int_{qU_0}^{E_0} \frac{\mathrm{d}N}{\mathrm{d}E}(E_0, m_\nu^2) \cdot R(E, qU_0)\mathrm{d}E, \tag{2.11}$$

with $R(E, qU_0)$ being the response function. Due to the rather large density of tritium in the source, there is a non-negligible probability for electrons to scatter off tritium molecules and lose some amount of energy. The corresponding energy loss is characterized by the normalized energy loss function

$$f(\epsilon) = \frac{1}{\sigma_{\mathrm{inel}}} \cdot \frac{\mathrm{d}\sigma}{\mathrm{d}\epsilon} \tag{2.12}$$

with the electron energy loss ϵ and the inelastic cross section σ_{inel}. The response function can be obtained once the scattering probabilities for no scattering P_0, single scattering P_1, twofold scattering P_2 and so forth are known with great precision. While for the case of no scattering the transmission function just needs to be multiplied with P_0, for n-fold scattering it has additionally to be convoluted with the n-folded convoluted energy loss function. The result is the following equation

$$\begin{aligned} R(E, qU_0) = \; & P_0 \cdot T(E, qU_0) & + \\ & P_1 \cdot T(E, qU_0) \otimes f(\epsilon) & + \\ & P_2 \cdot T(E, qU_0) \otimes [f(\epsilon) \otimes f(\epsilon)] & + \\ & \dots \end{aligned} \tag{2.13}$$

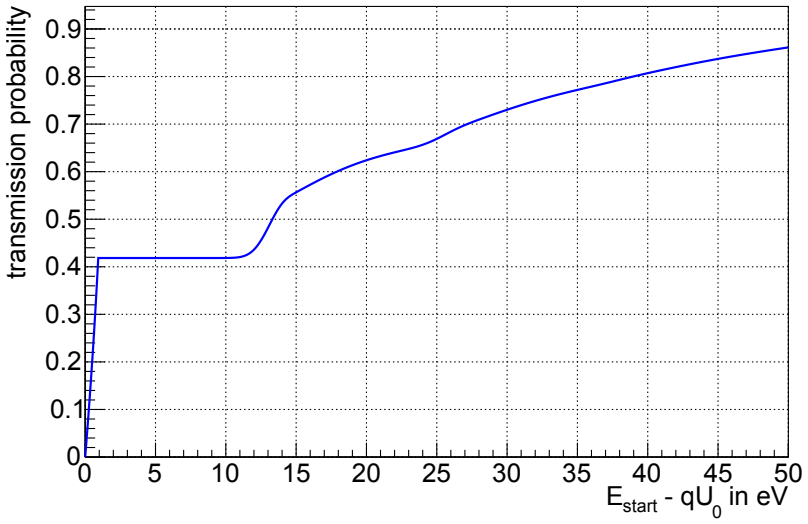

Figure 2.5: Response function as function of the surplus energy $E - qU_0$ for an isotropic source with $\theta_{\max} = 50.77°$ and a fixed spectrometer potential of $U_0 = 18.55\,\mathrm{kV}$. An inelastic cross section of $\sigma_{\mathrm{inel}} = 3.4 \cdot 10^{-22}\,\mathrm{m}^2$ and a column density of $\rho d = 5 \cdot 10^{21}\,\mathrm{m}^{-2}$ has been used for the calculation. As only $P_0 = 0.418$ of all electrons leave the source without experiencing any inelastic scattering on tritium molecules, the response function rises only to that level and stays at that plateau until after about 10 eV surplus energy the first scattered electrons get transmitted, as this is the minimal energy loss in inelastic scattering.

which is also shown as an example in figure 2.5 for the KATRIN reference values.

As can be seen, between a surplus energy $E - qU_0$ of 0 to about 10 eV, the shape of the response function is the same as the transmission function, but only rises to $P_0 = 0.418$, as this corresponds to the fraction of electrons that leave the source without experiencing inelastic scattering for that given setting. Due to the fact that the minimal energy loss of inelastic scattering is about 10 eV, there is a plateau in the function until more particles get transmitted for larger surplus energies.

More details on the energy loss function, the scattering probabilities and the calculation of the response function can be found in section 6.1.

As for the transmission function, this analytic description is only valid to first order, as the scattering off tritium molecules leads not only to energy losses but also to angular changes, which modifies the angular distribution and leads to slightly different scattering probabilities after the first scattering. Additionally, there is also an elastic scattering component, that needs to be taken into account, although its cross section is about 12 times lower. Also the scattering probabilities are angle-dependent, leading to a change of the angular distribution after the source apparatus. More details on this topic and the need to use Monte Carlo simulations for the modeling of the response function are discussed in chapter 6.

2.2 Main components

As outlined in the last section, the main components for a successful neutrino mass measurement are a high luminosity β-decay source with well-understood systematics, a high-precision spectrometer with well-defined transmission characteristics, a powerful tritium retention system to achieve a low source related background rate and a detector with a high efficiency for counting. While figure 2.6 gives an overview of the 70 m long beamline, the details of the individual components will be described in the following.

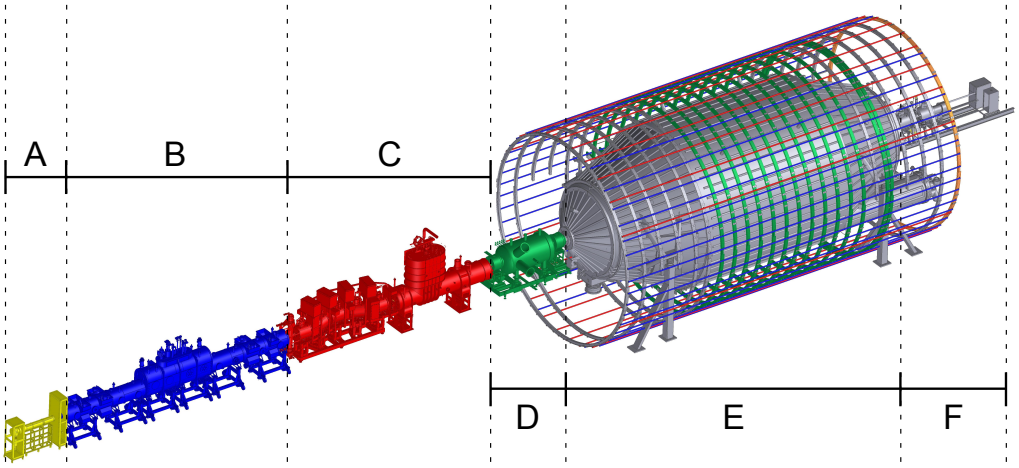

Figure 2.6: The 70 m long beamline of the KATRIN experiment, consisting of several main components: The rear section (A), used for calibration of the experiment and monitoring of the source, the WGTS, a windowless gaseous tritium source (B), followed by the transport section (C), used for differential and cryogenic pumping of tritium and magnetic guidance of the signal electrons to the spectrometers. The pre-spectrometer (D) is for rejection of low energy electrons and the big main spectrometer (E) for precise spectroscopy of the signal electrons that will be detected at the focal plane detector (F) afterwards.

2.2.1 Tritium source

KATRIN makes use of the concept of a windowless gaseous tritium source (WGTS) as β-decay emitter of highest luminosity and stability. Gaseous molecular tritium is injected at the center of the beam tube and pumped out at both ends by turbo molecular pumps (TMP). The pumped-out tritium will be collected and re-injected, thus forming a closed tritium cycle, the inner loop [Stu10]. This pumping concept avoids windows at both ends of the source's beam tube, restricting source related energy losses of signal electrons to energy losses by scattering of tritium gas. The cylindrical stainless-steel central beam tube has a length of 10 m, a diameter of 90 mm and is surrounded by 3 super conducting solenoids providing a nearly homogeneous magnetic field of $B_S = 3.6\,\mathrm{T}$, to guide the signal electrons out of the source. The length of the WGTS cryostat is increased to 16 m by two pumping sections, being attached on both ends, reducing the gas flow by a factor of 10^2. With a gas injection pressure of about 10^{-3} mbar and an operating temperature of $T = 30\,\mathrm{K}$, a stable column density of $\rho d = 5 \cdot 10^{17}\mathrm{cm}^{-2}$ can be achieved, which corresponds to a β-decay activity of the source of $A \approx 10^{11}\mathrm{Bq}$. The isotopic gas composition with a tritium purity larger than 95 % is monitored in-line and near time by a dedicated Laser Raman spectroscopy system, the LARA setup [Sch13, Fis14]. To achieve a stable operating temperature of $T = 30\,\mathrm{K}$, the beam tube is surrounded by a complex cooling system, using a novel two-phase neon beam tube cooling concept [Bod11, GBSS11]. This low temperature is not only required to minimize the tritium throughput, but also to reduce the effect of thermal Doppler broadening of the electron energies due to molecular motion. An even lower temperature is not advantageous, as it would lead to clustering of tritium molecules. A temperature fluctuation of $\Delta T < 30\,\mathrm{mK}$ is required to stabilize the column density at the 10^{-3} level. A larger variation of the column density would lead to fluctuations of the count rate and the response function, due to the changes in the scattering probabilities. The cooling concept has already been extensively tested at the WGTS demonstrator, showing a temperature variation of one order of magnitude better than the requirements [Hoe12, GBH+13]. The final WGTS cryostat is currently being assembled and scheduled to be completed in summer 2015. A CAD view and a schematic drawing of its main parts can be found in figure 2.7. Further information is available in [B+12].

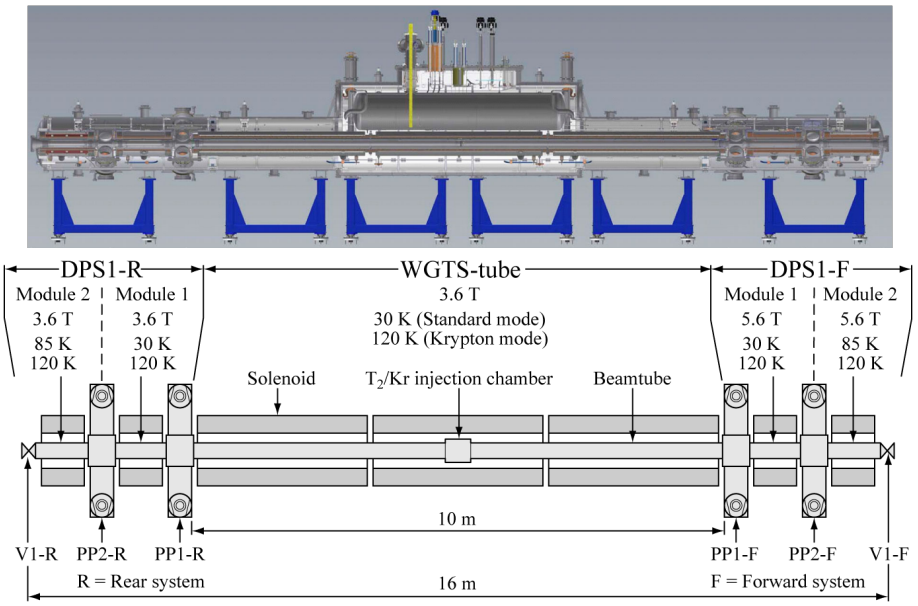

Figure 2.7: CAD model and schematic drawing of main parts of the windowless gaseous tritium source. Figure adapted from [Hoe12].

2.2.2 Rear section

The rear section at the downstream end of the WGTS cryostat has multiple monitoring and calibration purposes:

- The rear wall will define the plasma potential of the source [B$^+$12].
- Half of all electrons from the source will leave the WGTS in backwards direction, and most of the electron emitted in forward direction will be reflected at the electrostatic filter or due to magnetic reflection. Hence, almost all created electrons will hit the rear wall, where beta induced X-ray spectroscopy (BIXS) will be used to monitor the tritium activity [Röl11, R$^+$13].
- An angular resolved electron gun will be used in regular intervals to measure the actual source column density via inelastic scattering [Hug10, V$^+$11].
- Additionally, this electron gun is used to measure the energy loss function and the inelastic scattering cross section of the WGTS in a dedicated measurement campaign before the start of the long term KATRIN neutrino mass measurements, see section 6.1.

Further information about the technical details of the rear section, which is expected to be operational in summer 2015, can be found in [Bab14].

2.2.3 Transport section

The transport section connects the WGTS and the spectrometer section and is needed to reduce the tritium flow to the spectrometer. As outlined above, the WGTS is a high intensity source containing $5 \cdot 10^{19}$ tritium molecules, whereas the main spectrometer requires ultra high vacuum (UHV) conditions, with a tritium partial pressure lower than 10^{-20} mbar to keep the background below the design limits [Mer12]. Therefore, the transport section needs to reduce the tritium flow rate by 14 orders of magnitude, thus preventing tritium-related background in the spectrometer section. At the same time, signal electrons from the WGTS have to be guided adiabatically through the transport section to reach the spectrometers and the detector.

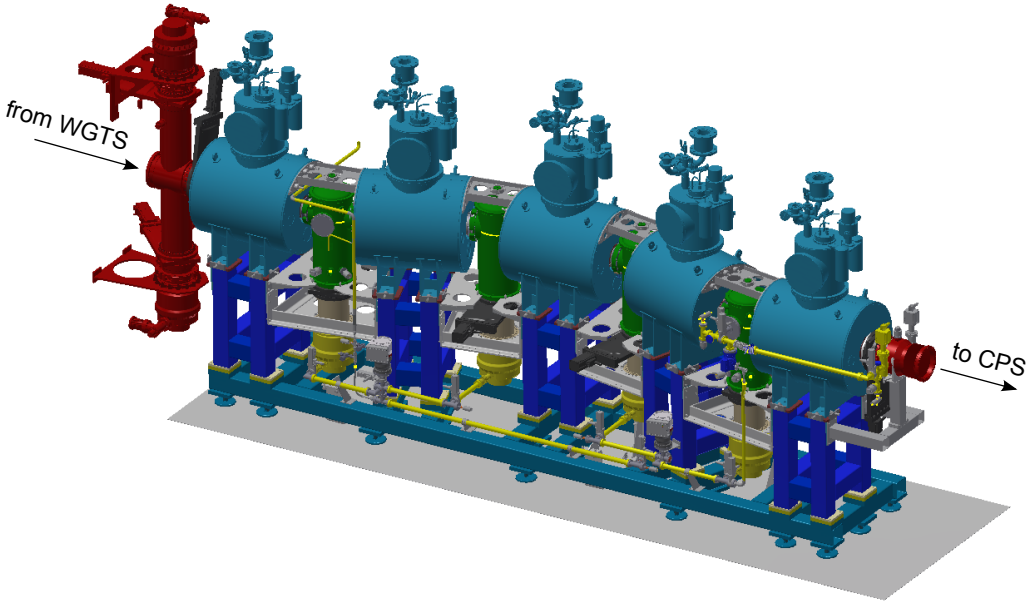

Figure 2.8: Differential pumping section. Four turbo molecular pumps (yellow) and the chicane geometry reduce the gas flow by 5 orders of magnitude, while 5 super conducting coils (turquoise) create a magnetic field of up to 5.5 T to guide the signal electrons through the beam tube (red). Figure adapted from [Jan15].

The transport section consists of two fundamental units, the differential pumping section (DPS) and the cryogenic pumping section (CPS), both being described in the following.

Differential pumping section

While the WGTS already includes two important differential pumping systems on both ends, the main differential pumping is achieved by the DPS, shown in figure 2.8. It is composed out of 5 beam tubes tilted by 20° against each other to avoid a direct line-of-sight for propagating tritium molecules. Between the beam tubes 4 pump ports are situated, each containing a large turbo molecular pump (TMP) with a tritium pumping speed of about 2400 l/s [Jan15], thus achieving a total gas flow reduction between 4 and 5 orders of magnitude. The 7 m long beam tube is surrounded by a system of 5 superconducting coils, creating a magnetic field of about 5.5 T to the transport signal electrons. Additionally the DPS beam tube is instrumented with a Fourier Transform-Ion Cyclotron Resonance (FT-ICR) diagnostic tool to determine the ion content originating from the WGTS [UD11, UD$^+$09]. As ions are charged particles, they are not affected by the differential or cryogenic pumping section, as the magnetic field will guide them through the chicanes of both units directly towards the spectrometer. Hence, a system of electrostatic dipole and blocking electrodes with positive potentials are also integrated into the DPS beam tube to actively remove ions [Rei09, Win11]. Further information about the DPS can be found in [Kos12] and [L$^+$12].

Cryogenic pumping section

The following cryogenic pumping section (CPS) consists of 7 beams tubes tilted in parts by 15°, again to make sure that tritiated molecules will hit the inner surface multiple times. In contrary to the DPS, the CPS does not employ turbo molecular pumps. The pumping of the CPS is based on the principle of cryo-sorption, as there is a 3 K cold layer of argon frost on the inner surface of several beam tube elements to adsorb tritium molecules. This will reduce the gas flow by another 7 orders of magnitude. When the

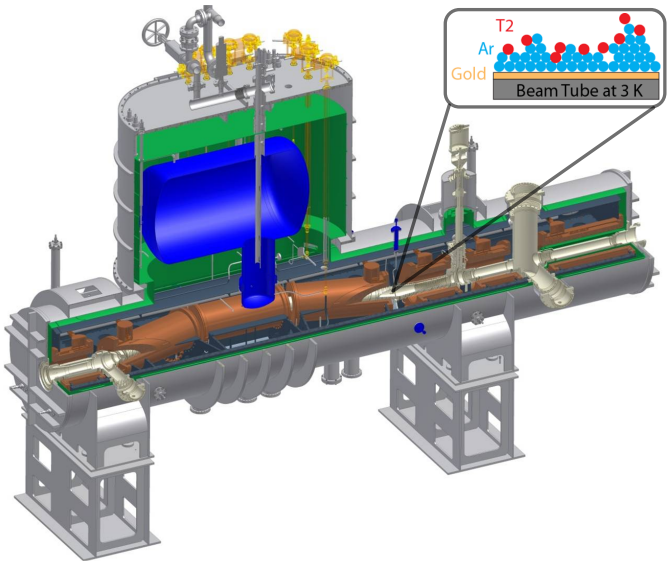

Figure 2.9: The cryogenic pumping section reduces the gas flow of tritiated molecules by 7 orders of magnitude. Tritiated molecules hit the cold beam tube surfaces covered by argon snow and are adsorbed there. The signal electrons are guided by 7 super conducting coils, producing a magnetic field of up to 5.6 T. Figure adapted from [Wan13].

surface is saturated to 1% with tritium, which should occur after approximately 3 months of continuous operation, the surface has to be regenerated by removing the tritiated argon frost layer. As in case of the DPS2, the CPS is also surrounded by superconducting magnets for the electron transport. Its 7 magnets create a maximal magnetic field of about 5.6 T. Further information about the CPS can be found in [G$^+$10] and [LD08].

2.2.4 The Spectrometers

The energy analysis of the β-decay electrons is performed by a tandem setup of electrostatic spectrometers, the pre-spectrometer and the large main spectrometer. Additionally a third spectrometer, the monitor spectrometer, is used in a separate beam line. All spectrometers implement the MAC-E filter technique, described in section 2.1.1.

Pre-spectrometer

The pre-spectrometer, with a length of 3.4 m and a diameter of 1.7 m, is the first spectrometer the signal electrons need to pass after the transport section and represents the first essentially tritium-free component in the beam line. The purpose of this spectrometer is to offer the option to be operated as pre-filter to reject signal electrons with a kinetic energy below about 18.3 keV, as these electrons do not contribute to the experiment's sensitivity on the neutrino mass. Thus the flux of signal electrons entering the sensitive main spectrometer could be reduced by up to 7 orders of magnitude. However, this arrangement would form a large Penning trap between pre- and main spectrometer, which can be avoided by operating the pre-spectrometer at vanishing potential [P$^+$12]. Besides the electrostatic field, created by putting pre-spectrometer vessel hull and a single inner wire system on high potential, two superconducting solenoids before and behind the vessel, creating a magnetic field of 4.5 T each, complete the MAC-E filter system with an intrinsic energy resolution of about $\Delta E \approx 70\,\mathrm{eV}$.

Until 2011, the pre-spectrometer was extensively used as a stand-alone test facility to study electron transport and background characteristics [Frä06, Hab09, Frä10, Gör10, Gro10, Mer12, Wan13].

Main spectrometer

The main spectrometer features a length of 23.3 m, a diameter of 10 m and a volume of 1240 m^3, and thus is the largest and arguably the most prominent component in the KATRIN experimental setup. Here, the high precision energy analysis of the signal electrons is performed, leading to the required dimensions, as detailed in section 2.1.1. The magnetic field, required for the MAC-E filter operation, is created by the second pre spectrometer solenoid PS2, generating a magnetic field of 4.5 T on the entrance side, and the pinch magnet with a magnetic field of 6.0 T on the exit side. Additionally, a large volume air coil system is installed, surrounding the main spectrometer, which will be detailed in section 2.2.5. A photo of the main spectrometer and the air coil system is reproduced in figure 2.10. The electrostatic retarding potential is created by putting the whole main spectrometer vessel on high voltage. On the inside, an inner electrode system with nearly massless wire electrodes is installed to fine tune the retarding potential and suppress background electrons originating from the vessel surface [Hug09, Zac09, Val06, Val09, Val10, Pra11]. Further information about the technical setup of the main spectrometer and its vacuum system can be found in [Gör14].

In summer 2013, the main spectrometer was commissioned for the first time in combination with the detector system. This commissioning phase will be described in more detail in chapter 4 and the performed transmission function measurements in this data-taking period are one of the main parts of this work and will be presented in chapter 5.

Monitor spectrometer

In parallel to the main KATRIN beam line, the former Mainz spectrometer is set up in a small second beam line, now acting as a monitor spectrometer. It has a length of about 4.0 m, a diameter of about 1 m but its MAC-E filter has the same energy resolution as the main spectrometer, $\Delta E = 0.93\,\mathrm{eV}$. Its inner wire system can be put on high voltage while the vessel hull remains at ground potential. The magnetic guiding field is provided by two super conducting magnets ($B = 6\,\mathrm{T}$) at both sides of the spectrometer, and additionally by 4 air coils, see figure 2.11. A solid-state krypton source emitting mono-energetic K-32 conversion electrons is used for monitoring purposes. Transmitted electrons are detected by a silicon based PIN-diode, after passing the spectrometer [Sle11, Zbo11, S^+13, Z^+13]. As the inner wire system of the monitor spectrometer is fed the same retarding high voltage as the main spectrometer, it can monitor the stability of the main retarding potential with high precision. By continuously measuring the width and position of the K-32 conversion line, even small drifts of the high voltage on the ppm or even sub-ppm scale can be detected [Erh12]. The monitor spectrometer was installed and commissioned at KIT between 2010 to 2012 [Gou10, Sch11b, Hau13]. Further information about the technical setup of the monitor spectrometer can be found in [E^+14].

2.2.5 Aircoil system

The magnetic field in the analyzing plane is dominated by the two pre-spectrometer (PS1, PS2) and the two detector solenoids (PCH, DET). Because of the considerable distance of these coils to the analyzing plane of more than 12 m, their magnetic field contribution is only about $B = 0.179\,\mathrm{mT}$. This low field value leads to multiple problems:

- In the center of the main spectrometer, the flux tube would have a radius of more than 11 m, not fitting into the spectrometer anymore.
- The earth's magnetic field, with its horizontal $B_{\mathrm{hor}} = 20.6 \cdot 10^{-6}\,\mathrm{T}$ and vertical $B_{\mathrm{ver}} = 43.6 \cdot 10^{-6}\,\mathrm{T}$ component at KIT Campus North, is not negligible anymore, and has a strong influence on the orientation and strength of the magnetic field at the analyzing plane.

Figure 2.10: A photo of the main spectrometer from the pre-spectrometer side, with the latter not installed yet. The main spectrometer is 23.3 m long and has a diameter of 10 m. It is surrounded by a large air coil system. The picture was taken in 2009.

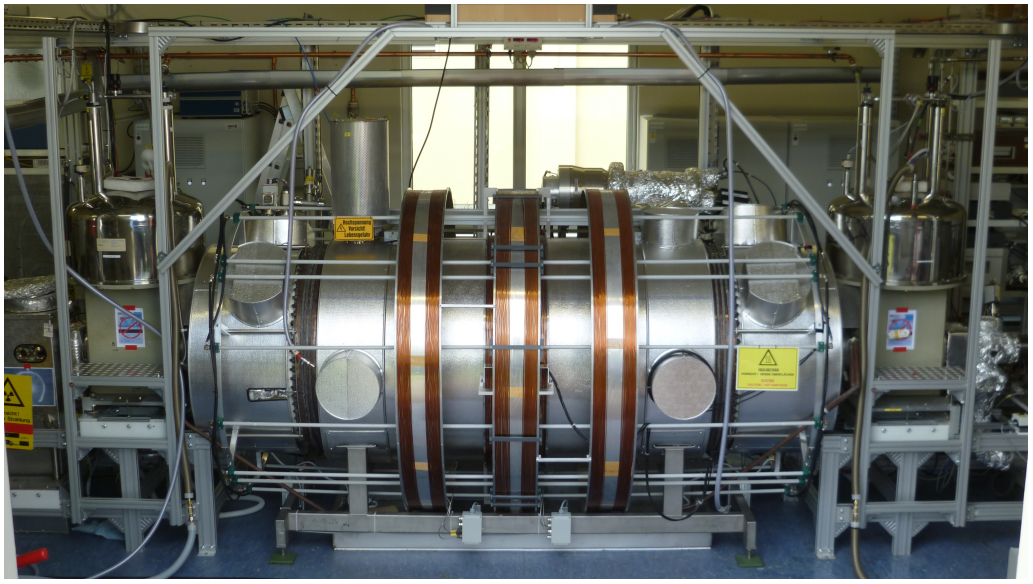

Figure 2.11: A photo of the monitor spectrometer with its 2 solenoids on both sides and surrounded by 4 aircoils (double layer in the center). Photo from [Erh12].

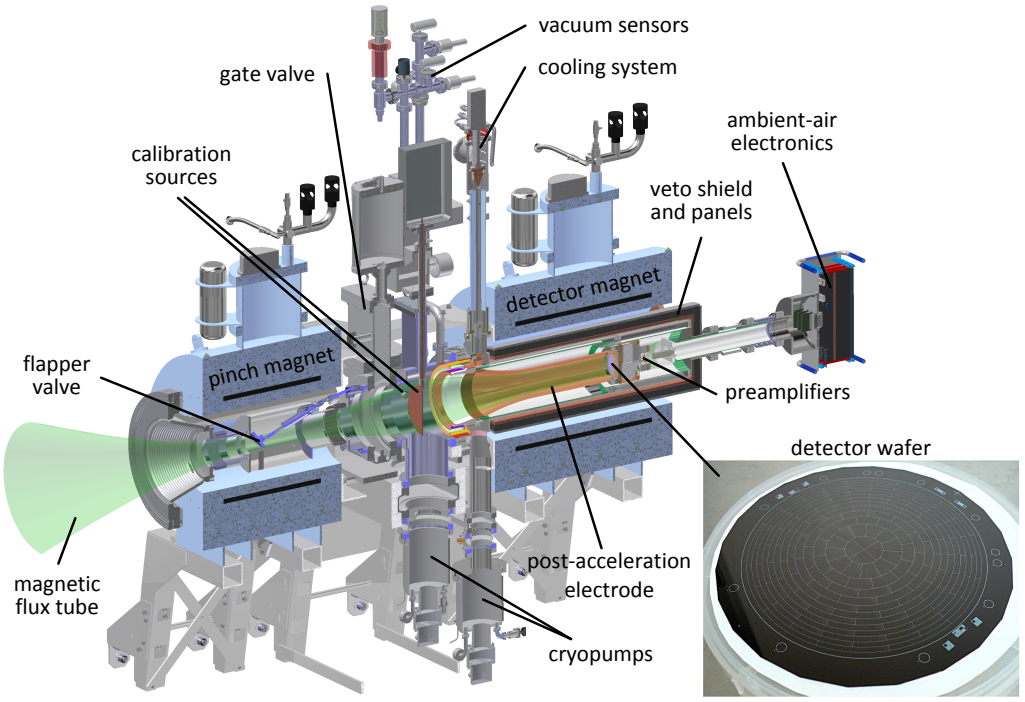

Figure 2.12: Focal plane detector system, with the silicon PIN-diode segmented into 148 pixels at the end. Adapted from [Sch14].

- Furthermore, as the entrance solenoid has a much smaller field than the exit solenoid (4.5 T compared to 6 T)[2], the magnetic flux tube inside the main spectrometer is asymmetric.

All these problems are significantly reduced and remedied by the air coil system, consisting of two units: The earth magnetic field compensation system (EMCS) and the low-field coil system (LFCS) [G+13]. The EMCS compensates the vertical and horizontal, non-axially symmetric components of the earth's magnetic field, consisting of 16 vertical and 10 horizontal cosine coils. On the other hand, the LFCS produces an axially symmetric magnetic guiding field, enhancing the stray field of the super conducting solenoids in the spectrometer to shape and fine-tune the flux tube. The LFCS consists of 15 large coils around the spectrometer, see figure 2.10. All coils are powered individually and can be used to optimize the magnetic field inside the spectrometer, see section 4.3.

2.2.6 Focal plane detector

Electrons passing the main spectrometer are guided onto the focal plane detector at the upstream end of the KATRIN setup, where they are counted, after the energy analysis in the MAC-E filter. The detector is a silicon based PIN-diode array with 148 pixels, housed on a monolithic silicon wafer of 9 cm sensitive diameter and 500 µm in thickness. The wafer is located in the middle of the detector solenoid, see figure 2.12. As a low intrinsic detector background is of major importance, the wafer is surrounded by a passive shield of lead and copper and an active veto system based on plastic scintillators to remove signals from incident cosmic rays. Additionally, a post acceleration electrode is installed in the detector system, allowing to shift signal electrons to a region of interest at higher energies with a more favorable detector-intrinsic background rate. Two super conducting solenoids belong to the detector system to guide the signal electrons to the wafer. The first is the pinch magnet, also being the magnet with the maximal magnetic field in the main KATRIN

[2]More precisely, the magnetic moments of the coils has to be considered, but the argument still holds.

beam line with $B = 6\,\mathrm{T}$, and the detector magnet surrounding the wafer with $B = 3.6\,\mathrm{T}$. Further information can be found in [Har12, Wal13, Sch14, A$^+$14].

2.3 Sensitivity

Since a MAC-E filter acts as an integrating spectrometer, the count rate recorded by the detector at different retarding potentials is an integral β-decay spectrum, as outlined above. When including the total number of tritium molecules N_{tot} in the source and the measuring time t_{U} spent at a specific retarding potential U, equation 2.11 can be completed to yield the total number of counted signal electrons

$$N_{\mathrm{S}}(qU_0, E_0, m_\nu^2) = N_{\mathrm{tot}} \cdot t_{\mathrm{U}} \int_{qU_0}^{E_0} \frac{\mathrm{d}N}{\mathrm{d}E}(E_0, m_\nu^2) \cdot R(E, qU_0)\mathrm{d}E. \tag{2.14}$$

Taking into account background events $N_{\mathrm{b}} = \Gamma \cdot t_{\mathrm{U}}$, which are considered to be Poisson distributed with a constant and energy-independent rate Γ, leads to

$$N_{\mathrm{th}}\left(qU_0, R_{\mathrm{s}}, R_{\mathrm{b}}, E_0, m_\nu^2\right) = R_{\mathrm{S}} \cdot N_{\mathrm{S}}\left(qU, E_0, m_\nu^2\right) + R_{\mathrm{b}} \cdot N_{\mathrm{b}}, \tag{2.15}$$

with the parameters R_{S} and R_{b} being relative contributions of signal and background rate. This theoretical description of an integral spectrum can now be compared to a real measured integral spectrum or to a simulated one. When minimizing the difference between measured and theoretical count rate at the individual potentials, the free parameters R_{s}, R_{b}, E_0 and m_ν^2 can be obtained:

$$\chi^2(R_{\mathrm{s}}, R_{\mathrm{b}}, E_0, m_\nu^2) = \sum_i \left(\frac{N_{\mathrm{exp}}(qU_i) - N_{\mathrm{th}}(qU_i, R_{\mathrm{s}}, R_{\mathrm{b}}, E_0, m_\nu^2)}{\sigma_{\mathrm{th}}(U_i)} \right)^2 \tag{2.16}$$

with the theoretically expected statistical fluctuation $\sigma_{\mathrm{th}}(U) = \sqrt{N_{\mathrm{s}} + N_{\mathrm{b}}}$ of the count rate. When employing toy Monte Carlo simulations, as described in more detail in section 3.4.2, a statistical uncertainty of m_ν^2 for the design parameters of the KATRIN experiment can be obtained

$$\sigma_{\mathrm{stat}} = 0.018\,\mathrm{eV}^2. \tag{2.17}$$

When assuming a systematic uncertainty of the same amount, which is a conservative limit given the known systematic uncertainties listed in the KATRIN design report [KAT05], the total error budget can be calculated by adding both quadratically to

$$\sigma_{\mathrm{tot}} = 0.025\,\mathrm{eV}^2. \tag{2.18}$$

In this case, KATRIN can measure a neutrino mass of $m_{\bar{\nu}_{\mathrm{e}}} = 350\,\mathrm{meV}/c^2$ with a 5σ significance. If no neutrino mass signal is observed, an upper limit of

$$m_{\bar{\nu}_e} < 200\,\mathrm{meV}/c^2 \ (90\%\,\mathrm{C.L.}) \tag{2.19}$$

can be derived, improving the current upper limit of the neutrino mass by one order of magnitude.

3. Simulation and analysis software

For a high precision experiment like KATRIN with a beam line extending for 70m a sophisticated simulation software is required which contains efficient and accurate algorithms to propagate electrons through complex electromagnetic fields and geometries. This is of particular importance for many diverse problems ranging from the investigation of background processes and estimates of their corresponding rates to the study of transmission properties where special emphasis has to be put on accurate description of energy losses during particle propagation through the extended setup. During the commissioning measurement, a large set of different field configurations can be tested experimentally and via detailed simulations. This allows to validate the simulations, which in turn evolve to form an accurate tool for evaluating the sensitivity of the entire experiment. Due to the large variety of applications, the simulation software needs to be very flexible, extensible and user-friendly.

This requirement is met by the Kassiopeia particle tracking package, which is a joint effort of members of the KATRIN collaboration. Over the course of this thesis, Kassiopeia has been significantly improved and refined since its first creation [Mer12]. This process has culminated in the recent release of version 3, which is now fully integrated with other simulation and analysis tools, thereby forming the large-scale simulation and analysis framework Kasper. Since its creation in 2010, Kassiopeia has been used by about 30 PhD and master theses within the KATRIN collaboration where particle tracking simulations were performed. Additionally, other experiments have started to use our particle tracking framework, such as the project 8 collaboration [MF09] or, more recently, the XENON 1t dark matter experiment [Wul14].

In section 3.1 an overview on the Kasper framework and modules included therein is given. The particle tracking framework Kassiopeia will be introduced in detail in section 3.2, followed by an overview of its geometry definitions and field calculation methods in section 3.3, both being independent modules of the Kasper framework. In section 3.4 the software tools to estimate neutrino mass sensitivities by generating and analyzing of toy Monte Carlo measurements will be introduced. Finally, section 3.5 will give an overview of the tools to analyse and optimize transmission properties which have been developed in the course of this thesis.

3.1 Overview of the simulation and analysis software package

Most of the simulation and analysis software developed within KATRIN is organized in one common C++ software framework, the KASPER suite. This software package is subdivided into different modules that can be compiled individually with the cmake build system [MH07], which enforces all parts of the code to remain compatible and to be linked correctly against each other. A limited number of external open source libraries is required, such as the ROOT analysis framework [ABB+09] for data storage and visualization, the popular BOOST library [Sch11a] for multiple general purposes, and the visualization toolkit VTK [SML06] for 3D visualization of geometries and particle tracks.

The common framework is a safeguard to guarantee compatibility and close interplay among the many different analysis and simulation modules as well as the functionally of multiple modules when combined within an application. The KASPER framework consists of the following modules, with the ones being relevant for the thesis in hand being described in more detail within this chapter:

- KOMMON: Collection of common functionalities used in most of the other modules, such as mathematical and physics constants, random number generation, tools for input/output, and mathematical utilities.
- KGEOBAG: Set of geometry shapes with extensible attributes and functionality, used for field calculations and particle navigation, described in section 3.3.1.
- KEMFIELD: Collection of electromagnetic field solving algorithms, described in section 3.3.3.
- KASSIOPEIA: Particle tracking simulation package, described in section 3.2.
- KSC: Katrin specific code, such as geometrical models or experimental specific extension of the field solving and particle tracking software, being described in section 3.2.10.
- SSC: Calculation of the tritium β-decay spectrum and modeling of the source region, see section 3.4.1.
- KAFIT: Collection of minimizers and statistical tools for neutrino mass sensitivity studies. Described in section 3.4.2.
- KALI: Katrin library, providing data access for Slow Control sensors or run data through a web service layer, described in [Kle14].
- BEANS: Comprehensive suite of analysis tools for data taking with the focal plane detector, see description in [Cen14].
- DRIPS: Detector electronics simulation, see again [Cen14].
- KTRAP: Collection of analysis and simulation tools for investigation of the transmission properties, see section 3.5.

3.2 The particle tracking framework Kassiopeia

Beginning in 2010 various software developers from the KATRIN collaboration started to combine multiple different small tools for field calculation, particle generation and particle tracking in a combined, extensible, flexible, and user-friendly object-oriented particle tracking framework called KASSIOPEIA. Until today a large number of researcher from the level of post-doc, phd-student up to undergraduates from Karlsruhe Institute of Technology (KIT), Massachusetts Institute of Technology (MIT), the University of North Carolina

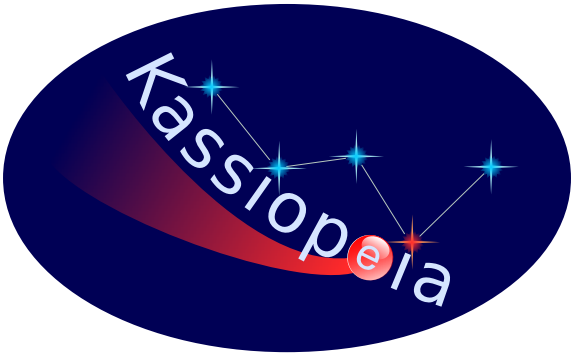

Figure 3.1: Logo of the particle tracking framework KASSIOPEIA.

(UNC) and the University of Münster (WWU) have contributed to the success of this software framework. Among the many people that created the first version, the contributions of S. Mertens [Mer12], D. Furse [Fur15] and W. Käfer [Käf12] should be emphasized.

Since then KASSIOPEIA has seen many different revisions with structural changes such as the incorporation into the KASPER framework, and the connection to the Geometry module KGEOBAG as well as the electromagnetic field solver KEMFIELD. These improvements allow users to utilize one common geometry for the entire simulation and to assign attributes like potentials to selected surfaces for field calculations. The interconnection to the data access library KALI and the detector electronic simulation DRIPS has opened the possibility to start simulations with specific experimental parameters as measured by the given sensors, for example the field driving current of a coil. As a consequence, the resulting energy spectrum of the simulation can directly be compared with the data recorded at the focal plane detector during a real measurement. In addition, very large amount of simplifications, speed improvements and refinements have been realized to meet the ever growing demands of the users of the KATRIN collaboration when investigating specific problems. The developments in the last few years leading to the current version of KASSIOPEIA 3 have been performed at led by D. Furse (MIT) [Fur15] and the author of the thesis at hand.

A detailed introduction to the working principle of KASSIOPEIA 3, highlighting its rich diversity of features and the user-friendly XML interface will be presented in this chapter. An overview of the general design and the internal structure will be given in section 3.2.1. The user interface with the powerful XML processor that allows advanced logical operations inside the configuration file will be introduced in section 3.2.1. The main components of the simulations are the physics modules to generate, propagate, navigate and to describe particle interactions and/or terminate particle tracks, will be introduced in sections 3.2.3 to 3.2.6. The highly flexible output system that allows custom-made data storage with a simple configuration will be detailed in section 3.2.7. This is followed by the introduction of the visualization modules in section 3.2.9 for graphical presentation of the simulation results in 2D with ROOT or 3D with VTK. In the last section 3.2.10 the most important parts of the KATRIN-specific code module will be described, which contains special extensions and models required for simulations of the experimental setup that have been separated from the main simulation package, to allow publication of the basic code to the physics community [FG+15].

3.2.1 General design

The goal of each particle tracking software and therefore also of KASSIOPEIA is to simulate the evolution of the physical state of multiple particles with very high precision and efficiency. The particle therefore represents a fundamental object, whose properties are

to be modified by the algorithms of the simulation software. The inherent properties of a particle, its mass m and electric charge q, are fixed during initialization, while the dynamic properties, such as its time t, position $\vec{x}$, and momentum $\vec{p}$, will evolve as the simulation progresses.

The evolution of multiple particles has to be organized into a specific data structure, which needs to be filled by the simulation, as explained in the next paragraph. Afterwards the basic simulation workflow will be detailed so that at the end of this section the modularity of the simulation algorithm can be presented, which is one of the main powerful features of KASSIOPEIA.

Organization structure

KASSIOPEIA's structure is organized into four intuitive levels of detail: Run, Event, Track and Step. A schematic representation of this classification is visualized in figure 3.2. The individual levels will be detailed in the following:

- **Step:** The lowest level of organization in the simulation is a step. It represents the evolution of a particle over a small amount of time and space from an initial to a final state. The propagation of the particle is achieved by solving the equations of motion and by considering a variety of interactions with the surrounding matter and fields. Additionally, navigation within the defined geometry is performed to detect the crossing of surfaces or space boundaries.
- **Track:** The complete evolution of a particle from its point of origin to its termination is polled together as a track, which can be seen as a sequential collection of steps. A particle and therefore a track, is typically created within an event generator or through an interaction like ionization. It can be terminated by a collection of terminators depending on specific states of the simulation. Additionally, a particle can also be terminated and a new one generated by the navigation when crossing a surface or changing a space, which thereby splits the track into two.
- **Event:** The next level of organization is an event, which is a collection of causally related tracks. Each event typically has one primary track corresponding to the primary particle created by a generator, and optionally additional secondary tracks created by splitting of the primary track or by new particles being generated during an interaction process. There are also specific generators which produce multiple causally related primary particles, for example in a radioactive decay sequence. Within one event, the primary particles created and all of their descendents are tracked step-by-step until they are terminated.
- **Run:** The highest level of organization within KASSIOPEIA is the run, which is a collection of events, whose number is pre-defined by the user in the configuration file. It represents one execution of the simulation for a fixed experimental setup. Multiple runs can be realized by running multiple KASSIOPEIA instances and merging the produced output files at the end.

Simulation workflow

The data structures introduced in the last paragraph need to be populated by the simulation algorithm. A simplified and schematic chart of the simulation work flow is visualized in figure 3.3. When the simulation is started, first the XML configuration file is parsed and the defined objects used in the simulation will be built and initialized as will be detailed in section 3.2.2. Then the event loop is executed n times and in each loop a user-specified generator will produce one or multiple initial particles. For each of these particles a track

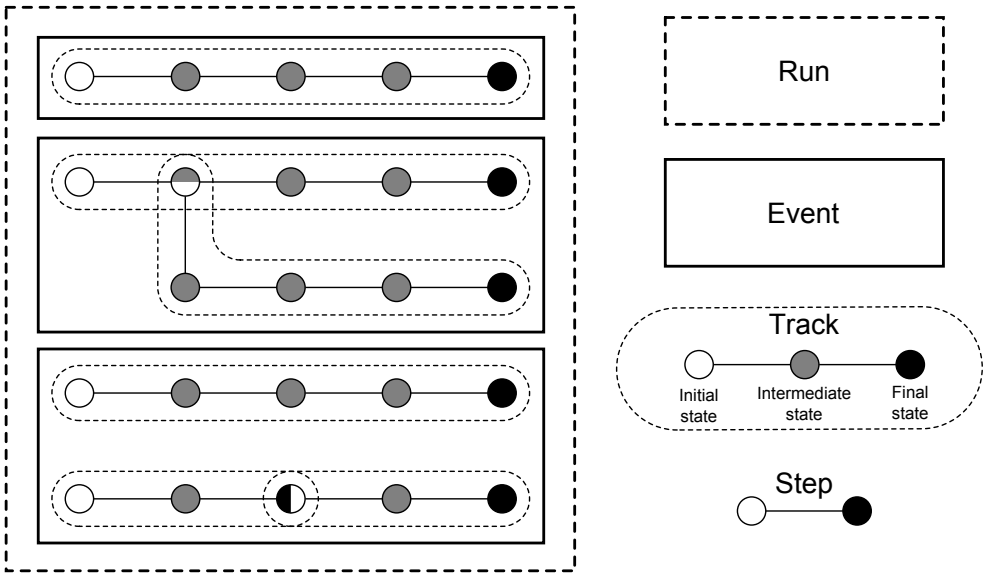

Figure 3.2: Schematic representation of a run with 3 events and a total of 6 tracks. Each track starts with an initial state (white) and ends with a final state (black). It consists of multiple steps - four for most of the given examples. Via interaction processes such as ionization within a track, a new particle and therefore a new track can be generated (track 3). Thus an event can consist out of multiple tracks, which is also the case for an event of a radioactive decay chain for example, creating multiple initial particles and therefore multiple tracks within one event (track 4 and 5). A track can be split if it crosses a surface or changes a geometrical space, thus ending the old track and starting a new one (track 5 and 6).

is created and consecutive steps are performed until the track is terminated. User-defined quantities of the track including the initial and finale particle state can then be written to disk before the next track is executed. If the tracking of all particles of the event is completed, including the one of secondary particles created within the tracks, the specific event being executed is finished and the corresponding event output is written. After all n events have been completed, the run output is written and the simulation ends after the deinitialization of all created objects.

The most important part for tracking of particles is the step loop, which is typically repeated a large number of times for each track. The schematic representation displayed in figure 3.3 corresponds to a simplification of a more sophisticated algorithm. In each step the particle is propagated by integrating its equations of motion for the user-defined step size. This is typically the most expensive part of the simulation as it involves many calculations of complex electric and magnetic fields, gradients and potentials. After the trajectory has been evaluated, the particle's mean free path length for the given interaction processes is calculated and the length at which the process will occur is diced. If this interaction length is smaller than the particle step's trajectory length, the position of the particle is adjusted accordingly and the interaction process is executed on the new final state of the particle. Additionally, the navigator checks if the particle has crossed any geometrical boundaries within the calculated trajectory. If this is the case, the state of the final particle is adjusted to the crossing position of its trajectory with the given geometrical boundary, which may induce a change of the whole configuration of the simulation for the next step, as will be detailed in the next paragraph. After the propagation, interaction and navigation of the step is done, and the particle has reached its final state for that step, the information about the step and its initial and final particle states can be written to the output. Subsequently, the active terminators are called to check if the particle has reached a certain physical state where the user has defined it to stop. If this is the case the track is finished, if not, then the steep loop is repeated.

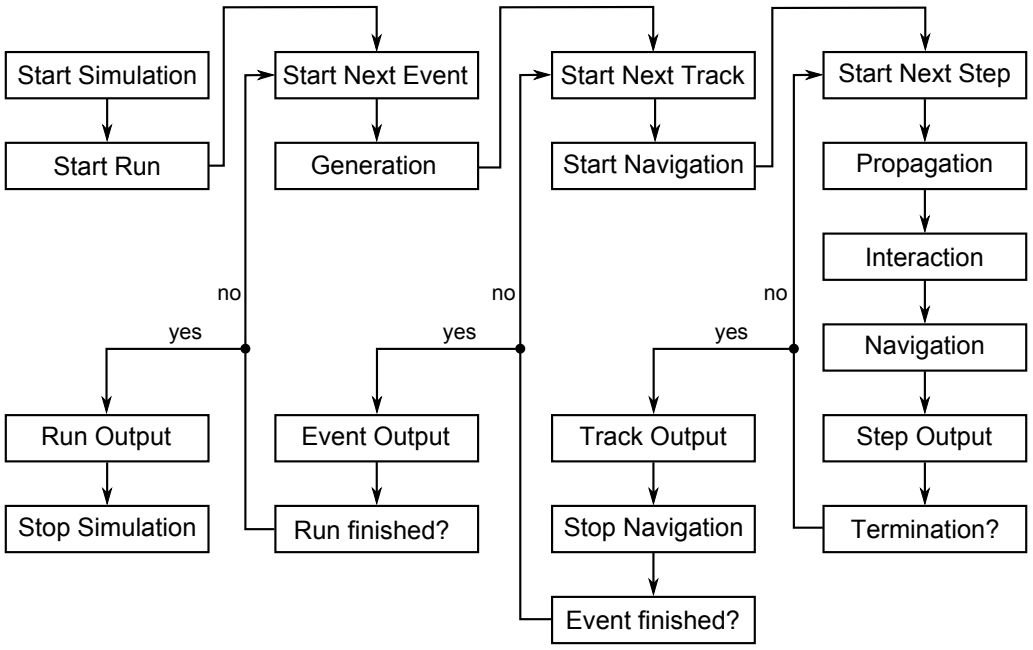

Figure 3.3: Simplified schematic representation of KASSIOPEIA's simulation algorithm, composed out of three loops over events, tracks and steps.

Modularity

The most powerful feature of KASSIOPEIA is its flexibility and modularity. The user can not only define the type of modules to be used in the simulations such as generators, field calculators or interactions, but the whole composition of the simulation algorithm can be changed depending on the particle's geometrical state. This is achieved first by the concept of a toolbox, where all objects that the user may use during the simulation are stored, second a structure of container classes, called root classes in KASSIOPEIA, for the main simulation algorithm, and third a command pattern to add, remove or replace parts of the simulation depending on the geometrical state.

- **Toolbox:** All objects of the simulation specified by the user are instantiated and stored in a so called toolbox when the XML configuration file is parsed (see next section 3.2.2). This is the case for physics modules such as particle generators, field calculators or interaction processes, but also for completely different objects such as output components (see section 3.2.7).
- **Root classes:** The simulation algorithm works with container classes for the different types of processes displayed in figure 3.3. These container classes within KASSIOPEIA are called root[1] classes, and there are two different types of them depending on whether multiple objects can be active at the same time, or only one. The root terminator, for example, can contain a list of multiple terminator objects, so when being called by the simulation algorithm, it will call all its "child" terminators. The root trajectory, however, being responsible for the propagation of the particle, can contain only one representation of equations of motion, although this equations can be composed of multiple terms. The root classes are typically filled with user-specified default objects at the beginning of the simulation, but they may also be totally empty. They will then be filled by the navigator depending on the geometrical state of the tracked particle.
- **Commands:** The way that root classes are filled by the navigator is totally open to

[1] Not be confused with classes of the ROOT package [ABB+09].

the user. In the configuration file one or multiple nested navigation geometries can be defined. As in the geometry library KGeoBag (see section 3.3.1) a basic distinction is made between a navigation space, a navigation side, which is a boundary surface of a space, and a navigation surface, which is a free surface. For each navigation geometry, a set of commands can be defined to be executed when the particle enters the corresponding geometry and to be reversed again when the particle has left it again. Nested geometries must be completely contained in a parent space. The processes of the parent space are still active inside the nested geometry, if not otherwise specified. These commands are typically defined to add or remove objects from the root classes, an example being given by adding an interaction to the root interaction for a certain surface. However, the commands can also be used to modify the objects in the root classes, for example replace a step size control in a certain trajectory representation. All objects in the toolbox that are referred to in one of the created commands (and therefore may be used at some time in the simulation) are initialized at the beginning. When an object is added to the simulation algorithm it gets activated and deactivated accordingly when being removed. At the beginning of each track the navigation is started and the simulations is put in a state depending on the geometrical position of the particle. At each step the navigator checks if the geometrical state of the particle has changed, and if so, will activate the corresponding navigation geometry and execute the associated commands. After each track is finished, the navigation is stopped and the state of the simulation is put back into the default mode.

With this concept it is possible to track particles through a variety of different lengths or physical processes within one simulation package by one single configuration file. A prime example is the entirety of the beam line where electrons are generated in a gaseous tritium source, will propagate through the about 70 m long experiment to finally enter the silicon detector. The physics processes will change on the path, for example from the scattering off tritium molecules in the source, over to the propagation being influenced by electromagnetic fields through the large dimensions of the UHV in the main spectrometer, and finally to solid-state physics where electron interactions with silicon material of the detector proceed on a scale of µm. This whole journey of up to 70 m of the particle can be described as a single track in Kassiopeia, as the simulation algorithm is adapted for each region of the experiment to perform the correct underlying physics.

3.2.2 Initialization

A simulation run with Kassiopeia is completely defined by a configuration file. In this file all simulation input data are defined and created. This includes the entire geometry of the experiment, all kinds of different physics processes that may be executed in the simulation, up to the level of output and the written down quantities. Furthermore, the navigation geometry and also the basic properties of the simulation such as the used random seed and the number of generated events are set up. The configuration files for Kassiopeia are based on the Extensible Markup Language (XML) as specified in [BPSM+08] with additional features and extensions. The XML parser of Kassiopeia is composed of a chain of multiple XML processors and the parsing of the information is performed sequentially in the so called SAX style. First an XML tokenizer creates tokens out of the data stream from the file, which are then fed into the chain of XML processors. These processors may modify the stream of tokens until the last processor in the chain finally creates the desired object. The individual processors available within Kassiopeia and therefore the features of its configuration language are described in the following.

- **Variables:** There are three different types of variables that can be defined in a configuration file: Local variables, global variables and external variables. While

local variables are only valid within the file where they have been defined, the scope of global variable is valid until they are revoked. Both can only be defined once, while external variables can be defined multiple times, even on the command line with the argument "-r name=value". For external variables, the value of its first definition is used, while a later definition can be seen as a default value, in case no definition has occurred before. All variables are referred to by the squared bracket, as shown in the following examples.

```
<!-- definition of local, global and external variables -->
<define name="path" value="/path/to/file"/>
<global_define name="detector_position_z" value="13.9337"/>
<external_define name="seed" value="123"/>

<!-- use of variables -->
<transformation displacement="0. 0. [detector_position_z]"/>

<!-- revoking of variables -->
<global_undefine name="detector_position_z"/>
```

- **Inclusion:** Configuration files can be included from other configuration files. The whole included file is parsed before the parsing of the original file is continued. The organization of large configuration files can therefore be improved if the geometry is put into a separate file for example.

```
<include name="[path]/file.xml"/>
```

- **Formulas:** Mathematical formulas can be used in element or attribute fields of the configuration file and will be interpreted by the TF1 class of the ROOT library. In addition to variables from the configuration file, all functions from the ROOT or C standard math library can be used. The formulas need to be surrounded by curly braces to be interpreted by the formula processor, which sends the resulting double precision number down the chain to the next processor.

```
<define name="amplitude" value="1.5"/>
<define name="phase" value="45"/>
<define name="result" value="{[amplitude]*cos(TMath::Pi()*[phase]/180.0)}"/>
```

- **Terminal printing:** When using the variable and formula system extensively, especially in definitions of complex geometries, it is often useful to print single variables to the screen while parsing the configuration file for debugging purposes.

```
<print name="result" value="[result]"/>
```

- **Conditions:** Conditions can be used to exclude a certain XML block from being parsed. The value of the attribute "condition" will be evaluated by the formula processor and if the result is true the lines within the "if block" are parsed. The expression for the condition can also contain logical operators and conditions can also be nested.

```
<external_define name="ac_setting" value="3.8"/>

<if condition="{[ac_setting] eq 3.8}">
    <define name="ac_1_current" value="28.6"/>
    <!-- etc. -->
</if>

<if condition="{[ac_setting] eq 9.0}">
    <define name="ac_1_current" value="95.2"/>
    <!-- etc. -->
</if>
```

- **Loops:** Loops can be very useful for groups of related content, especially in geometry definitions, as the lines in the configuration files can be reduced drastically. When creating a loop, a variable is defined with a start, an end and a step increment value. In the body of the loop block the variable can be referred to with squared brackets. Loops can also be nested.

```
<loop variable="index" start="1" end="13" step="1">
    <electromagnet current="[ac_[index]_current]" ... />
</loop>
```

- **Tags:** Tags can be used to group related objects, which can later be referred to by the common tag.

```
<tag name="magnet_tag">
    <cylinder_tube_space name="pinch_magnet_space" ... />
    <cylinder_tube_space name="detector_magnet_space" ... />
</tag>
```

- **Serializations:** A configuration file can also be serialized and written down again with all variables and formulas resolved and all loops enrolled. This can be useful to save the configuration file for a given simulation with all the used variables, also if they have been defined on the command line. The resulting file can be parsed by KASSIOPEIA again. To create a serialized file, the following XML line needs to be put somewhere in the configuration file.

```
<serialization file="serialization_config_output.xml"/>
```

- **Access to slow control data:** By making use of the KALI module it is possible to directly access the slow control data base and use sensor data as input for the simulation. For each sensor a unique identifier has been given, the so called KATRIN number. Multiple sensors can be grouped into a KALI call, if they belong to the same log group. For each database request, the start and end time, as well as the number of significant digits of the return values can be defined. Instead of the start and end time, also a corresponding start and end run identifier can be defined. The value of the sensors can be used in the remaining XML file by referring to it by its name and squared brackets, such as the user defined variables.

```
<kali starttime="[starttime]" endtime="[endtime]" digits="5">
    <katrinnumber name="vessel_voltage" value="436-WHV-0-9999-0003"/>
    <katrinnumber name="dipole_west_voltage" value="436-WHV-0-9999-0005"/>
    <katrinnumber name="dipole_east_voltage" value="436-WHV-0-9999-0006"/>
</kali>
```

3.2.3 Generation of particles

At the beginning of each event a particle generator needs to generate a set of particles. Besides the definition of a particle's intrinsic nature via its mass and charge, it needs to be fully characterized by seven parameters: position, momentum and time. While the type of the particle and therefore its inherited properties can easily be specified by an id, following the PDG particle numbering pattern [Par14], the generation of its dynamic properties is broken up into a independent substructure consisting out of four generators for the particle's properties of time, position, energy and direction. For the discussion of particle motions in a MAC-E filter, the setting of energy and direction is more appropriate then the use of the momentum vector.

For each of the four independent generators of time, position, energy and direction the values of interest, for example the three variables of the position, can be set independently by so called value generators. A set of these value generators can be used for all the

four generators, leading to large possibility of combinations. The value generators within KASSIOPEIA are:

- **Fix:** A fixed value defined by the user.
- **Uniform:** The value is drawn from a uniform distribution between a defined minimum and maximum value.
- **Gauss:** The value is drawn from a Gaussian distribution between a defined minimum and maximum value with a mean μ and standard deviation σ.
- **Formula:** The value is drawn between a minimum and maximum value according to a density distribution of user-defined formula.
- **Set:** A defined number of values is generated equally distributed between a start and an end value.
- **List:** A list of values is used where each value in the list has to be specified by the user.
- **Cylindrical:** The value is drawn from a cylindrical distribution, for example used for a uniform density distribution in cylindrical coordinates.
- **Spherical:** The value is drawn from a spherical distribution, for example used for an isotropic direction distribution.

These value generators can be used or combined within the four composite generators for time, position, energy and direction. Additionally, there are special generators for most of these types, which do not make use of the composite value mechanism.

- **Time generator:** The particle's time generator is the simplest of the available generators, as there is just one composite generator with a single selectable value generator for the time distribution.
- **Position generator:** For the generation of the particle's initial position, multiple composite generators are available, as the position variables can be expressed as x, y, and z in a rectangular representation, r, ϕ and z in a cylindrical representation, or r, θ, and ϕ in a spherical representation. For each composite generator optionally a reference coordinate system of a space or a surface of the geometry can be set. Additional generators are available to initiate a random position in a space or on a surface, as defined in the geometry, or for the generation of particles on the surface or the volume of a specified magnetic flux.
- **Energy generator:** Besides the composite energy creator with a single selectable value generator, there are more sophisticated energy generators for the radioactive decay sequences of specific unstable isotopes of radon, krypton or lead available. Based on the radioactive decay scheme, multiple electrons can be created.
- **Direction generator:** To generate an initial direction for a particle a composite generator is available in a spherical representation, with the result that for the variables of θ and ϕ a value generator can be selected.

The following XML example describes a generator that will create electrons in the source region with a fixed time and a cylindrical composite position, consisting of a fixed radius, a set of four ϕ values and a list of two z positions at the beginning and at the end of the source. The energy is drawn from a uniform distribution and the direction is drawn from an isotropic distribution. For one event a total 8 particles will be created with the fixed position combinations from the set and list, and a new randomly drawn energy and direction for each.

```
<ksgen_generator_composite name="wgts_generator" pid="11">
    <time_composite>
        <time_fix value="0."/>
    </time_composite>
    <position_cylindrical_composite>
        <r_fix value="{4.0e-3}"/>
        <phi_set value_start="0.0" value_stop="270.0" value_count="4.0"/>
        <z_list add_value="{[wgts_center]-5}" add_value="{[wgts_center]+5}"/>
    </position_cylindrical_composite>
    <energy_composite>
        <energy_uniform value_min="18570" value_max="18575"/>
    </energy_composite>
    <direction_spherical_composite>
        <theta_spherical angle_min="0." angle_max="50.77"/>
        <phi_uniform value_min="0." value_max="360."/>
    </direction_spherical_composite>
</ksgen_generator_composite>
```

3.2.4 Propagation of particles

The propagation of particles or more specifically the calculation of their corresponding trajectories, evidently is the most important part in a particle tracking software. This implies integrating the equations of motion which are represented as first order ordinary differential equations. Within KASSIOPEIA all continuous physics processes are represented as terms in the overall equation of motion. This includes the propagation of the particle, but also radiative synchrotron losses, which can be added to the overall equations of motion. Correspondingly, all terms are integrated numerically together. Depending on the choice of variables used for the full physical state of a particle, the terms for the equations of motion adopt different representations, also called trajectories in KASSIOPEIA. This method will be introduced in the following together with the differential equation terms for the different physics processes. After that the integrators to solve the differential equations in conjunction with the step size controls required will be presented.

Exact Trajectory

When dealing with an exact trajectory, the physical state of the propagating particle is described by a set of variables: the time t, the three positions components $\vec{r}$, and the three momentum components $\vec{p}$. The representation of the propagation term in the equation of motions of a particle with charge q in an electric and magnetic field $\vec{E}$ and $\vec{B}$ is given by the Lorentz equation. The terms for the ordinary differential equations for the variables of the exact representation are therefore:

$$\begin{aligned} \frac{\mathrm{d}t}{\mathrm{d}t} &= 1, \\ \frac{\mathrm{d}\vec{r}}{\mathrm{d}t} &= \frac{\vec{p}}{\gamma m}, \\ \frac{\mathrm{d}\vec{p}}{\mathrm{d}t} &= q\left(\vec{E} + \frac{\vec{p}\times\vec{B}}{\gamma m}\right) \end{aligned} \tag{3.1}$$

with the rest mass of the particle m and the relativistic Lorentz factor γ.

For the synchrotron emission term the derivation of the differential equation term can be found for example in [Fur13]. The result is an additional term in the differentiation of the momentum $\vec{p}$ that is

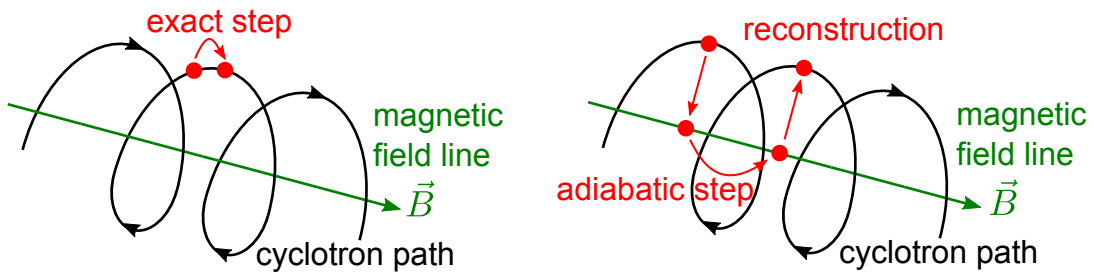

(a) Exact trajectory (b) Adiabatic trajectory

Figure 3.4: Illustration of the exact trajectory (a) and the adiabatic trajectory (b). In the adiabatic trajectory the guiding center position is propagated, which allows a much larger step size. The exact particle's position is reconstructed afterwards.

$$\frac{\mathrm{d}\vec{p}}{\mathrm{d}t} = -\frac{\mu_0}{6\pi c}\frac{q^4\vec{p}}{mp^2}\left(\gamma\xi_1 + \gamma^2\xi_2 + \gamma^3\xi_3\right) \tag{3.2}$$

with the vacuum permeability μ_0 and

$$\begin{aligned} \xi_1 &= E_T^2 + B_V^2\frac{p^2}{m^2}, \\ \xi_2 &= -2E_U B_V \frac{p}{m}, \\ \xi_3 &= E_U^2 + E_V^2 \end{aligned} \tag{3.3}$$

where the index T denotes the component in direction of the momentum $\vec{p}$, U the direction of $\vec{p}\times\vec{B}$, and $V = T \times U$.

Adiabatic Trajectory

If the magnetic and electric fields are nearly constant within a cyclotron radius of the particle, the first adiabatic invariant $\gamma\mu$ remains conserved along the trajectory of the particle, as discussed in section 2.1. With this approximation the physical state of the particle can be represented by its time t, the position at the guiding center of the motion $\vec{r}_\mathrm{c}$ and the components of the particle momentum parallel and perpendicular to the magnetic field $p_\parallel$ and $p_\perp$, as well as the gyration phase ϕ. The advantage of using this adiabatic trajectory is the much larger step size that is possible now compared to the case of calculating an exact trajectory, as the curvature in the propagation of the guiding center position is much smaller than for the propagating of the real particle position. The exact position of the particle will be reconstructed from the guiding center after the propagation, as visualized in figure 3.4.

In case of the adiabatic representation, the propagation terms in the ordinary differential equation assume the following form:

$$\begin{aligned}
\frac{\mathrm{d}t}{\mathrm{d}t} &= 1, \\
\frac{\mathrm{d}\vec{r_c}}{\mathrm{d}t} &= \frac{p_\parallel}{m\gamma}\frac{\vec{B}_\mathrm{c}}{B_\mathrm{c}}, \\
\frac{\mathrm{d}p_\parallel}{\mathrm{d}t} &= -\frac{p_\perp^2}{2\gamma m B_\mathrm{c}}\left(\vec{\nabla}B_\mathrm{c} + q\vec{E}_\mathrm{c}\right)\cdot\frac{\vec{B}_\mathrm{c}}{B_\mathrm{c}}, \\
\frac{\mathrm{d}p_\perp}{\mathrm{d}t} &= \frac{p_\perp p_\parallel}{2\gamma m B_\mathrm{c}}\vec{\nabla}B_\mathrm{c}\cdot\frac{\vec{B}_\mathrm{c}}{B_\mathrm{c}}
\end{aligned} \tag{3.4}$$

Two additional terms need to be added to this propagation terms to account for gyration and drift caused by the magnetron motion. The gyration term can be derived from the cyclotron frequency of the particle and is

$$\frac{\mathrm{d}\phi}{\mathrm{d}t} = \frac{qB_\mathrm{c}}{m\gamma}, \tag{3.5}$$

while the additional terms for the drift motion are more complicated as they modify the guiding center position and the momentum components [Fur13]

$$\begin{aligned}
\frac{\mathrm{d}\vec{r}_\mathrm{c}}{\mathrm{d}t} &= \frac{\vec{E}_\mathrm{c}\times\vec{B}_\mathrm{c}}{B_\mathrm{c}^2} + \frac{2p_\parallel^2 + p_\perp^2}{qm(\gamma+1)B_\mathrm{c}^3}\vec{B}_\mathrm{c}\times\vec{\nabla}B_\mathrm{c}\frac{\vec{B}_\mathrm{c}}{B_\mathrm{c}}, \\
\frac{\mathrm{d}p_\parallel}{\mathrm{d}t} &= \frac{q\gamma m}{p_\parallel}\vec{E}_\mathrm{c}\cdot\frac{\mathrm{d}\vec{r}_\mathrm{c}}{\mathrm{d}t} - \frac{p_\perp^2}{2p_\parallel B_\mathrm{c}}(\vec{\nabla}\vec{B}_\mathrm{c}\cdot\frac{\mathrm{d}\vec{r}_\mathrm{c}}{\mathrm{d}t})\cdot\frac{\vec{B}_\mathrm{c}}{B_\mathrm{c}}, \\
\frac{\mathrm{d}p_\perp}{\mathrm{d}t} &= \frac{p_\perp}{2B_\mathrm{c}}(\vec{\nabla}\vec{B}_\mathrm{c}\cdot\frac{\mathrm{d}\vec{r}_\mathrm{c}}{\mathrm{d}t})\cdot\frac{\vec{B}_\mathrm{c}}{B_\mathrm{c}}
\end{aligned} \tag{3.6}$$

For synchrotron radiation an additional term needs to be added to the differential equation of the perpendicular momentum component [Fur13]:

$$\frac{\mathrm{d}p_\perp}{\mathrm{d}t} = -\frac{\mu_0}{6\pi c}\frac{q^4}{m^3}\vec{B}_\mathrm{c}^2 p_\perp\gamma. \tag{3.7}$$

Magnetic Trajectory

An additional trajectory type within KASSIOPEIA is the "magnetic trajectory" to visualize magnetic field lines. This is achieved by creating a pseudo particle which is represented only by its time t and position $\vec{r}$, so that particle properties such as kinetic energy or polar angle are undefined. In this context, it is interesting to note that electrons with a kinetic energy in the keV regime will posses rather small cyclotron radii along magnetic field line. Accordingly, a magnetic trajectory is a good approximation for the path of such an electron, while considerably speeding up the time required to track a particle, even with respect to an adiabatic trajectory.

The term for the ordinary differential equation for this case simply is

$$\frac{\mathrm{d}\vec{r}}{\mathrm{d}r} = \frac{\vec{B}}{B}. \tag{3.8}$$

Integrators

The terms of the ordinary differential equations have to be integrated numerically. In the case of KASSIOPEIA this is done using the 8th order Runge-Kutta integrator, which requires exact 13 evaluations per step [Glü08, Sha91]. Additionally, the combination of Runge-Kutta integrators of different orders can be used for internal error estimation [FG86].

Controls

The computation of a step is critical in terms of performance, as this usually requires to calculate the electromagnetic variables at multiple positions within the particle's step. Accordingly, the number of calculated steps for each track should be reduced as much as possible. This must be done carefully, as the accuracy in calculating the particle motion will decrease for larger step sizes, which can lead to a violation of the total energy conservation. The step size of the particle therefore needs to be adjusted to the specific requirements of the user. This customization is handled by step size controls, which are part of the tracking module of KASSIOPEIA. A step size control suggests a specific step size in the dimension of time to the integrator at the beginning of each step. After the step has been performed the step size control may accept or reject the current step, and suggest a new step size. It is also possible to use multiple step size controls simultaneously with the smallest suggestion being used. In the following several step size controls available within Kassiopeia are presented:

- **time:** Fixed time step as defined by the user.
- **length:** Fixed trajectory length for each step, being calculated from the current velocity of the particle.
- **cyclotron:** The step size is based on a fraction of the cyclotron radius of the particle. This leads to small steps in high magnetic fields and large steps in low magnetic fields. This method is used for most trajectory calculations in KATRIN.
- **energy:** The step size is dynamically adjusted to keep the violation of the total energy within a user-defined range.

Bindings

All parts of the trajectory module, such as step size controls, specific terms in the differential equation, or even the integration method can be replaced during the simulation depending on the geometrical state of the particle, as described in section 3.2.1. In the following an XML example with the three described trajectory types is presented.

```
<kstraj_trajectory_exact name="trajectory_exact">
    <integrator_rk8 name="integrator_rk8"/>
    <term_propagation name="term_propagation"/>
    <control_cyclotron name="control_cyclotron" fraction="{1. / 32.}"/>
</kstraj_trajectory_exact>

<kstraj_trajectory_adiabatic name="trajectory_adiabatic">
    <integrator_rk8 name="integrator_rk8"/>
    <term_propagation name="term_propagation"/>
    <term_gyration name="term_gyration"/>
    <term_drift name="term_drift"/>
    <term_synchrotron name="synchrotron"/>
    <control_cyclotron name="control_cyclotron" fraction="4.0"/>
</kstraj_trajectory_adiabatic>

<kstraj_trajectory_magnetic name="trajectory_magnetic">
    <integrator_rk8 name="integrator_rk8"/>
```

```
    <term_propagation name="term_propagation" direction="forward"/>
    <control_time name="control_time" time="1.e-2"/>
</kstraj_trajectory_magnetic>
```

3.2.5 Interaction of particles

The interaction processes within KASSIOPEIA are separated into space interactions and surface interactions. While space interactions will occur as a function of a given probability during particle propagation through a dense medium, surface interactions are enforced when the particle reaches a surface which has a specific interactions attached to it.

Space interactions

For particles moving with a velocity v through a medium with a target number density of n, the probability for an interaction with cross section of σ to occur after time t can be calculated according to

$$P(t) = 1 - \exp\left(-\frac{t \cdot v}{\lambda}\right) \tag{3.9}$$

where the mean free path is defined as

$$\lambda = \frac{1}{n \cdot \sigma}. \tag{3.10}$$

In KASSIOPEIA the parameters n, v and σ are calculated as mean values for the initial and final position of the particle on the step step. The density of the medium is calculated by a separate density module, for example by defining a constant density, with properties defined by user input variables such as partial gas pressure and temperature. The cross section σ corresponds to the sum of all individual cross sections of interaction processes for this scattering module. The time for the next scattering to take place can be obtained according to

$$t_{\text{scat}} = -\ln\left(1 - P(t)\right) \cdot \frac{\lambda}{v} \tag{3.11}$$

by drawing $P(t)$ from a uniform distribution between 0 and 1. If this scattering time is larger than it takes the particle to complete the current step, no scattering will take place. On the other hand, if $t_{\text{scat}} < t_{\text{step}}$, the trajectory of the particle is repeated with a step size identical to the scattering time so that the properties of the particle are according to their values just before the scattering will take place. After that, a decision on the specific scattering process, typically elastic or inelastic scattering, is being made, based on their individual cross section contribution. Finally, the scattering process is executed, thereby modifying the properties of the particle while optionally creating new particles.

Scattering types

Scattering processes are treated in the simulation in a modular way so that each process can be handled individually by a so called scattering calculator. This unit is targeted to calculate the cross section depending on the properties of a particle and to execute the interaction process. Multiple calculators with the same species can then be grouped to a scattering module.

The dominant gas species in the main spectrometer is molecular hydrogen, while in the source region this is tritium, with the scattering properties of both isotopes being very

similar. The corresponding cross sections, energy losses and angular changes for elastic [NDS85], [LH94], [TRC83], excitation [ABG94], [CM95] and ionization processes [Rud91] are implemented within different scattering calculators, one for each process.

Further scattering processes for different species can be implemented easily, for example by importing data from the LXcat database [Pit13], which has been done for the processes of electron scattering off argon [PAB+13].

In addition, specific scattering calculators to describe electron interactions in silicon are available. These were adapted from the KESS package [Ren11] and now are completely integrated into KASSIOPEIA.

Surface Interactions

Surface interactions differ from space interactions as they are enforced when the particle crosses a specific surface. The associated surface interaction has to decide whether the particle is transmitted to the next space or reflected back to the actual space. This will modify the properties of the particle accordingly, and result in an angular or energy change when crossing the surfaces of different materials. Of particular importance are processes where particles enter from vacuum into the solid silicon detector or the rear wall.

Bindings

The scattering modules and their sub-components such as the above discussed scattering or density calculators can be replaced during the simulation depending on the actual state of the particle. While space interactions are assigned to specific spaces and will be activated as soon as the particle enters that space, surface interactions are assigned to a geometrical surface and will only be active when the navigation state of the particle is on that specific surface. In the following, an XML example for hydrogen scattering inside the main spectrometer space and interaction with the silicon detector is presented. The silicon interaction consists of a surface interaction when entering the detector space and a space interaction for scattering off the silicon substrate while the particle propagates through the detector.

```
<!-- scattering on hydrogen molecules inside the spectrometer -->
<ksint_scattering name="hydrogen_scattering">
    <calculator_hydrogen name="hydrogen_calculators" elastic="true"
                         excitation="true" ionisation="true" />
    <density_constant temperature="300." pressure_mbar="1.e-10"/>
</ksint_scattering>

<!-- scattering in the silicon of the detector -->
<ksint_scattering name="kess_scattering">
    <inelastic_bethefano name="kess_bethe_fano" PhotoAbsorption="true"
                         AugerRelaxation="false"/>
    <elastic_elsepa name="kess_elastic"/>
    <define name="avogadro_const" value="{6.022141e+23}"/>
    <define name="silicon_molar_volume" value="{12.06*1.e-6}"/>
    <density_constant name="silicon_density"
                      density="{[avogadro_const]/[silicon_molar_volume]}"/>
</ksint_scattering>

<!--  surface interaction, used when entering the detector -->
<kess_surface_interaction name="kess_backscattering" siliconside="inside"/>
```

3.2.6 Termination of particles

The trajectory of a particle has to be terminated once a specific user-defined condition is met. This condition to terminate the propagation of the actual particle can be defined in a

very flexible way, for example when the particle hits the detector after having propagated through the experiment, or by identifying a specific particle property that makes further tracking meaningless, such as when a defined minimal kinetic energy is reached or an undesired direction of the particle manifests. A selection of terminators available within KASSIOPEIA are presented in the following. A particle is terminated

- **min and max z:** once its final state is out of the specified range for the z-position.
- **min and max r:** once its final state is out of the specified range for the radial distance to the z-axis.
- **min and max kinetic energy:** once its final state is out of the specified range of its kinetic energy.
- **min and max longitudinal kinetic energy:** once its final state is out of the specified range of its longitudinal kinetic energy component, according to its momentum parallel to the magnetic field.
- **max time:** once its total propagation time is larger than specified by the user.
- **max length:** once its total propagation length is larger than specified by the user.
- **max steps:** once its total number of steps is larger than specified by the user.
- **trapped:** once its total number of longitudinal momentum sign changes are above a user defined value. This can be used to stop particles that are trapped, but also to terminate particles that get reflected in a MAC-E filter when setting the value to one.
- **death:** if this terminator is active. It is typically placed in a space where the particle should not be or on a surface where the particle should stop.
- **secondaries:** if it is a secondary particles that was created for example in an ionization process.
- **min distance:** once its minimal distance to a set of defined spaces or surfaces is less than a user defined value.
- **output:** once a specified arbitrary output variable (see section 3.2.7) is out of the specified range.

As a terminator module is a small class with a simple structure, additional terminators as required by the user can easily be added. Like all other modules, terminators can be attached to specific navigation spaces or surfaces of the simulation and will only be active once the particle enters that specified geometry. In the following an XML example with a few terminators is presented.

```
<ksterm_max_z name="term_max_z" z="13.93"/>
<ksterm_min_z name="term_min_z" z="-44.0"/>"/>
<ksterm_trapped name="term_trapped" max_turns="1"/>
<ksterm_secondaries name="term_secondaries"/>
<ksterm_max_steps name="term_max_steps" steps="{1e6}"/>
<ksterm_min_energy name="term_min_energy" energy="18540"/>
<ksterm_output name="term_max_scattering"
               component="track_number_of_scatterings" max_value="3"/>
```

3.2.7 Output

The output that will be written to disk for a given simulation depends on the user definition on the type of particle properties that need to be stored for further analysis. A static

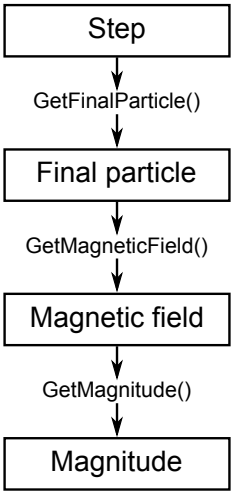

Figure 3.5: Schematic representation of the output component system for the magnitude of the magnetic field at the end of each step. From each object in the toolbox, like the step class in this example, a chain of output components can be created by calling the corresponding getter functions. The last object of the chain can be grouped with other output components and added to the writer, and will then be written to disk in an interval level according to the chosen organization level.

output system that writes down fixed particle properties after each track or even step is therefore not desirable. This is evidently the case when running Monte Carlo simulations with millions of tracks, each track containing millions of steps, as the disk space required to save the simulated information can easily reach problematic dimensions.

Therefore, the output system for the recent version of KASSIOPEIA was designed in a highly flexible way that allows the user to define each individual output component in the XML configuration for the four levels of detail run, event, track and step. It is thus not only possible to store exactly the amount of information that is required, but also this system can easily be extended to include each desired information from each object of the simulation into the output data stream.

In the following the working principle of the output components will be introduced. Then the analysis logic that can be applied to the output stream while writing to disk will be presented, which is followed by a description of the available output writers and readers.

Output components

The output can be configured in a chain-like system starting with a simulation object that has been put into the toolbox. By calling a getter function of the simulation object and repeating the procedure for the resulting object, a chain can be produced with the desired output variable at the end. This will be explained in the following for the example of the magnitude of the magnetic field at the end of each step. A schematic representation is shown in figure 3.5 and the corresponding XML binding required is as follows

```
<ks_component_member name="step_final_particle" field="final_particle"
                     parent="step"/>
<ks_component_member name="final_magnetic_field" field="magnetic_field"
                     parent="step_final_particle"/>
<ks_component_member name="final_magnetic_field_magnitude" field="magnitude"
                     parent="final_magnetic_field"/>
```

The first output component of the chain is the final particle of the step which is created by calling the corresponding function of the step object. The parent of the first output component in each chain needs to be an object stored in the toolbox. From the particle object

the output component of the magnetic field can be created by calling its corresponding function. The data type of the magnetic field output component is a vector with the three components B_x, B_y and B_z, which could also be directly written to the output file. In the case of the given example another output component is added to the chain to obtain the magnitude of the magnetic field vector, which is of scalar data type.

Multiple output components with desired information about the simulation need to be grouped together before they can be added to the object writing the output. Each group corresponds to a tree in the ROOT data structure, which is written simultaneously. When adding an output group to the writer object, the user can choose the level at which this group should be written, i.e. each step, track, event or run. Output groups at step level can be connected to the navigation geometry as any other simulation module and will therefore only be active when the particle is in this corresponding region. An example for a group of step outputs is listed in the following.

```
<ks_component_group name="output_step_basics">
    <component_member name="step_id" field="step_id"
                      parent="step"/>
    <component_member name="time" field="time"
                      parent="step_final_particle"/>
    <component_member name="position" field="position"
                      parent="step_final_particle"/>
    <component_member name="magnetic_field" field="magnetic_field"
                      parent="step_final_particle"/>
    <component_member name="electric_potential" field="electric_potential"
                      parent="step_final_particle"/>
    <component_member name="kinetic_energy" field="kinetic_energy_ev"
                      parent="step_final_particle"/>
    <component_member name="polar_angle_to_b" field="polar_angle_to_b"
                      parent="step_final_particle"/>
</ks_component_group>
```

Although the examples only made use of the step particle's properties for the output, basically each information of the simulation to be obtained with a getter function can be used to construct a chain of output components in the XML configuration file.

Analysis logic

In addition to the large flexibility of the output system, where the user can define exactly which variable at which interval or geometrical state should be recorded, it is also possible to apply a simple analysis logic to the output stream. This is highly useful, if a user is only interested in the maximal kinetic energy of each track for example, but does not want to record the energy information for each step. Storing all this information and perform the analysis after the Monte Carlo is finished, would increase the required disk space significantly.

The available analysis logic for output components within KASSIOPEIA is implemented by determining a minimal, a maximal and an integral value. These output components can be used at any level, but the resulting component should be used at least one level higher than the parent component. For example, the maximal value of a variable which is updated at step level should only be recorded at track level or higher. Additionally, there is a math output component, which can combine arbitrary output components of the same level with a user-defined function.

In the following XML example a math output component is used to calculate the longitudinal kinetic energy component of the particle at each step, using the output components of kinetic energy and the polar angle between the particle momentum and the magnetic field. Furthermore, a minimum output component is used to record the minimal longitudinal kinetic energy, which can be written down for each track.

```
<ks_component_member name="step_final_particle"
                     field="final_particle"
                     parent="step"/>
<ks_component_member name="kinetic_energy"
                     field="kinetic_energy_ev"
                     parent="step_final_particle"/>
<ks_component_member name="polar_angle_to_b"
                     field="polar_angle_to_b"
                     parent="step_final_particle"/>
<ks_component_math name="longitudinal_kinetic_energy"
                   term="x0*cos(x1*TMath::Pi()/180.)*cos(x1*TMath::Pi()/180.)"
                   component="kinetic_energy"
                   component="polar_angle_to_b"/>
<ks_component_minimum name="min_long_kin_energy"
                      component="longitudinal_kinetic_energy"/>
```

Writers and Readers

Apart from a simple ASCI writer, the main writer for KASSIOPEIA is based on the binary data format of a ROOT file with a tree structure. For each selected group of output components of the four organization levels of run, event, track and step, a tree is created with the data objects as branches. Additional meta information is also stored which allows a correct reconstruction of the data. For a simple analysis of the data, the files can be viewed and plotted with a few clicks using the ROOT TBrowser. For a more advanced analysis logic the user has the possibility to write own analysis tools within the KASSIOPEIA package. With the provided reader classes the saved data is reconstructed automatically for user-friendly access.

3.2.8 Navigation

The task of the navigation module is to make sure that the simulation algorithm is always in the state of the current geometry, which houses the particle, as defined by the user in the configuration file. At the beginning of each track the navigator needs to check the geometry of the initial particle position and adjust the simulation algorithm accordingly. After each step the navigator checks if the current space was left, a child space was entered or a surface was crossed. This is done by calculating the distance to all relevant navigation geometries. As a caching system is used, these distances are not computed at each step, but only if the length of the particle's trajectory exceeds the cached limit. If a crossing of any navigation boundary is detected, the position of the final particle is adjusted to the exact geometrical position of the intersected surface.

If this surface is associated with a change of the simulation algorithm, the corresponding commands are executed and the next step of the particle is a surface step, meaning no propagation takes places and only the interaction associated to this surface is executed. Afterwards, the navigator checks if the particle has been reflected or transmitted, depending on the result of the surface interaction. Subsequently, the appropriate commands of the correct space for the particle's next step are executed.

If the crossed surface is part of a space change, without commands attached to it, the navigator will adjust the simulation algorithm according to the corresponding commands. If a space was left, the reverse commands attached to this space are executed, and if a new space is entered, the commands attached to this navigation space are applied. When entering a nested space, the particle is still inside the outer space, and the reverse commands for exiting are not executed. The commands for entering a space therefore have to be defined sequentially.

The change of the simulation algorithm is achieved by commands, which can be used to modify the root classes, as detailed in section 3.2.1. The definition of these commands in the XML configuration file is shown in the following example, where a simulation is set up in a world space with a cylindrical inner volume. When the particle enters this inner volume, the propagation should switch to the exact method, the step output should be written and the particle should be terminated when reaching the bottom surface.

```
<ksgeo_space name="space_world" spaces="world">
    <!-- add trajectory -->
    <command parent="root_trajectory" field="set_trajectory"
             child="trajectory_adiabtic"/>
    <!-- add terminators -->
    <command parent="root_terminator" field="add_terminator" child="term_min_z"/>
    <command parent="root_terminator" field="add_terminator" child="term_max_z"/>
    <!-- define which modules should be used in the inner volume-->
    <geo_space name="inner_volume" spaces="world/inner_volume">
        <!-- replace adiabatic trajectory with exact trajectory -->
        <command parent="root_trajectory" field="clear_trajectory"
                 child="trajectory_adiabatic"/>
        <command parent="root_trajectory" field="set_trajectory"
                 child="trajectory_exact"/>
        <!-- add another terminator -->
        <command parent="root_terminator" field="add_terminator"
                 child="term_min_energy"/>
        <!-- add step output -->
        <command parent="write_root" field="add_step_output"
                 child="output_step_basics"/>
        <!-- define modules on the bottom surface of the inner volume -->
        <geo_side name="bottom_surface" surfaces="world/inner_volume/bottom">
            <command parent="root_terminator" field="add_terminator"
                     child="term_death"/>
        </geo_side>
    </geo_space>
</ksgeo_space>
```

The example shown consists of two navigation spaces and a navigation side. The main navigation space is the world space, with an attached command to set the adiabatic trajectory to the root trajectory object and more commands to add terminators to the root terminator. The world space has an inner volume, with is of special interest to the user in the given example. In this volume the trajectory is replaced by first defining commands for removing the old adiabatic trajectory and then setting the exact trajectory to the root trajectory object. An additional terminator is added in this new space and also the step output is activated by adding an output group to the root writer. The particle should be terminated when reaching the bottom surface of the inner volume. As the corresponding surface is part of a navigation space, it is referred to as navigation side and a command is attached to it which adds a death terminator.

The available command pattern is not limited to the modification of the root classes only, but can be used to modify any object registered in the toolbox, like changing the step size control of a trajectory object or adding a scattering calculator to a scattering module.

3.2.9 Visualization

There are two different visualization options available within Kassiopeia, the 2D Root visualization and the 3D VTK visualization. Both options are completely configurable in the XML configuration file and can be set up to display for example the desired geometry before the simulation starts or the resulting tracks after the simulation is finished.

2D visualization with ROOT

The ROOT visualization module enables simple 2D plots of the simulation components based on the functionality of the ROOT framework. The desired information is drawn into a canvas, which the user can interact with, like zooming in a desired region or modifying the label or colors. The visualization is organized into specific painter objects, each painter fulfilling a designed task. The following painters are available within KASSIOPEIA:

- **Geometry painter:** Paints the intersection of user-defined geometry elements with a 2D plane. The origin and the normal axis of the plane can be configured by the user arbitrarily. Surfaces are displayed as black lines and spaces as green shapes.
- **Track painter:** The track painter reads the output file produced by the simulation and paints the progress of the tracked particles if step data is available. The user can choose the plane the tracks are projected onto as well as the color pattern that should be used for the visualization. Either a set of fixed color patterns can be used, or steps or tracks can be colored individually according to a specified variable of the output data.
- **Potential painter:** Calculates the electric potential values within a defined area and step size and paints the resulting contour plot.
- **Zonal harmonics painter:** Calculates and paints the zonal harmonic convergence region for a specific field setting (see section 3.3.3).
- **Focal plane detector painter:** Paints the geometry of the focal plane detector with its 148 pixels and colors the individual pixels according to the energy deposit of particles in the wafer.

Multiple painters can also be combined to use the same canvas, for example the geometry painter and the track painter. Figure 3.6 shows an example of a visualization with the ROOT painters. The geometry painter and the track painter are combined to draw the results of a simulation of particles propagating through the main spectrometer. The focal plane detector painter is used to visualize the pixel pattern of particles reaching the wafer.

3D visualization with VTK

In addition to the 2D visualization using ROOT, it is also possible to make use of the functionality of the visualization toolkit (VTK) to create 3D graphics of geometries and tracks. As the ROOT visualization module, KASSIOPEIA's VTK module is organized into painters, a geometry and a track painter, among others. When selected in the XML configuration file, an interactive window will open before or after the simulation with the desired visualization. Additionally, a file in the VTK format is written down, which can be opened and edited with tools like PARAVIEW [HAL04], which provides access to a rich variety of graphical options. An image created with PARAVIEW that shows the same geometry and tracks as in the ROOT example is provided in figure 3.7.

3.2.10 KATRIN-specific code

KASSIOPEIA in its most recent version 3 was implemented with the target to be a general particle tracking package with the usage in other experiments outside of KATRIN. Therefore all KATRIN-specific parts of the software were integrated into a specific module, called KSC (KATRIN specific code), allowing to publish the software for general use without the KATRIN-specific parts. For KATRIN-specific calculations, the KSC flag can be activated to access the full KATRIN version of KASSIOPEIA.

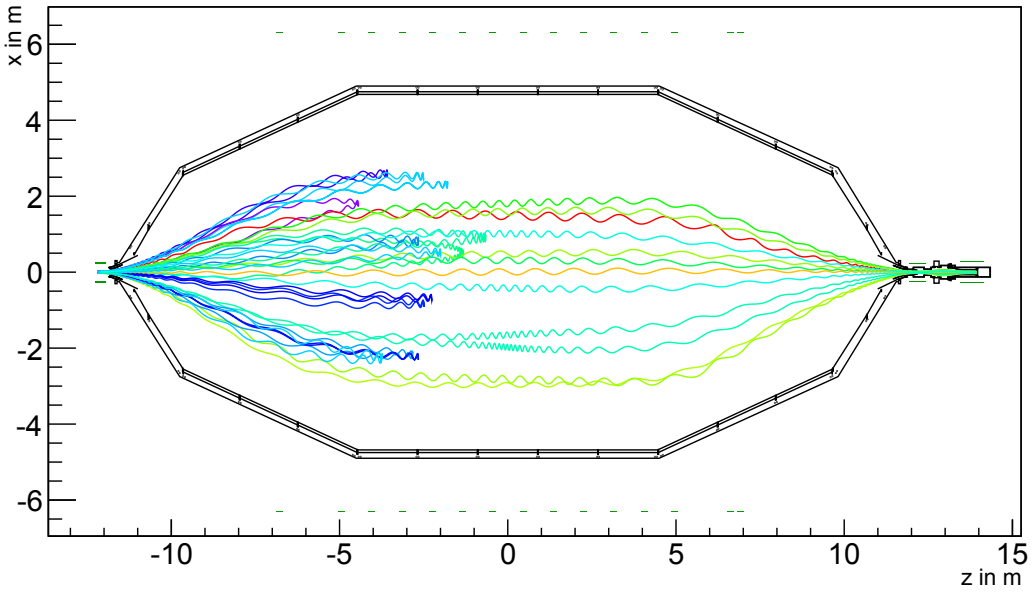

(a) Geometry and track painter

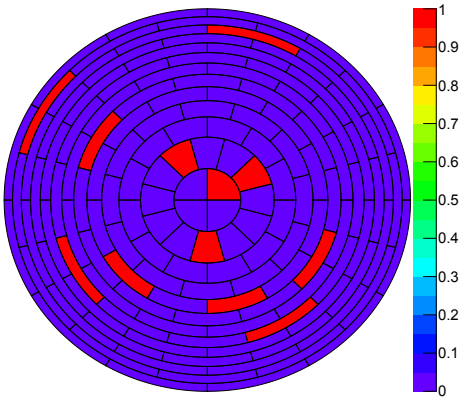

(b) Focal plane detector painter

Figure 3.6: Example Kassiopeia run with 25 particles being tracked through the main spectrometer and visualized with the ROOT painters. The geometry of the main spectrometer electrodes and the magnet system are displayed in the z-x plane together with the simulated tracks (a). The coloring is according to the initial kinetic energies of the particles with small values in blue and large values being displayed in red. The focal plane detector painter (b) shows the pixel pattern of the particles at the detector. In this specific simulation case, muons were chosen instead of the reference case of electrons, to obtain rather large and visible cyclotron radii.

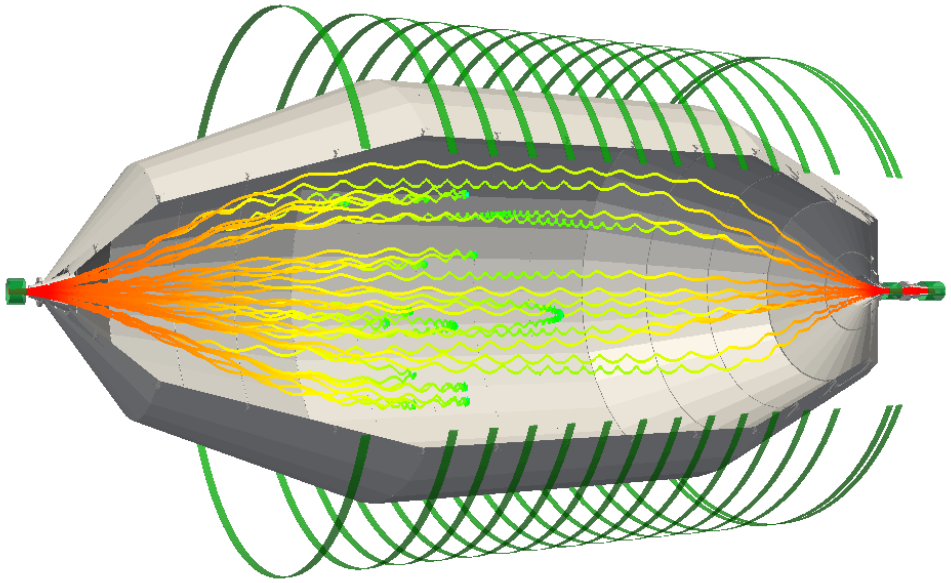

Figure 3.7: The same Kassiopeia run with 25 tracked particles through the main spectrometer as shown in figure 3.6 is now written to a VTK file and visualized with the Paraview software. This time the individual steps have been colored according to the longitudinal kinetic energy of the particle with small values in blue and large values being displayed in red.

Geometrical models

The most important parts of KSC are related to the geometrical models of the experiment. This includes the multiple axially symmetric electrode models for the pre-spectrometer, main spectrometer, detector section and of the transport section and the monitor spectrometer. Additionally, there are models for all solenoids and coils used within the 70 m long experimental setup.

These models are based on simple geometrical shapes defined within XML configuration files which were combined by proper placement and rotation (see section 3.3.1.) These geometries can be used for field calculations by adding electromagnetic properties to them, or navigation purposes in the simulation, as detailed in section 3.2.8.

All individual geometrical models may employ specific coordinate systems, however, when combining various models for a larger simulation, the global coordinate system of KATRIN should be used, which is visualized in figure 3.8.

Additional objects

A variety of additional KATRIN-specific simulation objects exist, such as objects based on the source and spectrum calculation package SSC (see section 3.4.1). These objects include a special generator and density module to calculate particle positions and interaction probabilities for the expected gas density of the windowless gaseous tritium source. Also, a special scattering module for tritium interaction has been implemented, as detailed in section 6.3.

Other examples are generators or terminators related to the focal plane detector to generate particles on the surface of the wafer for specific pixel numbers or pixel rings. This is especially useful for field line tracking and the determination of the magnetic flux as seen by the detector.

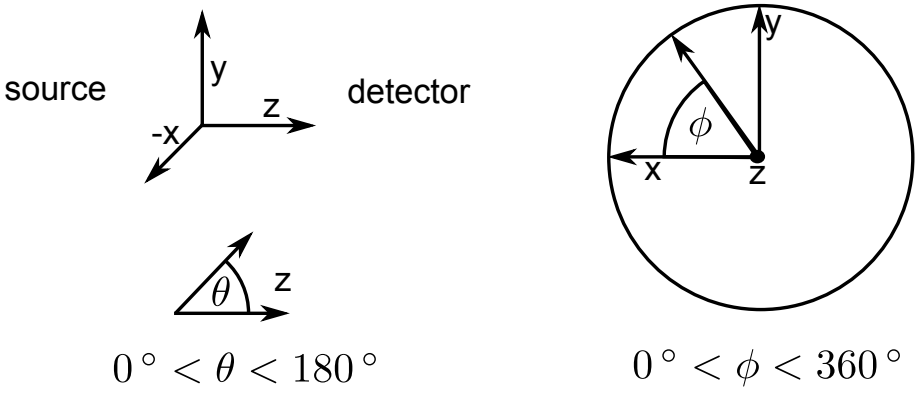

Figure 3.8: The coordinate system used within KASSIOPEIA. The z-axis points from the source to the detector and the y-axis points to the top. The x-axis points in the correct direction to complete the right handed system. The origin (0,0,0) of the coordinate system is in the center of the main spectrometer. The polar coordinates θ and ϕ are defined as visualized.

3.3 Geometry and electromagnetic field calculations

Two key imperatives for particle tracking are geometry definitions and field calculation methods, which were put into separate modules within the KASPER framework. These will be presented briefly in the following.

3.3.1 Geometry module

The geometry module of the KASPER package, KGEOBAG, comprises geometrical classes for a large number of different shapes, linear algebra methods, structures for the relation between geometrical elements and an extension system to add arbitrary properties to shapes.

Shapes

The available shapes are divided into different types of surfaces and spaces. Both can be constructed from an XML configuration file by defining the necessary attributes that are required for the specific geometrical element. Each single shape being created with its own coordinate system depending on the attribute values chosen by the user. In the following example a box space, a cylinder space and a disk surface are constructed.

```
<box_space name="box_A" xa="0.0" ya="0.0" za="0.0"
                        xb="1.0" yb="1.0" zb="1.0" />
<cylinder_space name="cylinder_C" z1="-0.4" z2="0.4" r="0.3"/>
<disk_surface name="disk_a" z="0.0" r="0.1"/>
```

The origin of the box is located in one of its corners, while the origin for the cylinder is in its center.

Beside the above given examples for basic shapes, it is also possible to construct more complex arbitrary shapes. To do so, a set of points is defined which is connected either by lines or arcs. The resulting poly-line can be rotated or extruded to create non-trivial surfaces or spaces. All the features of the XML system as described in section 3.2.2 can be used, such as loops, variable definitions, and mathematical operations. This significantly reduces the amount of lines needed to describe a large number of similar geometrical objects. In addition, more complex type of spaces and surfaces are available to model the as-built experimental setup of the KATRIN beam-line.

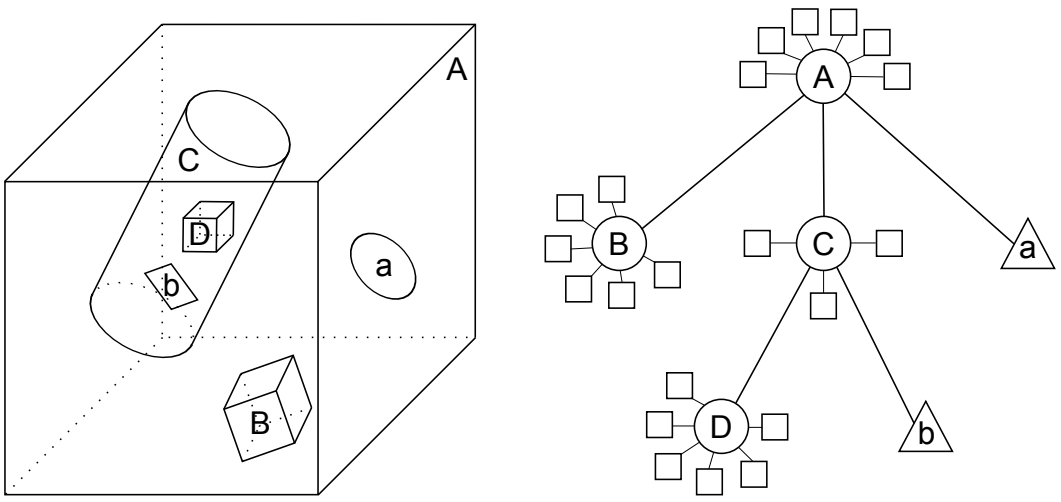

(a) Nested spaces and surfaces (b) Tree structure

Figure 3.9: A set of nested spaces and surfaces (a) and its representation as a tree structure (b). In this example circles represent spaces, squares represent boundary surfaces and triangles represent free surfaces.

Structure

Surface and spaces have to be placed and related to each other to form a nested relationship. Spaces automatically contain a set of boundary surfaces and may also contain other spaces or surfaces. The policy of KGeoBag is that child spaces or child surfaces need to be completely contained within their nesting parent space with no protrusion being allowed.

When a space or surface element is placed inside another space, multiple transformations can be applied to rotate or displace the child space with respect to the coordinate system of the parent space. A nested geometry example with the shapes of the previous section is shown in the following.

```
<space name="outer_box" node="box_A">
    <space name="inner_cylinder" node="cylinder_C">
        <transformation rotation_euler="90 60 -90"/>
        <transformation displacement="0.5 0.5 0.5"/>
    </space>
    <surface name="inner_disk_a" node="disk_a">
        <transformation rotation_euler="90 45 -90"/>
        <transformation displacement="0.5 0.5 0.8"/>
    </surface>
</space>
```

A visualization of the example with additional elements is drawn in figure 3.9 together with its corresponding geometry tree. The tree is used to store the geometry relation internally. When referring to a specific space or surface, the address in the tree is required, as shown in the next paragraph.

Extensions

The geometrical shapes of the KGeoBag module feature an extension system which allows to append arbitrary information to the object. These extensions may contain different types of data for surfaces and spaces.This can be, for the example, the color of a geometrical shape, to be used by a visualization module or an extension with electromagnetic attributes such as the current in a space, or the potential on a surface. The electromagnetic extension

are of prime importance for the field calculation module to compute electromagnetic fields for the given geometry.

In the following an example for an electromagnet is shown, where a current is added to the cylinder of the example of the previous section.

```
<electromagnet spaces="outer_box/inner_cylinder" current="50"/>
```

3.3.2 Field calculation methods

When tracking charged particles, the precise and fast calculation of the magnetic and electric fields is of key importance. In the following the methods to calculate magnetic and electric fields will be detailed together with the KEMField module, where they are being implemented.

Magnetic field calculation

The magnetic field calculation methods used within Kassiopeia can be divided into two separate categories, depending on the geometry of the field generating object:

- **Discrete methods:** The magnetic field generated by complex geometrical forms can be calculated via discrete methods by subdivision of the geometry into numerous small elements. This is a very flexible method, but at the expense of offering a rather slow computation speed only. The discrete calculation method introduced in this section is the integrated Biot-Savart method.
- **Axially symmetric methods:** When the geometrical form is constrained to be axially symmetric, the computation speed can be improved significantly. The methods introduced in this section are making use of elliptic integrals and the zonal harmonic expansion. The latter method has the advantage of being about two orders of magnitude faster to compute, however, the drawback in this case arises from of a required pre-computation step.

Integrated Biot-Savart

The magnetic field generated by an electric current I in a line segment $\mathrm{d}s$ at the position $\vec{r}$ can be calculation according to Biot-Savart's law with

$$\mathrm{d}\vec{B} = \frac{\mu_0}{4\pi} \cdot \frac{I\mathrm{d}\vec{s} \times \vec{r}}{r^3} \tag{3.12}$$

with the magnetic permeability μ_0. Complex shapes can be approximated by creating a number of discretized line current segments, so that for each line segment the magnetic field contribution $\vec{B}_i$ can be calculated by integrating along the line segment $\mathrm{d}\vec{s}_i$. The total magnetic field can then be obtained by summing the individual contributions of the line segments

$$\vec{B}_{\mathrm{total}} = \sum_{i=1}^{N} \vec{B}_i. \tag{3.13}$$

Evidently, the accuracy of this approximation will increase when using a larger number of line segments N, however this comes at the expense of a considerable slower computation speed.

Elliptic integrals

For a thin coil, Biot-Savart's law can be expressed in terms of the complete elliptic integrals of first (I) and second (II) kind:

$$\begin{aligned} K(k) &= \int_0^{\pi/2} \frac{\mathrm{d}\theta}{1-k^2\sin^2\theta} && (I), \\ E(k) &= \int_0^{\pi/2} \sqrt{1-k^2\sin^2\theta}\,\mathrm{d}\theta && (II), \\ \Pi(n,k) &= \int_0^{\pi/2} \frac{\mathrm{d}\theta}{(1-n^2\sin^2\theta)\sqrt{1-k^2\sin^2\theta}} && (III). \end{aligned} \tag{3.14}$$

For a realistic coil with length Z and thickness R, the complete elliptic integral of the third kind (III) is also needed to account for the length and reduce the problem to a one-dimensional integration in radial direction.

The axial and magnetic field components B_z and B_r for an infinitesimal thin solenoid can be calculated according to

$$\begin{aligned} B_z &= \hat{B}_z(Z_{\max}) - \hat{B}_z(Z_{\min}), \\ B_r &= \hat{B}_r(Z_{\max}) - \hat{B}_r(Z_{\min}), \end{aligned} \tag{3.15}$$

with

$$\begin{aligned} \hat{B}_z(Z) &= -\tfrac{\mu_0\lambda}{\pi} \cdot \tfrac{(z-Z)R}{(R+r)S} \left[K(k) + \tfrac{R-r}{2R}(\Pi(n,k) - K(k)\right], \\ \hat{B}_r(Z) &= -\tfrac{\mu_0\lambda}{\pi} \cdot \tfrac{R}{S} \left[2\tfrac{E(k)-K(k)}{k^2} + K(k)\right], \end{aligned} \tag{3.16}$$

and the parameters $S = \sqrt{(r+R)^2 + (z-Z)^2}$, $k^2 = \frac{4Rr}{S^2}$, $n^2 = \frac{4Rr}{(R+r)^2}$ and the linear current density λ [Gar63, Wan13]. The elliptic integrals can be solved with Carlson's method [P+07].

The advantage of this elliptic integral method is the possibility to calculate the magnetic field at any point without the need to discretize the coils in many elements and to use the direct method. Yet, due to the elliptical integration steps, the computation time is still rather large.

Zonal harmonic expansion

A much faster method makes use of the zonal harmonic expansion [Glü11b], where the magnetic field at a point $p(z,r)$ can be expressed in terms of the Legendre polynomial expansion and its derivative at a source point z_0 on the symmetry axis.

For a point p being located within the so called central convergence radius ρ_{cen} of its next source point z_0 (see figure 3.10), the magnetic field can be calculated with the central expansion

$$\begin{aligned} B_z &= \sum_{n=0}^{\infty} B_n^{\mathrm{cen}} \cdot \left(\tfrac{\rho}{\rho_{\mathrm{cen}}}\right)^n \cdot P_n(u), \\ B_r &= -s \cdot \sum_{n=1}^{\infty} \tfrac{B_n^{\mathrm{cen}}}{n+1} \cdot \left(\tfrac{\rho}{\rho_{\mathrm{cen}}}\right)^n \cdot P_n'(u), \end{aligned} \tag{3.17}$$

with the distance ρ between the point p and the source point z_0 and with $s = \sin(\theta)$ and $u = \cos(\theta)$. P_n are the Legendre polynomials of grade n and B_n^{cen} are the corresponding source point coefficients. The central expansion converges faster for small ratios of ρ/ρ_{cen}, which means that using a large number of source points is of advantage, as the overall convergence region will increase. On the other hand, for each source point a number of coefficients has to be calculated beforehand, and the closest source point needs to be found for any field calculation.

As the central expansion is only valid within its convergence radius ρ_{cen}, a remote expansion is needed to calculate the magnetic field values at positions p larger than the remote convergence radius ρ_{rem}

$$\begin{aligned} B_z &= \sum_{n=2}^{\infty} B_n^{\text{rem}} \cdot \left(\frac{\rho_{\text{rem}}}{\rho}\right)^{n+1} \cdot P_n(u), \\ B_r &= -s \cdot \sum_{n=2}^{\infty} \frac{B_n^{\text{rem}}}{n} \cdot \left(\frac{\rho_{\text{rem}}}{\rho}\right)^{n+1} \cdot P_n'(u), \end{aligned} \tag{3.18}$$

with the remote coefficients B_n^{rem} (see figure 3.11). As in case of the central expansion, the series will converge faster if the ratio ρ_{rem}/ρ is small. The central as well as the remote source point coefficients depend on the used solenoid geometry as well as the currents and will be automatically stored to disk and used again for the same settings within Kassiopeia.

It is also possible to compute the field of multiple coils that do not share a common symmetry axis by dividing the coils into corresponding groups. For each group a set of source points can be calculated and the magnetic field can be obtained in the group's coordinate system. The magnetic field of each group is then transformed back into the reference system and the fields are summed up.

The zonal harmonic method is much faster compared to elliptic integrals, but even in case of a fine spacing of source points the magnetic field can not be calculated in all regions, for example very close to the coils. Therefore, a combination of both methods is used for maximal speed and flexibility. For most cases within the KATRIN beam line, the magnetic field parameters inside the beam tubes are needed, where the zonal harmonic expansion is valid.

Electric field calculation

The calculation of the electric field and potential can also be divided into discrete and axially symmetric methods. For axially symmetric geometries, elliptic integrals and zonal harmonic expansions similar to the magnetic field calculation can be used. In contrast to the magnetic field however, which is generated by an electric current, a quantity that can be directly measured, the electric potential and field is created by a charge distribution, which is usually not known a priori. The charge density distribution depends on the voltage on the individual electrodes but also strongly on their geometry, as the charge densities are influenced by their surroundings. There exists a variety of methods for electric field calculation such as the finite difference method [LeV07], the finite element method [BS08] and the boundary element method [Gib08]. The first two methods divide the volume into a meshed grid, so they are not applicable to the exceedingly large dimensions of the KATRIN experiment, due to the ensuing computer memory bottleneck. The boundary element method (BEM) is thus the preferred method for KATRIN, as it is efficient for problems with small surface to volume ratios.

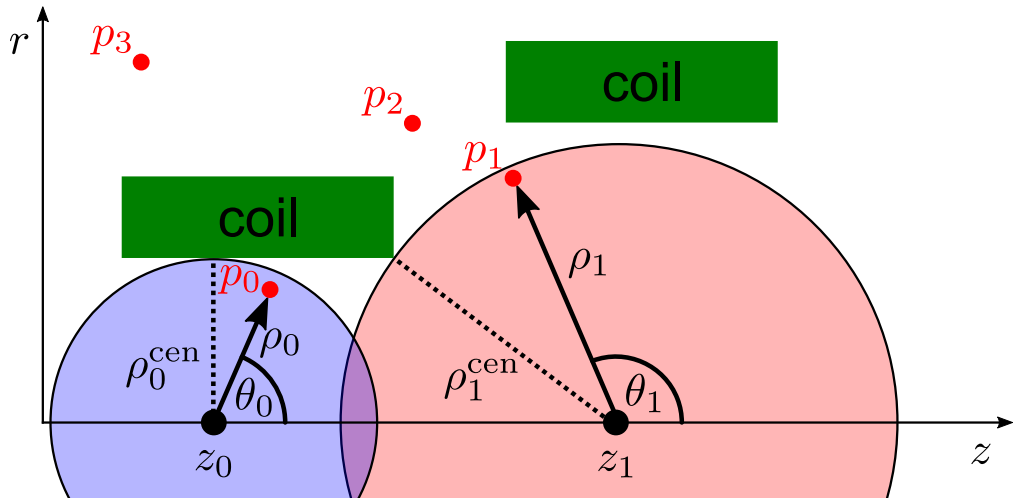

Figure 3.10: Central convergence region for two different source points z_0 (blue) and z_1 (red) on the symmetry axis. The magnetic field at point p_0 can be calculated with the central expansion for source point z_0 and the magnetic field for point p_1 can be calculated with the central expansion for source point z_1. The magnetic fields at the points p_2 and p_3 can not be calculated with the central expansion, as they are not in the convergence region of any source point.

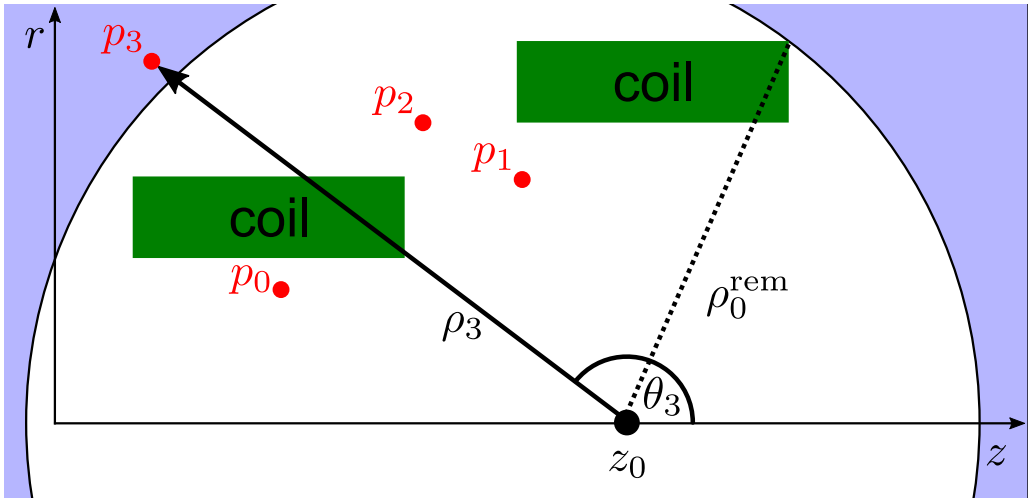

Figure 3.11: Remote convergence region for the source point z_0 on the symmetry axis (blue). The magnetic field at point p_3 can be calculated with the remote expansion for source point z_0. The magnetic fields at the points p_0, p_1 and p_2 can not be calculated with the remote expansion, as they are not in the convergence region of any source point.

Boundary element method

When applying BEM, the electrode geometry needs to be split into a large number of small subelements. On each subelement surface the charge density is approximated to be distributed homogeneously. The discretization into surface elements allows to adapt the model to complex shapes with variable levels of detail and accuracy. The discretization of a geometry S into N subelements

$$S = \sum_{j=1}^{N} S_j, \tag{3.19}$$

evidently will lead to a better accuracy for larger numbers of N, again at the expense of increasing amounts of required computation time and memory.

In a first step the individual charge densities σ_j for each element S_j need to be calculated. They are related to the applied electrostatic potential on each electrode by

$$U_i = \sum_{j=1}^{N} C_{ij}\sigma_j, \tag{3.20}$$

with the Coulomb-matrix-elements $C_{ij} = C_j(\vec{r_i})$, which can be calculated according to

$$C_j(\vec{r_i}) = \frac{1}{4\pi\epsilon_0} \int\limits_{S_j} \frac{1}{|\vec{r_i} - \vec{r}_S|} \mathrm{d}^2\vec{r}_S. \tag{3.21}$$

The charge densities can be obtained by solving the linear algebraic equation system (3.20) by making use of the Gauss-Jordan-algorithm, for example [P+07]. As the required computation time and memory will grow with the size of the matrix as N^2, the possible number of elements is limited. This can be handled by employing iterative solvers, such as the Robin Hood algorithm, for example [F+12]. The calculated charge densities for a specific geometry and applied potential are automatically stored to disk for later use within Kassiopeia.

To calculate the electric potential at a specific point $\vec{r}$, it is necessary to integrate over all subelements to obtain

$$\Phi(\vec{r_i}) = \frac{1}{4\pi\epsilon_0} \int\limits_{S} \frac{\sigma(\vec{r_S})}{|\vec{r} - \vec{r}_S|} \mathrm{d}^2\vec{r}_S. \tag{3.22}$$

The computation speed for this direct method scales with the number of subelements N and is therefore not very fast for large N. As in case of the magnetic field calculation, the electric field of an axially symmetric geometry can be calculated using elliptic integrals and zonal harmonic expansions [Glü11a] with the same advantages and disadvantages as detailed in the last section.

3.3.3 KEMField

The field calculation methods introduced above are comprised in the KEMField package, written by T.J. Corona [Cor14]. KEMField is a module of the Kasper framework and is used for the field calculations within Kassiopeia.

The geometry of the experimental setup is defined in XML configuration files, as detailed in section 3.2.10, and can be directly fed into KEMField for fast and accurate field calculation. For axially symmetric models, the field parameters can be calculated using the zonal harmonic expansion as detailed in the previous section.

Additionally, a detailed 3D model of the main spectrometer based on CAD data has been implemented, including details resulting from the deformation of the vessel hull due to gravity. This model consists of about $5 \cdot 10^6$ elements of triangles, rectangles and line segments. A visualization of the geometry is provided in figure 3.12. Due to this large number of elements the calculation of the charge densities is a huge challenge which can only be performed successfully by employing a hybrid MPI and GPU parallel algorithm. This computation takes about a week on a cluster with more than 3500 nodes [Cor14].

The calculation of the electric field requires a summation over all $5 \cdot 10^6$ elements. The evaluation of a single field point therefore takes about one second on a single CPU. This is much too slow for Monte Carlo particle tracking simulations, as even in the fast adiabatic approximation the propagation of a particle through the whole experiment needs a few thousand steps, each requiring 13 field evaluations.

Nevertheless, the detailed model is extremely useful and important for single field calculations inside the main spectrometer, especially near the analyzing plane in the center, which is needed to analyze the measurements of the radial potential inhomogeneity in chapter 5. In figure 3.13 a visualization of a calculation of the potential in the analyzing plane is shown.

3.4 Tools to estimate the neutrino mass sensitivity

To estimate the sensitivity of the KATRIN experiment to the neutrino mass and to study the influence of different experimental parameters of this key parameter, a sophisticated model of the resulting electron spectrum measured at the detector is required as well as a set of powerful statistical tools for the analysis. This is provided by the Kasper modules SSC and KaFit, both are introduced in the following sections.

3.4.1 Source and Spectrum Calculation

The Source and Spectrum Calculation (SSC) module implements the computation of source-specific properties and the calculation of differential and integrated tritium β-decay spectra. The initial steps of development were based on the works of W. Käfer and M. Hötzel [Käf12, Hoe12]. This works were further improved by M. Kleesiek [Kle14] to include additional systematic effects and in particular complex numerical tools for higher performance and accuracy.

As the SSC module is a module within Kasper, its initialization is realized by the same building system with the full user friendly XML initialization process, as introduced in section 3.2.2.

Modeling of the source

The calculation of the gas dynamic properties of the source section is one of the major tasks of the SSC software module. The 10 m long source region can be subdivided into individual segments, so called voxels. For each one, critical key parameters such as local density, velocity, and temperature of the tritium gas can be calculated and allocated. A longitudinal segmentation into slices along the beam axis is the minimum requirement to account for inhomogeneities of the gas dynamics or the magnetic field. In addition, SSC allows a radial and azimuthal segmentation following the pixel pattern of the detector

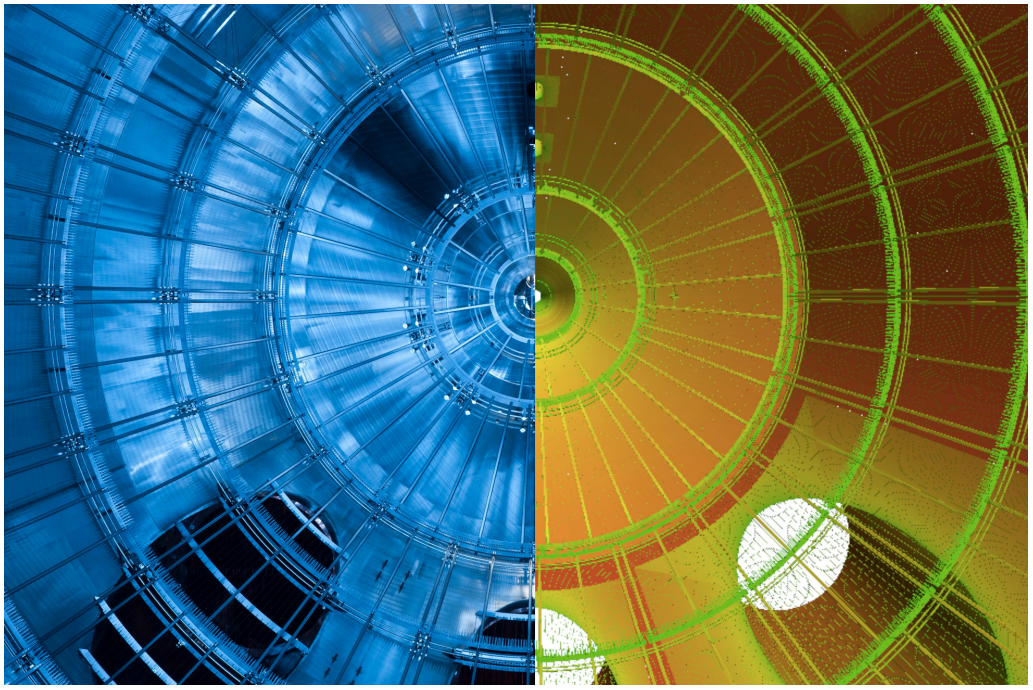

Figure 3.12: A side-by-side comparison of a photograph looking downstream inside KATRIN's main spectrometer (left) and its representation in KEMFIELD (right). Picture from [Cor14]

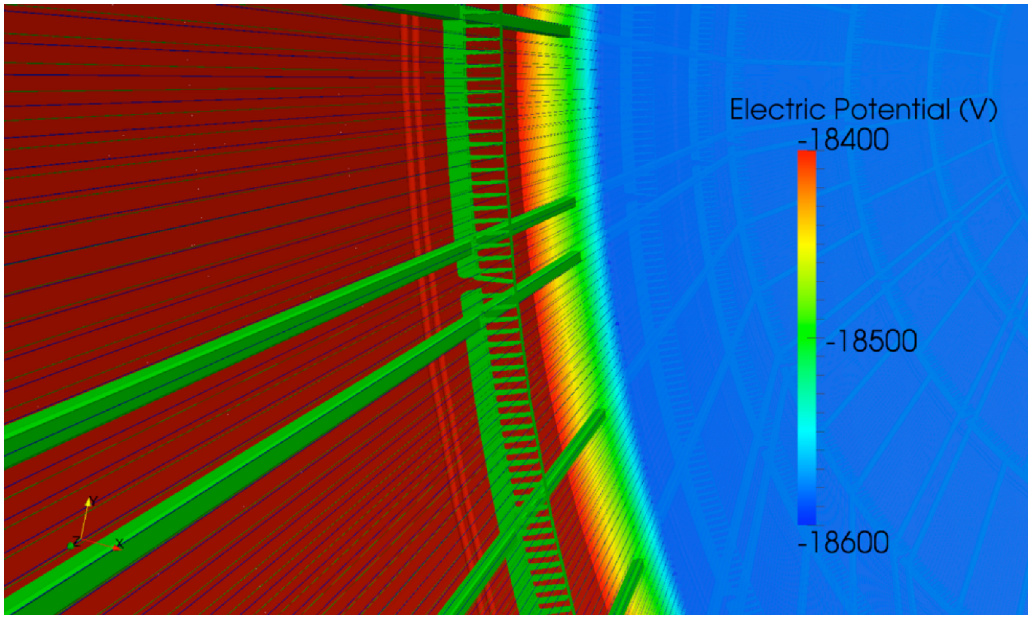

Figure 3.13: Visualization of the inner wires of the main spectrometer and the corresponding detailed 3D potential simulation. The vessel hull (red) is on −18.4 kV, the wire holding structure with the outer wire layer (green) and on −18.5 kV and the inner wires (blue) on −18.6 kV. The surface of the analyzing plane is also colored according to the local electric potential. Simulation and picture by T. Corona.

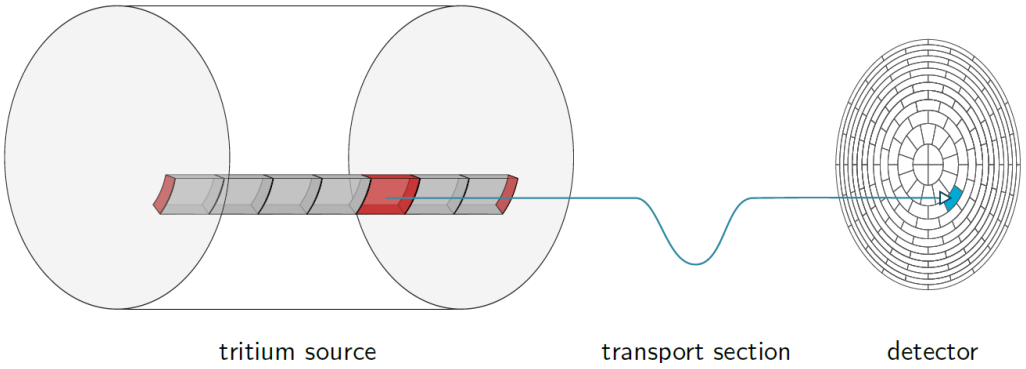

Figure 3.14: Schematic segmentation of the source into voxels in radial and azimuthal direction according to the detector pixels and additionally axially along the beam direction. Figure from [Kle14].

wafer. In doing so each part of the source with its parameters can be mapped to a specific pixel, as illustrated in figure 3.14.

To calculate the gas density and velocity, a sophisticated model based on the full solution of the Boltzmann equation is used. It covers gas dynamics from the hydrodynamical regime at high pressure at the injection ports up to the free-molecular regime observed at low pressure at the pumping ports [Hoe12]. The gas density is proportional to the total number of tritium molecules, and thus the β-decay activity of a source voxel. A voxel also has a specific scattering probabilities for signal electrons scattering off tritium gas. Furthermore, the voxel-specific bulk velocity of the gas along the beam line leads to an energy shift of the spectrum, due to Doppler broadening.

The temperature profile along the source beam tube influences not only the density of the tritium gas, but the thermal gas movement, which also causes a Doppler broadening of the differential β-decay spectrum. From the experimental point of view, this implies that the temperature is monitored constantly [GBH+13], with actual thermistor data being used as input to calculate the temperature of individual voxels.

When calculating the magnetic field in the source, the field solvers and geometric models of Kassiopeia and KEMField can be used. Together with a pre-defined magnetic flux volume, the radius for each voxel can be calculated depending on the local magnetic field strength. The source magnetic field also defines the maximal polar angle θ_{max}, which is 50.77 °, for the two reference values of $B_{\mathrm{S}} = 3.6\,\mathrm{T}$ and $B_{\mathrm{max}} = 6.0\,\mathrm{T}$. This maximal polar angle is not constant over the whole source, but it depends on the local magnetic field. This fact will influence the shape of the transmission function, the elastic and inelastic scattering probabilities of electrons, the radiative energy losses caused by synchrotron radiation, and finally also the absolute rate.

Differential tritium spectrum

The differential tritium β-decay spectrum is calculated according to classical Fermi theory, as introduced in section 1.3.3. This description is refined by several modifications that need to be included being of comparable size to a non vanishing neutrino mass. Details with respect to the most important modifications, are highlighted in the following, with more details in [Hoe12, Kle14].

- **Fermi function:** The Fermi function $F(Z', E)$ describes the Coulomb interaction between the daughter nucleus with charge Z' and the outgoing electron with energy E. In case of tritium β-decay, the outgoing electron is attracted by the positively charged nucleus, thus shifting the spectrum to slightly lower energies.

- **Radiative corrections:** When electrons are emitted within the Coulomb field of a nucleus, they experience energy losses due to their interaction with virtual and real photons. This correction only becomes relevant close to the tritium endpoint.
- **Final states distribution:** In the molecular decay of T_2 to the daughter molecule $(^3HeT)^+$, rotational, vibrational and electronic states can be excited. These states are represented by a final state distribution with an excitation energy E_F and probability P_f. As the excitation energy of the final states will reduce the maximal possible electron energy in the decay, the spectrum is modified. The resulting β-decay spectrum is thus a superposition of a large number of single branches, each one with a lower effective endpoint, weighted by the final states probability. Moreover, as the source does not only consist of pure T_2, but also incorporates smaller amounts of the tritiated hydrogen isotopologues DT and HT, the corresponding decay into daughter nuclei with different final state distributions have to be included.
- **Nuclear recoil:** After the decay process of tritium, the daughter molecule $(^3HeT)^+$ experiences a recoil and carries away a small amount of kinetic energy. This energy is nearly constant close to the tritium endpoint with a typical value of about 1.7 eV.
- **Doppler effect:** The thermal motion and the bulk velocity of tritium molecules in the source region will lead to a broadening of the energy spectrum as described above. This is mathematically handled as a convolution of the β-decay spectrum with a Maxwellian distribution.

Integral tritium spectrum

As the KATRIN experiment will observe an integral spectrum of the β-decay electrons, owing to its MAC-E filter measurement principle, the expected signal rate at an applied retarding potential $\dot{N}_S(qU_0)$ is an integral of the differential spectrum rate $\frac{dN}{dE}$ and the response function $R(E, qU_0)$ of the apparatus. Considering the segmentation of the source, an integral rate can be computed for each detector pixel j, where the corresponding voxels in longitudinal direction are aggregated to an effective segment. The integral rate for each retarding potential U_0 and pixel j can then be expressed as

$$\dot{N}_S^j(qU_0) = N_T^j \, \epsilon_{det}^j \, \frac{\Omega^j}{4\pi} \int_{qU_0}^{E_0} \frac{dN^j}{dE}(E_0, m_\nu^2) \cdot R^j(E, qU_0) dE, \tag{3.23}$$

with the total number of tritium nuclei N_T and the detector efficiency ϵ_{det} corresponding to pixel j. The solid angle $\Omega = 2\pi \cdot (1 - \cos(\theta_{max})$ accounts for electrons being emitted with a polar angle larger than θ_{max}, which are not able to reach the detector due to magnetic reflection. This factor needs to be accounted for, as the response function is normalized to θ_{max}.

More details about the analytical calculation and the Monte Carlo simulation of the response function will be presented in section 6.1.

3.4.2 KaFit

The KaFit module, developed by M. Kleesiek [Kle14], contains a variety of statistical tools and probability models to extract a neutrino mass from observed data. It also allows to study the impact of systematics and measurement strategies on the neutrino mass sensitivity. The sensitivity is a statement about the combined statistical and systematic

uncertainties of the experiment. Due to the statistical nature of an observation, an experiment can not determine the true value of the neutrino mass for example, but it has to make a best-fit estimate (measurement) and state a confidence interval.

To study the sensitivity and the impact of different systematics, KaFit generates toy measurements, which can be investigated with a set of different probability models and statistical methods for parameter fitting and confidence interval construction.

Generating a toy measurement

To simulate a 3-year-long neutrino mass measurement with the KATRIN experiment, the integrated signal rate for each retarding potential $\dot{N}(qU_0)$, as calculated with the SSC module according to equation 3.23, needs to be multiplied with the total measurement time spent at this retarding potential t_{qU_0}. This leads to the mean number of β-decay signal electrons at the potential qU_0 counted by the detector

$$N_{\mathrm{S}}(qU_0) = \dot{N}(qU_0) \cdot t_{qU_0}. \tag{3.24}$$

The set of applied retarding potentials together with the time spent at each point is called the measuring time distribution, which can be configured arbitrarily. The actual measuring time distribution has a large impact on the neutrino mass sensitivity, as the influence of a non-vanishing neutrino mass is more prominent close to spectrum endpoint, where the count rate is rather low. More information about the measuring time distribution and strategies for its optimization can be found in [Kle14].

To generate a toy measurement, the total number of counts on the detector for each retarding potential is calculated by drawing from a Poissonian with $\lambda = N_{\mathrm{S}}(qU_0)$ and adding a background contribution corresponding to its probability distribution. Multiple models can be used for the background, for example a background of Poissonian nature or a background model based on radon decay with a non-trivial time structure [Mer12, Kle14, Ört14].

It is important to note that the calculation of rates and β-decay spectra within KaFit is purely based on analytical methodes. This is of great benefit in terms of computation speed, but to incorporate all details of the measurement apparatus, a more comprehensive particle tracking Monte Carlo simulations has to be performed, as detailed in chapter 6.

Sensitivity calculation from ensemble tests

To estimate the neutrino mass from a toy measurement, the difference between the simulated measurement and the theoretical probability model needs to be minimized. This can be described by a Likelihood function, or approximated by a chi-square statistic

$$\chi^2(m_\nu^2, E_0, A_{\mathrm{S}}, R_{\mathrm{b}}) = \sum_i \sum_j \left(\frac{N^j_{\mathrm{meas}}(qU_i) - N^j_{\mathrm{th}}(qU_i, m_\nu^2, E_0, A_{\mathrm{S}}, R_{\mathrm{b}})}{\sigma^j_{\mathrm{th}}(U_i)} \right)^2 \tag{3.25}$$

with the applied retarding potentials U_i, the detector pixel j, and the 4 free fit parameters of the squared neutrino mass m_ν^2, the tritium endpoint E_0, the signal amplitude A_{S}, and mean background rate R_{b}. For the reference measuring time distribution [KAT05] 41 different retarding potentials are used. If the segmentation of the detector is activated for all 13 rings, the total number of summands is 533, and for a full detector segmentation of 148 pixels the χ^2-sum consists out of 6068 terms in total.

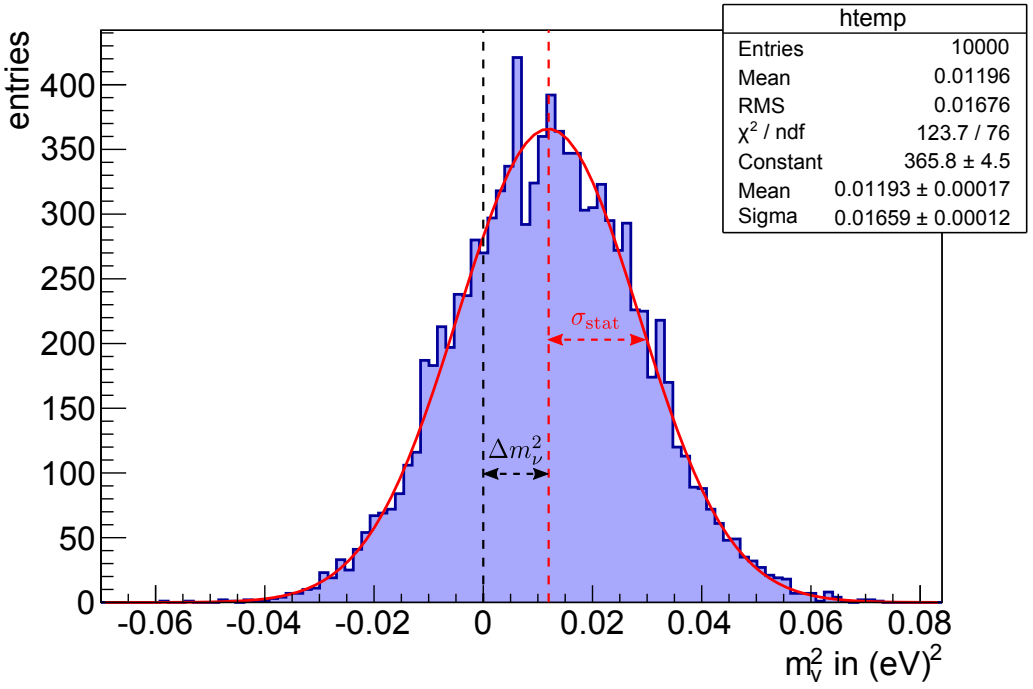

Figure 3.15: Example of an ensemble test with 10000 fits and an input neutrino mass of $m_\nu = 0\,\mathrm{eV}$. A systematic shift was induced on purpose by using different experimental parameters for the toy measurements and the theoretical model. A Gaussian function was fitted to the distribution of obtained values of m_ν^2 with $\mu = 11.9 \cdot 10^{-3}$ and $\sigma = 16.6 \cdot 10^{-3}$. The induced systematic error can be determined by the shift of the Gaussian distribution from the input value of the neutrino mass, and its standard deviation is a measure of the statistical sensitivity.

For the minimization of the chi-square term a set of different minimizers is available within the KaFit module, like Minuit from the Root library [ABB+09], or a selection of Markov Chain Monte Carlo algorithms [Kle14].

The statistical sensitivity on the neutrino mass as well as the impact of systematics can be obtained by performing ensemble tests. In this method a large number of random toy measurements is generated. By minimizing the chi-square function in equation 3.25, a best-fit estimate of m_ν^2 is obtained for each generated toy measurement. The resulting distribution of the obtained values for m_ν^2 is filled into a histogram and plotted in figure 3.15 for an example ensemble test with a sample size of 10000 and an input neutrino mass of $m_\nu = 0\,\mathrm{eV}$. Additionally, the magnetic field in the analyzing plane B_A was set to a different value in the theoretical model and the toy measurement. By fitting a Gaussian function to the obtained distribution, its mean μ and standard deviation σ can be determined.

The difference between the mean of the Gaussian function and the input neutrino mass of $\Delta m_\nu^2 = 11.9 \cdot 10^{-3}\,(\mathrm{eV})^2$ can be interpreted as systematic error caused by the difference in the parameter values between the toy measurement and the theoretical model used for the fit. When repeating this ensemble test for a set of experimental parameters, their impact on the measured neutrino mass m_ν can be obtained. In this way the required stability or knowledge of the absolute values of key experimental parameters can be established. The total systematic error budget for KATRIN is envisaged to $\sigma_\mathrm{sys} = 17.0 \cdot 10^{-3}\,(\mathrm{eV})^2$ [KAT05], thus the individual contributions of experimental parameters need to be much lower.

The standard deviation of the Gaussian function of $\sigma = 16.6 \cdot 10^{-3}$ can be interpreted as the statistical sensitivity of the squared neutrino mass. The 90% C.L. sensitivity of the

neutrino mass can then be constructed by

$$S_{m_\nu} = \sqrt{1.645 \cdot \sigma_{\mathrm{tot}}} \tag{3.26}$$

with

$$\sigma_{\mathrm{tot}} = \sqrt{\sigma_{\mathrm{stat}}^2 + \sigma_{\mathrm{sys}}^2} \tag{3.27}$$

being the quadratically combined statistical and systematic uncertainty on m_ν^2. The sensitivity (90% C.L.) on the neutrino mass for the standard deviation of the given example of $\sigma_{\mathrm{stat}} = 16.6 \cdot 10^{-3}\,(\mathrm{eV})^2$ and the envisaged systematical error of $\sigma_{\mathrm{sys}} = 17.0 \cdot 10^{-3}\,(\mathrm{eV})^2$ can thus be calculated to $S_{m_\nu} = 198\,\mathrm{meV}$.

An application of the possibility to perform ensemble test with the SSC and KaFit modules will be given in section 5.5, where the influence of the radial inhomogeneity of the electrostatic retarding potential and the electromagnetic field in the analyzing plane will be investigated. In chapter 6 the response function of the KATRIN experiment will be obtained by a Monte Carlo tracking simulation and the appertaining effects will be compared to the analytical calculations of the SSC module, and the influence on the neutrino mass measurement caused by their neglection will be presented.

3.5 Simulation and analysis of transmission properties

The KATRIN Transmission Analysis Package (KTrAP) consists of multiple tools to investigate, simulate and analyze transmission properties of electrons through the beam line. It is a module of the Kasper package and makes extensive use of most of the other modules, like KEMField for field calculation, Kassiopeia for field line and particle tracking, KaFit for parameter estimation, and KaLi and Beans for access as well as analysis of measured data. KTrAP has been designed and developed by the author of the thesis at hand. Some parts, such as the optimization of the analyzing point positions, are based on other contributions [Wan13], which have been put into the objective oriented extensible structure, which can be configured with an XML file.

The main parts of KTrAP are the determination of the analyzing point positions of the main spectrometer, depending on the electromagnetic configurations (section 3.5.1), and the simulation and analysis of transmission functions (section 3.5.2).

3.5.1 Determination and optimization of the analyzing point positions

Evidently, the electromagnetic properties of the MAC-E filter are of prime importance in high-resolution tritium β-decay spectroscopy, in particular the electric potential and magnetic field at the analyzing plane. The position of the analyzing plane does not necessarily coincide with the very center of the main spectrometer. Also, in general, it will not be a 2D plane at all. The analyzing point for each field line will depend on the rather complicated interplay of the electrostatic potential and the magnetic field. The determination and optimization of these analyzing points plays an important role in the SDS commissioning measurements, which will be detailed in chapter 4, where also the implemented mathematical and physical models will be introduced. In the following a brief overview on the tools will be given.

Determination of the analyzing point positions

To determine the distribution of analyzing points for a specific field line, the minimal longitudinal kinetic energy along the electron's path has to be found, as will be detailed in section 4.3. The simulation to obtain these field lines can be done using Kassiopeia by setting up a corresponding XML configuration file. Then the KTrAP object calculates the longitudinal kinetic energy using the information of the magnetic field and electric potential at each field line point. To do so, KTrAP is added in the XML configuration file after the Kassiopeia sequence to be automatically executed when the simulation is finished. Additionally, visualization objects can be added to show the progress of chosen electromagnetic parameters along the field line and finally the position of analyzing points (see section 4.3.4).

Depending on the electromagnetic settings of the main spectrometer the simple yet fast axi-symmetric models are not sufficient anymore, so a full 3D model of the main spectrometer (see section 3.3.3) is needed for precise calculation of the actual analyzing points. In contrast to particle tracking, where the usage of the slow 3D model is limited, the simulation of field lines only relies on the magnetic field. The electric potential to calculate the longitudinal kinetic energy can thus be added later. KTRaP makes use of this fact and can automatically parallelize the potential calculations with the 3D model on a cluster, leading to fast and accurate results (see section 4.3.5).

Optimization of the analyzing point positions

The distribution of analyzing points can be optimized, in particular with respect to their distance from the center position of the main spectrometer. This can be done by defining specific criteria for the magnetic field properties, as will be detailed in section 4.3.2, and by varying the currents of the 14 coils of the LFCS to achieve the pre-defined requirements. This corresponds to a minimization problem, and KTrAP thus makes use of the variety of available minimizers of the KaFit module for its solving. The defined criteria for the magnetic field, as well as the required minimizer can be set up in an XML-configuration file.

3.5.2 Transmission function simulation and analysis

KTrAP comprises a variety of different tools for the precise study of simulated or measured transmission functions. This enables the investigation of various influences, the refinement of the needed measurement strategy and the optimization of the analyzing procedure. The two most important functionalities are introduced briefly in the following.

Transmission function creation

A transmission function for a MAC-E filter can be described by the observed number of counts (or the rate) as function of the energy of the transmitted electrons with respect to the analyzing point potential. Within KTrAP a common file format is used to describe a transmission function, both for measured or simulated data. Also, data obtained from the fitting procedures, such as background, amplitude or the radial potential offset are stored in the file, too.

This transmission function can be created for example from measured data using a Beans analysis sequence, where, depending on the measurement run number, the used voltages and detector rates for its sub-runs are retrieved from the data base with KaLi. In case of a Kassiopeia simulation, multiple output files with different electron energies or spectrometer potentials are automatically combined. This has the advantage that all analysis tools can be used both for measurement and simulation data.

Determination of source and spectrometer properties

An important task of transmission function measurements is to determine key spectrometer properties such as the analyzing point electric potential and magnetic field, as will be detailed in chapter 5. This is only possible once the energy and angular distributions of the source, for example an electron gun, are well known (see section 5.1.5). With the tools provided in KTRAP, these distributions can be extracted from dedicated electron gun measurements to be stored in a file for later use. Multiple distributions are available, in particular a Gaussian distribution, but it is also possible to extract the energy distribution numerically (see section 5.2).

Once the source properties are known, and the analytical model derived in section 5.1 is used, the spectrometer properties can be obtained by fitting the model to measured transmission functions using a user-defined minimizer from KAFIT. This is detailed in section 5.4 in the framework of the analysis of radial potential inhomogeneities in the analyzing plane.

4. Commissioning measurements of the spectrometer and detector section

During summer of 2013, an extensive four month measurement campaign was undertaken, in which the main spectrometer and the focal plane detector system were operated together the first time as a combined instrument. This commissioning of the spectrometer and detector section (SDS) is an important part of the thesis at hand, as the author contributed significantly to the results through electromagnetic simulations, run time coordination and the measurement and analysis of the transmission properties of the main spectrometer, the latter being described in chapter 5. The main goal of the first SDS commissioning measurements was the confirmation of the proper functioning of the main spectrometer in its role as high resolution MAC-E filter system with regards to its transmission characteristic and background composition. Additionally, all hardware and slow control components were tested together the first time, and the analysis and simulation software was to be validated with real measurement data. The achieved success in all these fields of work is an important milestone for the KATRIN experiment, in particular as only a few sub-components with non-optimal performance could be identified. These sub-components were significantly improved afterward for the next SDS commissioning measurement phase currently taking place in late 2014.

The focus of this chapter is to give an overview of the first SDS commissioning measurements and provide a description of all required preconditions for an analysis of the transmission function measurements in chapter 5. In the first section 4.1, the hardware used during the SDS commissioning, its deviations from the reference KATRIN beamline setup, like the integration of an electron gun at the entrance of the main spectrometer instead of the pre-spectrometer, and the performance of the individual subcomponents are described. The verification of the precise alignment of the focal plane detector system and the electron gun, as described in section 4.2, is an important requirement for the analysis and interpretation of transmission function measurements. Before the start of the SDS commissioning measurements, the electromagnetic field configuration of the main spectrometer had to be optimized with regards to transmission properties. The optimization process and the achieved results will be presented in section 4.3. The monitoring of the magnetic field is an important task and was realized by the magnetic field monitor, as described in section 4.4. It turned out to be an essential quality assurance tool during the SDS commissioning measurements, as it reduced operating mistakes in the magnetic field configuration significantly. Finally, a short summary about the results of the per-

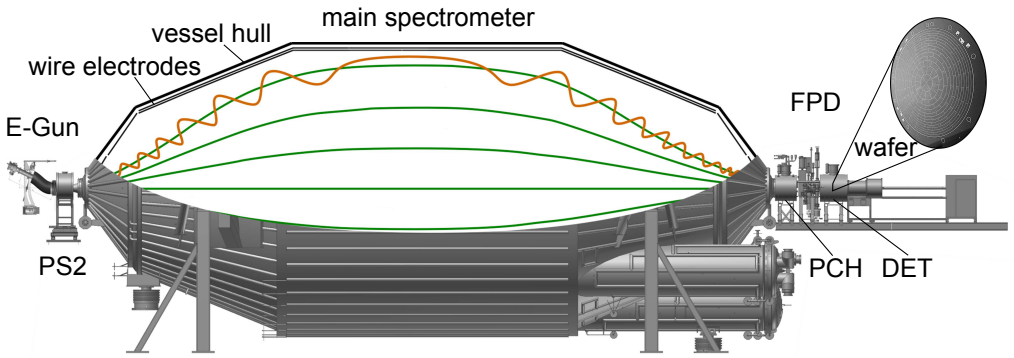

Figure 4.1: The 30 m long beamline for the first SDS commissioning measurements consists of the big main spectrometer vessel in the center, an electron gun (E-Gun) on the south side (left) and the focal plane detector system (FPD) on the north side (right), containing a silicon wafer with 148 pixels. The magnet system consists out of four superconducting solenoids, the pre-spectrometer magnets 1 and 2 (PS1 (not shown) and PS2) and the pinch (PCH) and detector (DET) magnets. The large scale air coil system surrounding the vessel is not shown. The vessel hull is put on high potential by the high voltage system, typically at $U \approx -18.5\,\mathrm{kV}$ while the inner electrode system is put on an additional negative potential of $\Delta U \approx 100\,\mathrm{V}$. Inside the main spectrometer magnetic field lines are drawn, the top one being orbited by an electron flying from the electron gun through the spectrometer to the detector. Its cyclotron motion has been artificially increased for this sketch.

formed background measurements during the SDS commissioning phase will be presented in section 4.5.

4.1 Hardware configuration and performance

The hardware in use during the first commissioning measurements of the spectrometer and detector section (SDS) will be detailed in the following. A schematic side view of the 30 m long experimental setup is provided in figure 4.1. The most prominent component in the center is the main spectrometer whose background and transmission conditions were the prime target of this measurement phase. It will be described in detail in section 4.1.1 together with its vacuum system. The double layer inner wire system, which fine-tunes the electrostatic potential and suppresses background processes, could only be used in a single wire configuration in the SDS commissioning measurement, due to a short circuit that developed during the preceding bake out phase. The inner electrode system, the consequences of the non-functionalities of double layer configurations, and its sophisticated high voltage system will be described in more detail in section 4.1.2. Magnets in use for the SDS commissioning measurements are the two pre-spectrometer solenoids on the south side of the spectrometer (PS1, PS2) and the two detector solenoids on the north side (PCH, DET), completed by 14 large aircoils of the low field correction system (LFCS) and 2 cosine coils of the earth magnetic field compensation system (EMCS). The solenoids have not been operated at their design fields for different reasons, as detailed in section 4.1.3. On the north side of the spectrometer the detector system with its segmented 148 pixel silicon wafer is installed as in the final KATRIN setup. Its operation conditions in the SDS commissioning measurements are described in 4.1.4. Instead of the pre-spectrometer an angular selective electron gun was installed on the south side of the main spectrometer during the SDS commissioning measurements, which is described in 4.1.5, and which was used to generate electrons with a specific energy and angular distribution to investigate the spectrometer transmission properties.

4.1.1 Main spectrometer vessel and vacuum system

The main spectrometer is the world's largest ultra high vacuum recipient in operation. Together with the magnet system it forms the most advanced MAC-E filter for precision electron spectroscopy up to 35 keV. The spectrometer vessel was manufactured by *MAN DWE GmbH* out of stainless-steel (grade 316LN/1.4429) with a thickness between 25 and 32 mm and has a mass of 200 t. With a length of 23.3 m and an inner diameter of 9.8 m it has a total volume of 1240 m^3 and an inner surface of 690 m^2. On both ends of the spectrometer vessel, specially developed beam pipes with in-line flapper valves are installed, which allow the attachment of the electron gun and the detector system, without breaking the vacuum in the main spectrometer. Two DN200 full-metal gate valves, which are installed at the electron gun and at the detector provide an additional possibility to separate both sub-components within the measurement phase for stand-alone preparations or calibrations. They also act as rather fast safety switches in case of Penning discharges.

Vacuum system

For the investigation of transmission properties the actual vacuum attributes in the main spectrometer are less relevant. However, an excellent ultra-high vacuum (UHV) inside the vessel is of key relevance to keep the background level below the ambitious design goal of 10 mcps. Therefore, the main spectrometer is equipped with a sophisticated UHV pumping system based on active elements in form of turbomolecular pumps (TMP) and passive ones implemented as non-evaporable getters (NEG) to allow pressures down to 10^{-11} mbar. A NEG pump is located in each of the three major pump ports, which are welded on the conical detector side of the main spectrometer. These pump ports have an inner diameter of 1.7 m, a length of 3 m, and each contains a total of 1 km of *SAES St 707* getter strips which provide a combined pumping speed for hydrogen of about 10^6 l/s. Additionally, a liquid nitrogen-based baffle system [Gör14] is installed in each pump port to prevent the emanation of radon isotopes from the NEG pumps into the vessel by cryogenic sorption. Radon emanation is a major source of background as described in 4.5.4. Attached to two of the three pump ports are a total number of 6 *Leybold Turbovac MAG W 2800* TMPs installed in a cascaded setup with a combined pumping speed for hydrogen of about 10^5 l/s [W$^+$14].

Bake out

Preceding the SDS commissioning measurements a dedicated bake-out phase of the main spectrometer took place in January 2013. The bake-out is not only necessary to improve the vacuum conditions by releasing gas components such as H_2O molecules from the inner surface but also to activate the passive NEG pumps. To bake out a massive stainless steel vessel to a temperature regime up to 350° C a large scale heating system is required. This is implemented as 0.5 MW oil-based heating system, manufactured by *HTT*. As heat transfer fluid *Malotherm* oil was used, supported by electric heating tapes placed on all protruded parts like the pump ports. The temperature was increased up to 300° C. At that point the bake-out cycle had to be stopped and the temperature was ramped down again, as several short circuits in the inner electrode system developed, as described in more detail in the next section. The total length of the baking cycle was about a month, as the temperature could only be ramped slowly to avoid large temperature gradients at the wire electrode modules. More details about the UHV system and the baking cycle can be found in [Gör14].

Achieved pressure during SDS Commissioning Measurements

Due to the incomplete activation of the NEG pumps as a result of the shortened bake-out process and owing to an air leak that opened during the cool down which could

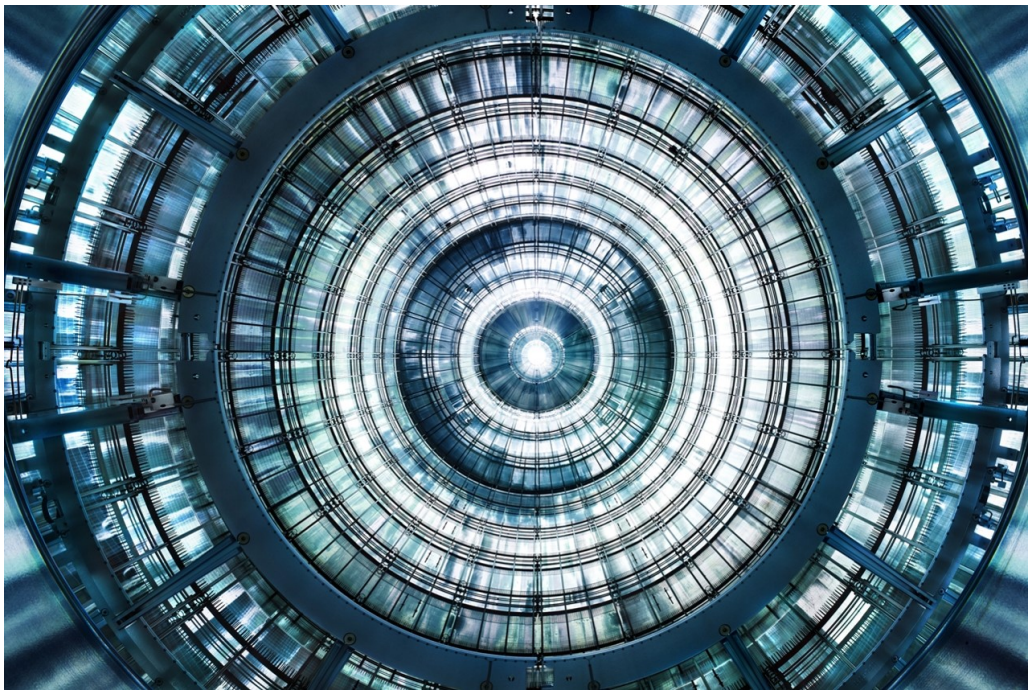

Figure 4.2: Photo of the inner surface of the main spectrometer. The whole surface is covered by more than 2300 wires with a diameter of 200 and 300 µm, mounted on 248 modules. Photo from KIT.

only be repaired provisionally, the pressure in the main spectrometer vessel during the commissioning measurements was (only) in the order of 10^{-10} mbar [GTW13]. This is one order of magnitude above the design value, but still sufficient for the measurements that were carried out [BBB+14].

4.1.2 Inner electrodes and high voltage system

The entire main spectrometer vessel is elevated to a negative high voltage in order to provide the retarding potential for the MAC-E filter. Therefore, the vessel support structures are insulated against high voltage of up to −35 kV and the main spectrometer beam line is insulated with ceramic cones on both sides to allow its connection to the grounded electron gun and the grounded detector system.

Inner electrode system

As visible in figure 4.2, nearly the complete inner surface of the main spectrometer vessel is equipped with a modular double-layered wire electrode system. It consists of 248 modules, distributed on 15 rings arranged coaxially to the beam line, as shown in figure 4.3. It comprises more than 23000 wires in total, with diameters of 200 and 300 µm. On both ends of the spectrometer, full-metal ground electrodes made of pure aluminium and field correcting anti-Penning electrodes made of titanium are installed. All inner wire electrode rings, which are additionally split into an east and a west part, and both anti-Penning electrodes can be put on separate potentials, which is required for the following reasons:

- The wire electrode modules can be put on a negative potential compared to the spectrometer vessel hull, with a maximum applicable potential offset of 1 kV. This creates an electric field between the wire modules and the spectrometer vessel and allows to shield electrostatically against low-energy electrons released from the inner vessel surface by cosmic muons, radioactivity or field emission. As the sophisticated

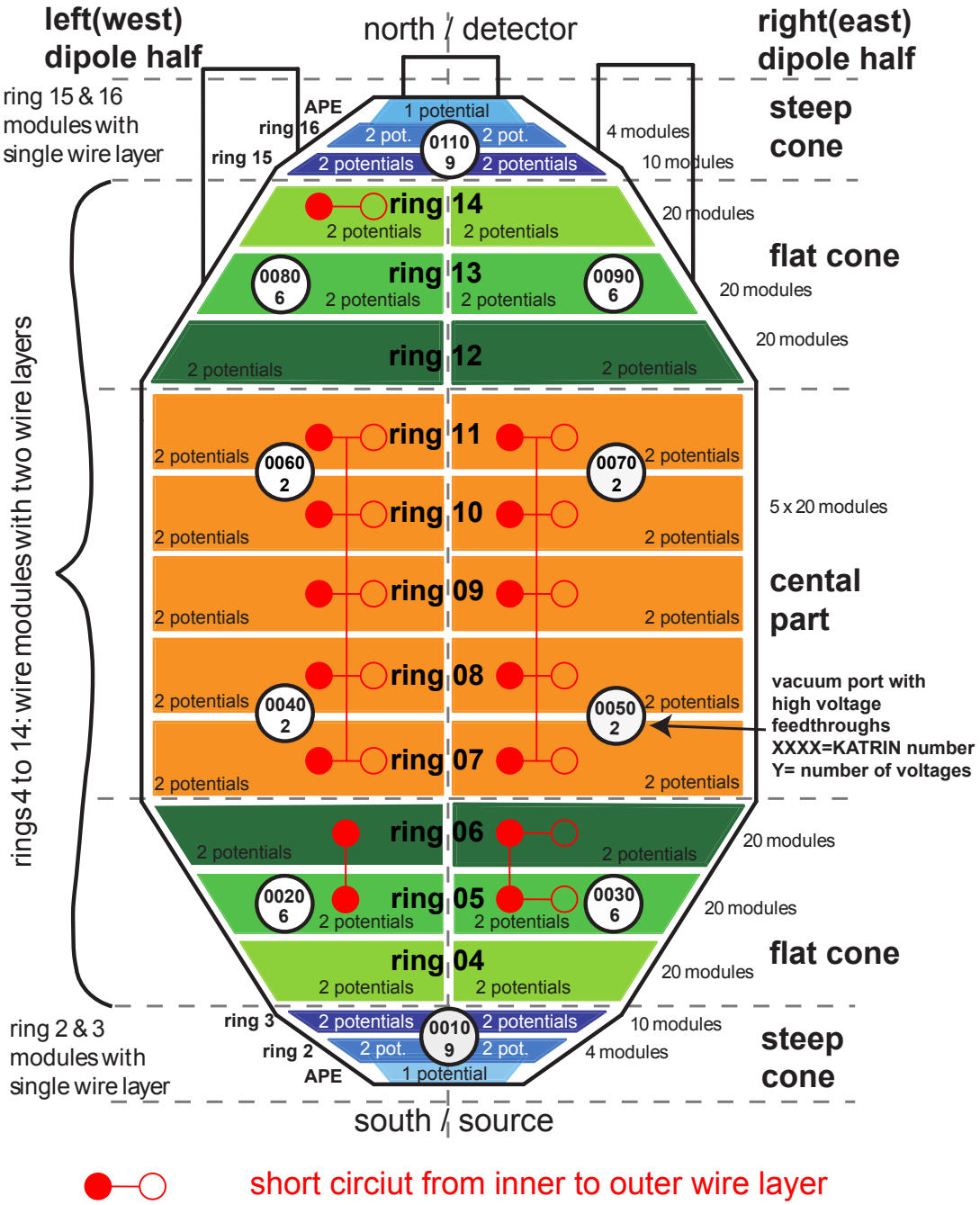

Figure 4.3: Overview of the 16 inner electrode rings of the main spectrometer. Additionally, the short circuits, that developed during the bake out phase, have been outlined. Figure adapted from [HOZW13]

holding structure of the wires is on the same potential as the wires, its non-negligible mass will contribute to background electrons. Therefore, all wire modules, except those in the steep cones, have a second inner wire layer. This inner layer is isolated from the holding structure and can therefore be put on a different potential for additional electrostatic shielding, leading to a total expected shielding factor of about 10^2 [KAT05]. With the dominant magnetic shielding factor of 10^5 a total background reduction of the order of 10^7 can be expected (see section 4.5.1.

- As the individual wire module rings can be elevated onto different potentials, the MAC-E filter retarding potential can be fine-shaped to optimize the electron transmission conditions and filter properties, see section 4.3).
- The coaxial alignment of the electrode system relative to the main spectrometer axis was verified by laser tracker measurements, demonstrating that the wire rings form an almost perfect circle with local deviations of 0.5 mm. The vessel on the other hand is subject to deformations caused by its own weight in the order of 20 mm [Jur09]. Accordingly, the deviations in the homogeneity and axial symmetry of the electrostatic field caused by the vessel deformation is greatly suppressed by the perfectly aligned wire modules [BCG$^+$13].
- Fluctuations on the main spectrometer vessel potential, caused for example by electronic noise originating from devices attached to the vessel like TMPs, are suppressed similarly [BBB$^+$14].
- Additionally, the electrode system is divided into two half shells, an eastern and a western part. With a maximum applicable potential difference of 1 kV between the two half shells, a static or pulsed electric dipole can be created. This dipole can be used to efficiently remove stored low-energy electrons in the sub-keV range via the resulting $\vec{E} \times \vec{B}$ drift [Wan13].

More detailed technical information about the inner electrode system can be found in [Hug09, Zac09, Val06, Val09, Val10, Pra11].

Short circuits in the inner electrode system

During the bake-out phase of the main spectrometer in January 2013, multiple electrical short circuits developed in the inner electrode system. The reason for these short circuits result from the inner high-voltage distribution lines which run from the high voltage feedthroughs on the top of the spectrometer to the wire modules. These 4 mm thick connections are made out of copper beryllium (CuBe) which suffered from thermally induced deformations in the bake-out phase. Due to gravity they bended downwards and in various cases they touched the wire holding structure, leading to a short circuit between the inner and outer wire layer [HOZW13]. As a result, most of the wire modules could only be used in a one wire layer configuration, as illustrated in figure 4.3. The consequences of this drawback are a reduced electrostatic shielding, as the inner wire layer is on the same potential as the outer wire layer and the support structure. While the large surface of the main spectrometer can be electrostatically shielded, the massive support structure of inner electrode system remains unshielded, which is expected to increase the muon-related background rate by a factor of 10 [BCG$^+$13].

An additional consequence is the influence of the complex holding structure on the homogeneity and axial symmetry of the electrostatic retarding potential. For radii above 3.7 m, parts of the support structure (c-beams) cause a strong azimuthal dependency of the potential, and the wire holding combs on the edge of each wire module cause a shift of the maximal potential away from the middle of the spectrometer [BCG$^+$13].

Therefore, the short circuits play a crucial role in the investigation of the main spectrometer transmission properties, which is an essential part of the thesis in hand. Due to short circuits' influence, the transmission properties are more difficult to determine (see chapter 5), and they are also different than in a setup which is supposed to be used for the neutrino mass measurements. Additionally, the transmission properties were also modified by other components in an undesired way, like the magnet system alignment or the high voltage distribution system as detailed in the next sections. Hence, the motivation for the determination of the transmission properties during the first SDS commissioning measurements was also to test and validate the developed simulation software and analysis models.

High voltage distribution system

Due to the large number of individually applicable potentials to the inner electrode system and the requirement for precise and stable voltages up to 35 kV at the ppm level, a sophisticated high voltage distribution system is needed [Kra14]. In the SDS commissioning measurements, less precise high voltage devices were used than in the final KATRIN setup to protect the highly sensitive equipment, as this was the first time the main spectrometer and all inner electrodes were put on high voltage. The topology used in the SDS commissioning measurement is given in figure 4.4. The main spectrometer vessel is operated at a common potential provided by a single high voltage power supply with a range of up to 35 kV, while the remaining power supplies sit on a high voltage rack on the common potential and add an additional offset potential to the inner electrodes. The main power supplies used to provide an offset between vessel and inner electrodes are the two dipole power supplies. There is one unit for the east half of the spectrometer and one for the west half, both providing a potential of up to 1 kV. Additionally, there are 46 offset power supplies, 23 for each dipole half, adding a supplementary offset of up to 500 V to the dipole potentials. Therefore, the effective potential on a certain wire layer is the sum of the common, dipole and offset potentials. While the common and the dipole potentials only have a precision of about 10^{-3} of their nominal value, the lower voltage power supplies for the offset potentials are working with high precision of better than 10 mV when regulated at voltages above 0.5 V [BBB$^+$14].

High voltage configurations during SDS Commissioning Measurements

From the point of view of high voltage usage, the SDS commissioning measurements can be divided into two separate parts. For about the first half of the measurement time, it was not possible to apply high voltage to the main spectrometer vessel due to safety regulations. Only the inner electrode system could be used and the maximal possible retarding potential was limited to 1 kV. Furthermore, both electrode half shells have been operated with the same power supply, as the dipole mode was not required at that time.

After all safety regulations had been fulfilled to put high voltage on the main spectrometer, the second part of the SDS commissioning measurements had been carried out with high voltage on the vessel and a separate power supply for each dipole half, as described in the previous section.

A logical consequence of the described high voltage topology which is of significant importance to transmission function measurements is the resulting distortion in the symmetry of the electrostatic retarding potential. The limited precision and reproducibility of the two power supplies for the two half shells of the inner electrodes led to a potential difference between the east and the west part of the spectrometer of 0.4 V, resulting in a static dipole inside the spectrometer volume. An additional voltage difference between the modules arises from the offset power supplies, which only work with high precision when regulated at voltages above 0.5 V. When they were not actively used, which means their

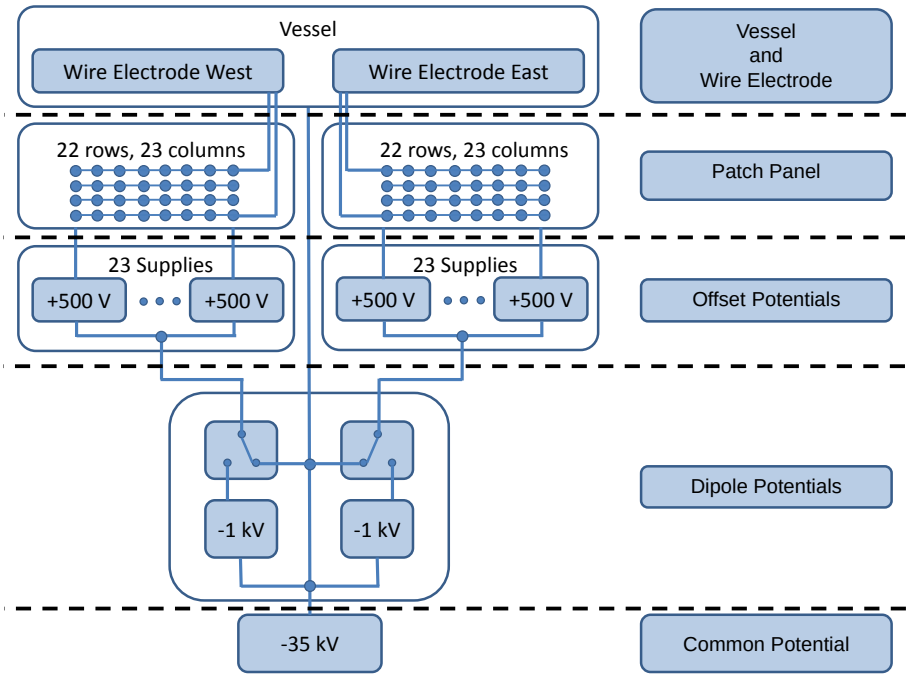

Figure 4.4: High voltage distribution system for the SDS commissioning measurements. The main spectrometer vessel is fed by a common supply of up to 35 kV. The east and west side of the wire electrodes are fed separately by two dipole potential power supplies up to 1 kV, sitting on the common potential and can be enabled by relays. Each inner wire layer can now be customly connected to one of the 46 offset power supplies with an additional offset of up to 500 V. Figure from [BBB+14]

set point was set to zero, they still produce output potentials of up to 2 V. The power supplies for the central cylindrical part of the spectrometer had the largest offset, although being most important for the analyzing plane potential. This does not only imply that there is an additional dipole field in the spectrometer, but it breaks the mirror symmetry of the electric potential in the middle of the vessel, as inner electrodes on the north side of the spectrometer have a slightly different potential than inner electrodes on the south side.

During the SDS commissioning measurements this effect remained unnoticed, the dipole was only discovered after the measurement phase was finished. However, as the actual values of the potentials of all power supplies were measured continuously and written to a database, the exact potential on each wire module can be reconstructed. While the influence of this effect on the measured background rate still is under investigation, its impact on the transmission function measurements is significant: The originally calculated magnetic settings (see section 4.3) do not imply optimized transmission conditions anymore and the analysis of transmission function measurements gets much more complicated, as detailed in chapter 5.

4.1.3 Magnet system

During the SDS commissioning phase the magnetic flux tube featured a field direction from detector to source. It was produced by 4 solenoids, 14 large air coils of the low field correction system (LFCS) and 2 cosine coils of the earth magnetic field compensation system (EMCS). Their specifications and the settings in use during the SDS commissioning phase are detailed in the following.

Table 4.1: Overview of the solenoids in use during the SDS commissioning measurements, with the design axial z position, the field generating current I and the resulting magnetic field B in the center of the magnet.

solenoid	z position in m	current I in A	magnetic field B in T
PS1	-15.500	103.8	3.0
PS2	-12.104	149.7	4.3
PCH	12.184	72.6	5.0
DET	13.784	54.6	3.5

Superconducting solenoids

The two s.c. solenoids of the focal plane detector system are the pinch (PCH) and the detector (DET) magnet, both arranged coaxially to the beam line with the beam tube being installed in their warm bores. Both magnets can produce a maximal magnetic field of 6 T and are operated in persistent mode, which means that the superconducting coil is short circuited and forms a superconducting loop. The magnet will therefore preserve its magnetic field, although the power supply is switched off. Due to technical constraints, the magnetic field of the pinch magnet was limited to 5 T during the SDS commissioning measurements. For the detector magnet, a magnetic field of 3.5 T was used.

The two solenoids on the other side of the main spectrometer are the pre-spectrometer s.c. magnets, labelled PS1 and PS2, both capable of producing a maximal magnetic field of 4.5 T. In contrast to the detector solenoids, the pre-spectrometer solenoids are operated in driven mode, which means that the superconducting coils are connected to the power supplies continuously. The pre-spectrometer was not installed during the SDS commissioning measurements, as the space between the two pre-spectrometer magnets was reserved for the electron gun, see section 4.1.5. The PS1 magnet therefore was positioned closer to the electron gun and powered to a magnetic field of 3.0 T only. The second pre-spectrometer magnet PS2 was placed at its design position at the entrance of the main spectrometer with a magnetic field of 4.3 T.

An overview of the solenoids, their actual z position at the beam axis, their field-generating current I and the resulting magnetic field B in their center can be found in table 4.1. While the current of the two detector solenoids could be measured rather precisely (in the order of a few mA [Cry08]), before switching to persistent mode, the current of the two pre-spectrometer solenoids could only be obtained by reading the displays on the power supplies. As these values were not continuously monitored and written to a database the actual currents and therefore also the magnetic field suffers an imprecision in the order of a few ampere for the nominal value of about 150 A. In addition, both magnets were ramped up and down multiple times during the SDS commissioning measurements by different operators.

Large volume air coil system

As outlined in section 2.2.5, the magnetic flux tube in the main spectrometer produced by the superconducting solenoids has to be modified by additional measures. The magnetic field in the analyzing plane is too small to contain the desired flux tube volume of 191 Tcm^2 inside the spectrometer. The shape of the flux tube is asymmetric, due to the different type of magnets, different fields and different positions on both sides. Also, the earth magnetic field in the analyzing plane is not negligible anymore and deforms the flux tube even further. As countermeasures, a large volume air coil system is installed around the main spectrometer, as shown in figure 4.5. It consists of two independent sub-systems,

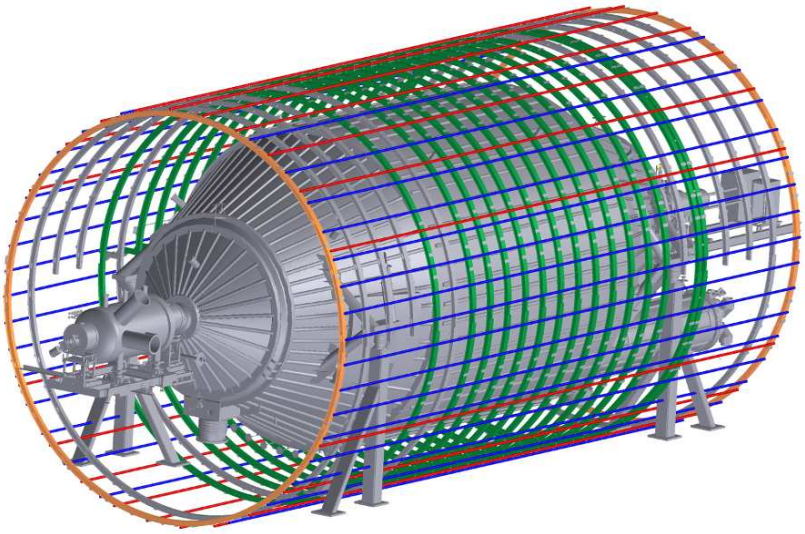

Figure 4.5: The main spectrometer vessel surrounded by the large volume air coil system. The 14 coils of the LFCS are painted in green color. The blue and red straight segments belong to the vertical and horizontal EMCS. They are connected via circular segments at the orange end rings.

the low field correction system LFCS and the earth magnetic field compensation system EMCS [G+13].

Low field correction system - LFCS

The LFCS is composed of 14 large coils, which are arranged coaxially to the main spectrometer vessel with a radius of 12.6 m. Each coil is powered separately by a *Delta Elektronika SM3000* power supply to allow flexibility in adjusting the field layout. The power supplies are limited to a maximum current between 100 and 125 A, corresponding to a maximum magnetic field in the analyzing plane of 1 mT. Figure 4.6 shows the magnetic flux tube, as seen by the detector with the reference values of the SDS commissioning measurements, with and without LFCS contribution. It is clearly visible that the LFCS is essential to create a symmetric flux tube that fits into the main spectrometer vessel.

During the SDS commissioning measurements multiple settings for the LFCS were in use. For regular measurements of the spectrometer MAC-E filter properties the magnetic field was optimized with regard to the transmission conditions, as detailed in section 4.3. The two most important settings are a low magnetic field setup, commonly referred to as "3.8 Gauss setting", and a high magnetic field setup, commonly referred to as "9 Gauss setting". The individual LFCS currents for those settings are summarized in table 4.2 and their derivation is detailed in section 4.3. The names of these settings originate from the magnetic field in the analyzing plane produced by all coils. It is important to note that the total magnetic field in the analyzing plane, considering also the non-compensated earth magnetic field component along the spectrometer axis of 20 μT, is $3.6 \cdot 10^{-4}$ T and $8.8 \cdot 10^{-4}$ T respectively.

Earth magnetic field compensation system - EMCS

The earth magnetic field at the KATRIN experiment is $B_{\text{earth}} = 48.2\,\mu\text{T}$, with the components in the KATRIN coordinate system of $B_{\text{x}} = 5.0\,\mu\text{T}$, $B_{\text{y}} = -43.6\,\mu\text{T}$ and $B_{\text{z}} = 20.0\,\mu\text{T}$ [Nat]. As shown in figure 4.7, the magnetic flux tube would be deformed significantly due to its presence without proper countermeasures.

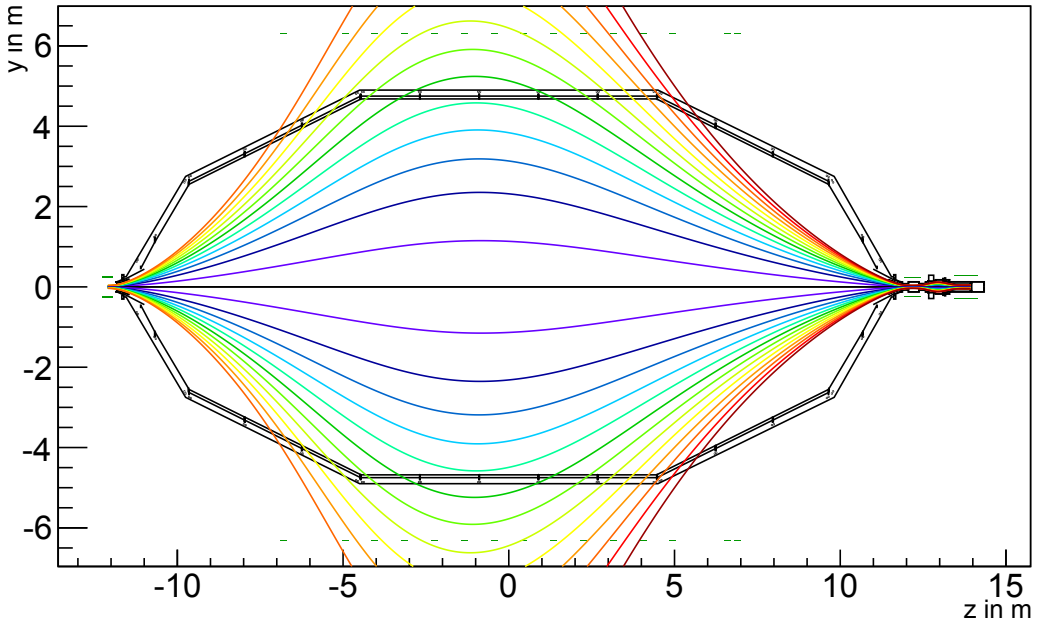

(a) LFCS switched off

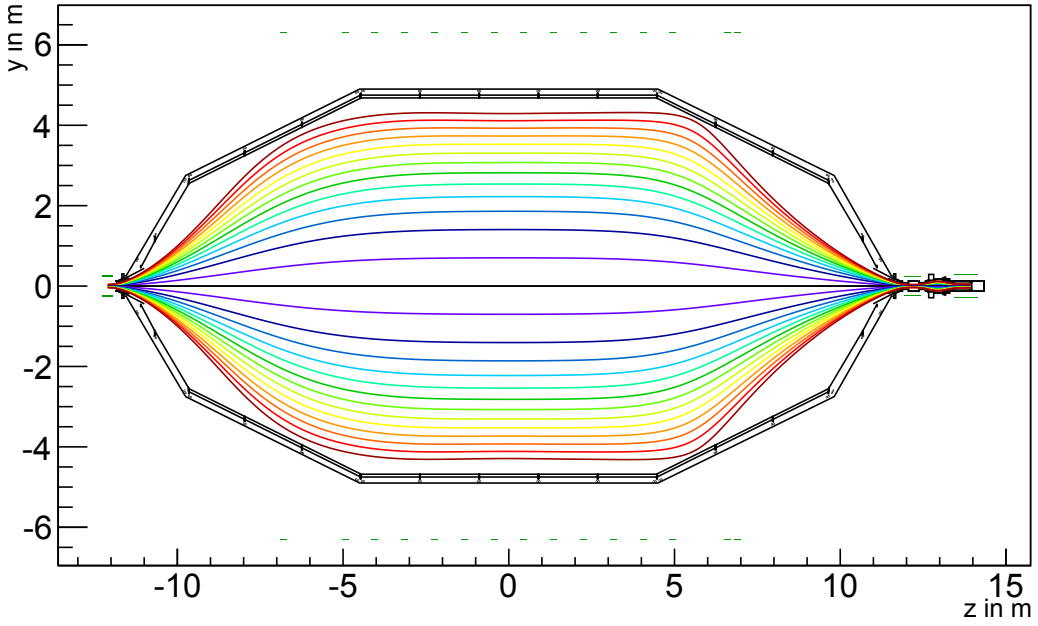

(b) LFCS at 3.8 Gauss setting

Figure 4.6: Influence of the LFCS on the magnetic flux tube in the main spectrometer. Displayed is the magnetic flux as seen by the detector with the reference values of the SDS commissioning measurements. Each field line corresponds to a detector ring, as shown in figure 4.8, with a full detector magnetic flux of 207 Tcm^2. Without the LFCS (a), the flux tube is asymmetric and only the part of the inner 5 detector rings fits into the spectrometer vessel. The flux tube produced with the reference 3.8 Gauss setting on the other hand, is symmetric and fits into the main spectrometer vessel completely.

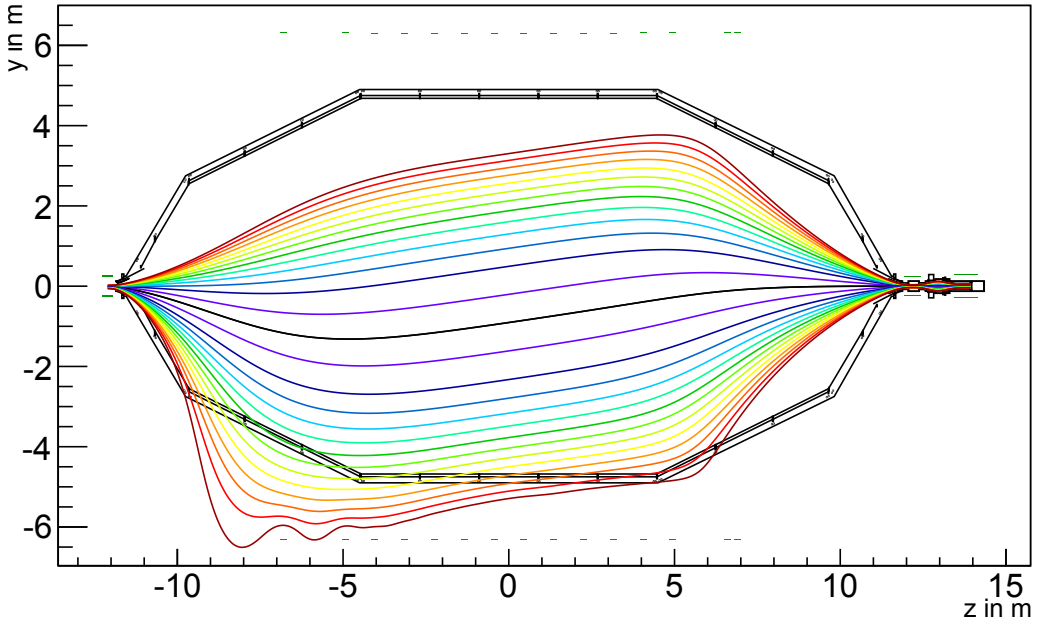

(a) z-x plane without EMCS

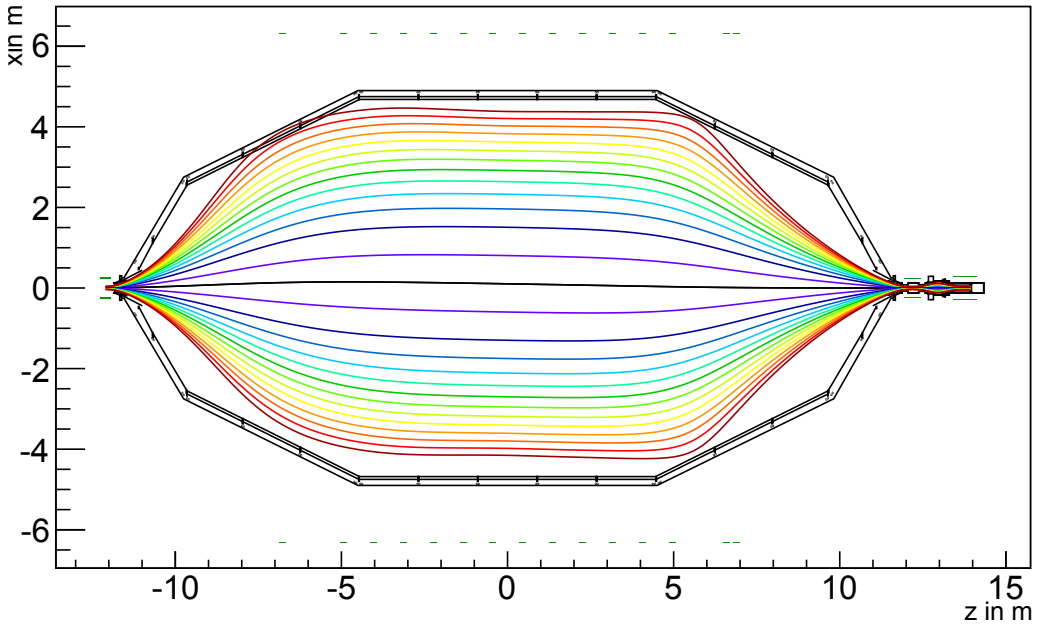

(b) z-y plane without EMCS

Figure 4.7: Influence of the EMCS on the magnetic flux tube in the main spectrometer. Displayed is the magnetic flux as seen by the detector with the reference values of the SDS commissioning measurements. Each field line corresponds to a detector ring, as shown in figure 4.8, with a full detector magnetic flux of about $207\,\mathrm{Tcm}^2$. Without the EMCS, the flux tube is deformed by the non axial components of the earth magnetic field. The deformation on the vertical axis (a) is much larger than on the horizontal axis (b), as the corresponding magnetic fields are $B_\mathrm{y} = -43.6\,\mu\mathrm{T}$ and $B_\mathrm{x} = 5.0\,\mu\mathrm{T}$, respectively.

Table 4.2: Overview of the LFCS parameters during the SDS commissioning measurements, with the design axial z position and the field creating current I for the low magnetic field 3.8 Gauss setup and the high magnetic field 9 Gauss setup. Note that the double aircoil 14 has a reversed polarity, creating a magnetic field from the source to the detector, in contrast to all other coils and solenoids.

LFCS coil index	z position in m	current I in A	
		3.8 G setting	9 G setting
1	-6.788	28.6	95.2
2	-4.938	24.0	99.8
3	-4.040	17.3	48.9
4	-3.139	22.1	98.8
5	-2.238	33.5	100.0
6	-1.338	36.4	74.0
7	-0.442	35.8	98.2
8	0.456	54.1	96.6
9	1.354	10.2	80.9
10	2.256	52.1	90.4
11	3.156	32.0	61.3
12	4.058	20.1	99.0
13	4.952	29.8	97.6
14a	6.606	51.8	36.2
14b	6.904	51.8	36.2

The earth magnetic field compensation system of KATRIN is composed of two independent cosine coil systems, one for the vertical and one for the horizontal component of the earth magnetic field. In principle, there is no action required to compensate the earth field component along the beam axis B_z, as this axisymmetric component can be adjusted with the LFCS. The EMCS utilizes a modified spherical cosine coil system [Cla38, EO66], which can produce homogenous magnetic fields. The current loops surrounding the main spectrometer are distributed according to a cos-current density distribution, thus creating a constant homogenous magnetic field inside the main spectrometer in both horizontal and vertical direction. For a compensation of the earth magnetic field's non axisymmetric components, currents of $I_{\text{vertical}} = 50\,\text{A}$ and $I_{\text{horizontal}} = 9.1\,\text{A}$ were used during the SDS commissioning measurements [BBB$^+$14].

4.1.4 Focal plane detector

The focal plane detector (FPD) system is connected to the main spectrometer via a custom made in-line beam flapper valve. The pinch and detector magnet fields guide the incoming electrons onto the detector wafer which is located at a z-position of 13.934 m in a magnetic field of 3.26 T. With a sensitive diameter of 90 mm, the corresponding magnetic flux mapped by the detector is $207\,\text{Tcm}^2$. Figure 4.8 shows the detector wafer with its equally sized 148 pixels, grouped into 12 rings and 4 additional bulls-eye center pixels. Moreover, the color pattern used for field line simulations throughout this thesis is shown, for field lines starting on the boundary of the pixel rings. Two pixels (78 and 89) were not usable during the SDS commissioning measurements, as they were exhibiting a small electric resistance between them [BBB$^+$14].

The FPD system includes a post-acceleration electrode which at present allows to accelerate electrons by up to 10 kV, thereby shifting signal electrons to a window at higher energies with a more favorable intrinsic detector background rate. The post-acceleration also allows to detect electrons with extremely small kinetic energies in the measurement

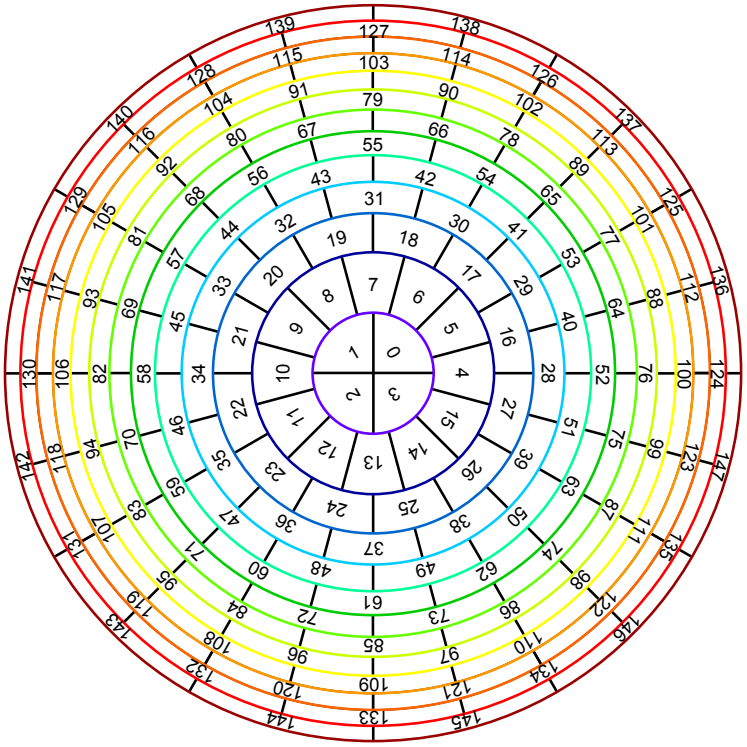

Figure 4.8: Sketch of the detector wafer with its 12 rings and the central bulls-eye, yielding a total of 148 pixels. The color pattern displayed is used throughout this thesis for the visualization of field line simulations.

campaigns where no high voltage is applied on the spectrometer vessel. These low-energy background electrons originate from the spectrometer inner surface or correspond to signal electrons produced by the electron gun, usually having a kinetic energy well below the detection threshold. These electrons would thus not be detectable without the additional energy boost by the post acceleration.

For the data acquisition of the digitized detector traces, a pair of trapezoidal filters is implemented in field programmable gate arrays (FPGAs). For the SDS commissioning measurements a shaping length of $L = 1.6\,\mu s$ and a gap length of $G = 0.2\,\mu s$ for the trapezoidal filter were used, resulting in a noise threshold of 7 keV and an FWHM energy resolution of 2 keV for 18.6 keV electrons [Sch14].

4.1.5 Electron gun

The electron gun is an indispensable tool to investigate the transmission properties of the main spectrometer. It has to provide electrons with a well-defined energy and angular distribution. Additionally, it should be able to cover the full magnetic flux tube of the main spectrometer. Therefore, it is mounted on a UHV manipulator for precise positioning of the electron starting spot. As shown in figure 4.9, the central design elements of the electron gun consists of two parallel plates, both being located in a rotatable box inside a vacuum chamber. Electrons created by the photoelectric effect on the back plate get accelerated in a two-step process. First a high electric field between the back and the front plate accelerates the electrons in a non-adiabatic way. By doing so and rotating the box and its two inner plates, the electron gun produces specific polar angles, as illustrated in figure 4.10. The second part of the acceleration between the front plate and the end of the box, which is on ground potential, is then of adiabatic type with conserved magnetic moment μ. For the creation of photo electrons, UV light is used, originating from an optical fiber with a diameter of 200 µm. The fiber is glued onto a stainless steel holder and evaporated

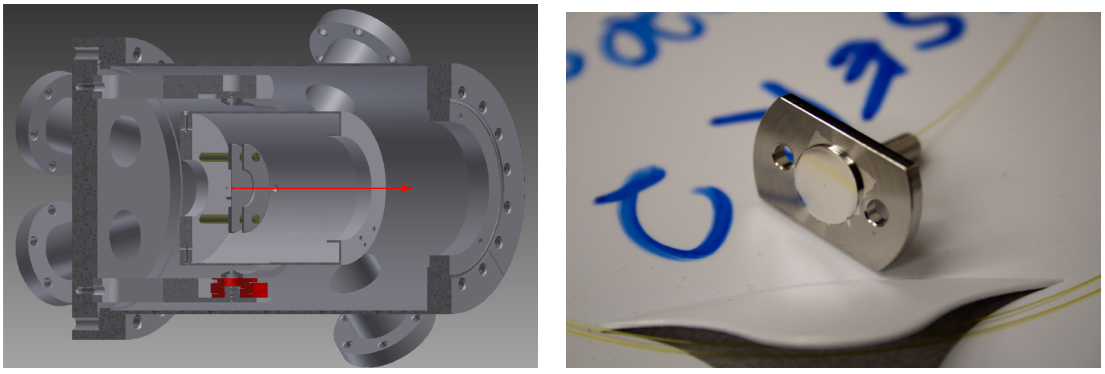

(a) Electron gun chamber (b) Electron gun fiber

Figure 4.9: CAD drawing of the electron gun(a) with its vacuum chamber and the rotatable box containing the front and back plate. Electrons are produced at the back plate, being first accelerated in a high electric field by the front acceleration plate, and after that by a lower electric field until the end of the box. The electrons are produced by the photoelectric effect by shining UV light on a silver surface. Hence, an optical fiber with a diameter of 200 µm is glued into a stainless steel holder(b) and plated with a 40 nm silver layer, which is then illuminated from the back. Figure adapted from [HBJ+13].

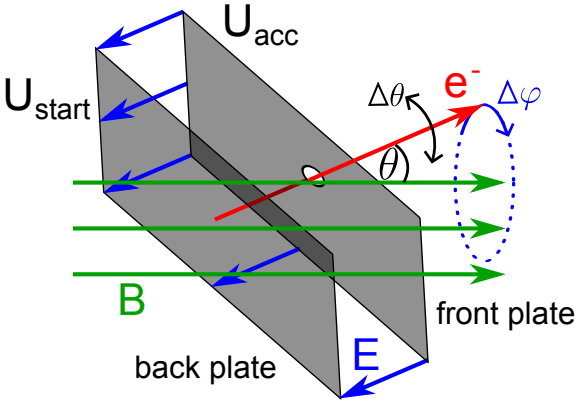

Figure 4.10: Illustration of the e-gun working principle. Electrons are generated at the back plate of a plate capacitor and are accelerated in a high electrostatic field, created by the potential difference between the back and the front plate. The plates can be rotated relative to the magnetic field, thus defining the starting polar angle, as the acceleration between the plates is non adiabatic. Figure adapted from [Wan13].

with a 40 nm silver layer. Thereby the silver is illuminated from the back, producing photo electrons that are able to leave the silver layer on the front side [Hei12, Win14, Zac14].

The rotation of the plates allows for the angular selectivity. This tasks was originally foreseen to be done by piezo-ceramic actuators. However, due to problems with the piezo elements in the UHV conditions during the SDS commissioning measurements, these devices could only be used as precision read-out units for the actual rotation angle of the box. Accordingly, the actual rotation mechanism had to be changed. This was done by connecting an extension pin to the electrode assembly, which was moved on two axes by linear stepper motors through a vacuum feedthrough [HBJ+13].

Light sources

As a light source, a UV laser as well as different UV emitting LEDs were used. The commercial laser was produced by *InnoLas Holding GmbH* and is a pulsed frequency-quadrupled laser system operating at 266 nm. While the intrinsic length of the laser

pulses is 20 ns, the frequency can be chosen between 20 and 100 kHz. By tuning the power and the frequency of the laser, an electron rate of a few kcps was achieved. A water cooler is used to stabilize the laser temperature at 25° C for constant light yield.

As a second option different types of UV emitting LEDs can be used, with peak wavelengths ranging from 265 nm to 315 nm and a rather broad FWHM of about 10 nm. Additionally, a tunable monochromator module can be inserted between the LED and the optical fiber to scan the wavelengths reaching the photo cathode, thereby changing the surplus energy of the produced electrons. When operating the light source at large wavelengths close to the work function of the silver cathode, a small surplus energy and therefore a very sharp energy distribution can be produced, however at the cost of a reduced electron rate.

For the investigation of the transmission properties, the UV LEDS are the favored light source, due to the sharper energy distribution of the produced photo electrons when working close to the work function of silver. However, at the end of the measurement phase, when the silver layer of the electron gun was degraded, only the laser was able to produce a sufficient electron rate.

High voltage

As the electron gun has to produce electrons with kinetic energies up to 18.6 keV comparable in energy to the main spectrometer potential, high voltage for the acceleration is necessary. Instead of using its own high voltage supply, the electron gun is supported by the high voltage of the main spectrometer, which allows a precise setting and read back of the voltage difference between electron gun and main spectrometer. As illustrated in figure 4.11, the back plate of the electron gun, where the electrons are produced and which defines their total kinetic energy, is supported by the dipole west power supply with an additional offset from a battery pack of about −90 V and an *ISEG EHS 8205P* power supply with a range from zero to 300 V. This setup allows to set the voltage difference between the back plate of the electron gun and the main spectrometer wire potential in a range from −90 to 210 V, which is more than sufficient for transmission function measurements. There the voltage difference is typically scanned only a few volts below and above the transmission edge. This voltage difference is measured very precisely (5 mV) with a 7.5 digit *NI-PXI DMM 4071* multimeter.

The high voltage of the acceleration plate is supported by the main spectrometer vessel potential with an additional offset being produced by an *ISEG NHQ 226* power supply in a range from 0 to 6 kV. Therefore, a voltage difference between the back and the front plate in the range from 0 to 7 kV can be achieved.

Manipulator

In addition to rotating the inner plates to define the polar angle of the produced electrons, the whole electron gun assembly can be moved in horizontal and vertical direction to cover the full flux tube. Therefore, electrons can be injected along a specific field line and be transmitted along it through the spectrometer to a particular detector pixel, during a transmission measurement. The electron gun vacuum chamber is attached to the end of a UHV manipulator, as shown in figure 4.12. The manipulator can be turned in horizontal and vertical direction by 23°, although this was limited during the SDS commissioning measurements to 20° due to safety reasons.

Electron gun performance during SDS commissioning measurements

During the SDS commissioning, the electron gun emerged as an important device, not only for transmission function measurements, but also for many supplementary measurements.

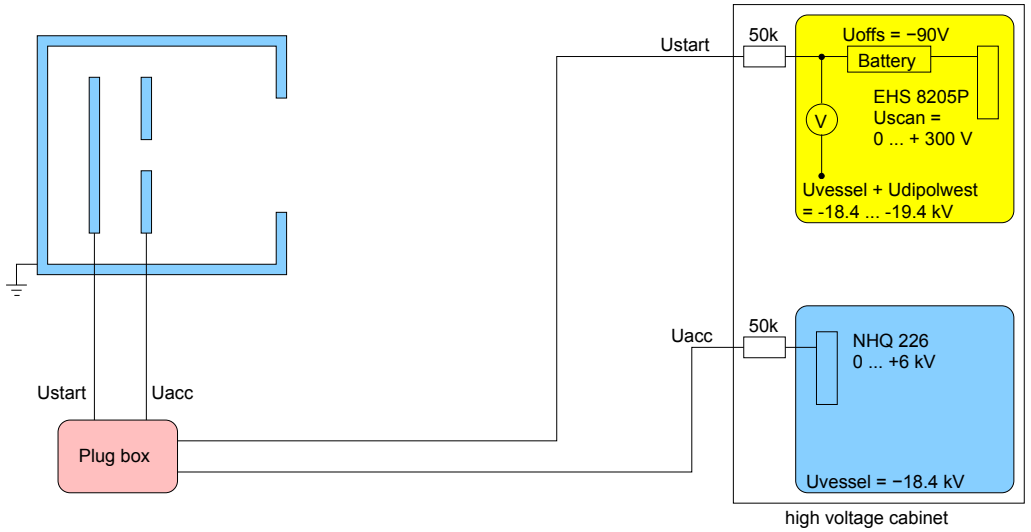

Figure 4.11: The high voltage for the electron gun is supported by the vessel and wire potential of the main spectrometer, according to the illustrated scheme. Figure adapted from [BBB+14].

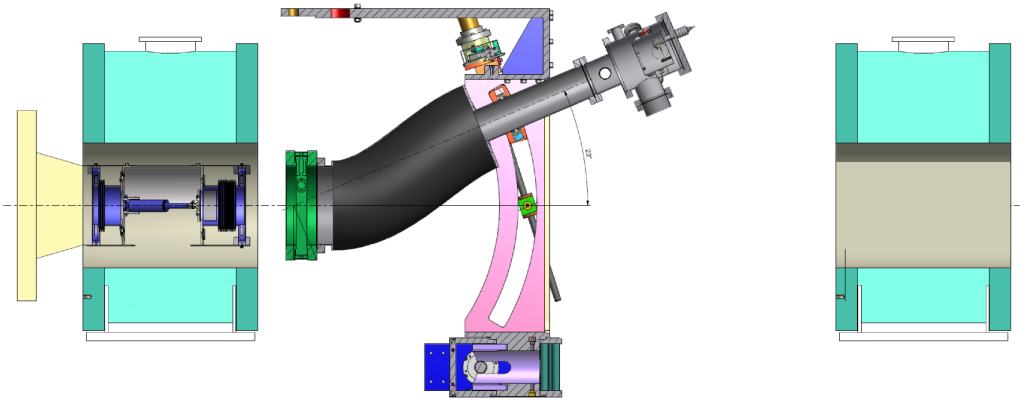

Figure 4.12: UHV Manipulator between the two pre-spectrometer solenoids with the electron gun attached to its end. It can be rotated in horizontal and vertical direction by 20°. The connection to the main spectrometer is on the left side. Figure adapted from [HBJ+13].

These areas of application include the detector characterization, the test of the system's time-of-flight capability, or as a tool to investigate the wire integrity [BBB+14]. Although a lot of measurements could be done successfully, some major drawbacks were identified. The intermediate solution of the box rotation device did not work as smoothly as expected, causing discharges inside of the electron gun and measurement time losses. Additionally, the high voltage of the electron gun was not stable at 18.6 kV. Therefore, only one transmission measurement could be taken at nominal high voltage, while later measurements had to be performed at reduced high voltage values of maximal 15.6 kV, to not risk the integrity of the system. Due to the several discharges caused by the box rotation and high voltage problems, the silver layer degraded very fast and had to be replaced multiple times. Therefore, the produced energy distribution was not stable during the SDS commissioning phase and for the measurements at the end of the commissioning phase, the only usable light source having a sufficient intensity to produce a suitable electron rate was the UV laser. Last but not least, the angular selectivity did not work as expected, due to a variety of mechanical reasons [Zac14].

Owing to the lack of angular selectivity, transmission function measurement could only be used to determine the electric potential inside the main spectrometer, but not the magnetic field. The radial potential inhomogeneity was measured successfully, but not the absolute potential, due to the unstable silver layer and work function. This is no major drawback, as it is the radial inhomogeneity that needs to be known with a precision of about 30 mV. The requirements on the true value of the absolute potential are much less stringent, these will be detailed in chapter 5.

4.2 Alignment of the sub components

For proper analysis of the transmission function data taken over the course of the SDS commissioning measurements, the alignment and recording of deviations from the nominal positions of all individual subsystems are essential. When comparing data with simulations, the exact field line path of electrons propagating through the main spectrometer and the precise points of intersection in the analyzing plane need to be known. To determine the misalignment of the electron gun system relative to the SDS apparatus, two independent approaches were persued. First, a measurement was performed of the mechanical misalignment relative to the second pre-spectrometer solenoid (PS2), as well as an alignment relative to the detector wafer, using the electron gun to send electrons through the spectrometer onto the wafer. For the second approach, the misalignment of the whole FPD system relative to the main spectrometer axis needs to be known first, as being summarized in the following section.

4.2.1 Alignment of the FPD system

The challenging task of the alignment of the detector system is described and discussed in more detail in [Sch14]. When the detector system was connected to the main spectrometer, the tilt of its vacuum chamber relative to the spectrometer axis was measured to be 0.25°, using a *FaroArm* [Far14]. Additionally, the post-acceleration electrode with the detector wafer flange inside the vacuum chamber does not share the same axis as the chamber, with a relative tilting of 0.1°. As these misalignments could not be altered due to limited hardware adjustment possibilities, the pinch and detector magnet were tilted in such a way to share a similar axis as the vacuum system, thereby guiding a larger magnetic flux of signal electrons onto the wafer.

Figure 4.13 visualizes the transported magnetic flux as mapped by the wafer, including misalignment data as provided by [Sch14, Har15]. The z-y-plane has been chosen for the

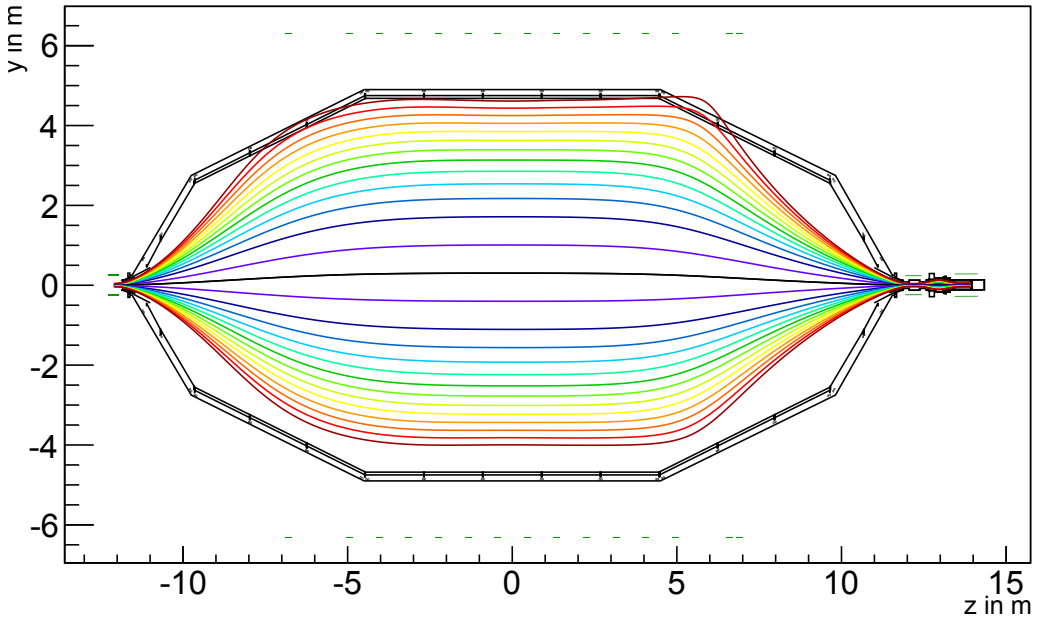

(a) Flux tube in the main spectrometer

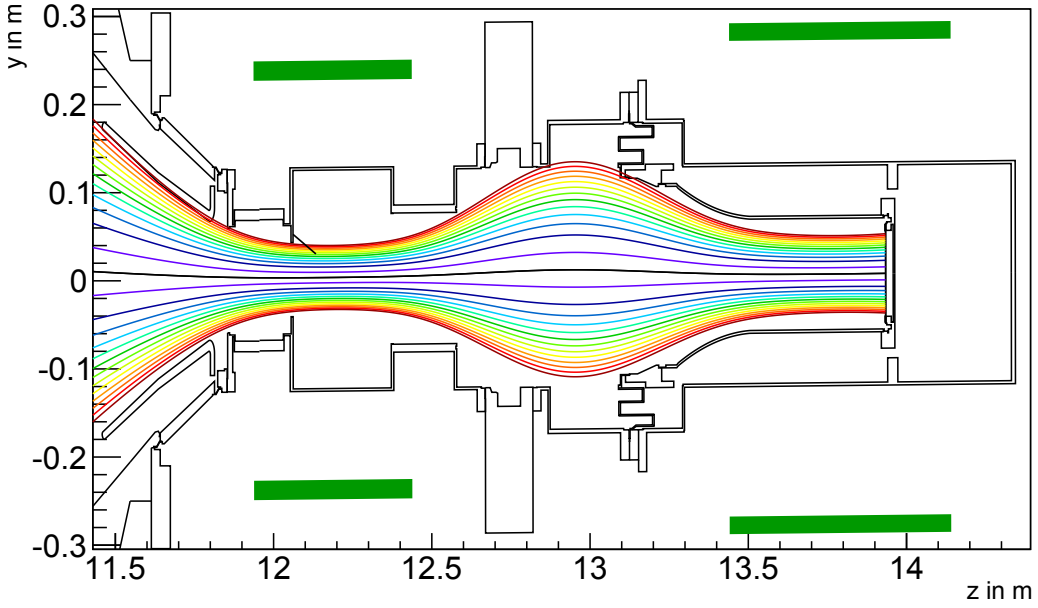

(b) Flux tube in the detector system

Figure 4.13: Simulated flux tube with the tilted detector system in the z-y-plane. Each field line corresponds to the inter-pixel boundary of a detector ring, as illustrated in figure 4.8. Due to the tilted pinch and detector magnet, and the axially shifted detector wafer, the flux tube in the main spectrometer (a) is not axially symmetric anymore. Parts of the upper pixels are shadowed by the partially opened in-line beam flapper valve, as illustrated at $z = 12.1\,\mathrm{m}$ inside the FPD system (b). Additionally, some upper pixels on the outermost ring are hit by secondary electrons from the post-acceleration electrode that is also touched by the mapped flux tube.

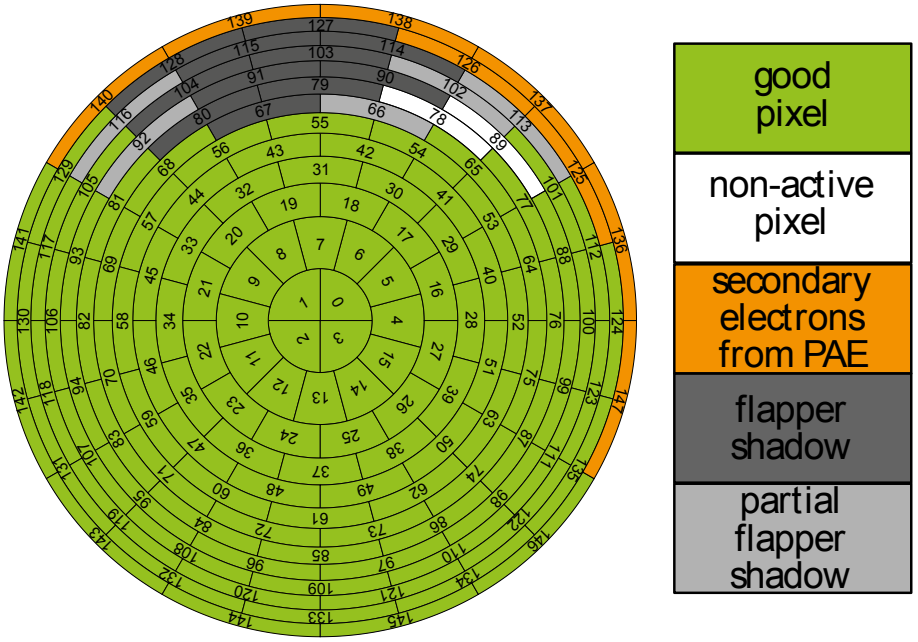

Figure 4.14: Schematic view of the detector wafer with an illustration of the operational state of the individual pixels. In total 122 of 148 detector pixels were used for data analysis during the SDS commissioning measurements. Figure from [Sch14].

visualization, as the misalignment is more dominant there than in the z-x-plane. It is clearly visible that the flux tube is not axially symmetric in the spectrometer anymore and is indeed actually touching the vessel for the upper detector pixels. When having a closer look at the flux tube inside the detector system, it can be observed that the flux tube also touches the post acceleration electrode, mapped by the outermost pixel ring at its top part. Additionally, the only partially closed in-line beam flapper valve shadows a large part of the upper detector pixels. The alignment of the FPD system has been closer investigated by simulations and measurements in [Sch14] with the main focus on assigning those pixels suffering from the flapper shadow, or being influenced by background from secondary electrons originating from the post-acceleration electrode. In total only 122 out of 148 detector pixel could be used during the SDS commissioning measurements as illustrated in figure 4.14.

Although the axes of the pinch and detector solenoids were adjusted to the axis of the vacuum chamber, there is still an offset between the center of the detector wafer and the magnetic flux tube. This displacement has also been investigated in [Sch14] and is stated there to be $\Delta x = 1.843\,\text{mm}$ and $\Delta y = 3.111\,\text{mm}$. This means that the wafer is shifted to the top by Δy and to the right by Δx, as measured relative to the central axis of the magnetic flux tube.

4.2.2 Alignment of the EGun system

The electron gun is attached to a UHV manipulator which can be rotated horizontally and vertically, as stated in section 4.1.5. The manipulator is connected to the second pre-spectrometer magnet (PS2) and its turning point has an axial position of $z_{\text{manip}} = -12.333\,\text{m}$. The distance of the electron gun's fiber surface to the turning point is $r_{\text{manip}} = 1.206\,\text{m}$. This leads to the following equations for the position of the fiber surface:

$$\begin{aligned} x &= -r_{\text{manip}} \cdot \cos(\alpha_{\text{v}}) \cdot \sin(\alpha_{\text{h}}) + x_{\text{offset}} \\ y &= r_{\text{manip}} \cdot \sin(\alpha_{\text{v}}) + y_{\text{offset}} \\ z &= -r_{\text{manip}} \cdot \cos(\alpha_{\text{v}}) \cdot \cos(\alpha_{\text{h}}) + z_{\text{manip}} \end{aligned} \tag{4.1}$$

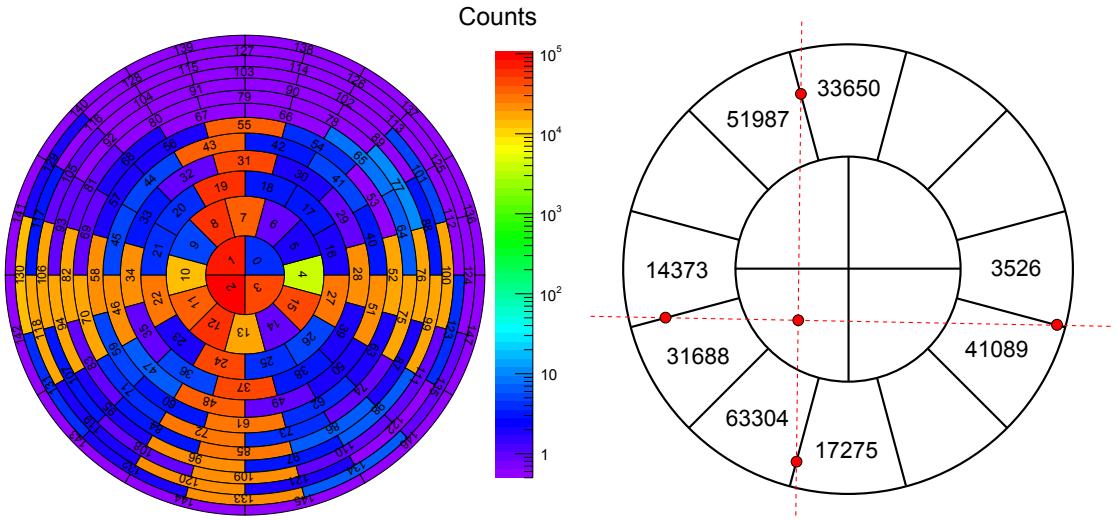

(a) Measurement (b) Detector hits for crossing point calculation

Figure 4.15: The electron gun has been moved in a vertical and a horizontal straight line while sending a continuous electron beam onto the detector. The resulting pixel distribution is illustrated in (a). From the relative number of detector hits on the neighboring pixels in the first detector ring, the crossing positions can be calculated as schematically shown in (b). The point of the intersection is at $\Delta x = -3.275\,\text{mm}$ and $\Delta y = -3.373\,\text{mm}$.

The horizontal and vertical manipulator angles are given by α_h and α_v, respectively, and the misalignment offsets by x_offset and y_offset. A measurement with the *FaroArm* was performed to determine the relative offset of the manipulator to the second pre-spectrometer magnet, yielding values of $x_\text{offset} = -1.6\,\text{mm}$ and $y_\text{offset} = 0.9\,\text{mm}$ [HBS+13].

As the alignment of the pre-spectrometer magnets has not been measured as precisely as the one of the magnets of the FPD system, their tilting and offset are not known, thus one supposes an ideal alignment. A potential misalignment of the pre-spectrometer magnets leads to an additional misalignment of the manipulator and also to a change in the magnetic flux. Therefore, an electron-optical measurement with the electron gun has been performed to determine the relative offset to the detector wafer. The result can be used to calculate the offset to the spectrometer axis. This has been realized by setting the electron gun to a small surplus energy, grounding the main spectrometer and by moving the manipulator from $\alpha_\text{v} = -20\,^\circ$ to $\alpha_\text{v} = +20\,^\circ$. Thereby a vertical line on the detector was mapped. By moving from $\alpha_\text{h} = -20\,^\circ$ to $\alpha_\text{h} = +20\,^\circ$ the corresponding horizontal line was mapped. The combined pixel distribution of the electron hits on the focal plane detector for these two measurements is shown in figure 4.15 (a).

Due to the characteristic shape of the detector pixels and the given detector offsets, two neighboring pixels of the first detector ring were hit with the electron gun beam on opposite sides for each measurement. This allows to very accurately determine the central beam position on pixel 2 when the manipulator is set to its initial position at zero degree, as the spot size of the electron beam on the detector has a diameter of less than 20 µm. Supposing a constant scanning speed of the manipulator, at least in the central part of the detector, the relative number of detector hits on two neighboring pixels on ring 1 are used to determine the exact crossing position of the corresponding pixel boundary. The crossing positions on both opposite sides of this ring are connected with a straight line and the intersection point of the horizontal and the vertical scan can be obtained, as schematically shown in in figure 4.15 (b). A detailed derivation of the formulas used for the stated determination of the crossing positions can be found in [Sta13].

Table 4.3: Overview of offset values of the electron gun relative to the flux tube.

offset	Δx in mm	Δy in mm
EGun relative to FPD	-3.275	-3.373
FPD relative to flux tube	1.843	3.111
EGun relative to flux tube at FPD	-1.432	-0.262
EGun relative to flux tube at EGun	-14.154	-2.590

The obtained values $\Delta x = -3.275\,\text{mm}$ and $\Delta y = -3.373\,\text{mm}$ have to be corrected by the relative offset of the detector wafer to the central axis of the magnetic flux tube of $\Delta x = 1.843\,\text{mm}$ and $\Delta y = 3.111\,\text{mm}$ as stated in the previous section. This leads to a relative shift on the detector wafer which is caused by the electron gun misalignment of $\Delta x = -1.432\,\text{mm}$ and $\Delta y = -0.262\,\text{mm}$. This shift can not be translated directly to the mechanical misalignment of the electron gun, as the magnetic field at the central fiber position at $z = -13.539\,\text{m}$ is $B_{\text{EGun}} = 0.0336\,\text{T}$, whereas the central magnetic field at the wafer surface at $z = 13.934\,\text{m}$ is $B_{\text{wafer}} = 3.283\,\text{T}$. Due the conservation of the magnetic flux, the offset at the electron gun can be calculated according to

$$r_{\text{EGun}} = \sqrt{\frac{B_{\text{wafer}}}{B_{\text{EGun}}}} \cdot r_{\text{wafer}}. \tag{4.2}$$

This results in $\Delta x = -14.154\,\text{mm}$ and $\Delta y = -2.590\,\text{mm}$. A summary of the offset values of this calculation is given in table 4.3.

Using these values in the formulas for the electron gun's starting position in equation 4.1, tracking simulations which explicitly include these stated misalignments were performed to check for internal consistency. For the vertical and horizontal line scan, 1000 particles were started at the electron gun's position, equally distributed between $\alpha_{\text{v,h}} = -20\,^\circ$ and $\alpha_{\text{v,h}} = 20\,^\circ$ for each scan. Additionally, a measurement with the electron gun moving in a circle at a fixed total angle of $\alpha = 14\,^\circ$ was performed and a corresponding simulation carried out. The pixel distributions for the measurements and the simulations are compared in figure 4.16. The visible agreement between measurement and simulation verifies that the misalignment of the electron gun relative to magnetic flux tube of the main spectrometer has been found and understood. This is an important requirement for the analysis of transmission function measurements as discussed in chapter 5.

4.3 Optimization of the electromagnetic field

As pointed out above in section 2.1.2, the precise knowledge of the transmission function is of paramount importance for a successful neutrino mass determination. To compute the transmission function, the magnetic field and electric potential at the analyzing plane need to be known. Due to the inherent MAC-E filter characteristics of the main spectrometer and its magnet system, the electric potential and the magnetic field are not constant over the analyzing plane, but suffer radial inhomogeneities, as plotted in figure 4.17. This fact can be taken into account in the analysis, as the focal plane detector offers a matching radial resolution, due to its 12 rings and the central bulls-eye. Therefore, a corresponding transmission function can be calculated for each pixel. However, the remaining variations of the potential and the magnetic field within one pixel leads to a broadening of the corresponding transmission function. Hence, the total radial inhomogeneity needs to be minimized.

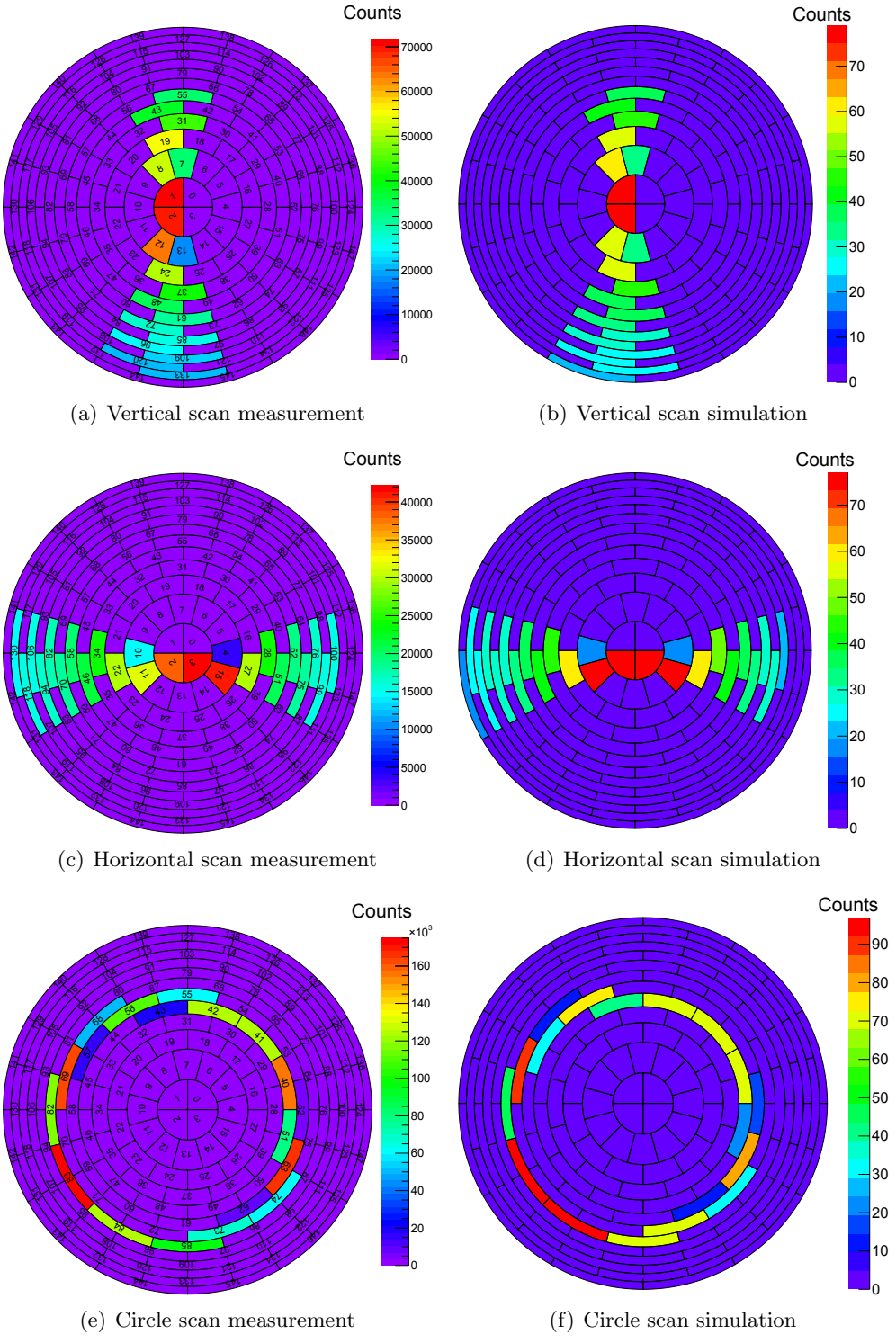

(a) Vertical scan measurement

(b) Vertical scan simulation

(c) Horizontal scan measurement

(d) Horizontal scan simulation

(e) Circle scan measurement

(f) Circle scan simulation

Figure 4.16: Comparison of pixel distributions for measurements and simulations based on an electron gun offset of $\Delta x = 14.154\,\text{mm}$ and $\Delta y = 2.590\,\text{mm}$ and a misalignment of the detector system as stated in section 4.2.1. The outer rings of the vertical (a) and horizontal (c) measurements have been excluded, due to an excess in rate caused by starting and stopping the manipulator before and after the line scan. The agreement in the pixel hit pattern is convincing, as the simulated line scans lead to the same vertical and horizontal offset on the detector as in the measurement. In the circular scans (e and f), the identical pixels were hit both in the simulation as in the measurement, although the distribution of the counts vary slightly. This is caused by the manipulator not performing an ideal circle but a zig-zag path approximating an ideal circle, caused by a difference in speed between the vertical and horizontal rotation axes.

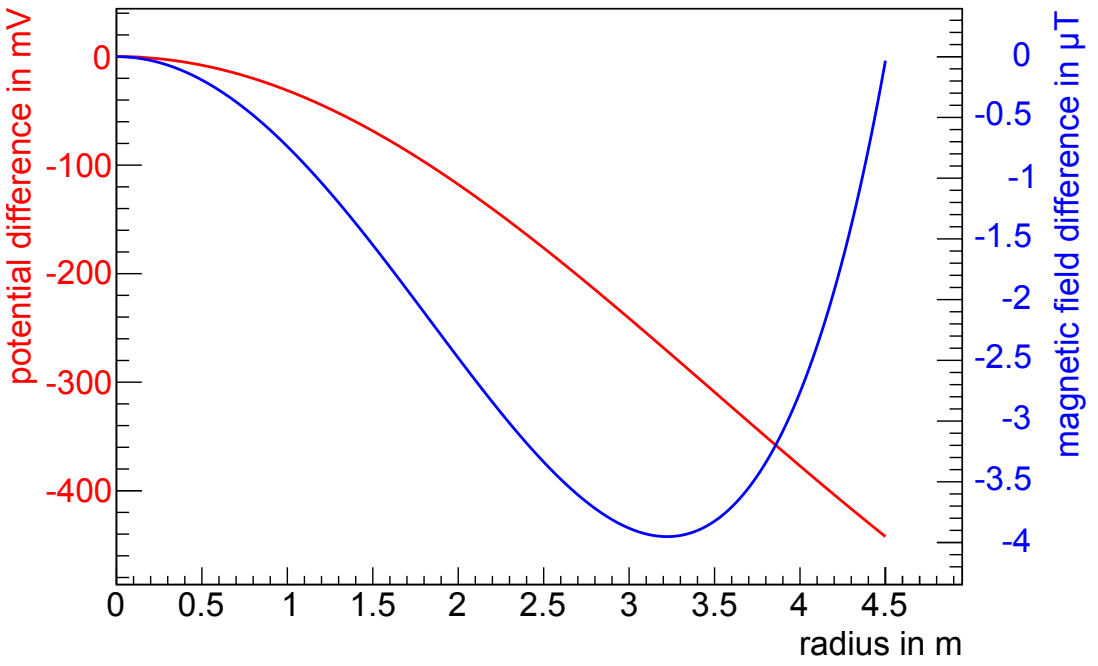

Figure 4.17: Radial inhomogeneity of the electrostatic potential at the analyzing plane $z = 0\,\mathrm{m}$ for a default short-circuit electrode configuration of $U_{\mathrm{vessel}} = -18.5\,\mathrm{kV}$ and $U_{\mathrm{wire}} = -18.6\,\mathrm{kV}$. The absolute potential in the middle of the spectrometer at $r = 0\,\mathrm{m}$ is smaller than in a region close to the wires, which start at $r = 4.68\,\mathrm{m}$, due to the effect of the ground electrode. The radial magnetic field inhomogeneity for the 3.8 Gauss magnet setup can be shaped using the air system surrounding the spectrometer vessel. The shown 3.8 Gauss setup is already optimized for small magnetic inhomogeneities, as detailed in chapter 4.3.

The analyzing point for a field line is the point in the spectrometer where the longitudinal kinetic energy of an electron propagating along this field line reaches its minimum. The analyzing points for all field lines are not necessarily in the middle of the spectrometer at $z = 0\,\mathrm{m}$. This position can be different for each field line, and even depends on the starting polar angle θ. The actual position of the analyzing point thus results from the complicated interplay between the magnetic adiabatic collimation by the magnetic field gradient and the decrease of the longitudinal kinetic energy by the retarding potential, as described in section 2.1.

The goal of this section is thus the optimization of the electromagnetic field, which in an optimal way results in a conjunction of all analyzing points at the analyzing plane at $z = 0\,\mathrm{m}$. The determination of the position of the analyzing points will be detailed in section 4.3.1, followed by an explanation of the requirements of the electromagnetic fields to achieve a common analyzing plane for radial positions at $z = 0\,\mathrm{m}$, in section 4.3.2. This requires an automated optimization of the LFCS currents, as first described in [Wan13, G$^+$13], which will be summarized in section 4.3.3. The optimization for the SDS commissioning measurements has been performed by N. Stallkamp ([Sta13]), using the KTRAP framework, as described in section 3.5. These optimizations were concluded before the start of the SDS commissioning measurements and the results, being used for entire measurement phase, are presented in section 4.3.4. The impact on the transmission conditions caused by tilted solenoids, short-circuited wire electrodes and the asymmetric potential configurations (the latter only discovered after the end of the SDS commissioning measurements) will finally be presented in section 4.3.5.

4.3.1 Determination of the analyzing point

An electron with an initial kinetic energy E_S and polar angle θ_S at a specific point $\vec{P}_S$ will propagate along a magnetic field line through the spectrometer to the detector. The point where the longitudinal kinetic energy of the electron is minimal is called analyzing point $\vec{P}_A$.

The total kinetic energy of the electron at any point $\vec{P}$ along its trajectory is determined by its starting conditions through energy conservation

$$E_{tot} = E_S + qU_S = E_P + qU_P, \tag{4.3}$$

with the electron charge q and the electric potential U. Energy losses due to synchrotron radiation and scattering off residual gas molecules can be neglected here.

The electron's momentum $\vec{p}$ is composed of a longitudinal component $\vec{p}_\parallel$ along the magnetic field line and a transversal component $\vec{p}_\perp$ perpendicular to it. Making use of a non-relativistic relation

$$E = \frac{p^2}{2m}, \tag{4.4}$$

the kinetic energy can also be expressed with a longitudinal and a transversal component

$$E = E_\parallel + E_\perp. \tag{4.5}$$

The transversal component then can be expressed as

$$E_\perp = E \cdot \sin^2(\theta) \tag{4.6}$$

with the electron's polar angle θ relative to the magnetic field line.

As the first adiabatic invariant $\gamma\mu$ (see equation 2.2) remains constant along the electron's trajectory within the main spectrometer, as detailed in section 2.1, the two transversal energy components $E_{S,\perp}$ and $E_{P,\perp}$ can be related by

$$\frac{\gamma_S + 1}{2} \cdot \frac{E_{S,\perp}}{B_S} = \frac{\gamma_P + 1}{2} \cdot \frac{E_{P,\perp}}{B_P} \tag{4.7}$$

with the relativistic Lorentz factor γ and the magnetic field magnitude B.

To get the longitudinal kinetic energy at the point $\vec{P}$ along the trajectory, equations 4.3, 4.5 and 4.6 need to be put into equation 4.7 and solved for $E_{P,\parallel}$:

$$E_{P,\parallel} = q(U_S - U_P) + E_S \cdot \left(1 - \sin^2(\theta_S) \cdot \frac{B_P \cdot (\gamma_S + 1)}{B_S \cdot (\gamma_P + 1)}\right) \tag{4.8}$$

With this equation, the longitudinal kinetic energy for a given initial state can be calculated along its field line and the position of its minimal value can be obtained, being called the analyzing point $\vec{P}_A$.

4.3.2 Optimization of the analyzing points

The axial homogeneity of the electric potential and the magnetic fields is largest in the center of the main spectrometer at $z = 0\,\mathrm{m}$. If the analyzing points for all field lines are at that position, the resulting analyzing potentials and magnetic fields are more robust with regards to slight deviations of the analyzing point position, due to intrinsic inaccuracies of the experimental setup. Additionally, there is an intrinsic axial spread of the analyzing points for a single field line, depending on the polar angle θ. This increases the systematic

error on the analyzing potential and magnetic field, which can be minimized if the analyzing point is in the center of the spectrometer, where the axial homogeneity is largest. Therefore, the analyzing points need to be optimized to be as close to $z = 0\,\mathrm{m}$ as possible, where they form a common analyzing plane.

For the following determination and optimization of the analyzing point position, the electron starting position is chosen to be the center of the second pre-spectrometer magnet. The starting kinetic energy is discussed by making use of the so called transmission energy E_{tr}, being the initial energy an electron needs at its starting position to just be transmitted through the spectrometer. This means its longitudinal kinetic energy $E_{\mathrm{P},\parallel}$ vanishes at the analyzing point. As this point is not known before the calculation, it is assumed to be in the middle of the spectrometer at $z = 0\,\mathrm{m}$. From equation 4.8 follows an expression for the transmission energy:

$$E_{\mathrm{tr}} = \frac{q(U_{\mathrm{A}} - U_{\mathrm{S}})}{1 - \sin^2(\theta_{\mathrm{S}}) \cdot \frac{B_{\mathrm{A}} \cdot (\gamma_{\mathrm{S}}+1)}{B_{\mathrm{S}} \cdot (\gamma_{\mathrm{A}}+1)}} \tag{4.9}$$

The position of the analyzing points depends on the accurate interplay between the electrostatic retardation potential, which decreases the longitudinal kinetic energy component on the one hand, and on the magnetic adiabatic collimation on the other hand, which transforms transversal into the longitudinal kinetic energy. The interplay of both must be carefully adjusted to avoid an electrostatic reflection of the electron before the transformation from transversal to longitudinal kinetic energy is completed. A plot of the electrostatic potential and magnetic field magnitude along the central field line is shown in figure 4.18. The electrostatic potential rapidly drops after entering the spectrometer, but it is homogenous in the center. For an initial polar angle of $\theta = 0\,^\circ$, the analyzing point is only defined by the minimum of the electrostatic potential, according to equation 4.8, which is at $z = 0\,\mathrm{m}$ if the inner electrodes are operated as designed.

Likewise, the magnetic field drops rapidly when entering the spectrometer due to the increasing distance to the super conducting solenoids to reach its minimum in the center of the spectrometer at $z = 0\,\mathrm{m}$. However, in contrast to the electric potential, the minimum of the magnetic field does not necessarily result in a minimum of the longitudinal kinetic energy at that position. When considering equation 4.8 with an initial non-zero polar angle, the magnetic term increases when moving away from the magnetic minimum, thereby decreasing the longitudinal kinetic energy.

Therefore, a very homogenous magnetic field close to the analyzing plane is required, so that an increase in longitudinal kinetic energy caused by the decreasing magnetic field, when moving closer to the analyzing plane, is compensated by a decrease in longitudinal kinetic energy due to the electrostatic potential. Another possible solution is a small local maximum of the magnetic field at $z = 0\,\mathrm{m}$, causing the magnetic term in equation 4.8 to decrease when moving closer to the analyzing plane, resulting in a minimal kinetic energy at the magnetic field maximum.

When optimizing the transmission properties, a major challenge is the non-trivial optimization of the magnetic field to obtain high homogeneity close to the analyzing plane, as detailed in section 4.3.3. The electrostatic potential, in contrast, is already very homogenous by design, which is sufficient for the transmission properties if a common pitfall is avoided, the early retardation.

Early retardation

When operating the main spectrometer at default values with a short-circuited electrode configuration of $U_{\mathrm{vessel}} = -18.5\,\mathrm{kV}$ and $U_{\mathrm{wire}} = -18.6\,\mathrm{kV}$, the retarding potential drops

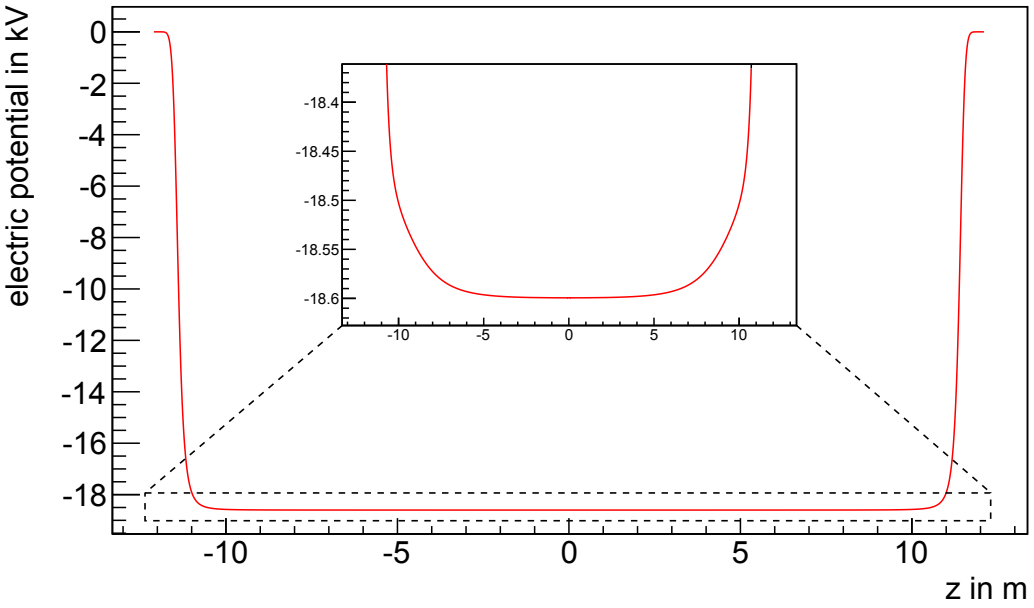

(a) Potential

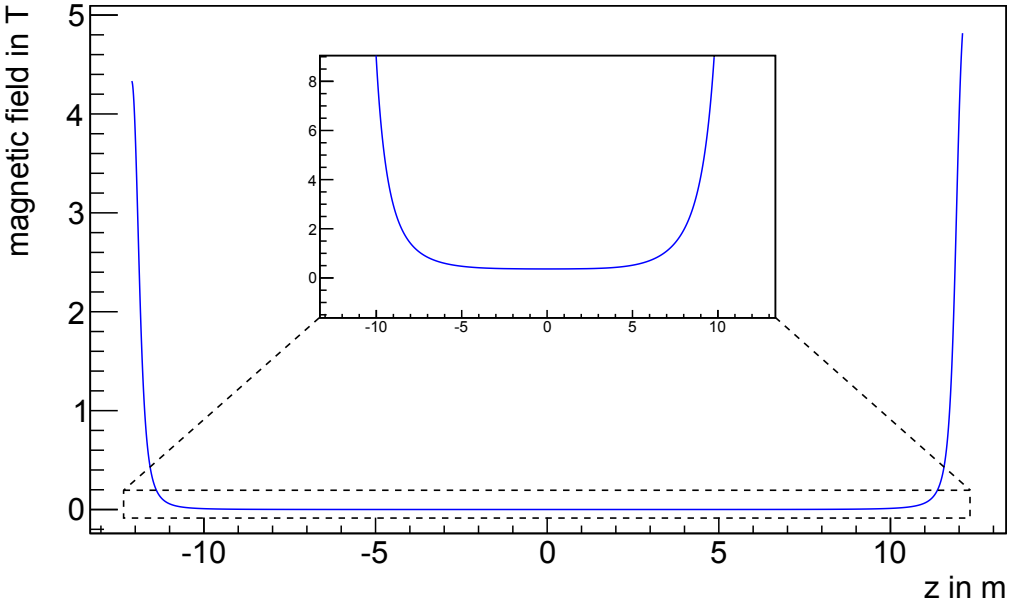

(b) Magnetic field

Figure 4.18: Electrostatic potential (a) and magnetic field magnitude (b) along the central field line for a default short-circuit electrode configuration of $U_{\text{vessel}} = -18.5\,\text{kV}$ and $U_{\text{wire}} = -18.6\,\text{kV}$ and the magnetic 3.8 Gauss setup. Both drop rapidly at $z \approx -11\,\text{m}$ and have their minimum in the center of the spectrometer at $z = 0\,\text{m}$.

rapidly after the electrons have passed the ground electrode and enter the steep cone at $z \approx 11\,\mathrm{m}$, as shown in figure 4.18 (a). The magnetic field, however, has not yet dropped to low enough values to transform a sufficient amount of transversal energy into the longitudinal component, causing the electron to be reflected, even in cases where it would have enough kinetic energy to pass the analyzing plane later on. This effect is called early retardation and is illustrated in figure 4.19, where the theoretical longitudinal kinetic energy of a particle has been plotted along the central field line for different initial polar angles. As soon as the longitudinal kinetic energy reaches zero, the particle is reflected. While this effect has no impact on particles with a small initial polar angle, electrons with a initial polar angle larger than $\theta \approx 30\,^\circ$ are reflected back already at $z \approx -11\,\mathrm{m}$ for the given example.

This can be avoided by attenuating the rapid potential drop via reducing the electrostatic potential of the steep cone electrodes. When an additional positive offset of 100 V is put on the steep cone wire electrodes, the effect vanishes, as shown in figure 4.20. The default short-circuit electrode configuration therefore needs to be adjusted to be $U_{\mathrm{vessel}} = -18.5\,\mathrm{kV}$, $U_{\mathrm{wire}} = -18.6\,\mathrm{kV}$ and $U_{\mathrm{steepcone}} = -18.5\,\mathrm{kV}$. This important additional steep cone offset is used in all following potential configurations throughout this thesis.

4.3.3 Optimization of the LFCS currents

The optimization of the magnetic field inside the spectrometer with regard to the transmission properties is also a non-trivial task. The radial and axial homogeneity of the magnetic field in the analyzing plane need to be maximized within the constraints given by the design magnetic field value. This can be done by adjusting the field driving currents of the 14 coils of the LFCS. However, the parameter space of the 14 LFCS coils with a current range from 0 A to 100 A is quite large. Therefore, an automatic optimization routine is more practical and also yields better results than an optimization by hand.

For a mathematical optimization the goal needs to be defined in a so called objective function, which has to be optimized numerically. The free parameters of the optimization are the 14 LFCS currents with the external constraints of the minimal and maximal technically allowed currents. As for the given problem, several goals and requirements need to be fulfilled simultaneously, accordingly, the optimization needs to minimize a multi-objective problem. This can be described as an objective function

$$F = \sum_{k=1}^{N} w_k O_k, \tag{4.10}$$

with the individual objectives O_k and the corresponding weights w_k. By choosing appropriate weights, the relative importance of the different objectives can be influenced. The used objectives for the optimization of the transmission properties are described in the following:

1. **Magnetic field strength:** Depending on the type of measurement to be undertaken or the desired energy resolution of the spectrometer, an absolute value of the magnetic field at the center of the spectrometer B_{set} ($z = 0\,\mathrm{m}, r = 0\,\mathrm{m}$) can be defined. The squared difference to the actual value, obtained by a calculation with all the solenoids and the LFCS with its free parameters, is the first objective:

   $$O_1 = (B_{\mathrm{actual}} - B_{\mathrm{set}})^2 \tag{4.11}$$

   This objective also results in the flux tube fitting into the spectrometer vessel, if a set value above 0.3 mT is chosen. Due to technical limitations of the manageable LFCS currents, the maximal possible magnetic field in the center is 1.1 mT.

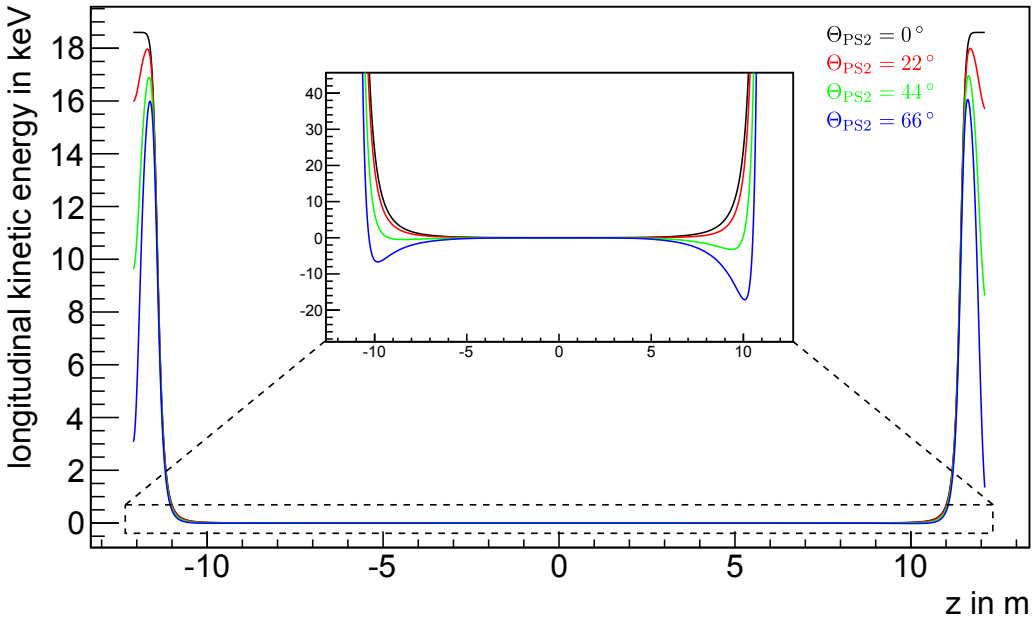

Figure 4.19: Longitudinal kinetic energy for the central field line with different initial polar angles. A default short-circuit electrode configuration of $U_{\text{vessel}} = -18.5\,\text{kV}$ and $U_{\text{wire}} = -18.6\,\text{kV}$ and the 3.8 Gauss magnetic setup have been used. The longitudinal kinetic energy increases at first, when the electron moves away from the PS2 magnet due to the magnetic adiabatic collimation as the magnetic field decreases. When the potential starts to drop at $z \approx -11.5\,\text{m}$, the longitudinal kinetic energy decreases accordingly. For very high polar angles the longitudinal kinetic energy drops below zero at $z \approx -10\,\text{m}$, as shown in the zoomed region, which would result in a reflection of the electron. For field lines closer to the wires, the effect is even more distinct.

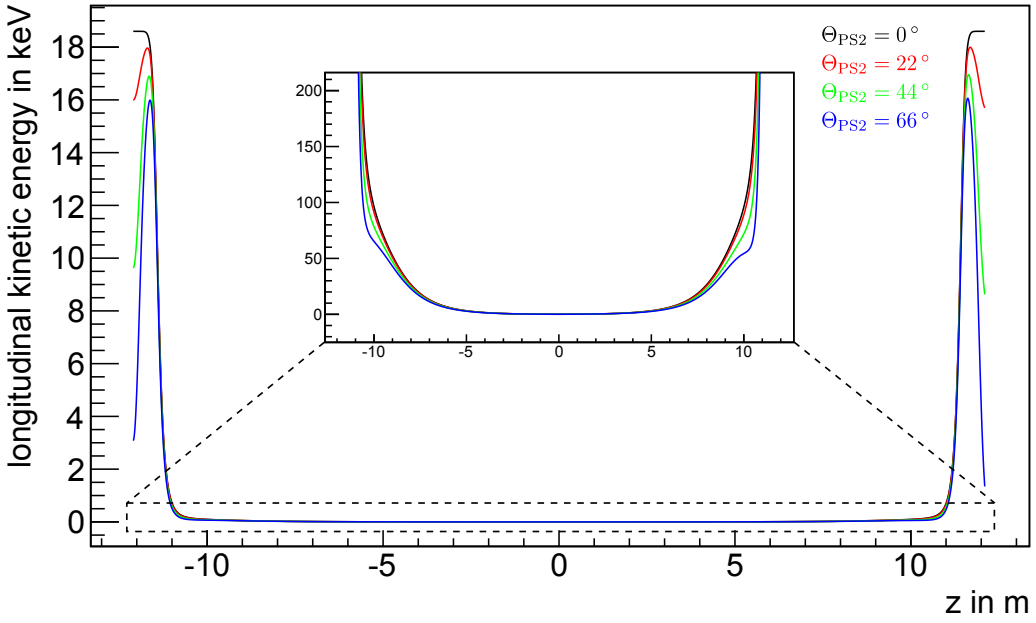

Figure 4.20: Longitudinal kinetic energy for the central field line with different initial polar angles and an additional offset of 100 V on the steep cone electrodes. In contrast to the default setup in figure 4.19, the longitudinal energy does not drop below zero at $z = -10\,\text{m}$, thus avoiding the early retardation.

2. **Radial magnetic field homogeneity:** The second objective is similar to the first one, but this time multiple points with different radii are used to optimize the radial magnetic field homogeneity. A defined number N of typical 10 points up to a maximal radius defined by the given flux tube are therefore used to calculate the magnetic field values. The sum of the squared differences to the set value is then the next objective:
$$O_2 = \frac{1}{N}\sum_{p=1}^{N}(B_{\text{actual},p} - B_{\text{set}})^2 \tag{4.12}$$

3. **Axial magnetic field homogeneity:** The third objective minimizes the axial magnetic field homogeneity, by calculating the gradient in z direction for all radial points as used in the second objective. By minimizing the maximal gradient of this points, the axial magnetic field homogeneity is improved:
$$O_3 = \max\left|\frac{\mathrm{d}B_{\text{actual},p}}{\mathrm{d}z}\right| \tag{4.13}$$

The most CPU-time consuming part of the minimization routine is the magnetic field evaluation, which has to be computed at multiple positions for each step of the minimization. Depending on the chosen minimizer and starting conditions, the minimization requires thousands of steps and a corresponding large number of slow field computations. This can be significantly improved, if the magnetic fields for the given points are only computed once for a LFCS setting of $I = 1\,\text{A}$ on all air coils. The magnetic field of the LFCS can then easily be computed by a super-position of the individual coils contributions B_{j}, weighted with their applied currents I_{j}. The total magnetic field during the optimization can then be obtained by
$$B_{\text{total}} = B_{\text{solenoids}} + B_{\text{earth}} + \sum_{j=1}^{14} I_j B_j. \tag{4.14}$$

This optimization routine is implemented in the KTRAP framework (see 3.5), and the options, including a choice of different minimizer from the KASPER framework, can easily be configured in an xml file by the user.

The results that have been obtained for the SDS commissioning measurements will be presented in the next section.

4.3.4 Results

For the SDS commissioning measurements different optimized magnetic field setups were created for different magnetic field strengths in the analyzing plane. The two most important ones for this thesis are given by a low magnetic field settings with total field of 0.36 mT, and a high magnetic field setting with a total field of 0.88 mT in the center of the main spectrometer. As all used coils (without the earth magnetic field) for these setting create an analyzing plane magnetic field of 0.38 mT (3.8 G) and 0.90 mT (9.0 G) respectively, these have commonly been called “3.8 Gauss” and “9 Gauss setting”, despite the lower central field value of $\Delta B = 0.02\,\text{mT}$. This name convention will also be used throughout this thesis. The LFCS currents for these settings have been stated in table 4.2.

To crosscheck the obtained magnetic field settings for the analyzing point positions, field line simulations were performed using KTRAP. The electric field input for the calculation comprises a fast axi-symmetric main spectrometer and detector model with the default short-circuited electrode configuration of $U_{\text{vessel}} = -18.5\,\text{kV}$, $U_{\text{wire}} = -18.6\,\text{kV}$,

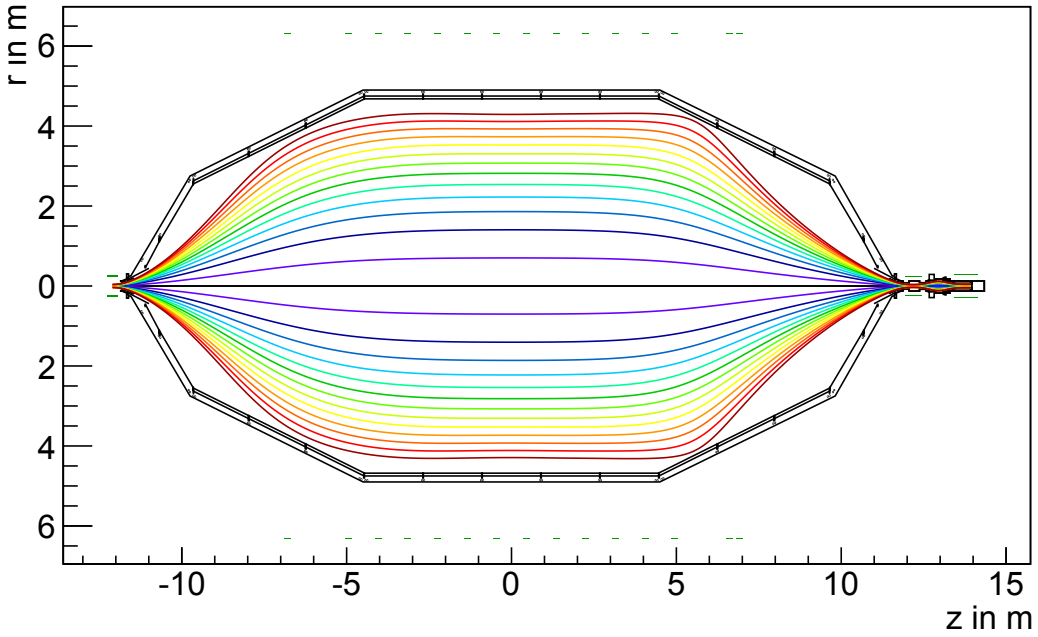

Figure 4.21: Field line simulation for the 3.8 Gauss setup. The field lines start in the PS2 magnet at the entrance of the main spectrometer and end in the focal plane detector system on the wafer. One field line for each detector ring has been calculated, according to figure 4.8. While the flux tube looks symmetric, small deviations can be seen on the outer field line (red) at $z \approx \pm 6\,\mathrm{m}$.

$U_{\mathrm{steepcone}} = -18.5\,\mathrm{kV}$, and a detector post acceleration of $U_{\mathrm{PAE}} = 10.0\,\mathrm{kV}$. For the magnet setup, the design positions without additional displacement and rotation were used.

Exemplary plots for the 3.8 Gauss setup will be shown in the following, starting with a trajectory overview in figure 4.21, where one field line for each detector ring is displayed, with a color coding according to figure 4.8. The electrostatic potentials and magnetic field magnitudes along these field lines are shown in figure 4.22 and figure 4.23, respectively. The corresponding longitudinal kinetic energy is displayed in figure 4.24 with the maximal initial polar angle in the entrance magnet of $\theta = 66\,^{\circ}$. The resulting minimum of the longitudinal kinetic energy is for all field lines within a few cm to the center of the main spectrometer at $z = 0\,\mathrm{m}$. The exact minimum positions, also for different initial polar angles, are displayed in figure 4.25. In this configuration, even for the outer field lines the deviation of the analyzing points is only in the order of 10 mm, which is more than sufficient, as the electrostatic potential and magnetic field is very homogeneous in this small range.

For the 9 Gauss setup the flux tube radius in the analyzing plane is smaller, and an excellent homogeneity of the magnetic field is therefore easier to achieve. The field lines for this setup are shown in figure 4.26 and the analyzing plane positions are illustrated in figure 4.27. In contrast to the low magnetic field setup, the deviation between the different field lines is much smaller, while the variation within one field line for different polar angles is more prominent. Nevertheless, the deviation from $z = 0\,\mathrm{m}$ is only a few mm, and therefore even better than in the 3.8 Gauss setup.

4.3.5 Transmission conditions during the SDS commissioning measurements

While the optimization of the transmission conditions has been performed in prior to the SDS commissioning measurements yielding impressive results as shown in the last section,

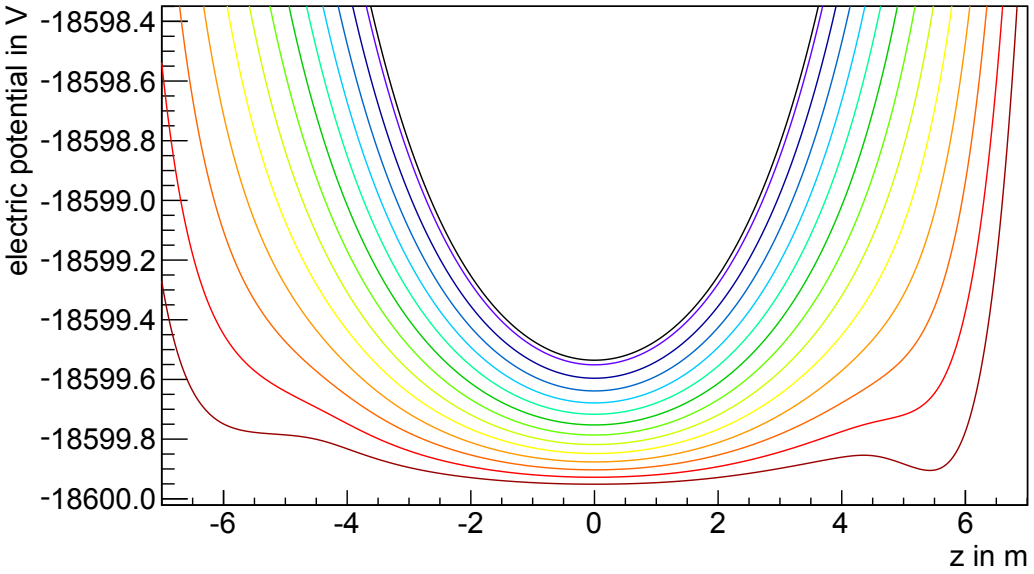

Figure 4.22: Electrostatic potential curves for the 3.8 Gauss setup shown in figure 4.21. The potential minimum of all field lines is in the center of the spectrometer at $z = 0\,\mathrm{m}$. The slight asymmetry is caused by the different distance to the wire electrodes on both sides, due to the asymmetry of the magnetic field lines. The different minimal potential for each field line at the analyzing plane, the radial potential inhomogeneity, is 400 mV, as already shown in figure 4.17.

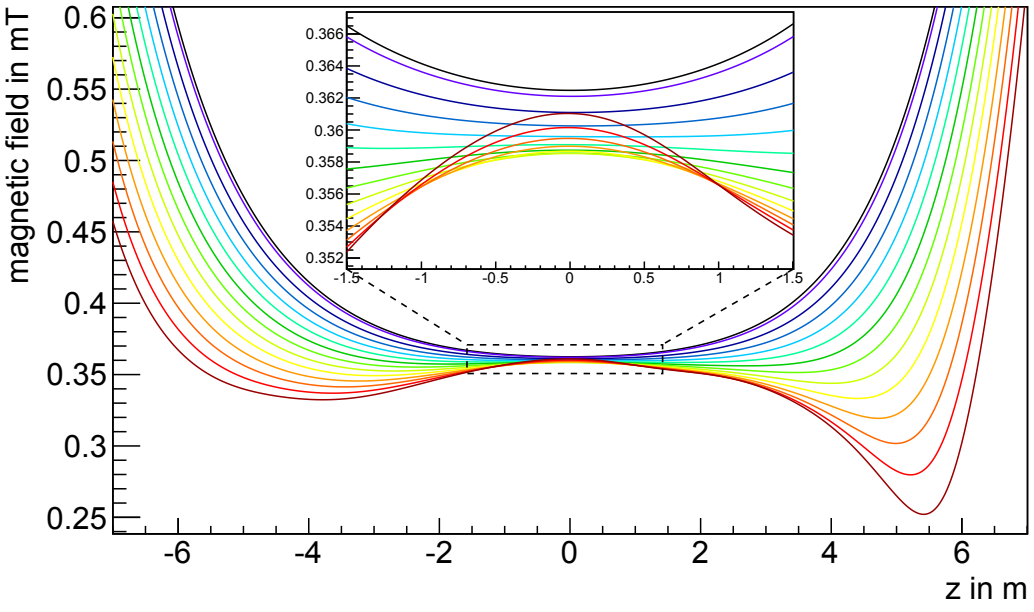

Figure 4.23: Magnetic field curves for the 3.8 Gauss setup shown in figure 4.21. While the magnetic field has a global minimum in the center of the main spectrometer for the field lines of the inner detector pixels, the outer field lines feature a local magnetic field maximum. Both lead to a minimum of the longitudinal kinetic energy if the homogeneity is sufficient, as explained in section 4.3.2. The total magnetic field in the center of the main spectrometer is 0.36 mT, while the shown setup comprises only a very small radial magnetic field inhomogeneity of 4 µT, as already shown in figure 4.17.

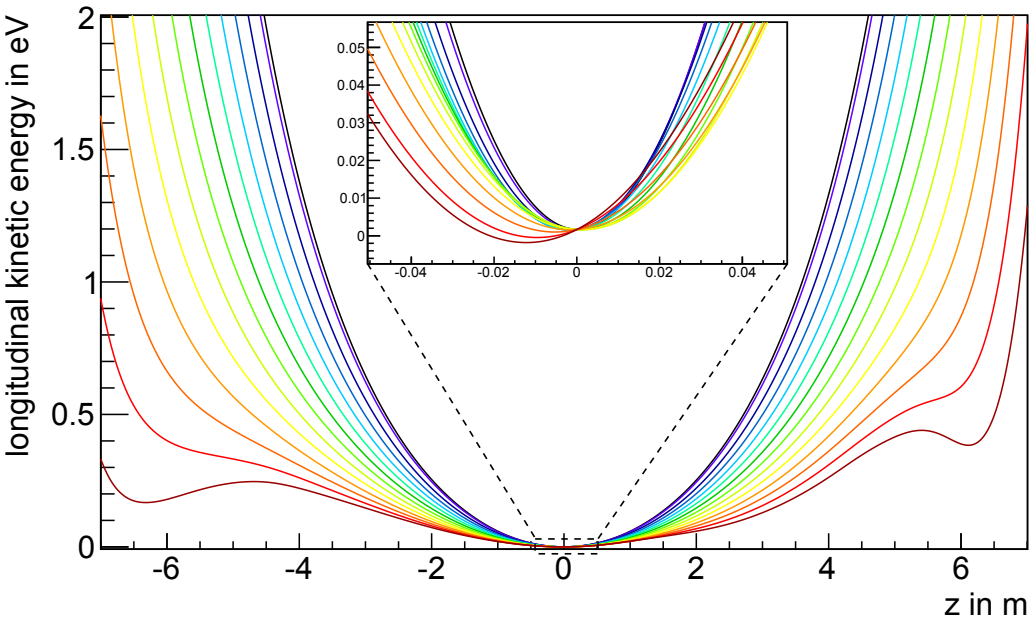

Figure 4.24: Longitudinal kinetic energy curves for the for the 3.8 Gauss setup shown in figure 4.21. The used initial polar angle in the entrance magnet of the main spectrometer is the maximum possible angle before magnetic reflection occurs of $\theta = 66°$. While the positions of the minimal longitudinal kinetic energy seem to be at $z = 0\,\mathrm{m}$, a more closer look in the zoomed region shows small deviation in the order of 10 mm. The field lines of the outer detector rings, having a large radius in the main spectrometer, show the largest deviation.

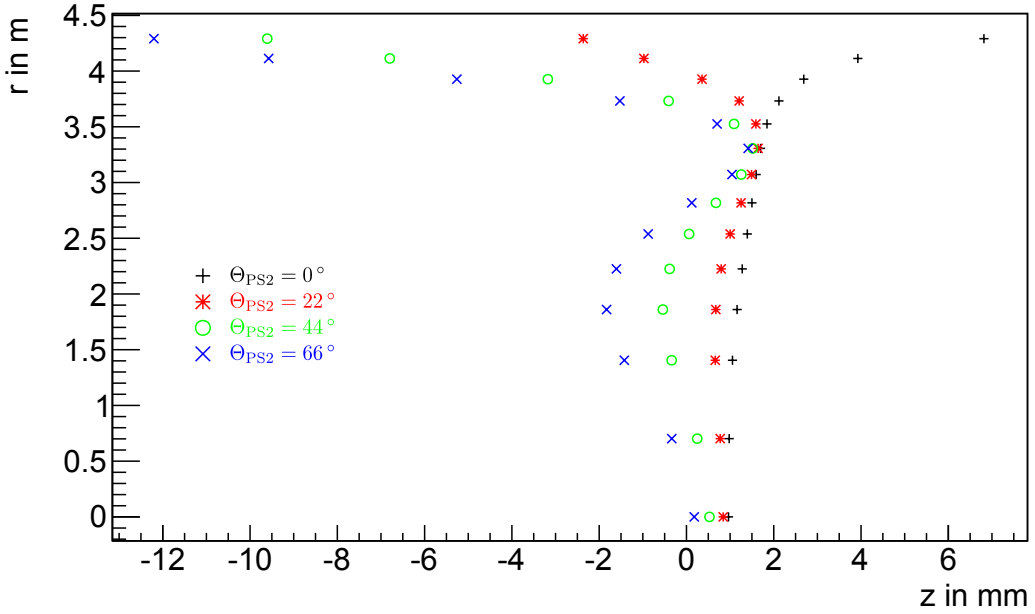

Figure 4.25: Analyzing plane position curves for the 3.8 Gauss setup shown in figure 4.21 with four different initial polar angles. There is a variation within one field line for different polar angles and also a deviation for the different field lines from $z = 0\,\mathrm{m}$. The deviation is most prominent for the outer field lines, but even there it is only in the order of 10 mm.

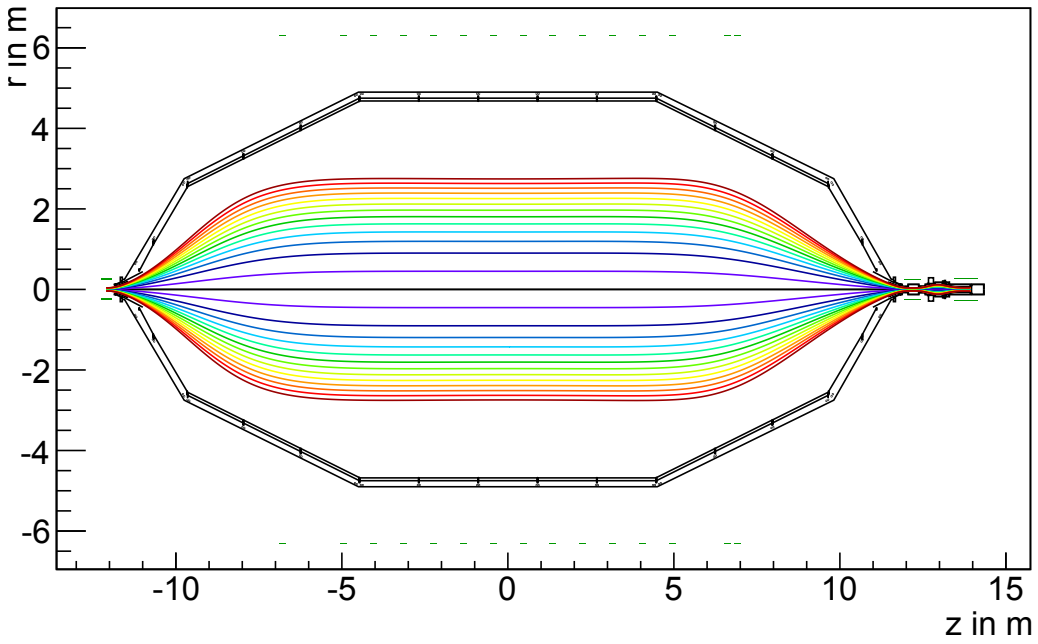

Figure 4.26: Field line simulation for the 9 Gauss setup. The field lines start in the PS2 magnet at the entrance of the main spectrometer and end in the focal plane detector system on the wafer. One field line for each detector ring has been calculated, according to figure 4.8. Due to the high central magnetic field of 0.88 mT, the flux tube in the center of the main spectrometer is smaller than in the 3.8 Gauss setup.

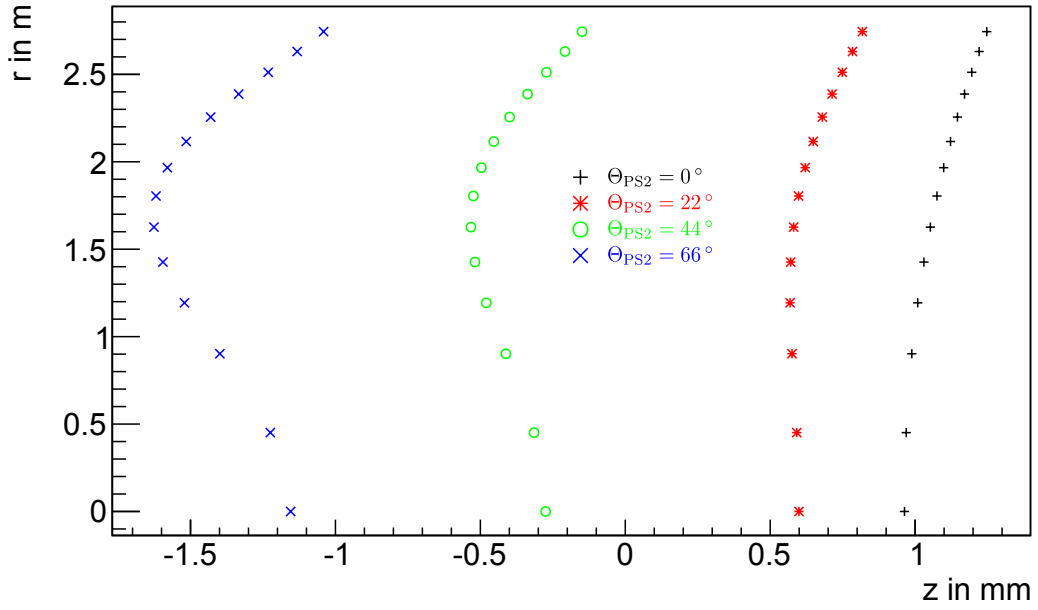

Figure 4.27: Analyzing plane position curves for the 9 Gauss setup shown in figure 4.21 with four different initial polar angles. The variation within one field line for different polar angles is more prominent than the deviation between different field lines. However, the deviation from $z = 0$ m is only a few mm.

hardware-related issues (see section 4.1) occurring during the measurement phase, have a big influence on the transmission conditions.

- The misalignment of the detector system does not only cause slightly different magnetic field values in the center of the main spectrometer due to the misaligned detector solenoids, but it also results in different magnetic field lines hitting a specific pixel due to the displaced and rotated wafer. The influence of these effects on the transmission conditions is still small, because outer detector rings, being the most critical ones due to their proximity of the corresponding field lines to the main spectrometer vessel and air coil system can be neglected, as they are shadowed by the in-line beam flapper valve, as discussed in section 4.2.1.
- The short circuit between the inner and outer wire layers of the central inner electrode modules has a significant effect on the transmission conditions of the outer field lines. As the inner wire layer can only be elevated on the same potential as the outer wire layer, the non-axi-symmetric influence of the wire holding structure is no longer shielded efficiently. Additionally, the gaps between the wire modules, housing special elements to compensate the potential rise caused by the gap, lead to a global potential minimum at the position of the gap for field lines close to the wire electrodes. More details about the influence of the short circuit on the transmission conditions caused by the wire holding structure can be found in [BCG+13].
- The potential configuration, caused by the high voltage scheme discussed in section 4.1.2, has a significant influence on the transmission conditions, as all individual electrode modules are put on an individual potential. Besides the dipole voltage, caused by the voltage difference between the west and the east electrode half shells, the shift of the minimal electrical potential away from the analyzing plane at $z = 0\,\mathrm{m}$, caused by the broken north-south symmetry, also needs to be considered.

All these effects have been incorporated into the simulation. The non-axi-symmetric parts of the wire holding structure and the potential configuration breaking also axi-symmetry, can only be calculated by making use of a realistic 3D-model of the main spectrometer, as introduced in 3.3.3. However, this entails the distinct disadvantage of a rather large computation speed compared to the fast axi-symmetric model used before. The 3.8 Gauss setup field lines with the tilted and displaced focal plane detector system are shown in figure 4.28. For the following simulations only field lines hitting active detector pixels detailed in figure 4.14 have been considered. Two typical voltage configurations in use for transmission function measurements, one without and one with high voltage on the main spectrometer vessel, will be investigated in the following.

High voltage phase

A generic example of a potential configuration during the high voltage measurement phase is given by the set $U_{\mathrm{vessel}} = -15.5\,\mathrm{kV}$, $U_{\mathrm{wire}} = -15.6\,\mathrm{kV}$ and $U_{\mathrm{steepcone}} = -15.5\,\mathrm{kV}$. The exact potentials on the individual wire electrode modules are summarized in table A.2. It can be clearly seen that there is a dipole voltage of about 0.4 V and the north-south mirror symmetry is also slightly broken.

Due to the broken axial symmetry, the electrostatic potential, the magnetic field and therefore also the longitudinal kinetic energy and the analyzing plane position do not longer depend only on the radius, but also on the full x-y position. The potential along the field lines on the z-x plane is drawn in figure 4.29, and the corresponding longitudinal kinetic energy is drawn in figure 4.30. The longitudinal kinetic energy has been computed for a theoretical particle propagating along its corresponding field line, starting with the transmission energy to be just transmitted at $z = 0\,\mathrm{m}$. As these values have been computed

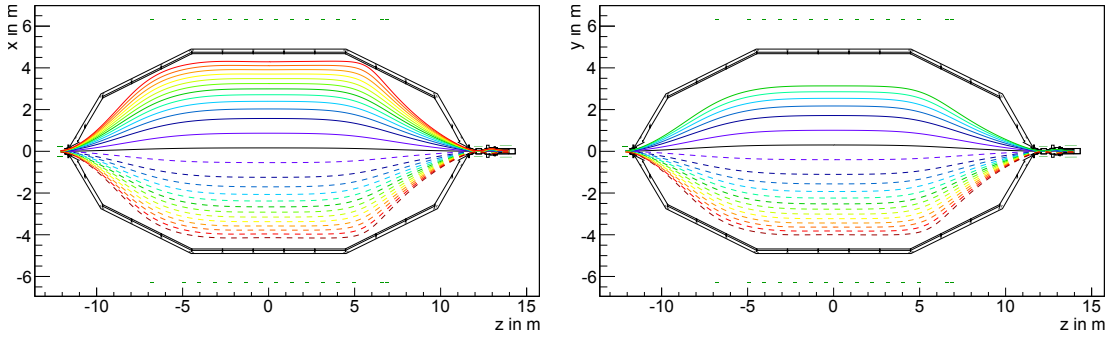

(a) z-x plane (top view)

(b) z-y plane (side view)

Figure 4.28: Field line simulation with the tilted FPD system for the 3.8 Gauss setup. The field lines start in the PS2 magnet at the entrance of the main spectrometer and end at the focal plane detector system on the wafer. One field line for each detector ring has been calculated, according to figure 4.8 but only field lines hitting usable detector pixels, according to figure 4.14, have been drawn. Due to the broken axial symmetry, the z-x plane (a) and the z-y plane (b) are drawn individually. Field lines ending on detector rings with negative x or y values, have been drawn with dashed lines.

for all points of the field line, negative kinetic energies show up as soon as the analyzing point diverges from the central position. These positions can not be obtained by the particle, as it is reflected as soon as its longitudinal kinetic energy reaches zero. The minimum for each field line is the analyzing point position, which is visualized for all field lines in the z-x and the z-y plane in figure 4.31 and figure 4.32.

The results show that there is a deviation of up to 0.9 m between the analyzing points of the different field lines and also the variation between different polar angles is up to 0.2 m. Therefore, the analyzing points do not form a simple analyzing plane as for an optimized setup as shown in the last section and the analysis of transmission functions measurements with this setting needs to incorporate all these effects, as it will be done in chapter 5.

No high voltage phase

For the measurement phase without high voltage on the main spectrometer vessel, the potential configuration is quite different, with the vessel being grounded and only one dipole power supply being used for both inner electrode half shells. The exemplary potential configuration shown here is $U_{\text{vessel}} = 0.0\,\text{V}$ and $U_{\text{wire}} = -1000\,\text{V}$. The exact potentials on the individual wire electrode modules are summarized in table A.4. Although only one dipole power supply was used, there is still a dipole of up to 1.2 V between the west and east parts of the modules, caused by the offset power supplies. Additionally, there is a large difference between the individual module rings of up to 2 V, breaking the north-south symmetry significantly.

Similar to the high voltage settings, field line simulations for this setup were performed as well. The potential along the field lines on the z-x plane is drawn in figure 4.33 and the corresponding longitudinal kinetic energy is displayed in figure 4.34. The resulting positions of the analyzing points for all field lines in the z-x and the z-y plane are visualized in figures 4.35 and 4.36.

Also, for the investigated setting without high voltage on the main spectrometer vessel, the positions of analyzing points show deviations of up to 2 m. Additionally, all analyzing point positions are shifted by a value of about 0.8 m in z direction (north) towards the detector section. This is caused by the potential configuration, as the north flat cone modules have a lower potential than the mirrored ones on the south side of the spectrometer. Also

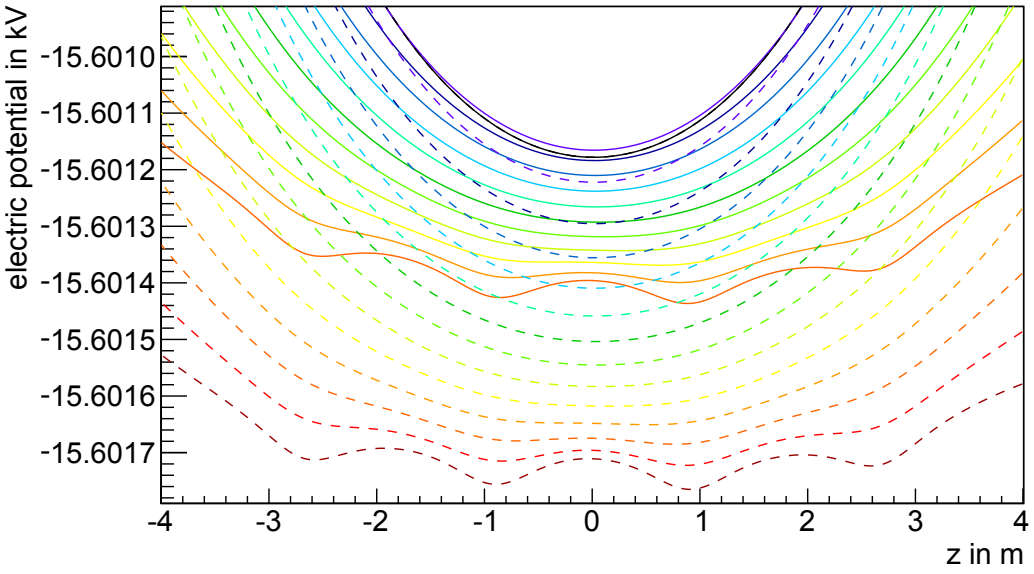

Figure 4.29: Electrostatic potential curves for the SDS high voltage setting as summarized in table A.2. The potential is plotted for the field lines on the z-x plane according to figure 4.28 (a). For the outer field lines, the potential minimum is no longer in the center of the spectrometer at $z = 0\,\mathrm{m}$, but at the gaps between the cylindrical wire modules at $z = \pm 0.9\,\mathrm{m}$, due to the short-circuit of the inner and outer wire layer. The absolute potential difference between the solid (west part) and the dashed (east part) lines is caused by the dipole potential.

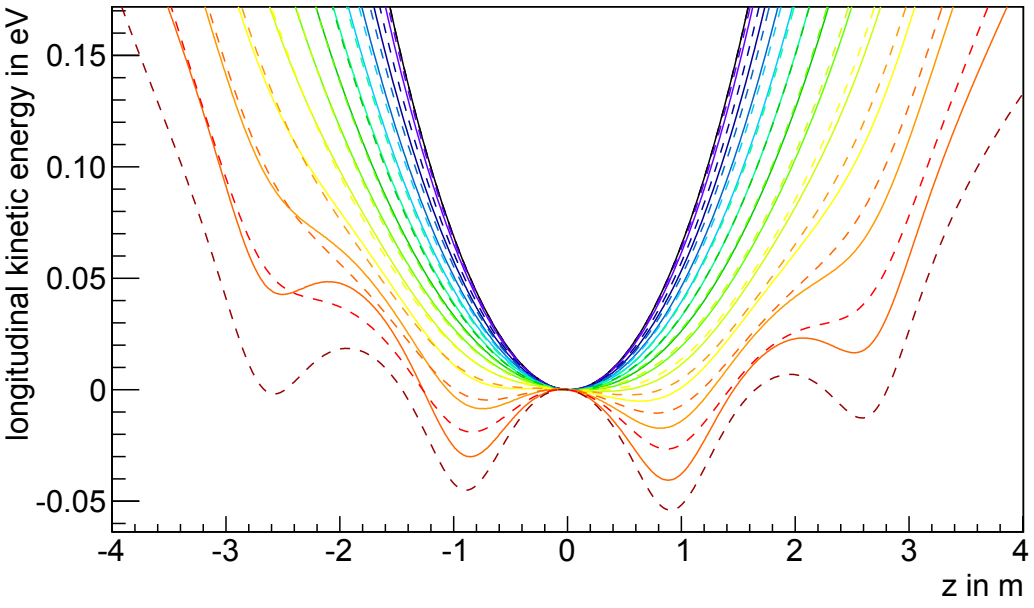

Figure 4.30: Longitudinal kinetic energy curves for the SDS high voltage setting as summarized in table A.2. The longitudinal kinetic energy is plotted for the field lines on the z-x plane according to figure 4.28 (a) with an initial polar angle of $\theta = 66°$. For the outer field lines, the minimum positions are strongly influenced by the potential minima at the wire module gaps at $z = \pm 0.9\,\mathrm{m}$. Negative kinetic energies in the plot occur due to definition of its zero value at $z = 0\,\mathrm{m}$, as explained in the text.

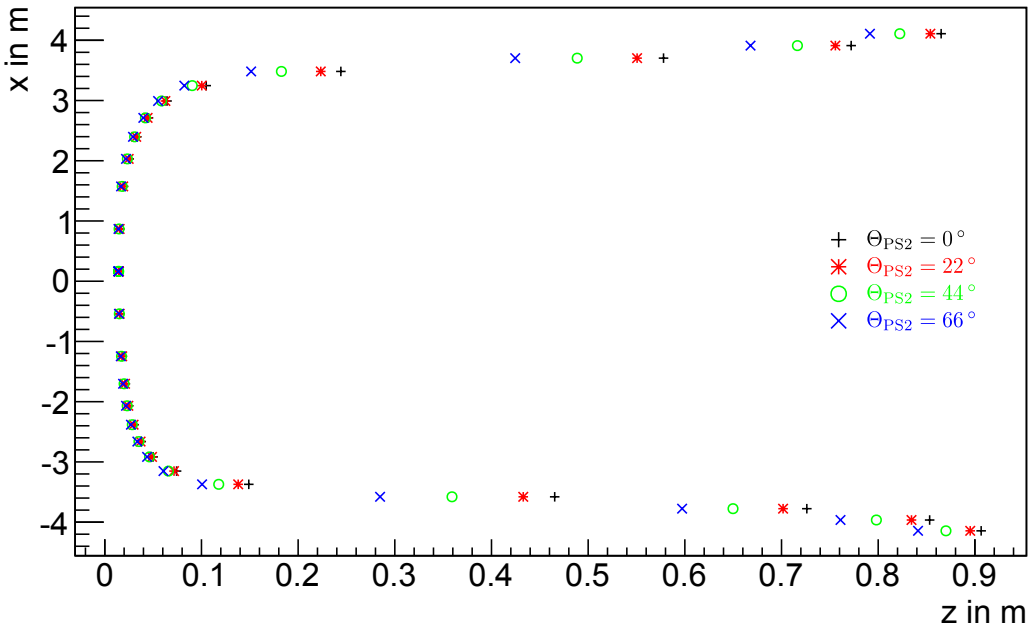

Figure 4.31: Analyzing points for the SDS high voltage setting for the field lines in the z-x plane for four different initial polar angles. There is not only a variation of the analyzing position due to the different polar angles, but also a large difference between the individual field lines, especially for the outer ones. The analyzing plane positions of the outer field lines move to $z = 0.9\,\mathrm{m}$, due to the potential minimum caused by gaps between the wire modules in the short-circuit configuration.

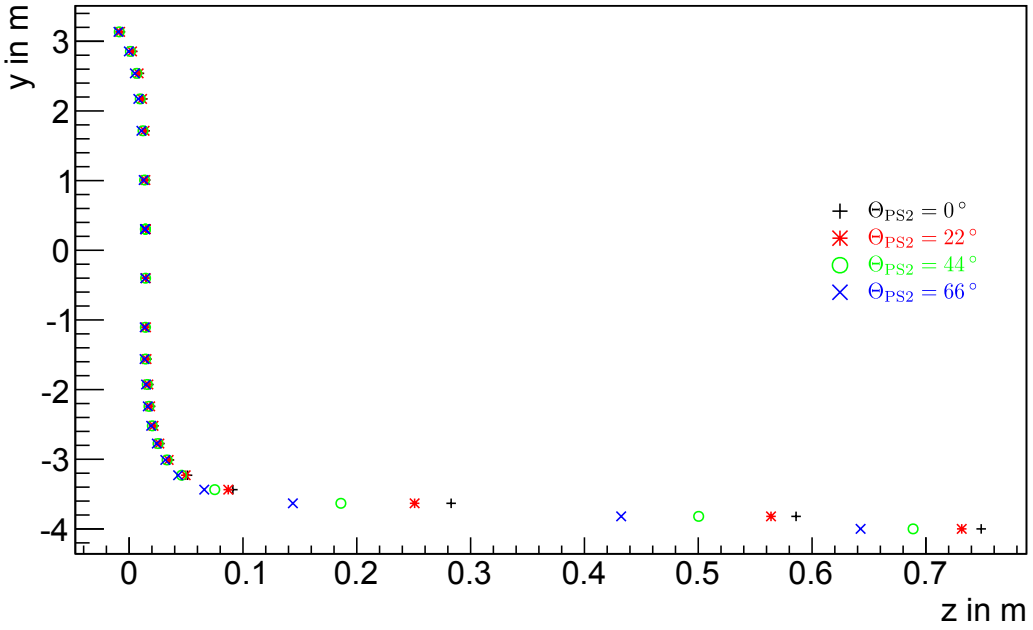

Figure 4.32: Analyzing points for the SDS high voltage setting for the field lines in the z-y plane for four different initial polar angles. There is not only a variation of the analyzing position due to the different polar angles, but also a large difference between the individual field lines, especially for the outer ones at negative y values. The outer field lines of the upper part are not displayed, as they are blocked by the in-line beam flapper valve.

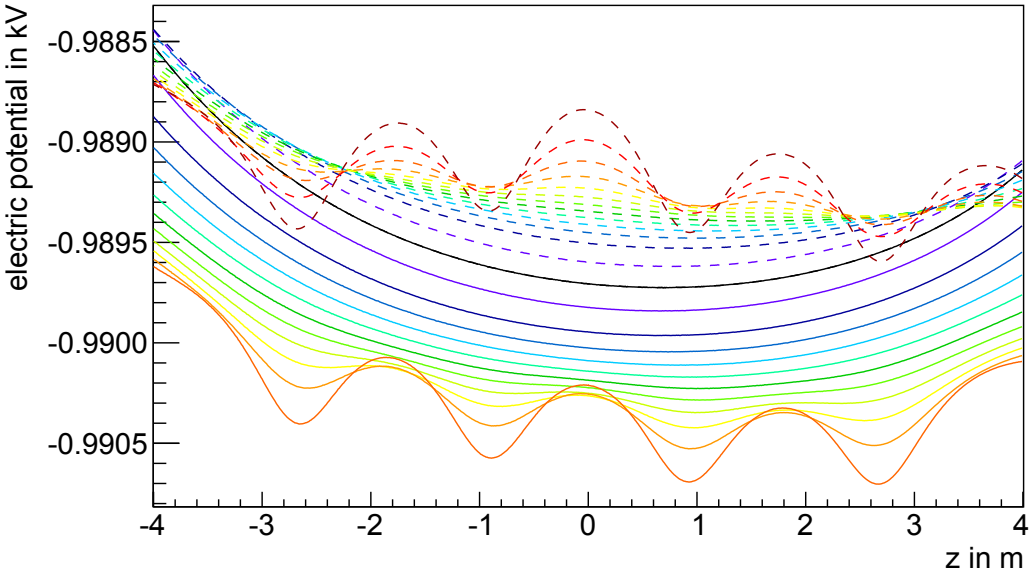

Figure 4.33: Electrostatic potential curves for the SDS setting without high voltage as summarized in table A.4. The potential is plotted for the field lines on the z-x plane according to figure 4.28 (a). Similar to the setting with high voltage, the outer field lines feature local potential minima at the gaps between the cylindrical wire modules at $z = \pm 0.9\,\mathrm{m}$, due to the short-circuit of the inner and outer wire layer. Additionally, the global minimum for the inner field lines is shifted to $z \approx 0.8\,\mathrm{m}$, due to the lower potential on the north flat cone, than on the south flat cone, especially on the east part. The absolute potential difference between the solid (east part) and the dashed (west part) lines is caused by the dipole between the west and east electrodes, being even more prominent than in the high voltage example.

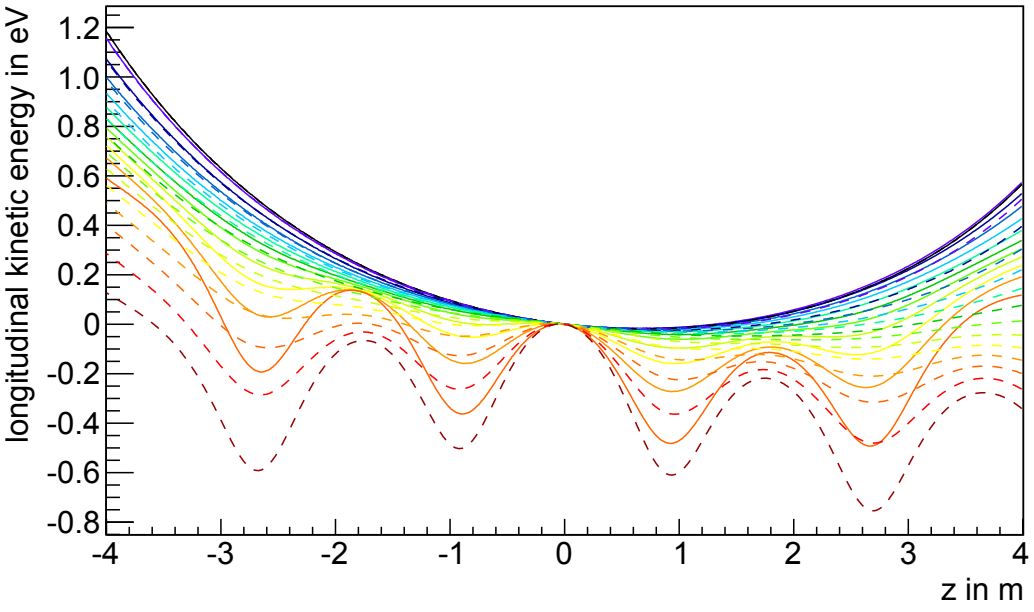

Figure 4.34: Longitudinal kinetic energy curves for the SDS setting without high voltage as summarized in table A.4. The longitudinal kinetic energy is plotted for the field lines on the z-x plane according to figure 4.28 (a) with an initial polar angle of $\theta = 66°$. The minimum positions are strongly influenced by the potential minima as shown in figure 4.33. The minima of the outer field lines are caused by the wire module gaps, but additionally the global minimum is shifted towards $z \approx 0.8\,\mathrm{m}$, due to the broken north-south symmetry of the electrostatic potential. Negative kinetic energies in the plot occur due to definition of its zero value at $z = 0\,\mathrm{m}$, as explained in the text.

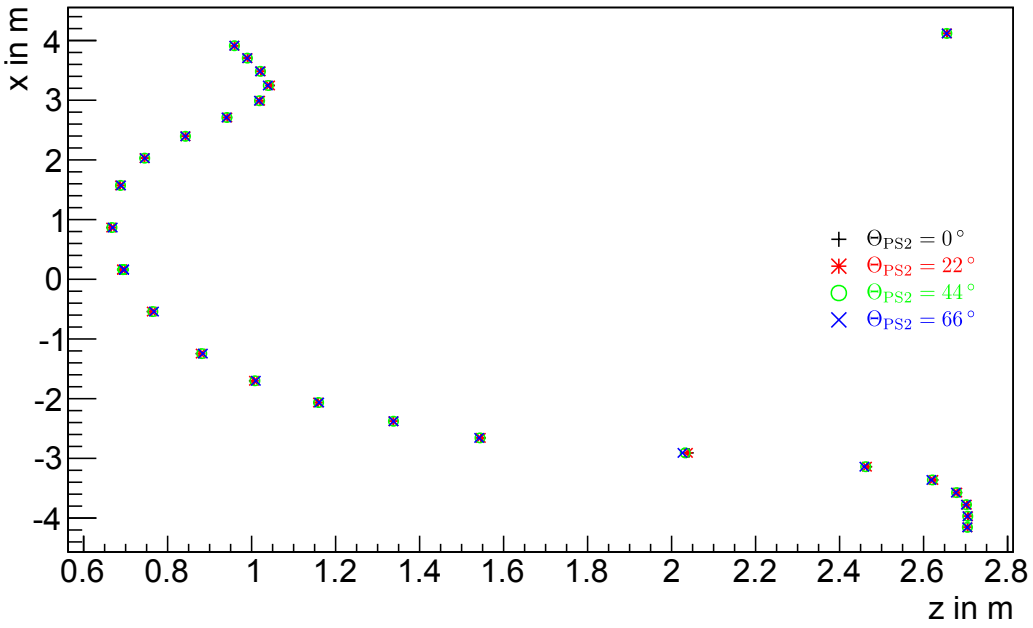

Figure 4.35: Analyzing points for the setting without high voltage for the field lines in the z-x plane with four different initial polar angles. While the variance in the analyzing point positions for different polar angles is very small, the position for different field lines has a very large spread with values up to $z = 2.7\,\mathrm{m}$.

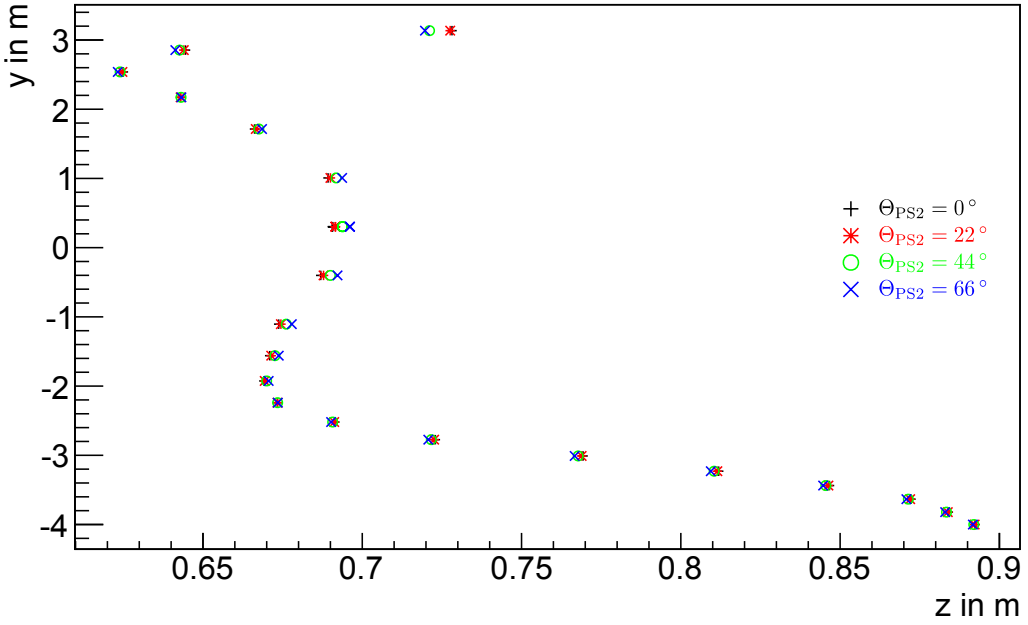

Figure 4.36: Analyzing points for the setting without high voltage for the field lines in the z-y plane with four different initial polar angles. As in the z-x plane, the variance in the analyzing point positions for different polar angles is very small, but the spread of positions for different field lines is much smaller than in the z-x plane. Moreover, all points are shifted to positive z values significantly.

for the measurements without high voltage, the analyzing points do not form a simple analyzing plane as for an optimized setup as shown in the last section. Evidently, the analysis of transmission functions measurements with this setting needs to incorporate all these effects, as done in chapter 5.

4.4 Monitoring of the magnetic field

The magnet system in operation during the SDS commissioning measurements, with its 4 s.c. solenoids and its large number of air coils in the LFCS and the EMCS (see section 4.1.3), is highly flexible in precise shaping of the magnetic field. Although some default settings have been calculated, as detailed in section 4.3, which were in use for the most important background and transmission measurements, many supplementary measurements with entirely different magnetic field setups were performed, including asymmetric field setups, where the magnetic field lines connect the detector wafer to the spectrometer vessel surface.

These setups not only required an adjustment of the currents of the power supplies driving the magnetic coils, but often also a change in polarity. For the hardware components in use this can imply a manual rewiring of the corresponding power supplies in the basement of the main spectrometer building. While the magnets of the detector system were operating in a fixed configuration during the SDS commissioning measurements, the remaining power supplies have been adjusted regularly: those of the two pre-spectrometer magnets, the 14 units for the LFCS and the 2 PSUs for the EMCS. While the current of the PS1 and PS2 were not monitored continuously, owing to technical data processing issues, the current of all LFCS and EMCS power supplies was written to the Slow Control database every few seconds. However, only the absolute values of the currents were recorded, and not the actual polarities.

To ensure the correct magnetic settings, the operator thus has to check the polarity of each coil manually using a compass, before a measurement starts. This interaction is not only inconvenient and rather time-consuming, but also touches safety issues as the basement of the main spectrometer building can not be accessed while the spectrometer vessel has been ramped up to high voltage. Therefore, a magnetic field monitor was developed, which was running during the SDS commissioning measurements for easy and fast visual check of the magnetic field settings.

4.4.1 Magnetic field monitor

The concept of the magnetic field monitor is a simple visualization of the magnetic flux in the main spectrometer based on the actual values of the coil currents, so that the operator obtains a visualization of changes to the coil currents immediately. It is then possible, for example, to check if the flux tube touches an electrode as a result of a magnetic field value which is too low, or to verify which specific detector ring is connected to a specific part of the vessel in an asymmetric setup.

The magnetic field monitor is incorporated into the Kassiopeia particle tracking package (see chapter 3), using many of its features. The actual values of the magnetic coil currents are automatically read from the Slow Control database, using its data access layer KaLi (see [Kle14]). With this information a magnetic field object can be created for calculation of the actual field lines from the detector wafer rings through the main spectrometer to the pre-spectrometer magnet PS1. For different EMCS settings in general, the field lines are no longer axi-symmetric. Therefore, they are visualized, together with the main spectrometer vessel and the detector system, in both the z-x and the z-y plane. Additionally, all current values of the individual coils are displayed to the operator screen, and in the center of

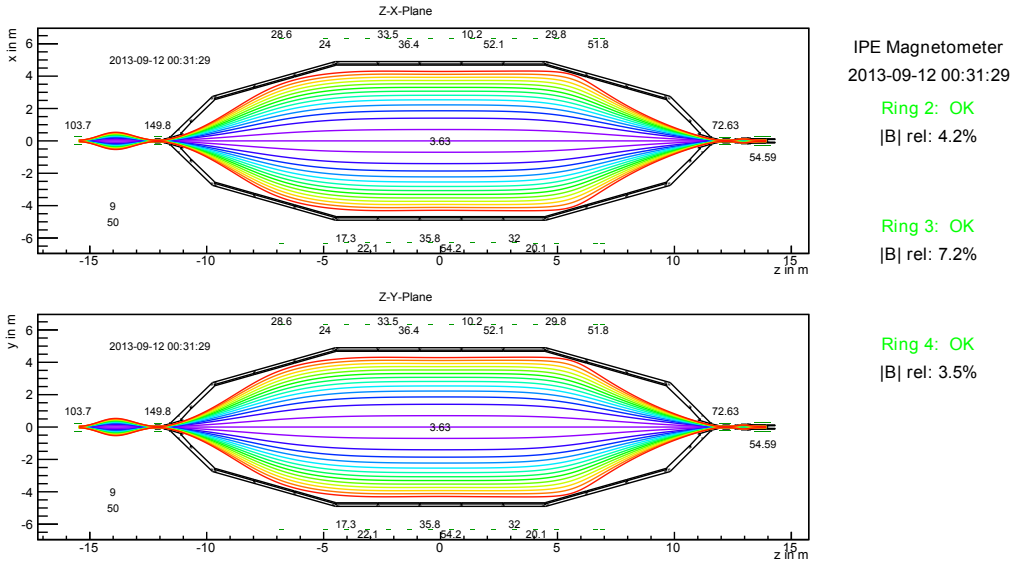

Figure 4.37: Output display of the magnetic field monitor. The actual currents of all coils (except the pre-spectrometer magnets) are read from the database and a corresponding field line simulation is done in the z-x and z-y plane. The operator can therefore easily see the resulting flux tube based on his chosen current values. Additionally, 24 magnet sensors, installed on 3 rings around the main spectrometer vessel, are read out and the value is compared to a calculation based on the actual current values. If the relative difference is larger than 10 %, an alarm is displayed and the operator should check the coils for their polarity.

the spectrometer the central magnetic field value is shown. Figure 4.37 shows an example of this online magnetic field monitor for an arbitrarily chosen moment during the SDS commissioning measurement phase. The creation of the output display takes less than 30 seconds, including all database calls to obtain actual current values, with all magnetic field and trajectory calculations done. Also, the operator has the possibility to interact with the output display, for example by zooming into a desired region, so the magnetic flux tube can easily be checked for collisions with the spectrometer or focal plane detector electrodes.

Additionally, the information from the 24 magnetometers of type KMZ10B and KMZ20M ([Erh15]), which are installed in 3 rings around the main spectrometer vessel, are being used. By comparing the actual magnetic field readings of these sensors with the corresponding magnetic field calculations based on the actual coil currents, a consistency check can be done. Due to the missing exact position and orientation data of the sensors during the first SDS measurement phase, only the magnitude of the magnetic field could be used for comparison, with a relative precision of about 10 %. For each sensor ring the monitor output displays the relative difference between measurement and calculation and triggers a warning if the relative difference is larger than 10 %, as shown in figure 4.37. Small changes in the actual currents can therefore not be detected, but incorrect polarities or failure of single coils can easily be identified as they usually result in a mismatch between the measured and calculated field values of more than 10 %.

After setting up the magnetic field monitor, the unit was always running permanently and being displayed on a separate run control monitor in the control room during the remainder of the SDS commissioning measurement phase. It proved to be a very useful tool, minimizing time periods with incorrect magnetic field settings significantly. To improve the limited precision of the magnetic field sensors, a new set of high precision magnetometers is currently being installed with inclinometers and laser-guided position determination [Ada15, Erh15].

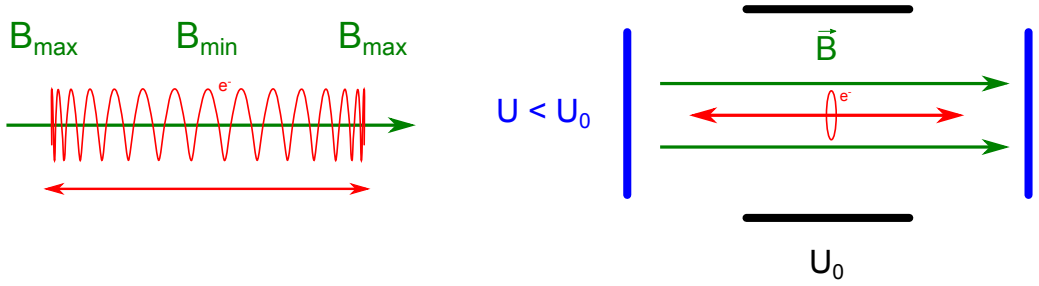

(a) Magnetic mirror trap (b) Penning trap

Figure 4.38: Two different types of stored particles in a MAC-E filter are shown. Sketch (a) shows a magnetically stored particle, that is trapped due to the magnetic mirror effect. In a penning trap (b) however, the particle is stored due to the potential well caused by the electrode configuration.

4.5 Measurements

During the entire SDS commissioning measurements, which lasted about 4 months, a large amount of data subdivided into more than 4000 individual runs was taken over hundreds of different measurements. This included calibrations, the commissioning of individual hardware components, auxiliary measurements, proof-of-principle measurements for background removal methods and many more [BBB+14].

The two most important objectives for the SDS commissioning measurements were the investigation of the transmission properties of the main spectrometer and the determination of the background composition. The measurement of the transmission properties is a major part of this thesis and will thus be discussed separately in chapter 5. The background has been investigated in detail in [Gör14, Sch14, Lei14], but the most important results will be summarized in the following section, preceded by an overview of the principal background processes in a MAC-E filter.

4.5.1 Background processes in a MAC-E filter

In the present understanding there are three generic background sources that can occur in a MAC-E filter experiment: Magnetically stored particles, Penning traps, and electron emission from inner surfaces. All these sources are based on different production mechanisms and have been intensively studied at the predecessor experiments at Mainz and Troitsk, and also the pre-spectrometer test experiment [K+05, Frä10, Gör10, Gro10, Mer12, Wan13]. All particles created from these sources usually have a rather low kinetic energy of less than 1 keV. However, when leaving the spectrometer, these particles are accelerated by the applied retarding potential towards the detector and therefore produce a signal in the detector energy spectrum in the same energy window as signal electrons, the region-of-interest. In the following, the different background sources are described in more detail.

Magnetically stored particles

In case that charged particles are created inside the volume of the spectrometer, they can be trapped due to the magnetic mirror effect. As explained in section 2.1.1, particles propagating towards the increasing magnetic field at the entrance or exit region of the main spectrometer will transform their longitudinal kinetic energy into the transversal component, so that their polar angle θ increases. When θ reaches a critical value of 90°, the longitudinal kinetic energy vanishes and the particle will be reflected. Particles starting in a low magnetic field region with high magnetic fields on both sides like in the main spectrometer are thus very likely to be trapped, as shown in figure 4.38 (a). A prime

source for creation of charged particles inside the spectrometer volume at UHV conditions are radioactive decays of single tritium or radon atoms. While background from tritium only needs to be considered once the tritium source is connected to the spectrometer (which was not the case during SDS commissioning measurements), the background component originating from radon decay plays an important role and will be detailed in section 4.5.4.

Penning traps

A Penning trap is formed by a localized volume in which charged particles are stored by an interplay of magnetic and electrostatic fields. These particles are confined in radial direction by the magnetic field and in axial direction by the potential well, as sketched in figure 4.38 (b). A single stored electron in a trap can produce a considerable number of background events via messenger particles such as ions or photons, which leave the trap to produce further secondary particles inside the sensitive flux tube volume. Very small volumes in the order of cm^3 are sufficient to produce background rates in the range of 10^3 cps [Hil11, Mer12, Wan13].

In order to avoid the creation of Penning traps, the electrodes in the main spectrometer were designed on the basis of electromagnetic field calculations and simulations such as the KASSIOPEIA package, and lessons learned at predecessor experiments and in particular at the pre-spectrometer setup [Frä10].

Electron emission from inner surfaces

The inner surfaces of the main spectrometer vessel of $690\,m^2$ and its inner electrode system of $460\,m^2$ are potential areas for electron emission which is a primary concern for the KATRIN experiment. The main source for electron emission are cosmic rays (mainly minimal ionizing muons [Lei14]) that interact with the stainless steel vessel of the spectrometer, thereby creating secondary electrons. Environmental and intrinsic radioactivity can also create secondary electrons on the surface, but only in much lesser numbers. More details about the electron background induced by cosmic muons and the undertaken countermeasures are described in section 4.5.3.

Additionally, all sharp edges and areas with non-negligible surface roughness at the inner electrode system can generate high electric field strengths within a narrow region. This can lead to field electron emission, where low-energy electrons are able to leave the surface by the tunnel effect. This can be avoided by using potential settings where the voltage offset between the vessel and inner electrode system is less than 250 V, as investigated in [Sch14].

4.5.2 Background measurements

After the high voltage of the main spectrometer was ramped up and the detector valve was opened, a 24-hour background measurement was initialized. For the potential configuration, the default short-circuit setup was used with $U_{\text{vessel}} = -18.5\,\text{kV}$, $U_{\text{wire}} = -18.6\,\text{kV}$, $U_{\text{steepcone}} = -18.5\,\text{kV}$ and $U_{\text{PAE}} = 10\,\text{kV}$. For the magnetic field the 3.8 Gauss setup was used.

The resulting rate at the detector is plotted in figure 4.39 and its mean value in the region of interest between 25.6 and 30.6 keV is (781.9 ± 2.7) mcps. The achieved background rate below 1 cps is one of the major successes of the SDS commissioning measurement, as no evident Penning trap or Penning discharges were observed, in contrast to the pre-spectrometer test setup, which experienced these background-generating processes when being ramped up for the first time [Frä10]. Nevertheless, the ambitious goal of measuring the neutrino mass with a sensitivity of $m_\nu = 200\,\text{meV}/c^2$ at 90 % C.L. requires a

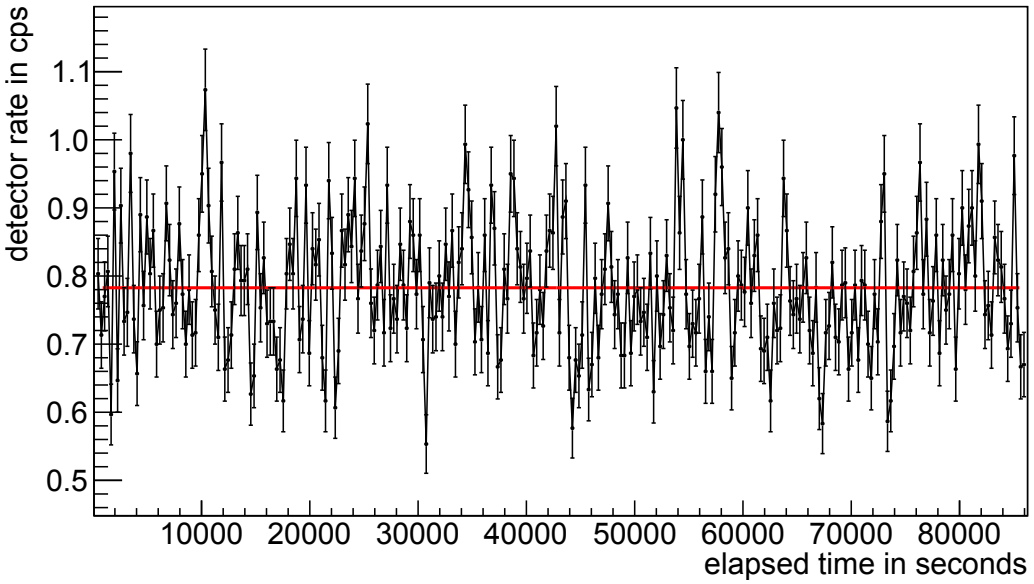

Figure 4.39: Total background rate at a high voltage configuration of −18.6 kV with the 3.8 Gauss magnetic setup. The mean rate is (781.9 ± 2.7) mcps.

total background rate below 10 mcps in the region of interest. Therefore, a further reduction of the background is mandatory, which requires a detailed understanding of the measured background composition. Supplementary measurements [BBB+14] showed that main contributions to the background originate from single radon atoms decaying in the main spectrometer volume, and cosmic muons creating secondary electrons on the inner main spectrometer surface, both being discussed in the following.

4.5.3 Muon induced background

Due to the large size of the spectrometer and in particular due to the required large tritium infrastructure, the KATRIN experiment can not be operated in an underground laboratory as other low background experiments. Therefore, the large flux of cosmic rays is of great concern for the background rate. The total expected muon flux on the surface of the main spectrometer is between 75 and 79 kcps [BBB+14]. There, muons interact with the stainless steel walls to produce secondary electrons. These are a major source of background, if entering the sensitive flux tube. The mechanism of secondary electron production is described in more detail in [Mer12, Wan13, Lei14].

Countermeasures

In order to prevent secondary electrons created at the spectrometer surface from entering the sensitive flux tube, two independent shieldings are available in the main spectrometer.

- The dominant part is played by magnetic shielding, which is a natural feature of a MAC-E filter experiment. Due to the Lorentz force, electrons are constrained to a cyclotron motion around the guiding magnetic field line and are therefore reflected back to their point of production at the surface, as illustrated in figure 4.40 (a). However, deviations from an ideal axial symmetry, caused for example by tilted magnets or a dipole potential configuration as stated in sections 4.1.2 and 4.2.1, will lead to radial drifts of electrons into the sensitive flux tube volume [Lei14]. In total, the magnetic shielding is expected to reduce the background by a factor of about 10^5.

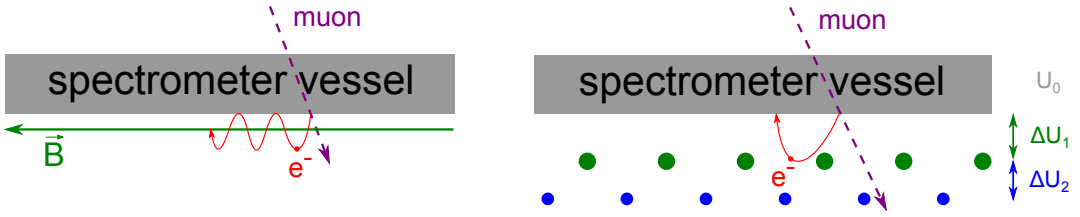

(a) Magnetic shielding (b) Electrostatic shielding

Figure 4.40: Sketch of the working principle of magnetic (a) and electrostatic (b) shielding. While the Lorentz force prevents the particles from moving perpendicular to the magnetic field lines at the magnetic shielding, the electrostatic shielding repels the particles through the wire electrodes, which are negative with regard to the spectrometer vessel.

- The electrostatic shielding plays a sub-dominant role and is achieved by the wire electrode system installed at the inner surface of the main spectrometer, as detailed in section 4.1.2. As the two wire layers can be operated at a negative potential offset with respect to the main spectrometer vessel, secondary electrons created at the vessel surface are repelled for initial kinetic energies of $E_{\text{kin}} < q(\Delta U_1 + \Delta U_2)$, as illustrated in figure 4.40. During the SDS commissioning measurements, the inner wire layer could however only be operated with the same potential as the outer wire layer, due to electric shorts in the system. For a two wire layer electrostatic shielding a total reduction factor of 10^2 is expected.

4.5.4 Radon induced background

Large parts of the inner main spectrometer surface, such as the welding seams of the spectrometer vessel, and auxiliary units such as the NEG pumps with their total strip length of 3 km, are major sources of emanation of the neutral radon isotopes ^{219}Rn, ^{220}Rn, and ^{222}Rn. These isotopes originate from the primordial isotopes ^{235}U, ^{232}Th, and ^{238}U through α- and β-decay chains. The neutral radon atoms are unaffected by the magnetic or electrostatic shielding of the MAC-E filter. Thus, emanation processes will lead to a homogenous radon distribution inside the volume of the main spectrometer vessel. The two isotopes ^{219}Rn and ^{220}Rn have relatively short half-lifes of $\tau_{1/2} = 3.96(1)$ s and $\tau_{1/2} = 55.6(1)$ s, respectively, and therefore will usually decay inside the spectrometer before being pumped out by the turbomolecular pumps with an effective pump-out time of about 360 s [Gör14]. The isotope ^{222}Rn on the other hand with its half-life period of $\tau_{1/2} = 3.82$ d is largely pumped out by the TMPs before it can decay, and can therefore be neglected in the following discussion [FE04].

On the atomic scale, the radon α-decay into ^{215}Po and ^{216}Po is a complex process, involving internal conversion, inner shell shake-off, atomic relaxation and atomic-shell reorganization sub-processes. This leads to the emission of multiple electrons in the energy range from a few eV to hundreds of keV, as sketched in figure 4.41. This Radon background model is described in more detail in [Frä10, Mer12, WDF+13a, Wan13, WDF+13b].

Depending on their polar angle, primary electrons associated with radon decay are stored with high probability in the MAC-E filter due to the magnetic bottle effect, as explained in section 4.5.1. While the trapped particle performs a fast axial oscillation caused by the magnetic mirror, it also follows a cyclotron motion around its magnetic field line and exhibits a rather slow azimuthal magnetron motion around the magnetic field axis, as shown in figure 4.42. Due to scattering off residual gas atoms and molecules in the UHV of the main spectrometer and emission of synchrotron radiation, the electron loses energy and is cooled. The cool-down time strongly depends on the initial energy of the primary

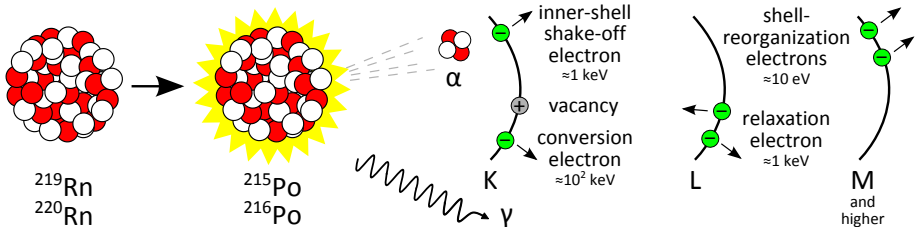

Figure 4.41: Overview of electron emissions accompanying the α-decay of radon. Processes like shake-off, conversion and shell relaxation produce multiple electrons with energies from a few eV up to several hundred keV. Figure from [Sch14].

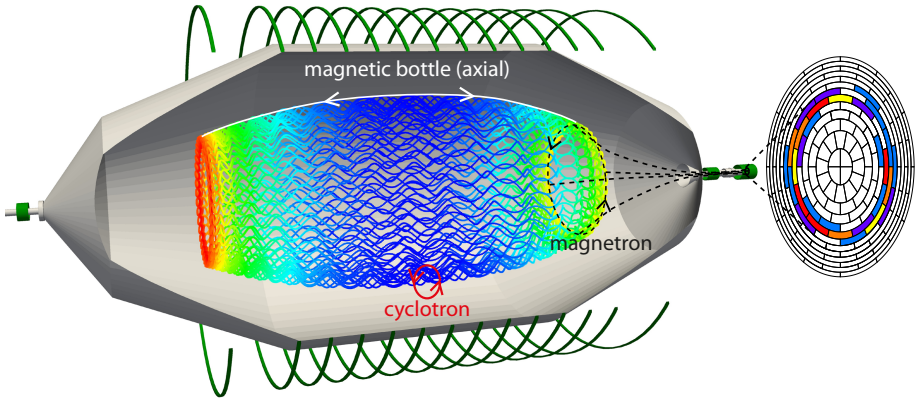

Figure 4.42: Simulation of the trajectory of a primary electron originating from a radon decay, which is magnetically trapped inside the main spectrometer. While performing a fast axial motion due to the magnetic mirror, it performs a cyclotron motion around its magnetic field line and furthermore a slow azimuthal magnetron motion around the spectrometer axis. During its cool down process caused by scattering off residual gas and synchrotron radiation, it produces low-energy secondary electrons via ionization. These low-energy secondary electrons are more likely to escape the magnetic trap and are accelerated either to the entrance of the main spectrometer or to the detector section, where they produce a characteristic ring shaped-distribution on the detector wafer. Figure from [BBB$^+$14].

electron and the pressure inside the main spectrometer. It can last for up to an hour for primary electron energies of several keV at a pressure of 10^{-10} mbar [Wan13]. During this rather long cool-down process, a cascade of low-energy secondary electrons is produced via residual gas ionization. The number of generated secondaries depends on the initial energy of the primary particle. Each inelastic scattering process causes on average an energy loss of 37 eV for the primary electron [Sch14], so hundreds of secondary particles can be produced by a single primary electron with an initial kinetic energy of several keV. As secondary electrons are created with a small kinetic energy, they are more likely to escape the magnetic trap, so that they can be guided onto the detector wafer. Due to the magnetron circle of the primary particle in the main spectrometer volume, the hit pattern of secondary particles on the focal-plane detector wafer has a characteristic ring-shaped structure, as visualized in figure 4.42.

Countermeasures

In order to reduce the radon induced background in the main spectrometer, a direct approach is to prevent emanating radon atoms from entering the sensitive flux tube. For the radon atoms emanating from the NEG pumps, which have a big contribution to the radon background, this can be implemented rather easily. As the NEG pumps are installed in the three big pump ports being connected to the vessel, a liquid nitrogen cooled baffle

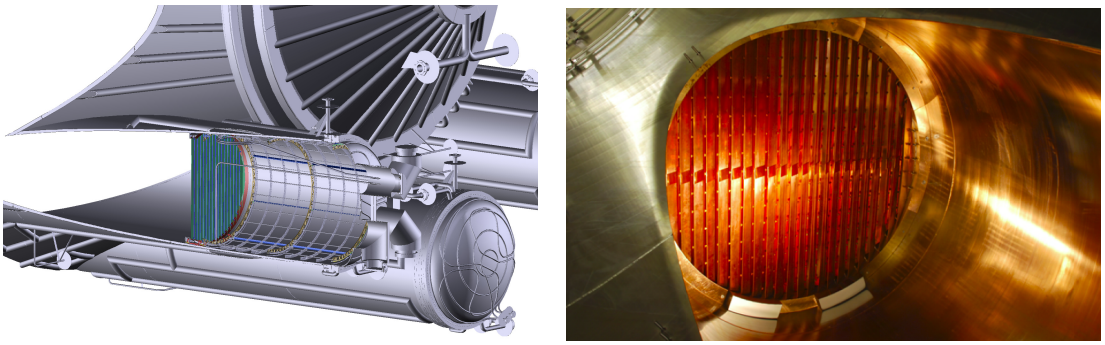

(a) CAD drawing of pump port with baffle

(b) Photo of baffle, from inside

Figure 4.43: CAD drawing of the three big pump ports of the main spectrometer (a). The liquid nitrogen cooled baffle is installed at the connection of the pump port to the spectrometer. A photo shows the cryogenic copper baffle system (b) from inside the main spectrometer. The baffle prevents a direct line-of-sight from the NEG pump within the pump port and the sensitive spectrometer volume, thus preventing emanated radon from entering and decaying inside the flux tube. Figures adapted from [Kle14] and [Gör14].

system made of copper was installed in each of the pump ports between the NEG pumps and the sensitive spectrometer volume, as shown in figure 4.43. It prevents a direct line-of-sight for radon emanating from the NEG pumps, while maintaining the ultra-high vacuum conditions in the main spectrometer. The copper surface, when cooled down to the cryogenic temperatures of liquid nitrogen will cryotrap radon atoms, thereby preventing their subsequent decay inside the sensitive flux tube volume. Additionally, radon atoms originating from the inner spectrometer surface also have a chance to be adsorbed on the cold baffle surface. The baffle system was carefully designed so that it does not significantly compromise the effective NEG pumping speed for hydrogen and tritium. A more detailed description of its technical implementation can be found in [Gör14].

In addition to the passive method of the liquid nitrogen cooled baffle, several active methods were tested during the SDS commissioning measurements to reduce the radon induced background. These techniques intend to break the storage condition of the primary trapped electron, removing it in radial direction from the MAC-E filter before a cascade of secondary electrons by ionizing collisions is created. This can be achieved by modifying the electromagnetic settings, using a pulsed electric dipole [Wan13], a magnetic pulse [Hil11, Wan13] or the method of electron cyclotron resonance [Mer12].

4.5.5 Results

The baffle system was installed before the SDS commissioning phase and its influence with respect to radon-induced background could be investigated by cooling it down to liquid nitrogen temperatures. A four hour measurement was performed with the same settings as for the 24 hour background measurement without activated baffle system. The resulting mean rate in the region of interest is (472.6 ± 5.7) mcps. The different radial rate distributions are shown in figure 4.44.

With supplementary measurements, such as under artificially elevated vacuum conditions inside the main spectrometer to reduce the storage times of the primary electrons, it has been shown that the baffle reduces a considerable fraction of the radon-induced background [Sch14]. The remaining background of (472.6 ± 5.7) mcps is therefore attributed to the muon-induced component [Lei14].

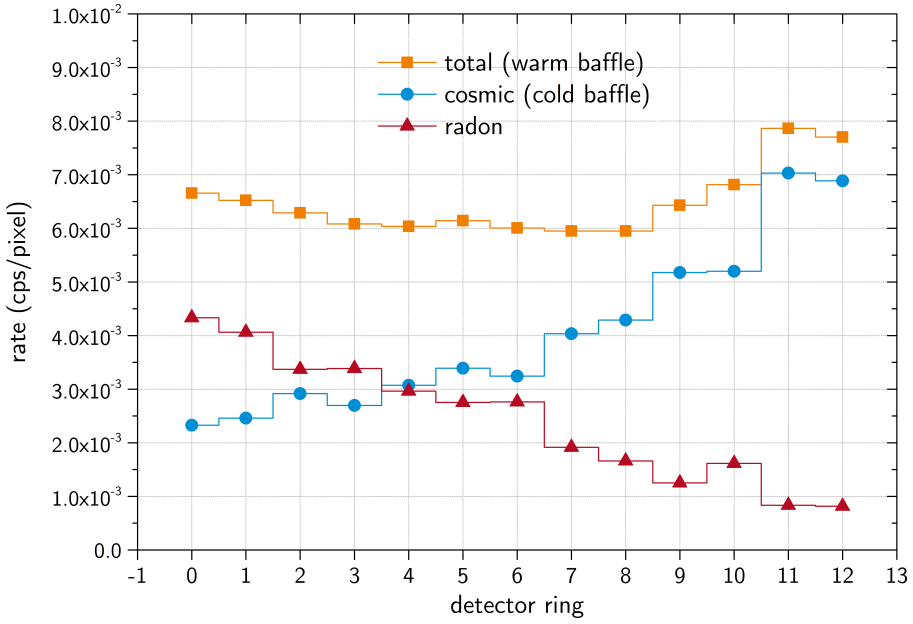

Figure 4.44: Radial background distributions with warm (yellow) and cold (blue) baffle. The difference of both (red) is therefore originating from radon. The remaining background with cold baffle is expected to be dominated by cosmic particles. Figure from [Kle14].

4.6 Conclusion

The SDS commissioning measurements performed in summer 2013 turned out to be very successfully, as the interplay of all hardware and slow-control components could be demonstrated. Furthermore, the complex analysis and simulation software could be validated with experimental data. Nevertheless, a few subcomponents were subject to technical issues. Due to the short-circuited wire electrode modules, the inner electrodes could only be used in a single layer configuration. This limited the efficiency of the electric shielding and therefore increased the measured background rate, as secondary electrons originating from the wire holding structure could not be shielded anymore. Additionally, the short circuit deteriorated the transmission conditions on outer field lines, owing to the altered shape of the electrostatic potential close to the wire electrodes. The scheme of the high voltage distribution was very flexible, but also resulted in slightly different potentials on each wire module, thereby causing among other things, an electric dipole field across the main spectrometer.

The misalignment of the focal-plane detector system entailed a slight reduction in the efficiency of the detector, as some pixels could not be used for the analysis. However, the misalignment did not compromise the planned measurements, as it could be incorporated into the analysis and simulations. This is also valid for the apparent misalignment of the electron gun, as its offset could be quantified. The corresponding measurements show an agreement on a pixel level when comparing to KASSIOPEIA particle tracking simulations.

The calculated magnetic field configurations for optimal transmission conditions with a common analyzing plane for all field lines and polar angles in the middle of the spectrometer at $z = 0\,\mathrm{m}$ were compromised by the short circuit in the electrode system and especially by the non-intended potential configuration. The resulting transmission conditions lead to a highly twisted analyzing plane. However, this did not harm the transmission function measurements significantly, as all these effects are considered in the analysis.

The most important physics objective of the first SDS commissioning phase, the investigation of the MAC-E filter system with regard to transmission properties and background

composition have thus been met. The required preconditions for the analysis of measured transmission functions like the misalignment of the subcomponents and the determination of the analyzing point positions have been detailed within this chapter. In the next chapter the magnetic guidance and the electrostatic retardation of the MAC-E filter system will be confirmed showing good agreement of the measured data with corresponding KASSIOPEIA simulations. The measured background rate of below 1 cps is also a great success for the first operation of such a large UHV vessel. As a neutrino mass measurement with a sensitivity of 200 meV at 90 % C.L. requires a background rate lower than 10 mcps, there is still significant room for improvement. The main reasons for the measured background rate are expected to be a result of the short circuits in the inner electrode system, and the deviation from the axial symmetry caused by the misaligned solenoids, both resulting in less efficient magnetic and electrostatic shielding mechanisms. As these issues were fixed partially after the measurement phase was finished, a lower background rate is expected for the next SDS commissioning phase starting at the end of 2014.

5. Measurement of the transmission properties of the main spectrometer

To successfully determinate the neutrino mass with a sensitivity of $200\,\mathrm{meV}/^2$ at 90% C.L., the transmission function of the main spectrometer has to be known very precisely, as the differential tritium β-decay spectrum is measured in an integral mode, as outlined in chapter 2. The transmission function of the main spectrometer for the molecular tritium source with its isotropic angular distribution and at a fixed initial electron energy can not be measured directly. It has to be calculated from an analytical formula, or obtained via Monte Carlo simulations, as will be detailed in chapter 6. An important input parameter for both methods is the layout of the magnetic field and the electrostatic potential inside the main spectrometer and the radial inhomogeneity of both quantities. These can be measured by using a quasi monoenergetic, angular selective electron gun, as done in the commissioning measurements of the spectrometer and detector section. Due to specific hardware issues with the electron gun, as stated in the previous chapter, only the radial potential inhomogeneity could be determined.

As the hardware settings of the entire SDS part of KATRIN are not yet in their final stage of functionality, the focus of the potential measurements discussed here is set on developing a sophisticated measurement and analysis strategy to validate the current models. First, the theoretical aspects of the transmission function will be discussed in section 5.1. The basic formulas that are needed for transmission function calculations will be presented and the different influences of source and spectrometer properties and their correlation will be discussed and visualized in examples. Afterwards an analysis strategy to extract the source properties from transmission function measurements will be presented in section 5.2 on the basis of electron gun measurements during the SDS commissioning measurements. Monte Carlo particle tracking simulations that were performed will be discussed in section 5.3, showing an excellent agreement of simulated and measured data. The key section of this chapter is the analysis of the radial potential inhomogeneity measurements, performed for different electrostatic settings of the main spectrometer in section 5.4. A comparison with potential simulations based on a fully detailed 3D main spectrometer model reveals a precision of about 30 mV for the measured radial potential inhomogeneity of the main spectrometer's high voltage settings. Finally, sensitivity studies will be carried out in section 5.5 to investigate the influence of different spectrometer properties on the obtained neutrino mass and to deduce the mandatory precision requirements for the radial potential inhomogeneities of the electrostatic potential and magnetic field.

5.1 Theoretical aspects of the transmission function

The shape of the transmission function depends on the non-trivial interplay between multiple source and spectrometer properties. In the following section (5.1.1) basic formulas to calculate the transmission function are presented. For the SDS commissioning phase, where transmission function measurements were performed with an electron gun, the basic formulas have to be adapted, as shown in section 5.1.2. The individual influence of the source properties, the energy and the angular distribution, as well as the spectrometer properties on the shape and position of the transmission function will be detailed in section 5.1.3 and 5.1.4, while the correlation of these properties will be discussed subsequently in section 5.1.5.

5.1.1 Basic formulas for transmission function calculation

The shape of the transmission function depends on different source and spectrometer properties, which are best discussed by the transmission energy, as described in equation 4.9:

$$E_{\mathrm{tr}} = \frac{q(U_{\mathrm{A}} - U_{\mathrm{S}})}{1 - \sin^2(\theta_{\mathrm{S}}) \cdot \frac{B_{\mathrm{A}} \cdot (\gamma_{\mathrm{S}}+1)}{B_{\mathrm{S}} \cdot (\gamma_{\mathrm{A}}+1)}}. \tag{5.1}$$

The spectrometer properties are defined solely by the electrostatic potential U_{A} and the magnetic field B_{A} at the analyzing point, when the electromagnetic setup has been optimized with regards to the transmission conditions, as detailed in section 4.3. The source properties are described by the starting energy E_{S} and starting polar angle θ_{S} of an electron propagating through the spectrometer. Only electrons with a starting kinetic energy E_{S} larger than the transmission energy E_{tr} will pass the MAC-E filter to be counted at the detector.

When considering a source with fixed starting energy E_{S} and polar angle θ_{S}, the variation of the spectrometer potential U_{A} will results in a transmission function $T(U_{\mathrm{A}})$, which can be described by a step function

$$T(U_{\mathrm{A}}) = \Theta(E_{\mathrm{S}} - E_{\mathrm{tr}}(U_{\mathrm{A}})), \tag{5.2}$$

which is 0 for $E_{\mathrm{S}} < E_{\mathrm{tr}}$ and 1 for $E_{\mathrm{S}} \geq E_{\mathrm{tr}}$.

For non-monoenergetic sources, such as an electron gun, the starting energy of the electrons E_{S} is described by a distribution $F(E_{\mathrm{S}})$. The fraction of electrons with a starting energy E_{S} bigger than the transmission energy E_{tr} are transmitted, so that the transmission function can be expressed with the following integral

$$T(U_{\mathrm{A}}) = \int_{E_{\mathrm{tr}}(U_{\mathrm{A}})}^{\infty} F(E_{\mathrm{S}}) \mathrm{d}E_{\mathrm{S}}. \tag{5.3}$$

For electrons with a fixed polar angle θ_{S}, the transmission function is simply the integral of the energy distribution of electrons from the source. However, when considering also an angular distribution of the source, the situation gets more complicated. For a fixed starting polar angle θ_{S}, an electron is transmitted if its starting kinetic energy E_{S} exceeds the transmission energy E_{tr}, as already discussed. For this fixed transmission energy E_{tr}, electrons with a smaller starting polar angle are also transmitted, however. Hence, for a given starting energy E_{S}, a transmission polar angle θ_{tr} can be defined where all electrons

with polar angles equal to or below θ_{tr} will pass the MAC-E filter. The transmission polar angle θ_{tr} can easily be obtained by inverting equation 5.1, which results in:

$$\theta_{\mathrm{tr}}(E_{\mathrm{S}}) = \arcsin\left(\sqrt{\frac{E_{\mathrm{S}} - q(U_{\mathrm{A}} - U_{\mathrm{S}})}{E_{\mathrm{S}}} \cdot \frac{B_{\mathrm{S}}}{B_{\mathrm{A}}} \cdot \frac{(\gamma_{\mathrm{A}} + 1)}{(\gamma_{\mathrm{S}} + 1)}}\right). \tag{5.4}$$

For an arbitrary angular distribution of the source $\omega(\theta)$, the transmission function can be expressed as a double integral

$$T(U_{\mathrm{A}}) = \int_{E_{\mathrm{tr}}(U_{\mathrm{A}})}^{\infty} \int_{0}^{\theta_{\mathrm{tr}}(E_{\mathrm{S}})} \omega(\theta)\mathrm{d}\theta \cdot F(E_{\mathrm{S}})\mathrm{d}E_{\mathrm{S}}, \tag{5.5}$$

where the inner integral can be seen as a weighting factor for each single energy E_{S} of the energy distribution $F(E_{\mathrm{S}})$, as only a fraction of the angular distribution may have a small enough polar angle to pass the filter.

5.1.2 Transmission functions during SDS commissioning measurements

Due to several boundary conditions of the SDS commissioning measurements the formulas for the calculations of the transmission functions presented above need to be modified.

Boundary conditions

In an electron gun measurement, UV light shinning on a silver cathode releases electrons via the photoelectric effect. These electrons are then accelerated as the cathode is on a negative potential of U_{EGun}. The total kinetic energy of these electrons before entering the main spectrometer can therefore be expressed as

$$E_{\mathrm{S}} = qU_{\mathrm{EGun}} + E_{\mathrm{kin}}, \tag{5.6}$$

with E_{kin} denoting the energy distribution of the electrons released by the photoelectric effect, i.e. before the acceleration by the electron gun's anodes.

The total electrostatic analyzing potential U_{A} is not constant for different field lines, but exhibits a radial inhomogeneity, as described in section 4.3. U_{A} thus needs to be expressed relative to a directly measurable electrode potential, for which the potential of the inner electrodes U_{IE} was chosen. The potential of the analyzing point for a specific field line can therefore be expressed as

$$U_{\mathrm{A}} = U_{\mathrm{IE}} + \Delta U_{\mathrm{r}}. \tag{5.7}$$

As shown in the last chapter, the analyzing point for a specific field line is not necessarily located in the middle of the spectrometer at $z = 0\,\mathrm{m}$, but may be subject to changes depending on the electromagnetic field configuration. Furthermore, as will be shown later in this chapter, the potentials for the individual analyzing points do not only depends on the radius, but also on the full x-y position, as the potential in the main spectrometer is not axial symmetric. Nevertheless, the terminology will be kept constant throughout this chapter.

As the real voltage for the different inner electrode modules was actually not exactly equal in the actual measurement, the radial potential offset is defined here relative to west half

cone of the cylindrical inner electrode section of the main spectrometer. The absolute potential there is given by

$$U_{\mathrm{IE}} = U_{\mathrm{DW}} + U_{\mathrm{CW}}, \tag{5.8}$$

with the absolute voltage of the dipole west power supply U_{DW}, and the voltage caused by the cylinder west offset power supply U_{CW}.

The absolute potential of the inner electrodes U_{IE} and also the potential of the electron gun U_{EGun} could not be measured very precisely, with an uncertainty estimation to be of the order of a few volt. This fact prohibits the calculation of the precise difference between the total kinetic energy of the electrons E_{S} and the analyzing point potential U_{A}, which is needed for the transmission function calculations. However, the voltage difference between the cathode of the electron gun and the dipole west potential was measured very precisely, as described in section 4.1.2. This voltage difference is called ΔU_{EGun} and defined as

$$\Delta U_{\mathrm{EGun}} = U_{\mathrm{DW}} - U_{\mathrm{EGun}}. \tag{5.9}$$

As the offset power supply for the cylinder west was set to zero at all times, and as a significant deviation of the actual voltage was only present for the radial potential measurements without high voltage (see section 5.4.6), the identity $U_{\mathrm{DW}} = U_{\mathrm{IE}}$ will be used in the following.

Adapted formulas

Taking into account the boundary conditions described above, the expression for the maximal transmission polar angle from equation 5.4 can be rewritten to

$$\theta_{\mathrm{tr}}(\Delta U_{\mathrm{EGun}}) = \arcsin\left(\sqrt{\frac{E_{\mathrm{kin}} - q(\Delta U_{\mathrm{EGun}} + \Delta U_{\mathrm{r}})}{E_{\mathrm{S}}} \cdot \frac{B_{\mathrm{S}}}{B_{\mathrm{A}}} \cdot \frac{\gamma_{\mathrm{A}} + 1}{\gamma_{\mathrm{S}} + 1}}\right), \tag{5.10}$$

with the initial kinetic energy E_{kin} of the electrons and the precise measured voltage difference ΔU_{EGun}. As the electron has a vanishingly small kinetic energy at the analyzing plane, the approximation $\gamma_{\mathrm{A}} = 1$ is valid. The other Lorentz factor can be expressed as $\gamma_{\mathrm{S}} = \frac{E_{\mathrm{S}}}{mc^2} + 1$ with the electrons rest mass m and the starting energy E_{S}.

The integral for the calculation of the transmission function, as stated in equation 5.5, also needs to be modified accordingly to

$$T(\Delta U_{\mathrm{EGun}}) = \int_{-(\Delta U_{\mathrm{EGun}} + \Delta U_{\mathrm{r}})}^{\infty} \int_{0}^{\theta_{\mathrm{tr}}(\Delta U_{\mathrm{EGun}})} \omega(\theta)\mathrm{d}\theta \cdot F(E_{\mathrm{kin}})\mathrm{d}E_{\mathrm{kin}}, \tag{5.11}$$

with the initial energy distribution $F(E_{\mathrm{kin}})$ before the electron acceleration. As it is not possible to derive an expression for the transmission energy (see equation 5.1), which does depend only on ΔU_{EGun}, and not on the absolute potential at the analyzing point U_{A}, the lower boundary for the outer integral needs to be changed to $-(\Delta U_{\mathrm{EGun}} + \Delta U_{\mathrm{r}})$, which is the correct integration boundary for an initial polar angle of zero degree. For larger polar angles, however, the integration boundary is too low, but the equation is still correct, as the transmission polar angle is zero for these energies and the inner integral will thus cancel these contributions.

In the following sections, exemplary transmission functions for different source and spectrometer properties will be calculated to investigate and separate their specific influences on the transmission function.

5.1.3 Influence of the source properties

The influence of source properties on the shape and position of the transmission function is of major importance, as spectrometer properties can only be determined successfully, if the energy and the angular distribution of the source is precisely known. For the following toy examples, Gaussian distributions

$$f(x) = \frac{1}{\sigma\sqrt{2\pi}} \exp^{-\frac{1}{2}(\frac{x-\mu}{\sigma})^2} \tag{5.12}$$

were used, for key parameters such as energy and angular distribution, each with mean value μ and standard deviation σ. Additionally, mono-energetic or mono-angular distributions were used in some examples to better emphasize the specific influences.

Energy distribution

Four different energy distributions for the initial kinetic energy inside the electron gun before the acceleration were investigated, as plotted in figure 5.1 (a). The "perfect case" is a mono-energetic line at $E_{\mathrm{kin}} = 0\,\mathrm{eV}$ (red), as these electrons possess a kinetic energy of $E_{\mathrm{S}} = qU_{\mathrm{EGun}}$ before entering the spectrometer, and therefore are transmitted exactly at $\Delta U_{\mathrm{EGun}} = 0\,\mathrm{V}$, as plotted in the step function in figure 5.1 (b). When the energy of the incoming UV light photons does not perfectly match the work function of the cathode material, the photo-electrons are released with an initial kinetic energy, as visualized with the blue line for the selected initial energy $E_{\mathrm{kin}} = 0.3\,\mathrm{eV}$. As these electrons are transmitted already at a lower voltage difference ΔU_{EGun}, the corresponding transmission function in figure 5.1 (b) moves to the left by exactly this amount of initial kinetic energy.

In realistic scenarios, the initial energy is not mono-energetic, but displays a distribution with a specific width, represented by a Gaussian distribution in this example. Two Gaussian energy distributions with standard deviations of $\sigma_{\mathrm{e}} = 0.05\,\mathrm{eV}$ and $\sigma_{\mathrm{e}} = 0.1\,\mathrm{eV}$ are selected here, as shown in figure 5.1 (a), together with their corresponding transmission functions in figure 5.1 (b). The former step function from a mono-energetic line is transformed to a broad shape with a width reflecting the Gaussian energy distribution. For this generic example, the transmission function can actually by described analytically by an error function, as it represents the cumulative distribution function for a Gaussian probability density function. For the presented calculations, a single polar angle of $\theta = 0\,^\circ$ was chosen to turn off effects associated with an angular distribution, and a radial potential offset of $\Delta U_{\mathrm{r}} = 0\,\mathrm{V}$.

Angular distribution

For the visualization of the influence of the angular distribution, three different polar angles are selected: $\theta = 0\,^\circ$, $\theta = 20\,^\circ$ and $\theta = 40\,^\circ$. Besides these sharp δ-functions (dashed lines), Gaussian distributions with $\sigma_{\mathrm{a}} = 5\,^\circ$ are considered as well, as shown in figure 5.2 (a). As the polar angles are only defined for positive values, its magnitude has been plotted on the x-axis, resulting in an apparently different shape for $\theta = 0\,^\circ$, although the same standard deviation has been used for all distributions.

The corresponding transmission functions for a fixed initial kinetic energy of $E_{\mathrm{kin}} = 0\,\mathrm{eV}$ are plotted in figure 5.2 (b). For these calculations a radial potential offset of $\Delta U_{\mathrm{r}} = 0\,\mathrm{V}$, a source and analyzing plane magnetic field of $B_{\mathrm{S}} = 4.333\,\mathrm{T}$ and $B_{\mathrm{A}} = 3.6 \cdot 10^{-4}\,\mathrm{T}$ and a total kinetic energy of $E_{\mathrm{S}} = 18600\,\mathrm{eV}$ were used. The dashed step functions, belonging to the distributions with fixed polar angles, get shifted to the right for larger initial polar angles, as additional surplus energy is required to pass the potential barrier for $\theta > 0\,^\circ$.

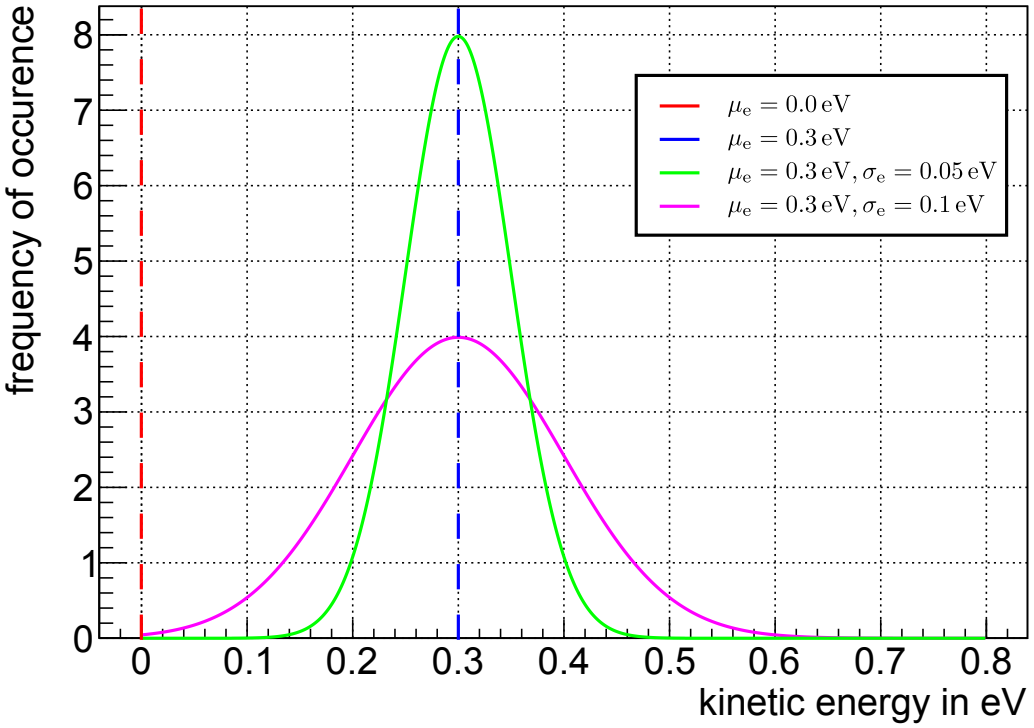

(a) Energy distributions

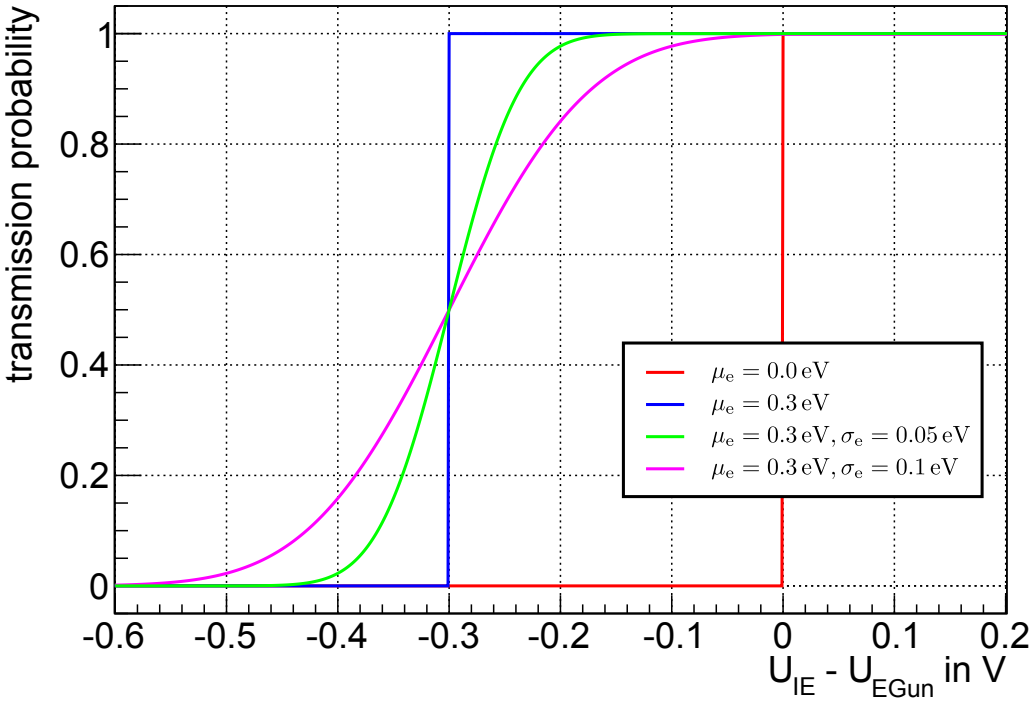

(b) Transmission functions

Figure 5.1: The influence of the energy distribution of the source is visualized with four different energy distributions (a) resulting in four different transmission functions (b). The mono-energetic nature of the initial energies $\mu_e = 0.0\,\mathrm{eV}$ and $\mu_e = 0.3\,\mathrm{eV}$ result in sharp step functions, while the Gaussian energy distributions lead to broader shapes reflecting the width of the initial distribution. As the initial kinetic energy of the electrons, except the mono-energetic red line, is bigger than zero before being accelerated by the electron gun potential to $E_S = qU_{EGun} + E_{kin}$, these electrons get transmitted already for negative values of ΔU_{EGun}. For the calculations a single polar angle of $\theta = 0\,^\circ$ and a radial potential offset of $\Delta U_r = 0\,\mathrm{V}$ were used.

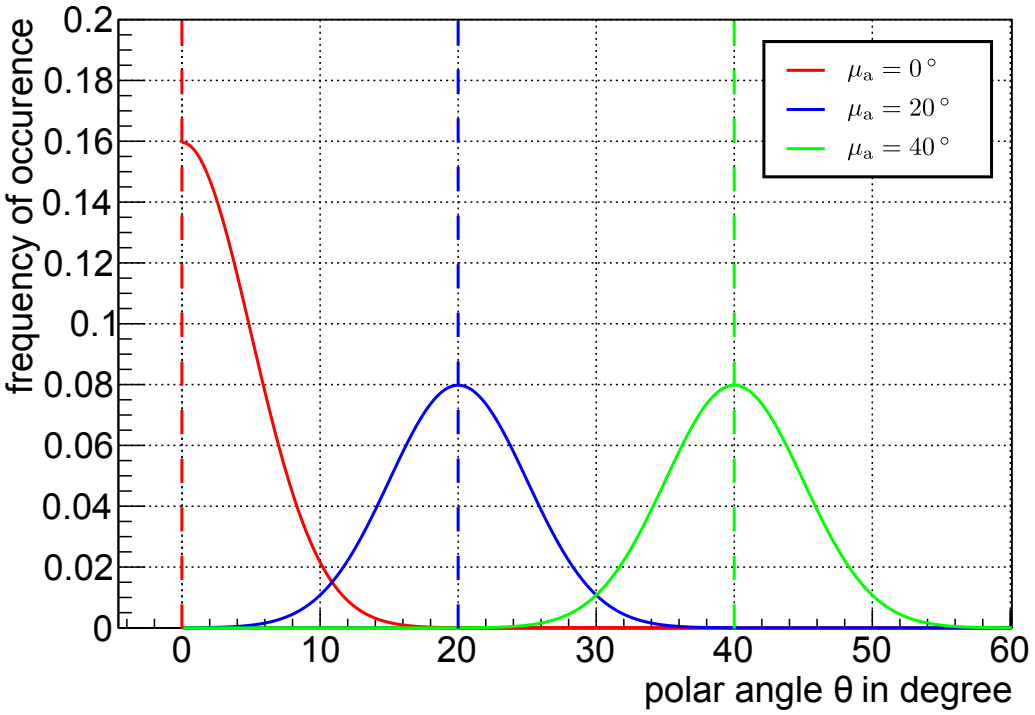

(a) Angular distributions

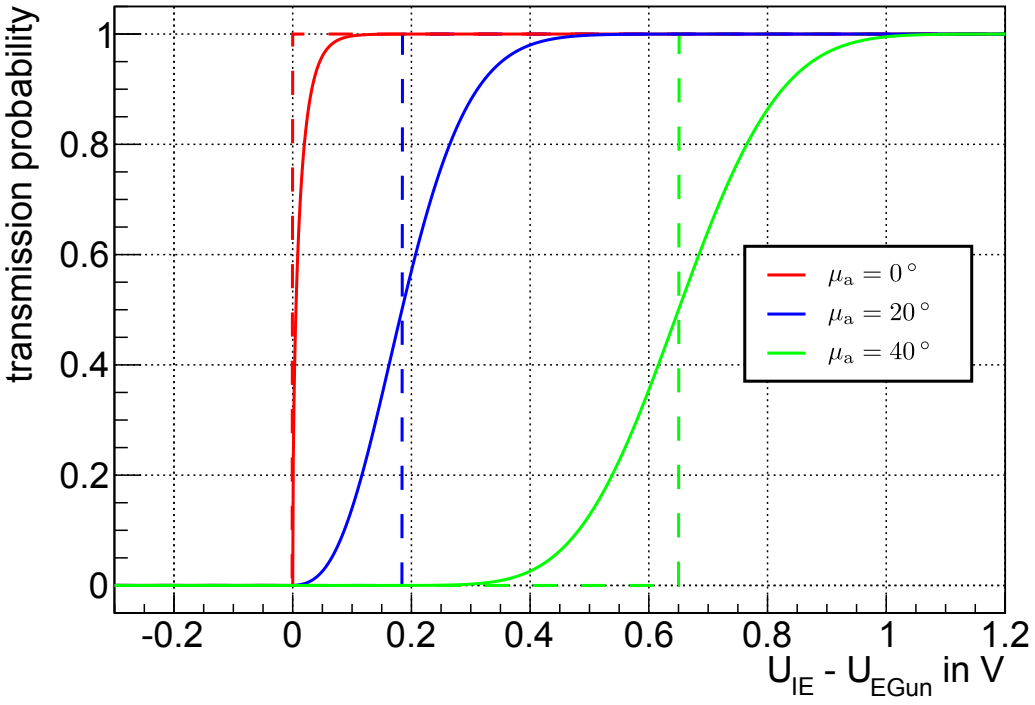

(b) Transmission functions

Figure 5.2: The influence of the angular distribution of the source is visualized for six different polar angle distributions (a) resulting in six transmission functions (b). Three different polar angles are selected, with fixed polar angles of 0 °, 20 °, 40 ° (dashed lines) and Gaussian distributions around these values with $\sigma_a = 5\,°$. For higher polar angles, additional surplus energy is needed to pass the MAC-E filter, therefore the transmission function is shifted to the right. The relative shift for larger angles is higher and therefore also the width of the transmission function with a large initial polar angle is bigger than for lower ones. The settings for the calculations are $E_{kin} = 0\,\text{eV}$, $\Delta U_r = 0\,\text{V}$, $B_S = 4.333\,\text{T}$, $B_A = 3.6 \cdot 10^{-4}\,\text{T}$ and $E_S = 18600\,\text{eV}$.

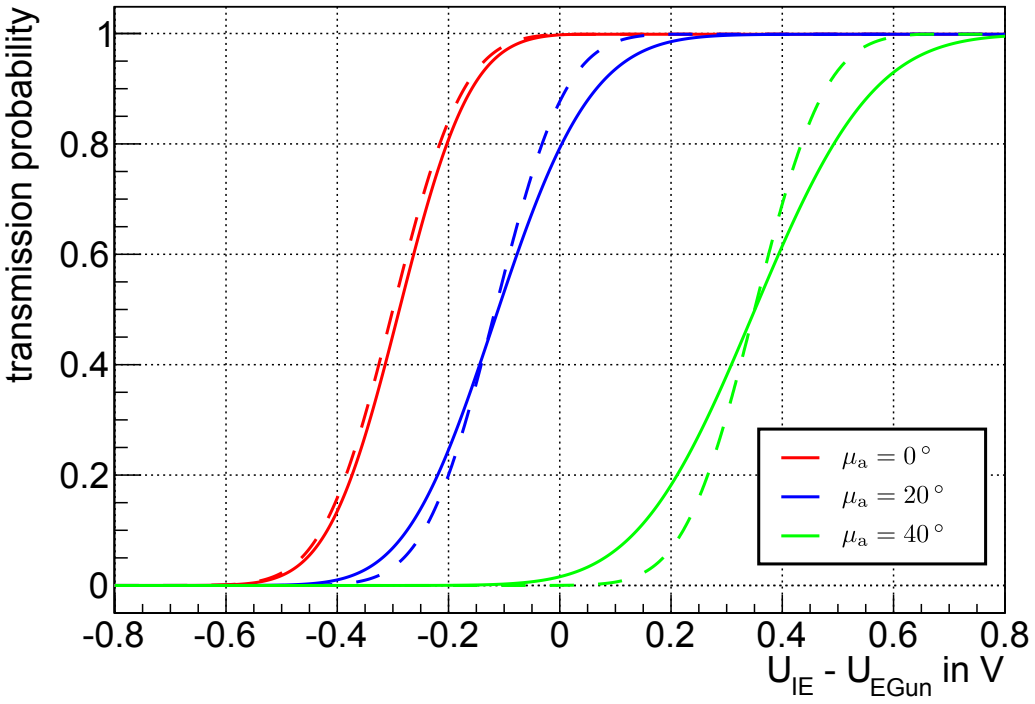

Figure 5.3: The influence of the combined effect of specific energy and angular distributions of the source on the transmission function is visualized. A Gaussian energy distribution with $\mu_e = 0.3\,\text{eV}$ and $\sigma_e = 0.1\,\text{eV}$ was used, and different angular distributions were selected according to figure 5.2 (a), where the dashed lines correspond to fixed values of θ. The spectrometer settings for the calculations are identical to figure 5.2.

Due to the non linear relation between the initial polar angle θ and the transmission energy E_{tr} (see equation 5.1), the transmission function with $\theta = 40\,°$ is shifted much further than the transmission function with $\theta = 20\,°$. The additional required surplus energy increases with $\sin^2(\theta)$ and therefore the relative shift increases until $\theta = 45\,°$. However, the relative shifts decrease again for larger polar angles.

In case of Gaussian polar angle distributions, the corresponding transmission functions get broadened, as expected. Compared to a Gaussian energy distribution, the broadening is not symmetric, nor does the same standard deviation lead to the same width of the transmission function, as visible in figure 5.2 (b), where the transmission function for $\theta = 40\,°$ is much broader then for $\theta = 20\,°$ or $\theta = 0\,°$. The latter is a special case, as the minimal possible polar angle is $\theta = 0\,°$, hence the Gaussian distribution only leads to additional initial angles with a higher value, and none with a lower one. Therefore, some electrons need additional surplus energy, but evidently none need less to be transmitted so that the corresponding transmission function broadens only in the direction of higher energies. It is also important to note that, in contrast to the Gaussian energy distribution, the resulting transmission function for a Gaussian polar angle distribution can not be described by an error function.

To demonstrate the combined effect of energy and angular distribution, transmission functions with the same polar angle distributions and corresponding colors are plotted in figure 5.3, though this time the kinetic energy was defined by a Gaussian distribution with $\mu_e = 0.3\,\text{eV}$ and $\sigma_e = 0.1\,\text{eV}$. The effect of the energy distribution alone is visible at the transmission functions with dashed lines, where a single polar angle was used and the combined effect is plotted in full lines, where the transmission functions are additionally broadened by the Gaussian polar angle distribution. The broadening is not symmetric and more distinct for higher polar angles.

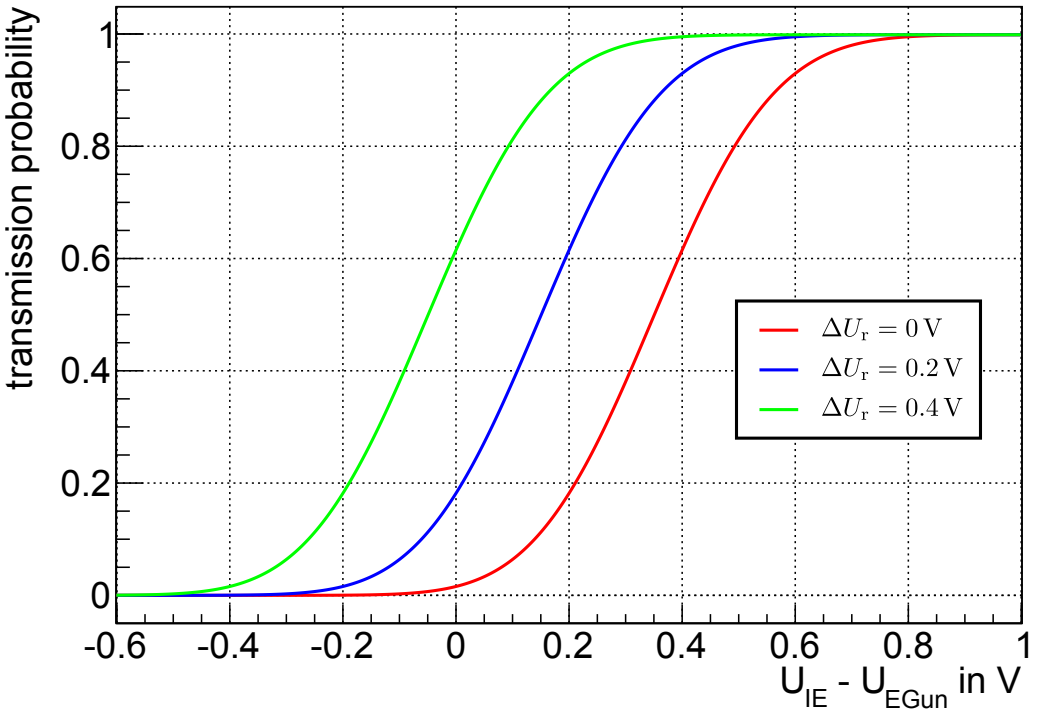

Figure 5.4: The influence of the retarding potential of the spectrometer on the transmission function is visualized for three different values of ΔU_r. The shape of the transmission function does not change at all, only its position is modified. For the calculation a source with an energy distribution of $\mu_\mathrm{e} = 0.3\,\mathrm{eV}$ and $\sigma_\mathrm{e} = 0.1\,\mathrm{eV}$ and an angular distribution of $\mu_\mathrm{a} = 40\,^\circ$ and $\sigma_\mathrm{a} = 5\,^\circ$ was used.

5.1.4 Influence of the spectrometer properties

The determination of spectrometer properties is the essential goal of transmission function measurements, in particular the absolute values and the radial dependency of the electrostatic retarding potential and the magnetic field in the analyzing plane.

Retarding potential

The retarding potential of different radial positions in the analyzing plane can be described by a radial potential offset ΔU_r, as defined in equation 5.7. Figure 5.4 shows three transmission functions with different values for ΔU_r. For these calculations an energy distribution of $\mu_\mathrm{e} = 0.3\,\mathrm{eV}$ and $\sigma_\mathrm{e} = 0.1\,\mathrm{eV}$ and an angular distribution of $\mu_\mathrm{a} = 40\,^\circ$ and $\sigma_\mathrm{a} = 5\,^\circ$ were used, with identical settings for B_S, B_A and E_S as before.

As it is clearly visible in the figure, a different retarding potential does not change the shape of the transmission function, but causes a shift to the left (right) side to lower (higher) values of the voltage difference, depending on the actual value of ΔU_r. In case of a positive value of ΔU_r the absolute retarding potential at the analyzing point is reduced, so that less surplus energy is needed to pass the MAC-E filter and therefore the transmission starts at lower values of ΔU_EGun.

Magnetic field

To demonstrate the influence of the magnetic field in the analyzing plane on the transmission function, the above calculations were repeated with the identical settings, except for a different magnetic field. Figure 5.5 compares transmission functions with magnetic fields of $B_\mathrm{A} = 3.6 \cdot 10^{-4}\,\mathrm{T}$ and $B_\mathrm{A} = 8.8 \cdot 10^{-4}\,\mathrm{T}$ in the analyzing plane. Additionally, transmission functions with fixed polar angles have been plotted with dashed lines. In

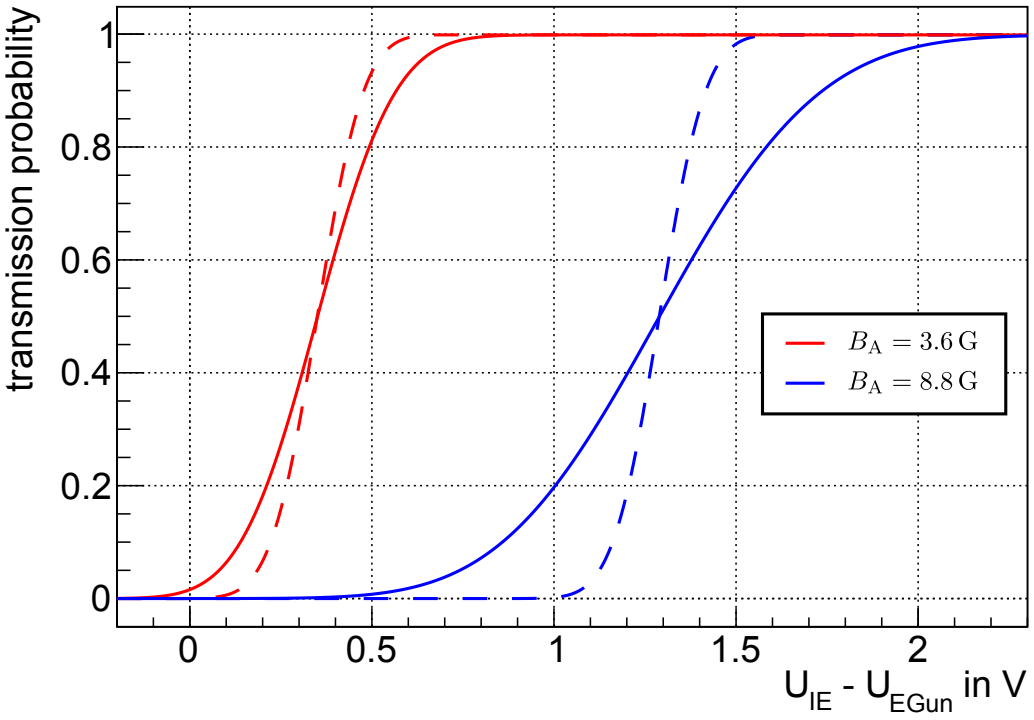

Figure 5.5: The influence of the magnetic field in the analyzing plane on the transmission function is visualized for two different values of B_A. For the calculation a source with an energy distribution of $\mu = 0.3\,\mathrm{eV}$ and $\sigma = 0.1\,\mathrm{eV}$ and an angular distribution of $\mu = 40\,^\circ$ and $\sigma = 5\,^\circ$ was used, while the dashed lines represent fixed polar angles of $\theta = 40\,^\circ$. A higher magnetic field does not only shift the transmission function to higher values of ΔU_EGun, but also broadens it significantly.

case of a higher magnetic field, an electron with fixed polar angle needs additional surplus energy to pass the retarding potential, as the magnetic adiabatic collimation works not as efficiently, as at a lower field. Therefore, the transmission starts at higher values of ΔU_EGun. In case of Gaussian angular distributions, the transmission functions are not only shifted but their width increases as well due to the same effect. For transmission functions with a polar angle of $\theta = 0\,^\circ$ (not shown), the magnetic field does not influence the transmission properties, as electrons are already collimated.

5.1.5 Correlation of the parameters

From the examples given in the last section it is obvious that a set of source and spectrometer properties is correlated as these parameters modify the transmission function in the same way. It is therefore a non-trivial challenge to disentangle spectrometer properties from transmission functions. In the following, the impact of correlated parameters leading to the same effect on the transmission function will be discussed.

Position of the transmission function

A shift of the transmission function result from the following parameters:

- **Radial potential offset ΔU_r:** Different values of ΔU_r lead to a shift of the transmission function, as demonstrated in figure 5.4. The goal of the transmission function analysis is to measure this shift to determine the potential offset.
- **Surplus energy of the initial kinetic energy of the electrons:** A difference in the initial kinetic energy of the electrons created by the photoelectric effect in the electron gun leads to an equivalent shift in the transmission function measurement.

Therefore the initial kinetic energy needs to be known precisely, for example by determining the UV light wavelength distribution and the work function of the cathode material.

- **Initial polar angle:** A different initial polar angle also does shift the transmission function, as demonstrated in figure 5.3 for example. The shift between two different polar angles θ_1 and θ_2 can be calculated according to

$$\Delta E_\theta = E_\mathrm{S} \cdot \frac{B_\mathrm{A}(\gamma_\mathrm{S}+1)}{B_\mathrm{S}(\gamma_\mathrm{A}+1)} \cdot (\sin^2(\theta_1) - \sin^2(\theta_2)). \tag{5.13}$$

  For the above defined default values of B_S, B_A and E_S, a small angular change from $\theta_1 = 40\,^\circ$ to $\theta_2 = 45\,^\circ$ already leads to a shift of $\Delta E_\theta = 137\,\mathrm{mV}$.

- **Analyzing plane magnetic field:** A different magnetic field in the analyzing plane also results in a shift of the transmission function, as demonstrated in figure 5.5. The shift can be calculated analogously according to

$$\Delta E_{B_\mathrm{A}} = E_\mathrm{S} \cdot \frac{\Delta B_\mathrm{A}}{B_\mathrm{S}} \cdot \frac{\gamma_\mathrm{S}+1}{\gamma_\mathrm{A}+1} \cdot \sin^2(\theta). \tag{5.14}$$

  With the same settings as before and a polar angle of $\theta = 40\,^\circ$, a change by $\Delta B_\mathrm{A} = 1.0 \cdot 10^{-4}\,\mathrm{T}$ corresponds to a shift of $\Delta E_{B_\mathrm{A}} = 180\,\mathrm{mV}$.

While the first two parameters (ΔU_r, E_kin) do only result in a shift of the transmission function position, the latter two (θ_S, B_A) also modify its shape and the width.

Shape of the transmission function

A variety of parameters will also influence the shape and width of the transmission function:

- **Shape of the kinetic energy distribution:** The shape of the energy distribution directly propagates to the shape of the transmission function. For a Gaussian energy distribution with a standard deviation σ and a fixed polar angle the transmission function can therefore be described by an error function with the width σ, as illustrated in figure 5.1.

- **Shape of the polar angle distribution:** The shape of the polar angular distribution also influences the shape of the transmission function. For a broader angular distribution, the width of the transmission function will increase. In contrast to the broadening caused by the energy distribution, the contribution of the width of the angular distribution to the broadening of the transmission function is non linear in nature and also not symmetric, as shown in figure 5.2.

- **Mean value of the initial polar angle:** The broadening of the transmission function due to the angular distribution is influenced by the mean value of the initial polar angle. For different polar angles an angular distribution with the same standard deviation σ results in different widths of the transmission functions, as demonstrated in figure 5.2.

- **Analyzing plane magnetic field:** The same is true for the analyzing plane magnetic field, with a different magnetic field resulting in a different width of the transmission function, as demonstrated in figure 5.5.

5.2 Extracting the source properties from transmission function measurements

As detailed in the last section, an electron source with well understood energy and angular distributions is essential to successfully derive the spectrometer properties. From the modeling side, this goal requires detailed simulations of the rather complex electrostatic fields of the inner electron gun electrodes and to perform particle tracking from the fiber surface, where the photo electrons are created, through the acceleration electrode to the exit of the electron gun and the entrance of the main spectrometer, as has been done for example in [Zac14]. Alternatively, as done throughout this thesis, the source properties can be determined by analyzing specific transmission function measurements at the main spectrometer. The advantage here is that these do not depend on results from simulations. On the other hand, due to the correlation of source and spectrometer properties as described in 5.1.5, their effect has to be decoupled by a suitable sequence of measurements with the following strategy, as proposed in [Wan13], to determine the

1. energy distribution of the source by measuring at low voltage (see section 5.2.1),
2. angular selectivity by varying the polar angle (see section 5.2.2),
3. angular distribution for a fixed polar angle by fitting the measured transmission function (see section 5.2.3).

During the next sections these three steps will be explained in more detail on the basis of measurements taking during the SDS commissioning phase. It will become evident, however, that due to different hardware issues, such as an unstable work function of the silver layer of the electron gun and problems with the angular selectivity, a complete disentanglement was not possible for the performed measurements.

5.2.1 Energy distribution of the source

The energy distribution of the source has a direct influence on the shape of the measured transmission function. This also holds for the angular distribution, whose influence on the shape of the transmission function also depends on the magnetic field in the analyzing plane. Thus, to extract the energy distribution of a measured transmission function, specific settings have to be chosen where the influence of the angular distribution is negligible. This can be achieved by a configuration with:

- A low magnetic field in the analyzing plane, as this reduces the spread of the transmission function caused by the finite angular distribution of the source.
- A "neutral" position of the rotatable plates of the electron gun to produce initial polar angles close to $\theta = 0\,^\circ$, as the finite angular spread has the lowest influence on the transmission function shape at this setting.
- A low retarding voltage of the main spectrometer, being the most important parameter here. For an inner electrode potential of $U_{\mathrm{IE}} = -200\,\mathrm{V}$ the required total kinetic energy for transmission is also about $E_{\mathrm{S}} \approx 200\,\mathrm{eV}$. According to equation 5.13 the energy shift between two initial polar angles, which results in a broadening of the transmission function for a continuous angular distribution, can be calculated. For the given settings of $E_{\mathrm{S}} = 200\,\mathrm{eV}$, $B_{\mathrm{A}} = 3.6 \cdot 10^{-4}\,\mathrm{T}$, $B_{\mathrm{S}} = 4.333\,\mathrm{T}$ and the two polar angles $\theta_1 = 0\,^\circ$ and $\theta_2 = 5\,^\circ$ the result is $\Delta E_\theta = 0.1\,\mathrm{meV}$. Therefore, the extremely small broadening caused by the angular distribution for such a setup can be ignored completely.

Therefore, a transmission function measurement has been performed with the following settings:

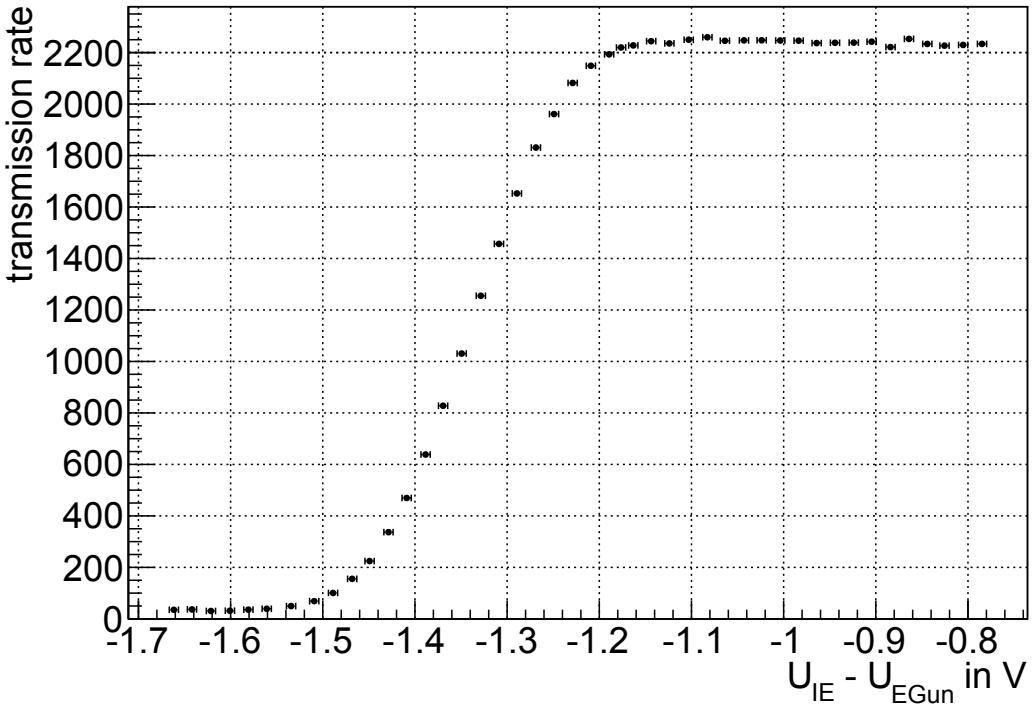

Figure 5.6: Transmission function with the 310 nm UV LED at $U_{\mathrm{IE}} = -200\,\mathrm{V}$ and the 3.8 G magnetic setup. The width of the transmission function is dominated by the energy distribution of the source, which can be extracted from this measurement. The systematic uncertainty on the voltage is 5 mV according to the precision of the used digital volt meter (see section 4.1.2). The not visible statistical error on the rate has been propagated from the Poisson error on the total counts.

- **High voltage:** The spectrometer vessel was grounded and the inner electrodes were put on $U_{\mathrm{IE}} = -200\,\mathrm{V}$ using the dipole power supplies. The post acceleration potential was set to $U_{\mathrm{PAE}} = 10\,\mathrm{kV}$ to detect these low energetic electrons.
- **Magnets:** The default 3.8 G setup was used, as stated in table 4.2.
- **Electron gun:** A 310 nm UV LED was used as a light source with the monochromator also set to 310 nm. The LED was powered by a pulse generator with a pulse rate of 100 kHz and a pulse length of 100 ns. The manipulator of the electron gun was set to the neutral position, corresponding to the central field in the middle of the spectrometer, hitting pixel number 2 on the focal plane detector. The rotatable plates have also been set to their neutral position, to produce initial polar angles around $\theta = 0\,^{\circ}$.

While the spectrometer potential was kept stable, the potential of the electron gun was varied in steps of 20 mV, with a measuring interval of 30 seconds at each voltage setting. The resulting transmission function is plotted in figure 5.6, as function of the voltage difference between inner electrodes and electron gun $\Delta U_{\mathrm{EGun}} = U_{\mathrm{IE}} - U_{\mathrm{EGun}}$.

To extract the source energy distribution from the transmission function, two basics steps needs to be done.

- **Determination of the shape of the energy distribution:** As the main spectrometer is an integration filter, the shape of the energy distribution can be obtained by a numerical differentiation of the measured transmission function. If the shape is assumed to be Gaussian, an error function can be fitted to the measured transmission function to obtain the parameters of the Gaussian distribution. Both cases will be presented in the following.

- **Determination of the mean kinetic energy:** The total kinetic energy of the electrons and also the mean of the obtained distribution can not be measured directly, as long as the radial potential offset is unknown. However, the kinetic energy can be obtained in principle, in case that the exact wavelength distribution of the light source and the work function of the cathode material are known.

Determination of the shape of the energy distribution

To extract the energy distribution of the source without specific assumptions on its shape a differentiation of the transmission function T has to be done:

$$F(\Delta U_{\mathrm{EGun}}) = \frac{\partial T(\Delta U_{\mathrm{EGun}})}{\partial \Delta U_{\mathrm{EGun}}}. \tag{5.15}$$

Here a numerical differentiation using Lagrange's formula was performed

$$F(\Delta U_i) = a_{i-1} \cdot T(\Delta U_{i-1}) + a_i \cdot T(\Delta U_i) + a_{i+1} \cdot T(\Delta U_{i+1}), \tag{5.16}$$

with the specific measured potential values ΔU_i replacing $\Delta U_{\mathrm{EGun},i}$. The prefactors are defined as

$$\begin{aligned} a_{i-1} &= \tfrac{\Delta U_i - \Delta U_{i+1}}{(\Delta U_{i-1} - \Delta U_i)\cdot(\Delta U_{i-1} - \Delta U_{i+1})}, \\ a_i &= \tfrac{2\cdot\Delta U_i - \Delta U_{i-1} - \Delta U_{i+1}}{(\Delta U_i - \Delta U_{i-1})\cdot(\Delta U_i - \Delta U_{i+1})}, \\ a_{i+1} &= \tfrac{\Delta U_i - \Delta U_{i-1}}{(\Delta U_{i+1} - \Delta U_{i-1})\cdot(\Delta U_{i+1} - \Delta U_{i-1})}. \end{aligned} \tag{5.17}$$

For the first and last data points, with only one neighboring point, the simpler Taylor's theorem is applied:

$$\begin{aligned} F(\Delta U_1) &= \tfrac{T(\Delta U_2) - T(\Delta U_1)}{\Delta U_2 - \Delta U_1}, \\ F(\Delta U_n) &= \tfrac{T(\Delta U_n) - T(\Delta U_{n-1})}{\Delta U_n - \Delta U_{n-1}}. \end{aligned} \tag{5.18}$$

The result of this differentiation on the measured transmission function is plotted in figure 5.7. Here, in addition, all outer data points on both sides were removed, as soon as the energy distribution reached zero, to get rid of undesired fluctuations. The area below the curve has been normalized to 1. The displayed correlated errors are calculated using error propagating taking into account the errors on the rate and the voltage difference.

Determination of the mean kinetic energy

As the obtained energy distribution depends on the parameter ΔU_{EGun}, while a representation as a function of E_{kin} is needed, the x-axis has to be transformed according to $E_{\mathrm{kin}} = q(\Delta U_{\mathrm{EGun}} + \Delta U_{\mathrm{r}})$. This can not be done, as ΔU_{r} is not known a priori, being an objective of the transmission measurements.

Another possibility to obtain the mean kinetic energy is to make use of the relation from the photoelectric effect

$$E_{\mathrm{kin}} = \frac{hc}{\lambda} - \Phi_{\mathrm{EGun}}, \tag{5.19}$$

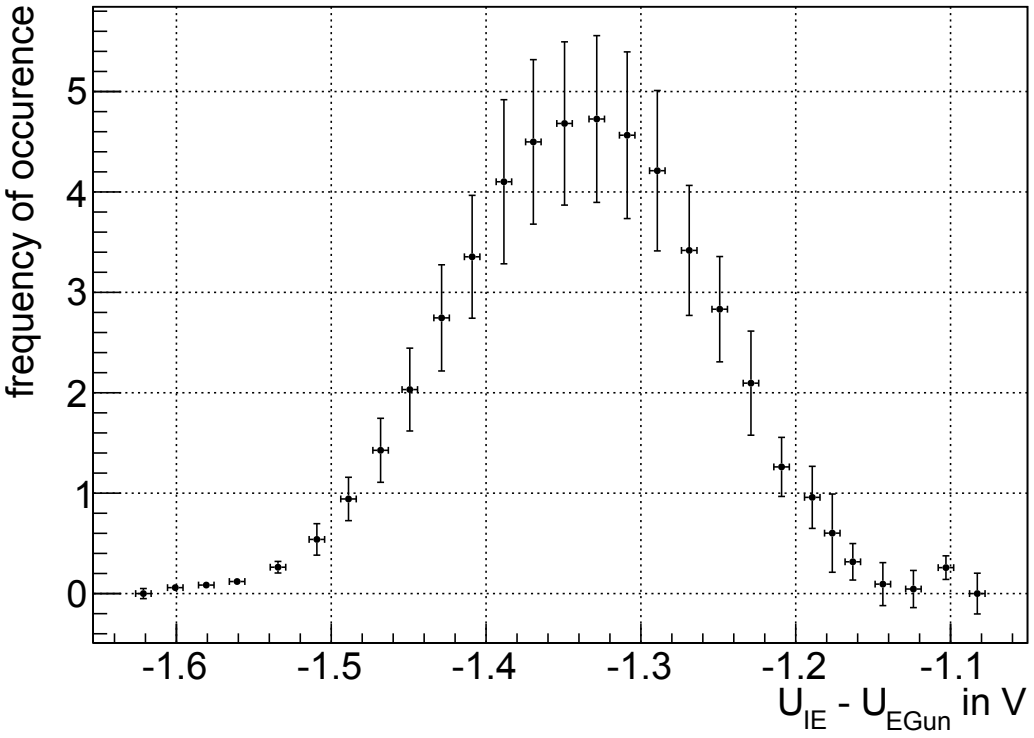

Figure 5.7: Numerical differentiation of the transmission function plotted in figure 5.6. The outer points on both sides have been removed and the area below the curve normalized to 1. The error has been calculated by propagating the error of the rate and of the voltage.

with the Planck constant h, the speed of light c, the mean wavelength of the light source λ and the work function of the electron gun's cathode Φ_{EGun}. The work function of the silver cathode was measured to $\Phi_{\mathrm{EGun}} = (3.9\,\mathrm{eV} \pm 0.1)\,\mathrm{eV}$ at a different setup before the electron gun was installed [Win14]. However, due to changing surface properties of the silver layer in the vacuum of the main spectrometer and overall rather unstable conditions of the silver layer, such as degradation from multiple discharges and the subsequent replacing of the fiber, as described in section 4.1.5, this measured value could not be used.

Therefore, a new strategy to determine the mean kinetic energy has been followed, based on the fact that the kinetic energy of all released electrons is always positive. The lowest energy electrons should thus have a kinetic energy approaching zero, as these were created by photons with an energy matching the work function exactly. This can be done, by integrating the energy distribution in figure 5.7, and by choosing an upper integration boarder, which represents the electrons with the lowest kinetic energy, so that the integral covers 99.9 % of the total area. The point on the position of the upper integration boarder is set to a kinetic energy of zero and the remaining points within the boarders are transformed accordingly. The result is plotted in figure 5.8, where the peak of the distribution is now at about $E_{\mathrm{kin}} = 0.25\,\mathrm{eV}$.

It is important to note that due to the rather arbitrary definition of the mean kinetic energy, the determination of ΔU_{r} is affected directly. How this issue can be handled will be covered in section 5.4.

Gaussian energy distribution

For a Gaussian energy distribution, its parameters can be obtained without numerical differentiation. As the integral of a Gaussian distribution can be described by an error function, the measured transmission function can be fitted by

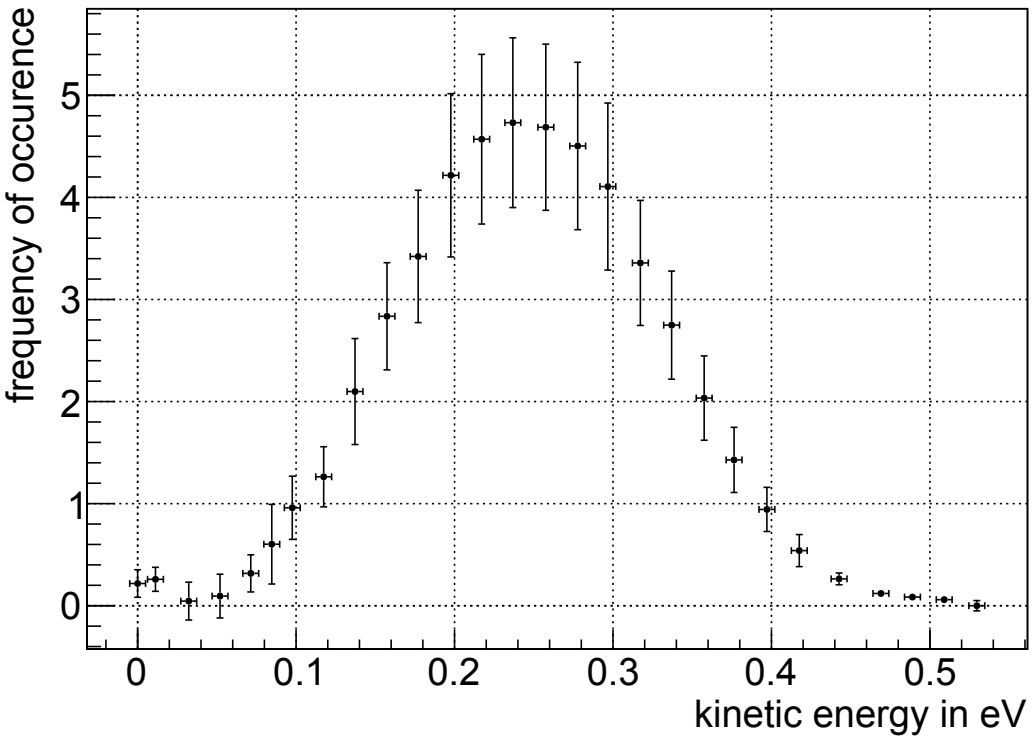

Figure 5.8: Energy distribution of the electron gun with the 310 nm UV LED as light source, obtained by numerical differentiation and axis transformation of the transmission function in figure 5.6. The peak of the distribution is at $E_{\mathrm{kin}} \approx 0.25\,\mathrm{eV}$.

$$\frac{a}{2} \cdot \left[1 + \mathrm{erf}\left(\frac{\Delta U_{\mathrm{EGun}} - \mu_{\mathrm{e}}}{\sqrt{2}\sigma_{\mathrm{e}}})\right)\right] + b, \tag{5.20}$$

with the amplitude a, the background b and the mean μ_{e} and standard deviation σ_{e} of the distribution. The fitted function and the measured points are plotted in figure 5.9 together with the obtained parameters.

As in case of the numerical differentiation, the x-axis also needs to be transformed to obtain the energy distribution as function of E_{kin}. This can be done exactly with the same procedure, which leads to a new mean value of $\mu_{\mathrm{e}} = 0.247\,\mathrm{eV} \pm 2 \cdot 10^{-4}\,\mathrm{eV}$. The resulting energy distribution is plotted in figure 5.10 together with the one obtained numerically. The excellent matching of the numerical energy distribution and the Gaussian function strongly seems to back the assumption that the energy distribution can be described by a Gaussian function. This is not the case in general, however, as the example given is only one out of few measured energy distributions with such a good agreement. Other measured energy distributions with different light sources and different conditions of the silver cathode show different shapes which can only be described numerically.

5.2.2 Angular selectivity of the source

When referring to the actual polar angle θ of the electrons as produced by the electron gun, it is important to state also the position at which θ occurs, as the polar angle changes with the magnetic field, which is subject to change along the electrons trajectory. Within this thesis this reference point is always located at the center of the PS2 magnet, the entrance magnet of the main spectrometer. With a magnetic field of $B_{\mathrm{S}} = 4.333\,\mathrm{T}$ there, the maximal initial polar angle which is not magnetically reflected at the pinch magnet with $B_{\mathrm{max}} = 5\,\mathrm{T}$ is $\theta_{\mathrm{max}} = 68.6\,^{\circ}$, according to equation 2.5.

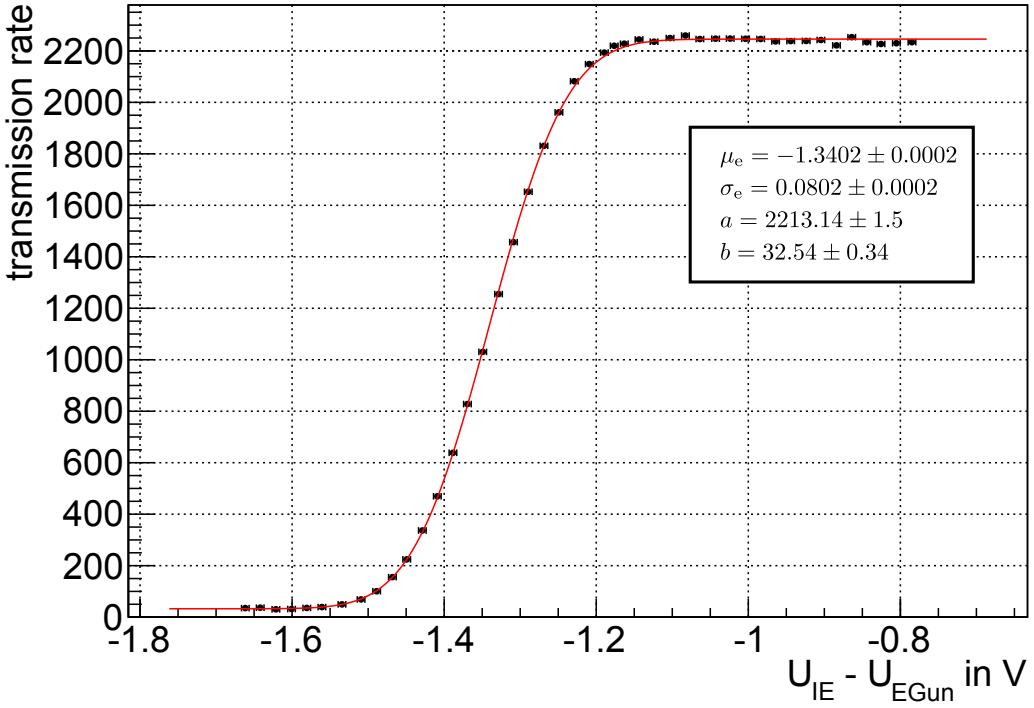

Figure 5.9: Plot of the fitted error function (red) together with the measured points. The obtained fit parameters are displayed in the box.

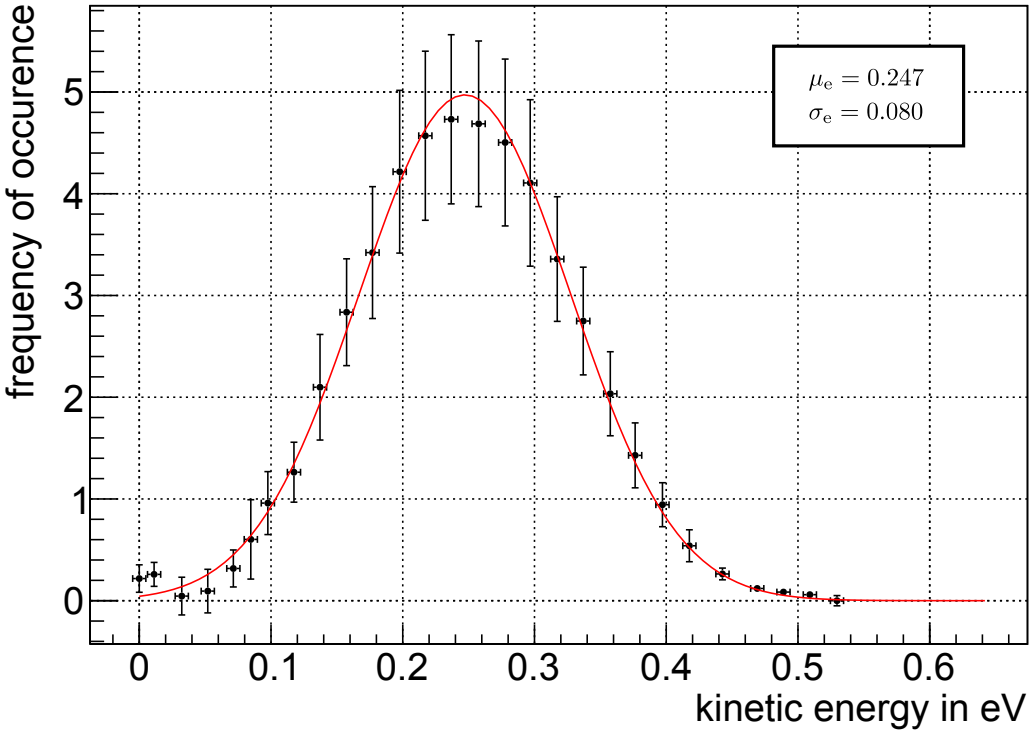

Figure 5.10: Numerical and Gaussian energy distribution of the electron gun with the 310 nm UV LED as light source. The Gaussian function shows a good agreement with the numerical obtained distribution.

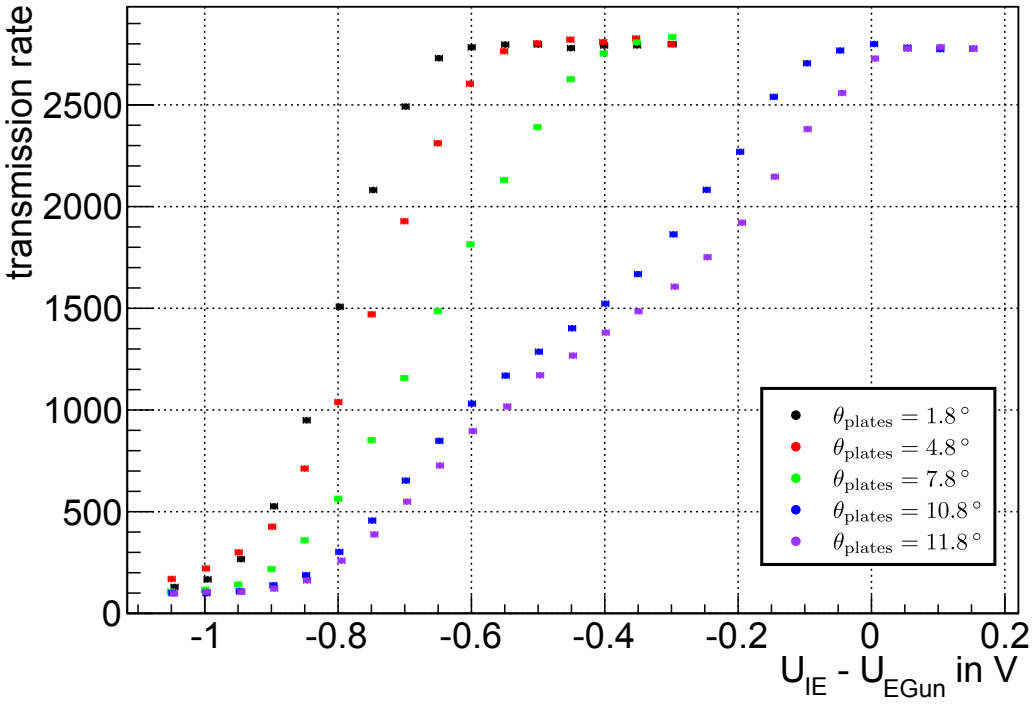

Figure 5.11: Transmission function measurements for five different plate angles. As expected, the initial polar angle increases for higher plate angles and the transmission functions shift to higher surplus energies. However, the size of the shift is much smaller than expected. Additionally, the spread of the transmission function increases substantially for large plate angles and results in a hump-like structure.

As detailed in section 4.1.5, the initial polar angle θ can be changed by rotating the electron gun's plates to a different angle θ_{plates}. For an increased value of θ_{plates} the electron gun produces electrons with a larger polar angle θ, which leads to a shift of the transmission function to higher surplus energies, as demonstrated in figure 5.2. The largest effect can be produced by adopting the high magnetic field 9 G setup and by choosing the full retarding potential $U_{\text{IE}} = -18600\,\text{kV}$. According to equation 5.13 the expected shift between the minimal polar angle of $\theta = 0\,^\circ$ and the maximal polar angle $\theta = 68.6\,^\circ$ in the entrance magnet of the main spectrometer with this setup is $\Delta E = 3.3\,\text{eV}$.

First, a value of θ_{plate} which produces the minimal initial polar angles θ has to be found, which is not necessarily $\theta_{\text{plate}} = 0\,^\circ$. It depends on the position of the manipulator, as the whole electron gun and also it's inner plates rotate when the manipulator is moved, changing the direction of the magnetic field relative to the axis of the plates. The minimal initial polar angle θ can be obtained by choosing a value of ΔU_{EGun} residing in the middle of the transmission edge and by then rotating the plates slightly forth and back until the count rate of the electron gun at the detector is maximal. By doing so, a plate angle of $\theta_{\text{plates}} = 1.8\,^\circ$ was determined. After that the plate angle was increased in steps of $3\,^\circ$ up until the maximal mechanical limit of $11.8\,^\circ$ to calibrate the relation between θ_{plate} and the corresponding initial polar angle θ. The maximal polar angle of $\theta = 68.6\,^\circ$ can thereby be determined, as the transmission rate drops for higher angles due to the magnetic mirror effect.

For different values of θ_{plate} in a range from $1.8\,^\circ$ to $11.8\,^\circ$, a variety of transmission functions was measured by varying the electron gun potential in 50 mV steps. For increasing polar angles θ the transmission function is expected to shift to higher surplus energies, until finally at the maximal polar angle of $\theta = 68.6\,^\circ$ a shift of $\Delta E = 3.3\,\text{eV}$ is achieved. The result of the measurement is plotted in figure 5.11. In principle, the transmission func-

tions indeed shift to higher surplus energies for larger plate angles, but the shift is much smaller and the additional spread is much larger than expected. Additionally, the start of the transmission edge does shift only marginally, while its width increases significantly for larger plate angles. This means that rotating the plates in the electron gun does not produce specific larger polar angles, but mainly broadens its angular distribution.

Multiple tests were performed during the SDS commissioning phase to investigate possible reasons for this non-expected functionality in angular selectivity. It was only after the measurement phase was finished and the electron gun was completely disassembled, that multiple mechanical reasons were discovered leading to the stated behavior [Zac14].

Due to these issues with respect to angular selectivity, all remaining measurements were performed with a minimal polar angle of $\theta = 0\,^\circ$. The consequence is that the magnetic field in the analyzing plane can not be determined by performing transmission function measurements, as the remaining angular distribution at $0\,^\circ$ is not sensitive enough for this task. Nevertheless, the angular distribution is still important when determining the analyzing plane potential, as the position of the transmission function can be fitted more precisely, in case that the exact shape is known.

5.2.3 Angular distribution of the source

For a pre-defined plate angle, the angular distribution of the source can be determined by measuring a transmission function, on condition that the energy distribution is already known, a finite angular distribution broadens the transmission function further. Again, this is best done at a high magnetic field in the analyzing plane and at full retarding potential to maximize the effect. Therefore, a transmission function was measured with the following settings:

- **High voltage:** The spectrometer vessel was put on $U_{\text{vessel}} = -18500\,\text{V}$ and the dipole power supplies were set to $-100\,\text{V}$ for an overall potential on the inner electrodes of $U_{\text{IE}} = -18600\,\text{V}$. The post acceleration potential is not needed at this setting and has been deactivated.
- **Magnets:** The high magnetic field 9 G setup was used, as stated in table 4.2.
- **Electron gun:** The same light source as in section 5.2.1 was used, the 310 nm UV LED with monochromator. As this measurement took place only a few hours after the measurement of the energy distribution, the silver cathode is expected to be in the same condition. The manipulator of the electron gun was set to the neutral position of $\alpha_{\text{v}} = \alpha_{\text{h}} = 0\,^\circ$, hitting pixel 2 on the focal plane detector as before. The rotatable plates have been set to the position where an initial polar angle of $\theta = 0\,^\circ$ is expected.

Again, the spectrometer potential was kept stable and the electron gun's potential was varied in steps of 30 mV, measuring the electron gun rate at the detector over 30 second intervals at each voltage setting. The resulting transmission function, as function of the voltage difference between inner electrodes and electron gun $\Delta U_{\text{EGun}} = U_{\text{IE}} - U_{\text{EGun}}$ is plotted in figure 5.12.

The measured transmission function can be described with the two integrals of the already known energy distribution $F(E_{\text{kin}})$ and the desired angular distribution $\omega(\theta)$, as stated in equation 5.11. As the two integrals are not independent from each other, the determination of an arbitrary numerical angular distribution is a complicated procedure. Therefore, the angular distribution is assumed to be Gaussian, which is sufficient for the analysis tasks to be performed. Doing so, the transmission function can be fitted according to

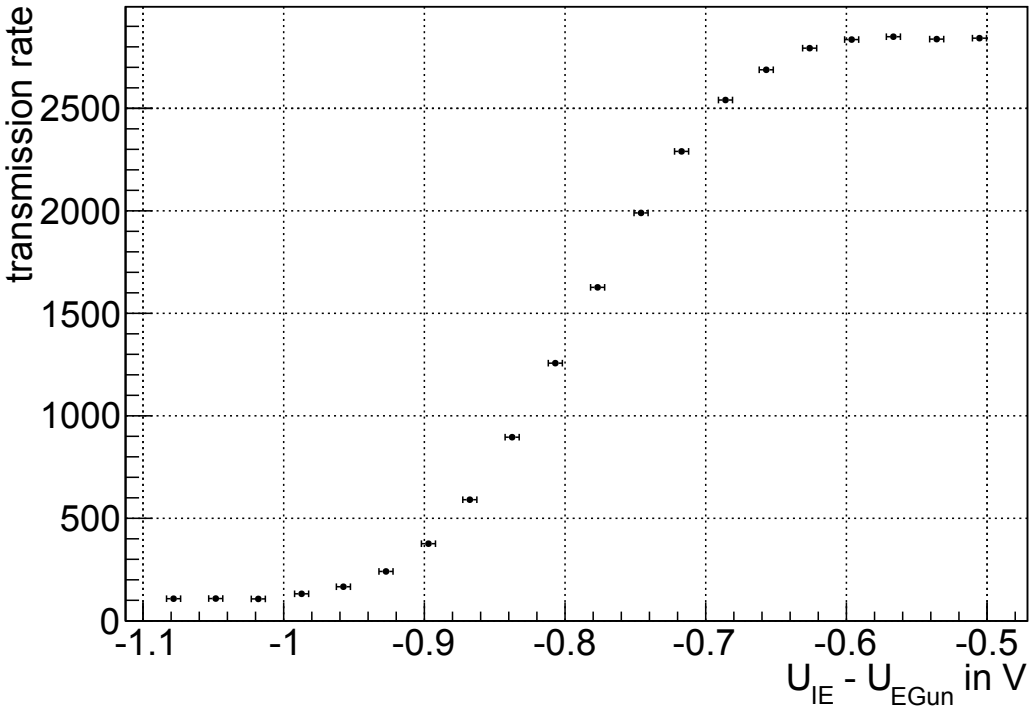

Figure 5.12: Plot of the transmission function at −18.6 kV with the 310 nm UV LED at the 9 G magnetic field setup. At each setting of ΔU_{EGun} a 30 seconds measurement has been taken. The obtained width of the transmission function is slightly broader than the one measured at low voltage (figure 5.6) with the same source, due to the influence of the angular distribution.

$$T(\Delta U_{\mathrm{EGun}}) = a \cdot \left(\int_{-(\Delta U_{\mathrm{EGun}}+\Delta U_{\mathrm{r}})}^{\infty} \int_{0}^{\theta_{\mathrm{tr}}(\Delta U_{\mathrm{EGun}})} \frac{1}{\sigma_{\mathrm{a}}\sqrt{2\pi}} \exp^{-\frac{1}{2}(\frac{\theta-\mu_{\mathrm{a}}}{\sigma_{\mathrm{a}}})^2} \mathrm{d}\theta \cdot F(E_{\mathrm{kin}}) \mathrm{d}E_{\mathrm{kin}} \right) + b, \tag{5.21}$$

with θ_{tr} as defined in equation 5.10 and four fit parameters: the amplitude a, the background b, the radial potential offset ΔU_{r}, and the standard deviation of the angular distribution σ_{a}. The mean of the Gaussian distribution had to be fixed to $\mu_{\mathrm{a}} = 0$, due to the correlation with ΔU_{r} and σ_{a}, as a different μ_{a} shifts the transmission function like a change in ΔU_{r} and increases the width like a change in σ_{a}. But as a plate angle has been chosen where the initial polar angle is expected to be minimal, the true mean of the angular distribution should indeed be close to $\mu_{\mathrm{a}} = 0$, as assumed. For similar reasons the analyzing plane magnetic field in the formula had to be fixed to $B_{\mathrm{A}} = 8.8 \cdot 10^{-4}$ T, although this value is obtained from magnetic field calculations only. This is another reason why this measurement is done at a high magnetic field, where the field is dominated by the field shaping coils and additional background components such as the magnetic materials in the hall or a not fully compensated earth magnetic field can be neglected.

The fitted function is plotted in figure 5.13 together with the measurement points, the obtained fit parameters and the residuals. For the width of the angular distribution a value of $\sigma_{\mathrm{a}} = (4.66 \pm 0.11)^\circ$ was obtained. In general, the fitted function shows a rather good agreement with the measured data points with a reduced $\chi^2 = 3.7$ and residuals lying within a range of 1 % for most of the points. This implies that model of the electron gun used here based on the obtained parameters describes the measurements very well and can thus be used for further analysis.

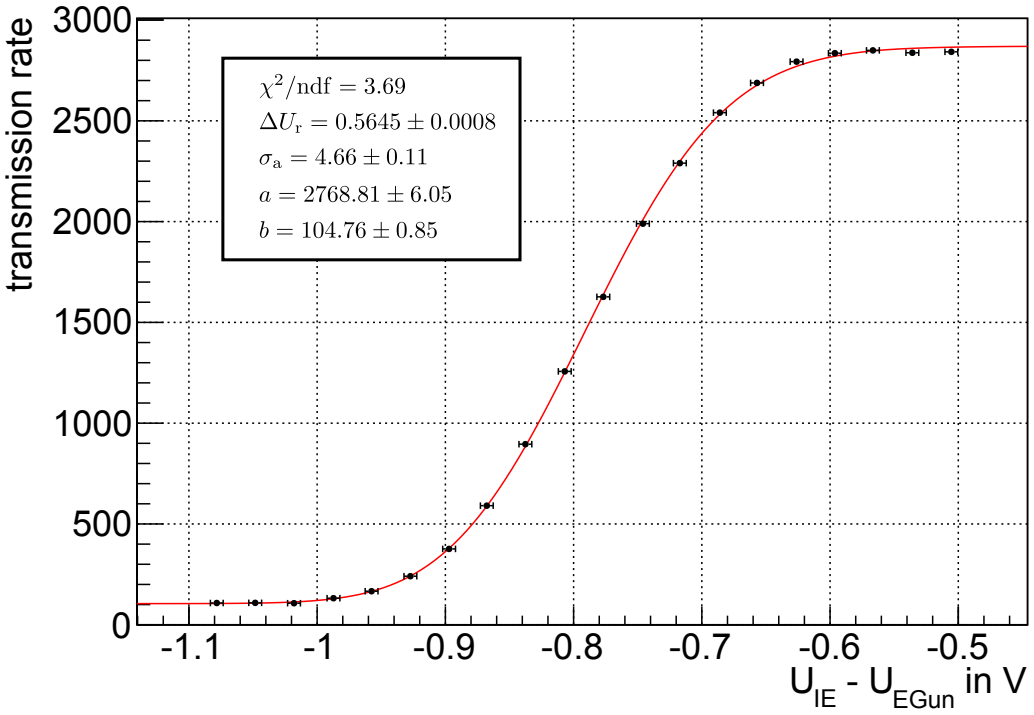

(a) Fit of the transmission function

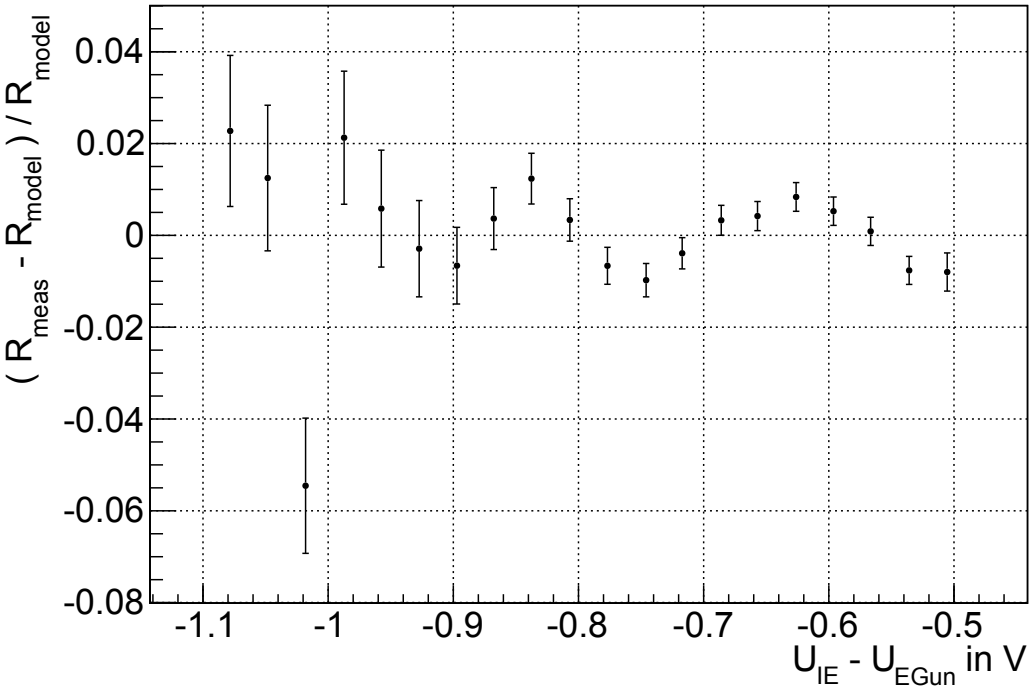

(b) Residuals

Figure 5.13: Plot of the fitted transmission function (red) together with the measured points (a). The obtained fit parameters are displayed in the box. The plotted residuals (b) show a good agreement in the range of 1 % for most of the points.

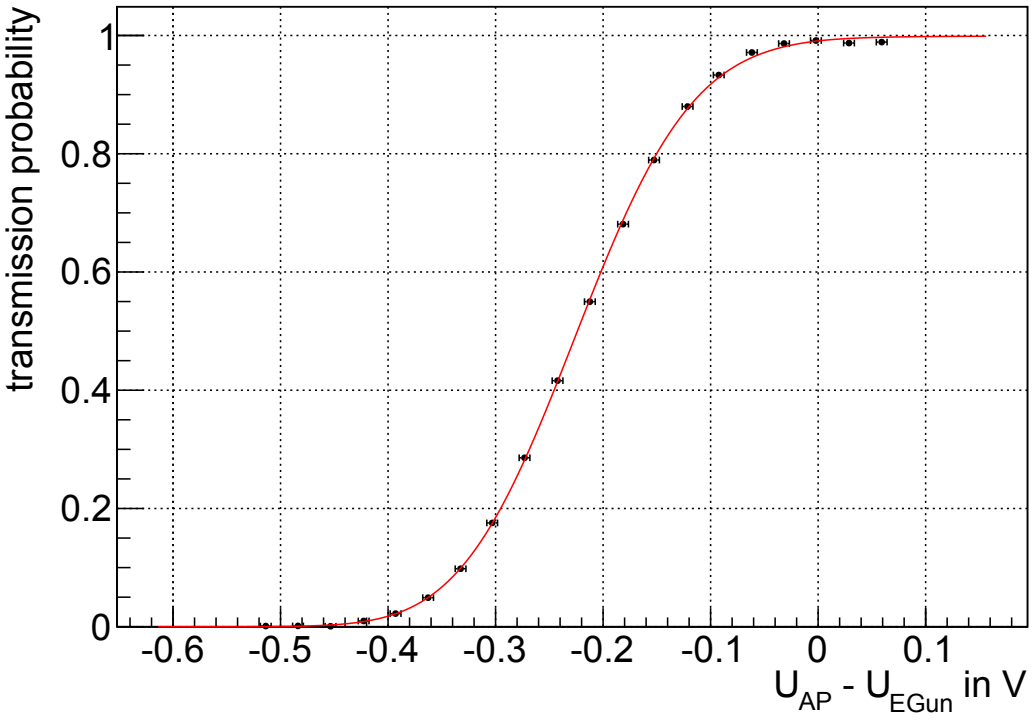

Figure 5.14: Plot of the normalized transmission function with the parameters obtained from the fit. Additionally, the x-axis has been rescaled to show the potential difference between the analyzing plane and the electron gun.

As the amplitude and background parameters have been obtained by the fit, a normalized transmission function can now be calculated with a transmission probability between zero and unity. This is useful when comparing different transmission functions, as the obtained rate was not constant for different light sources and furthermore decreased over time scales of days. Additionally, with the knowledge of the radial potential offset ΔU_r, the x-axis can be rescaled to show the difference between the analyzing point potential U_A and the electron gun potential U_EGun. The obtained transmission functions for the fit and the measured data points are plotted in figure 5.14.

5.3 Monte Carlo simulation of the transmission function with particle tracking

When knowing the properties of the electron gun and the main spectrometer, the transmission function can be analytically calculated as shown in the last sections. But these equations are only valid if the adiabatic invariant $\gamma\mu$ remains constant along the trajectory, as described in section 2.1. If this is not the case, the conversion from transversal to longitudinal kinetic energy, and vice versa, does not work as described in the analytical model. Accordingly, electrons with large polar angle would not be able to pass the main spectrometer, despite starting with sufficient kinetic energy. In the experiment not all electrons produced by the electron gun would be registered by the detector. As the rate of electrons produced at the electron gun is not measured independently, but only with the entire SDS apparatus, a loss of electrons would not be visible in the measurement. Since the main spectrometer was designed to guide signal electrons in a fully adiabatic way, the validity of the analytical model can be expected. Nevertheless, it is still important to perform transmission function simulations with exact particle tracking to compare the obtained results with the measured data and analytical calculations.

For these reasons, a Monte Carlo simulation was set up with KASSIOPEIA to simulate the

transmission function at high voltage from the last section. The settings of the Monte Carlo simulation are described in the next section (5.3.1), followed by the results obtained (5.3.2) and a comparison with the measued data (5.3.3).

5.3.1 Settings of the Monte Carlo simulation

For the simulations all known properties of the SDS commissioning measurements were incorporated, and exactly the same settings as in the measurement of the transmission function were used.

- **Electrostatic field:** For the simulation of the electrostatic field a fully axially symmetric model of the main spectrometer and the detector section was used. The main spectrometer vessel and the steep cone were set to $U_{\text{vessel}} = -18500\,\text{V}$ and all inner electrodes on $U_{\text{IE}} = -18600\,\text{V}$. The post acceleration electrode was deactivated, as in the measurement.
- **Magnetic field:** For the simulation of the magnetic field the magnet system with the two pre-spectrometer and two detector solenoids and the LFCS system was used with the 9 G setup, as stated in section 4.1.3. The tilting of the pinch and detector magnet as described in section 4.2.1 has been incorporated.
- **Particle generation:** All electrons have been generated in the center of the PS2 magnet, at a position $z = -12.10375\,\text{m}$, and with non-zero radial offsets due to the misalignment of the electron gun, as detailed in section 4.2.2, of $x = -1.246\,\text{mm}$ and $y = -0.228\,\text{mm}$, respectively, which corresponds to the neutral position of the electron gun manipulator.
- **Energy distribution:** As the spectrometer potential is kept constant, the starting energy of the electrons is supposed to vary for different values of ΔU_{EGun}. The mean of the Gaussian distribution $\mu_{\text{e}} = 0.247\,\text{eV}$ of the kinetic energy was obtained in the last section. To this value the acceleration potential is added, resulting in $\mu_{\text{e}} = q(U_{\text{IE}} - \Delta U_{\text{EGun}}) + 0.247\,\text{eV}$. As standard deviation a value $\sigma_{\text{e}} = 0.080\,\text{eV}$ is used. The drawn values of the initial kinetic energy for one transmission point at $\Delta U_{\text{EGun}} = -0.7\,\text{V}$ are visualized in figure 5.15.
- **Angular distribution:** For the angular distribution a generator with a Gaussian distribution with $\mu_{\text{a}} = 0\,^\circ$ and $\sigma_{\text{a}} = 4.66\,^\circ$ was used. The drawn values of the initial polar angle for one transmission point at $\Delta U_{\text{EGun}} = -0.7\,\text{V}$ are visualized in figure 5.16.
- **Particle tracking:** For the particle tracking the exact trajectory with the Runge-Kutta 8 integrator and 16 steps per cyclotron motion was used, as introduced in section 3.2. The particles were stopped when they did hit the surface of the focal plane detector wafer, or when they turned around in the main spectrometer due to the retarding potential.

A total of 81 different sub runs with values of ΔU from $-1.10\,\text{V}$ to $-0.30\,\text{V}$ in steps of $10\,\text{mV}$ were simulated, each including 10^5 generated and tracked electrons.

5.3.2 Results of the Monte Carlo simulation

A track of a transmitted electron passing the main spectrometer is visualized in figure 5.17. The electron started in the entrance magnet of the main spectrometer with enough kinetic energy to be transmitted at the retarding potential and stops at the silicon surface of the detector wafer. A track like this has been calculated for all of the $8 \cdot 10^6$ generated electrons, a fraction of those passing the MAC-E filter and reaching the detector as in

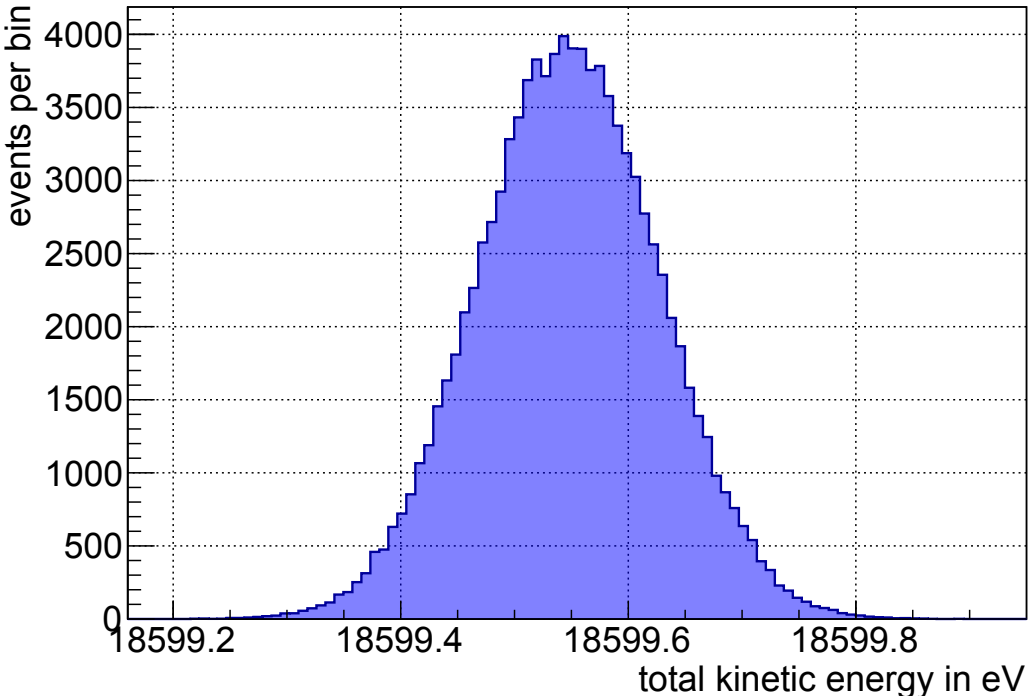

Figure 5.15: Initial total kinetic energy distribution of the Monte Carlo simulation for $\Delta U_{\mathrm{eGun}} = -0.7\,\mathrm{V}$ with 10^5 events. The initial total kinetic energy was drawn from a Gaussian distribution with the mean $\mu_{\mathrm{e}} = q(U_{\mathrm{IE}} - \Delta U_{\mathrm{EGun}}) + 0.247\,\mathrm{eV}$ and standard deviation of $\sigma_{\mathrm{e}} = 0.080\,\mathrm{eV}$.

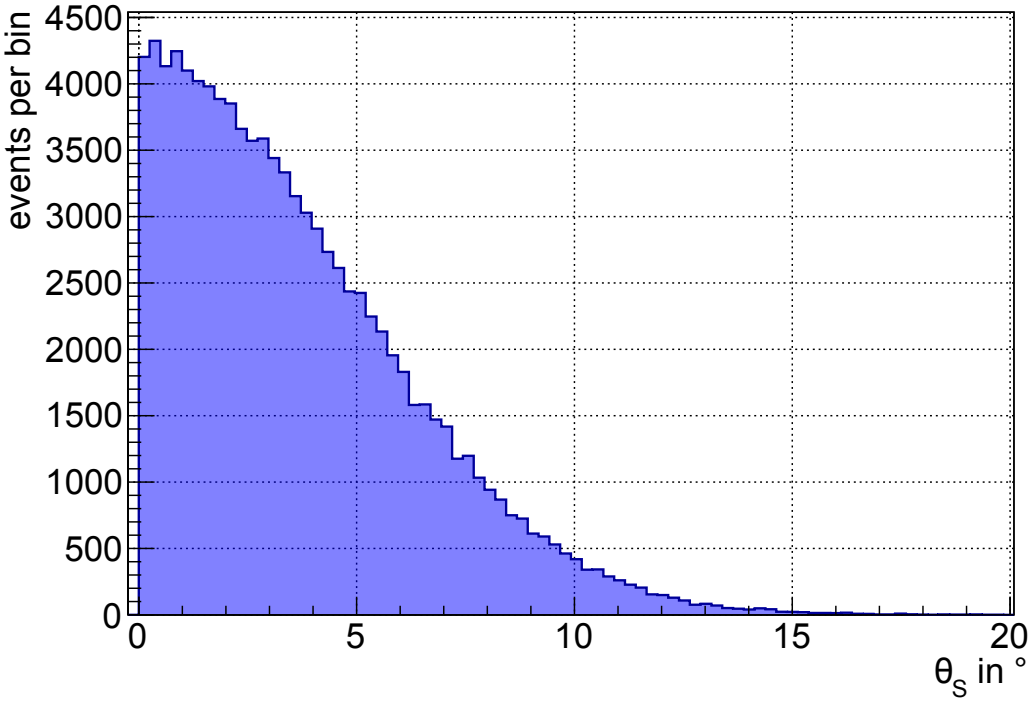

Figure 5.16: Initial polar angle distribution of the Monte Carlo simulation for $\Delta U_{\mathrm{eGun}} = -0.7\,\mathrm{V}$ with 10^5 events. The initial polar angle was drawn from a Gaussian distribution with $\mu_{\mathrm{a}} = 0\,^\circ$ and a standard deviation of $\sigma_{\mathrm{a}} = 4.66\,^\circ$. Note that the polar angle is defined only between $\theta = 0\,^\circ$ and $\theta = 180\,^\circ$ and the distribution is adjusted accordingly.

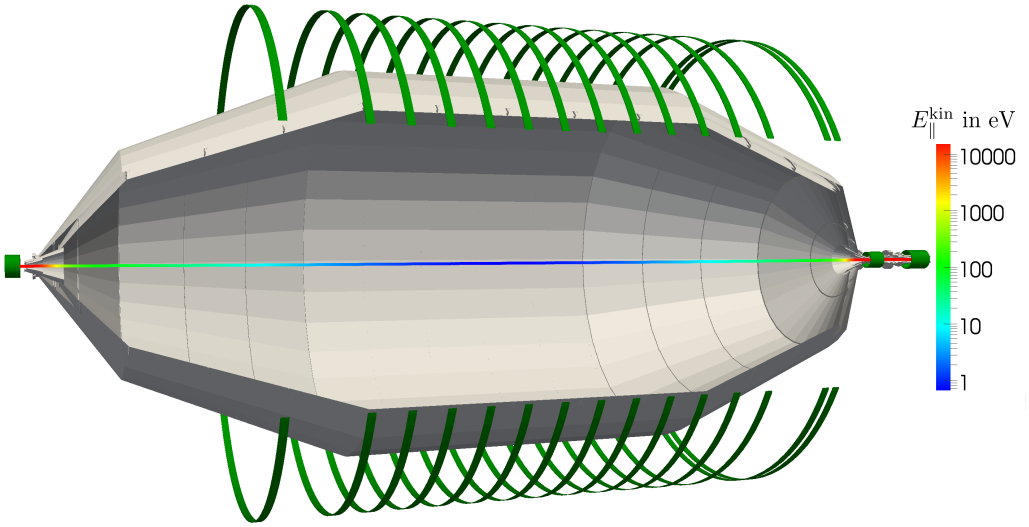

Figure 5.17: Trajectory of an electron inside the main spectrometer for the transmission function simulation. The particle starts inside the entrance magnet on the left side, passes the main spectrometer and the retarding potential close to the axis and enters the focal plane detector system on the right side before the track gets terminated when the electron hits the silicon surface. The color coding is according to the longitudinal kinetic energy, starting at $E_{\parallel} \approx 18600\,\text{eV}$ and reaching less than 1 eV in the analyzing plane in the middle of the spectrometer.

the shown example, while the remainder are reflected by the retarding potential. The transmission probability for each sub run can easily be calculated as

$$T(\Delta U_{\text{EGun}}) = \frac{k(\Delta U_{\text{EGun}})}{n}, \tag{5.22}$$

with k being the number of transmitted particles for that sub run, and $n = 10^5$ denoting the total number of generated electrons per sub run. The errors on the transmission probability were calculated with

$$\sigma = \sqrt{\frac{(k+1)(k+2)}{(n+2)(n+3)} - \frac{(k+1)^2}{(n+2)^2}}, \tag{5.23}$$

according to [UX08].

The simulated transmission function reaches full transmission for sufficiently high surplus energies, where all of the generated particles reach the detector, so that no electrons are reflected due to non-adiabatic motion. For further analysis of the exact shape and width of the simulated transmission function, a comparison of the measurement and the analytical model will be done in the next section, where also a plot of the Monte Carlo transmission function is presented in figure 5.18.

5.3.3 Comparison with measured data

To compare the simulated and measured transmission function, both need to be plotted as function of the potential difference between the analyzing point U_{A} and the electron gun U_{EGun}, including the radial potential offset ΔU_{r}. The latter parameter was determined for the measurement in the last section to $\Delta U_{\text{r}} = 0.565\,\text{V}$, and can be calculated for the simulation to $\Delta U_{\text{r}}^{\text{sim}} = 0.464\,\text{V}$. The difference results from the simplified axially symmetric model, which offers the distinct advantage of fast computation speed in contrast to the

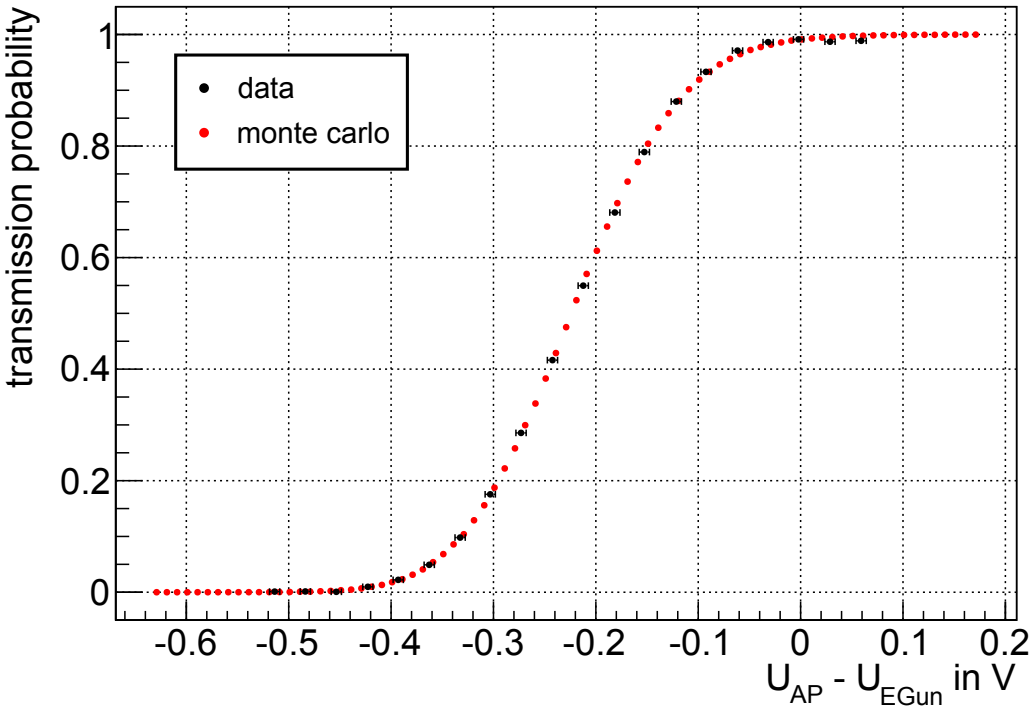

Figure 5.18: The comparison of the transmission function from the Monte Carlo simulation with the measured data shows a good agreement.

full 3D model, which is too slow to be used for Monte Carlo simulations. The electrostatic potential at the starting position of $U_S = -0.007\,\mathrm{V}$ also needs to be incorporated into the shift of the simulated transmission function. The resulting plots for the measured and simulated transmission function are shown in figure 5.18, showing a very good agreement.

Finally, a comparison between the Monte Carlo simulation, based on exact particle tracking and the analytical model, which is only valid for adiabatic motions, needs to be done to validate the analytical model. Both are plotted in figure 5.19, together with their residuals. The agreement of both curves again is very good with the residuals for the upper half of the transmission function falling within a range of 10^{-3}. For lower starting energies the residuals including their errors, get larger, which is caused by the finite number of simulated particles in conjunction with the very low transmission probability.

The main conclusion of this section is the important fact that the measured transmission data can indeed be reproduced by Monte Carlo simulations with very good accuracy. The analytical model, despite its adiabatic approximation, is thus certainly valid to describe the measured data.

5.4 Measurement of the radial potential inhomogeneity in the analyzing plane

The focus of this chapter is set on the measurement of transmission properties of the main spectrometer to obtain information on the radial inhomogeneity of the electrostatic potential and magnetic field in the analyzing plane.

Due to issues with the angular selectivity of the electron gun, as stated in section 5.2.2, a reliable determination of the actual magnetic field in the analyzing plane is not possible using transmission function measurements. Therefore, the following studies will focus on the determination of the radial inhomogeneity of the potential in the analyzing plane for different electrostatic field settings. This will also demonstrate the functionality of

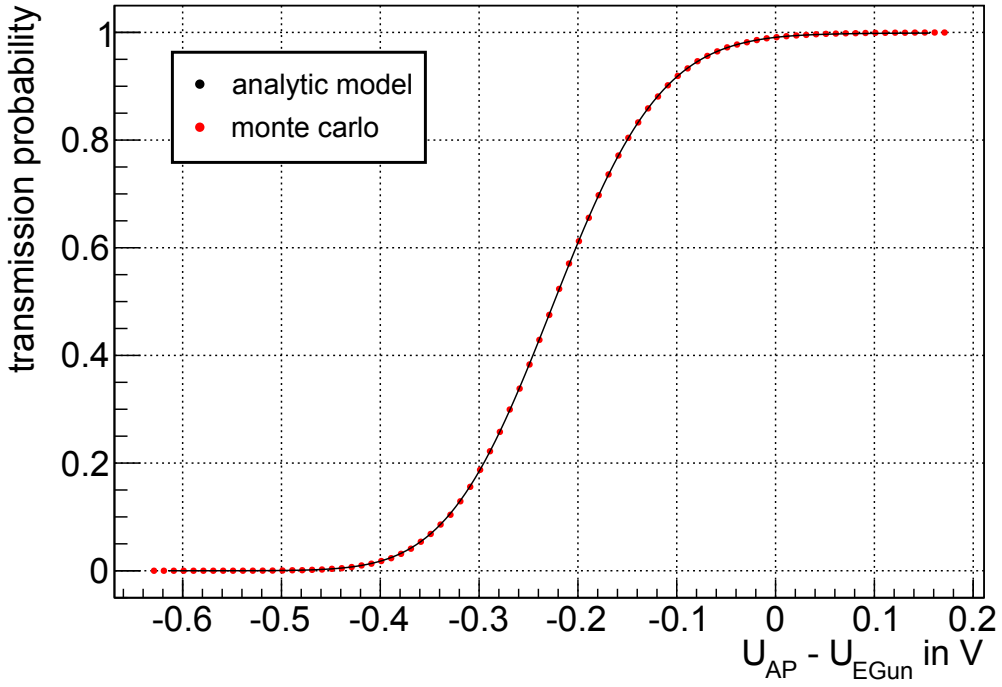

(a) Monte Carlo and analytical transmission function

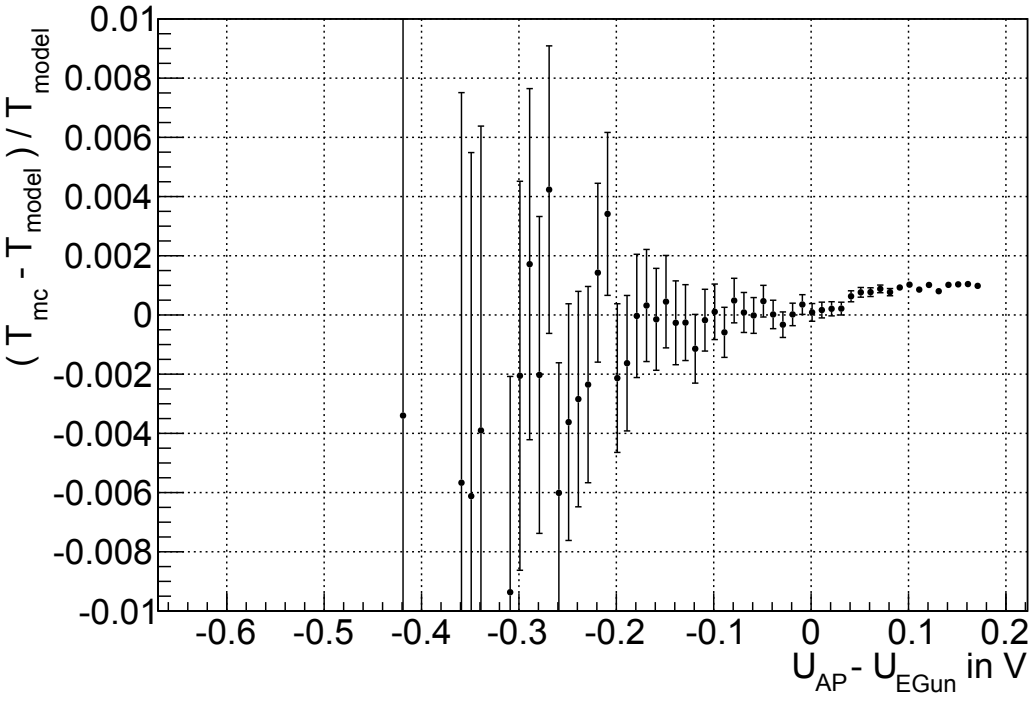

(b) Residuals

Figure 5.19: Comparison of the transmission function from the Monte Carlo simulation with the analytic model as presented in the last section (a). The corresponding residuals are plotted below (b). For most of the upper part of the transmission function, the residuals are within the range of 10^{-3}, but for the lower part the residuals increase, due to the finite amount of simulated particles and the transmission probability close to zero.

the evolved analysis procedure and the developed software tools, and is also intended to validate the simulation software and models via a dedicated comparison of the measured data with performed simulations.

The required precision of the radial potential inhomogeneity measurement can be estimated by considering the potential inhomogeneity for a single pixel. As the total radial inhomogeneity in the analyzing plane of the main spectrometer is expected to be of the order of 400 mV, as presented in section 4.3, the inhomogeneity over a single pixel ring (out of 13) can be approximated to be about 30 mV. In this simple approach this value can be taken as the required precision of the radial potential inhomogeneity measurements, while a more detailed investigation will be done in section 5.5.

Several radial potential measurements were performed during the SDS commissioning phase in a configuration without high voltage on the main spectrometer vessel, and also in a later stage with full working high voltage functionality. The radial potential measurements performed in both phases differ significantly from each other not only in the electromagnetic setup, but also with respect to the used light source and the applied electron gun manipulator settings, and therefore also the mapped positions inside the main spectrometer. In the following, the analysis procedure will be detailed for the two different electrode settings in the high voltage phase.

Initially, when performing a measurement to determine the radial potential offset in the analyzing plane, the manipulator of the electron gun needs to be set to various positions, resulting in different electron trajectories through the main spectrometer mapped onto specific pixel hits on the focal plane detector. For each of the manipulator positions selected, the exact position of the analyzing point in the middle of the main spectrometer had to be determined by a field line tracking simulation, as will be outlined in section 5.4.1. The corresponding potential offset can be extracted from a transmission function measurement, as will be shown in section 5.4.2. The systematic errors for the position of the analyzing point and the extracted radial potential offsets are estimated in section 5.4.3, and the resulting plots of the radial potential inhomogeneity will be shown and discussed in section 5.4.4. This is followed by a comparison with corresponding simulations in section 5.4.5. Finally, in section 5.4.6, the same analysis procedure is applied to the measurements without high voltage and the obtained results will be presented and discussed.

5.4.1 Determination of the analyzing plane positions

In the configuration with an elevated vessel, two different electromagnetic setups were used for the radial potential measurement. In both cases, the overall potential of the inner electrodes was set to $U_{\mathrm{IE}} = -15600\,\mathrm{V}$, as the electron gun could not be operated at a higher potential at this measurement series due to discharges at the electron gun's electrodes. In the setting A, the offset between vessel and inner electrodes was set to 100 V, and in setting B the difference was 200 V. Details about the exact potential configuration of the individual electrode modules of the main spectrometer for these settings can be found in appendix A. The post acceleration electrode of the focal plane detector was not activated, while the voltage difference between the electron gun plates was set to 100 V and the magnet system has been set to the 3.8 G setup on both settings.

For the setting A, 10 different values of the horizontal electron gun manipulator angle α_{h} were used, for scanning the analyzing plane potential shape in main spectrometer in horizontal direction. For setting B the same horizontal scan was done, however with only 5 different manipulator angles. For the angles selected, the field lines determining the electron tracks were simulated. Field lines started at the electron gun according the formula given in 4.1 and propagated through the main spectrometer to the detector wafer. The simulation incorporated all settings as used in the measurements. The geometry during the

SDS commissioning measurements was exactly reproduced, including the misalignment of the detector system and the electron gun, as described in section 4.2. The resulting field lines are visualized in figure 5.20, the blue ones corresponding to the manipulator angles used in setting B, while in setting A all displayed field lines correspond to electron tracks which were used in the measurements.

The resulting simulation based pixel hits at the detector wafer are shown in figure 5.21 together with the pixel distributions of the measurement for all transmission functions taken for setting A. Most importantly, identical pixels were hit both in the simulation as in the measurement. Correspondingly, the misalignment of the electron gun and the focal plane detector system is expected to be incorporated correctly in the simulation so that the resulting electron trajectories are expected to match the ones from the measurement.

The position of the analyzing point for each field line does not necessarily coincide with $z = 0\,\mathrm{m}$, as the given setup is not optimized for transmission conditions. This is due to the misaligned detector magnets, the short circuit in the inner electrode system and the asymmetric potential settings, as detailed in section 4.1. Therefore, the analyzing points differ strongly from $z = 0\,\mathrm{m}$ (as shown in section 4.3.5) and thus have to be determined by calculating the position of the minimal longitudinal kinetic energy for each field line, as demonstrated in section 4.3. This can only be done by using a detailed electrostatic 3D model of the main spectrometer ([Cor14]), which incorporates the short circuits and the asymmetric potential settings as stated in appendix A.

The resulting analyzing plane positions are listed in tables 5.1 and 5.2 for the two settings A and B, respectively.

5.4.2 Determination of the analyzing plane potentials

To determine the analyzing plane potential, or more precisely the radial potential offset, the properties of the used electron gun need to be known. For both radial potential measurements during the high voltage phase, the UV laser was used as light source. As stated above, it produces a much broader energy distribution than the UV LED. However, at that time the laser was the only light source available able to produce a suitable electron rate, as the silver cathode was already heavily degraded. The laser was pulsed with a frequency of 100 kHz at a pulse length of 2 µs. To determine the energy and angular distribution of the electron gun in this configuration, two transmission functions measurement were performed, one at low voltage and one at high voltage with the 9 G magnetic field setting prior to the radial potential measurements. The procedures outlined in section 5.2 to extract the energy and angular distribution were performed, and the energy distribution obtained is plotted in figure 5.22. The shape deviates notably from a Gaussian, so the numerical distribution was used for the following analysis. The angular distribution was assumed to be Gaussian with a mean of $\mu_\mathrm{a} = 0\,^\circ$, wit the fit revealing a standard deviation of $\sigma_\mathrm{a} = 4.98\,^\circ$, which is in agreement with the angular distribution obtained for the 310 nm LED in section 5.2.3.

For each manipulator position selected a transmission function was measured with a step size of 100 mV, lasting 20 seconds for each sub run. To deduce the radial potential offset, each measured transmission function is fitted according to equation 5.21 with the energy and angular distributions as described before. The three free fit parameters now are the amplitude a, the background b and the radial potential offset ΔU_r. The results obtained for the radial potential offsets are summed up in tables 5.1 and 5.2 for settings A and B, respectively.

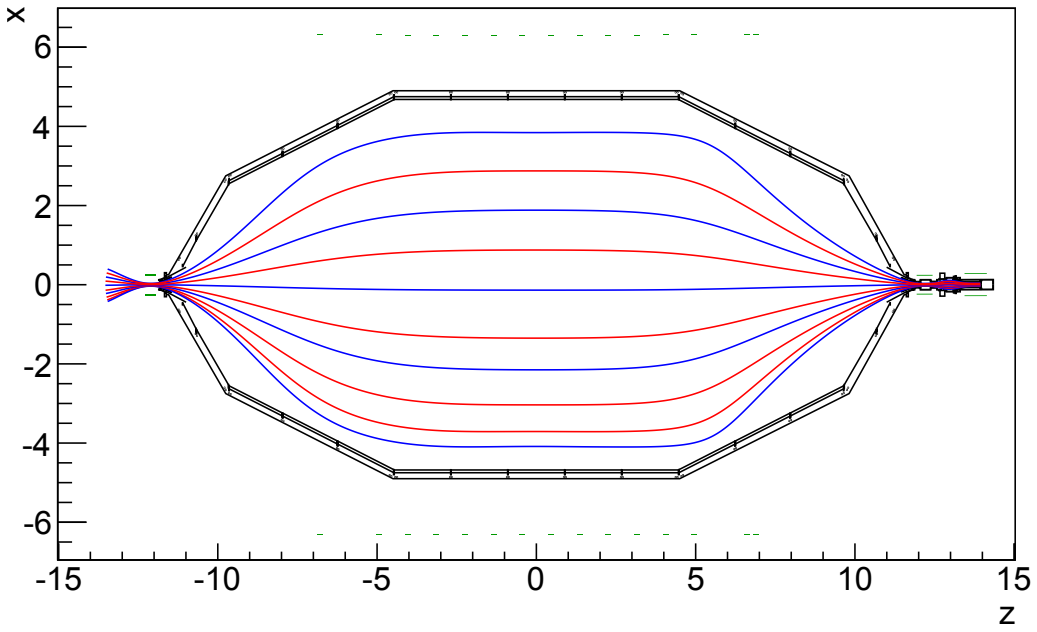

Figure 5.20: Visualization of the field lines for the transmission function measurements during the high voltage phase. All field lines start at the electron gun (not displayed) at the left side, and are tracked through the main spectrometer to the detector. While all plotted field lines correspond to the manipulator angles used in setting A, for the setting B only transmission measurements along the blue field lines were performed.

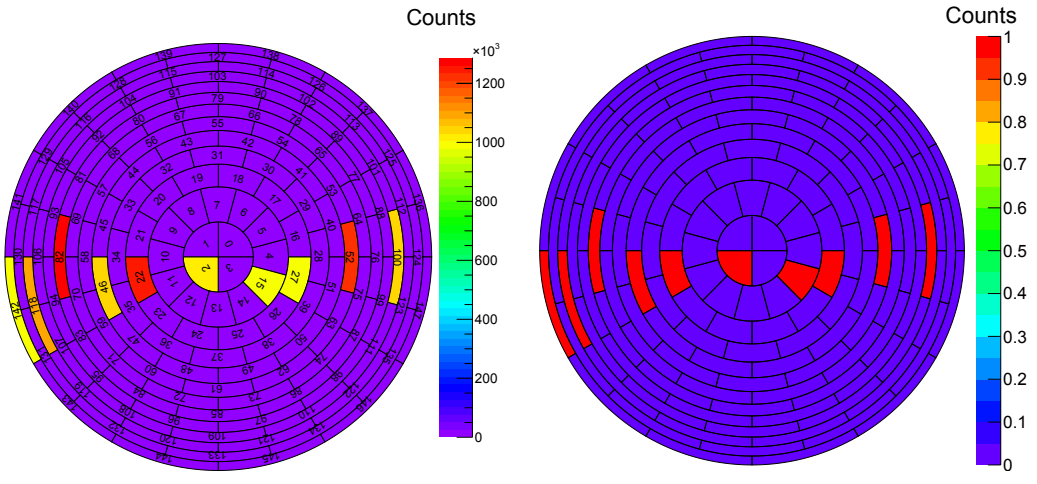

(a) Measurement (b) Field line simulation

Figure 5.21: Comparison of the measured (a) and simulated (b) pixel distributions for the manipulator angles of setting A. The manipulator angle subset of setting B corresponds to the pixels 142, 46, 2, 27 and 100. The measured electron tracks can be reproduced by the simulation, with identical pixels being hit for the manipulator angles selected.

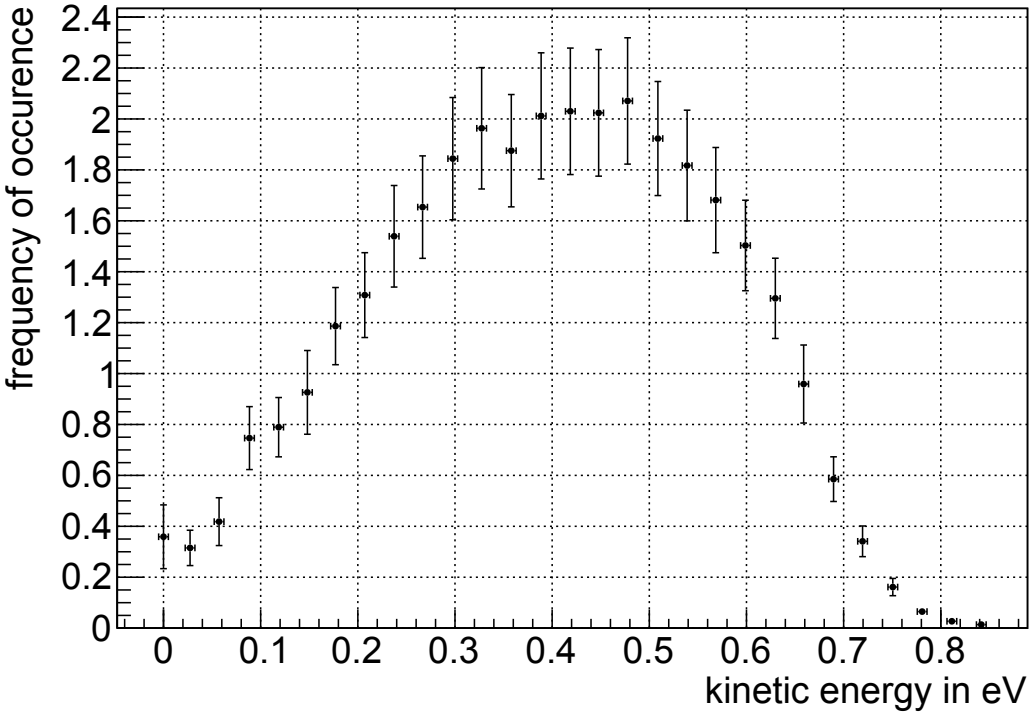

Figure 5.22: Energy distribution of the electron gun with the UV laser for the radial potential measurements at high voltage. The mean of the numerical distribution is at 0.42 eV with a standard deviation of 0.26 eV.

Table 5.1: Overview of the transmission function measurements for all 10 manipulator angles at setting A with the determined analyzing point positions and radial potential offsets.

run id	α_h in °	α_v in °	pixel	x_A in m	y_A in m	z_A in m	ΔU_r in V
7740	20	0	142	-4.090	-0.027	0.898	0.298
7730	18	0	118	-3.710	-0.027	0.652	0.374
7751	14.5	0	82	-3.036	-0.027	0.066	0.477
7758	10	0	46	-2.150	-0.027	0.028	0.600
7763	6	0	22	-1.350	-0.027	0.019	0.725
7765	0	0	2	-0.137	-0.027	0.015	0.840
7782	-5	0	15	0.876	-0.027	0.016	0.841
7778	-10	0	27	1.883	-0.027	0.022	0.796
7780	-15	0	52	2.875	-0.027	0.052	0.718
7772	-20	0	100	3.844	-0.027	0.693	0.611

Table 5.2: Overview of the transmission function measurements for all 5 manipulator angles at setting B with the determined analyzing point positions and radial potential offsets.

run id	α_h in °	α_v in °	pixel	x_A in m	y_A in m	z_A in m	ΔU_r in V
7787	20	0	142	-4.090	-0.027	0.937	1.291
7786	10	0	46	-2.150	-0.027	0.074	1.614
7785	0	0	2	-0.137	-0.027	0.045	1.802
7788	-10	0	27	1.883	-0.027	0.054	1.731
7789	-20	0	100	3.845	-0.027	0.801	1.507

5.4.3 Error estimation

The systematic effects leading to errors when determining the analyzing plane position and radial potential offsets will be detailed in the following.

Error estimation for the radial potential offset

Multiple systematic effects contribute to the errors of the measured potential offset in the analyzing plane. The most important one is related to the energy distribution. As the surplus energy for the photo electrons was arbitrarily defined, as detailed in section 5.2.1, an unaccounted offset directly translates into a measured potential offset. However, this additional offset is identical for all measured transmission functions, as long as the same energy distribution is used. The shape of the radial potential inhomogeneity is therefore unaffected. Furthermore, a small unaccounted shift on the overall potential for all pixels does not lead to a systematic error on the neutrino mass, as long as the potential differences for the individual pixels are known correctly, as will be shown in section 5.5. Therefore, only systematic effects that undergo changes for each transmission function measurement, need to be accounted for.

The first systematic considered is the digital volt meter reading of ΔU_{EGun} with a precision of 5 mV, resulting in an error on the radial potential offset of that value. The other systematic is related to the initial polar angle of the produced electrons, leading to an error on the radial potential offset of 2.9 mV for an estimated error on the electron gun plate angle of $\theta_{\mathrm{plates}} = 1.5\,^{\circ}$. The calculation leading to this assessment will be detailed in the following.

For each measurement during the radial potential scan, the manipulator arm was used to rotate the electron gun and send the electrons on a different trajectory through the main spectrometer. Therefore, also the angle of the electron gun plates relative to the magnetic field was changed. Although the angular selectivity is not working correctly, as detailed in section 5.2.2, for small plate angles a shift of the angular distribution to higher polar angles is possible. Hence for each setting of the manipulator angles α_{h} and α_{v}, the corresponding angle of the rotatable plates θ_{plates} was adjusted to the neutral position again. However, a small deviation can not be excluded, leading to larger initial polar angles θ of the electrons, even for the selected 100 V difference between the two electron gun plates. This gives rise to a systematic error on the measured potential, as a different initial polar angle θ results in a shift of the transmission function.

To estimate the shift caused by a slight deviation of the plate angle the relation between the plate angles θ_{plates} and the produced initial polar angles of the electrons θ needs to be determined. This can be done by measuring two transmission functions with different plate angles for identical electron gun and main spectrometer settings as in setting A, but now with a 9 G magnetic field setup to increase the visible effect. First a transmission function with a setting producing electrons with a minimal initial polar angle was measured at $\theta_{\mathrm{plates}} = 1.8\,^{\circ}$. For the next measurement the angle was increased to $\theta_{\mathrm{plates}} = 7.6\,^{\circ}$. To estimate the polar angle of the electrons θ produced by this change of the plate angle of $\Delta\theta_{\mathrm{plates}} = 5.8\,^{\circ}$, the mean value of the angular distribution of the electrons for the second measurement needs to be found. Therefore, the first transmission function was fitted with a fixed mean of the Gaussian angular distribution of $\mu_{\mathrm{a}} = 0\,^{\circ}$, in this case the fit resulted in $\Delta U_{\mathrm{r}} = 0.82$ and $\sigma_{\mathrm{a}} = 4.49\,^{\circ}$. Fixing those values for the fit of the second function, where the potential is not changed and the angular distribution is supposed to be similar, results in a mean of the angular distribution of $\mu_{\mathrm{a}} = 10.35\,^{\circ}$. The measured transmission functions and their fits are plotted in figure 5.23.

For the measurements with an elevated vessel potential, the error on the electron gun plate angle is assumed to be less than $\theta_{\mathrm{plates}} = 1.5\,^{\circ}$, which leads to a maximal mean value of the

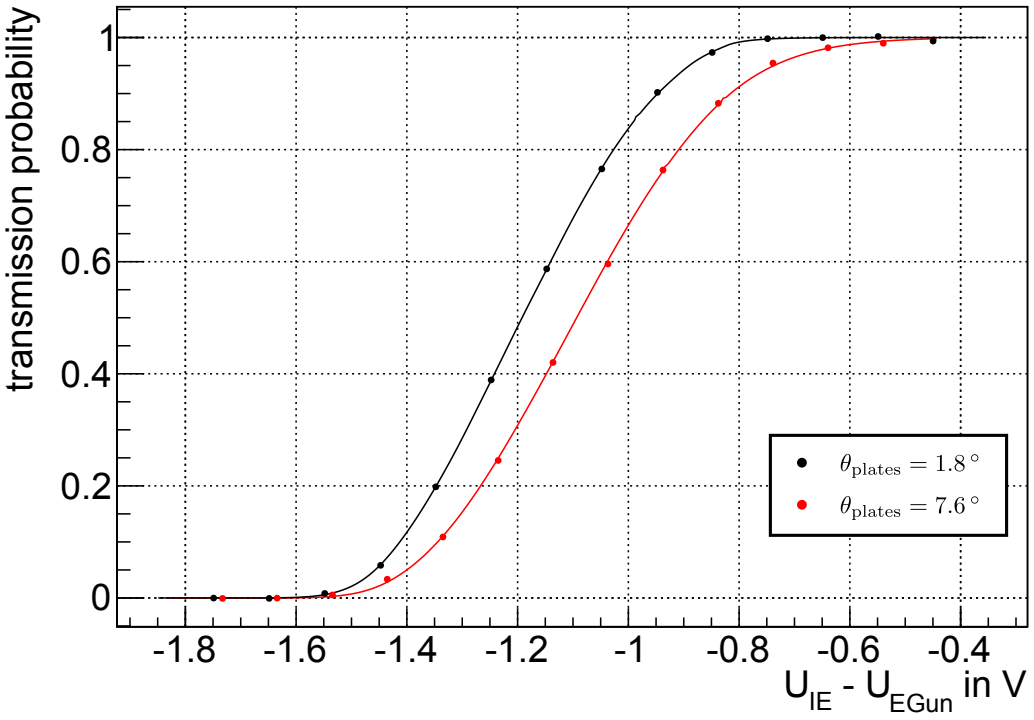

Figure 5.23: Transmission functions with different plate angles and the corresponding fitted functions. While the electron gun with a plate angle of $\theta_{\text{plates}} = 1.8\,^\circ$ is assumed to produce electrons with a polar angle distribution with a mean of $\mu_{\text{a}} = 0\,^\circ$, a setting with a plate angle difference of $\Delta\theta_{\text{plates}} = 5.8\,^\circ$ results in a mean of the electrons angular distribution of $\mu_{\text{a}} = 10.35\,^\circ$, causing the transmission function to shift to the right.

polar angular distribution of the electrons of $\mu_{\text{a}} = 2.68\,^\circ$, when assuming a linear relation. According to equation 5.13, the energy difference between two transmission functions with polar angles of $\theta_1 = 0.0\,^\circ$ and $\theta_2 = 2.68\,^\circ$ for the given parameters in the high voltage settings of $E_{\text{S}} = 15.6\,\text{keV}$, $B_{\text{A}} = 3.6 \cdot 10^{-4}\,\text{T}$ and $B_{\text{S}} = 4.333\,\text{T}$ is $\Delta E = 2.9\,\text{meV}$.

Including the error from the digital volt meter of 5 mV, the total systematic uncertainty for the radial potential measurements at elevated vessel potential can be stated as $\sigma_{\Delta U_{\text{r}}} = 7.9\,\text{mV}$.

Error estimation for the analyzing point position

The errors on the analyzing plane positions can be estimated taking into account the following systematics:

- **Alignment of the electron gun relative to the focal plane detector:** The misalignment of the electron gun and the detector system was integrated into the field line simulation, leading to the same pixels being hit in the simulation as in the measurement. Therefore, half of the width of the outer pixel can be used as an estimation for the maximal unaccounted shift of about $\Delta x = \Delta y = 0.9\,\text{mm}$.
- **Additional unconsidered magnetic stray fields:** Possible geometric deviations from the axially symmetric magnets, like a possible small tilt of the pre-spectrometer magnets, the EMCS coils forming not a perfect circle and stray fields from magnetic materials in the spectrometer building were not included in the field line simulation. Nevertheless, as the pixel distribution of the measurement could be reproduced by the simulation, small local effects are estimated to be maximal of the same order as the alignment error of $\Delta x = \Delta y = 0.9\,\text{mm}$ at the wafer.

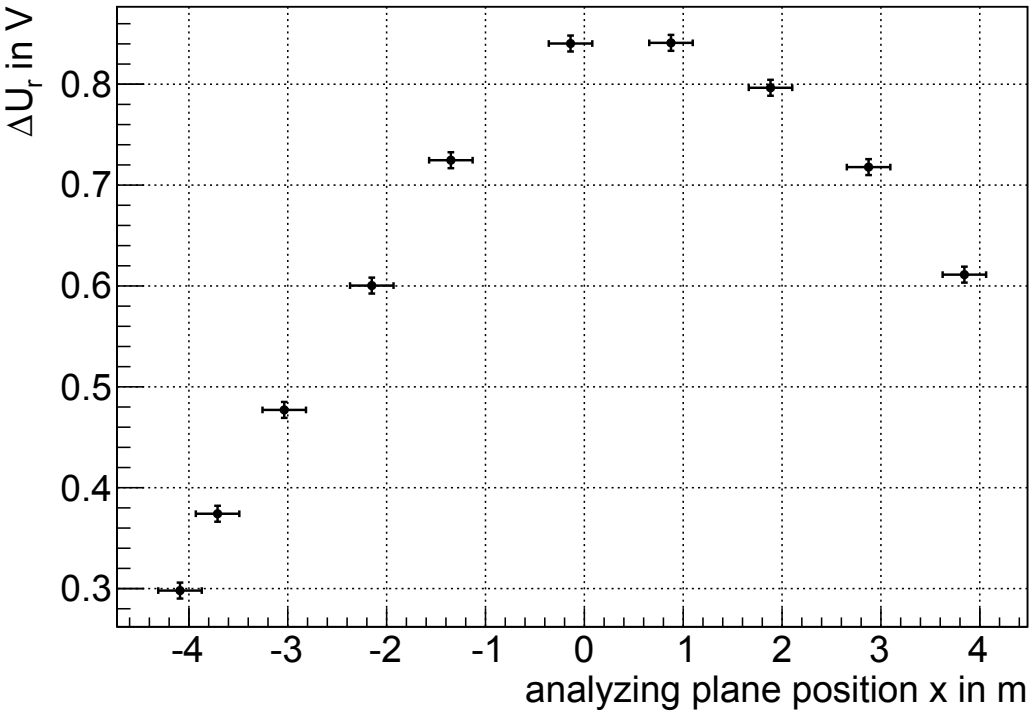

Figure 5.24: Plot of the measured radial potential offsets for setting A, with respect to the x component of the determined analyzing point position.

- **Offset of the magnetic flux tube to the main spectrometer vessel:** Field-emission measurements performed in [Sch14] revealed a misalignment of the spectrometer vessel, or at least the inner electrode system, relative to the magnetic flux tube, resulting in an offset at the detector of $\Delta x = 0.5\,\text{mm}$ and $\Delta y = 0.2\,\text{mm}$.

These estimated maximal offsets for the individual systematics can be added up to $\Delta x = 2.3\,\text{mm}$ and $\Delta y = 2.0\,\text{mm}$ and need to be scaled to the position of the analyzing plane due to the conservation of the magnetic flux. Although the magnetic field for the different analyzing points is not constant, a value of $B_\text{A} = 3.6 \cdot 10^{-4}\,\text{T}$ can still be used for all points of this estimation. With a magnetic field at the wafer of $B_\text{wafer} = 3.283\,\text{T}$, an estimated error for all analyzing points can be calculated according to equation 4.2 to $\sigma_x = 0.220\,\text{m}$ and $\sigma_y = 0.191\,\text{m}$.

5.4.4 Results

The values obtained for the radial potential offset and the corresponding analyzing point position, as summarized in tables 5.1 and 5.2 for settings A and B, respectively, can now be visualized together with the estimated errors in figure 5.24 and figures 5.25.

As expected, the radial potential offset is largest in the middle of the spectrometer and drops to both sides, but it is not symmetric. The difference between the outermost measured values at about $x = +4\,\text{m}$ (west side) and $x = -4\,\text{m}$ (east side) is of the order of 0.4 V for setting A, and 0.2 V for setting B. In a first estimation this can be fully explained by the applied high voltage configuration (see appendix A), as the difference between the west and the east part of the inner electrodes on the cylindrical modules is about 0.37 V for setting A and 0.20 V for setting B. Also the larger radial potential offset for setting B with a difference between the inner electrodes and the spectrometer vessel of $\Delta U_\text{wire} = 200\,\text{V}$, compared with $\Delta U_\text{wire} = 100\,\text{V}$ at setting A, can be expected qualitatively, as the radial potential offset scales approximately linearly with ΔU_wire.

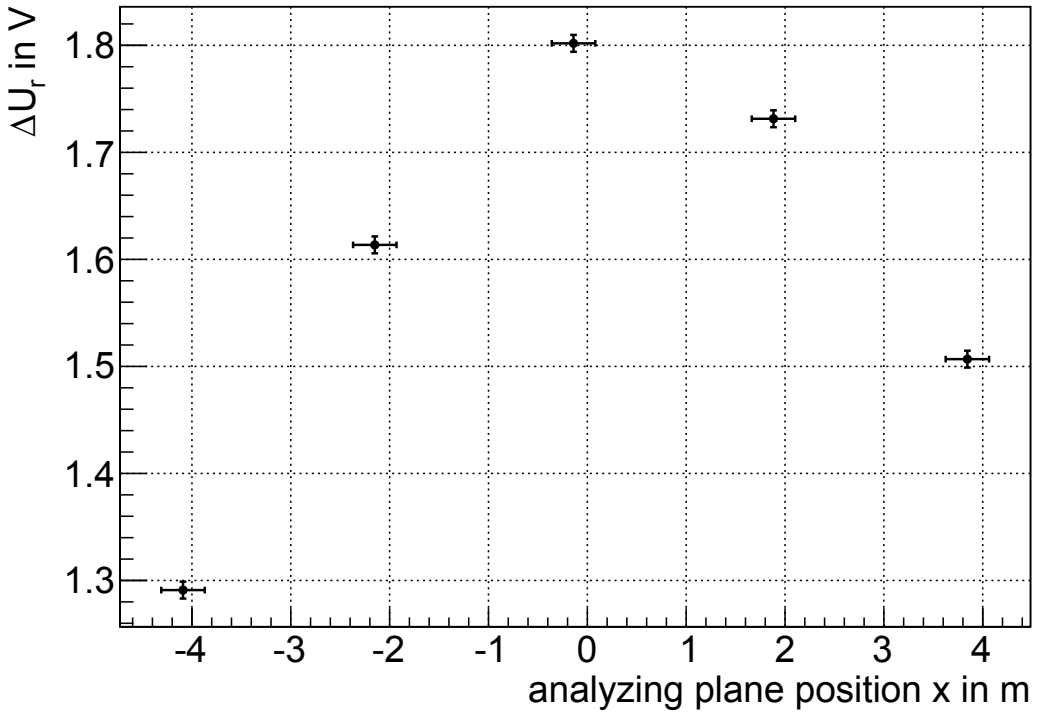

Figure 5.25: Plot of the measured radial potential offsets for setting B, with respect to the x component of the determined analyzing point position.

For a more quantitative evaluation of the measured radial potential offsets, electrostatic potential calculations need to be performed as described in the next section.

5.4.5 Comparison with potential simulations

To compare the measured radial potential inhomogeneity with electrostatic potential calculations, a sophisticated 3D model of the main spectrometer is required, which incorporates all geometrical elements inside the vessel with great detail, including the deformation of the vessel hull as well as detailed models of the complex wire electrode modules [Cor14]. In this model, all potentials of the individual electrodes were set to the measured values from the power supplies, as stated in appendix A.

For each setting, the potential has to be calculated not only at the determined analyzing plane positions, but also in between the measured positions, and even closer to the inner electrodes than in the measurement. As the analyzing plane positions do not form a simple line, these 100 points in total were obtained using a Lagrange interpolation. For these positions the absolute potentials were computed and the potential offset relative to the inner electrode on the west cylindrical part was calculated. The resulting values are plotted together with measured data in figures 5.26 and 5.27 for the settings A and B, respectively.

The absolute values of the radial potential offsets of measurement and simulation are not expected to be identical, due to the effects of the unknown spectrometer work function and the uncertainty on the energy scale of the electrons produced by the electron gun, as detailed in section 5.4.3. Therefore, an absolute offset $\Delta U_{\mathrm{offset}}$ was added to the simulated values of ΔU_{r}. As these two properties should not have changed for the two different measurement settings, the offset value is expected to be similar for both. From a fit the values of $\Delta U_{\mathrm{offset}} = -0.327\,\mathrm{V}$ for setting A and of $\Delta U_{\mathrm{offset}} = -0.316\,\mathrm{V}$ for setting B were obtained. With this shift in vertical direction, the measured values of the radial potential offsets are in good agreement with the simulated potentials, as illustrated in

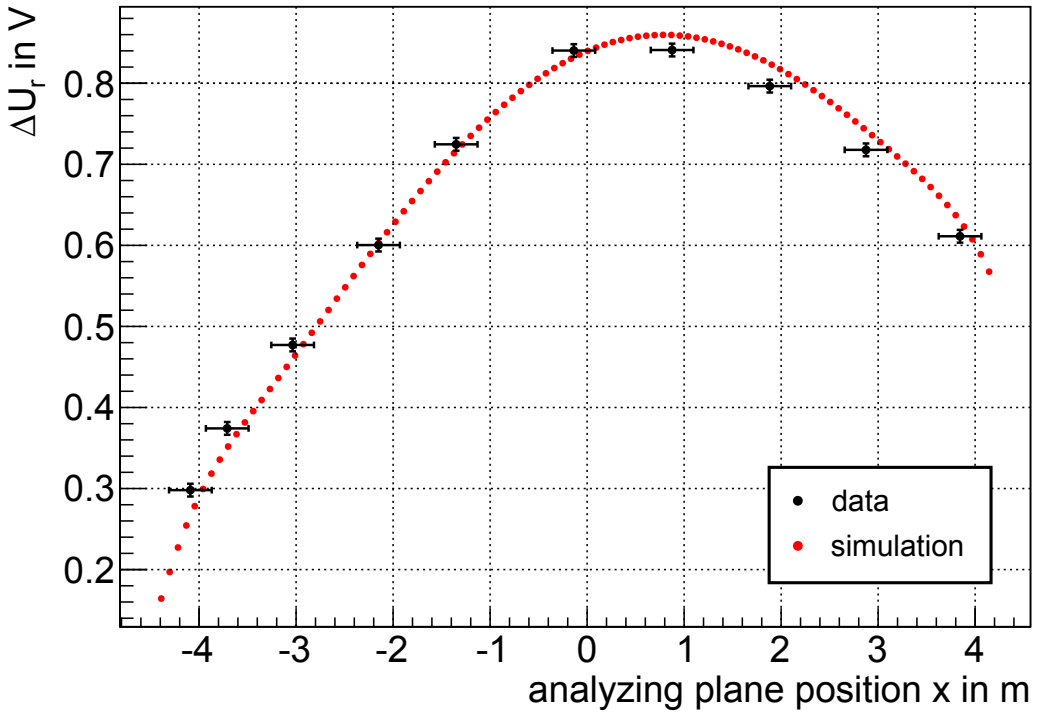

Figure 5.26: Comparison of measured and simulated radial potential offsets for setting A. For the simulated values an absolute offset $\Delta U_{\text{offset}} = -0.327\,\text{V}$ was added. The measured data shows a very good agreement with the simulated potentials.

figure 5.28. The maximal difference between measurement and simulation is about 30 mV, which coincides with the required precision, as stated in the beginning of this section. Additionally, the difference for most points on the positive x-axis is negative, but positive for points on the negative x-axis, which may be caused by an unaccounted shift in the calculations of the analyzing points. For a system with improved alignment, the achieved precision in determining the radial potential inhomogeneity is therefore expected to be even better.

5.4.6 Measurements without high voltage

In addition to the described radial potential measurements at elevated vessel potential described in the last sections, also radial potential measurements without high voltage on the spectrometer vessel were performed. In this measurements the electrostatic settings for the main spectrometer vessel were even more complex, with a higher dipole field, larger deformations of the analyzing plane and a larger radial potential inhomogeneity. It will be shown that the radial potential inhomogeneity still can be determined with nearly identical accuracy as in the example with high voltage.

Settings

With the main spectrometer vessel being grounded, only the inner electrodes were elevated to $U_{\text{IE}} = -1000\,\text{V}$ to form the retarding potential of the main spectrometer. Due to the rather low energy nature of the electrons produced, of about $E_{\text{S}} = 1000\,\text{eV}$, the post acceleration of the focal plane detector system was set to $U_{\text{PAE}} = 10\,\text{kV}$. For the magnetic field, the standard 3.8 G setting was used.

Two different radial potential measurements were performed to scan the spectrometer vessel in two diagonal directions, orthogonal to each other. Although the electrodes of the main spectrometer were set to the same values for both measurements, the resulting

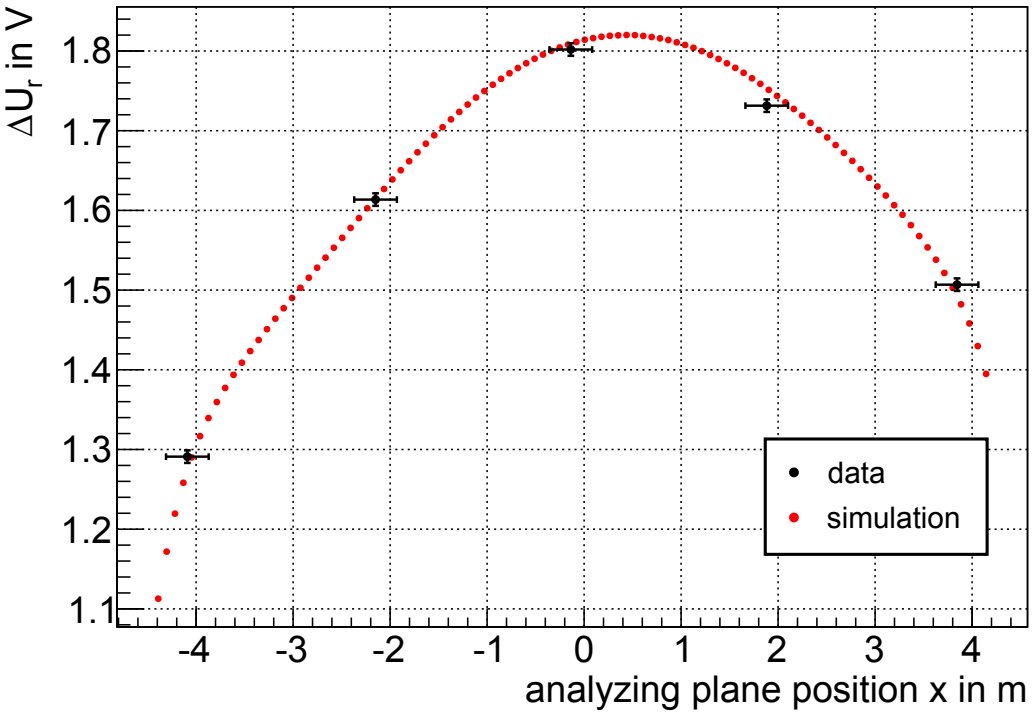

Figure 5.27: Comparison of measured and simulated radial potential offsets for setting B. For the simulated values an absolute offset $\Delta U_{\text{offset}} = -0.316\,\text{V}$ was added. The measured data show a very good agreement with the simulated potentials.

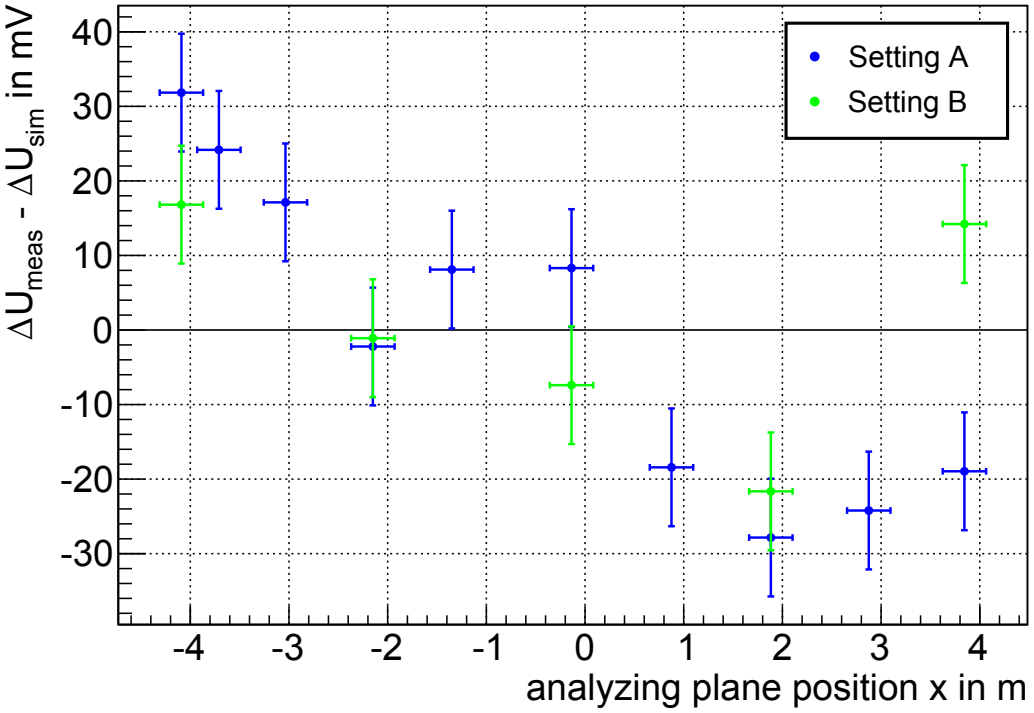

Figure 5.28: The difference between measured and simulated potential for setting A (blue) and B (green) is within the range of 30 mV.

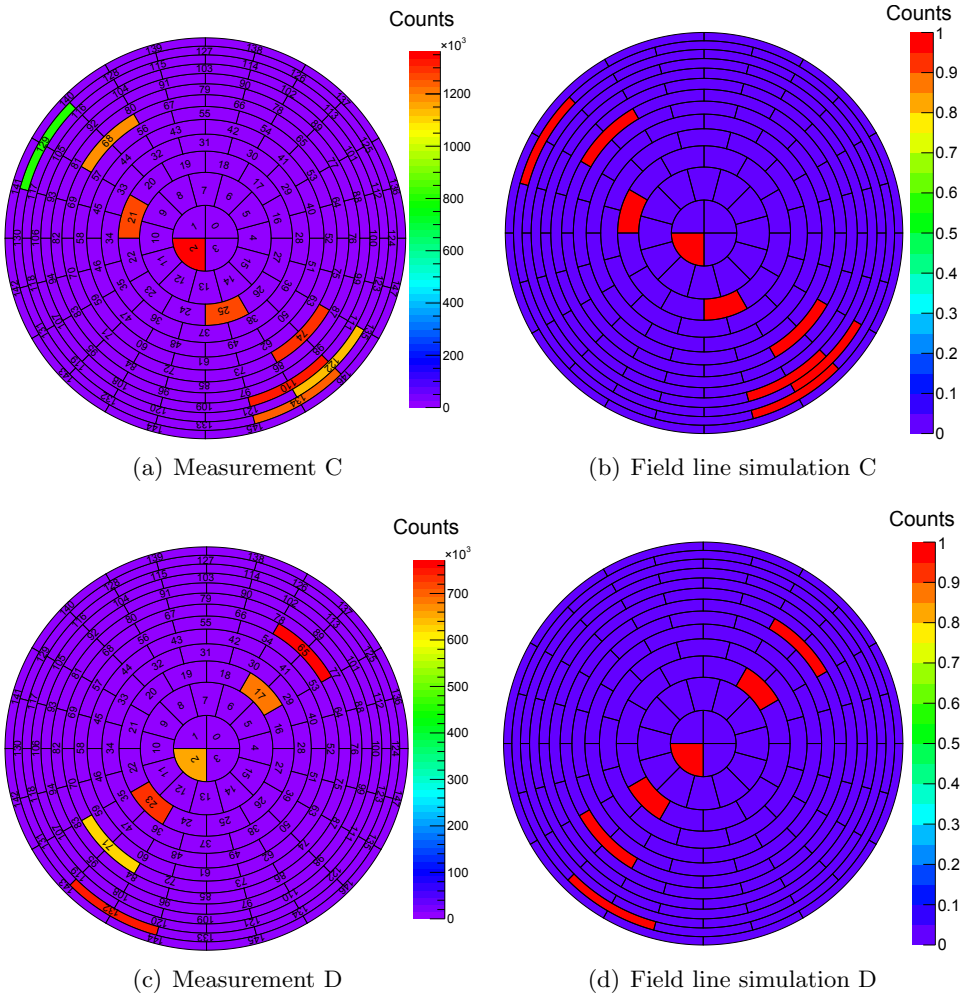

(a) Measurement C

(b) Field line simulation C

(c) Measurement D

(d) Field line simulation D

Figure 5.29: Comparison of the measured and simulated pixel distributions for the manipulator angles of the setting C and D. Two diagonal scans of the main spectrometer were performed, orthogonal to each other. The measured electron tracks can be reproduced by the simulation, as the identical pixels were hit for the manipulator angles selected.

actual values on the inner electrodes differ and the two measurements have to be analyzed independently. The actual values for the two measurements with the settings called C and D are stated in appendix A. The two different diagonal scans of the main spectrometer, are visualized by the detector hit pattern in figure 5.29. Again, the simulation of the field lines shows a good agreement with the measurement, as an identical pixel pattern is observed for both settings. Therefore, the same error estimation for the analyzing point position is assumed as in the high voltage measurement, namely $\sigma_x = 0.220\,\mathrm{m}$ and $\sigma_y = 0.191\,\mathrm{m}$.

The light source used for the electron gun at the radial potential measurements without high voltage was a LED at 290 nm, pulsed with a frequency of 100 kHz at a pulse length of 100 ns. The energy distribution was obtained in an independent measurement between the radial potential measurements of the setting C and D. As the measurements were performed without high voltage, the angular distribution of the electrons is assumed to be fixed at $\theta = 0\,^\circ$ and therefore neglected in the analysis. When turning the electron gun manipulator, the plate angles of the electron gun were not adjusted to the "neutral" position for each manipulator position. Therefore, a maximal deviation of the plate angles of $\theta_{\mathrm{plates}} = 5\,^\circ$ is estimated, resulting in an error on the obtained radial potential offset of 2 mV (see section 5.4.3). Including the error from the digital volt meter of 5 mV, the total systematic uncertainty for the radial potential offset is therefore $\sigma_{\Delta U_\mathrm{r}} = 7.0\,\mathrm{mV}$.

Table 5.3: Overview of the transmission function measurements for all 9 manipulator angles at setting C with the determined analyzing point positions and radial potential offsets.

run id	α_h in °	α_v in °	pixel	x_A in m	y_A in m	z_A in m	ΔU_r in V
6225	-14.40	-14.00	134	2.668	-2.839	-0.999	8.160
6227	-13.54	-13.16	122	2.513	-2.673	-0.999	8.242
6229	-12.67	-13.16	110	2.354	-2.506	-0.946	8.295
6231	-10.36	-10.08	74	1.921	-2.061	0.764	8.437
6233	-5.47	-5.32	25	0.965	-1.104	0.630	8.681
6235	0.00	0.00	2	-0.137	-0.027	0.711	8.932
6237	5.47	5.32	21	-1.237	1.048	0.859	9.044
6239	10.37	10.08	68	-2.191	2.001	0.941	9.121
6241	14.40	14.00	129	-2.931	2.774	0.907	8.366

Table 5.4: Overview of the transmission function measurements for all 6 manipulator angles at setting D with the determined analyzing point positions and radial potential offsets.

run id	α_h in °	α_v in °	pixel	x_A in m	y_A in m	z_A in m	ΔU_r in V
6361	-12.25	12.00	65	2.277	2.392	0.888	8.178
6363	-7.55	7.50	17	1.377	1.490	0.683	8.515
6365	0.00	0.00	2	-0.137	-0.027	0.715	8.857
6367	3.75	-3.75	23	-0.894	-0.785	0.827	8.910
6369	8.50	-8.50	71	-1.830	-1.739	1.128	8.944
6371	12.85	-12.55	132	-2.649	-2.542	0.960	8.914

Results

The results of the fitted radial potential offsets and the simulated positions of the analyzing points are summarized in tables 5.3 and 5.4 for the measurements at setting C and D, respectively. The resulting radial potential offset is much larger than for the measurements with high voltage on the vessel, due to much larger voltage difference between the inner wires and the spectrometer vessel of $\Delta U = 1000\,\mathrm{V}$.

In figure 5.30 and figure 5.31 the shape of the radial potential inhomogeneity is plotted relative to the x-component of the analyzing point position. Again, the simulated potential values were shifted for the same reasons as before. For setting C an absolute potential offset of $\Delta U_{\mathrm{offset}} = -0.396\,\mathrm{V}$ was obtained and for setting D the fit revealed $\Delta U_{\mathrm{offset}} = -0.394\,\mathrm{V}$. This is an excellent agreement, due to the fact that the value is expected to stay constant over the two measurements for identical electron gun properties. As the electron gun properties are in fact not truly identical to the high voltage measurements, the difference of about 60 mV in the potential offsets obtained in the last section can be explained.

The difference between the measured and simulated radial potential offsets is illustrated in figure 5.32, which is in the range of 50 mV for most of the points. This is not as good as in the measurements with high voltage, but the precisions achieved for this special setting with a rather large dipole being present of more than 1 V and in view of the large difference between vessel and inner wire layer of 1000 V, is only slightly larger than the required range of 30 mV. For measurements with an improved alignment and without dipole field, a much better precision is expected.

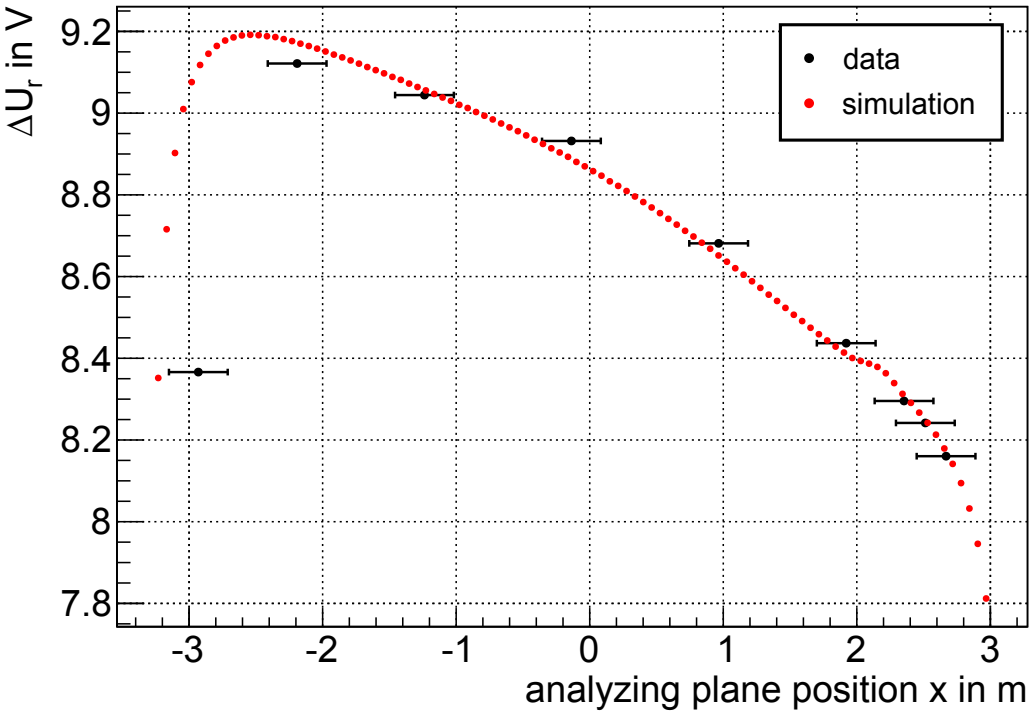

Figure 5.30: Comparison of measured and simulated radial potential offsets for setting C. For the simulated values an absolute offset $\Delta U_{\text{offset}} = -0.396\,\text{V}$ is added. The measured data show good agreement with the simulated potentials, with the only exception being the position of the point at $x = -3\,\text{m}$.

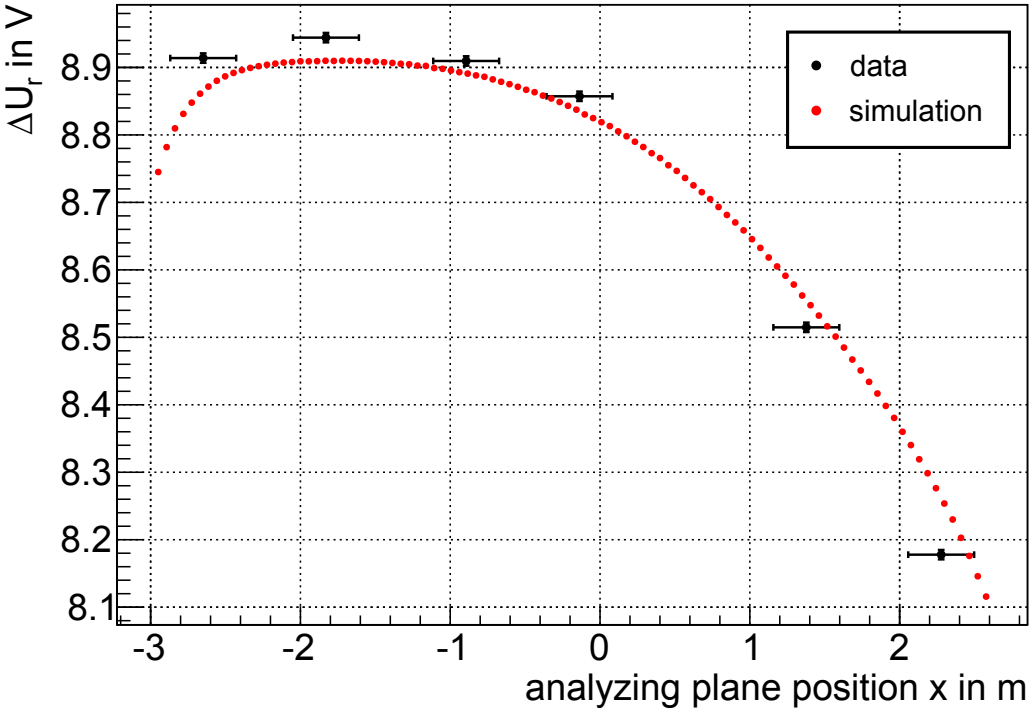

Figure 5.31: Comparison of measured and simulated radial potential offset for setting D. For the simulated values an absolute offset $\Delta U_{\text{offset}} = -0.394\,\text{V}$ is added. The measured data show again good agreement with the simulated potentials.

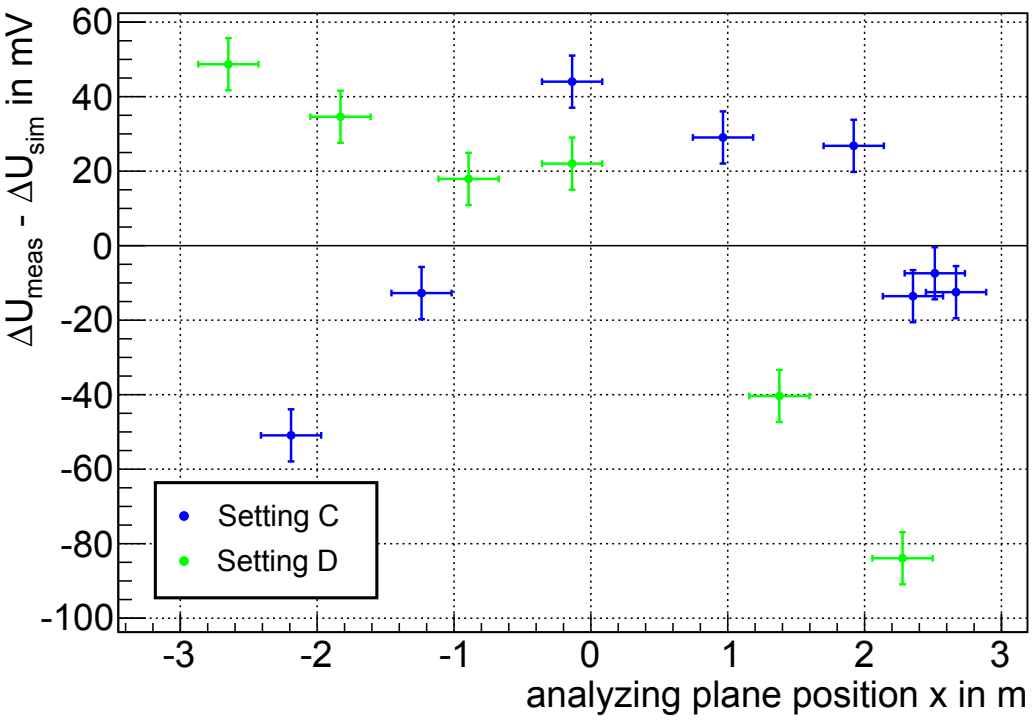

Figure 5.32: Differences between measured and simulated potentials for setting C (blue) and D (green). For most of the points these are within the range of 50 mV.

5.5 Influence on the neutrino mass sensitivity

The true absolute potential value in the analyzing plane and its radial slope can only be measured with limited precision. To investigate the systematic error associated with an imprecise knowledge of the analyzing plane potential or magnetic field, sensitivity estimations with respect to the measured neutrino mass were performed, using the KaFit module and the method of ensemble tests (see section 3.4).

5.5.1 Requirement

As the total systematic error budget of KATRIN on the squared neutrino mass m_ν^2 is limited to a value of $\sigma_{\text{sys}} = 17 \cdot 10^{-3}\,\text{eV}^2$, the maximal allowed systematic error of the analyzing plane potential or magnetic field can be deduced. With the requirement that the systematic error caused by the analyzing plane potential or magnetic field should not increase the total systematic error more than a fraction of 1 %, the maximal allowed value is $|\Delta m_\nu^2| = 2.4 \cdot 10^{-3}\,\text{eV}^2$, in case of quadratic error summation.

5.5.2 Settings

For the following studies the electromagnetic settings of the SDS commissioning measurements were used, that is a 3.8 G magnetic field layout together with an axially symmetric electric configuration with $U_{\text{vessel}} = -18.5\,\text{kV}$ and $U_{\text{IE}} = -18.6\,\text{kV}$. The plots for the corresponding radial inhomogeneity are displayed in figure 4.17 in section 4.3. The sensitivity calculations were performed with a radial detector segmentation of 13 rings, to investigate the influence of the radial potential and magnetic field inhomogeneity. The potential and magnetic field values used for each pixel ring together with their offsets are listed in table 5.5. Here, the radial offset for the potential is defined relative to the potential of the inner electrodes as $\Delta U_{\text{r}} = U_{\text{A}} - U_{\text{IE}}$ (i.e. as before), and the radial offset for the magnetic field is defined relative to its value in the middle of the spectrometer as $\Delta B_{\text{r}} = B_{\text{A}} - B(r = 0)$.

Table 5.5: Radial potential and magnetic field offsets for each detector ring as used in the sensitivity calculations. The offset of the potential is relative to the inner electrode potential of $U_{\mathrm{IE}} = -18600.0\,\mathrm{V}$, and the offset of the magnetic field is relative to the value at $r = 0$ of $B_{\mathrm{A}} = 3.625 \cdot 10^{-4}\,\mathrm{T}$. The mean value of the potential offset is 233 mV with $\sigma = 125\,\mathrm{mV}$ and the mean value of the magnetic field offset is $-28.7 \cdot 10^{-4}\,\mathrm{mT}$ with $\sigma = 11 \cdot 10^{-4}\,\mathrm{mT}$.

detector ring	U_{A} in V	ΔU_{r} in mV	B_{A} in $10^{-4}\,\mathrm{T}$	ΔB_{r} in $10^{-4}\,\mathrm{mT}$
0	-18599.536	464	3.625	0
1	-18599.570	430	3.617	-8
2	-18599.616	384	3.607	-18
3	-18599.658	342	3.599	-26
4	-18599.697	303	3.593	-32
5	-18599.734	266	3.589	-36
6	-18599.769	231	3.586	-39
7	-18599.802	198	3.585	-40
8	-18599.833	167	3.586	-39
9	-18599.862	138	3.588	-37
10	-18599.890	110	3.592	-33
11	-18599.915	85	3.598	-27
12	-18599.939	61	3.606	-19

Table 5.6: Reference simulation parameters for the sensitivity estimation of the radial offsets. All values are default settings as stated in [KAT05], only the analyzing plane field settings are different, as the potential and the magnetic field incorporate a radial dependency according to table 5.5.

parameter	setting
column density	$\rho d = 5 \cdot 10^{17}\,\mathrm{cm}^{-2}$
magnetic flux	$191\,\mathrm{Tcm}^2$
inelastic scattering cross section	$\sigma_{\mathrm{inelast}} = 3.456 \cdot 10^{-18}\,\mathrm{cm}^2$
magnetic fields	$B_{\mathrm{S}} = 3.6\,\mathrm{T}$
	$B_{\mathrm{max}} = 6.0\,\mathrm{T}$
	$B_{\mathrm{A}} \approx 3.6 \cdot 10^{-4}\,\mathrm{T}$
tritium purity	$\epsilon_{\mathrm{T}} = 0.95$
background rate	$\dot{N}_{\mathrm{b}} = 0.01\,\mathrm{cps}$
detector efficiency	$\epsilon_{\mathrm{det}} = 0.9$
measurement time distribution	$t = 3\,\mathrm{years}$, default
tritium endpoint	$E_0 = 18575\,\mathrm{eV}$
detector segmentation	12 rings + bullseye
total systematical error	$\sigma_{\mathrm{sys}} = 0.017\,\mathrm{eV}^2$

Table 5.7: Influence of the analyzing plane potential on the neutrino mass sensitivity for a reference ensemble test without radials offsets, and an ensemble test with radial offsets as listed in table 5.5. In addition, an ensemble test was performed where the radial potential offsets are used in the simulation, but are ignored in the analysis, which results in systematic shifts on the squared neutrino mass m_ν^2 and the endpoint E_0. The errors for the obtained values are 10^{-4} for $\sigma_{\mathrm{stat}}^{m_\nu^2}$ and Δm_ν^2 and $2 \cdot 10^{-4}$ for ΔE_0.

potential in simulation	potential in analysis	$\sigma_{\mathrm{stat}}^{m_\nu^2} \cdot 10^{-3}$ in eV^2	$\Delta m_\nu^2 \cdot 10^{-3}$ in eV^2	ΔE_0 in mV	sensitivity on m_ν in meV (90 % C.L.)
constant	constant	16.6	<0.1	< 0.02	197.7
radial	radial	16.7	<0.1	< 0.02	198.0
radial	constant	16.6	-3.6	228	198.8

The experimental parameters for the ensemble tests correspond to the default settings in [KAT05] and are summarized in table 5.6. The effects of the potential and the magnetic field were examined separately. For both the effect of an error on the absolute value and also the error on the radial inhomogeneity were investigated. For the electrostatic potential an error on the absolute value does not lead to a systematic shift on the measured neutrino mass, but the shape of the radial inhomogeneity is important, as it will be detailed in section 5.5.3. For the magnetic field the absolute value in the analyzing plane needs to be known rather precisely, this will be outlined in section 5.5.4.

5.5.3 Influence of the analyzing plane electrostatic potential

To investigate the influence of the absolute value of the analyzing plane potential and its radial inhomogeneity on the neutrino mass sensitivity of the experiment a variety of ensemble tests with 10^4 samples each were performed. When using different experimental parameters in the analysis than in the simulation, systematic errors on the experimental observables like the squared neutrino mass will be introduced on purpose. Thereby, the effect of unaccounted changes of experimental parameters can be investigated. For a given maximal allowed systematic error, a requirement on the precision of the experimental parameter can then be stated.

First, an ensemble test was performed for the reference configuration without radial potential offsets, as well as a comparable test, where the radial potential offsets of table 5.5 were used for both simulation and analysis. The resulting statistical sensitivities on the neutrino mass and the resulting systematics, the shifts on the squared neutrino mass m_ν^2 and the endpoint E_0 are listed in table 5.7. For the two cases, the obtained shifts are smaller than the errors caused by the limited sample size. When the radial potential offset is considered, the neutrino mass sensitivity degrades marginally. Subsequently, a third ensemble test was performed where the radial potential offsets in the analysis were ignored on purpose, although being considered in the corresponding simulation. This results in a shift of the squared neutrino mass of $\Delta m_\nu^2 = -3.6 \cdot 10^{-3}\,\mathrm{eV}^2$, and of the endpoint of $\Delta E_0 = 228\,\mathrm{mV}$.

The shift of the squared neutrino mass is rather small compared with the shift of the endpoint. Nevertheless, it is slightly larger than the required maximal systematic error of $|\Delta m_\nu^2| = 2.4 \cdot 10^{-3}\,\mathrm{eV}^2$, and thus the radial potential offset can not be ignored in the final neutrino mass analysis. The shift of the endpoint is caused by the unaccounted mean value of the absolute potential of 233 mV. The shift of the squared neutrino mass is caused by the unaccounted radial inhomogeneity, as will be shown in the following.

Table 5.8: Influence of a global unaccounted potential offset in the analyzing plane on the neutrino mass sensitivity. A global potential offset does not lead to any systematic effect on the neutrino mass, only in the determination of the endpoint E_0. For large offsets the sensitivity gets worse, as the measurement time distribution is not optimized any more. The errors for the obtained values are 10^{-4} for $\sigma^{m_\nu^2}_{\text{stat}}$ and Δm_ν^2 and $2 \cdot 10^{-4}$ for ΔE_0.

unaccounted ΔU in mV	$\sigma^{m_\nu^2}_{\text{stat}} \cdot 10^{-3}$ in eV^2	$\Delta m_\nu^2 \cdot 10^{-3}$ in eV^2	ΔE_0 in mV	sensitivity on m_ν in meV (90 % C.L.)
-1000	18.8	<0.1	-1000	204.2
-500	16.9	<0.1	-500	198.6
-100	16.6	<0.1	-100	197.7
100	16.7	<0.1	100	198.0
500	17.3	<0.1	500	199.7
1000	18.6	<0.1	1000	203.6

Influence of the absolute value

To thoroughly test the effect of an unaccounted offset value on the absolute potential, multiple ensemble tests were performed. In all cases the same shape of the radial potential inhomogeneity was used for simulation and analysis, however, in the simulation an additional global offset of ΔU was added. The values of ΔU used and the results obtained are listed in table 5.8. Even in case of large unaccounted potentials no systematic shifts of the squared neutrino mass will follow. The offset on the absolute voltage is absorbed by the obtained endpoint parameter E_0, which is shifted accordingly.

However, the sensitivity on the neutrino mass worsens significantly in case of large shifts of the absolute potential in the analyzing plane. This is due to the adopted fixed measuring time distribution. As the influence of the neutrino mass is more prominent close to the endpoint of the spectrum, a shift of the absolute potential in the analyzing plane effectively leads to a shift of the measuring time distribution so that the largest measuring time is not spent at the optimal position of the spectrum anymore. This effect can be compensated by adapting the measuring time distribution according to the mean value of the absolute potential in the analyzing plane.

Influence of the radial inhomogeneity

As a global shift of the radial potential offset does not lead to systematic errors in the neutrino mass, but only to a shift of the endpoint E_0, the effect of a different radial potential inhomogeneity needs to be investigated. Therefore, ensemble tests were performed where the potential offset for all detector rings was randomly drawn from a Gaussian distribution with mean $\mu = 0\,\text{V}$, but different values of its standard deviation σ_U. In the analysis all detector rings were set to 0 V, in order to investigate the influence of this unaccounted relative offset.

For each value of σ_U, a total of 10 different radial potential shapes was computed and for each one an ensemble test with 10^4 toy measurements were performed. The resulting mean value of the systematic error on the squared neutrino mass is listed in table 5.9 together with the values for σ_U. The results are also visualized in figure 5.33. For values of σ_U below 50 mV the resulting systematic error on the squared neutrino mass stays below the required limit of $|\Delta m_\nu^2| < 2.4 \cdot 10^{-3}\,\text{eV}^2$.

Therefore, the radial potential offsets need to be known with a precision better than 50 mV, which has been achieved in the course of the high voltage measurements detailed in section 5.4.5. An error on the absolute potential however, does not lead to a systematic error on

Table 5.9: Systematic shifts on the squared neutrino mass due to an unaccounted radial potential inhomogeneity for different values of σ_U. The statistical sensitivity is $1.64 \cdot 10^{-3}\,\mathrm{eV}^2$ for all values. The errors of $\sigma^{m^2_\nu}_{\mathrm{stat}}$ and Δm^2_ν are 10^{-4}.

unaccounted σ_U in mV	$\Delta m^2_\nu \cdot 10^{-3}$ in eV^2	sensitivity on m_ν in meV (90 % C.L.)
10	-0.3	197.1
20	-0.6	197.2
30	-1.0	197.2
50	-2.1	197.5
70	-3.9	198.5
100	-7.9	202.4

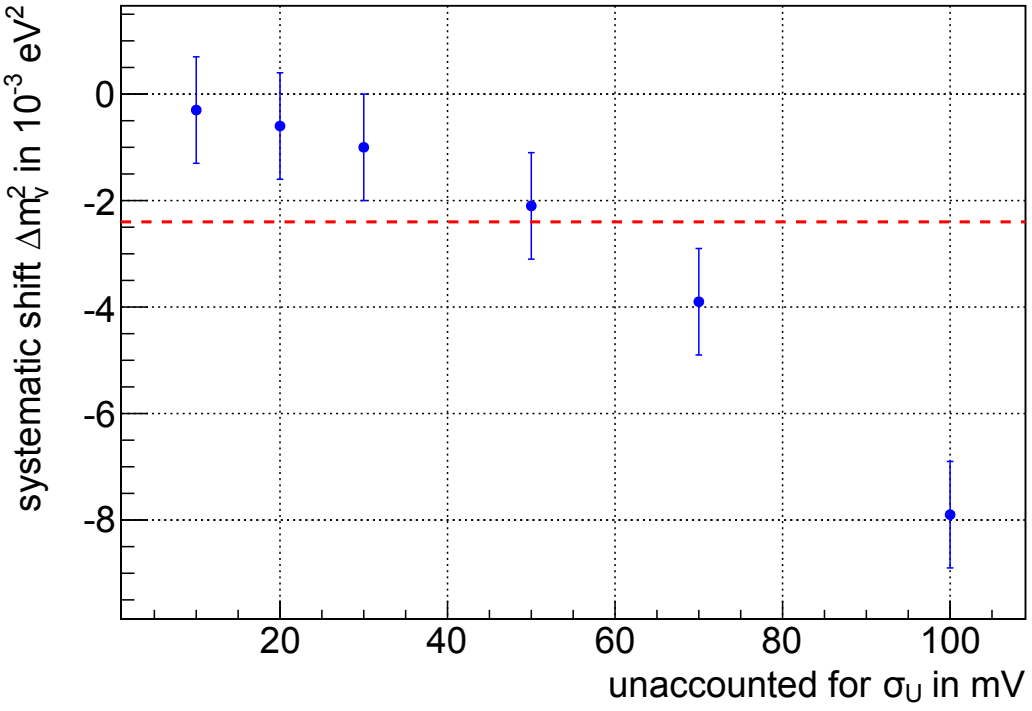

Figure 5.33: Systematic shifts on the squared neutrino mass due to an unaccounted radial potential inhomogeneity for different errors of σ_U. The dotted red line marks the required maximal allowed shift of $-2.4 \cdot 10^{-3}\,\mathrm{eV}^2$. The shown error bars are increased by a factor of 10 for better visibility.

Table 5.10: Influence of the analyzing plane magnetic field on the neutrino mass sensitivity for a reference ensemble test without any radial offsets, an ensemble test with radial offsets as stated in table 5.5 and two ensemble tests where the radial magnetic field offsets were used in the simulation, but ignored in the analysis where a constant magnetic field of different values was assumed. The errors for the obtained values are 10^{-4} for $\sigma^{m_\nu^2}_{\text{stat}}$ and Δm_ν^2 and $2 \cdot 10^{-4}$ for ΔE_0.

magnetic field in simulation	magnetic field in analysis	$\sigma^{m_\nu^2}_{\text{stat}} \cdot 10^{-3}$ in eV^2	$\Delta m_\nu^2 \cdot 10^{-3}$ in eV^2	ΔE_0 in mV	sensitivity on m_ν in meV (90 % C.L.)
constant	constant	16.6	<0.1	< 0.02	197.7
radial	radial	16.5	<0.1	< 0.02	197.4
radial	constant center	16.4	3.3	4.8	198.1
radial	constant mean	16.5	-0.2	-0.03	197.4

the neutrino mass, but the statistical sensitivity worsens significantly, if the measuring time distribution is not adapted accordingly.

It is important to state that the effect of a radial potential offset is not the same as in case of a high voltage fluctuation, although both effects seem to be similar at first glance. A high voltage fluctuation of σ_U leads to a systematic error on the squared neutrino mass of $\Delta m_\nu^2 = -2\sigma_U^2$, according to [OW08]. However, in contrast to high voltage fluctuations, a given radial potential inhomogeneity stays the same over the entire measurement period and thus is independent of the applied retarding potential. Therefore, the required precision on the radial potential offset is less stringent than on high voltage fluctuations, where a fluctuation with $\sigma_{\text{hv}} = 60\,\text{mV}$ already results in a systematic error on the squared neutrino mass of $\Delta m_\nu^2 = 7.2 \cdot 10^{-3}\,\text{eV}^2$ [KAT05].

5.5.4 Influence of the analyzing plane magnetic field

Although the analyzing plane magnetic field could not be determined during the SDS commissioning measurements, its required precision for the later neutrino mass analysis can be obtained analogously as performed for the potential. Its effect is rather interesting, as it is different to the requirements of the precision of the radial potential offsets.

As before, multiple ensemble tests were performed: A reference setting without radial magnetic field offsets in both simulation and analysis, and a setting where the radial offsets as listed in table 5.5 were used. Furthermore, ensemble tests for two additional settings were performed, in which the radial magnetic field offset of the simulations was ignored in the analysis. In the first setting, a constant magnetic field was used in the analysis, with a value as the center pixel of $B = 3.625 \cdot 10^{-4}\,\text{T}$ (setting constant center). In the second setting, a mean value of the radial offsets of $B = -0.029 \cdot 10^{-4}\,\text{T}$ was considered, resulting in an constant magnetic field used in the analysis of $B = 3.596 \cdot 10^{-4}\,\text{T}$ (setting constant mean).

The obtained systematic errors and the sensitivity on the neutrino mass for all 4 settings are listed in table 5.10.

When including the radial magnetic field offsets, the sensitivity on the neutrino mass improves marginally, which is caused by the slightly lower mean value of the magnetic field in the analyzing plane and the resulting improved energy resolution. When ignoring the radial magnetic field inhomogeneity, the resulting systematic error on the neutrino mass strongly depends on the constant value of the magnetic field that is used in the analysis. For the analysis using the magnetic field value at the center, a systematic error on the squared neutrino mass of $3.3 \cdot 10^{-3}\,\text{eV}^2$ results, which is more than the required

Table 5.11: Influence of a global unaccounted magnetic field offset in the analyzing plane on the neutrino mass sensitivity. A negative offset of the magnetic field leads to a positive shift on the squared neutrino mass and vice versa. The errors for the obtained values are 10^{-4} for $\sigma^{m_\nu^2}_{\text{stat}}$ and Δm_ν^2 and $2 \cdot 10^{-4}$ for ΔE_0.

unaccounted ΔB in 10^{-4} T	$\sigma^{m_\nu^2}_{\text{stat}} \cdot 10^{-3}$ in eV^2	$\Delta m_\nu^2 \cdot 10^{-3}$ in eV^2	ΔE_0 in mV	sensitivity on m_ν in meV (90 % C.L.)
-0.100	16.6	11.8	16.7	208.9
-0.050	16.4	6.0	8.4	200.2
-0.020	16.7	2.3	3.3	198.5
-0.010	16.5	0.9	1.6	197.5
0.010	16.6	-1.6	-1.7	197.9
0.020	16.5	-2.7	-3.4	198.0
0.050	16.3	-6.2	-8.4	200.2
0.100	16.4	-12.1	-16.7	208.9

maximum of $2.4 \cdot 10^{-3}\,\text{eV}^2$. However, when using the mean value of the magnetic field for all detector rings in the analysis, the resulting systematic error on the squared neutrino mass is negligible.

For the magnetic field, the mean value is thus much more important in contrast to the potential. The radial inhomogeneity however does not seem to play an important role in the neutrino mass analysis. In the following sections, the influence of the absolute value and the radial inhomogeneity will be investigated separately.

Influence of the absolute value

To test the effect of an unaccounted shift of the absolute value of the magnetic field, multiple ensemble tests were performed, where the identical shapes of the radial magnetic field inhomogeneity were used both for simulation and analysis, however the simulation incorporated an additional global offset of ΔB. The values of ΔB used and the results obtained are listed in table 5.11 and visualized in figure 5.34.

An unaccounted shift of the mean value of the magnetic field can not be compensated by a shift of the resulting endpoint as in the case for the electrostatic potential. For the absolute field value, even small shifts will lead to relative large systematic errors on the squared neutrino mass. The induced systematic errors are symmetric, with a negative shift of the absolute value leading to a positive shift of the squared neutrino mass and vice versa. To meet the requirement on the systematic error of $|\Delta m_\nu^2| < 2.4 \cdot 10^{-3}\,\text{eV}^2$, the absolute value of the magnetic field in the analyzing plane has to be known within a range of $[-2.2\,\mu\text{T}, 1.8\,\mu\text{T}]$, which is about 0.55 % of the nominal magnetic field of $3.6 \cdot 10^{-4}$ T.

In addition, the impact of different absolute magnetic field values in the analyzing plane was investigated under the assumption that their true values are known precisely. Hence, ensemble tests were performed for the three main magnetic field settings in use during the SDS commissioning measurement. The results are aggregated in table 5.12. If the magnetic field in the analyzing plane is increased, the energy resolution of the MAC-E filter will broaden in a likewise manner, which in turn leads to a reduced statistical sensitivity on the squared neutrino mass.

Influence of the radial inhomogeneity

As shown above, the absolute mean value of the analyzing plane magnetic field has to be known better than $2\,\mu$T. In the following the influence of the radial inhomogeneity will

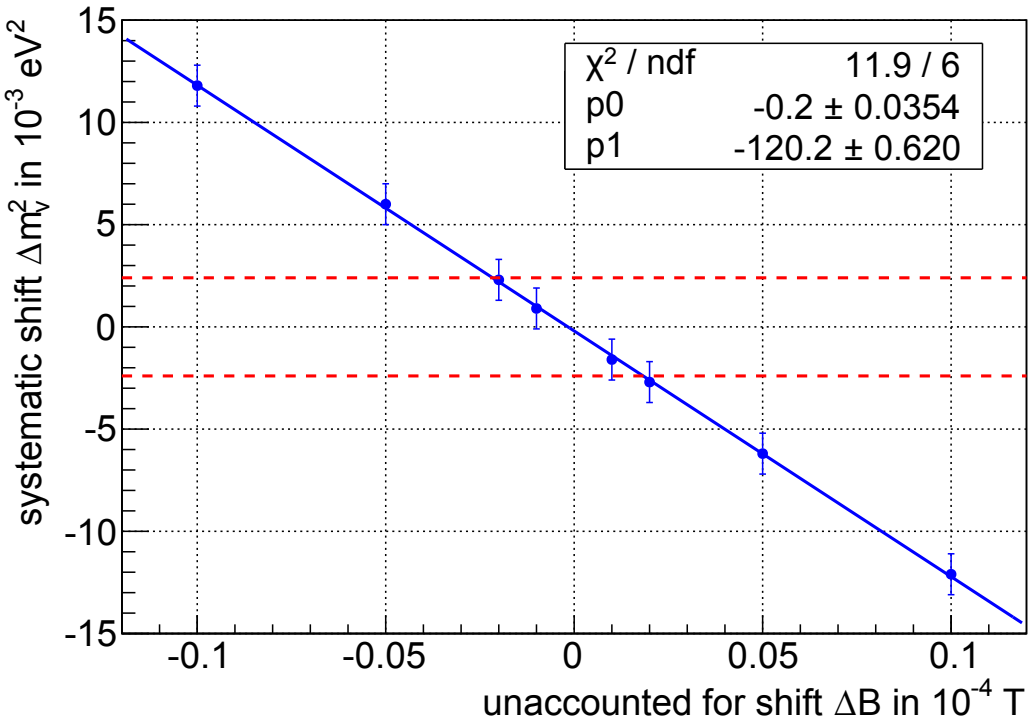

Figure 5.34: Systematic shifts on the squared neutrino mass due to unaccounted for absolute magnetic field shifts of ΔB. The dotted red lines marks the maximal allowed shift of $|\Delta m^2_\nu| = 2.4 \cdot 10^{-3}\,\mathrm{eV}^2$. The fitted linear function reveals the allowed deviation range of $[-2.2\,\mu\mathrm{T}, 1.8\,\mu\mathrm{T}]$. The shown error bars are increased by a factor of 10 for better visibility.

Table 5.12: Influence of the overall magnetic field strength in the analyzing plane on the neutrino mass sensitivity for the three magnetic field settings used in the SDS commissioning measurements. For settings with a higher magnetic field, the energy resolution broadens and the sensitivity on m^2_ν is slightly reduced.

magnetic field at AP in 10^{-4} T	energy resolution ΔE in eV	$\sigma^{m^2_\nu}_{\mathrm{stat}} \cdot 10^{-3}$ in eV^2	sensitivity on m_ν in meV (90 % C.L.)
3.6	1.16	16.6	197.6
4.8	1.49	17.0	198.9
8.8	2.73	21.8	213.3

Table 5.13: Systematic shifts on the squared neutrino mass due to an unaccounted radial magnetic field inhomogeneity for different values of σ_B. The statistical sensitivity is $1.65 \cdot 10^{-3}\,\mathrm{eV}^2$ for all cases. The errors of $\sigma^{m_\nu^2}_{\mathrm{stat}}$ and Δm_ν^2 are 10^{-4}.

unaccounted σ_B in $10^{-4}\,\mathrm{T}$	$\Delta m_\nu^2 \cdot 10^{-3}$ in eV^2	sensitivity on m_ν in meV (90 % C.L.)
0.05	-0.2	197.4
0.1	-0.7	197.5
0.2	-2.4	197.9
0.3	-5.4	199.9

be investigated. For a given radial shape, variations of the magnetic field for individual detector rings are possible without changing the mean value, as deviations from individual rings chancel each other.

To investigate this effect, ensemble tests were performed again with the following settings: In the simulations the magnetic field offset for each detector ring was drawn from a Gaussian distribution with a mean of $\mu = 0\,\mathrm{T}$ and different values of its standard deviation σ_B. For the analysis, a constant magnetic field offset for all rings was used with the mean value of the distribution from the simulation. By doing so, the effect of an incorrect assumption on the mean value is excluded and the effect of the different radial shape can be investigated. For each value of σ_B used, a total of 10 different radial magnetic field shapes were computed and for each one an ensemble test with 10^5 toy measurements was performed. The resulting mean value of the systematic error on the squared neutrino mass is given in table 5.13 together with the values used for σ_B.

Due to the cancellation of the contribution on the shift of the squared neutrino mass of detector rings with positive and with negative magnetic field offsets, the resulting systematic error is rather small, but not zero. As in case of the uncertainty on the electrostatic potential inhomogeneity or HV fluctuation, the resulting systematic error is a negative squared neutrino mass.

A variation of about $20\,\mu\mathrm{T}$ is within the specific requirements, which is 10 times larger than for an unaccounted mean value. Nevertheless, as the requirement on the mean value is much stricter, the magnetic field offset for the individual pixel rings still needs to be known with a precision of about $2\,\mu\mathrm{T}$, otherwise the mean value can not be determined with a high enough accuracy.

5.6 Conclusion

In this chapter, a method to determine the transmission properties of the main spectrometer was presented. Also the radial inhomogeneity of the potential was investigated for different spectrometer settings and compared to potential simulations. As a major outcome of these studies it can be stated that the achieved precision on this important experimental parameter is within the calculated requirements.

In doing so, a theoretical analytical model to describe the transmission function was derived and the influence of different source and spectrometer properties on the shape and position of the transmission function was discussed and visualized for realistic examples. It could be demonstrated that a determination of the spectrometer properties requires the properties of the source, in particular its energy and angular distribution, to be known, as spectrometer and source properties showing an intrinsic correlation. A method was presented which allows to extract the important source properties from transmission function

measurements. The functionality of this novel ansatz could be demonstrated with data from transmission function measurements taken during the SDS commissioning.

To verify the derived analytical model, Monte Carlo-based particle tracking simulations were performed with KASSIOPEIA. When comparing the resulting transmission function with measured data and the analytical model, an excellent agreement is observed.

As a key achievement of this chapter, the radial inhomogeneity of the analyzing potential was investigated, based on an analytical transmission model which allows to determine the potential at the analyzing point for a given electron gun manipulator position. To determine the position of analyzing points, the effect of non-optimized transmission conditions was considered. The resulting radial potential inhomogeneity for two different electrostatic configurations with elevated vessel showed a non-symmetric behavior with an east-west asymmetry. This was caused by a hardware-based asymmetric potential configuration on the inner electrodes of the main spectrometer. This shows the power of transmission studies which have revealed the subtle, yet important electric dipole field between the east and the west part of the inner electrodes.

Follow-on simulations of the potential were performed with a realistic 3D model of the main spectrometer. The calculated potential configuration was compared with the measured data. With the exception of a constant offset, which originates from the uncertainty of the energy scale of the produced electrons and the work function of the main spectrometer vessel, the measured radial potential inhomogeneity matches the simulated one within 30 mV, which is of major importance.

The same analysis was performed also for measurements with a different electrostatic potential setting based on a grounded vessel and potential of -1 kV on the inner electrodes. In this non-standard configuration an even larger electrostatic dipole was observed than before, with the measured radial potential inhomogeneity matching the corresponding simulation within about 50 mV.

Finally, a series of ensemble tests were carried out to investigate the sensitivity and resulting systematic error on the neutrino mass measurement with KATRIN for different spectrometer properties such as the radial inhomogeneities of the potential and magnetic field. From the results obtained, specific requirements for the true values and their precision can be stated. For the electrostatic potential, the values for each pixel ring need to be known with a precision better than 50 mV, while a global offset does not lead to systematic errors on the neutrino mass, as long as the measurement time distribution is adapted accordingly. For the magnetic field, the radial inhomogeneity is less important, but its true mean value needs to be measured better than 2 μT.

The analysis methods and theoretical models which were developed in the framework of this thesis, and the corresponding software are indispensable tools to determine the properties of the main spectrometer. Both models and analysis methods will be applied to the measurements carried out in the current SDS commissioning phase and finally also in the neutrino mass analysis. Owing to significant improvements in the electron gun hardware targeted to provide a working angular selectivity and an overall optimized alignment of all sub-components the achieved precision of these future measurement is expected to improve. This is complemented by recent progress in precision measurements of the magnetic field in the analyzing plane.

6. Precise modeling of the response function via global Monte Carlo simulations

To successfully determine neutrino masses with a sensitivity of 200 meV at 90% C.L. a precise knowledge of the transmission function of the main spectrometer is mandatory. However, more importantly, the complete response function of the experiment, which is an extension of the transmission function and includes energy loss processes in the gaseous source and in the transport section, is required to be known with very high precision. This response function can not be measured directly, as it strongly depends on the source properties, just as the transmission function. For the neutrino mass analysis the response function is required to be known for an isotropic source emitting electrons with a fixed initial energy and an initial position distribution according to the WGTS gas density.

Therefore, the response function has to be calculated analytically or to be obtained by performing large-scale Monte Carlo simulations of particles propagating through the whole experimental setup using Kassiopeia. The results of these Monte Carlo simulations will be presented in this chapter and it will be shown that a simple analytical model of the response function is insufficient to be used in the neutrino mass analysis, as it is only valid in a first order approximation. A total of seven necessary individual modifications were identified and their influences on the neutrino mass sensitivity were quantified. Subsequently, the analytical model was refined to include the required modifications based on the findings of the Monte Carlo simulation.

First, the analytical calculation of the response function, as described in the KATRIN design report [KAT05] will be detailed in section 6.1. The necessary ingredients contain the analytical formula for the transmission function of an isotropic source, the energy loss function and the scattering probabilities. Afterwards the motivation to use a particle tracking Monte Carlo simulation will be discussed in section 6.2. Although an analytical calculation is much faster and easier to handle than large-scale Monte Carlo simulations of electrons propagating through the whole KATRIN experiment, the merits of the latter approach will be underlined. The implementation within Kassiopeia and the setup of the Monte Carlo simulation will then be described in section 6.3, together with the validation of the crucial physics modules used in the simulation, such as the validity of adiabatic particle tracking over the experimental setup. This is of crucial importance, as it decreases the required computation time by many orders of magnitude. The calculation of synchrotron

energy losses will be validated as well, as this radiative process plays an important role for the exact shape of the response function. The results of the Monte Carlo simulation will be presented in section 6.4 and the obtained response function is compared to the analytical model. As the resulting deviations are unacceptable within the KATRIN error budget, the analytical model needs to be refined, which is presented in section 6.5. There, a total of seven individual modifications are identified and an extension of the analytical model is presented, which includes these required refinements. For each of the individual effects its influence on the neutrino mass sensitivity is calculated based on ensemble tests, and furthermore the required accuracy on experimental parameters, such as the source magnetic field or the inelastic cross section, are presented. Finally, the response function of the refined analytical model will be compared to the data of the Monte Carlo simulation, showing an excellent agreement within the statistical errors.

6.1 Analytical calculation of the response function

The MAC-E filter principle used at the KATRIN experiment results in a measured electron spectrum at the detector which is an integrated spectrum. From this a non-vanishing neutrino mass has to be extracted by analyzing the shape of the differential spectrum $\frac{\mathrm{d}N}{\mathrm{d}E}(E_0, m_\nu^2)$. For each retarding potential U of the main spectrometer, the measured integral rate can be expressed as

$$\dot{N}_\mathrm{S}(qU) = N_\mathrm{T}\,\epsilon_\mathrm{det}\,\frac{\Omega}{4\pi}\int_{qU}^{E_0}\frac{\mathrm{d}N}{\mathrm{d}E}(E_0, m_\nu^2)\cdot R(E, qU)\mathrm{d}E, \tag{6.1}$$

with the total number of tritium nuclei N_T in the source, the detector efficiency ϵ_det and the response function $R(E, qU)$. When the response function R is normalized to θ_max, which is a commonly used description, the solid angle $\Omega = 2\pi\cdot(1-\cos(\theta_\mathrm{max}))$ accounts for electrons being emitted with a polar angle larger than θ_max, that are not able to reach the detector due to magnetic reflection.

The response function $R(E, qU)$ denotes the probability of an electron, emitted in the source with starting energy E, to reach the detector. $R(E, qU)$ is an extension of the transmission function $T(E, qU)$, as it also includes scattering processes in the source. At each scattering process, the electron loses a specific amount of energy ϵ, which results in a required larger surplus energy $E - qU$ for the electron to be transmitted through the MAC-E filter and be counted at the detector.

In the following, the basic form of the response function and its composition will be presented, as described previously in [KAT05], [Hoe12] or [Kle14]. Additional modifications developed in the course of this thesis will be detailed in section 6.5.

The response function $R(E, qU)$ can be expressed as

$$\begin{aligned} R(E, qU) &= \int_{\epsilon=0}^{E-qU} T(E-\epsilon, qU)\cdot(\overline{P}_0\delta(\epsilon) + \overline{P}_1 f(\epsilon) + \overline{P}_2(f\otimes f)(\epsilon) + ...)\mathrm{d}\epsilon \\ &= \int_{\epsilon=0}^{E-qU}\sum_{i=0}^{N} T(E-\epsilon, qU)\cdot\overline{P}_i\cdot f_i(\epsilon)\,\mathrm{d}\epsilon, \end{aligned} \tag{6.2}$$

with the averaged scattering probabilities $\overline{P}_i$ for i-fold scattering up to N scatterings and the energy loss function $f_i(\epsilon)$. Electrons leaving the source without inelastic scattering

($i = 0$) do not lose energy so that $f_0(\epsilon) = \delta(\epsilon)$. For i-fold scattering, the energy loss function $f(\epsilon)$ needs to be convoluted i times.

For the gaseous source of KATRIN, the transmission function $T(E, qU)$ for an isotropic and mono-energetic source has to be known. For this special case an analytical formula can be derived, which will be presented in section 6.1.1. The energy loss function $f(\epsilon)$ will then be described in section 6.1.2 before the calculation of the scattering probabilities P is detailed in section 6.1.3.

6.1.1 Transmission function for an isotropic, mono-energetic source

The general description of the transmission function of section 5.1 can be used to derive an analytical formula of the transmission function for an isotropic and mono-energetic source.

The polar angular distribution of an isotropic source can be described as

$$\omega(\theta) = \sin(\theta), \tag{6.3}$$

which can be entered into equation 5.5 to obtain the transmission function as function of a fixed starting energy E_S, resulting in

$$\begin{aligned} T(E_\mathrm{S}) &= \int_0^{\theta_\mathrm{tr}(E_\mathrm{S})} \omega(\theta)\mathrm{d}\theta \\ &= 1 - \cos\left[\theta_\mathrm{tr}(E_\mathrm{S})\right]. \end{aligned} \tag{6.4}$$

Simplifying the expression of the transmission angle θ_tr from equation 5.4 with $U = U_\mathrm{A}$, as $U_\mathrm{S} = 0$ and the non relativistic approximation of $\gamma_\mathrm{S} = \gamma_\mathrm{A}$ leads to

$$\theta_\mathrm{tr}(E_\mathrm{S}) = \arcsin\left(\sqrt{\frac{E_\mathrm{S} - qU}{E_\mathrm{S}} \cdot \frac{B_\mathrm{S}}{B_\mathrm{A}}}\right), \tag{6.5}$$

which can be entered into equation 6.4 using the relation $\cos(\arcsin(\sqrt{x})) = \sqrt{1-x}$, resulting in

$$T(E_\mathrm{S}, qU) = 1 - \sqrt{1 - \frac{E_\mathrm{S} - qU}{E_\mathrm{S}} \cdot \frac{B_\mathrm{S}}{B_\mathrm{A}}}. \tag{6.6}$$

As the term in the square root can be negative or larger than one, both implying unphysical results, the following case differentiation is to be done

$$T(E_\mathrm{S}, qU) = \begin{cases} 0 & E_\mathrm{S} - qU < 0 \\ 1 - \sqrt{1 - \frac{E_\mathrm{S} - qU}{E_\mathrm{S}} \cdot \frac{B_\mathrm{S}}{B_\mathrm{A}}} & 0 \leq E_\mathrm{S} - qU \leq \frac{B_\mathrm{A}}{B_\mathrm{S}} E_\mathrm{S} \\ 1 & E_\mathrm{S} - qU > \frac{B_\mathrm{A}}{B_\mathrm{S}} E_\mathrm{S}, \end{cases} \tag{6.7}$$

to describe the transmission function for an isotropic source with starting energy E_S. The function equals zero, if the surplus energy of the electrons $E_\mathrm{S} - qU$ is negative, as no particles can pass the electrostatic filter in that case. As soon as the starting energy E_S is as large as the retarding potential, electrons with zero polar angles are transmitted. Electrons with larger polar angles are transmitted when the surplus energy increases, until

finally all electrons are transmitted. This will happen once the surplus energy is larger than the so called energy resolution, which is $\Delta E = \frac{B_\mathrm{A}}{B_\mathrm{S}} E_\mathrm{S}$.

In a configuration where the magnetic field in the source does not represent the maximal magnetic field of the experiment, electrons starting with a high polar angle in the source will not reach the detector, as they are reflected magnetically, as described in section 2.1. According to equation 2.5, electrons starting with a polar angle higher than θ_max are not transmitted. Therefore, the transmission function stops rising after all electrons with polar angles below θ_max are transmitted, which happens at a surplus energy of $\frac{B_\mathrm{A}}{B_\mathrm{max}} E_\mathrm{S}$. This limits the width of the transmission function and reduces the energy resolution to $\Delta E = \frac{B_\mathrm{A}}{B_\mathrm{max}} E_\mathrm{S}$. A normalization can then be applied to make sure that the transmission function stays in the range between zero and unity, resulting in:

$$T(E_\mathrm{S}, qU) = \begin{cases} 0 & E_\mathrm{S} - qU < 0 \\ \frac{1-\sqrt{1-\frac{E_\mathrm{S}-qU}{E_\mathrm{S}} \cdot \frac{B_\mathrm{S}}{B_\mathrm{A}}}}{1-\sqrt{1-\frac{B_\mathrm{S}}{B_\mathrm{max}}}} & 0 \leq E_\mathrm{S} - qU \leq \Delta E \\ 1 & E_\mathrm{S} - qU > \Delta E. \end{cases} \tag{6.8}$$

This analytical formula is, however, only valid for a single field line with an analyzing potential U and magnetic field B_A. The effect of a radial electric potential and a magnetic field inhomogeneity has been investigated in section 5.5. Moreover, further modifications due to synchrotron energy losses or a modified angular distribution due to the scattering in the source need to be taken into account, as it will be detailed in section 6.5.

6.1.2 Energy loss due to inelastic scattering

KATRIN is designed to avoid large energy losses of signal electrons by using a windowless gaseous tritium source and by guiding the electrons from the source to the detector in an adiabatic way. As certain energy losses can not be avoided, the sources thereof have to be known precisely and included in the neutrino mass analysis. The most prominent effect is the well known energy loss due to inelastic scattering of electrons off tritium molecules in the source region. It depends on the inelastic scattering cross section σ_inel and the energy loss function $f(\epsilon)$, which is a normalized probability distribution

$$f(\epsilon) \propto \frac{1}{\sigma_\mathrm{inel}} \frac{\mathrm{d}\sigma}{\mathrm{d}\epsilon} \tag{6.9}$$

with the energy loss ϵ and the differential cross section $\frac{\mathrm{d}\sigma}{\mathrm{d}\epsilon}$.

The inelastic cross section and the energy loss function for electrons with kinetic energies of $\approx 18\,\mathrm{keV}$ scattering off tritium molecules have both been measured in [ABB+00]. The inelastic scattering cross section was determined to $\sigma_\mathrm{inel} = (3.40 \pm 0.07) \cdot 10^{-18}\,\mathrm{cm}^2$, and a functional form was fitted to the energy loss function of

$$f(\epsilon) = \begin{cases} A_1 \exp^{-2(\frac{\epsilon-\epsilon_1}{\omega_1})^2} & \text{for } \epsilon < \epsilon_c \\ A_2 \frac{\omega_2^2}{\omega_2^2 + 4(\epsilon-\epsilon_2)^2} & \text{for } \epsilon \geq \epsilon_c \end{cases} \tag{6.10}$$

with the parameters $A_1 = 0.204 \pm 0.001$, $A_2 = 0.0556 \pm 0.0003$, $\omega_1 = 1.85 \pm 0.02$, $\omega_2 = 12.5 \pm 0.1$, $\epsilon_2 = 14.30 \pm 0.02$ and a fixed $\epsilon_1 = 12.6$. To obtain a continuous transition between the two parts of $f(\epsilon)$, a value $\epsilon_c = 14.09$ was chosen. The Gaussian part describes the energy loss due to excitation, while the Lorentzian part describes the energy loss due to ionisation of tritium molecules. A graphical representation is shown in figure 6.1.

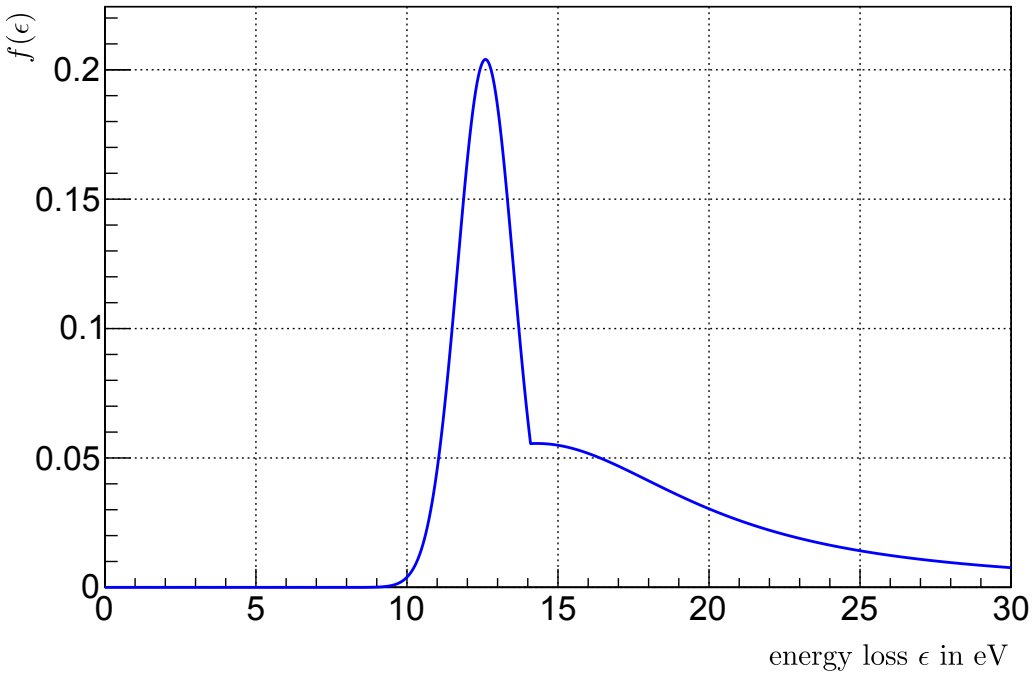

Figure 6.1: Energy loss function $f(\epsilon)$ for inelastic scattering of electrons on tritium molecules as determined in [ABB+00]. The parametrization consists of a Gaussian part due to excitation and a Lorentzian part due to ionisation processes. The minimal energy loss for inelastic scattering is about 10 eV.

The accuracy of $\approx 2\,\%$ for the inelastic cross section σ_{inel} and the energy loss function $f(\epsilon)$ measured in [ABB+00] are not sufficient enough for the ambitious goal of KATRIN [KAT05]. Both parameters have to be determined in a dedicated measurement campaign before the start of the neutrino mass measurements. Using the rear section electron gun (see section 2.2.2) to measure the count rate at the detector at different electron energies and column densities of the source apparatus, the inelastic cross section and the energy loss function can be obtained by a deconvolution procedure [Wol08, Kra11] or can be directly extracted [Zie13].

6.1.3 Scattering probabilities

For a given density distribution of gas inside the tritium source, the scattering probabilities P_i for an electron propagating through the source and scattering i times can be calculated. These scattering probabilities for a single electron do not only depend on its position inside the source, but also on its starting polar angle, as both parameters will lead to a different path length of the electron's trajectory through the tritium gas. Because of the low probability to scatter off a single tritium molecule, the number of scatterings during propagation can be calculated according to a Poisson distribution

$$P_i(z,\theta) = \frac{(\lambda(z,\theta)\cdot\sigma_{\text{inel}})^i}{i!}\exp^{-\lambda(z,\theta)\cdot\sigma_{\text{inel}}}, \tag{6.11}$$

with λ being the effective column density. An electron starting at position z with polar angle θ thus has to propagate through

$$\lambda(z,\theta) = \frac{1}{\cos(\theta)}\int_{z'=z}^{L/2}\rho(z')\,\mathrm{d}z' \tag{6.12}$$

Table 6.1: Scattering probabilities for the KATRIN reference configuration, a column density of $\rho d = 5 \cdot 10^{21}\,\mathrm{m}^{-2}$, an inelastic cross section of $\sigma_{\mathrm{inel}} = 3.456 \cdot 10^{-18}\,\mathrm{cm}^2$ and the magnetic fields of $B_{\mathrm{S}} = 3.6\,\mathrm{T}$ and $B_{\mathrm{max}} = 6\,\mathrm{T}$.

number of scatterings	probability
0	0.413
1	0.293
2	0.167
3	0.079
4	0.032

with the length of the source apparatus L and the axial density distribution $\rho(z)$.

Taking into account the angular distribution $\omega(\theta)$ of the source, the mean scattering probabilities for a specific axial position z can be calculated according to

$$\overline{P}_i(z) = \int_{\theta=0}^{2\pi} \omega(\theta) \cdot P_i(z,\theta)\,\mathrm{d}\theta. \tag{6.13}$$

Using an isotropic distribution of $\omega(\theta) = \sin(\theta)$ and a maximal polar angle of θ_{max} results in

$$\overline{P}_i(z) = \frac{1}{1-\cos(\theta_{\mathrm{max}})} \int_{\theta=0}^{\theta_{\mathrm{max}}} \sin(\theta) \cdot P_i(z,\theta)\,\mathrm{d}\theta. \tag{6.14}$$

The mean scattering probabilities for the whole source tube, which enter into equation 6.2, can be obtained when integrating over the length L and the density profile $\rho(z)$ of the source

$$\overline{P}_i = \frac{1}{\rho d} \int_{z=-L/2}^{+L/2} \rho(z) \cdot \overline{P}_i(z)\,\mathrm{d}z, \tag{6.15}$$

with the total column density ρd. For a constant magnetic field of the source, the average scattering probabilities are independent of the function $\rho(z)$.

For the default KATRIN configuration the scattering probabilities up to $i = 4$ are listed in table 6.1.

With these descriptions of the transmission function, the energy loss function and the scattering probabilities, the response function of equation 6.2 can be calculated and visualized in figure 6.2. In contrast to typical representations found for example in [KAT05], here the response function is not normalized to $\theta_{\mathrm{max}} = \arcsin(\sqrt{\frac{B_{\mathrm{S}}}{B_{\mathrm{max}}}})$, but to all electrons emitted in forward direction ($\theta = 90\,^\circ$), thus changing the scale of the y-axis. This normalization is chosen for all response and transmission functions plotted within this chapter for the reason that θ_{max} is not a constant value due to the axial magnetic field inhomogeneities along the entire extended source tube (see section 6.5.1).

The characteristic plateau of the response function for surplus energies between about 1 eV and 10 eV is a result of the fraction of electrons leaving the source without experiencing

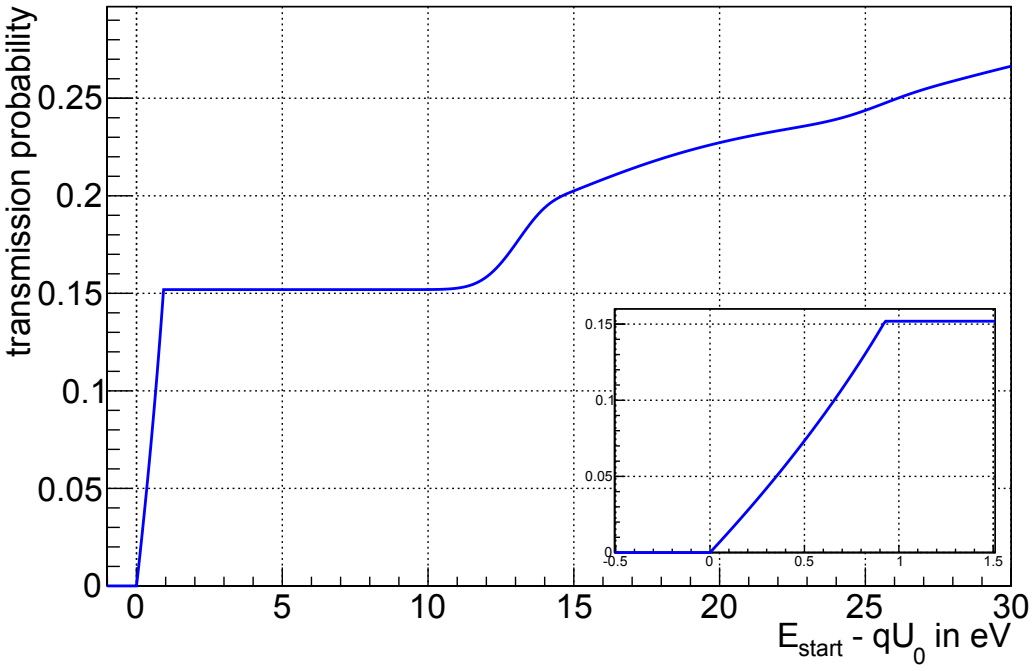

Figure 6.2: Example of a response function for the KATRIN reference configuration, calculated for a column density of $\rho d = 5 \cdot 10^{21}\,\mathrm{m}^{-2}$, an inelastic cross section of $\sigma_{\mathrm{inel}} = 3.456 \cdot 10^{-18}\,\mathrm{cm}^2$ and magnetic fields of $B_{\mathrm{S}} = 3.6\,\mathrm{T}$, $B_{\mathrm{max}} = 6\,\mathrm{T}$ and $B_{\mathrm{A}} = 3.0 \cdot 10^{-4}\,\mathrm{T}$. The response function takes into account all electrons emitted in forward direction. A more detailed zoom to the region of the transmission function is shown in the inlay.

an inelastic scattering process, as the corresponding minimal energy loss of this process is about 10 eV. Electrons scattering once or multiple times will lose at least 10 eV of kinetic energy. Correspondingly, they require an equivalent surplus energy to pass the MAC-E filter to reach the detector.

6.2 Motivation for a full Monte Carlo simulation

The response function of the KATRIN experiment can be calculated analytically with rather small computational effort. However, this calculation is only an approximation, as a variety of effects are not considered in such an analytical model, for example magnetic field inhomogeneities, angular changes due to scattering processes or energy losses due to emission of synchrotron radiation. These effects can be studied and included by performing large-scale Monte Carlo simulations, where electrons are generated in the source tube and propagate through the whole experimental setup until reaching the detector wafer or being magnetically or electrostatically reflected. Thereby a more realistic response function can be obtained, which can be compared with the initial analytical model, so that the influence of neglected effects can be studied and quantified.

As these kinds of large-scale Monte Carlo simulations are very time consuming (see section 6.3.6), they can not be produced with sufficient statistics in short time, as is needed when fitting a model to the obtained integral spectrum to deduce the neutrino mass. However, the results of the Monte Carlo simulation are essential in order to refine the analytical model and to adapt it to the results of the simulation. This approach will ensure that the relevant effects are not neglected.

The Monte Carlo simulations performed within the scope of this thesis were focused on the effects caused by the transport of electrons from the source section to the detector, in particular by incorporating all effects of scattering off tritium molecules and energy

losses caused by synchrotron radiation. Source-related effects such as variations in the temperature or density profile are currently investigated in a separate thesis [Kuc16]. Detector-related effects, caused by back-scattering and the finite dead-layer in the silicon wafer are not yet included in the Monte Carlo simulation, but these effects can be easily investigated separately, as the required processes were integrated in the provided particle tracking framework KASSIOPEIA. Additionally, the simulations were performed for electrons created on the central beam axis, thus neglecting any radial potential and magnetic field inhomogeneities in the main spectrometer, as these issues were already discussed separately in section 5.5.

6.3 Implementation with Kassiopeia and validation of involved physics processes

Before starting a large-scale Monte Carlo simulation it is important to validate the involved physics processes and optimize the computation speed.

Accordingly, the adiabatic approximation of the electron transport through the whole KATRIN beam line will first be tested and confirmed in section 6.3.2. The scattering logic of KASSIOPEIA can be tested by comparing analytical scattering probabilities with simulated ones, which will be presented in section 6.3.3. The corresponding energy losses of the scattering module will be discussed in section 6.3.4 and compared to the energy loss function used in the analytical calculation. In section 6.3.5 energy losses caused by synchrotron radiation will be tested. Finally, in section 6.3.6, the numerical energy losses and performance of the simulation will be presented and optimized.

But first of all, the setup of the Monte Carlo simulation will be presented in the next section.

6.3.1 Setup of the Monte Carlo simulation

- **Geometry:** The geometry used for the Monte Carlo simulation consists of axially symmetric models of the pre-spectrometer, the main spectrometer and the focal plane detector. For the transport section and the source, both being at ground potential, a rather simple axi-symmetric cylinder has been used as approximation instead of the complex beam tube. This was done in order not to break the axial symmetry of the electric field, which would slow down the calculation significantly. For the magnetic configuration all 62 coils of the KATRIN beam line have been used, including the large number of superconducting solenoids with correction coils in the transport section, as well as the air coil system around the main spectrometer. A visualization of the geometrical elements used for representing the entire beam line is presented in figure 6.3 together with the transported magnetic flux of 191 Tcm^2.

- **Magnetic setup:** For the magnetic configuration the reference setup for the KATRIN experiment is used. This includes the non-homogenous magnetic field in the WGTS with a value in the center of about $B_\mathrm{S} = 3.6\,\mathrm{T}$, and the maximal magnetic field at the pinch magnet of $B_\mathrm{max} = 6.032\,\mathrm{T}$. For the air coils a setting which has been optimized with regards to the transmission conditions is used with a value in the middle of the main spectrometer of $B_\mathrm{A} = 3.474 \cdot 10^{-4}\,\mathrm{T}$. The procedure of optimizing the transmission conditions were discussed in detail in section 4.3. The currents used for the air coils together with the values for all other solenoids are listed in appendix B. The resulting magnetic field variation along the whole beam line is plotted in figure 6.4.

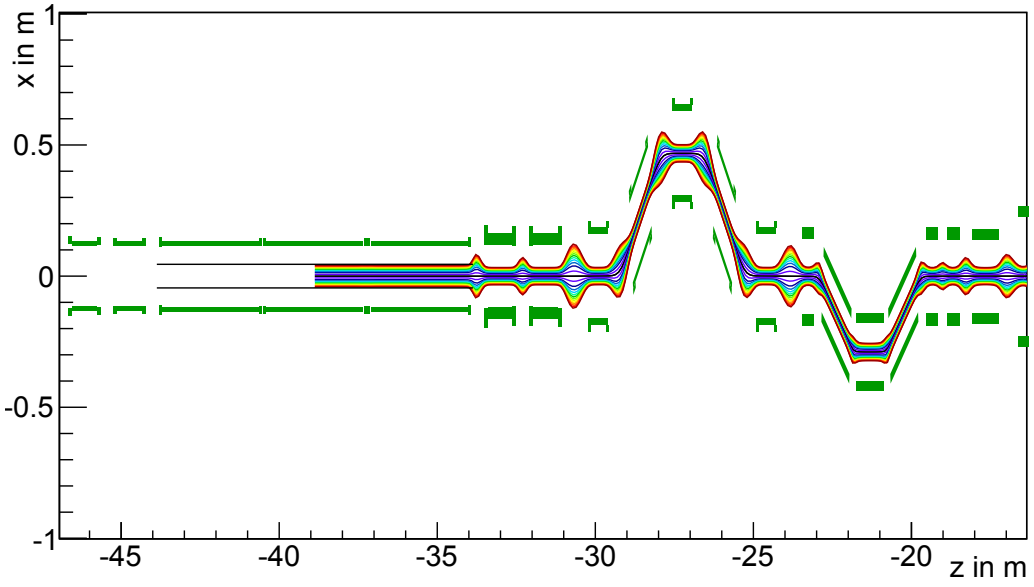

(a) Transport section

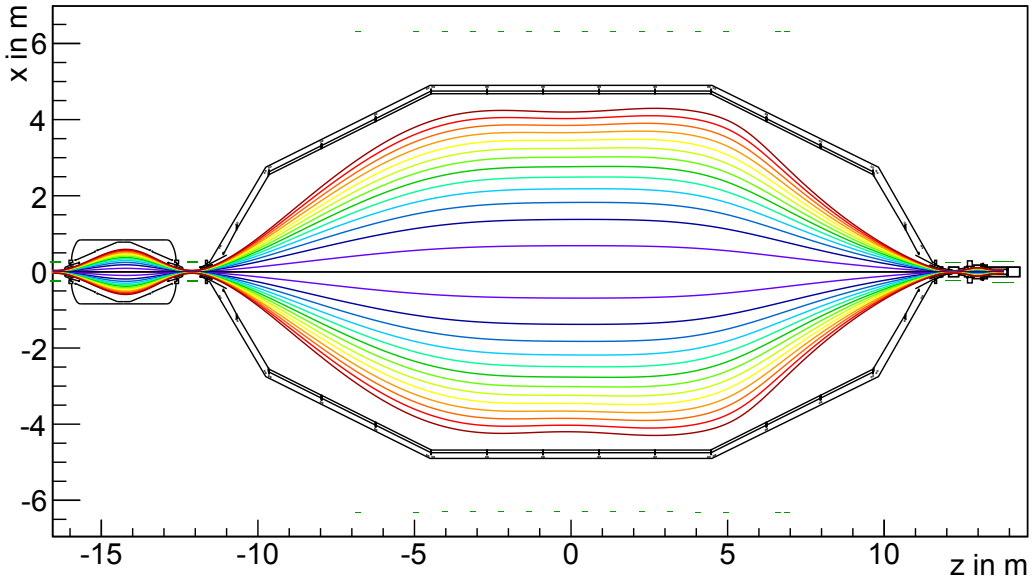

(b) Spectrometer section

Figure 6.3: Flux tube for the whole KATRIN beam line from the center of the WGTS to the detector wafer. The field lines are colored according to the corresponding pixel rings. In the transport section (a) the beam tube is not visualized, only the relevant tritium containing part in the WGTS, the 10 m long WGTS tube. The magnetic flux, and therefore also the signal electrons, are guided through the chicanes of the pumping and transport section, before reaching the spectrometer section (b), where the tandem MAC-E filter setup of pre-spectrometer and main spectrometer leads to an increased flux tube radius due to the low magnetic field in the middle of each.

- **Electric setup:** The inner wire electrodes of the main spectrometer are put on a potential of $-18445\,\mathrm{V}$, resulting in an analyzing potential in the middle of the spectrometer of $U_\mathrm{A} = -18544.142\,\mathrm{V}$. With the endpoint of the tritium β-decay spectrum of 18575 eV, this results in a response function with surplus energies of up to 31 eV. The potential of the inner wires of the pre-spectrometer is set to $-18300\,\mathrm{V}$, while the transport beam tube is on ground potential. The detailed electrostatic setup is listed in appendix B.
- **Particle generation:** All electrons for the Monte Carlo simulation are generated within the 10 m long central beam tube element of the WGTS according to the calculated column density distribution of the tritium gas, as visualized in figure 6.5. This neglects the small contribution to the overall column density in the DPS cryostat and the rear section. The starting kinetic energy is drawn from a uniform distribution between 18544 and 17575 eV. The starting polar angle is diced isotropically with a maximal angle of 60 °. For the given magnetic field of the source and the pinch magnet, the maximal starting polar angle that an electron can possess, without being magnetically reflected, is about 50 °. A significantly higher maximal polar angle is chosen in the simulation to account for electrons changing their polar angle when scattering off tritium molecules.
- **Particle propagation:** The particles are propagated using an adiabatic trajectory, which will be detailed in section 6.3.2. A term for the emission of synchrotron radiation is added, as introduced in section 3.2.4. If the particle is still within the WGTS, scattering off tritium molecules is performed depending on the local gas density. The full range of elastic and inelastic energy losses and the corresponding angular changes are used (see section 6.3.4). The particle is terminated when crossing the surface of the silicon wafer, or when being reflected by the retarding potential or the magnetic field.

6.3.2 Adiabatic approximation of the electron transport

Using exact particle tracking as described in section 3.2.4 is the most accurate method of particle propagation for studying the interactions of β-decay electrons in the WGTS and transporting them to the detector. Unfortunately this is not a very fast method, as the simulation of a single electron track requires many million steps with 13 field evaluations per step, and a corresponding computation time in the order of half an hour (see section 6.3.6).

A much faster tracking method makes use of the adiabatic approximation as introduced in section 3.2.4. This approach reduces the required number of steps by about two orders of magnitude. Though, it can only be used if the adiabatic approximation is valid for the given electromagnetic setup.

This assumption can be tested by the following procedure: A number of electrons with an isotropic angular distribution is started in the middle of the WGTS and tracked with the exact method through the transport section to the main spectrometer to obtain its longitudinal kinetic energy at the analyzing plane position. Using the electric potential and magnetic field values of the particle's initial and final guiding center position, its longitudinal kinetic energy at the analyzing plane can also be calculated in an adiabatic approximation with equation 4.8. By comparing the longitudinal kinetic energy obtained for the two cases of exact tracking and of the adiabatic approximation a quantitative result with respect to the validity of the adiabatic approximation can be obtained.

In figure 6.6 the corresponding difference between the exact and adiabatic longitudinal kinetic energy is plotted as a function of the starting polar angle θ for a total of 10^3

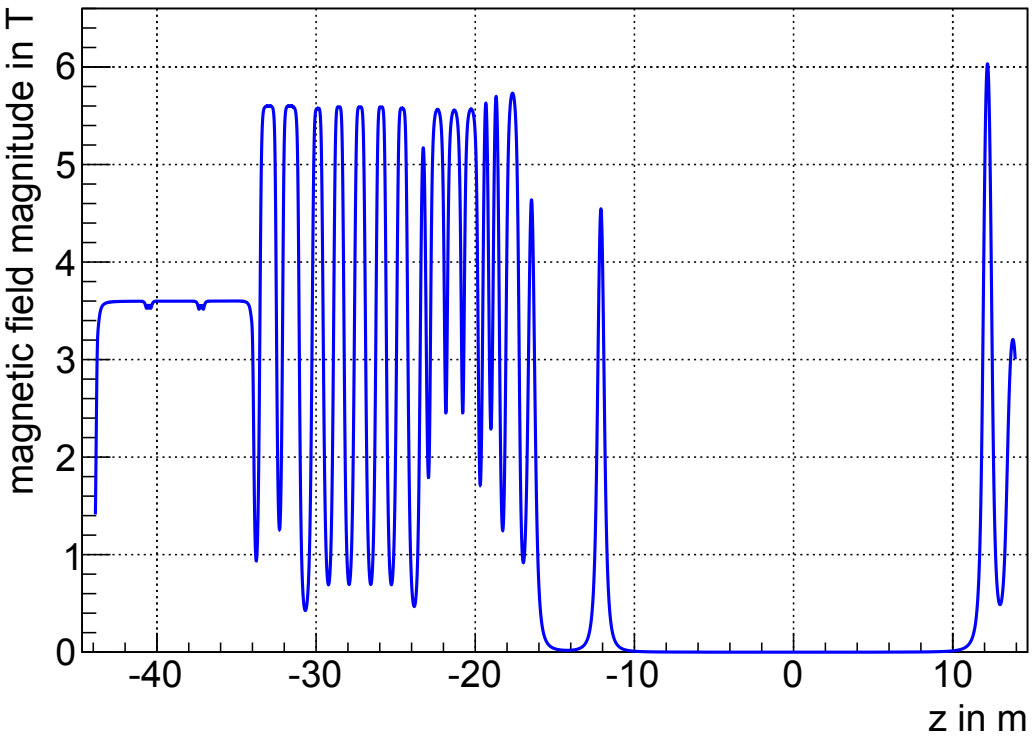

Figure 6.4: Magnetic field along the KATRIN beam line. The magnetic field in the WGTS (left) is about 3.6 T, followed by the many solenoids of the transport section with a field of up to 5.6 T. In center of the pre-spectrometer the magnetic field drops to about 0.02 T and in the center of the main spectrometer to $3.474 \cdot 10^{-4}$ T. The magnetic field is maximal at the pinch magnet with 6.032 T.

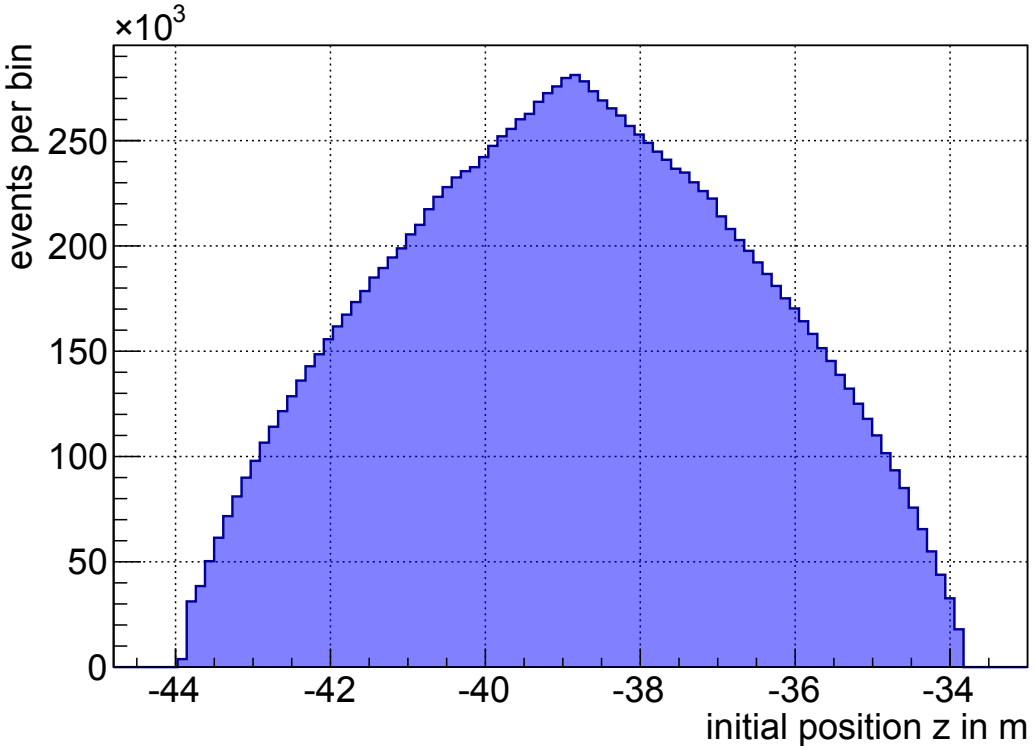

Figure 6.5: Initial position within the WGTS for 15 Million generated electrons. A simple one dimensional density profile for the tritium gas distribution within the WGTS was used.

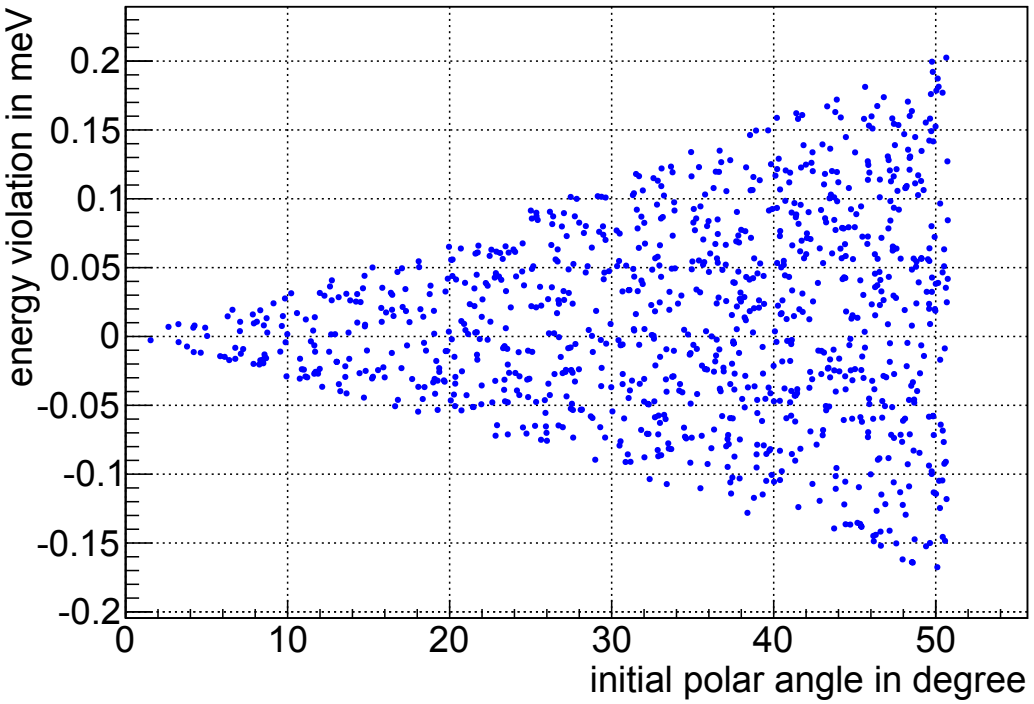

Figure 6.6: Energy violation caused by the adiabatic approximation for electrons starting with an isotropic distribution at the center of the WGTS and propagating to the analyzing plane. The mean absolute energy violation is 0.06 meV.

started electrons. The energy violation is larger for electrons with a larger initial polar angle, amounting to a value of up to 0.2 meV for electrons starting with $\theta_{\max}$. The mean value of the absolute energy violation is 0.06 meV. Compared with the filtering width of the main spectrometer of $\Delta E \approx 1\,\mathrm{eV}$, or the energy loss due to synchrotron radiation of about 85 meV, this error caused by the adiabatic approximation is negligible.

6.3.3 Scattering probabilities

The scattering module of KASSIOPEIA, as introduced in section 3.2.5, calculates the scattering probabilities on a step by step basis, by dicing the path length until the next scattering takes place and executing the correct scattering process if it occurred within the current step. The scattering probabilities of the analytical model are calculated using a Poisson distribution, as detailed in section 6.1.3.

The scattering module of KASSIOPEIA can be tested by comparing the number of scattering events at each simulated track with the analytically calculated scattering probabilities. This can be done by generating particles inside the WGTS according to the tritium gas density profile and by tracking them to the end of the source tube. When using a constant magnetic field of $B_{\mathrm{S}} = 3.6\,\mathrm{T}$ while deactivating elastic scattering processes and angular changes, a comparison with the analytical calculations is possible. This has been done for a total of 10^5 particles, starting with a maximal polar angle of $\theta = 50.77\,^\circ$ with the reference source column density of $\rho d = 5 \cdot 10^{21}\,\mathrm{m}^{-2}$ and an inelastic cross section of $\sigma_{\mathrm{inel}} = 3.456 \cdot 10^{-18}\,\mathrm{cm}^2$.

The resulting scattering probabilities together with the analytical values from section 6.1.3 are listed in table 6.2. The values obtained by particle tracking agree with the analytical values within their statistical errors.

Table 6.2: Scattering probabilities obtained by particle tracking and comparison with analytical values. Both values agree within the statistical error of the MC simulation.

number of scatterings	probability	
	particle tracking	analytical
0	0.415 ± 0.002	0.413
1	0.292 ± 0.002	0.293
2	0.166 ± 0.001	0.167
3	0.079 ± 0.001	0.079
4	0.031 ± 0.001	0.032

6.3.4 Energy loss due to scattering

The scattering module in KASSIOPEIA is composed of multiple different physics processes, each with its own cross section and energy loss distribution, as detailed in section 3.2.5. For electrons scattering off tritium molecules, the physics processes include electronic excitations, dissociation, rotation, vibration and ionization of tritium molecules. The models used and the underlying data are derived for molecular hydrogen, which is expected to be a good approximation for tritium, as electronic excitations and ionization processes depend only to a very small degree to the actual isotope.

The source model includes also elastic scattering processes, caused by the Coulomb interaction between the electron and the tritium nuclei. This leads to small energy losses of typically a few meV only, while inelastic processes, i.e. the excitation, dissociation and ionization processes, will lead to energy losses of about 11 eV at least. Rotation processes are very unlikely due to their small cross section at electron energies of 18600 eV. Due to their small energy losses they are treated as elastic processes for practical reasons. More information about KASSIOPEIA's scattering modules and the implemented processes can be found in section 3.2.5.

The resulting energy loss for an electron with a kinetic energy of 18600 eV is plotted in figure 6.7. The elastic processes can be found on the left side at sub-eV energy losses, the central peak structure between 10 and 15 eV is caused by excitation and the following peaks at about 15 eV by dissociation. The subsequent continuum at higher energies is a result of ionization processes. Additionally, the energy loss function used in the analytical calculation has been plotted, which is based on an analytical formula that is fitted on measured data [ABB+00], as described in section 6.1.2.

Although elastic processes can be deactivated, there still is an obvious difference between the energy loss function obtained by KASSIOPEIA with all relevant physics processes modeled individually, and the analytical energy loss function. This leads to a large difference in the response functions obtained with both methods, as has been shown in [Pom14].

The energy loss function to be used in the final neutrino mass analysis will be obtained from a dedicated energy loss measurement campaign before the start of the long-term experiment. This will also be the case for the required inelastic cross section. Therefore, a scattering module was implemented into KASSIOPEIA with a user-defined cross section and energy loss function. At the same time the angular change is calculated according to the same formulas as in the tritium scattering code. Thereby, the Monte Carlo simulation includes a realistic angular change on scattering, while the used cross section as well as the energy loss function are identical as in the analytical calculation.

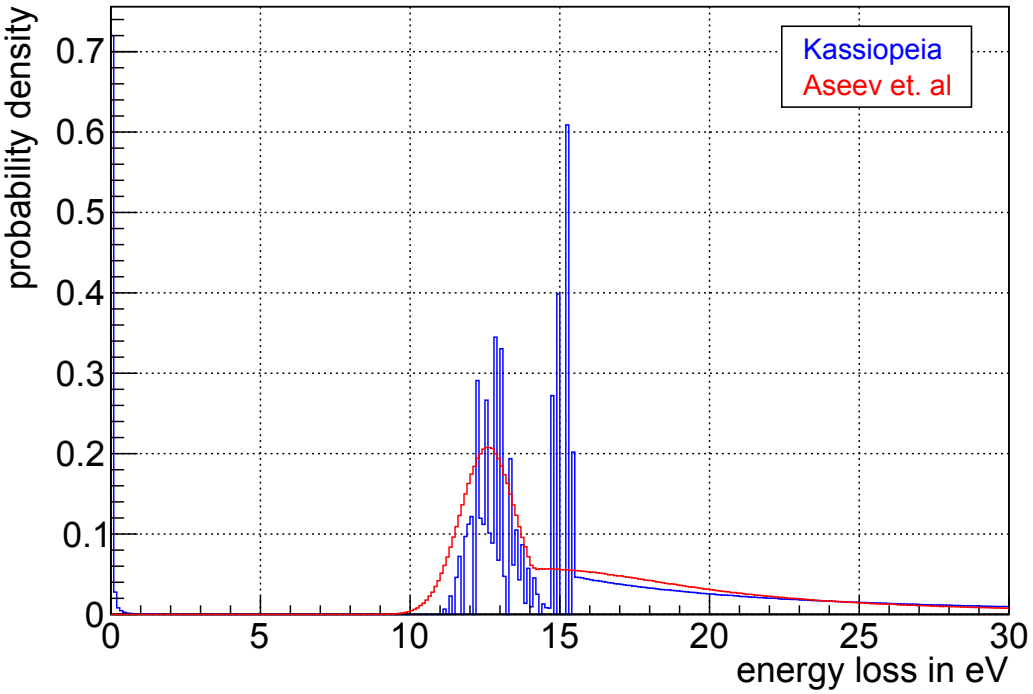

Figure 6.7: Scattering energy loss for electrons with a kinetic energy of 18575 eV as computed with KASSIOPEIA (blue) and as used in the analytical calculation (red).

6.3.5 Energy loss due to synchrotron radiation

Charged particles propagating along cyclotron tracks in magnetic fields will lose energy due to the emission of synchrotron radiation. Within KASSIOPEIA, these radiative energy losses are accounted for via a separate term in the overall equations of motion. In general, synchrotron emission will reduce the transversal momentum component of the propagating electrons, the formulas used were presented in section 3.2.4.

The non-relativistic energy momentum relation of $E = \frac{p^2}{2m}$ can be used to obtain an approximation for the energy loss caused by synchrotron radiation based on equation 3.7:

$$\Delta E = \frac{-\mu_0}{3\pi c}\frac{q^4}{m^3} \cdot B^2 \cdot E_\perp \cdot \gamma \cdot t \tag{6.16}$$

The transveral kinetic energy component can be expressed as $E_\perp = E\sin^2(\theta)$, while the propagation time $t = \frac{s}{\cos(\theta)v}$ spent in a magnet of length s is proportional to the path length of the electron. Therefore, the synchrotron losses of an electron with kinetic energy E which propagates in a constant magnetic field B will depend on its polar angle θ only. Consequently, for large polar angles these losses are largest, while vanishing completely for polar angles of $\theta = 0\,^\circ$.

As an example, an electron is considered with kinetic energy $E = 18600\,\text{eV}$ and polar angle of $\theta = 45\,^\circ$ propagating through a magnet with a length $s = 10\,\text{m}$ and constant magnetic field of $B = 3.6\,\text{T}$: In this configuration the energy loss can be calculated to $\Delta E = 8.7\,\text{meV}$. A corresponding KASSIOPEIA simulation, which is more exact due to incorporating the full relativistic calculations and considering the differential energy loss, reveals a synchrotron energy loss of $\Delta E = 8.5\,\text{meV}$.

In [KAT05] the synchrotron energy losses for the entire KATRIN beam line, from the WGTS to the analyzing plane in the main spectrometer, were expected to not exceed $\Delta E = 142\,\text{meV}$.

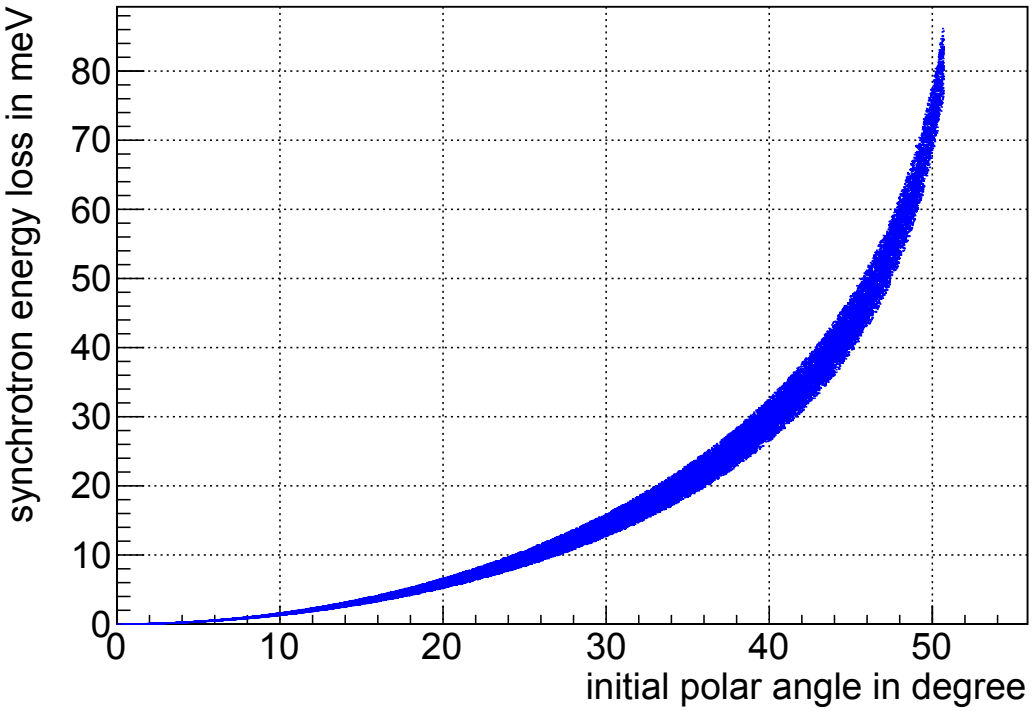

Figure 6.8: Synchrotron energy loss for electrons starting in the WGTS and propagating through the transport section to the analyzing plane in the main spectrometer. The synchrotron energy loss depends on the polar angle θ. Electrons starting at the rear side of the WGTS lose up to 85 meV, while electrons starting on the front side lose only up to 75 meV due to their shorter path length. The initial polar angle is normalized to a magnetic field of 3.6 T.

The result obtained with the help of particle tracking and the actual magnet geometry is shown in figure 6.8. Depending on the actual polar angle θ and the axial starting position in the WGTS, the electrons will lose up to 85 meV in synchrotron radiation before reaching the analyzing plane in the middle of the main spectrometer.

6.3.6 Numerical energy loss and performance

Even the method of particle tracking on a step by step basis has to be considered as an approximation only for a real particle motion, as the propagation process for a real particle is continuous. Large field gradients within a step or a large curvature due to small cyclotron radius thus requires small step sizes. The resulting numerical error of a particle track caused by a finite step size can be quantified by comparing the initial total energy of the particle to its final value. As this is a conserved quantity, and if interaction processes are deactivated, any deviation can be traced back to be due to the finite step size.

On the other hand, the performance of the simulation depends linearly on the number of calculated steps for a specific track. Decreasing the step size and thereby increasing the number of steps inevitably will lead to larger computation times. Therefore, a compromise for the step size needs to be found where numerical energy losses are tolerable and a viable computation time is maintained.

Figure 6.9 shows an analysis of the numerical energy violation relative to the initial particle energy for the case of exact tracking with a rather fine-grained step size amounting to a fraction of $\frac{1}{50}$ of a cyclotron period only. In this investigation, the particle started on axis in the center of the WGTS with an initial polar angle of $\theta = 45\,^\circ$ and an initial kinetic energy of 18600 eV and was then tracked through the entire beam line up to the detector. The resulting energy violation of only about 11 µeV is more than sufficient in view of the

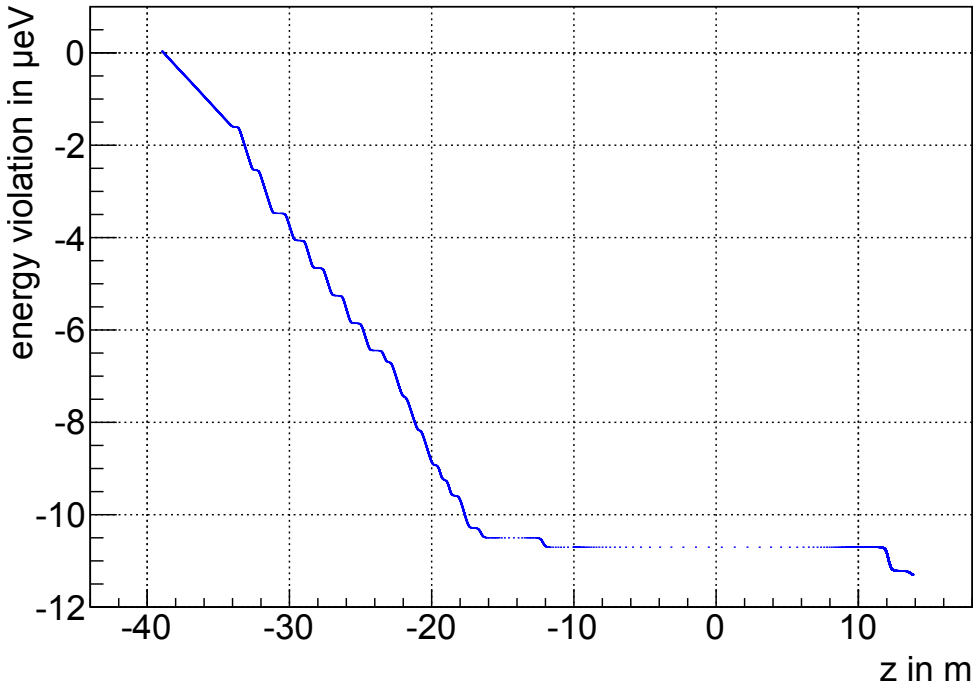

Figure 6.9: Numerical energy losses for exact tracking based on a step size fraction of $\frac{1}{50}$ of a cyclotron period. For a trajectory from the center of the WGTS to the detector the total energy of the electron deviates by about 11 µeV from its initial value.

targeted neutrino mass sensitivity of the experiment. However, a total of $2.72 \cdot 10^6$ steps had to be performed for a single particle, resulting in a computation time[1] of 27 minutes.

This long computation time for a single track is not feasible in high statistics applications. A reduction of the number of steps by a factor of two only, resulting in a computation time of 13.5 minutes for a single track, will however lead to an increase in the numerical inaccuracy and corresponding energy violation by several orders of magnitude up to a value of 6 meV, which is not tolerable anymore.

As electron propagation through the transport section is fully adiabatic in the energy regime of interest (i.e. 18.6 keV) as shown in section 6.3.2, the adiabatic approximation can be used for particle tracking. We recall that in this approximation not the real particle position is tracked on a step by step basis but the guiding center of the motion, so that much larger step sizes are possible (see section 3.2.4).

When using the adiabatic tracking method and a step size of four cyclotron periods, the total number of steps for the whole track reduces significantly to a value of $13.6 \cdot 10^3$, equivalent to a computation time for a single track of only 17 seconds. The corresponding numerical energy violation is of the order of 5 µeV, which is even better than in the exact case. Table 6.3 gives an overview of different tracking methods and step sizes together with their corresponding computation time and numerical energy violation.

The computation speed can be improved even further by using variable step sizes, depending on the region the particle is passing. Thereby smaller step sizes can be enforced in regions with high field gradients, and larger ones in regions with low field gradients. This strategy can be easily realized using the navigation algorithm provided by KASSIOPEIA, as detailed in section 3.2.8. This solution reduces the computation time further down to about 6 seconds per track with an identical numerical energy violation of 5 µeV, as shown in figure 6.10.

[1] on an Intel Core i7 CPU with 2.9 GHz

Table 6.3: Numerical energy violation and performance for different tracking methods and step sizes for electrons tracks from the center of the WGTS to the detector.

tracking method	step size in cyclotron fractions	number of steps in 10^3	computation time in min : s	energy violation in µeV
exact	1 / 50	2720	27 : 00	11
exact	1 / 32	1740	17 : 00	600
exact	1 / 25	1360	13 : 30	6000
adiabatic	4	14	00 : 17	5
adiabatic	8	7	00 : 09	500
adiabatic	variable	5	00 : 06	5

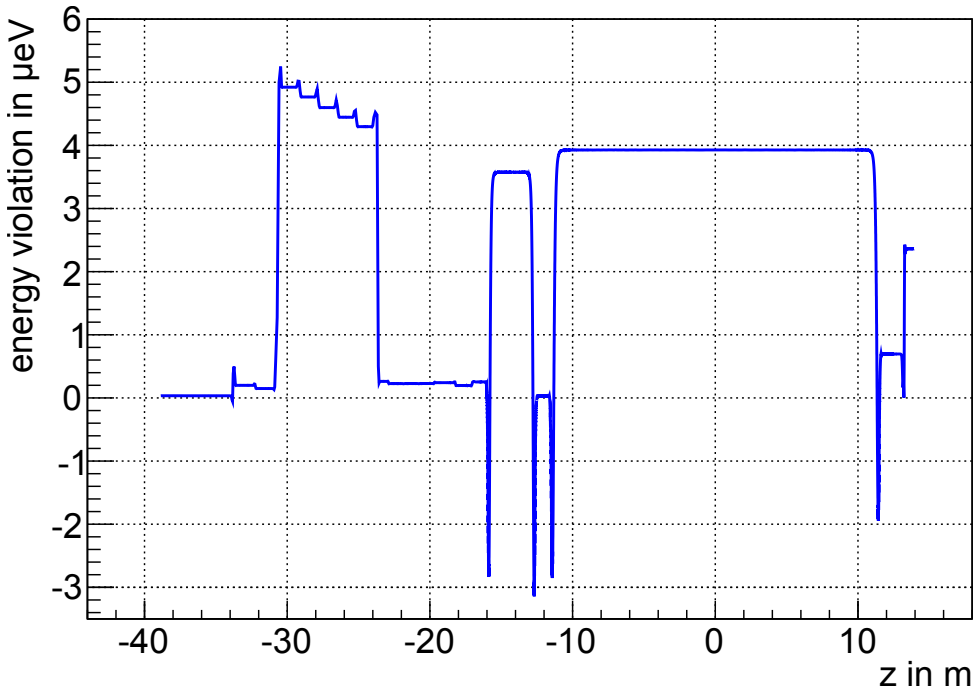

Figure 6.10: Numerical energy losses for adiabatic tracking based on a variable step size ranging from half the fraction of a cyclotron period up to a step size of over 20 cyclotron periods in regions with homogeneous fields. For a trajectory from the center of the WGTS to the detector the total energy of the electron is violated by not more than 5 µeV.

For the examples presented, an electron with an initial polar angle of 45 ° was considered. The numerical energy loss, the required number of steps and therefore also the computation time will increase slightly for larger polar angles and decreases for lower ones. Moreover, in the Monte Carlo simulation of the response function not all electrons need to be tracked onto the detector. Tracks can be discarded once the particle turns around, which is the case for a reflection by the potential barrier of the MAC-E filter or magnetic reflection in the pinch magnet or even earlier in the transport system. Also particles which lose too much energy by scattering off tritium molecules to pass the spectrometer can directly be stopped in the WGTS. Therefore, the simulation of 10^3 particles for the response function Monte Carlo currently takes about 1 hour on a single CPU core, allowing high statistics investigations.

6.4 Results and comparison with the analytical model

To examine small deviations between response functions obtained with particle tracking and the analytical calculation, a large number of electrons has to be simulated to achieve adequate statistical errors. Therefore, a total number of 75 million electrons were simulated with a required time of about 75000 CPU-hours. This could only be accomplished using multi-core grid computing system, where the total number of electrons is divided into smaller packages which are simulated in parallel.

In this large-scale effort, particles did not start with fixed energy values, but their initial energy was randomly distributed in a range of surplus energies from $0 - 30\,\mathrm{eV}$. In the subsequent analysis, the binning scheme and therefore the statistical error per bin can be chosen freely. In the most important region of the response function corresponding to surplus energies from $0 - 1.2\,\mathrm{eV}$ (i.e. the region of the transmission function), a rather fine binning with a total of 20 equally sized bins was chosen. For the subsequent plateau region up to a surplus energy of 10 eV only 3 further bins were used to increase the statistics for each point. The remaining part of the response function beyond 10 eV was divided into 40 equally sized bins. Due to the finer binning in the transmission region, most of the particles of the Monte Carlo simulation were thus started with a surplus energy lower than 1.2 eV, increasing the statistics there.

For each bin, the total number of started electrons n and the number of electrons reaching the detector k were counted to obtain the transmission probability

$$T(E - qU) = \frac{k}{n}, \tag{6.17}$$

with the surplus energy $E - qU$ at the center of the bin. The statistical errors on the obtained transmission probabilities were calculated with

$$\sigma = \sqrt{\frac{(k+1)(k+2)}{(n+2)(n+3)} - \frac{(k+1)^2}{(n+2)^2}}, \tag{6.18}$$

according to [UX08].

The resulting response function is shown in figure 6.11 (a), together with the analytical model as described in section 6.1. The statistical errors of the Monte Carlo simulation are not visible due to their small size. To first order the analytical model and the Monte Carlo data agree well. A closer look at the transmission region in figure 6.11 (b), reveals clear deviations of Monte Carlo simulation and analytical calculation, however.

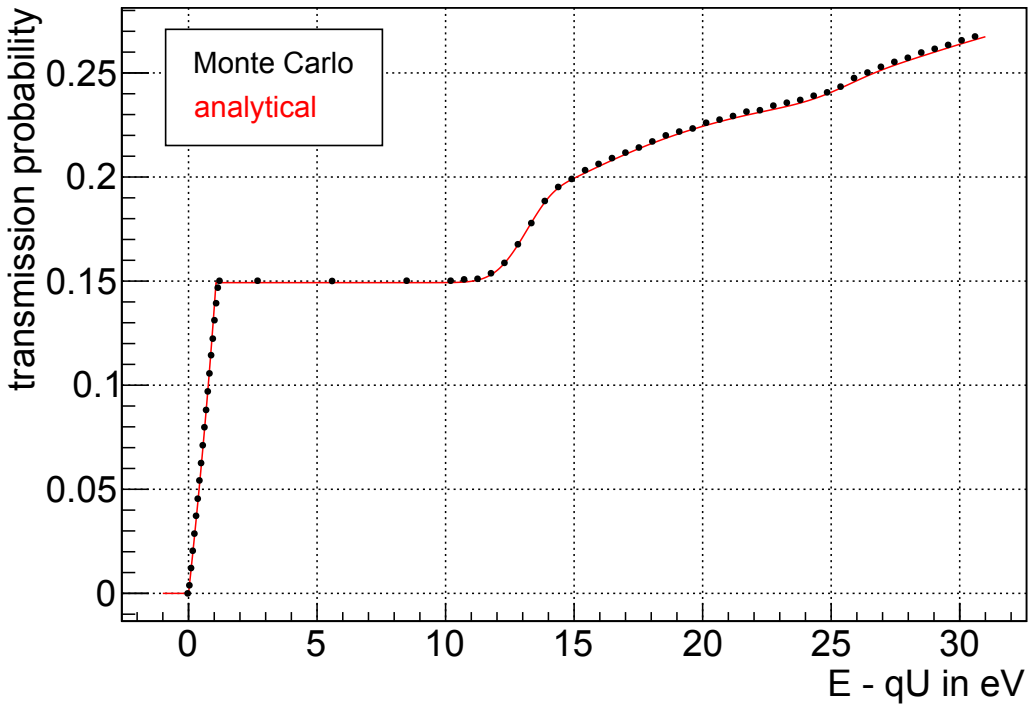

(a) Response function

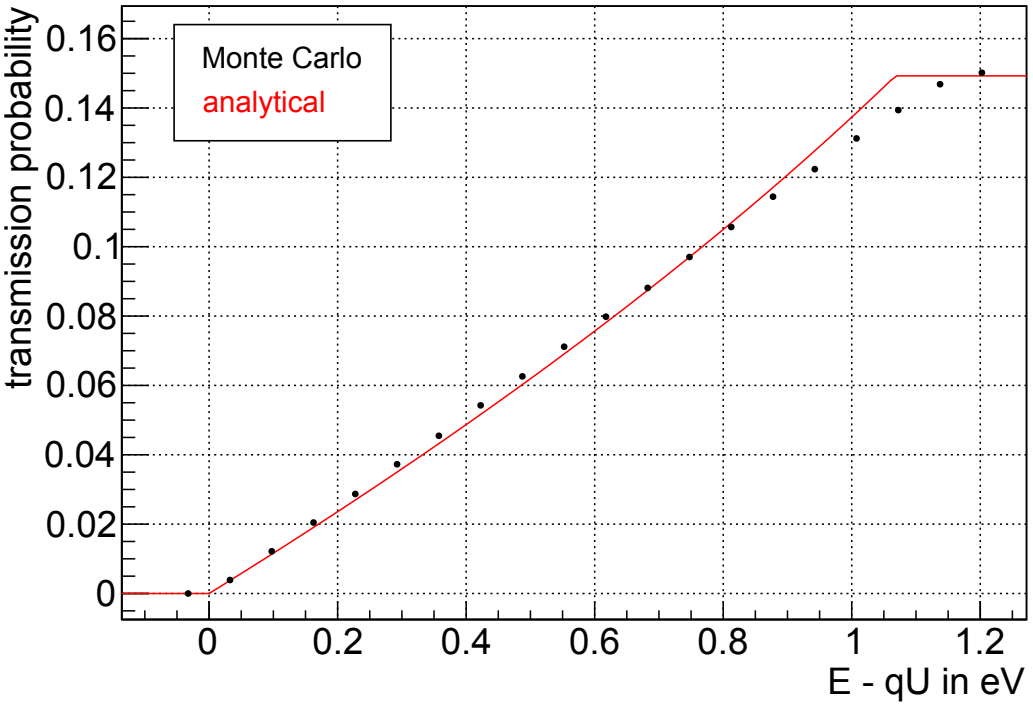

(b) Transmission function region

Figure 6.11: Results of the Monte Carlo response function and comparison with the analytical model. To first order, the Monte Carlo data and the analytical model agree rather well (a). A zoom into the transmission region (b) shows clear deviations.

Figure 6.12 shows the relative difference between the Monte Carlo data and the analytical model. For most parts of the response function, the relative deviations are of the order $5 \cdot 10^{-3}$, which means that the rate of the analytical model is too low. For the transmission region the observable deviations become much larger, reaching up to a value of 8 %, and also changing their sign from the lower part to the upper part of the transmission edge.

The analytical model used for the response function, as described in section 6.1 and [KAT05], clearly is not sufficient to describe the more realistic transmission probability obtained by the Monte Carlo simulation. The large deviations in the region of the transmission function are clearly unacceptable. However, even the rather small deviation for higher surplus energies would lead to a non-negligible systematic shift on the obtained neutrino mass if this model would be used in the final neutrino mass analysis.

In the following section a total of seven identified individual modifications to the analytical model will be introduced. The corresponding systematic shifts of each contribution induced on the neutrino mass will be presented, if it is not considered in the final neutrino mass analysis. The most significant contribution is the energy loss by synchrotron radiation, leading to a systematic error of $\Delta m_\nu^2 = -24.1 \cdot 10^{-3}\,\mathrm{eV}^2$ if left unconsidered. This alone would reduce the sensitivity on the neutrino mass to 235.9 meV (90 % C.L.).

It will then be shown that once all these identified effects are incorporated, the refined analytical model will match the Monte Carlo simulation within statistical errors.

6.5 Refinement of the analytical model and systematic shifts of the neutrino mass

In this section, the seven individual effects will be introduced, their influence on the response function will be quantified, the corresponding modifications to the analytical model will be presented and a comparison with the response function obtained by Monte Carlo particle tracking simulation will be performed. The effects investigated are the following:

- magnetic field inhomogeneities in the WGTS (see section 6.5.1)
- relativistic corrections (see section 6.5.2)
- synchrotron radiation (see section 6.5.3)
- modified angular distribution (see section 6.5.4)
- angular changes by inelastic scattering (see section 6.5.5)
- energy losses and angular changes by elastic scattering (see section 6.5.6)

Additionally, for each effect its impact on the neutrino mass sensitivity will be presented if left unconsidered in the final analysis. Furthermore, the requirements on the accuracy of the source magnetic field, on the synchrotron energy losses, and on the inelastic cross section and energy loss function will be derived and presented. To do so, detailed sensitivity estimations were performed using the KaFit module and the method of ensemble tests as presented in section 3.4. This method was already introduced when describing the investigation of the analyzing plane potential and magnetic field and presented in section 5.5.

Ensemble test settings and requirements

The parameters for the analytical calculation of the response function and the sensitivity estimations are listed in table 6.4. Here, default settings were used for most of the parameters, except for the magnetic fields, where parameters identical to the Monte Carlo

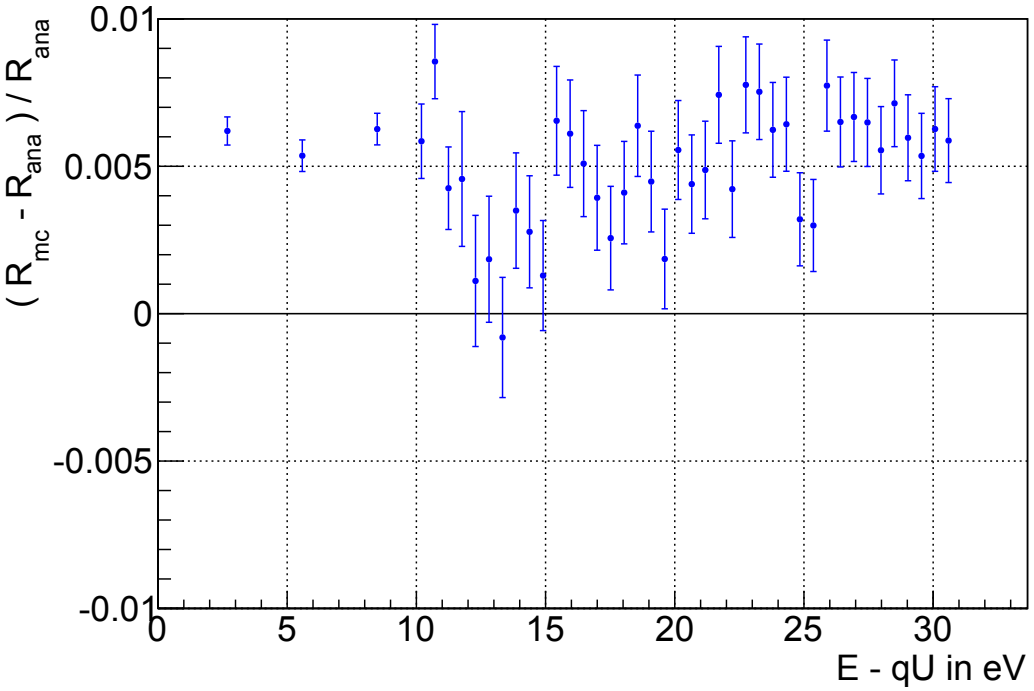

(a) Response function

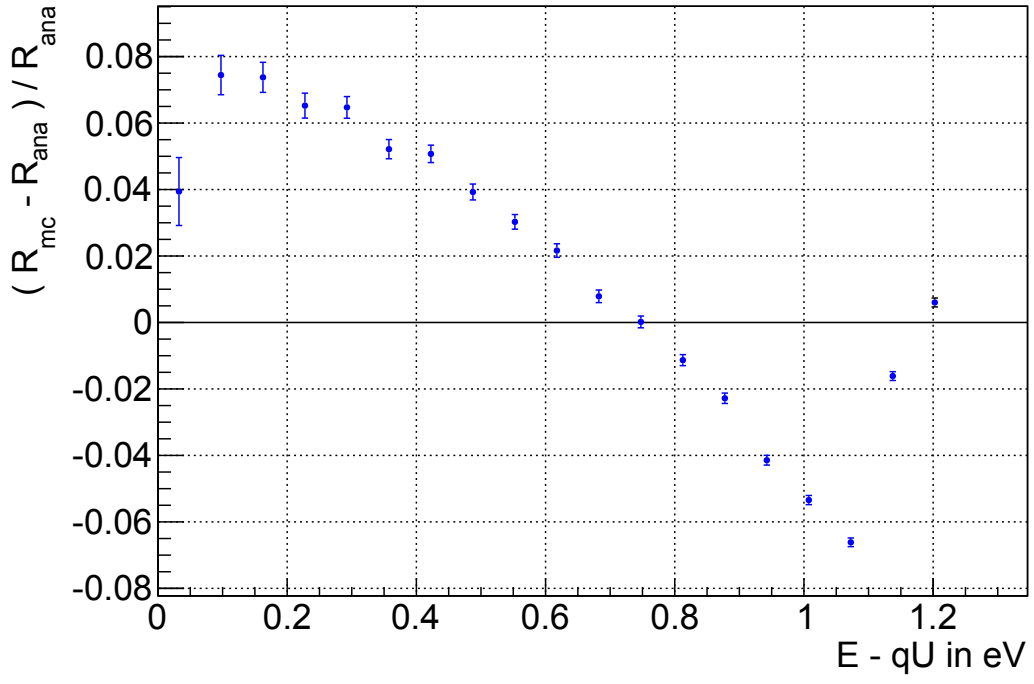

(b) Transmission function region

Figure 6.12: Relative difference of the Monte Carlo response function and the analytical model. For surplus energies higher than a few eV (a) the relative deviation is of the order of $5 \cdot 10^{-3}$. For the region of the transmission function (a), the deviations are much larger, reaching values up to 8 %.

Table 6.4: Parameters for the analytical response function calculation and sensitivity estimations. All values are default settings as stated in [KAT05], except the magnetic field values, where parameters identical to the Monte Carlo simulation were used, including a realistic, non homogenous source magnetic field.

parameter	setting
column density	$\rho d = 5 \cdot 10^{17}\,\mathrm{cm}^{-2}$
magnetic flux	$191\,\mathrm{Tcm}^2$
inelastic scattering cross section	$\sigma_{\mathrm{inelast}} = 3.456 \cdot 10^{-22}\,\mathrm{m}^2$
magnetic fields	$B_{\mathrm{S}} \approx 3.6\,\mathrm{T}$ (non homogeneous)
	$B_{\mathrm{max}} = 6.032\,\mathrm{T}$
	$B_{\mathrm{A}} = 3.474 \cdot 10^{-4}\,\mathrm{T}$
tritium purity	$\epsilon_{\mathrm{T}} = 0.95$
background rate	$\dot{N}_{\mathrm{b}} = 0.01\,\mathrm{cps}$
detector efficiency	$\epsilon_{\mathrm{det}} = 0.9$
measurement interval	$[E_0 - 30\,\mathrm{eV}, E_0 + 5\,\mathrm{eV}]$
measurement time distribution	$t = 3\,\mathrm{years}$, reference setting
tritium endpoint	$E_0 = 18575\,\mathrm{eV}$
total systematical error	$\sigma_{\mathrm{sys}} = 0.017\,\mathrm{eV}^2$

simulation were used. These parameters include a realistic analyzing plane magnetic field with optimized transmission conditions and a central field of $B_{\mathrm{A}} = 3.474 \cdot 10^{-4}\,\mathrm{T}$ as well as a non-homogenous realistic source magnetic field in the WGTS (see section 6.5.1). The maximal magnetic field in the pinch magnet reaches a value of $B_{\mathrm{max}} = 6.032\,\mathrm{T}$ due to the additional influence of the detector magnet close by. For the measurement interval a default setting was chosen, which uses scanning potentials up to 30 eV below the endpoint E_0, as the Monte Carlo simulation of the response function was performed with surplus energies of up to $\approx 30\,\mathrm{eV}$. For all ensemble tests a sample size of 10^5 was used.

In the KATRIN design report [KAT05] the required precision of the analytical calculation of the response function and the maximal allowed induced systematic error on the neutrino mass are not described. The effects considered there were restricted to the magnetic field variation in the WGTS with a maximal systematic shift of $\sigma_{\mathrm{sys}} = 2 \cdot 10^{-3}\,\mathrm{eV}^2$ and the elastic scattering with a maximal systematic shift of $\sigma_{\mathrm{sys}} = 5 \cdot 10^{-3}\,\mathrm{eV}^2$.

Therefore, as in the case of the induced shift by the analyzing plane potential and magnetic field inhomogeneity, a maximal allowed shift for each of the individual contributions is defined. With the requirement that each systematic error should not increase the total systematic error budget of $\sigma_{\mathrm{sys}} = 17 \cdot 10^{-3}\,\mathrm{eV}^2$ by more than a fraction of 1 %, a maximal allowed shift of $|\Delta m_\nu^2| = 2.4 \cdot 10^{-3}\,\mathrm{eV}^2$ results, when assuming quadratic error summation.

6.5.1 Magnetic field inhomogeneities in the WGTS

The magnetic field in the 10 m long beam tube of the WGTS is not constant along the beam tube axis due to the three s.c. solenoid configuration, with small gaps between them. In these gaps the magnetic field drops slightly, although correction coils are installed to mitigate this effect (compare figure 6.3 (a) for the magnet geometry). Additionally, the magnetic field at the rear and front end parts of the source tube drops significantly. In figure 6.13 the magnetic field is plotted along the z-axis of the WGTS.

The consequences of this detailed source magnetic field are as follows. Electrons starting in a source magnetic field of B_{S} can only reach the detector if their maximal initial polar angle is below $\theta_{\mathrm{max}} = \arcsin(\sqrt{B_{\mathrm{S}}/B_{\mathrm{max}}})$, otherwise they are magnetically reflected at the

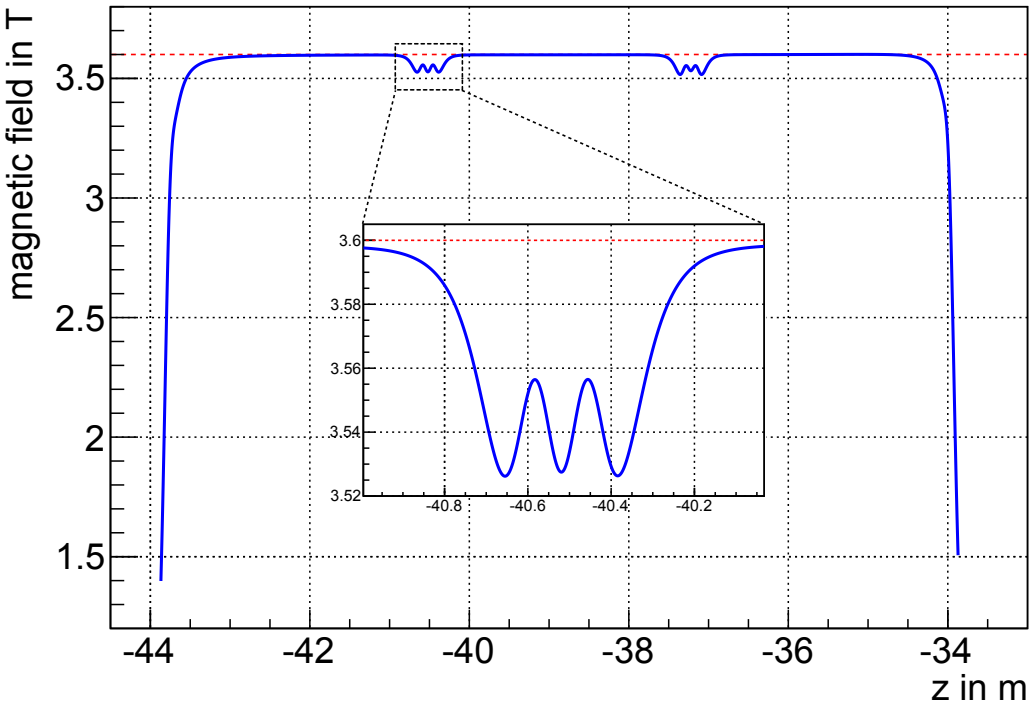

Figure 6.13: Magnetic field in the WGTS along the z-axis. The magnetic field is generated by 3 large s.c. solenoids, compare figure 6.3 (a). In the gaps between the magnet modules, the field drops slightly. On the front and rear end the field drops significantly due to the large gap to the next magnet of the DPS1. Additionally, the magnetic field increases slightly towards the front end. The red line marks a constant field of 3.6 T.

maximal magnetic field $B_{\max}$. The maximal initial polar angle is thus lower for particles starting in a region of the source with a reduced magnetic field. As a result of this different angular distribution, the scattering probabilities change slightly towards a higher probability for no scattering. Consequently, the response function is modified, mainly the important plateau region for surplus energies between 1 and 10 eV, corresponding to the particles which leave the source without undergoing an inelastic scattering process. As the tritium density is very low at the front and rear end parts of the WGTS (compare figure 6.5), only a small fraction of particles will start in this rather low magnetic field. However, the reduced magnetic field in the two gaps, where the tritium density is high, has a notable influence.

This magnetic field inhomogeneity can be accounted for in the analytical calculation of the response function by the concept of slicing the WGTS into many cylindrical segments, as introduced in section 3.4.1. For each slice, the response function can be calculated individually with the given local properties, such as the magnetic field and the scattering probabilities. By summing up the response functions over all individual slices, weighted by their local tritium column density ρd, the overall response function can be calculated

$$R(E, qU) = \frac{1}{\rho d_{\text{total}}} \sum_{i=1}^{N} \rho d_i \cdot R_i(E, qU) \tag{6.19}$$

with the number of used slices N.

A simplified model with an averaged source magnetic field consisting of a single slice only, as described in section 6.1, is clearly not sufficient. In figure 6.14 the plateau region for particles with surplus energies from $1 - 10$ eV of the Monte Carlo response function is plotted together with two analytically calculated response functions, based on a WGTS

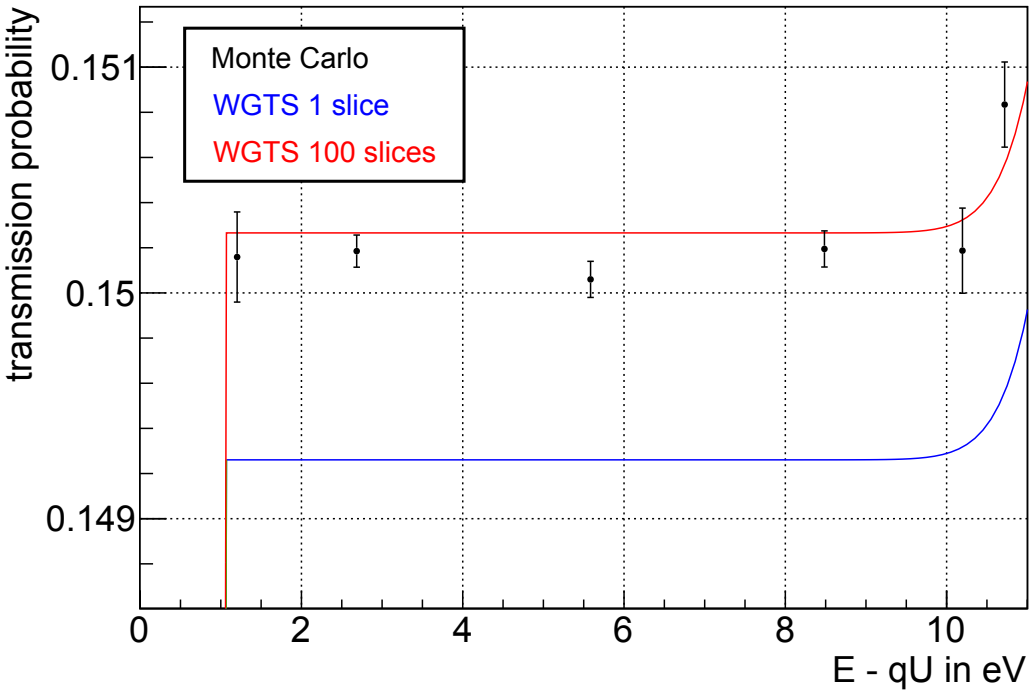

Figure 6.14: Plateau of the response function as obtained by the Monte Carlo simulation and for analytical calculations with different numbers of WGTS slices. A segmentation of the WGTS into multiple slices is necessary to account for the magnetic field inhomogeneities.

source profile segmented in 100 slices and one single slice. The model with a segmented WGTS of 100 slices describes the Monte Carlo data better than a simple single slices WGTS model. Increasing the number of slices to even higher number does not lead to further noticeable improvements, the only impact being an increase of computation time.

Systematic shift of the neutrino mass

To investigate the induced shift on the neutrino mass caused by the magnetic field inhomogeneities multiple ensemble tests were performed, with the WGTS being segmented into 100 or 200 slices in the simulation, where as in the analysis a reduced number of slices was used. The result is listed in table 6.5 and plotted in figure 6.15. If the simulated WGTS is segmented into 100 slices, an analysis with at least 10 segments is needed to fulfill the requirement of $|\Delta m_\nu^2| < 2.4 \cdot 10^{-3}\,\mathrm{eV}^2$. Using a number of least 50 is recommended to keep the induced statistical error as low as possible. Increasing the number of slices in the simulation even beyond a value of 200 has no additional benefit.

Requirement on the accuracy of the source magnetic field

In the Monte Carlo simulations as well as in the analytical calculations, identical magnetic field values for the WGTS were used. In the final experiment the magnetic field of the WGTS will only be known up to a yet unspecified accuracy, depending on the exact knowledge of the solenoid geometries, the field inducing currents and the calibrations of the corresponding power supplies. The influence of the accuracy can be tested by scaling the WGTS magnetic field with a relative offset, which is not being accounted for in the analysis.

The results of the performed ensemble tests are listed in table 6.6 and are plotted in figure 6.16. Even a relative offset of only 1 % leads to a systematic shift of $\Delta m_\nu^2 = -3.4 \cdot 10^{-3}\,\mathrm{eV}^2$ if unaccounted for in the analysis. The fit of a linear function reveals the maximal allowed relative deviation range of $[-8.7 \cdot 10^{-3}, 6.4 \cdot 10^{-3}]$.

Table 6.5: Systematic shifts on the neutrino mass due to an unaccounted for axial magnetic field inhomogeneity in the WGTS, which was divided into a different number of slices for the investigation. For all values the statistical sensitivity is assumed to be $1.66 \cdot 10^{-3}\,\mathrm{eV}^2$ and the error of Δm_ν^2 is $10^{-4}\,\mathrm{eV}^2$.

number of WGTS slices		$\Delta m_\nu^2 \cdot 10^{-3}$	sensitivity on m_ν
in the simulation	in the analysis	in eV^2	in meV (90 % C.L.)
100	1	-3.5	198.8
100	5	-3.2	198.6
100	10	-2.7	198.3
100	25	-1.6	197.9
100	50	-0.3	197.7
100	100	0.0	197.7
200	50	-0.3	197.7
200	100	<0.1	197.7

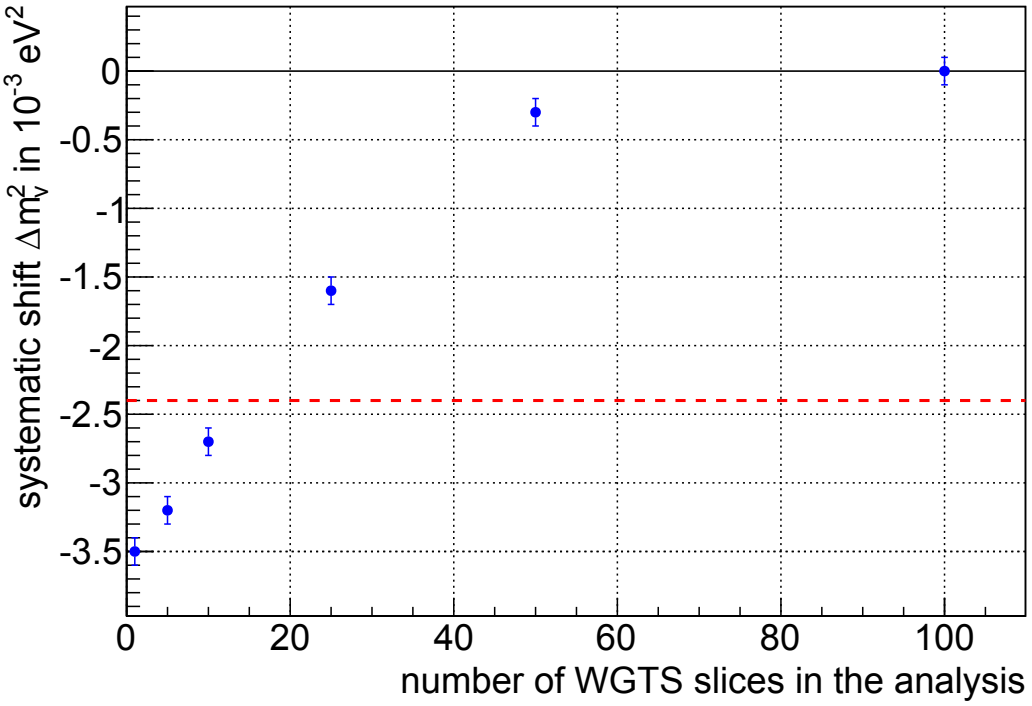

Figure 6.15: Systematic shifts on the neutrino mass due to an unaccounted for magnetic field inhomogeneity. The simulation of the WGTS was performed with 100 slices, while the number of slices was reduced in the analysis. The maximal allowed systematic shift of $\Delta m_\nu^2 = -2.4 \cdot 10^{-3}\,\mathrm{eV}^2$ is plotted as a dashed red line.

Table 6.6: Systematic shifts on the neutrino mass due to an unaccounted for relative magnetic field offset in the WGTS. For all values the statistical sensitivity is assumed to be $1.66 \cdot 10^{-3}\,\mathrm{eV}^2$ and the error of Δm_ν^2 is $10^{-4}\,\mathrm{eV}^2$.

unaccounted for relative source magnetic field offset	$\Delta m_\nu^2 \cdot 10^{-3}$ in eV^2	sensitivity on m_ν in meV (90 % C.L.)
0.100	-33.0	258.6
0.050	-16.3	217.7
0.020	-6.9	201.7
0.010	-3.4	198.7
0.008	-2.8	198.4
0.005	-1.9	198.0
-0.005	1.4	197.9
-0.008	2.2	198.1
-0.010	2.6	198.3
-0.020	5.6	200.4
-0.050	15.8	216.7
-0.100	30.6	225.4

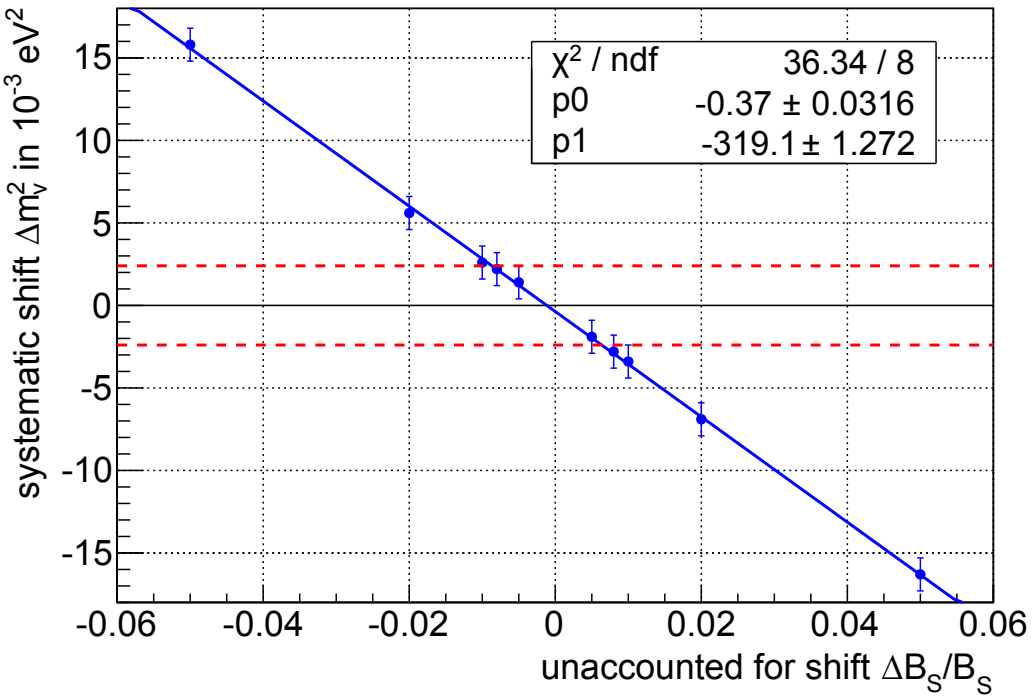

Figure 6.16: Systematic shifts on the neutrino mass due to an unaccounted for relative magnetic field offset. The dashed red lines show the maximal allowed shift of $|\Delta m_\nu^2| = 2.4 \cdot 10^{-3}\,\mathrm{eV}^2$. The fitted linear function reveals the allowed deviation range of $[-8.7 \cdot 10^{-3}, 6.4 \cdot 10^{-3}]$. The shown error bars are increased by a factor of 10 for better visibility.

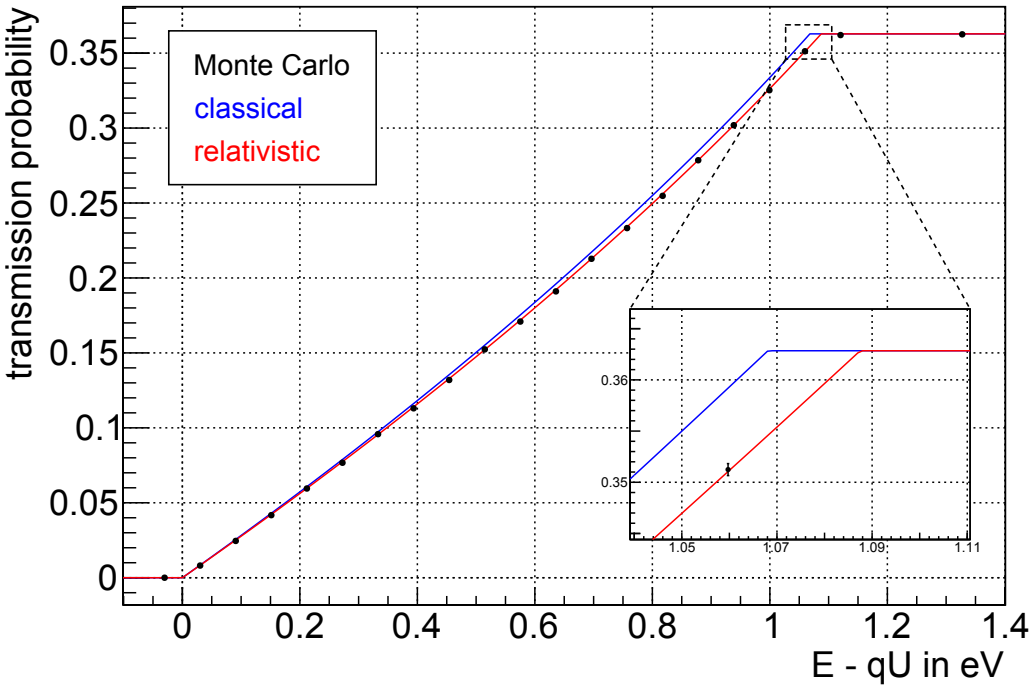

Figure 6.17: Monte Carlo simulation of the global transmission function for $5 \cdot 10^6$ started particles and its corresponding analytical calculation with and without relativistic corrections. The transmission function with relativistic corrections has an increased width of 1.8 % and clearly matches the Monte Carlo data.

6.5.2 Relativistic corrections

The analytical formula for the transmission function detailed in [KAT05] and described in section 6.1.1 is a non-relativistic approximation. With the relativistic Lorentz factor $\gamma = \frac{E}{mc^2} + 1$, a relativistic expression for the transmission function of an isotropic source can be stated as

$$T(E_\mathrm{S}, qU) = \begin{cases} 0 & E_\mathrm{S} - qU < 0 \\ \dfrac{1-\sqrt{1-\frac{E_\mathrm{S}-qU}{E_\mathrm{S}} \cdot \frac{B_\mathrm{S}}{B_\mathrm{A}} \cdot \frac{(\gamma_\mathrm{A}+1)}{(\gamma_\mathrm{S}+1)}}}{1-\sqrt{1-\frac{B_\mathrm{S}}{B_\mathrm{max}}}} & 0 \leq E_\mathrm{S} - qU \leq \Delta E \\ 1 & E_\mathrm{S} - qU > \Delta E \end{cases} \tag{6.20}$$

with the refined energy resolution $\Delta E = \frac{B_\mathrm{A}}{B_\mathrm{S}} E_\mathrm{S} \cdot \frac{(\gamma_\mathrm{S}+1)}{(\gamma_\mathrm{A}+1)}$. For electrons with an initial kinetic energy of $E_\mathrm{S} = 18575\,\mathrm{eV}$, the additional relativistic factor is $\frac{(\gamma_\mathrm{S}+1)}{(\gamma_\mathrm{A}+1)} = 1.018$, leading to a slight deterioration of the energy resolution by 1.8 %.

Figure 6.17 shows the results of a global Monte Carlo simulation for a total of $5{\cdot}10^6$ particles started in the WGTS. Energy loss effects such as scattering or synchrotron radiation were deactivated to obtain the pure transmission function. The corresponding analytical transmission functions are also plotted, with and without relativistic corrections. The deviation between the transmission functions for both cases is clearly visible. The Monte Carlo data match the analytical transmission function with relativistic corrections.

Systematic shift of the neutrino mass

If this relativistic correction to the transmission function is ignored in the analysis, a systematic error on the obtained neutrino mass is induced. The size of this effect has been

calculated by again running ensemble tests with a results of $\Delta m_\nu^2 = -7.6 \cdot 10^{-3}\,\mathrm{eV}^2$. As this is much higher than the stated requirement of $|\Delta m_\nu^2| < 2.4 \cdot 10^{-3}\,\mathrm{eV}^2$, this effect must not be ignored, especially since its implementation is rather straightforward.

6.5.3 Synchrotron radiation

From their point of origin in the WGTS to the analyzing plane, where the energy analysis takes place, electrons will lose up to 85 meV by synchrotron radiation, as shown in section 6.3.5. This synchrotron energy loss depends mainly on the polar angle θ of the electron. Due to the direct correlation of polar angle θ and synchrotron losses, the implication for the transmission function can be calculated. We recall that at the edge of the transmission function the required surplus energy of an electron to be transmitted directly depends on its initial polar angle. With a given relation between the initial polar angle of an electron and its synchrotron energy loss, which can be obtained from a Monte Carlo particle tracking simulation, a modification of the analytical calculation to include this effect is possible.

Additionally, the synchrotron energy loss does not only depend on the initial polar angle of the electron, but also on its axial position inside the WGTS. For large polar angles the difference between particles emitted at the rear and the front end of the WGTS beam tube is about 10 meV. Therefore, a two-dimensional distribution of the synchrotron energy loss $\Delta E_{\mathrm{sync}}(\theta, z)$ needs to be obtained. Due to the axial inhomogeneity of the magnetic field in the WGTS (see section 6.5.1), the initial polar angles need to be scaled to a constant magnetic field. For the following synchrotron energy loss investigations, a value of $B_{\mathrm{S}} = 3.6\,\mathrm{T}$ is used.

To obtain the required distributions of synchrotron energy losses, a particle tracking simulation was performed with particles starting at three distinct positions: the rear end, the front end and the center of the WGTS beam tube with initial polar angles from 0 to 51 ° for all cases. The electrons were tracked through the experiment up to the analyzing plane. The corresponding synchrotron energy losses are shown in figure 6.18. Using a Lagrangian interpolation with the given data, the synchrotron energy loss $\Delta E_{\mathrm{sync}}(\theta, z)$ for an electron starting inside the WGTS can be calculated.

For a given slice in the WGTS located at position z, the transmission function $T_{\mathrm{sync}}(E_{\mathrm{S}}, qU, z)$ can be calculated according to

$$T_{\mathrm{sync}}(E_{\mathrm{S}}, qU, z) = \begin{cases} 0 & E_{\mathrm{S}} - qU < 0 \\ T(E_{\mathrm{S}} - \Delta E_{\mathrm{sync}}(\theta_{\mathrm{tr}}, z), qU, z) & 0 \leq E_{\mathrm{S}} - qU \leq \Delta E \\ 1 & E_{\mathrm{S}} - qU > \Delta E \end{cases} \tag{6.21}$$

with the increased energy resolution $\Delta E = \frac{B_{\mathrm{A}}}{B_{\mathrm{S}}} E_{\mathrm{S}} \frac{(\gamma_{\mathrm{S}}+1)}{(\gamma_{\mathrm{A}}+1)} + \Delta E_{\mathrm{sync}}(\theta_{\mathrm{max}}, z)$ and the transmission polar angle

$$\theta_{\mathrm{tr}} = \arcsin\left(\sqrt{\frac{E_{\mathrm{S}} - \Delta E_{\mathrm{sync}}(\theta_{\mathrm{tr}}, z) - qU}{E_{\mathrm{S}}} \cdot \frac{B_{\mathrm{S}}}{B_{\mathrm{A}}} \cdot \frac{(\gamma_{\mathrm{A}}+1)}{(\gamma_{\mathrm{S}}+1)}}\right). \tag{6.22}$$

As the transmission polar angle θ_{tr} depends on the synchrotron energy loss ΔE_{sync} and vice versa, the equations need to be solved iteratively, starting with the calculation of θ_{tr} for $\Delta E_{\mathrm{sync}} = 0\,\mathrm{eV}$, which is already a good approximation. After a few iterations one achieves a typical precision for synchrotron energy losses of 10^{-3}.

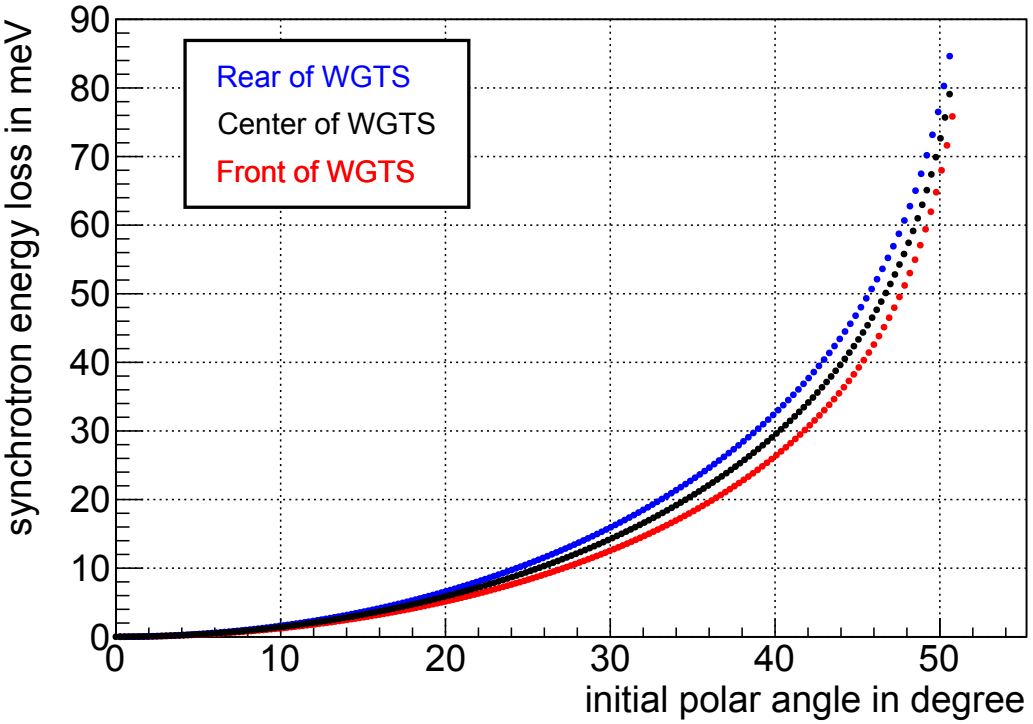

Figure 6.18: Synchrotron energy loss data for the analytical calculation of the transmission function plotted as function of the initial polar angle θ for different starting positions z inside the WGTS. The initial polar angles are normalized to a magnetic field of 3.6 T.

To compute $T(E, qU, z)$ transmission functions with arbitrary angular distributions can be used, such as the relativistic isotropic transmission function from section 6.5.2, or the transmission function with a modified angular distribution as will be introduced later in section 6.5.4.

Figure 6.19 shows the results of a global Monte Carlo simulation for a total of $5 \cdot 10^6$ particles generated in the WGTS according to the tritium gas density distribution. The effect of scattering was deactivated to obtain a transmission function which is only modified by synchrotron energy losses. The corresponding analytical transmission functions are also plotted again, with and without the modification introduced for synchrotron energy losses.

Due to the radiative energy losses, the transmission function is shifted to higher surplus energies, by 85 meV at the top and by 0 meV at the bottom, leading to an effective broadening of about 7 %. The agreement of the Monte Carlo data with the analytical calculation confirms the validity of the presented modification to the analytical calculation.

Systematic shift of the neutrino mass

If this correction for synchrotron losses to the transmission function is ignored in the final analysis, a systematic error on the neutrino mass is induced. The size of this effect was calculated by running ensemble tests to be $\Delta m_\nu^2 = -24.1 \cdot 10^{-3}\,\mathrm{eV}^2$, which would reduce the sensitivity on the neutrino mass to 235.9 meV (90 % C.L.). Therefore, this effect must be considered in the final neutrino mass analysis. Furthermore, also the accuracy of the synchrotron energy loss data used is important, which will be investigated in the next section.

Required accuracy of the synchrotron energy loss calculation

Radiative synchrotron energy loss can be obtained through high statistics particle tracking simulations incorporating the geometry and fields of magnets in the transport system,

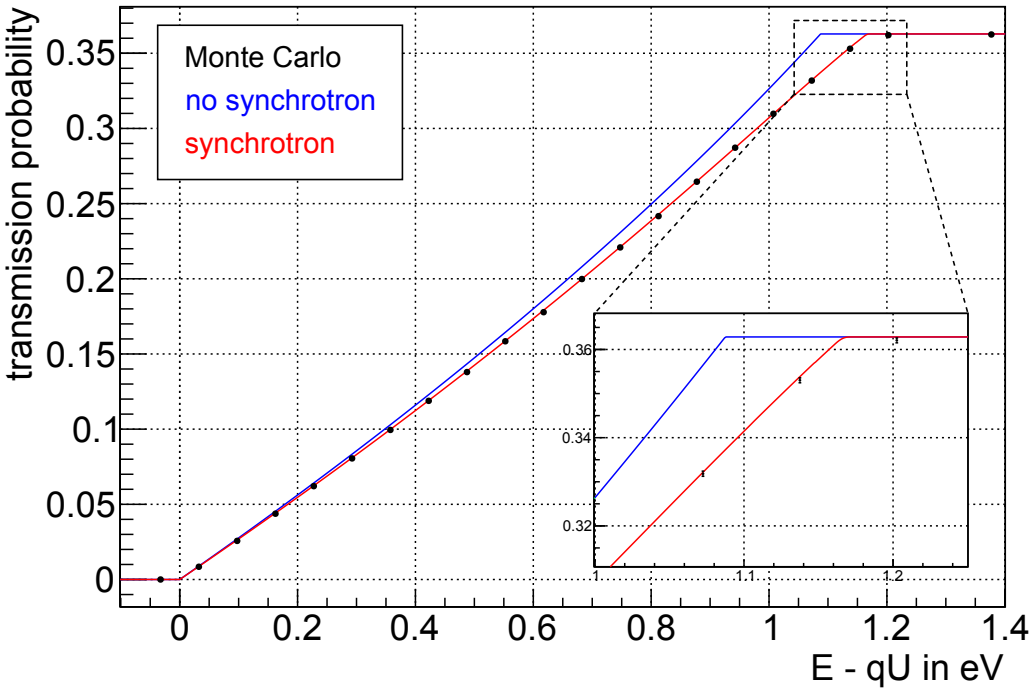

Figure 6.19: Monte Carlo simulation of the global transmission function including synchrotron energy loss for $5 \cdot 10^6$ generated particles. The analytically calculated transmission functions are also plotted, with and without the introduced modifications for synchrotron energy losses. The transmission function with synchrotron energy losses has a slightly larger width, increased by about 7 %, and matches the Monte Carlo data.

which are both only known with a limited accuracy. Consequently, also the synchrotron energy loss is only known with limited accuracy. The influence of this systematic error can be tested by artificially scaling the synchrotron energy loss with a relative factor which is assumed to be unaccounted for in the analysis.

The results of the ensemble tests performed are listed in table 6.7 and plotted in figure 6.20. The requirements on the accuracy are rather loose, as even an unaccounted for relative offset of 10 % will lead to a shift of only $\Delta m_\nu^2 = 2.1 \cdot 10^{-3}\,\mathrm{eV}^2$. The fit of a linear function reveals the maximal allowed relative deviation range of $[-11\,\%, 9\,\%]$. A calculation of synchrotron energy losses with an accuracy of better than 10 % can, however, easily be achieved using a sophisticated particle tracking framework such as KASSIOPEIA. In this respect the imperfect input parameters, such as the magnetic fields, have to be known with a much higher accuracy for other reasons (for example see section 6.5.1 for the requirement on the accuracy of the source magnetic field).

6.5.4 Modified angular distribution

Electrons generated from the β-decay of tritium are emitted isotropically inside the WGTS[2]. Depending on their polar angle θ, electrons close to E_0 will possess a certain probability $P_i(\theta)$ to leave the WGTS while experience an i-fold inelastic scattering. Electrons starting with a small polar angle will have a higher chance of leaving the source region without experiencing inelastic scattering than electrons starting with a large polar angle. Therefore, the angular distribution of electrons having undergone a specific number i of scatterings is no longer isotropic when entering the MAC-E filter for energy analysis. Consequently, the transmission function specified for an isotropic scenario, which was derived in section

[2] A tiny deviation is expected due to polarization of tritium molecules because of their spin in the magnetic field and the parity violation of the weak interaction, resulting in an error in the order of 10^{-7} [Ven03].

Table 6.7: Systematic shifts on the neutrino mass due to unaccounted for relative synchrotron energy losses. For all values the statistical sensitivity is assumed to be $1.66 \cdot 10^{-3}\,\mathrm{eV}^2$ and the error of Δm_ν^2 is $10^{-4}\,\mathrm{eV}^2$.

unaccounted for relative synchrotron energy loss offset	$\Delta m_\nu^2 \cdot 10^{-3}$ in eV^2	sensitivity on m_ν in meV (90 % C.L.)
-0.50	11.9	209.1
-0.20	4.5	195.5
-0.10	2.1	198.1
-0.05	0.9	197.8
-0.01	0.2	197.7
0.01	-0.5	197.7
0.05	-1.2	197.8
0.10	-2.6	198.3
0.20	-5.3	200.1
0.50	-12.7	210.5

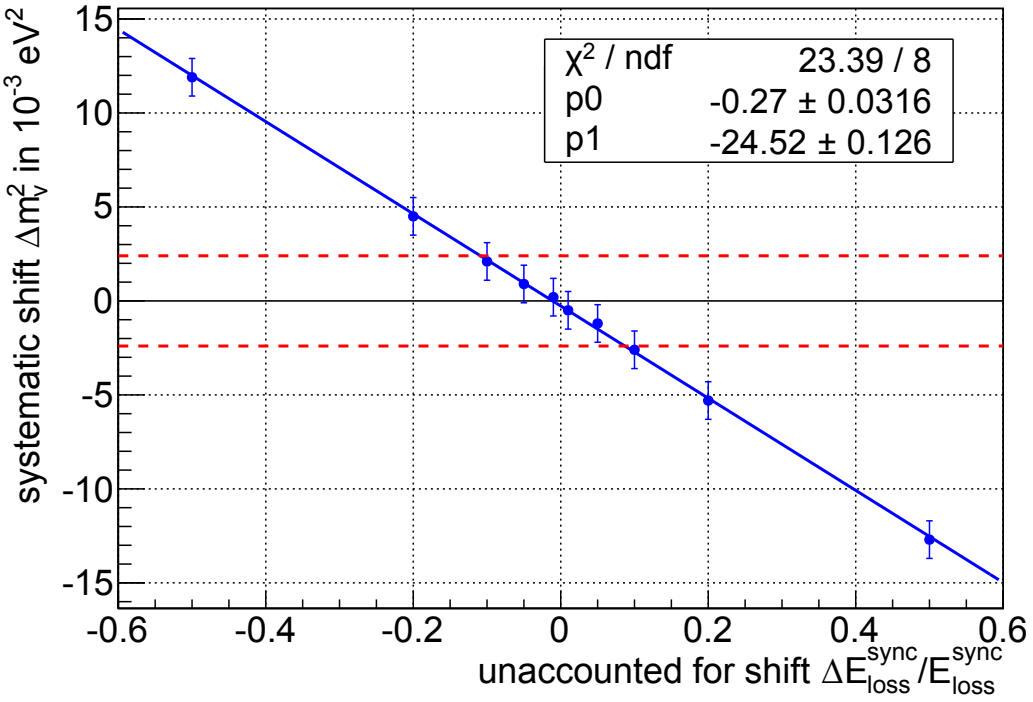

Figure 6.20: Systematic shifts on the neutrino mass due to an unaccounted for relative synchrotron energy loss offset. The dashed red lines show the maximal allowed shift of $|\Delta m_\nu^2| = 2.4 \cdot 10^{-3}\,\mathrm{eV}^2$. The fitted linear function reveals the allowed deviation range of $[-11\,\%, 9\,\%]$. The shown error bars are increased by a factor of 10 for better visibility.

6.1.1, is no longer valid. For each distribution of electrons experiencing exactly i-fold inelastic scattering processes in the WGTS, a separate transmission function $T_i^\star(E, qU)$ needs to be applied, which will be derived in the following. This investigation will not include angular changes caused by scattering processes, which will be discussed separately in section 6.5.5. This description is also valid for the transmission function of unscattered electrons $T_0^\star(E, qU)$, where the described effect actually has the largest impact.

To obtain the angular distribution of electrons after experiencing i-fold inelastic scatterings in the source, the original isotropic distribution $\omega(\theta) = \sin(\theta)$ needs to be weighted by the individual scattering probabilities $P_i(\theta)$

$$\omega_i(\theta) = \sin(\theta) \cdot P_i(\theta), \tag{6.23}$$

which can be entered into the general equation of the transmission function 5.5 to now obtain the transmission function as a function of the starting energy E_S, the spectrometer potential U and the number of experienced inelastic scatterings i:

$$T_i^\star(E_\mathrm{S}, qU) = \frac{1}{N} \int_{\theta=0}^{\theta_\mathrm{tr}(E_\mathrm{S},qU)} \sin(\theta) \cdot P_i(\theta) \mathrm{d}\theta, \tag{6.24}$$

with the normalization constant $N = \int_{\theta=0}^{\theta_\mathrm{max}} \sin(\theta) \cdot P_i(\theta) \mathrm{d}\theta$. Using the relation of equation 6.14, the normalization constant can be written as $N = (1 - \cos(\theta_\mathrm{max})) \cdot \overline{P}_i$, leading to

$$T_i^\star(E_\mathrm{S}, qU) = \int_{\theta=0}^{\theta_\mathrm{tr}(E_\mathrm{S},qU)} \frac{\sin(\theta) \cdot P_i(\theta)}{(1 - \cos(\theta_\mathrm{max})) \cdot \overline{P}_i} \mathrm{d}\theta \tag{6.25}$$

with the transmission polar angle

$$\theta_\mathrm{tr}(E_\mathrm{S}, qU) = \arcsin\left(\sqrt{\frac{E_\mathrm{S} - qU}{E_\mathrm{S}} \cdot \frac{B_\mathrm{S}}{B_\mathrm{A}} \cdot \frac{(\gamma_\mathrm{A} + 1)}{(\gamma_\mathrm{S} + 1)}} \right). \tag{6.26}$$

To prevent unphysical values, caused by the energy difference in the square root of equation 6.25, a case differentiation such as for an isotropic transmission function has to be done:

$$T_i^\star(E_\mathrm{S}, qU) = \begin{cases} 0 & E_\mathrm{S} - qU < 0 \\ \int_{\theta=0}^{\theta_\mathrm{tr}(E_\mathrm{S},qU)} \frac{\sin(\theta) \cdot P_i(\theta)}{(1 - \cos(\theta_\mathrm{max})) \cdot \overline{P}_i} \mathrm{d}\theta & 0 \leq E_\mathrm{S} - qU \leq \Delta E \\ 1 & E_\mathrm{S} - qU > \Delta E \end{cases} \tag{6.27}$$

Although not stated explicitly for reasons of simplicity, the transmission function $T_i^\star(E_\mathrm{S}, qU)$ also depends on the axial position z of the electrons generated inside the source, as evidently the single and the mean scattering probabilities $P_i(\theta)$ and $\overline{P}_i$ both depend on z.

Figure 6.21 shows calculations of the derived transmission functions $T_i^\star(E_\mathrm{S}, qU)$ for i-fold scattering from 0 to 3. When investigating response functions with a maximal surplus

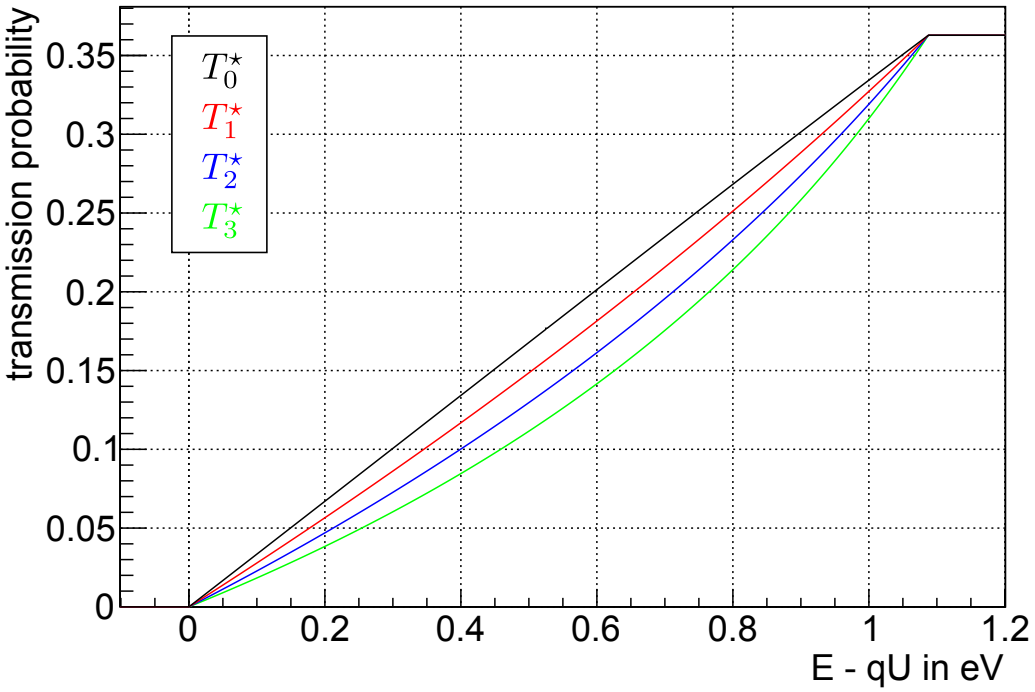

Figure 6.21: Transmission functions with modified angular distribution $T_i^\star$ with i-fold scattering from 0 to 3. The width of the transmission functions does not change due to the modified angular distribution, only the slope.

energy of 30 eV, only electrons experiencing maximal 3-fold inelastic scattering need to be considered, as each scattering process results in a minimal energy loss of 10 eV. The shape of the individual transmission functions clearly differs, due to the different angular distributions. Interestingly, the transmission function of unscattered electrons $T_0^\star$ now resembles a nearly straight line.

Figure 6.22 shows the result of a response function based on Monte Carlo simulation for a surplus energy of up to 1.2 eV with activated inelastic scattering, but without synchrotron radiation. The corresponding analytic response function, incorporating the modified transmission function $T_0^\star(E, qU)$, is also plotted, as well the one using the default transmission function for an isotropic distribution $T(E, qU)$. The plot clearly shows that Monte Carlo data is described by the modified transmission function correctly.

For unscattered electrons, corresponding to the transmission function visible at a surplus energy of up to 1.1 eV, the relative difference between the default isotropic transmission function T and the one with modified angular distribution $T_0^\star$ is up to 15 %. For higher surplus energies, however, corresponding to the transmission functions $T_1^\star$, $T_2^\star$ and $T_3^\star$, the effect is largely suppressed by the rather large energy losses due to inelastic scattering. The relative difference for the case where only the isotropic transmission function T for scattered electrons is used, is less than 10^{-3}, as plotted in figure 6.23.

Systematic shift of the neutrino mass

Should this modified calculation of the transmission function be ignored in the analysis, a systematic error on the derived neutrino mass is induced. By running ensemble tests the size of this effect was determined to be $\Delta m_\nu^2 = 11.9 \cdot 10^{-3}\,\mathrm{eV}^2$, which would lead to a diminished sensitivity on the neutrino mass of 212.8 meV (90 % C.L.). If only $T_0^\star$ is considered in the analysis, being by far the largest influence, and the remaining response function is calculated using the simple isotropic transmission function T, the resulting systematic shift on the neutrino mass is $\Delta m_\nu^2 = -2.3 \cdot 10^{-3}\,\mathrm{eV}^2$. This is just below the

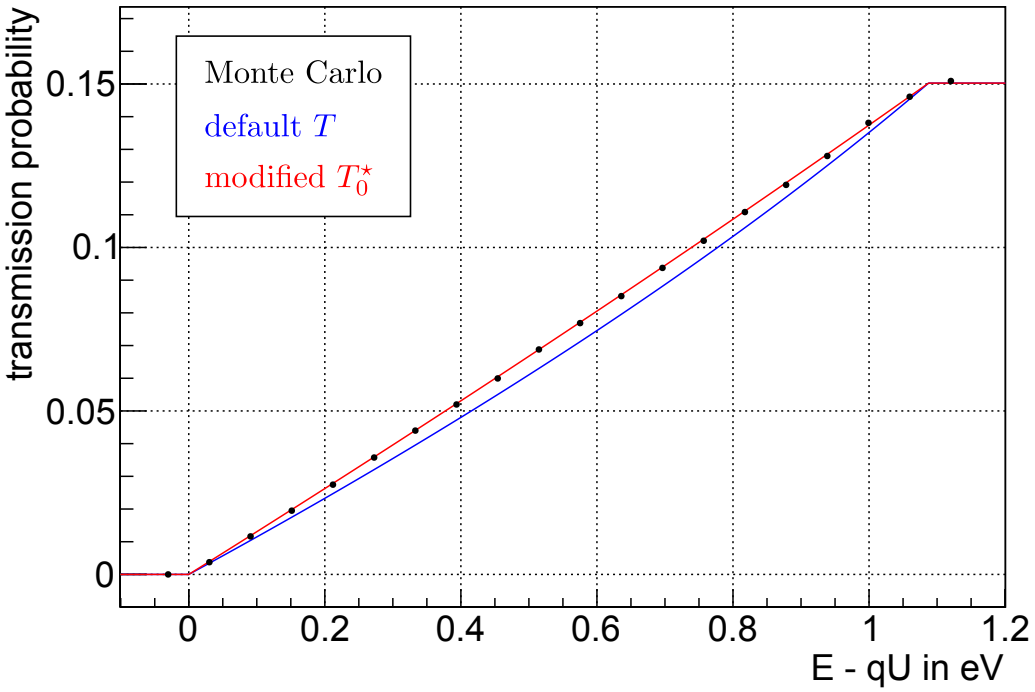

Figure 6.22: Monte Carlo simulation of the response function up to a surplus energy of 1.2 eV for $5 \cdot 10^6$ particles using inelastic scattering, but no synchrotron radiation. Additionally the modified transmission function for unscattered electrons $T_0^\star$ is plotted, as well as the default transmission function for an isotropic source T. The Monte Carlo data are best described by the derived transmission function for the modified angular distribution $T_0^\star$.

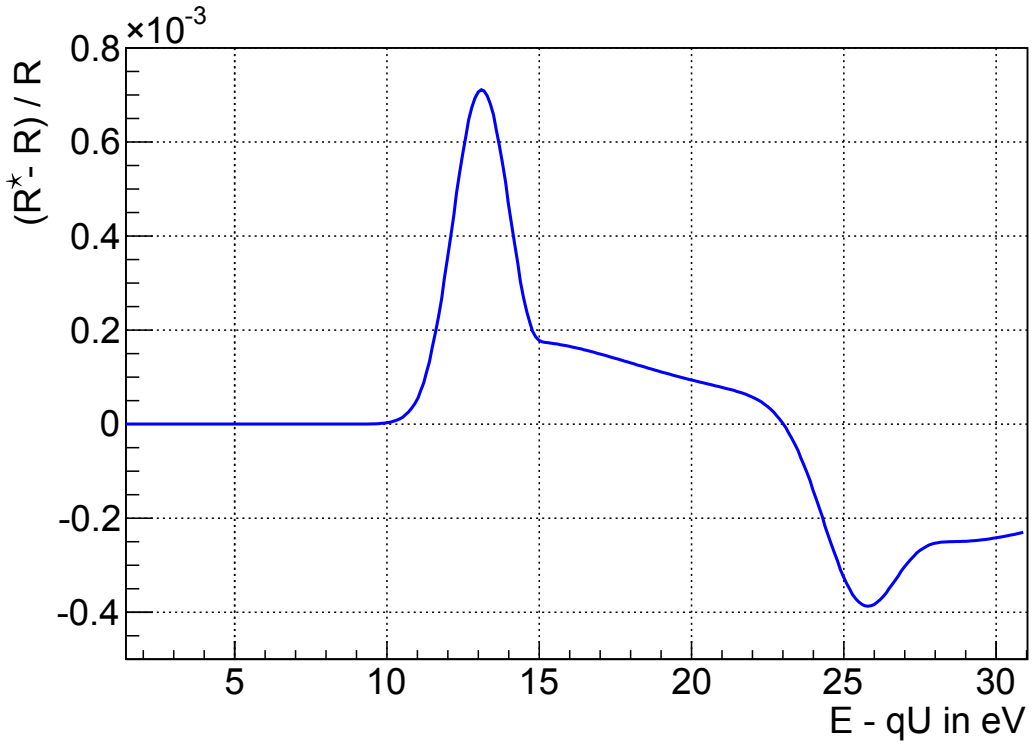

Figure 6.23: Relative difference between the response function based on a transmission functions with modified angular distributions $T_i^\star$ and the default transmission T. The difference is plotted for a surplus energy above 1.5 eV, thus showing only the influence of $T_1^\star$, $T_2^\star$ and $T_3^\star$, with the by far largest deviation caused by $T_0^\star$ shown separately in figure 6.22.

required limit of $|\Delta m_\nu^2| = 2.4 \cdot 10^{-3}\,\mathrm{eV}^2$, and is therefore a valid approximation. Its use may be advantageous in some cases, as the additional calculation of $T_i^\star$ for $i > 0$ slows down the computation significantly. However, it is still recommended to use the modified transmission functions for all relevant values of i, in order not to introduce additional systematic errors on the neutrino mass.

A similar investigation for the modified angular distribution was performed in [Tit04] and [Zie13], resulting in comparable values.

6.5.5 Angular changes by inelastic scattering

Each time an electron scatters inelastically off a tritium molecule in the source regime its polar angle θ will change by $\Delta\theta$. As the mean angular change of inelastic scattering in case of energy losses below 30 eV is 0.61 ° only, the impact on the shape of the response function is expected to be small. Furthermore, as the electrons up to a surplus energy of about 10 eV will leave the source without inelastic scattering, the effect of angular changes will only modify the response function for surplus energies larger than 10 eV.

The effect of angular changes through scattering can be included by modifying the calculation of the scattering probabilities. Thereby, the modified angular distribution is automatically included, if the transmission function $T^\star$ as detailed in the previous section is used. While P_0 is not altered, the probabilities for an electron to leave the source experiencing i-fold scattering processes need to be modified, as the polar angle is changed after the first scattering process, which will increase or decrease the remaining path length through the WGTS.

The default scattering probability calculation using a Poisson distribution was presented in section 6.1.3 for electrons starting in the source with initial polar angle θ, and a remaining column density of ρd to propagate through before leaving the WGTS as

$$P_i(\theta, \rho d) = \frac{(\rho d \cdot \sigma_{\mathrm{inel}})^i}{\cos(\theta)^i \cdot i!} \exp^{-\frac{\rho d \cdot \sigma_{\mathrm{inel}}}{\cos(\theta)}} . \tag{6.28}$$

To include the angular change $\Delta\theta$ during each scattering process, the remaining column density to be traversed by the electrons has to be divided into a number of n equal segments. For each segment, the scattering probabilities can then be calculated. For the segments which have been passed after a scattering has occurred, a modified polar angle will be used. The final result for the overall path length can be obtained by making use of combinatorics. A detailed derivation of the formulas to calculate the modified scattering probabilities $P_i^\star(\theta, \rho d)$ can be found in appendix C.

For a fixed angular change of $\Delta\theta$ the scattering probabilities $P_i^\star(\theta, \rho d)$ can be calculated recursively by

$$P_i^\star(\theta, \rho d) = P_1(\theta, \frac{\rho d}{n}) \cdot \sum_{k=1}^{n} P_0(\theta, \frac{\rho d}{n}(k-1)) \cdot P_{i-1}^\star(\theta + \Delta\theta, \rho d(1 - \frac{k}{n})), \tag{6.29}$$

which is only valid for large n. To complete the recursive description, $P_0^\star(\theta, \rho d)$ needs to be defined as

$$P_0^\star(\theta, \rho d) = P_0(\theta, \rho d) \cdot \Theta(\theta_{\max} - \theta) \tag{6.30}$$

with the Heaviside step function $\Theta(\theta_{\max} - \theta)$ accounting for particles with polar angles larger than $\theta_{\max}$, which have a zero probability of reaching the detector. For a given slice

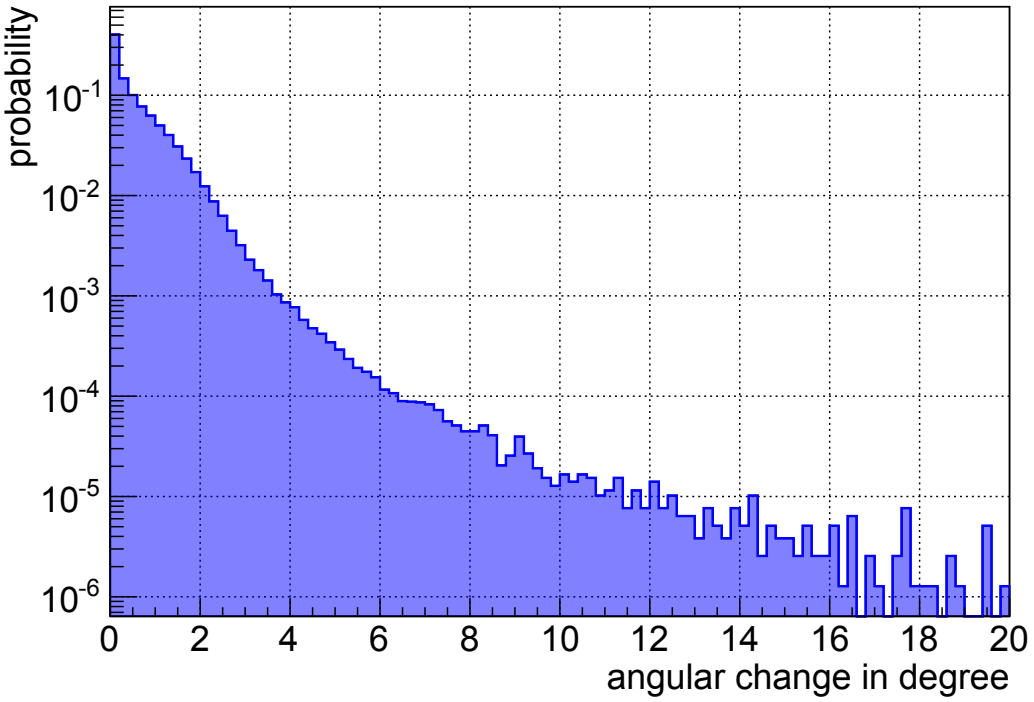

Figure 6.24: Angular change distribution of inelastic scattering for energy losses below 30 eV plotted in a logarithmic scale. The mean value of the distribution is 0.61 °.

in the WGTS and the specific angular change $\Delta\theta$ the mean scattering probabilities can be calculated by integrating over the forward angular distribution

$$\overline{P}_i^{\star}(\Delta\theta) = \int_{\theta=0}^{\pi/2} \sin(\theta) \cdot P_i^{\star}(\theta, \rho d)\, \mathrm{d}\theta. \tag{6.31}$$

Since also some of the electrons starting with a polar angle larger than $\theta_{\max}$ can reach the detector, if their polar angle is sufficiently decreased by scattering processes, the upper integration bound has been fixed at $\pi/2$ here to include all electrons starting in forward direction.

Finally, the mean scattering probabilities for a normalized distribution of angular changes $\omega(\Delta\theta)$ have to be obtained. A weighted sum of the individual scattering probabilities with the angular distribution can be expressed with the following integral:

$$\overline{P}_i^{\star} = \int_{\Delta\theta=0}^{\Delta\theta_{\max}} \frac{(\overline{P}_i^{\star}(\Delta\theta) + \overline{P}_i^{\star}(-\Delta\theta))}{2} \cdot \omega(\Delta\theta)\mathrm{d}\Delta\theta, \tag{6.32}$$

which also considers the fact that the particle's polar angle may either increase or decrease decrease by an angular change $\Delta\theta$.

The distribution $\omega(\Delta\theta)$ can again be obtained from KASSIOPEIA and is visualized in figure 6.24 for energy losses below 30 eV. The mean value of the distribution is 0.61 °, as large angular changes are very unlikely.

The probability for an electron to increase its polar angle via scattering by a specific amount is as large as the probability to decrease its polar angle by exact the same amount. Therefore, the resulting effect on the scattering probabilities is expected to be small and

Table 6.8: Effect of angular changes on the scattering probabilities P_1 and P_2 for an angular change between 0 and 10 ° at each inelastic scattering process. The scattering probabilities using the old calculations are listed also on the top line, and are used as reference values for the relative deviation calculation. The scattering probabilities for a realistic distribution of angular changes, as presented in figure 6.24 with a mean value of 0.61 °, are also listed. For each calculation the shift on the obtained squared neutrino mass Δm_ν^2 is given for the case where the angular change is ignored in the analysis. The error of Δm_ν^2 is $10^{-4}\,\mathrm{eV}^2$.

angular change $\Delta\theta$ in °	scat. prob. P_1	rel. deviation in 10^{-3}	scat. prob. P_2	rel. deviation in 10^{-3}	$\Delta m_\nu^2 \cdot 10^{-3}$ in eV^2
off	0.2930	0.0	0.1669	0.0	0.0
0	0.2930	0.0	0.1669	0.0	0.0
1	0.2929	-0.3	0.1668	-0.5	0.1
2	0.2928	-0.7	0.1666	-1.8	1.2
3	0.2926	-1.4	0.1662	-4.2	2.6
4	0.2923	-2.4	0.1656	-7.8	4.7
5	0.2920	-3.4	0.1648	-12.6	7.2
10	0.2889	-14.0	0.1582	-52.1	29.1
realistic	0.2929	-0.3	0.1668	-0.6	0.2

only caused by the asymmetry in the polar angle distribution. Due to the recursive calculation of the modified scattering probabilities $P_i^\star$ and the required large number n of segmentations ($n = 5000$ was used), the computation time for higher values of i grows exponentially. Therefore, only P_1 and P_2 were calculated with the presented formulas, while P_3 and higher were calculated with the default Poisson formula. This is a valid approximation, as for the response function with a surplus energy of up to 30 eV only P_0, P_1 and P_2 are relevant, as previously motivated.

Using different values of $\Delta\theta$ from 0 ° to 10 °, the mean scattering probabilities for the WGTS can be calculated. The results are presented in table 6.8 together with their relative differences to the scattering probabilities obtained with the former calculation method. Only P_1 and P_2 are listed, as P_0 is not affected by the angular changes. The scattering probabilities for $\Delta\theta = 0\,°$ agree perfectly with the values obtained from the default calculation, which is a good test for the derived formulas. As expected, the resulting change in the scattering probabilities is small. Even for an angular change of $\Delta\theta = 3\,°$ the relative deviation is only of the order of a few times 10^{-3}. Finally, a realistic distribution of angular changes as displayed in figure 6.24 was employed for the calculation of the scattering probabilities. The resulting relative deviations in P_1 and P_2 are only in the order of 10^{-4}.

The resulting effect on the response function is shown in figure 6.25 for the relative difference between a response function using no angular changes, and a response function based on the realistic angular distribution shown in figure 6.24. As expected, there is only an effect for electrons with a surplus energy above 10 eV, as electrons with less surplus energy will leave the WGTS unscattered. However, the effects observed are very small, being of the order of 10^{-4}. Therefore, no comparison with the data from the Monte Carlo simulation is displayed, as this tiny difference is within the statistical uncertainty related to the finite number of simulated electrons.

Systematic shift of the neutrino mass

The systematic shift on the obtained neutrino mass, if an angular change $\Delta\theta$ occurring at scattering is ignored in the analysis, has been outlined in table 6.8. Only if the angular

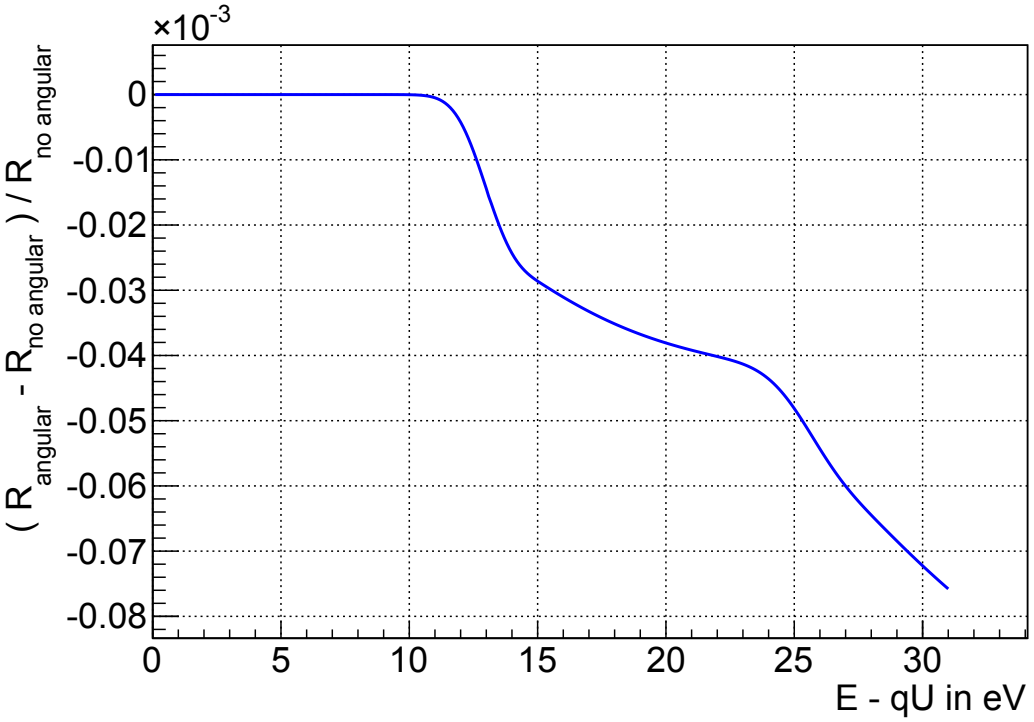

Figure 6.25: Relative difference of response functions which includes the angular changes during inelastic scattering processes, compared to a case of vanishing angular changes. There is only an effect for electrons with a surplus energy above 10 eV, as electrons with smaller surplus energies will leave the WGTS without scattering.

change at scattering were above 3 °, the induced systematic shift on the obtained neutrino mass would be relevant. For the realistic distribution of angular changes the resulting shift on the obtained neutrino mass is completely negligible. Therefore, the effects of angular changes due to inelastic scattering do not have to be considered explicitly in the final neutrino mass analysis.

6.5.6 Energy losses and angular changes by elastic scattering

In addition to the dominant process of inelastic scattering, there exists also the elastic interaction component, as discussed in section 6.3.4. Due to its small cross section of $\sigma_{\mathrm{el}} = 0.291 \cdot 10^{-18}\,\mathrm{cm}^2$ for electrons of $E = 18.6\,\mathrm{keV}$ compared to the inelastic cross section of $\sigma_{\mathrm{inel}} = 3.456 \cdot 10^{-18}\,\mathrm{cm}^2$, elastic scattering processes only play a minor role. Nevertheless, the effect of the corresponding energy losses and angular changes on the response function will be detailed in the following.

Energy losses by elastic scattering

The energy loss distribution resulting from elastic scattering processes can be computed with KASSIOPEIA, the results are presented in figure 6.26. In contrast to the inelastic component, the energy loss here is very small, with a mean value of only 45 meV.

The elastic energy loss function can be included in the response function calculation by combining it with the inelastic component to get a total energy loss function of

$$f(\epsilon)_{\mathrm{total}} = \frac{\sigma_{\mathrm{inel}}}{\sigma_{\mathrm{total}}} \cdot f(\epsilon)_{\mathrm{inel}} + \frac{\sigma_{\mathrm{el}}}{\sigma_{\mathrm{total}}} \cdot f(\epsilon)_{\mathrm{el}}, \tag{6.33}$$

with $\sigma_{\mathrm{total}} = \sigma_{\mathrm{el}} + \sigma_{\mathrm{inel}} = 3.747 \cdot 10^{-18}\,\mathrm{cm}^2$.

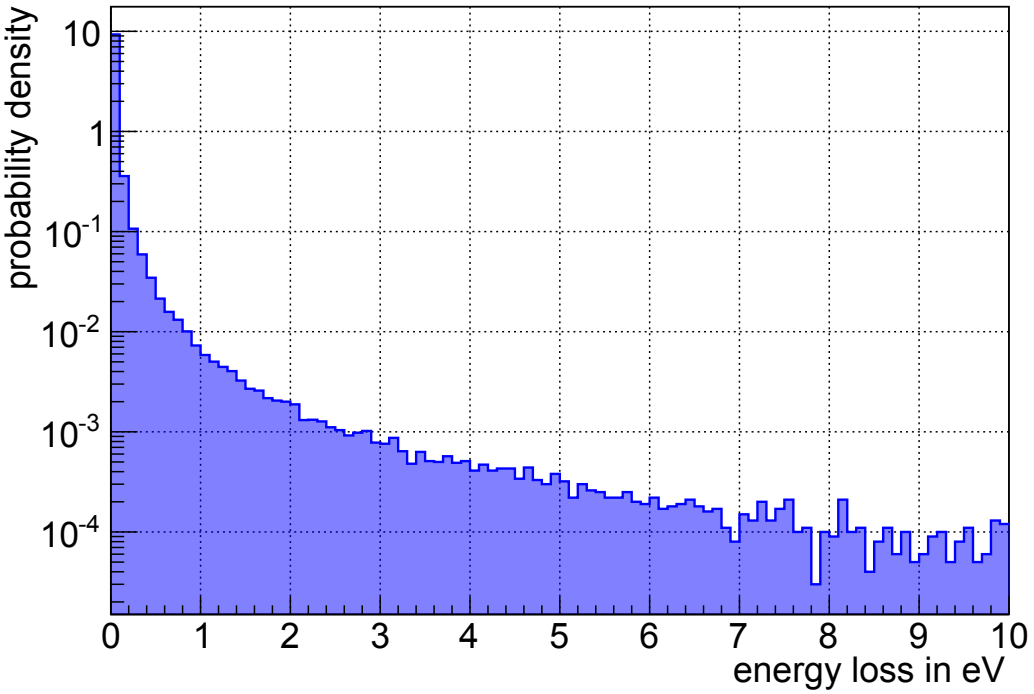

Figure 6.26: Elastic scattering energy loss in a logarithmic scale for electrons with a kinetic energy of 18575 eV as computed with KASSIOPEIA. The mean energy loss is 45 meV.

Figure 6.27 shows the response function when including energy losses by elastic scattering compared to the case where only inelastic energy losses are considered. The most significant change is observed in the region of the transmission edge and the plateau. Due to the elastic energy losses of only a few meV, the transmission width increases slightly and the transition to the formerly constant plateau is smeared out.

The relative difference between the response function both with and without elastic energy losses is plotted in figure 6.28. While for most of the region the relative difference is less than 10^{-3}, in the region of the transmission function the relative difference is most significant with values up to 6 % at the lower end of the transmission edge.

Angular changes by elastic scattering

While the effect of angular changes due to inelastic scattering can be ignored in the analysis, as shown in the last section, angular changes caused by elastic scattering will have a larger impact on the response function. This is due to larger angular changes during elastic scattering processes, with a mean angular change of 2.95 °. The distribution of angular changes during elastic scattering as obtained with KASSIOPEIA is plotted in figure 6.29.

As for the energy loss function, a combined angular change distribution $\omega(\Delta\theta)_{\text{total}}$ can be obtained, when adding the elastic and inelastic component weighted by their relative cross section contribution

$$\omega(\Delta\theta)_{\text{total}} = \frac{\sigma_{\text{inel}}}{\sigma_{\text{total}}} \cdot \omega(\Delta\theta)_{\text{inel}} + \frac{\sigma_{\text{el}}}{\sigma_{\text{total}}} \cdot \omega(\Delta\theta)_{\text{el}}. \tag{6.34}$$

This allows to include elastic angular changes in the response function calculation by modifying the scattering probabilities, as described in the previous section. As the correlation between a specific energy loss and the corresponding angular change is not considered, the described method is only an approximation. The mean angular change for the combined

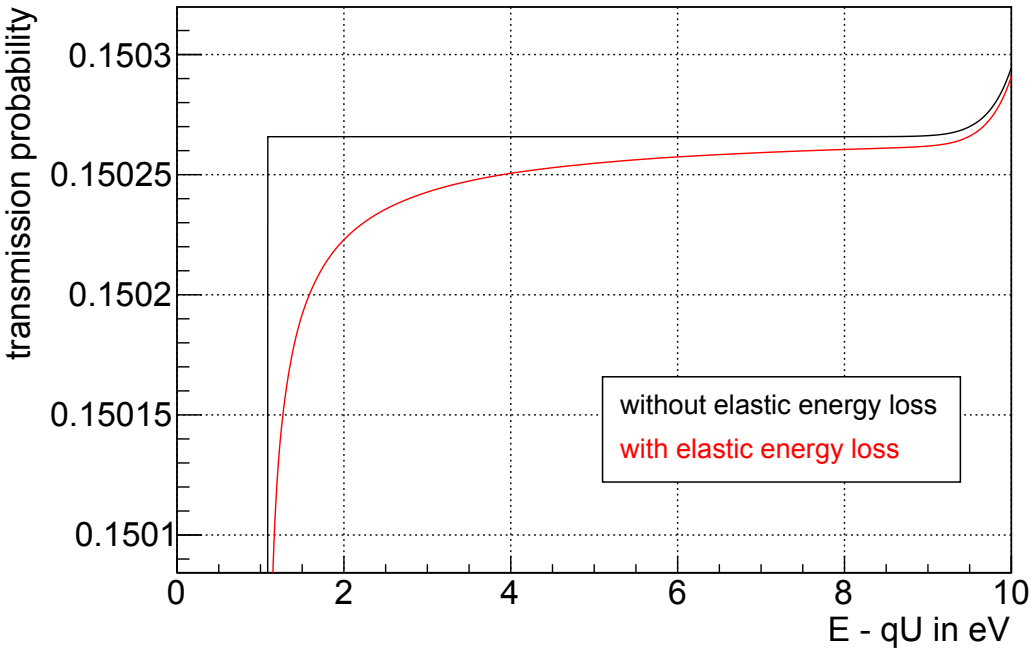

(a) Plateau region

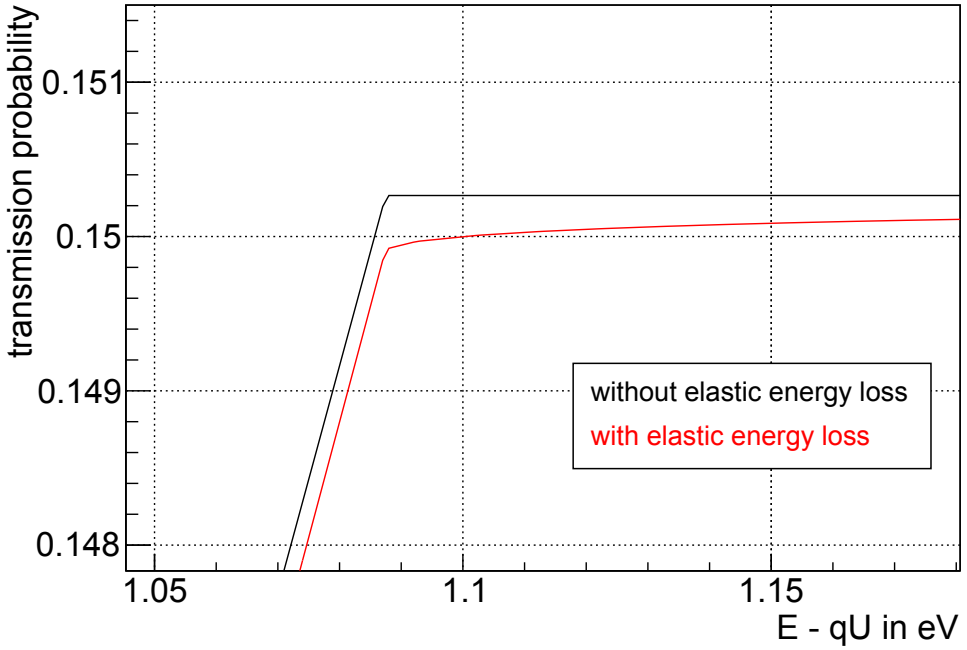

(b) Upper end of transmission edge

Figure 6.27: Response function with (red) and without (black) elastic energy losses in the region of the plateau (a) and at the upper end of the transmission edge (b). Due to elastic energy losses the transmission function gets broader and the transition to the plateau is smeared out.

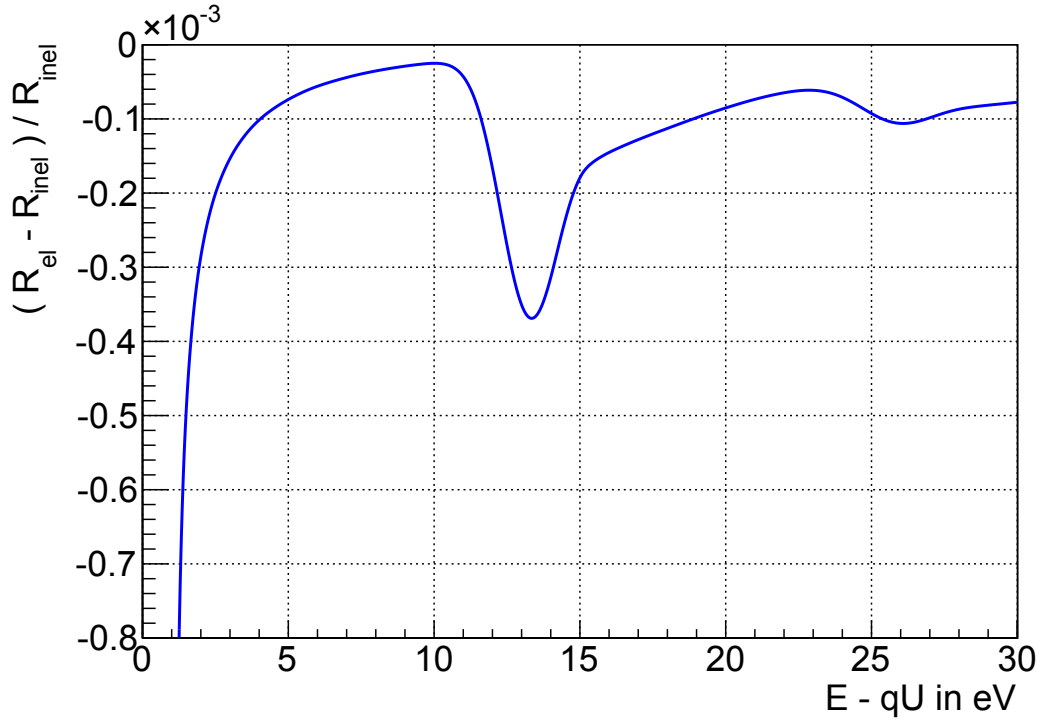

(a) Response function

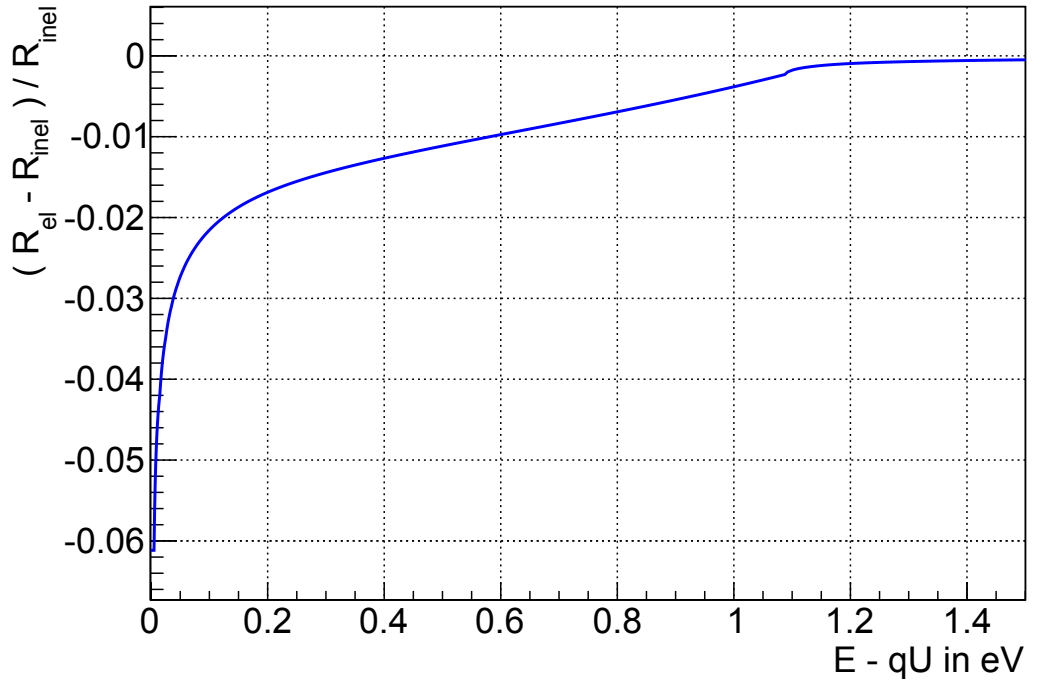

(b) Transmission region

Figure 6.28: Relative difference of the response function with elastic energy losses to the one without. For most of response function (a) the relative difference is less than 10^{-3}. For the region of the transmission function (b), the difference becomes significant with deviations up to 6%.

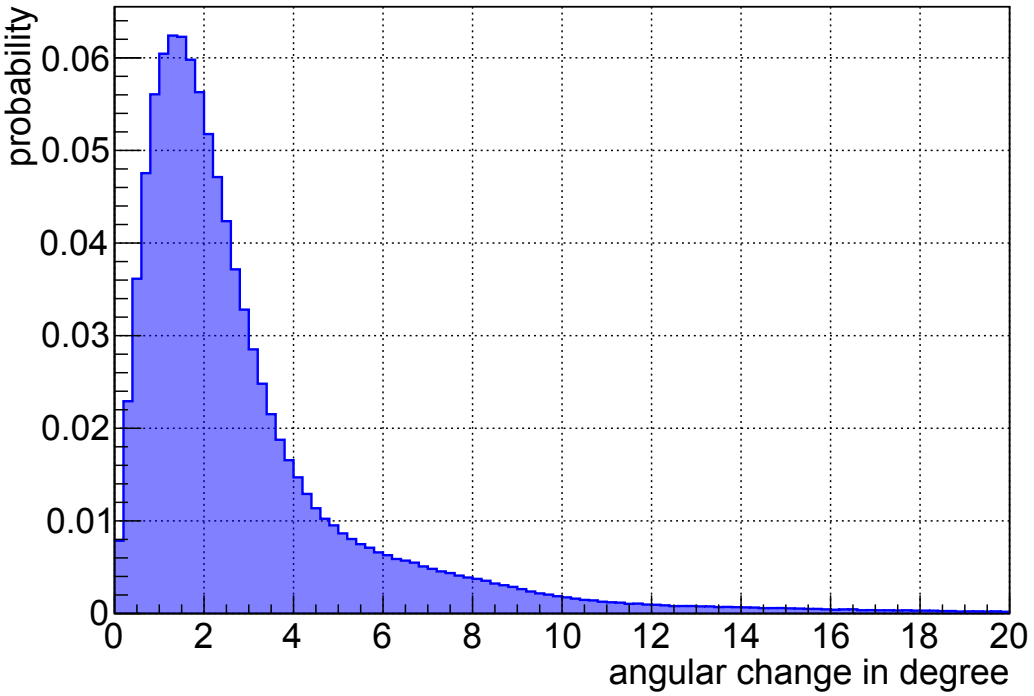

Figure 6.29: Angular change distribution of elastic scattering as obtained with KASSIOPEIA. The mean value of the distribution is 2.95 °.

distribution is 0.82 °, which is only slightly larger than for the angular change distribution when only taking into account inelastic scattering of 0.61 °

The changes in the scattering probabilities P_1 and P_2 for fixed angular changes are comparable to the ones presented in the previous section in table 6.8. However, the basic scattering probabilities without angular changes are slightly different, due to the increased total cross section.

The resulting effect on the response function is shown in figure 6.30. There, the relative difference is shown between a response function using elastic energy losses but no angular changes, and a response function, also incorporating angular changes for the combined angular change distribution with a mean value of 0.82 °. In contrast to the effect of inelastic angular changes, now also electrons with surplus energies below 10 eV are affected. The effect is of the order of $2 \cdot 10^{-4}$ and therefore twice as big as in the case with inelastic angular changes only.

Systematic shift of the neutrino mass

The systematic shifts of the neutrino mass in case that elastic scattering is not considered in the analysis are presented in table 6.9. Here the effects of ignoring only elastic energy losses or elastic angular changes were investigated separately. If the elastic energy losses are not accounted for in the analysis, a resulting shift of $\Delta m_\nu^2 = -2.1 \cdot 10^{-3}\,\mathrm{eV}^2$ was obtained by ensemble tests, which is in accordance with the value stated in [KAT05] of about $\Delta m_\nu^2 = 2.5 \cdot 10^{-3}\,\mathrm{eV}^2$.

The obtained shift of $\Delta m_\nu^2 = 0.7 \cdot 10^{-3}\,\mathrm{eV}^2$ when the angular changes are ignored is however much larger than in the inelastic case, although the mean value of the combined angular change distribution does increase only slightly. A reason for this is the width of the distribution, as for elastic scattering the probability of rather large angular changes is increased significantly. Furthermore, the effect of elastic angular changes will also modify the response function for surplus energies below 10 eV.

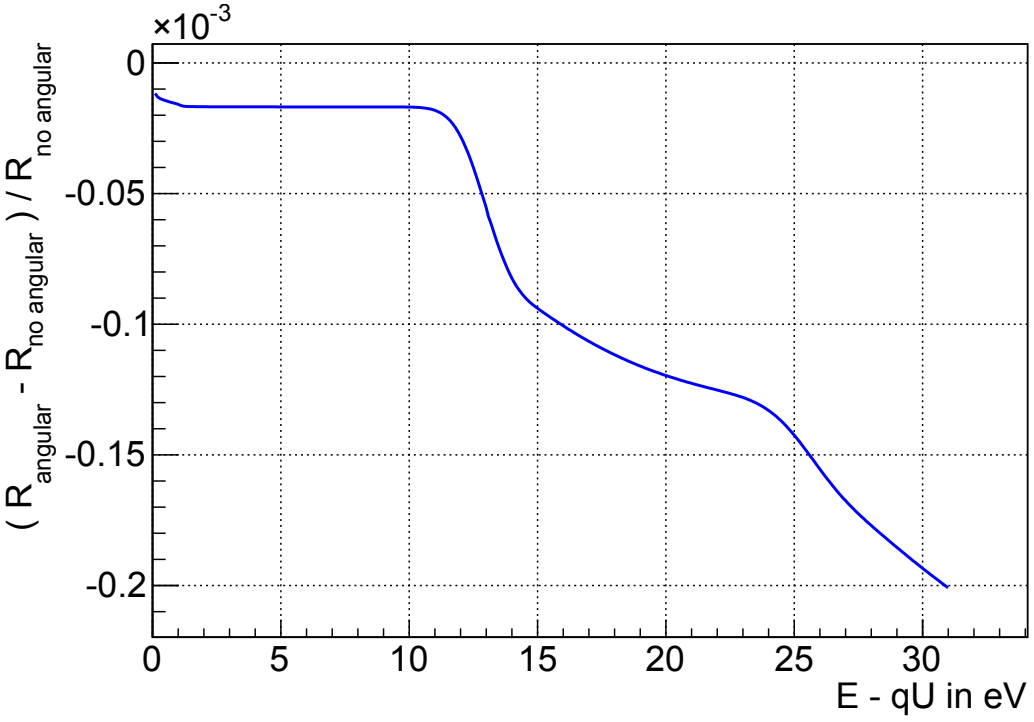

Figure 6.30: Relative difference of the response function using angular changes at inelastic and elastic scattering processes compared to no angular changes. Now there is also an effect for electrons with a surplus energy below 10 eV, due to the tiny energy loss of elastic scattering processes.

Table 6.9: Systematic shifts on the neutrino mass by elastic scattering if either energy losses, angular changes or both are ignored in the analysis. The induced shift on the neutrino mass caused by ignoring elastic energy losses and elastic angular changes are contrary and thereby cancel each other partly, when both are ignored. For all values the statistical sensitivity is assumed to be $1.66 \cdot 10^{-3}\,\mathrm{eV}^2$ and the error of Δm_ν^2 is $10^{-4}\,\mathrm{eV}^2$.

effect unaccounted for in the analysis	$\Delta m_\nu^2 \cdot 10^{-3}$ in eV^2	sensitivity on m_ν in meV (90 % C.L.)
elastic energy loss	-2.1	198.1
elastic angular change	0.7	197.7
both	-1.1	197.8

Table 6.10: Systematic shifts on the neutrino mass due to an unaccounted for relative inelastic cross section offset. For all values the statistical sensitivity is assumed to be $1.66 \cdot 10^{-3}\,\mathrm{eV}^2$ and the error of Δm_ν^2 is $10^{-4}\,\mathrm{eV}^2$.

unaccounted for relative inelastic cross section offset	$\Delta m_\nu^2 \cdot 10^{-3}$ in eV^2	sensitivity on m_ν in meV (90 % C.L.)
-0.010	11.6	208.6
-0.005	5.6	200.4
-0.003	3.5	198.8
-0.001	0.6	197.7
0.001	-1.9	198.0
0.003	-4.2	199.2
0.005	-6.5	201.3
0.010	-12.3	209.8

Nevertheless, the shift obtained when ignoring angular changes is still very low and may therefore not be required to be considered in the final neutrino mass analysis. The effect when ignoring elastic energy losses on the other hand is only slightly below the stated requirement of $|\Delta m_\nu^2| < 2.4 \cdot 10^{-3}\,\mathrm{eV}^2$ and should therefore be included.

6.5.7 Requirement on the accuracy of the inelastic cross section and energy losses

In the Monte Carlo simulations as well as in the analytical calculations an identical energy loss function and cross section was used to describe the process of inelastic scattering. These values are however only known with an accuracy of few times 10^{-2}, as detailed in section 6.1. This is clearly not sufficient as outlined in the KATRIN design report [KAT05]. Therefore, these parameters need to be measured in the course of a dedicated measurement campaign before the start of the long term neutrino mass measurements.

Requirement on the accuracy of the cross section

The required accuracy for the scattering cross section can be estimated by introducing a relative offset in the simulation which is unaccounted for in the analysis. The results of the performed ensemble tests for the inelastic cross section are listed in table 6.10 and are plotted in figure 6.31. As can be seen the requirements on the accuracy of the inelastic cross section are quite strict, as even a relative offset of 1 % will lead to a systematic shift of $\Delta m_\nu^2 = -12.3 \cdot 10^{-3}\,\mathrm{eV}^2$ if unaccounted for in the analysis. The fit of a linear function reveals the maximal allowed relative deviation range of $[-2.4 \cdot 10^{-3}, 1.6 \cdot 10^{-3}]$.

Requirement on the accuracy of the energy loss function

The requirements are more complicated to quantify for the inelastic energy loss function since its not just a scalar number but corresponds to a specific distribution. Therefore, the following two investigations were performed.

- The energy loss function can be scaled by an overall factor, corresponding to the values A_1 and A_2 when parametrizing the energy loss function as defined in section 6.1.2. If this factor would be inaccurately determined in the experiment or in case a normalization error would occur, a different energy loss function would results. The results of ensemble tests based on a relative offset of this factor being unaccounted for in the analysis are listed in table 6.11 and are plotted in figure 6.32. The requirements now are even more strict than on the cross section, as the fit reveals an allowed

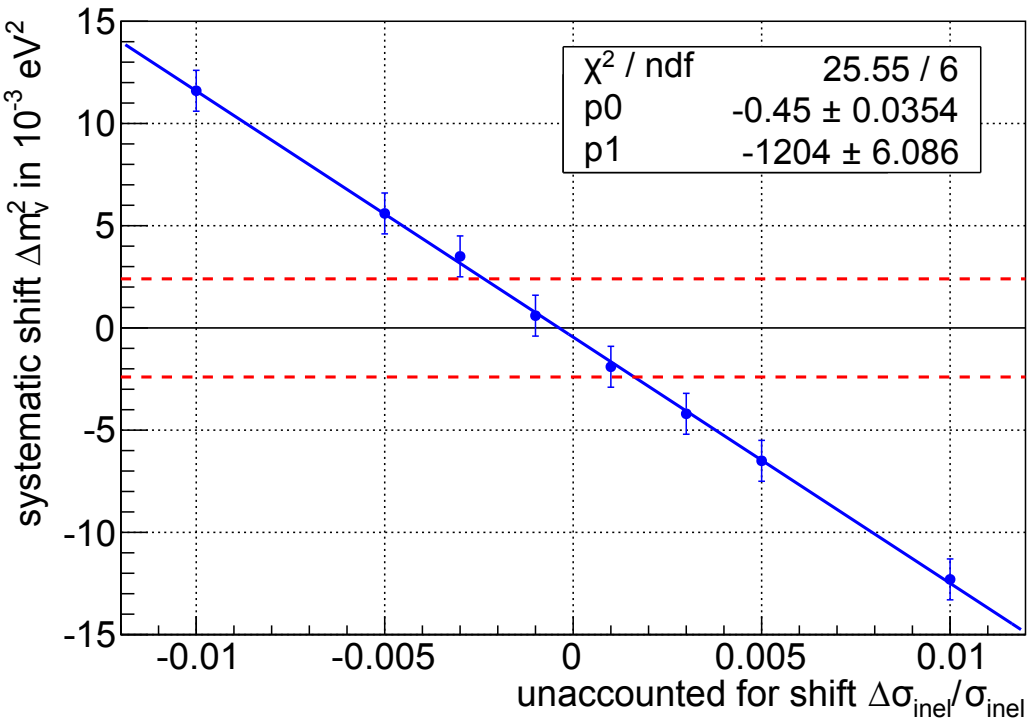

Figure 6.31: Systematic shifts on the neutrino mass due to an unaccounted for relative inelastic cross section offset. The dashed red lines show the maximal allowed shift of $|\Delta m_\nu^2| = 2.4 \cdot 10^{-3}\,\mathrm{eV}^2$. The fitted linear function reveals the allowed deviation range of $[-2.4 \cdot 10^{-3}, 1.6 \cdot 10^{-3}]$. The shown error bars are increased by a factor of 10 for better visibility.

relative deviation range of $[-1.1 \cdot 10^{-3}, 1.1 \cdot 10^{-3}]$ for a maximal shift of $|\Delta m_\nu^2| = 2.4 \cdot 10^{-3}\,\mathrm{eV}^2$.

- The energy loss function can also be shifted in energy, corresponding to different peak positions, as defined by the values ϵ_1 and ϵ_2 in the parametrization of the energy loss function in section 6.1.2. The results of ensemble tests incorporating an unaccounted for energy shift of the energy loss function in the analysis are listed in table 6.12 and are plotted in figure 6.33. For a maximal allowed neutrino mass shift of $|\Delta m_\nu^2| = 2.4 \cdot 10^{-3}\,\mathrm{eV}^2$, the allowed range of energy shifts can be narrowed down to $[-5.8\,\mathrm{meV}, 5.8\,\mathrm{meV}]$.

These rather simple approaches can of course not define the precise requirements on the accuracy of the shape of the energy loss function. Nevertheless, they are a good estimate of the order of magnitude of the accuracy required when obtaining the energy loss function from dedicated measurements before the start of regular data taking. The maximal allowed shift on the neutrino mass as used in the investigation is also quite strict, since for the determination of the energy loss function a required systematic shift of $|\Delta m_\nu^2| < 6 \cdot 10^{-3}\,\mathrm{eV}^2$ is stated in the design report [KAT05]. Investigations on the specific procedures to determine the energy loss function have declared that it seams to be feasible to obtain a sufficient accuracy for the energy loss function within the allowed corresponding systematic shift [Wol08, Kra11]. Further investigations with respect to the required accuracy of the inelastic cross section and energy loss function, as well as with regard to different measurement time intervals, are currently under investigation [Ant15].

6.5.8 Summary of the individual effects and resulting refined response function model

Having identified, quantified and included all seven individual effects in the analytical calculation of the response function, the comparison with the Monte Carlo data can be

Table 6.11: Systematic shifts on the neutrino mass due to an unaccounted for relative factor in the energy loss function. For all values the statistical sensitivity is assumed to be $1.66 \cdot 10^{-3}\,\mathrm{eV}^2$ and the error of Δm_ν^2 is $10^{-4}\,\mathrm{eV}^2$.

unaccounted for relative factor in the energy loss function in 10^{-3}	$\Delta m_\nu^2 \cdot 10^{-3}$ in eV^2	sensitivity on m_ν in meV (90 % C.L.)
-10.0	21.1	228.6
-5.0	10.3	206.4
-2.0	4.1	199.2
-1.0	2.0	198.1
-0.5	1.0	197.8
0.5	-1.0	197.8
1.0	-2.0	198.1
2.0	-4.1	199.2
5.0	-10.2	206.2
10.0	-20.4	227.0

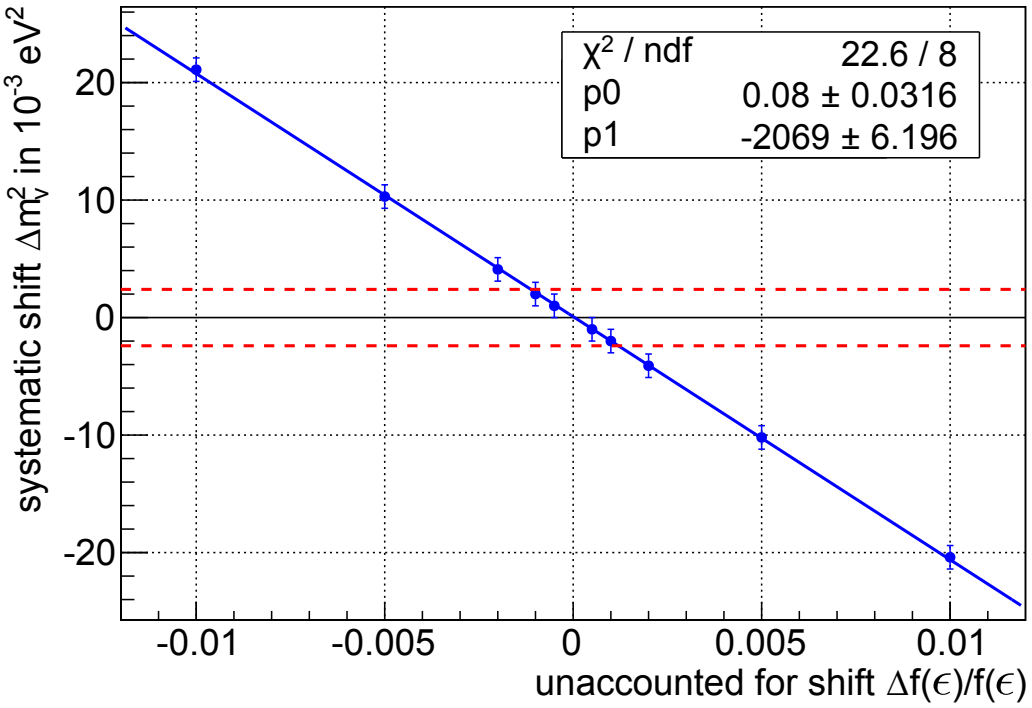

Figure 6.32: Systematic shifts on the neutrino mass due to an unaccounted for relative factor in the energy loss function. The dashed red lines show the maximal allowed shift of $|\Delta m_\nu^2| = 2.4 \cdot 10^{-3}\,\mathrm{eV}^2$. The fitted linear function reveals the allowed deviation range of $[-1.1 \cdot 10^{-3}, 1.1 \cdot 10^{-3}]$. The shown error bars are increased by a factor of 10 for better visibility.

Table 6.12: Systematic shifts on the neutrino mass due to an unaccounted for inelastic energy loss shift. For all values the statistical sensitivity is assumed to be $1.66 \cdot 10^{-3}\,\mathrm{eV}^2$ and the error of Δm_ν^2 is $10^{-4}\,\mathrm{eV}^2$.

unaccounted for shift of the energy loss function in meV	$\Delta m_\nu^2 \cdot 10^{-3}$ in eV^2	sensitivity on m_ν in meV (90 % C.L.)
-0.050	20.6	227.4
-0.020	8.2	203.3
-0.010	4.1	199.2
-0.005	2.1	198.1
-0.001	0.4	197.7
0.001	-0.4	197.7
0.005	-2.0	198.1
0.010	-4.1	199.2
0.020	-8.2	203.3
0.050	-20.7	227.7

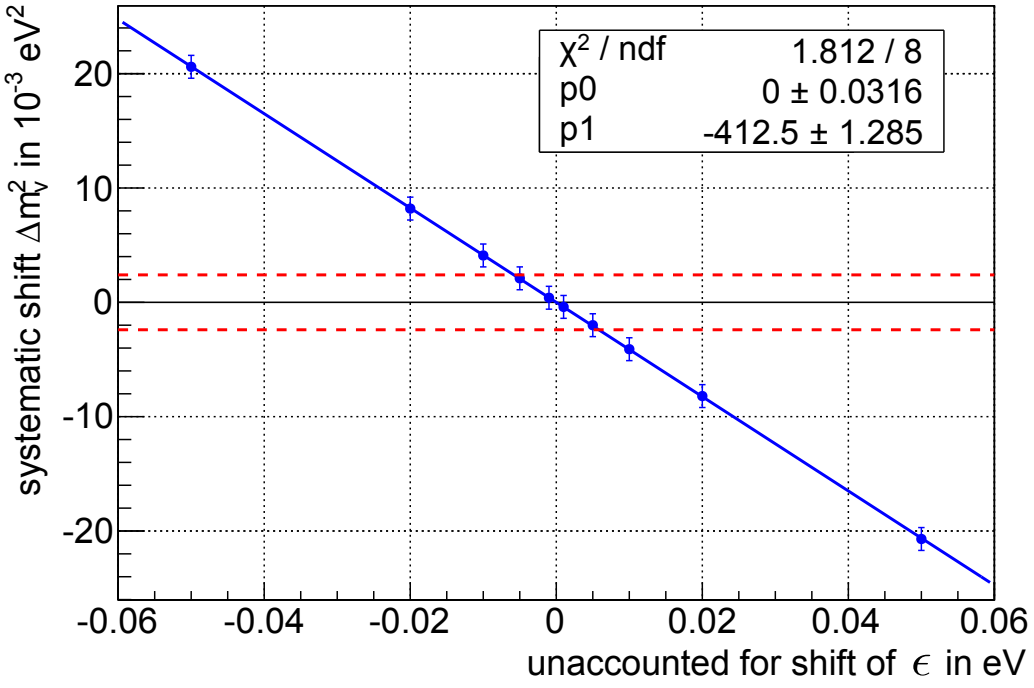

Figure 6.33: Systematic shifts on the neutrino mass due to an unaccounted for inelastic energy loss shift. The dashed red lines show the maximal allowed shift of $|\Delta m_\nu^2| = 2.4 \cdot 10^{-3}\,\mathrm{eV}^2$. The fitted linear function reveals the allowed deviation range of $[-5.8\,\mathrm{meV}, 5.8\,\mathrm{meV}]$. The shown error bars are increased by a factor of 10 for better visibility.

Table 6.13: Summary of the corrections to the response function as presented in this chapter and the resulting systematic shifts on the neutrino mass if one of the individual effects is ignored in the analysis. The neutrino mass sensitivity is calculated using a statistical sensitivity of $16.6 \cdot 10^{-3}\,\mathrm{eV}^2$ and a systematical base uncertainty of $17 \cdot 10^{-3}\,\mathrm{eV}^2$.

effect unaccounted for in the analysis	$\Delta m_\nu^2 \cdot 10^{-3}$ in eV^2	sensitivity on m_ν in meV (90 % C.L.)
source magnetic field inhomogeneity	-3.5	198.8
relativistic correction	-7.6	202.6
synchrotron radiation	-24.1	235.9
modified angular distribution	13.9	212.8
angular changes by inelastic scattering	0.2	197.7
energy losses by elastic scattering	-2.1	198.1
angular changes by elastic scattering	0.7	197.7

Table 6.14: Summary of the accuracy requirements for selected parameters. A maximal allowed systematic shift of $|\Delta m_\nu^2| = 2.4 \cdot 10^{-3}\,\mathrm{eV}^2$ was used for the calculation.

investigated effect	accuracy requirement range for the offset
source magnetic field	$[-0.9\,\%, 0.6\,\%]$
synchrotron energy loss	$[-11\,\%, 9\,\%]$
inelastic cross section	$[-0.3\,\%, 0.2\,\%]$
inelastic energy loss factor	$[-0.1\,\%, 0.1\,\%]$
inelastic energy loss shift	$[-5.8\,\mathrm{meV}, 5.8\,\mathrm{meV}]$

repeated. In doing so, an analytical response function was calculated including a WGTS segmentation of 100 slices, relativistic corrections, synchrotron energy loss corrections, all modified transmission functions $T_i^\star$, inelastic and elastic energy losses, and the modified scattering probabilities $P_i^\star$ as a result of angular changes caused by inelastic and elastic scattering processes.

The resulting response function is plotted in figure 6.34 together with the function based on the Monte Carlo simulation. No evident deviations are visible over the whole region of the response function. Even in the rather critical region at the transmission edge the refined analytical model matches the Monte Carlo simulation perfectly.

To obtain a more quantitative comparison, the relative difference between the response functions of the Monte Carlo and the refined analytical model is plotted in figure 6.35. For most parts of the response function the deviation is within the statistical error of the Monte Carlo simulation. Even at the transmission edge, where the old analytical model did show deviations of up to 8 %, most of the deviations of the refined model are within the statistical errors of the order of $5 \cdot 10^{-3}$.

All included corrections together with their individual contributions to the systematic error of the neutrino mass measurement in case of their omission are summarized in table 6.13. The most important ones are synchrotron radiation losses, modified angular distributions and relativistic corrections, while elastic energy losses and angular changes due to scattering processes play a minor role only.

In addition, the calculated requirements on the accuracy of experimental parameters are summarized in table 6.14 for a maximal allowed systematic shift of $|\Delta m_\nu^2| = 2.4 \cdot 10^{-3}\,\mathrm{eV}^2$.

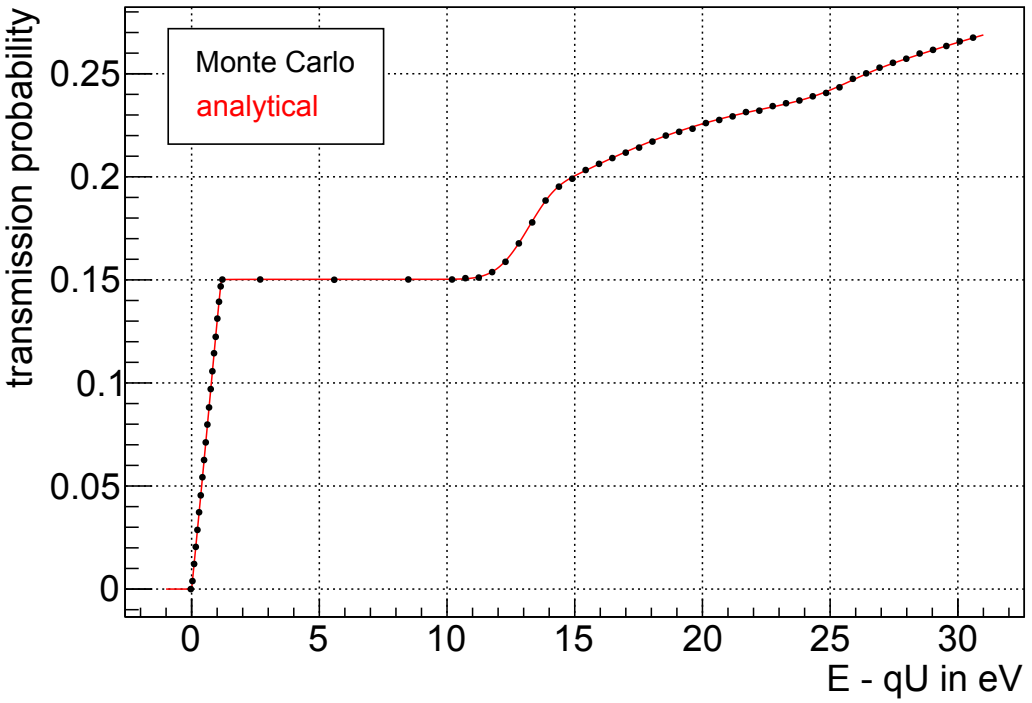

(a) Response function

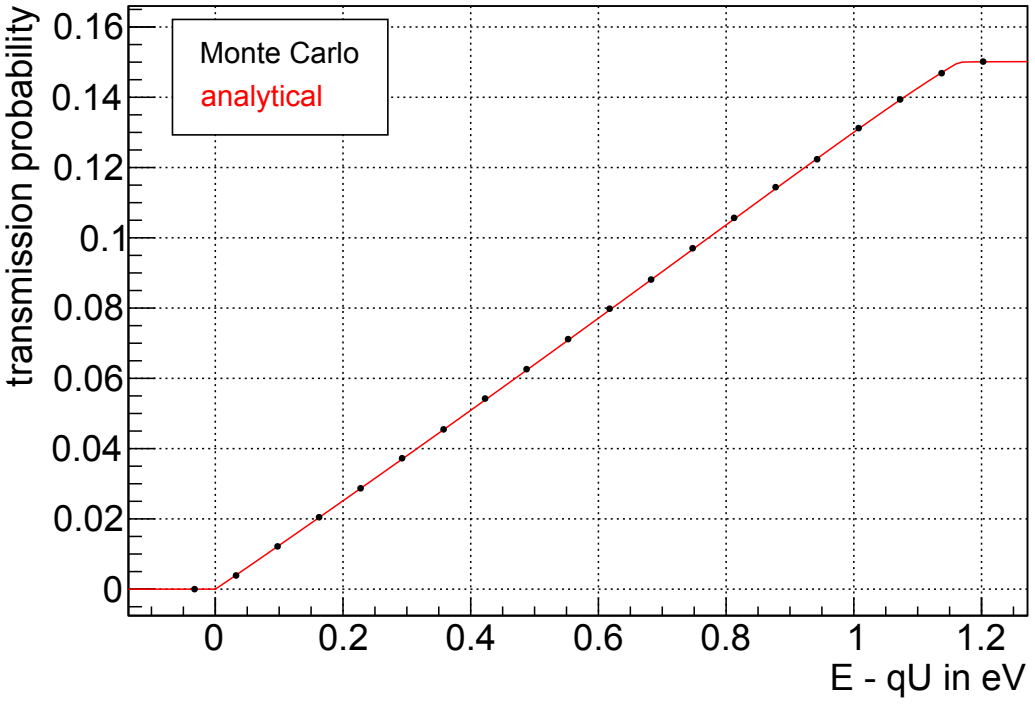

(b) Transmission function region

Figure 6.34: Results of the Monte Carlo response function and comparison with the refined analytical model. The refined analytical model now matches the Monte Carlo simulation perfectly.

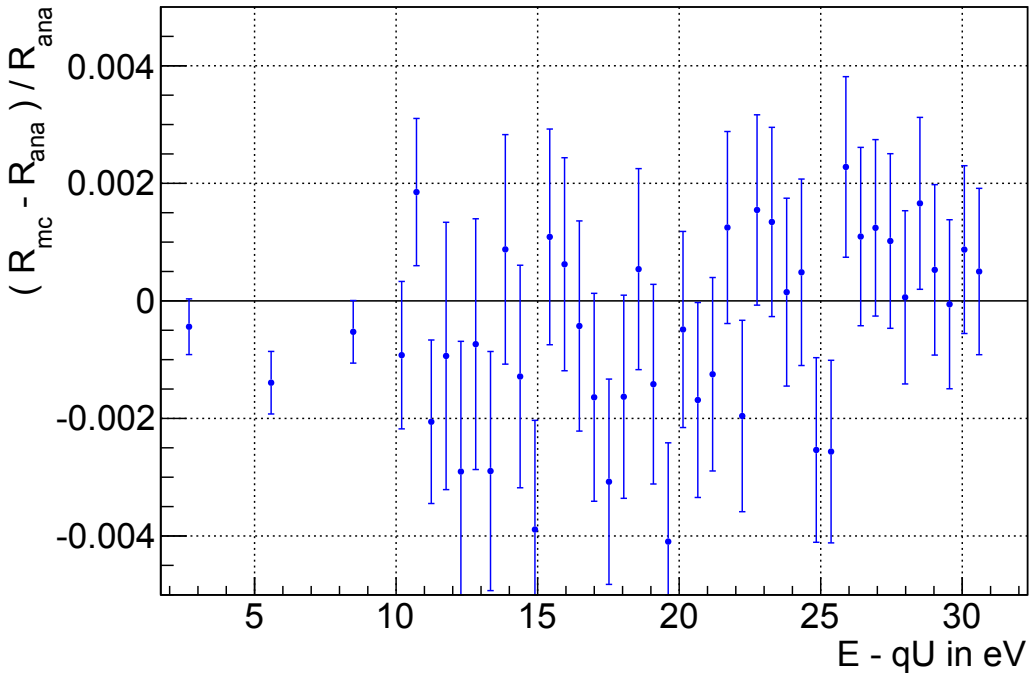

(a) Response function

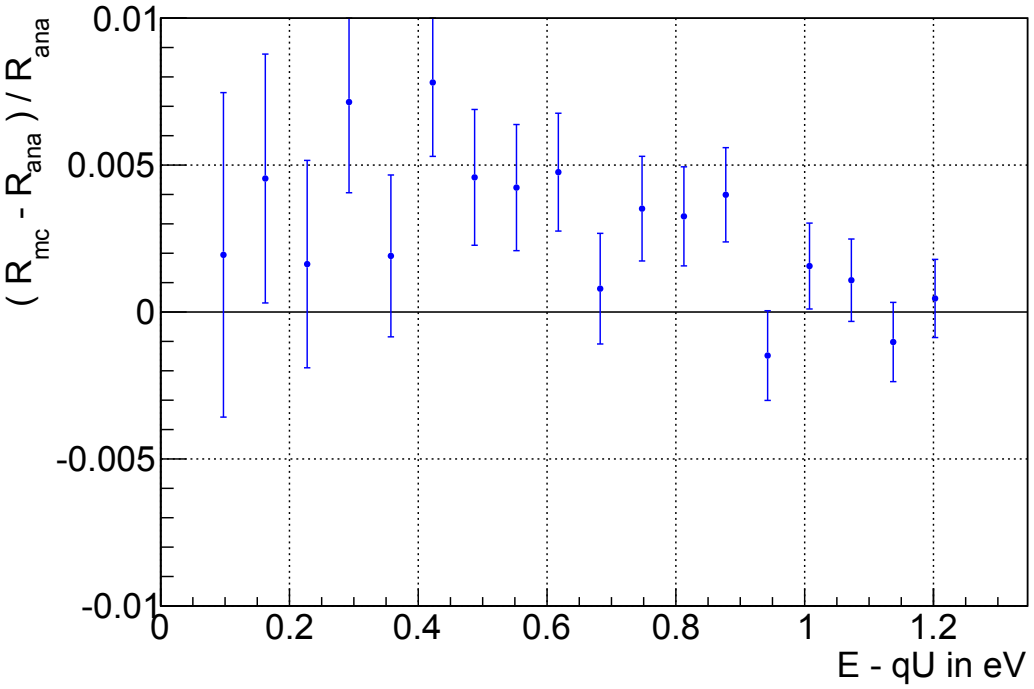

(b) Transmission function region

Figure 6.35: Relative difference of the Monte Carlo response function and the refined analytical model. For most of the points, the Monte Carlo simulation and the refined analytical model agree within statistical errors.

6.6 Conclusion

In this chapter the results of large-scale Monte Carlo simulations based on propagating electrons close to the endpoint E_0 through the entire KATRIN beam line from source to detector were presented. The obtained response function was compared to corresponding analytical models, which had to be refined by including a total of seven individual effects. For each of these effects, the influence on the neutrino mass sensitivity was presented in case that it is omitted in the final analysis. The resulting analytical model includes all the required effects, and, most importantly, it agrees with the response function obtained by the Monte Carlo simulation within statistical errors.

Starting with a description of an analytical response function, as given in [KAT05], the required formulas were derived. The setup of the Monte Carlo simulation using the most recent version of KASSIOPEIA was presented to describe the beam line geometry and corresponding electromagnetic fields. Several physics modules of the Monte Carlo simulation were validated such as the ones calculating energy losses through synchrotron radiation and scattering. It was shown that the adiabatic approximation for the electron transport is valid in the energy region-of-interest. This important approach together with further optimizations has decreased the required computation time by several orders of magnitude.

By comparison of the Monte Carlo simulation with the rather simple analytical model of the KATRIN design report, a total of seven effects influencing the shape of the response function were identified, which previously were not considered in the analytical model. These effects result from the inhomogeneous axial magnetic field in the WGTS, relativistic corrections, synchrotron energy losses, a modified shape of the transmission function as a result of polar angle-dependent scattering probabilities, angular changes by inelastic scattering processes, and energy losses by elastic scattering processes as well as angular changes by elastic scattering processes. For each individual contribution an extension of the analytical calculation was derived, graphically presented, and validated by the Monte Carlo simulation. Based on ensemble tests, the influence of each of these contributions on the neutrino mass sensitivity could be quantified. The most important ones are synchrotron radiation losses, modified angular distributions of source-scattered particles, and relativistic corrections, which must be taken into account in the final neutrino mass analysis. On the other hand, it could be shown that elastic energy losses and angular changes due to scattering processes only play minor roles since their corresponding systematic errors on m_ν are negligible.

In conclusion, the technique of high-statistics Monte Carlo simulations of signal electrons propagating through the whole experiment represents an essential new tool to describe the response function. Therein, the particle tracking software KASSIOPEIA developed in the course of this thesis, is of utmost importance for a better understanding of the experimental setup. The refined analytical model of the response function will be an indispensable analysis tool to push down the sensitivity for a successful determination of the neutrino mass even below the ambitious limit of $200\,\mathrm{meV}/c^2$ at 90% C.L.

7. Summary and Outlook

The discovery of neutrino flavor oscillation has given incontrovertible evidence for massive neutrinos, a breakthrough which points to new physics beyond the Standard Model of particle physics, in which neutrinos were originally assumed to be massless. The fundamental mass scale of neutrinos plays an important role for our understanding of the evolution of large-scale structures in our universe. This is a strong motivation for the determination of the absolute mass scale of neutrinos, as oscillation studies can only infer mass splittings. The Karlsruhe Tritium Neutrino experiment KATRIN, the next-generation tritium β-decay experiment, is targeted to determine the "effective mass of the electron anti-neutrino" $m_{\bar{\nu}_e}$ with a model-independent measurement. With a sensitivity of $200\,\mathrm{meV}/c^2$ at 90% C.L. ($350\,\mathrm{meV}/c^2$ at $5\,\sigma$) after five calendar years of operation, KATRIN will improve the current neutrino mass sensitivity obtained with its predecessor experiments by one order of magnitude. This is achieved by a precise measurement of the tritium β-spectrum close to the endpoint energy at 18.6 keV. The MAC-E filter principle, which allows high resolution spectroscopy by combining magnetic adiabatic collimation with electrostatic filtering, will be a cornerstone to a successful mass measurement.

The a priori knowledge of the exact shape of this filter is of utmost importance for a non-biased neutrino mass analysis. Two key parameters, the electrostatic potential and magnetic field together with their radial inhomogeneities in the center of the large main spectrometer vessel need to be measured with high precision. Apart from a very good understanding of the transmission function, a precise model of the complete response function of the experiment, including additional energy losses by scattering off gas molecules or by emission of synchrotron radiation, is required.

The three most important results of the work performed in the course of this thesis can be summarized briefly as follows and will be detailed thereafter:

- The development of the Kassiopeia particle tracking framework, which is a modular, extensible, efficient and user-friendly simulation software package. It is an indispensable tool used throughout the KATRIN collaboration for the modeling of experimental effects and the analysis of measured data.
- The measurement strategies and analysis methods developed in this thesis allow to determine the radial potential inhomogeneity in the analyzing plane of the main spectrometer. A key aspect here are transmission function measurements using a quasi mono-energetic angular selective electron emitter. After inclusion of specific

properties of the first SDS configuration an excellent agreement of measured data with corresponding simulations was obtained, which is within the derived accuracy limits for a successful neutrino mass determination.

- The first large-scale Monte Carlo simulation of the response function of the full experiment was performed by propagating electrons close to the endpoint E_0 through the entire experimental setup from the source to the detector. Based on these findings, a refined analytical model was derived, where a total of seven individual previously unconsidered effects were included and quantified with regard to their impact on the neutrino mass if omitted in the final analysis.

The particle tracking framework Kassiopeia

The Kassiopeia particle tracking simulation framework is a joint effort of various members of the KATRIN collaboration. The development of this powerful tool over the last few years was led and also mainly performed by D. Furse (MIT) and the author of the thesis at hand. The current version of Kassiopeia 3 is an extensible and object-oriented particle tracking framework which utilizes modern C++ techniques. Its modular and flexible design allows a large range of applications, in particular in case of a complex and demanding experiment such as KATRIN. Kassiopeia offers an efficient and accurate propagation of electrons through the complex field layouts and geometries of the experiment. This is essential for many tasks such as the currently ongoing investigation of background effects and estimates of corresponding rates. Also, the study of transmission properties including interaction processes and energy losses requires a detailed understanding of particle propagation. In addition, detailed simulations based on measurements performed during the extensive commissioning works are an important and accurate tool for evaluating the sensitivity of the entire experiment. The user-friendly xml configuration files allow inexperienced users to start a rather sophisticated particle tracking simulation, and the modular and extensible structure enables the convenient and fast addition of new physics modules.

The incorporation of the Kassiopeia code into the Kasper simulation and analysis framework provides access to geometry modules and electromagnetic field solvers. This allows to use one common geometry description for the entire simulation and to assign attributes like potentials to selected individual surfaces for the field calculation. An interface to the database allows to retrieve sensor parameters of the experiment and use them as input parameters for the simulation. Together with the connection to the detector electronics simulation this allows for the first time to generate an integral spectrum as will be measured in the real experiment.

With Kassiopeia it is possible to automatically generate a simulation configuration where parameters identical to the ones occurring during a measurement run can be employed. In brief, this allows to propagate β-decay electrons efficiently through the actual field configuration and geometries of the 70 m long experimental setup. In particular, processes such as scattering off tritium gas, synchrotron radiation energy losses as well as solid-state interactions in the silicon of the detector wafer up to the corresponding data acquisition chain are included.

The Kassiopeia framework is used both inside and outside of the KATRIN collaboration on a daily basis. Without this software it would not have been possible to analyze and interpret the results of the KATRIN SDS commissioning measurements correctly. Also, when estimating the experimental sensitivity and in view of a final neutrino mass analysis, Monte Carlo simulations performed with Kassiopeia have proven to be of major importance.

SDS commissioning measurements and determination of the transmission properties of the main spectrometer

During summer of 2013, an extensive four month measurement campaign was undertaken in which the main spectrometer together with the focal plane detector system were operated for the first time as a combined apparatus. This commissioning of the spectrometer and detector section (SDS) forms an important and integral part of the thesis at hand, as the author contributed significantly to the results through electromagnetic simulations, run time coordination and the measurement and analysis of the transmission properties of the main spectrometer. The SDS commissioning measurements turned out to be very successful, as the correct and reliable interplay of all hardware and slow-control components could be demonstrated. Moreover, the complex analysis and simulation software was validated with experimental data. A particular achievement of this first extended run period was the confirmation of the proper functioning of the magnetic guidance and electrostatic retardation of the high resolution MAC-E filter system of the main spectrometer. The transmission characteristic derived during the first SDS phase will be a valuable asset also in ongoing, more detailed studies of the next SDS phase.

To determine the transmission properties of the main spectrometer, a quasi mono-energetic angular selective electron emitter was used. By performing a transmission function measurement the electrostatic potential and magnetic field of a specific point inside the main spectrometer can be determined. To do so, two important tasks needed to be fulfilled first: The determination of a small-scale unavoidable misalignment of the electron gun, to calculate precise electron trajectories in the spectrometer, and the determination of the analyzing point of a specific field line. The misalignment of the electron gun relative to the flux tube was measured by moving its manipulator to draw a horizontal and vertical line on the detector. By comparing the relative rates of neighboring pixels the center of the cross could be determined precisely and by subtracting the misalignment of the detector wafer, the misalignment of the electron gun starting position was quantified to $\Delta x = -14.154\,\mathrm{mm}$ and $\Delta y = -2.590\,\mathrm{mm}$. The corresponding measurements show agreements on a pixel level, when compared to Kassiopeia particle tracking simulations. It could be shown that hardware-related issues such as the single voltage offset configuration of the inner electrodes, and the asymmetric potential configuration caused by the HV scheme resulted in non-optimum conditions. As a consequence, the analyzing points did not form a simple plane in the middle of the spectrometer, but were highly twisted, with deviations up to several meters for the outermost field lines. A proper analysis of transmission function measurements was only possible when considering these unexpected transmission conditions.

A sophisticated measurement and analysis strategy was worked out, which allows first to determine important properties of the electron gun, in particular its energy and angular distribution. Only by this a priori knowledge of e-gun properties is it possible to derive spectrometer properties such as electrostatic potential and magnetic field. This target was achieved by using an analytical model of the transmission function, which only depends on the energy and angular distribution of the source. The validity of this model was confirmed by performing Kassiopeia particle tracking simulation, showing an excellent agreement.

Due to hardware-related issues with respect to the angular selectivity of the electron gun, it was not possible to determine the magnetic field in the analyzing plane of the main spectrometer. However, the electrostatic potential and its radial shape could be investigated in detail. The resulting radial potential inhomogeneity for two different electrostatic configurations showed a non-symmetric behavior with an east-west asymmetry, which was caused by a hardware-based asymmetric potential configuration of the inner electrodes of the main spectrometer. This shows the power of transmission studies to reveal the exis-

tence of a subtle, yet important electric dipole field between the east and west parts of the inner electrodes.

Follow-on simulations of the potential were performed with a realistic 3D model of the main spectrometer. The calculated potential configuration was compared with the measured data. Apart from a constant offset, originating from the uncertainty of the energy scale of the produced electrons and the work function of the main spectrometer vessel, the measured radial potential inhomogeneity matches the simulated one within 30 mV. Finally, a series of ensemble tests were carried out to investigate the sensitivity and resulting systematic errors on the neutrino mass measurement with KATRIN for different spectrometer properties such as radial inhomogeneities of the potential and magnetic field. Based on the solid set of results obtained, specific requirements for the true values and their precision can be stated. For the electrostatic potential, the values for each pixel ring need to be known with a precision better than 50 mV. A global offset, however, does not worsen the neutrino mass sensitivity, as long as the measurement time distribution is adapted accordingly. For the magnetic field the radial inhomogeneity is less important, but its true mean value needs to be measured to better than 2 μT.

A major outcome of these studies is thus the statement that the radial inhomogeneity of the analyzing plane potential can be determined with a precision matching the calculated requirements by using the developed measurement strategies and analysis methods.

Monte Carlo simulation and modeling of the response function

Making use of the most recent version of KASSIOPEIA, a large-scale Monte Carlo simulation of the response function of the KATRIN experiment was set up. Several physics modules of the Monte Carlo simulation were validated such as the energy loss through synchrotron radiation and scattering. It was shown that the adiabatic approximation to describe the electron transport is a valid assumption. This and further optimizations decreased the required computation time by several orders of magnitude, resulting in a propagation time below one hour for 1000 β-decay electrons close to the tritium endpoint E_0.

A total of $75 \cdot 10^6$ electrons were generated in this process and the resulting response function was compared to the analytical model of the KATRIN design report. It was shown that the analytical model used there is insufficient for the neutrino mass analysis, due to the rather large deviations with respect to the Monte Carlo data. A total of seven individual effects influencing the shape of the response function were identified which previously had not been considered in the analytical model. For each individual contribution an extension of the analytical calculation was derived, graphically presented, and validated by the Monte Carlo simulation. Additionally, ensemble tests were performed to quantify the influence of each individual effect on the neutrino mass sensitivity if omitted in the final neutrino mass analysis. The most important contributions consists in radiative synchrotron losses, a modified angular distribution for unscattered electrons, relativistic corrections and magnetic field inhomogeneities in the WGTS. Without considering these effects in the final analysis, which can now be done conveniently on the basis of the presented refined analytical model, a design sensitivity of 200 meV/c^2 would not be achievable. As an example the effect of ignoring synchrotron radiation is considered, which would worsen the sensitivity to 235.9 meV/c^2. It was also shown that a relative accuracy of synchrotron energy loss calculations on the 10% scale are sufficient. This can easily be obtained using a dedicated particle tracking simulation code such as KASSIOPEIA. On the other hand it was demonstrated that elastic energy losses and angular changes due to scattering processes only play minor roles since their corresponding systematic errors on m_ν are negligible.

Furthermore, requirements on the accuracy of critical experimental parameters were investigated. Special emphasis has to be put on the source magnetic field, which needs to be known with an accuracy of 0.6%. Another important input for the response function are the inelastic scattering parameters. The inelastic cross section needs to be known with an accuracy of 0.2% to constrain the maximal systematic shift to $|\Delta m_\nu^2| = 2.4 \cdot 10^{-3}\,\mathrm{eV}^2$. The accuracy requirements for the energy loss function were calculated by considering an overall scaling factor as well as an energy shift, resulting in a maximal allowed unaccounted for factor of 0.1% and energy shift of 5.8 meV.

It was demonstrated that Monte Carlo simulations of signal electrons propagating through the entire experiment are an essential method to describe the response function. Again, the particle tracking software KASSIOPEIA, is mandatory to obtain a better understanding of the experimental setup. The refined analytical model of the response function worked out in this thesis will be essential to optimize the sensitivity and to a successfully determine of the neutrino mass even below the ambitious limit of $200\,\mathrm{meV}/c^2$ at 90% C.L.

Outlook

When determining important transmission properties of the main spectrometer, the analysis methods and theoretical models as well as the corresponding software developed in the framework of this thesis will be indispensable tools. Both models and analysis methods will be applied to the measurements of the current ongoing SDS commissioning phase and finally also in the neutrino mass analysis. Owing to significant improvements in the electron gun hardware targeted at providing angular selectivity and optimized alignment of all sub-components, the achieved precision of the ongoing and future measurements is expected to improve. Furthermore, a working angular selectivity also will allow to determine the important absolute value of the magnetic field inside the main spectrometer, on the basis of the measurement strategy and analysis models and software presented here.

The Monte Carlo simulation of the response function can be extended by adding effects of the focal plane detector, due to back-scattering and the finite dead-layer. Likewise, electrons backscattered from the rear wall in the CMS unit of KATRIN will have to be investigated, even when contributing only in a minor way to the signal region. Furthermore, the radial dependence of the response function needs to be investigated, as synchrotron energy losses are expected to vary slightly for larger radii. Moreover, mapping effects caused by the magnetron drift can be studied in this way. When investigating these suggested extensions, the effects of the radial dependence of key parameters and of detector-related effects can be studied rather easily with KASSIOPEIA simulations forming the essential underlying framework.

Appendix

A Potential setting during the transmission function measurements

Due to the high voltage topology in use during the SDS commissioning measurements, as described in section 4.1.2, the absolute potential is slightly different for each inner electrode module, affecting the position of the analyzing plane and the measurement of the radial potential offsets, as discussed in section 4.3.5 and 5.4.

An overview of the four most important potential settings for the transmission function measurements with the corresponding detector run numbers and potential set values is given in table A.1. The detailed potentials on all inner electrode modules for each setting are stated in table A.2, A.3, A.4 and A.5.

Table A.1: Overview of the potential configuration for the transmission function measurements with set values for the inner electrodes and resulting potentials on the vessel and west and east parts of the electrodes.

setting	runs	ΔU_{wire} set value in V	vessel potential in V	west potential in V	east potential in V
A	7719 to 7784	100	-15503.17	-15602.35	-15602.78
B	7785 to 7789	200	-15403.18	-15602.45	-15602.84
C	6225 to 6241	1000	0.0	-1000.05	-1000.05
D	6361 to 6381	1000	0.0	-1000.07	-1000.07

Table A.2: Actual potential values for the individual inner electrodes at setting A.

module id	module position	Potential U in Volt west	east	$U_{\text{west}} - U_{\text{east}}$ in V
2	steep cone south	-15512.24	-15502.78	-9.46
3	steep cone south	-15502.34	-15502.78	0.44
4	flat cone south	-15602.32	-15602.75	0.43
5-6	flat cone south	-15602.32	-15602.70	0.38
7-11	cylinder	-15602.32	-15602.69	0.37
12	flat cone north	-15602.32	-15602.75	0.43
13	flat cone north	-15602.33	-15602.75	0.42
14	flat cone north	-15602.30	-15602.77	0.47
15	steep cone north	-15502.35	-15502.78	0.44
16	steep cone north	-15502.34	-15502.78	0.44

Table A.3: Actual potential values for the individual inner electrodes at setting B.

module id	module position	Potential U in Volt west	east	$U_{\text{west}} - U_{\text{east}}$ in V
2	steep cone south	-15512.32	-15502.84	-9.48
3	steep cone south	-15502.45	-15502.84	0.39
4	flat cone south	-15602.43	-15602.81	0.39
5-6	flat cone south	-15602.43	-15602.65	0.22
7-11	cylinder	-15602.42	-15602.62	0.20
12	flat cone north	-15602.43	-15602.81	0.38
13	flat cone north	-15602.43	-15602.81	0.38
14	flat cone north	-15602.40	-15602.83	0.42
15	steep cone north	-15502.45	-15502.84	0.39
16	steep cone north	-15502.45	-15502.84	0.39

Table A.4: Actual potential values for the individual inner electrodes at setting C.

module id	module position	Potential U in Volt west	east	$U_{\text{west}} - U_{\text{east}}$ in V
2	steep cone south	-999.77	-999.94	0.17
3	steep cone south	-999.77	-999.84	0.07
4	flat cone south	-999.99	-999.99	0.00
5-6	flat cone south	-999.49	-998.35	-1.14
7-11	cylinder	-998.97	-997.76	-1.21
12	flat cone north	-999.90	-999.76	-0.15
13	flat cone north	-999.75	-999.86	0.11
14	flat cone north	-999.85	-999.39	-0.46
15	steep cone north	-999.91	-999.92	0.01
16	steep cone north	-999.81	-999.92	0.11

Table A.5: Actual potential values for the individual inner electrodes at setting D.

module id	module position	Potential U in Volt west	east	$U_{\text{west}} - U_{\text{east}}$ in V
2	steep cone south	-999.86	-999.99	0.13
3	steep cone south	-999.86	-999.90	0.03
4	flat cone south	-1000.02	-1000.03	-0.01
5-6	flat cone south	-999.61	-998.46	-1.15
7-11	cylinder	-998.93	-997.80	-1.13
12	flat cone north	-999.95	-999.82	-0.14
13	flat cone north	-999.81	-999.92	0.11
14	flat cone north	-999.92	-999.48	-0.44
15	steep cone north	-999.97	-999.98	0.01
16	steep cone north	-999.90	-999.98	0.08

Table B.6: Potential configuration for the response function simulations. The resulting analyzing potential in the center of the main spectrometer is $U_A = -18544.142\,V$.

electrode	potential in kV
transport beam tube	0.0
PS hull	-18.200
PS inner electrode	-18.300
MS hull	-18.345
MS outer wire	-18.445
MS inner wire	-18.545
MS steep cone	-18.445
FPD PAE	+10.00

B Settings used for the Monte Carlo Simulation of the response function

For the Monte Carlo simulation of the response function a combined axisymmetric model of the pre-spectrometer, main spectrometer and detector region was used. For the transport section and the source a simple cylinder beam tube was applied, as this whole region was set to zero potential. The used values for the individual electrode potentials are listed in table B.6.

For the magnetic field, all solenoids of the whole experiment were in use, including the aircoils of the main spectrometer. For the axial positions as well as the currents the reference values were used. Those are listed in table B.7.

Table B.7: Magnetic configuration for the response function simulations.

magnet module	z-position in m	current in A
DPS1R 1	-46.159	316.87
DPS1R 2	-44.728	316.87
WGTS 1	-42.168	313.23
WGTS 2	-38.871	313.23
WGTS 3	-35.573	313.23
DPS1F 1	-33.013	209.5
DPS1F 2	-31.583	209.5
DPS2F 1	-29.901	82.0
DPS2F 2	-28.573	82.0
DPS2F 3	-27.244	82.0
DPS2F 4	-25.915	82.0
DPS2F 5	-24.586	82.0
CPS 1	-23.270	200.0
CPS 2	-22.372	200.0
CPS 3	-21.315	200.0
CPS 4	-20.259	200.0
CPS 5	-19.337	200.0
CPS 6	-18.686	200.0
CPS 7	-17.657	200.0
PS 1	-15.500	157.0
PS 2	-12.104	157.0
LFCS 1	-6.788	0.5
LFCS 2	-4.938	0.0
LFCS 3	-4.040	4.8
LFCS 4	-3.139	7.1
LFCS 5	-2.238	6.6
LFCS 6	-1.338	19.4
LFCS 7	-0.442	57.2
LFCS 8	0.456	51.2
LFCS 9	1.354	22.7
LFCS 10	2.256	12.5
LFCS 11	3.156	7.7
LFCS 12	4.058	16.8
LFCS 13	4.952	15.9
LFCS 14a	6.606	42.1
LFCS 14b	6.904	42.1
PCH	12.184	87.115
DET	13.784	49.761

C Calculation of the scattering probabilities including angular changes

The default scattering probability calculation using a Poisson distribution was presented in section 6.1.3 for electrons starting in the source with initial polar angle θ, and a remaining column density of ρd to propagate through before leaving the WGTS as

$$P_i(\theta, \rho d) = \frac{(\rho d \cdot \sigma_{\text{inel}})^i}{\cos(\theta)^i \cdot i!} \exp^{-\frac{\rho d \cdot \sigma_{\text{ienl}}}{\cos(\theta)}} . \tag{7.1}$$

To include the angular change $\Delta\theta$ during each scattering process, first a recursive description of the scattering probabilities needs to obtained which only depends on P_0 and P_1. Therefore, the remaining column density to be traversed by the electrons has to be divided into a number of n equal segments. For each segment, the scattering probability can then be calculated individually and by making use of combinatorics the scattering probability for the whole column density can be obtained.

For example the probability for single scattering can be expressed as

$$P_1^\star(\theta, \rho d) = P_1(\theta, \frac{\rho d}{n}) \cdot P_0(\theta, \frac{\rho d}{n})^{n-1} \cdot n. \tag{7.2}$$

It is basically the product of the probability to scatter once in one segment and the probability not to scatter in all the remaining segments. The results has to be multiplied by the number of segments n to account for the possible cases and to finally obtain the probability to scatter once in the whole column density.

The probability for 2-fold scattering can be obtained analogously

$$\begin{aligned} P_2^\star(\theta, \rho d) = \quad & P_1(\theta, \tfrac{\rho d}{n})^2 \cdot P_0(\theta, \tfrac{\rho d}{n})^{n-2} \cdot \tfrac{n(n-1)}{2} \\ + \quad & P_2(\theta, \tfrac{\rho d}{n}) \cdot P_0(\theta, \tfrac{\rho d}{n})^{n-1} \cdot n. \end{aligned} \tag{7.3}$$

The second term is a results of the fact the there is also a small probability to scatter 2-fold in a single segment, which needs to be considered. However, when increasing the number of segments n, the probability for 2-fold scattering in a single segments becomes negligible small and the term can be ignored.

Therefore, a common formula for the scattering probability can be stated, which only depends on P_0 and P_1

$$P_i^\star(\theta, \rho d) = P_1(\theta, \frac{\rho d}{n})^i \cdot P_0(\theta, \frac{\rho d}{n})^{n-i} \cdot \binom{n}{i}, \tag{7.4}$$

with the binomial coefficients $\binom{n}{i}$. The formula is only valid for a large number of n for $i > 1$, as stated above.

To include angular changes at each scattering process the formula however needs to be modified further. It needs to be separated in scattering probabilities before a scattering took place and the ones after that. Again this will be demonstrated for the single-scattering example

$$P_1^\star(\theta, \rho d) = \sum_{k=1}^{n} P_0(\theta, \frac{\rho d}{n}(k-1)) \cdot P_1(\theta, \frac{\rho d}{n}) \cdot P_0^\star(\theta + \Delta\theta, \rho d(1 - \frac{k}{n})), \tag{7.5}$$

which is the product of the probability not to scatter in k segments, then the probability to scatter once in one segment and the probability to scatter in the remaining segments with a polar angle increased by $\Delta\theta$. The sum accounts for all possible segment for the scattering to take place. For the probability not to scatter after an angular change has occurred

$$P_0^\star(\theta, \rho d) = P_0(\theta, \rho d) \cdot \Theta(\theta_{\max} - \theta) \tag{7.6}$$

is used, to account for particles leaving the column density with a polar angle larger than $\theta_{\max}$, as they can not reach the detector due to the magnetic mirror effect.

Again, a common formula can be obtained

$$P_i^\star(\theta, \rho d) = P_1(\theta, \frac{\rho d}{n}) \cdot \sum_{k=1}^{n} P_0(\theta, \frac{\rho d}{n}(k-1)) \cdot P_{i-1}^\star(\theta + \Delta\theta, \rho d(1 - \frac{k}{n})), \tag{7.7}$$

which is again only valid for large numbers of n for $i > 1$.

With this modified scattering probability for a given θ and a given $\Delta\theta$ during scattering, the mean scattering probabilities can be obtained analogously as done before, which is shown in section 6.5.5.

List of Figures

1.1 Continuous energy spectrum of beta decay . . . 2
1.2 Solar neutrino energy spectrum . . . 4
1.3 Neutrino mass hierarchy . . . 10
1.4 Neutrinoless double beta decay . . . 12
1.5 Single beta decay . . . 14

2.1 Differential and integrated tritium beta decay spectrum . . . 20
2.2 MAC-E filter principle . . . 21
2.3 Cyclotron motion of electron in magnetic field and definition of polar angle 22
2.4 Transmission function for KATRIN reference values . . . 25
2.5 Response function for KATRIN reference values . . . 27
2.6 The beamline of the KATRIN experiment . . . 28
2.7 The windowless gaseous tritium source . . . 29
2.8 The differential pumping section . . . 30
2.9 The cryogenic pumping section . . . 31
2.10 The main spectrometer . . . 33
2.11 The monitor spectrometer . . . 33
2.12 The focal plane detector . . . 34

3.1 Kassiopeia logo . . . 39
3.2 Organization structure of a run . . . 41
3.3 Flow chart of the simulation algorithm . . . 42
3.4 Illustration of the exact and adiabatic trajectory . . . 48
3.5 Schematic representation of the output component system . . . 54
3.6 Visualization examples with the ROOT painters . . . 59
3.7 Visualization examples with the VTK painters . . . 60
3.8 Coordinate system used with Kassiopeia . . . 61
3.9 Tree structure of nested geometries . . . 62
3.10 Convergence region of the central zonal harmonic expansion . . . 66
3.11 Convergence region of the remote zonal harmonic expansion . . . 66
3.12 Geometry of the main spectrometer in KEMField . . . 69
3.13 Potential in the main spectrometer with the realistic 3D model . . . 69
3.14 Schematic segmentation of the source . . . 70
3.15 Ensemble test example . . . 73

4.1 SDS hardware overview . . . 78
4.2 Inner wire electrodes of the main spectrometer . . . 80
4.3 SDS wire modules overview with short circuits . . . 81
4.4 SDS high voltage setup . . . 84
4.5 Aircoil system . . . 86
4.6 Influence of the LFCS on the magnetic flux tube in the main spectrometer . 87
4.7 Influence of the EMCS on the magnetic flux tube in the main spectrometer 88

4.8 Detector wafer of the FPD system . . . 90
4.9 Electron gun overview . . . 91
4.10 Illustration of the e-gun working principle . . . 91
4.11 High voltage scheme for the electron gun . . . 93
4.12 UHV manipulator of the electron gun . . . 93
4.13 Flux tube with misaligned detector system . . . 95
4.14 Summary of shadowed pixels . . . 96
4.15 Electron gun alignment measurements . . . 97
4.16 Comparison of measurements and simulations of the electron gun alignment 99
4.17 Radial potential and magnetic field inhomogeneity in the analyzing plane . 100
4.18 Potential and magnetic field along the central field line . . . 103
4.19 Early retardation in the main spectrometer . . . 105
4.20 No early retardation in the main spectrometer . . . 105
4.21 Overview of field lines for the 3.8 G setup . . . 107
4.22 Potential plot for the 3.8 G setup . . . 108
4.23 Magnetic field plot for the 3.8 G setup . . . 108
4.24 Longitudinal kinetic energy plot for the 3.8 G setup . . . 109
4.25 Analyzing plane points for the 3.8 G setup . . . 109
4.26 Overview of field lines for the 9 G setup . . . 110
4.27 Analyzing plane points for the 9 G setup . . . 110
4.28 Overview of field lines for the tilted FPD system . . . 112
4.29 Potential plot for the SDS high voltage settings . . . 113
4.30 Longitudinal kinetic energy plot for the SDS high voltage settings . . . 113
4.31 Analyzing plane points for the SDS high voltage setup (z-x plane) . . . 114
4.32 Analyzing plane points for the SDS high voltage setup (z-y plane) . . . 114
4.33 Potential plot for the SDS settings without high voltage . . . 115
4.34 Longitudinal kinetic energy plot for the SDS settings without high voltage . 115
4.35 Analyzing plane points for the SDS setup without high voltage (z-x plane) . 116
4.36 Analyzing plane points for the SDS setup without high voltage (z-y plane) . 116
4.37 Magnetic field monitor . . . 118
4.38 Sketch of a magnetic mirror and a penning trap . . . 119
4.39 Total background during SDS . . . 121
4.40 Magnetic and electrostatic shielding . . . 122
4.41 Overview of electron emissions accompanying the α-decay of radon . . . 123
4.42 Simulation of magnetically trapped electron inside the main spectrometer . 123
4.43 The baffle on the main spectrometer pump ports . . . 124
4.44 Radial background distributions with warm and cold baffle . . . 125

5.1 Influence of the energy distribution on the transmission function . . . 132
5.2 Influence of the angular distribution on the transmission function . . . 133
5.3 Influence of energy and angular distribution on the transmission function . 134
5.4 Influence of the retarding potential on the transmission function . . . 135
5.5 Influence of the magnetic field on the transmission function . . . 136
5.6 Transmission function at $-200\,\mathrm{V}$ with the 310 nm UV LED . . . 139
5.7 Differentiation of the transmission function at $-200\,\mathrm{V}$ with the 310 nm UV LED . . . 141
5.8 Energy distribution of the electron gun with 310 nm UV LED . . . 142
5.9 Plot of the fitted error function . . . 143
5.10 Numerical and Gaussian energy distribution . . . 143
5.11 Transmission function measurements with different plate angles . . . 144
5.12 Transmission function at $-18.6\,\mathrm{kV}$ . . . 146
5.13 Fit of the transmission function at $-18.6\,\mathrm{kV}$ and residuals . . . 147

5.14 Normalized transmission function at −18.6 kV . . . 148
5.15 Initial total kinetic energy distribution of the Monte Carlo . . . 150
5.16 Initial polar angle distribution of the Monte Carlo . . . 150
5.17 Trajectory of electron inside the main spectrometer . . . 151
5.18 Comparison of the Monte Carlo transmission function with the measured data . . . 152
5.19 Comparison of the Monte Carlo transmission function with the analytic model 153
5.20 Field lines for the high voltage transmission function measurements . . . 156
5.21 Comparison of the measured and simulated pixel distribution for setting A 156
5.22 Energy distribution for the radial potential measurements at high voltage . 157
5.23 Transmission functions with different plate angle . . . 159
5.24 Plot of the measured radial potential offsets for setting A . . . 160
5.25 Plot of the measured radial potential offsets for setting B . . . 161
5.26 Comparison of measured and simulated radial potential offsets for setting A 162
5.27 Comparison of measured and simulated radial potential offsets for setting B 163
5.28 Difference between measured and simulated potential for setting A and B . 163
5.29 Comparison of the measured and simulated pixel distribution for settings C and D . . . 164
5.30 Comparison of measured and simulated radial potential offsets for setting C 166
5.31 Comparison of measured and simulated radial potential offset for setting D 166
5.32 Differences between measured and simulated potential for setting C and D . 167
5.33 Systematic shifts on the squared neutrino mass due to an unaccounted radial potential inhomogeneity . . . 171
5.34 Systematic shifts on the squared neutrino mass due to an unaccounted absolute magnetic field value . . . 174

6.1 Energy loss function for inelastic scattering on tritium molecules . . . 181
6.2 Example for a basic response function . . . 183
6.3 Flux tube visualization for the whole KATRIN beam line . . . 185
6.4 Magnetic field along the KATRIN beam line . . . 187
6.5 Initial position within the WGTS . . . 187
6.6 Energy violation caused by the adiabatic approximation . . . 188
6.7 Energy loss due to scattering . . . 190
6.8 Synchrotron energy loss at the KATRIN experiment . . . 191
6.9 Numerical energy loss for exact tracking . . . 192
6.10 Numerical energy loss for adiabatic tracking . . . 193
6.11 Results of the Monte Carlo response function and comparison with the analytical model . . . 195
6.12 Relative difference of the Monte Carlo response function and the analytical model . . . 197
6.13 Magnetic field in the WTGS . . . 199
6.14 Plateau of the response function for different number of WGTS slices . . . 200
6.15 Systematic shifts on the neutrino mass due to an unaccounted for magnetic field inhomogeneity . . . 201
6.16 Systematic shifts on the neutrino mass due to an unaccounted for magnetic field offset . . . 202
6.17 Relativistic correction of the transmission function . . . 203
6.18 Synchrotron energy loss data for the analytical calculation . . . 205
6.19 Synchrotron energy loss modification of the transmission function . . . 206
6.20 Systematic shifts on the neutrino mass due to an unaccounted for synchrotron energy loss offset . . . 207
6.21 Transmission functions with modified angular distribution . . . 209

6.22 Modified angular distribution of the transmission function 210
6.23 Relative response function difference by the modified angular distribution . 210
6.24 Angular change distribution of inelastic scattering 212
6.25 Relative response function difference by inelastic angular changes. 214
6.26 Energy loss due to elastic scattering 215
6.27 Response function with and without elastic energy losses 216
6.28 Relative difference of the response function with elastic energy losses to the one without 217
6.29 Angular change distribution of elastic scattering 218
6.30 Relative response function difference by elastic angular changes. 219
6.31 Systematic shifts on the neutrino mass due to an unaccounted for inelastic cross section offset 221
6.32 Systematic shifts on the neutrino mass due to an unaccounted for energy loss factor 222
6.33 Systematic shifts on the neutrino mass due to an unaccounted for for energy loss shift 223
6.34 Results of the Monte Carlo response function and comparison with the refined analytical model 225
6.35 Relative difference of the Monte Carlo response function and the refined analytical model 226

List of Tables

1.1 Leptons in the Standard Model . . . 3
1.2 Recent parameters for neutrino mixing and oscillation . . . 9

4.1 Overview of solenoid positions and currents at SDS . . . 85
4.2 Overview of LFCS positions and currents at SDS . . . 89
4.3 Position offset of the electron gun . . . 98

5.1 Overview of the transmission function measurements at setting A . . . 157
5.2 Overview of the transmission function measurements at setting B . . . 157
5.3 Overview of the transmission function measurements at setting C . . . 165
5.4 Overview of the transmission function measurements at setting D . . . 165
5.5 Radial potential and magnetic field offset for individual detector rings . . . 168
5.6 Reference simulation parameters for the sensitivity estimation of the radial offsets . . . 168
5.7 Influence of the analyzing plane potential on the neutrino mass sensitivity . 169
5.8 Influence of a global potential offset on the neutrino mass sensitivity . . . 170
5.9 Systematic shifts on the squared neutrino mass due to an unaccounted radial potential inhomogeneity . . . 171
5.10 Influence of the analyzing plane magnetic field on the neutrino mass sensitivity 172
5.11 Influence of a global unaccounted magnetic field offset on the neutrino mass sensitivity . . . 173
5.12 Influence of the overall magnetic field on the neutrino mass sensitivity . . . 174
5.13 Systematic shifts on the squared neutrino mass due to an unaccounted radial magnetic field inhomogeneity . . . 175

6.1 Default scattering probabilites . . . 182
6.2 Scattering probabilities obtained by particle tracking . . . 189
6.3 Numerical energy violation and performance . . . 193
6.4 Parameters for the analytical response function calculation and sensitivity estimations . . . 198
6.5 Systematic shifts on the neutrino mass due to an unaccounted for magnetic field inhomogeneity . . . 201
6.6 Systematic shifts on the neutrino mass due to an unaccounted for magnetic field offset . . . 202
6.7 Systematic shifts on the neutrino mass due to an unaccounted for synchrotron energy loss offset . . . 207
6.8 Effect of angular changes on the scattering probabilities and the neutrino mass . . . 213
6.9 Systematic shifts on the neutrino mass by elastic scattering . . . 219
6.10 Systematic shifts on the neutrino mass due to an unaccounted for cross section offset . . . 220

6.11 Systematic shifts on the neutrino mass due to an unaccounted for energy loss factor . . . 222
6.12 Systematic shifts on the neutrino mass due to an unaccounted for energy loss shift . . . 223
6.13 Summary of the corrections to the response function . . . 224
6.14 Summary of the accuracy requirements for certain parameters. . . . 224

A.1 Overview of the potential configuration for the transmission function measurements . . . 235
A.2 Actual potential values for setting A . . . 236
A.3 Actual potential values for setting B . . . 236
A.4 Actual potential values for setting C . . . 237
A.5 Actual potential values for setting D . . . 237
B.6 Potential configuration for the response function simulation . . . 238
B.7 Magnetic configuration for the response function simulation . . . 239

Bibliography

[A+02] C. E. Aalseth *et al.*, "Comment on 'Evidence for Neutrinoless Double Beta Decay'," *Mod. Phys. Lett. A*, vol. 17, no. 22, pp. 1475–1478, 2002.

[A+11] V. V. Aseev *et al.*, "Upper limit on the electron antineutrino mass from the troitsk experiment," *Phys. Rev. D*, vol. 84, no. 112003, 2011.

[A+14] J. F. Amsbaugh *et al.*, "Focal-plane detector system for the KATRIN experiment," *NIM A*, 2014.

[ABB+00] V. Aseev, A. Belesev, A. Berlev, E. Geraskin, O. Kazachenko, Y. Kuznetsov, V. Lobashev, R. Ostroumov, N. Titov, S. Zadorozhny, Y. Zakharov, J. Bonn, B. Bornschein, L. Bornschein, E. Otten, M. Przyrembel, C. Weinheimer, and A. Saenz, "Energy loss of 18 kev electrons in gaseous t and quench condensed d films," *The European Physical Journal D - Atomic, Molecular, Optical and Plasma Physics*, vol. 10, no. 1, pp. 39–52, 2000. [Online]. Available: http://dx.doi.org/10.1007/s100530050525

[ABB+09] I. Antcheva, M. Ballintijn, B. Bellenot, M. Biskup, R. Brun, N. Buncic, P. Canal, D. Casadei, O. Couet, V. Fine, L. Franco, G. Ganis, A. Gheata, D. G. Maline, M. Goto, J. Iwaszkiewicz, A. Kreshuk, D. M. Segura, R. Maunder, L. Moneta, A. Naumann, E. Offermann, V. Onuchin, S. Panacek, F. Rademakers, P. Russo, and M. Tadel, "ROOT - A C++ framework for petabyte data storage, statistical analysis and visualization," *Computer Physics Communications*, vol. 180, no. 12, pp. 2499 – 2512, 2009. [Online]. Available: http://www.sciencedirect.com/science/article/pii/S0010465509002550

[ABG94] G. Arrighini, F. Biondi, and C. Guidotti, "A study of the inelastic scattering of fast electrons from molecular hydrogen," *Mol. Phys.*, vol. 41, no. 6, pp. 1501–1514, 1994.

[Ada15] B. Adams, "Untersuchung magnetischer Materialien und Inbetriebnahme der Magnetfeldüberwachung am KATRIN-Hauptspektrometer," Master's thesis, KIT, 2015.

[ALE06] ALEPH Collaboration, DELPHI Collaboration, L3 Collaboration, OPAL Collaboration, SLD Collaboration, LEP Electroweak Working Group, SLD Electroweak and Heavy Flavour Groups, "Precision electroweak measurements on the Z resonance," *Physics Reports*, vol. 427, no. 5-6, pp. 257 – 454, 2006. [Online]. Available: http://www.sciencedirect.com/science/article/pii/S0370157305005119

[Ant15] J. Antoni, Master's thesis, KIT, 2015, in preparation.

[AW03] G. Altarelli and K. Winter, *Neutrino Mass*, ser. Springer Tracts in Modern Physics. Springer, 2003.

[B+01] J. Bonn *et al.*, "The mainz neutrino mass experiment," *Nucl. Phys. B Proc. Suppl.*, vol. 91, no. 1-3, pp. 273–279, 2001, neutrino 2000. [Online]. Available: http://www.sciencedirect.com/science/article/pii/S0920563200009518

[B+12] M. Babutzka *et al.*, "Monitoring of the operating parameters of the KATRIN Windowless Gaseous Tritium Source," *New Journal of Physics*, vol. 14, no. 10, p. 103046, 2012. [Online]. Available: http://stacks.iop.org/1367-2630/14/i=10/a=103046

[Bab14] M. Babutzka, "Design and development for the Rearsection of the KATRIN experiment," Ph.D. dissertation, KIT, 2014.

[BBB+14] J. Barrett, A. Beglarian, J. Behrens, T. Corona, G. Drexlin, S. Enomoto, M. Erhard, F. Fränkle, F. Glück, S. Görhardt, S. Groh, M. Haag, V. Hannen, F. Harms, D. Hilk, A. Kopmann, M. Kraus, M. Krause, B. Leiber, A. Müller, O. Rest, P. Rovedo, J. Schwarz, N. Stallkamp, N. Steinbrink, T. Thümmler, N. Trost, N. Wandkowsky, C. Weinheimer, K. Wierman, J. Wolf, and M. Zacher, "Results of the first KATRIN SDS measurement phase," 2014, internal KATRIN report.

[BCG+13] J. Behrens, T. Corona, F. Glück, S. Groh, N. Steinbrink, N. Wandkowsky, and C. Weinheimer, "EMD consequences of electrical shorts at the inner electrode system," 2013, internal KATRIN report.

[Bod11] T. Bode, "Optimierung des 2-phasen-kühlkonzepts für den WGTS-demonstrator von KATRIN," Master's thesis, KIT, 2011.

[Bor11] Borexino Collaboration, "Precision Measurement of the ^{7}Be Solar Neutrino Interaction Rate in Borexino," *Phys. Rev. Lett.*, vol. 107, p. 141302, 2011. [Online]. Available: http://link.aps.org/doi/10.1103/PhysRevLett.107.141302

[Bor12] ——, "First evidence of *pep* solar neutrinos by direct detection in borexino," *Phys. Rev. Lett.*, vol. 108, p. 051302, Feb 2012. [Online]. Available: http://link.aps.org/doi/10.1103/PhysRevLett.108.051302

[BP34] H. Bethe and R. Peierls, "The "Neutrino"," *Nature*, vol. 133, p. 532, 1934.

[BPSM+08] T. Bray, J. Paoli, C. M. Sperberg-McQueen, E. Maler, and F. Yergeau. (2008) Extensible Markup Language (xml) 1.0. [Online]. Available: http://www.w3.org/TR/xml/

[BPT80] G. Beamson, H. Q. Porter, and D. W. Turner, "The collimating and magnifying properties of a superconducting field photoelectron spectrometer," *Journal of Physics E: Scientific Instruments*, vol. 13, no. 1, p. 64, 1980. [Online]. Available: http://stacks.iop.org/0022-3735/13/i=1/a=018

[BS08] S. C. Brenner and L. R. Scott, *The mathematical theory of finite element methods*, ser. Springer Texts in Applied Mathematics. Springer, 2008.

[BSB05] J. N. Bahcall, A. M. Serenelli, and S. Basu, "New solar opacities, abundances, helioseismology, and neutrino fluxes," *Astrophys.J.*, vol. 621, pp. L85–L88, 2005.

[Cen14] Center for Experimental Nuclear Physics and Astrophysics. (2014) Annual Report. [Online]. Available: http://www.npl.washington.edu/annualreport2014

[Cha14] J. Chadwick, "Intensitätsverteilung im magnetischen Spektrum von β-Strahlen von Radium B+C," *Verh. d. Deutsch. Phys. Ges.*, vol. 15, p. 383, 1914.

[Cha32] ——, "Possible Existence of a Neutron," *Nature*, vol. 129, p. 312, 1932.

[Cla38] J. W. Clark, "A new method for obtaining a uniform magnetic field," *Review of Scientific Instruments*, vol. 9, no. 10, pp. 320–322, 1938. [Online]. Available: http://scitation.aip.org/content/aip/journal/rsi/9/10/10.1063/1.1752353

[CM95] Z. Chen and A. Z. Msezane, "Calculation of the excitation cross sections for the $^1\Sigma_u^+$ and $C^1\Pi_u^+$ states in $e-H_2$ scattering at 60 eV," *Phys. Rev. A*, vol. 51, no. 5, pp. 3745–3750, 1995.

[Cor14] T. Corona, "Methodology and Application of High Performance Electrostatic Field Simulation in the KATRIN Experiment," Ph.D. dissertation, Chapel Hill, 2014.

[CRH+56] C. L. Cowan, F. Reines, F. B. Harrison, H. W. Kruse, and A. D. McGuire, "Detection of the Free Neutrino: a Confirmation," *Science*, vol. 124, no. 3212, pp. 103–104, 1956. [Online]. Available: http://www.sciencemag.org/content/124/3212/103.short

[Cry08] Cryomagnetics Inc., "Model 4G Superconducting Magnet Power Supply," 2008, manual.

[D+62] G. Danby *et al.*, "Observation of high-energy neutrino reactions and the existence of two kinds of neutrinos," *Phys. Rev. Lett.*, vol. 9, no. 1, pp. 36–44, Jul 1962. [Online]. Available: http://prl.aps.org/abstract/PRL/v9/i1/p36_1

[Dav94] R. Davis, "A review of the Homestake solar neutrino experiment," *Prog. Part. Nucl. Phys.*, vol. 32, pp. 13–32, 1994. [Online]. Available: http://www.sciencedirect.com/science/article/pii/0146641094900043

[Day12] Daya-Bay Collaboration, "Observation of electron-antineutrino disappearance at Daya Bay," *Phys. Rev. Lett.*, vol. 108, 2012.

[DHMW13] G. Drexlin, V. Hannen, S. Mertens, and C. Weinheimer, "Current direct neutrino mass experiments," *Advances in High Energy Physics*, vol. 2013, p. 39, 2013. [Online]. Available: http://dx.doi.org/10.1155/2013/293986

[Dou12] Double Chooz Collaboration, "Reactor electron antineutrino disappearance in the Double Chooz experiment," *Phys. Rev. D*, vol. 86, 2012.

[E+14] M. Erhard *et al.*, "High-voltage monitoring with a solenoid retarding spectrometer at the KATRIN experiment," *Journal of Instrumentation*, vol. 9, no. 06, p. P06022, 2014. [Online]. Available: http://stacks.iop.org/1748-0221/9/i=06/a=P06022

[EHM87] S. R. Elliot, A. A. Hahn, and M. K. Moe, "Direct evidence for two-neutrino double-beta decay in ^{82}Se," *Phys. Rev. Lett.*, vol. 59, no. 18, pp. 2020–2023, 1987.

[EO66] J. E. Everett and J. E. Osemeikhian, "Spherical coils for uniform magnetic fields," *Journal of Scientific Instruments*, vol. 43, no. 7, p. 470, 1966. [Online]. Available: http://stacks.iop.org/0950-7671/43/i=7/a=311

[Erh12] M. Erhard, "Untersuchung der Langzeitstabilität des nuklearen Standards für die Energieskala des KATRIN-Experiments," Master's thesis, KIT, 2012.

[Erh15] ——, "Transmission characteristics of the KATRIN spectrometers regarding magnetic field properties," Ph.D. dissertation, KIT, 2015, in preparation.

[EXO14] EXO-200 Collaboration , "Search for majorana neutrinos with the first two years of exo-200 data," *Nature*, vol. 510, pp. 229–234, 2014. [Online]. Available: http://dx.doi.org/10.1038/nature13432

[F+12] J. Formaggio *et al.*, "Solving for nicro- and macro-scale electrostatic configurations using the Robin Hood algorithm," *Progress in Electromagnetics Research B*, vol. 39, no. 1, 2012.

[Far14] Faro, "FaroArm," 2014. [Online]. Available: http://www.faro.com/en-us/products/metrology/measuring-arm-faroarm/overview

[FCB99] R. B. Firestone, S. Y. F. Chu, and C. M. Baglin, "Table of Isotopes, 8th Edition," 1999.

[FE04] R. Firestone and L. P. Ekstroem, "WWW Table of Radioactive Isotopes, Version 2.1," *LBNL Isotopes Project - LUNDS Universitet*, 2004. [Online]. Available: http://ie.lbl.gov/toi/

[Fer34] E. Fermi, "Versuch einer Theorie der β-Strahlen," *Zeitschrift für Physik A*, vol. 88, pp. 161–177, 1934, 10.1007/BF01351864. [Online]. Available: http://dx.doi.org/10.1007/BF01351864

[FG86] S. Filippi and J. Gräf, "New Runge Kutta Nystroem formula-pairs of order 8(7), 9(8), 10(9) and 11(10) for differential equations of the form $y'' = f(x, y)$," *Journal of Computational and Applied Mathematics*, vol. 14, no. 3, pp. 361 – 370, 1986. [Online]. Available: http://www.sciencedirect.com/science/article/pii/0377042786900737

[FG+15] D. Furse, S. Groh *et al.*, "Kassiopeia: A Modern, Extensible C++ Particle Tracking Package," 2015, to be published.

[Fis14] S. Fischer, "Commissioning of the KATRIN Raman system and durability studies of optical coatings in glove box and tritium atmospheres," Ph.D. dissertation, KIT, 2014.

[Frä06] F. Fränkle, "Erste Messungen der elektromagnetischen Eigenschaften des KATRIN Vorspektrometers," Master's thesis, KIT, 2006.

[Frä10] ——, "Background Investigations of the KATRIN Pre-Spectrometer," Ph.D. dissertation, KIT, 2010. [Online]. Available: http://nbn-resolving.org/urn:nbn:de:swb:90-193929

[Fur13] D. Furse, "Derivation of Equations of Motion in the KASSIOPEIA Package," 2013, internal KATRIN report.

[Fur15] ——, Ph.D. dissertation, MIT, 2015, in preparation.

[G+10] W. Gil *et al.*, "The Cryogenic Pumping Section of the KATRIN Experiment," *Applied Superconductivity, IEEE Transactions on*, vol. 20, no. 3, pp. 316–319, June 2010.

[G+13] F. Glück *et al.*, "Electromagnetic design of the large-volume air coil system of the KATRIN experiment," *New Journal of Physics*, vol. 15, no. 8, p. 083025, 2013. [Online]. Available: http://stacks.iop.org/1367-2630/15/i=8/a=083025

[GAL99] GALLEX Collaboration, "GALLEX solar neutrino observations: results for GALLEX IV," *Phys. Lett. B*, vol. 447, no. 1-2, pp. 127–133, 1999.

[Gar63] M. W. Garrett, "Calculation of Fields, Forces, and Mutual Inductances of Current Systems by Elliptic Integrals," *Journal of Applied Physics*, vol. 34, no. 9, pp. 2567–2573, 1963. [Online]. Available: http://scitation.aip.org/content/aip/journal/jap/34/9/10.1063/1.1729771

[GBD+14] L. Gastaldo, K. Blaum, A. Doerr, C. Düllmann, K. Eberhardt, S. Eliseev, C. Enss, A. Faessler, A. Fleischmann, S. Kempf, M. Krivoruchenko, S. Lahiri, M. Maiti, Y. Novikov, P.-O. Ranitzsch, F. Simkovic, Z. Szusc, and M. Wegner, "The electron capture ^{163}ho experiment echo," *Journal of Low Temperature Physics*, vol. 176, no. 5-6, pp. 876–884, 2014. [Online]. Available: http://dx.doi.org/10.1007/s10909-014-1187-4

[GBH+13] S. Grohmann, T. Bode, M. Hötzel, H. Schön, M. Süßer, and T. Wahl, "The thermal behavior of the tritium source in KATRIN," *Cryogenics*, vol. 55, no. 0, pp. 5 – 11, 2013. [Online]. Available: http://www.sciencedirect.com/science/article/pii/S0011227513000076

[GBSS11] S. Grohmann, T. Bode, H. Schön, and M. Süßer, "Precise temperature measurement at 30 k in the KATRIN source cryostat," *Cryogenics*, vol. 51, no. 8, pp. 438 – 445, 2011. [Online]. Available: http://www.sciencedirect.com/science/article/pii/S0011227511001135

[GER06] GERDA Collaboration, "Status of the GERmanium Detector Array (GERDA) for the search of neutrinoless $\beta\beta$ decays of ^{76}Ge at LNGS," *Prog. Part. Nucl. Phys.*, vol. 57, no. 1, pp. 241–250, 2006.

[GER13] ——, "Results on neutrinoless double-β decay of ^{76}Ge from phase i of the gerda experiment," *Phys. Rev. Lett.*, vol. 111, p. 122503, Sep 2013. [Online]. Available: http://link.aps.org/doi/10.1103/PhysRevLett.111.122503

[Gib08] W. C. Gibson, *The Method of Moments in Electromagnetics*, ser. Springer Texts in Applied Mathematics. Chapman & Hall/CRC, 2008.

[Glü08] F. Glück, "Runge-Kutta method for numerical solution of differential equation system," 2008, internal KATRIN document.

[Glü11a] ——, "Axisymmetric electric field calculation with zonal harmonic expansion," *Progress In Electromagnetics Research B*, vol. 32, pp. 319–350, 2011. [Online]. Available: http://www.jpier.org/pierb/pier.php?paper=11042106

[Glü11b] ——, "Axisymmetric magnetic field calculation with zonal harmonic expansion," *Progress In Electromagnetics Research B*, vol. 32, pp. 351–388, 2011. [Online]. Available: http://www.jpier.org/pierb/pier.php?paper=11042108

[GM35] M. Goeppert-Mayer, "Double beta-disintegration," *Phys. Rev.*, vol. 48, no. 6, pp. 512–516, 1935.

[GNO05] GNO Collaboration, "Complete results for five years of GNO solar neutrino observations," *Phys. Lett. B*, vol. 616, no. 3-4, pp. 174–190, 2005.

[Gou10] J. Goullon, "Installation and commissioning of the monitor spectrometer," Master's thesis, KIT, 2010.

[Gör10] S. Görhardt, "Reduktion der durch Radon induzierten Untergrundprozesse in den KATRIN Spektrometern," Master's thesis, KIT, 2010.

[Gör14] ——, "Background Reduction Methods and Vacuum Technology at the KATRIN Spectrometers," Ph.D. dissertation, KIT, 2014. [Online]. Available: http://nbn-resolving.org/urn:nbn:de:swb:90-380506

[Gro10] S. Groh, "Untersuchung von UV-Laser induziertem untergrund am KATRIN Vorspektrometer," Master's thesis, KIT, 2010.

[GTW13] S. Görhardt, T. Thümmler, and J. Wolf, "Vacuum Conditioning of the KATRIN Main Spectrometer," 2013, internal KATRIN report.

[Hab09] F. Habermehl, "Electromagnetic measurements with the KATRIN Pre-Spectrometer," Ph.D. dissertation, KIT, 2009. [Online]. Available: http://nbn-resolving.org/urn:nbn:de:swb:90-135491

[HAL04] A. Henderson, J. Ahrens, and C. Law. (2004) The paraview guide. [Online]. Available: http://www.paraview.org/

[Har12] F. Harms, "Assembly and First Results of the KATRIN Focal-Plane Detector System at KIT," Master's thesis, KIT, 2012.

[Har15] ——, Ph.D. dissertation, KIT, 2015, in preparation.

[Hau13] N. Haussmann, "Development of Analysis Tools and Automatisation of Run Control for KATRIN," Master's thesis, KIT, 2013.

[HBJ+13] V. Hannen, S. Bauer, L. Josten, H.-W. Ortjohann, C. Weinheimer, D. Winzen, M. Zacher, and M. Zboril, "Main Spectrometer Electron-Gun Specification," 2013, internal KATRIN report.

[HBS+13] V. Hannen, J. Behrens, S.Groh, R. Jöhren, N. Steinbrink, C. Weinheimer, M. Zacher, and M. Zboril, "M3 Report - E-gun Characteristics," 2013, internal KATRIN report.

[Hei12] J. Hein, "Angular defined photo-electron sources for the katrin experiment," Master's thesis, Uni Münster, 2012. [Online]. Available: http://www.uni-muenster.de/Physik.KP/AGWeinheimer/theses/Diplom_Hendrik_Hein.pdf

[Hil11] B. Hillen, "Untersuchung von Methoden zur Unterdrückung des Spektrometeruntergrunds beim KATRIN Experiment," Ph.D. dissertation, Uni Münster, 2011. [Online]. Available: http://repositorium.uni-muenster.de/document/miami/1c6278eb-3176-4658-b37c-8133a3b12e3b/diss_hillen.pdf

[HLK+13] G. Hinshaw, D. Larson, E. Komatsu, D. N. Spergel, C. L. Bennett, J. Dunkley, M. R. Nolta, M. Halpern, R. S. Hill, N. Odegard, L. Page, K. M. Smith, J. L. Weiland, B. Gold, N. Jarosik, A. Kogut, M. Limon, S. S. Meyer, G. S. Tucker, E. Wollack, and E. L. Wright, "Nine-year wilkinson microwave anisotropy probe (wmap) observations: Cosmological parameter results," *The Astrophysical Journal Supplement Series*, vol. 208, no. 2, p. 19, 2013. [Online]. Available: http://stacks.iop.org/0067-0049/208/i=2/a=19

[Hoe12] M. Hoetzel, "Simulation and analysis of source-related effects for KATRIN," Ph.D. dissertation, KIT, 2012. [Online]. Available: http://nbn-resolving.org/urn:nbn:de:swb:90-312594

[HOZW13] V. Hannen, H.-W. Ortjohann, M. Zacher, and C. Weinheimer, "Electrical short circuits in the main spectrometer wire electrode," 2013, internal KATRIN report.

[Hug09] K. Hugenberg, "Design of the electrode system of the KATRIN main spectrometer," Master's thesis, Uni Münster, 2009.

[Hug10] ——, "An angular resolved pulsed UV LED photoelectron source for KATRIN," *Progress in Particle and Nuclear Physics*, vol. 64, no. 2, pp. 288 – 290, 2010, neutrinos in Cosmology, in Astro, Particle and Nuclear Physics International Workshop on Nuclear Physics, 31st course. [Online]. Available: http://www.sciencedirect.com/science/article/pii/S0146641009001094

[Jan15] A. Jansen, "The cryogenic pumping section of the KATRIN experiment - Design studies and experiments for the commissioning," Ph.D. dissertation, KIT, 2015, in preparation.

[Jur09] M. Juretzko, "Positioning of the Electrode Modules of the KATRIN Experiment by Using a Laser Tracker," *Optical 3-D Measurement Techniques IX*, vol. 2, pp. 91 – 98, 2009, A. Grün, H. Kahmen (eds.).

[K+01] K. Kodama *et al.*, "Observation of tau neutrino interactions," *Phys. Lett. B*, vol. 504, no. 3, pp. 218–224, 2001. [Online]. Available: http://www.sciencedirect.com/science/article/pii/S0370269301003070

[K+05] C. Kraus *et al.*, "Final results from phase II of the Mainz neutrino mass search in tritium," *Eur. Phys. J. C*, vol. 40, pp. 447–468, 2005.

[Kam96] Kamiokande Collaboration, "Solar Neutrino Data Covering Solar Cycle 22," *Phys. Rev. Lett.*, vol. 77, pp. 1683–1686, 1996.

[Kam13] KamLAND-Zen Collaboration, "Limit on neutrinoless $\beta\beta$ decay of ^{136}Xe from the first phase of kamland-zen and comparison with the positive claim in ^{76}Ge," *Phys. Rev. Lett.*, vol. 110, p. 062502, Feb 2013. [Online]. Available: http://link.aps.org/doi/10.1103/PhysRevLett.110.062502

[KAT05] KATRIN Collaboration, "KATRIN design report 2004," 2005.

[Käf12] W. Käfer, "Sensitivity Studies for the KATRIN experiment," Ph.D. dissertation, KIT, 2012. [Online]. Available: http://nbn-resolving.org/urn:nbn:de:swb:90-260214

[KK+01] H. V. Klapdor-Kleingrothaus *et al.*, "Evidence for neutrinoless double beta decay," *Modern Physics Letters A (MPLA)*, vol. 16, pp. 2409–2420, 2001. [Online]. Available: http://ejournals.wspc.com.sg/mpla/16/1637/S0217732301005825.html

[KKK06] H. V. KLAPDOR-KLEINGROTHAUS and I. V. KRIVOSHEINA, "The evidence for the observation of 0??? decay: The identification of 0??? events from the full spectra," *Modern Physics Letters A*, vol. 21, no. 20, pp. 1547–1566, 2006. [Online]. Available: http://www.worldscientific.com/doi/abs/10.1142/S0217732306020937

[KL13] S. F. King and C. Luhn, "Neutrino mass and mixing with discrete symmetry," *Rep. Prog. Phys.*, vol. 76, no. 056201, 2013.

[Kle14] M. Kleesiek, "A Data-Analysis and Sensitivity-Optimization Framework for the KATRIN Experiment," Ph.D. dissertation, KIT, 2014.

[Kos12] A. Kosmider, "Tritium Retention Techniques in the KATRIN Transport Section and Commissioning of its DPS2-F Cryostat," Ph.D. dissertation, KIT, 2012. [Online]. Available: http://nbn-resolving.org/urn:nbn:de:swb:90-289595

[KR83] P. Kruit and F. H. Read, "Magnetic field paralleliser for 2 pi electron-spectrometer and electron-image magnifier," *Journal of Physics E: Scientific Instruments*, vol. 16, no. 4, p. 313, 1983. [Online]. Available: http://stacks.iop.org/0022-3735/16/i=4/a=016

[Kra11] C. Kranz, "Optimierung der Methoden und Messprozeduren zur Entfaltung der Energieverlustfunktion beim KATRIN-Experiment," Master's thesis, Uni Münster, 2011. [Online]. Available: http://www.uni-muenster.de/Physik.KP/AGWeinheimer/Files/theses/Diplom_Christoper_Kranz.pdf

[Kra14] M. Kraus et al., "First commissioning of the KATRIN main spectrometer high voltage system," 2014, paper in preparation.

[Kuc16] L. Kuckert, "Simulation of the KATRIN tritium source and first measurements with the windowless gaseous tritium source (WGTS)," Ph.D. dissertation, 2016, in preparation.

[L+99] V. M. Lobashev *et al.*, "Direct search for mass of neutrino and anomaly in the tritium beta-spectrum," *Phys. Lett. B*, vol. 460, no. 1-2, pp. 227–235, 1999. [Online]. Available: http://www.sciencedirect.com/science/article/pii/S0370269399007819

[L+12] S. Lukic *et al.*, "Measurement of the gas-flow reduction factor of the KATRIN DPS2-F differential pumping section," *Vacuum*, vol. 86, no. 8, pp. 1126 – 1133, 2012. [Online]. Available: http://www.sciencedirect.com/science/article/pii/S0042207X11003800

[LD08] X. Luo and C. Day, "Test particle Monte Carlo study of the cryogenic pumping system of the Karlsruhe tritium neutrino experiment," *Journal of Vacuum Science and Technology A*, vol. 26, no. 5, pp. 1319–1325, 2008. [Online]. Available: http://scitation.aip.org/content/avs/journal/jvsta/26/5/10.1116/1.2956628

[Lei14] B. Leiber, "Investigations of background due to secondary electron emission in the katrin-experiment," Ph.D. dissertation, KIT, 2014. [Online]. Available: http://nbn-resolving.org/urn:nbn:de:swb:90-424154

[LeV07] R. J. LeVeque, *Finite Difference Methods for Ordinary and Partial Differential Equations: Steady-State and Time-Dependent Problems.* SIAM, 2007.

[LH94] J. Liu and S. Hagstrom, "Dissociative cross section of H_2 by electron impact," *Phys. Rev. A*, vol. 50, no. 4, 1994.

[LP12] J. Lesgourgues and S. Pastor, "Neutrino Mass from Cosmology," *Adv. in High Energy Phys.*, vol. 2012, no. 608515, 2012.

[LS85] V. M. Lobashev and P. E. Spivak, "A method for measuring the electron antineutrino rest mass," *Nucl. Instrum. Methods Phys. Res., Sect. A*, vol. 240, no. 2, pp. 305–310, 1985. [Online]. Available: http://www.sciencedirect.com/science/article/pii/0168900285906400

[LU00] L. L. Lucas and M. P. Unterweger, "Comprehensive Review and Critical Evaluation of the Half-Life of Tritium," *Journal of Research of the National Institute of Standards and Technology*, vol. 105, p. 541, 2000.

[Maj37] E. Majorana, "Teoria symmetrica dell elettrone e del positrone," *Il Nuovo Cimento (1924-1942)*, vol. 14, pp. 171–184, 1937.

[MAJ14] MAJORANA Collaboration, "The majorana demonstrator neutrinoless double-beta decay experiment," *Advances in High Energy Physics*, vol. 2014, p. 18, 2014. [Online]. Available: http://dx.doi.org/10.1155/2014/365432

[MAR06] MARE Collaboration, "The microcalorimeter arrays for a rhenium experiment (mare): A next-generation calorimetric neutrino mass experiment," *Nuclear Instruments and Methods in Physics Research Section A: Accelerators, Spectrometers, Detectors and Associated Equipment*, vol. 559, no. 2, pp. 346 – 348, 2006. [Online]. Available: http://www.sciencedirect.com/science/article/B6TJM-4HWXHC8-3/2/517cce3046104965432534fe70e5f30e

[MAR12] ——, "MARE-1 in Milan: Status and Perspectives," *J. Low Temp. Phys.*, vol. 167, pp. 1035–1040, 2012.

[Mer12] S. Mertens, "Study of Background Processes in the Electrostatic Spectrometers of the KATRIN experiment," Ph.D. dissertation, KIT, 2012. [Online]. Available: http://nbn-resolving.org/urn:nbn:de:swb:90-270589

[MF09] B. Monreal and J. Formaggio, "Relativistic cyclotron radiation detection of tritium decay electrons as a new technique for measuring the neutrino mass," *Phys. Rev. D*, vol. 80, p. 051301, Sep 2009. [Online]. Available: http://link.aps.org/doi/10.1103/PhysRevD.80.051301

[MH07] K. Martin and B. Hoffman, "An open source approach to developing software in a small organization," vol. 24, no. 1, pp. 54–7, 01 2007.

[MNS62] Z. Maki, M. Nakagawa, and S. Sakata, "Remarks on the unified model of elementary particles," *Prog. Theor. Phys.*, vol. 28, p. 870, 1962.

[MS85] S. P. Mikheyev and A. Y. Smirnov, "Resonance amplification of oscillations in matter and spectroscopy of solar neutrinos," *Sov. J. Nucl. Phys.*, vol. 42, pp. 913–917, 1985.

[Nat] National Geophysical Data Center, "On-line calculators to estimate current and past values of the magnetic field," homepage. [Online]. Available: www.ngdc.noaa.gov/geomag/magfield.shtml

[NDS85] H. Nishimura, A. Danjo, and H. Sugahara, "Differential Cross Sections of Electron Scattering from Molecular Hydrogen I. Elastic Scattering and Vibrational Excitation," *Journal of the Physical Society of Japan*, vol. 54, no. 5, 1985.

[NFB+05] S. Nagy, T. Fritioff, M. Björkhage, I. Bergström, and R. Schuch, "On the Q-value of the tritium β-decay," *Europhys. Lett*, vol. 74, p. 404, 2005.

[OW08] E. W. Otten and C. Weinheimer, "Neutrino mass limit from tritium beta decay," *Reports on Progress in Physics*, vol. 71, no. 8, p. 086201, 2008. [Online]. Available: http://stacks.iop.org/0034-4885/71/i=8/a=086201

[P+92] A. Picard *et al.*, "A solenoid retarding spectrometer with high resolution and transmission for keV electrons," *Nucl. Instrum. Methods Phys. Res., Sect. B*, vol. 63, no. 3, pp. 345–358, 1992. [Online]. Available: http://www.sciencedirect.com/science/article/pii/0168583X9295119C

[P+07] W. H. Press *et al.*, *Numerical Recipes 3rd Edition: The Art of Scientific Computing*, 3rd ed. New York, NY, USA: Cambridge University Press, 2007.

[P+12] M. Prall *et al.*, "The KATRIN pre-spectrometer at reduced filter energy," *New Journal of Physics*, vol. 14, no. 7, p. 073054, 2012. [Online]. Available: http://stacks.iop.org/1367-2630/14/i=7/a=073054

[PAB+13] L. C. Pitchford, L. L. Alves, K. Bartschat, S. F. Biagi, M. C. Bordage, A. V. Phelps, C. M. Ferreira, G. J. M. Hagelaar, W. L. Morgan, S. Pancheshnyi, V. Puech, A. Stauffer, and O. Zatsarinny, "Comparisons of sets of electron-neutral scattering cross sections and swarm parameters in noble gases: I. Argon," *Journal of Physics D: Applied Physics*, vol. 46, no. 33, p. 334001, 2013. [Online]. Available: http://stacks.iop.org/0022-3727/46/i=33/a=334001

[Par14] Particle Data Group, "The review of particle physics," 2014. [Online]. Available: http://pdg.lbl.gov/

[Pau30] W. Pauli, "Letter to Gauvereinstagung in Tübingen: "Sehr geehrte radioaktive Damen und Herren"," *published in R.Kronig and V. Weisskopf (Eds.), Wolfgang Pauli, Collected scientific Papers, Vol.2, Interscience, New York (1964)*, 1930.

[Per03] D. Perkins, *Particle Astrophysics*. Oxford University Press, 2003.

[Pit13] L. C. Pitchford, "Gec plasma data exchange project," *Journal of Physics D: Applied Physics*, vol. 46, no. 33, p. 330301, 2013. [Online]. Available: http://stacks.iop.org/0022-3727/46/i=33/a=330301

[Pla14] Planck Collaboration, "Planck 2013 results. XVI. Cosmological parameters," *Astronomy and Astrophysics*, vol. 571, p. 66, 2014. [Online]. Available: http://dx.doi.org/10.1051/0004-6361/201321591

[Pom14] C. Pommranz, "Implementation and Monte Carlo simulation of the KATRIN response function using Kassiopeia 3.0," Bachelor's thesis, KIT, 2014.

[Pon58] B. Pontecorvo, "Inverse beta processes and nonconservation of lepton charge," *Sov.Phys.JETP*, vol. 7, pp. 172–173, 1958.

[Pra11] M. Prall, "Background Reduction of the KATRIN Spectrometers: Transmission Function of the Pre-Spectrometer and Systematic Test of the Main-Spectrometer Wire Electrode," Ph.D. dissertation, Uni Münster, 2011.

[PW65] A. A. Penzias and R. W. Wilson, "A Measurement of Excess Antenna Temperature at 4080 Mc/s," *Astrophys. J.*, vol. 142, no. 1, pp. 419–421, 1965.

[R+13] M. Röllig *et al.*, "Activity monitoring of a gaseous tritium source by beta induced X-ray spectrometry," *Fusion Engineering and Design*, vol. 88, no. 6-8, pp. 1263 – 1266, 2013, proceedings of the 27th Symposium On Fusion Technology (SOFT-27); Liège, Belgium, September 24-28, 2012. [Online]. Available: http://www.sciencedirect.com/science/article/pii/S0920379612004632

[RCH+60] F. Reines, C. L. Cowan, F. B. Harrison, A. D. McGuire, and H. W. Kruse, "Detection of the Free Antineutrino," *Phys. Rev.*, vol. 117, no. 1, pp. 159–173, Jan 1960.

[Rei09] S. Reimer, "Ein elektrostatisches Dipolsystem zur Eliminierung von Ionen in der DPS2-F des KATRIN Experimentes," Master's thesis, KIT, 2009.

[Ren11] P. Renschler, "KESS - A new Monte Carlo simulation code for low-energy electron interactions in silicon detectors," Ph.D. dissertation, KIT, 2011. [Online]. Available: http://nbn-resolving.org/urn:nbn:de:swb:90-249597

[REN12] RENO Collaboration, "Observation of reactor electron antineutrino disappearance in the RENO experiment," *Phys. Rev. Lett.*, vol. 108, 2012.

[Röl11] M. Röllig, "Studien zu einem Röntgendetektorsystem zur Überwachung der KATRIN Tritiumquelle," Master's thesis, KIT, 2011.

[Ört14] J. Örtlin, "A detailed model of radon-induced background at the KATRIN experiment," Master's thesis, KIT, 2014.

[Rud91] M. E. Rudd, "Differential and total cross sections for ionization of helium and hydrogen by electrons," *Phys. Rev. A*, vol. 44, pp. 1644–1652, Aug 1991. [Online]. Available: http://link.aps.org/doi/10.1103/PhysRevA.44.1644

[S+04] M. Sisti *et al.*, "New limits from the Milano neutrino mass experiment with thermal microcalorimeters," *Nucl. Instr. Meth. Phys. A*, vol. 520, pp. 125–131, 2004.

[S+13] M. Slezák *et al.*, "Electron line shape of the KATRIN monitor spectrometer," *Journal of Instrumentation*, vol. 8, no. 12, p. T12002, 2013. [Online]. Available: http://stacks.iop.org/1748-0221/8/i=12/a=T12002

[SAG02] SAGE Collaboration, "Solar neutrino flux measurements by the Sovjet-American gallium experiment (SAGE) for half the 22-year solar cycle," *J. Exp. Theo. Phys.*, vol. 95, pp. 181–193, 2002.

[Sch97] N. Schmitz, *Neutrinophysik*. Teubner Studienbuecher, 1997.

[Sch11a] B. Schäling, *The Boost C++ Libraries*. XML Press, 2011.

[Sch11b] M. Schupp, "Inbetriebnahme des Monitorspektrometers und erste Messungen," Master's thesis, KIT, 2011.

[Sch13] M. Schlösser, "Accurate calibration of the Raman system for the Karslruhe Tritium Neutrino Experiment," Ph.D. dissertation, KIT, 2013. [Online]. Available: http://nbn-resolving.org/urn:nbn:de:swb:90-349674

[Sch14] J. Schwarz, "The detector system of the KATRIN experiment - Implementation and first measurements with the spectrometer," Ph.D. dissertation, KIT, 2014. [Online]. Available: http://nbn-resolving.org/urn:nbn:de:swb:90-427724

[Sco35] F. A. Scott, "Energy Spectrum of the β-Rays of Radium E," *Phys. Rev.*, vol. 48, pp. 391–395, 1935.

[Sha91] P. W. Sharp, "Numerical comparisons of some explicit Runge-Kutta pairs of orders 4 through 8," *ACM Trans. Math. Softw.*, vol. 17, pp. 387–409, September 1991. [Online]. Available: http://doi.acm.org/10.1145/114697.116811

[Sle11] M. Slezak, "The source of monoenergetic electrons for the monitoring of spectrometer in the KATRIN neutrino experiment," Master's thesis, Uni Prague, 2011.

[SML06] W. Schroeder, K. Martin, and B. Lorensen, *The Visualization Toolkit An Object-Oriented Approach To 3D Graphics, 4th Edition*. Kitware, Inc. publishers, 2006.

[SNO02] SNO Collaboration, "Direct Evidence for Neutrino Flavor Transformation from Neutral-Current Interactions in the Sudbury Neutrino Observatory," *Phys. Rev. Lett.*, vol. 89, no. 011301, 2002.

[SNO13] ——, "Combined analysis of all three phases of solar neutrino data from the sudbury neutrino observatory," *Phys. Rev. C*, vol. 88, p. 025501, Aug 2013. [Online]. Available: http://link.aps.org/doi/10.1103/PhysRevC.88.025501

[Sta13] N. Stallkamp, "Optimierung und erste messung der transmissionseigenschaften des katrin hauptspektrometers," Master's thesis, KIT, 2013.

[Stu10] M. Sturm, "Aufbau und Test des Inner-Loop-Systems der Tritiumquelle von KATRIN," Ph.D. dissertation, KIT, 2010. [Online]. Available: http://nbn-resolving.org/urn:nbn:de:swb:90-193551

[Sup98] Super-Kamiokande Collaboration, "Evidence for Oscillation of Atmospheric Neutrinos," *Phys. Rev. Lett.*, vol. 81, pp. 1562–1567, Aug 1998. [Online]. Available: http://link.aps.org/doi/10.1103/PhysRevLett.81.1562

[Sup10] ——, "Atmospheric neutrino oscillation analysis with subleading effects in Super-Kamiokande I, II and III," *Phys. Rev. D*, vol. 81, 2010.

[T2K14] T2K Collaboration, "Precise measurement of the neutrino mixing parameter θ_{23} from muon neutrino disappearance in an off-axis beam," *Phys. Rev. Lett.*, vol. 112, p. 181801, May 2014. [Online]. Available: http://link.aps.org/doi/10.1103/PhysRevLett.112.181801

[Tit04] N. Titov, "KATRIN Systematic - Response Function," 2004, internal KATRIN report.

[TRC83] S. Trajmar, D. F. Register, and A. Chutjian, "Electron scattering by molecules II. Experimental methods and data," *Phys. Rep.*, vol. 97, pp. 219–356, 1983.

[UD+09] M. Ubieto-Díaz *et al.*, "A broad-band FT-ICR Penning trap system for KATRIN," *International Journal of Mass Spectrometry*, vol. 288, no. 1-3, pp. 1 – 5, 2009. [Online]. Available: http://www.sciencedirect.com/science/article/pii/S138738060900236X

[UD11] M. Ubieto-Diaz, "Off-line commissioning of a non-destructive FT-ICR detection system for monitoring the ion concentration in the KATRIN beamline," Ph.D. dissertation, MPIK, 2011.

[UX08] T. Ullrich and Z. Xu, "Treatment of errors in efficiency calculations," 2008. [Online]. Available: http://arxiv.org/pdf/physics/0701199v1.pdf

[V+11] K. Valerius *et al.*, "Prototype of an angular-selective photoelectron calibration source for the KATRIN experiment," *Journal of Instrumentation*, vol. 6, no. 01, p. P01002, 2011. [Online]. Available: http://stacks.iop.org/1748-0221/6/i=01/a=P01002

[Val06] K. Valerius, "Electromagnetic design and inner electrode for the KATRIN main spectrometer," *Progress in Particle and Nuclear Physics*, vol. 57, no. 1, pp. 58 – 60, 2006, international Workshop of Nuclear Physics 27th course Neutrinos in Cosmology, in Astro, Particle and Nuclear Physics Ettore Majorana Center for Scientific Culture. [Online]. Available: http://www.sciencedirect.com/science/article/pii/S0146641005001353

[Val09] ——, "Spectrometer-related background processes and their suppression in the KATRIN experiment," Ph.D. dissertation, Uni Münster, 2009.

[Val10] ——, "The wire electrode system for the KATRIN main spectrometer," *Progress in Particle and Nuclear Physics*, vol. 64, no. 2, pp. 291 – 293, 2010, neutrinos in Cosmology, in Astro, Particle and Nuclear Physics International Workshop on Nuclear Physics, 31st course. [Online]. Available: http://www.sciencedirect.com/science/article/pii/S0146641009001100

[Ven03] D. Venos, "Angular distribution of β-particles in KATRIN experiment," 2003, internal KATRIN report.

[W+14] J. Wolf *et al.*, "Commissioning of the vacuum system of the KATRIN main spectrometer," *JINST*, 2014, paper in preparation.

[Wal13] B. Wall, "Karlsruhe Tritium Experiment: Detector System Commissioning and In-Situ PIN-Diode Array Dead-Layer Measurement," Ph.D. dissertation, Uni Washington, 2013.

[Wan13] N. Wandkowksy, "Study of background and transmission properties of the KATRIN spectrometers," Ph.D. dissertation, KIT, 2013. [Online]. Available: http://nbn-resolving.org/urn:nbn:de:swb:90-366316

[WDF+13a] N. Wandkowsky, G. Drexlin, F. M. Fränkle, F. Glück, S. Groh, and S. Mertens, "Modeling of electron emission processes accompanying radon-α-decays within electrostatic spectrometers," *New Journal of Physics*, vol. 15, no. 8, p. 083040, 2013. [Online]. Available: http://stacks.iop.org/1367-2630/15/i=8/a=083040

[WDF+13b] ——, "Validation of a model for radon-induced background processes in electrostatic spectrometers," *Journal of Physics G: Nuclear and Particle Physics*, vol. 40, no. 8, p. 085102, 2013. [Online]. Available: http://stacks.iop.org/0954-3899/40/i=8/a=085102

[Wei35] C. Weizsäcker, "Zur theorie der kernmassen," *Zeitschrift für Physik*, vol. 96, no. 7-8, pp. 431–458, 1935. [Online]. Available: http://dx.doi.org/10.1007/BF01337700

[Win11] A. Windberger, "Berechnungen und Simulationen zum Verhalten von Ionen in der differenziellen Pumpstrecke des KATRIN-Experiments," Master's thesis, KIT, 2011.

[Win14] D. Winzen, "Development of an angular selective electron gun for the KATRIN main spectrometer," Master's thesis, Uni Münster, 2014.

[Wol78] L. Wolfenstein, "Neutrino oscillations in matter," *Phys. Rev. D*, vol. 17, no. 9, pp. 2369–2374, 1978.

[Wol08] I. Wolf, "Entfaltung der Energieverlustfunktion beim KATRIN Experiment," Master's thesis, Uni Münster, 2008. [Online]. Available: http://www.uni-muenster.de/Physik.KP/AGWeinheimer/Files/theses/Diplom_Irina_Wolff.pdf

[Wul14] J. Wulf, "Electrostatic Field Simulations and Low-Temperature Measurements for a Xenon-based Dual-Phase Noble Gas Dark Matter Detector," Master's thesis, KIT, 2014.

[Z+13] M. Zboril *et al.*, "Ultra-stable implanted 83 rb/ 83 m kr electron sources for the energy scale monitoring in the KATRIN experiment," *Journal of Instrumentation*, vol. 8, no. 03, p. P03009, 2013. [Online]. Available: http://stacks.iop.org/1748-0221/8/i=03/a=P03009

[Zac09] M. Zacher, "Electromagnetic design and field emission studies for the inner electrode system of the KATRIN main spectrometer," Master's thesis, Uni Münster, 2009.

[Zac14] ——, "High-field electrodes design and an angular-selective photoelectron source for the KATRIN spectrometers," Ph.D. dissertation, Uni Münster, 2014.

[Zbo11] M. Zboril, "Solid electron sources for the energy scale monitoring in the KATRIN experiment," Ph.D. dissertation, Uni Münster, 2011.

[Zie13] S. Ziegler, "Die Extraktion der Energieverlustfunktion beim KATRIN Experiment," Master's thesis, KIT, 2013.

[Zub11] K. Zuber, *Neutrino physics - second edition.* CRC Press, 2011.

Danksagung

An dieser Stelle möchte ich allen ganz herzlich danken, die mich während meiner Promotion unterstützt haben und damit zum Gelingen dieser Doktorarbeit beigetragen haben. Ein ganz besonderes Dankeschön gebührt dabei folgenden Personen:

- Prof. Dr. Guido Drexlin, der mir die Promotion überhaupt ermöglicht hat, sowie die anspruchsvolle und abwechslungsreiche Aufgabenstellung und seine Unterstützung während der ganzen Promotionszeit.
- Prof. Dr. Wim De Boer, für die Übernahme der Aufgabe des Korreferenten dieser Doktorarbeit.
- Dr. Marco Kleesiek, für dessen große Hilfe bei der Berechnung des Tritiumspektrums, den Sensitivitätsanalysen, die immer schnelle Hilfe bei Softwareproblemen, sowie die freundschaftliche Atmosphäre in unserem gemeinsamen Büro.
- Dr. Daniel Furse, für die gute Zusammenarbeit bei der Entwicklung von Kassiopeia und seinen guten Ideen, sowie die lehrreiche gemeinsame Zeit am MIT.
- Dr. Nancy Wandkowsky, für viele lehrreiche Diskussionen, sowie ihre Unterstützung und Motivation während der Promotionszeit.
- Dr. Ferenc Glück, für die Hilfe und die zahlreichen Diskussionen zu physikalischen Fragen aller Art.
- Nikolaus Trost, für die hilfreiche Unterstützung bei Kassiopeia in den letzten Monaten.
- Dr. Susanne Mertens, für ihr immer offenes Ohr und ihre guten Ratschläge bezüglich meiner Doktorarbeit.
- Allen, die bei der Vorbereitung und der SDS Messphase beteiligt waren. Vor allem den Personen mit denen ich während der Messphase viel Zeit im Kontrollraum verbringen durfte, unter anderem Dr. Johannes Schwarz, Dr. T.J. Corona, Dr. Miroslav Zboril, Fabian Harms, Marcel Kraus, Jan Behrens sowie John Barrett.
- Dem Münster E-Gun Team um Dr. Volker Hannen sowie Dr. Michael Zacher, für die Bereitstellung der Elektronenkanone.
- Dr. Johannes Schwarz und Fabian Harms, für die Einbindung der Geometrien des Detektorsystems in Kassiopeia.
- Prof. Dr. Sanshiro Enomoto, für die Bereitstellung der Detektorsimulation und dessen Hilfe bei der Anbindung von Kassiopeia.
- Dr. T.J. Corona, für KEMField und die Berechnung der Ladungsdichten für meine Simulationen.

- Moritz Erhard, für die Diskussionen und seine Hilfe beim Analyisieren der Transmissionsmessungen.
- Dr. Martin Babutzka, für seine schnelle Hilfe bei Problemen mit Kalinka bzw. Tesla.
- Nils Stallkamp sowie Christian Pommranz, für ihre Vorarbeiten bezüglich der Magnetfeldoptimierung und der Monte-Carlo Simulation der Antwortfunktion.
- Dr. Susanne Mertens und Anton Huber, für die lehrreiche Zeit in Berkely auf der Suche nach sterilen Neutrinos.
- Dem Karlsruhe House of Young Scientists (KHYS), für die Förderung meines Auslandsaufenhaltes am Lawrence Berkeley National Laboratory (LBNL).
- Für das emsige Korrekturlesen der Arbeit sowie die dazugehörigen Diskussionen über Verbesserungen, danke ich Dr. Ferenc Glück, Dr. Marco Kleesiek, Dr. Susanne Mertens, Dr. Johannes Schwarz, Dr. Markus Steidl, Moritz Erhard, Nikolaus Trost sowie Ellen Groh.
- Allen Kollegen des IKP und auch TLK, für die tolle Arbeitsatmosphäre und die gemeinsamen Aktionen abseits von der Arbeit.

Außerdem danke ich meinen Eltern Ute Groh und Karlheinz Groh, die mich während meines gesamten Studiums nicht nur auf finanzielle Weise, sondern auch moralisch unterstützt haben.

Mein größter Dank geht an meine liebe Ehefrau Ellen Groh, dafür, dass sie immer an mich geglaubt und mich unterstützt hat, sowie ihren unglaublichen Einsatz in den letzten Monaten der Promotion, in denen sie es geschafft hat trotz Mehrfachbelastung durch Vollzeitarbeit, Betreuung unserer Tochter Katharina und Schwangerschaft mir immer den Rücken freizuhalten, wodurch das rechtzeitige Fertigstellen dieser Arbeit überhaupt erst möglich wurde.